# Nanomanipulation and In-Situ Electrical Characterisation of Nanowires

**Gemma Louise Kerr**

A dissertation submitted to the University of Surrey in accordance with the requirements of the degree of Doctor of Philosophy in the School of Electronics and Physical Sciences.

Submitted - September 2008.

# Acknowledgements

During the course of my research and writing of this thesis I have had the support of a number of people whom I would personally like to thank:

My supervisors Prof. Ravi Silva and Dr. David Carey for their support throughout this PhD. Without their helpful discussions, motivation and patience, this work would not have been possible.

Dr David Cox and Dr Paul Smith who have assisted with the practical aspects of this work and provided valuable discussions regarding the experimental work. I would also like to thank Dr Vlad Stolojan from the ATI for undertaking the TEM analysis and Miss Rossanna Grilli from the Materials Science Department for the AES analysis that is described within this thesis.

The Nano-electronics group (NEC), including Richard Smith and Damitha Adikaari for their technical advice and help with sample manufacture and equipment.

The EPSRC for their support of my PhD through funding.

Finally, I would to thank my family for their constant support during this work.

# Authors Declaration

This thesis is submitted for the degree of Doctor of Philosophy at the University of Surrey.

I declare that this work was carried out within the Nano-electronics group at the Advanced Technology Institute, School of Electronics and Physical Sciences between October 2004 and September 2008 under the supervision of Professor S. R. P. Silva and Doctor J. D. Carey. This work is original, except where indicated by special reference in the text and no part of this dissertation has been or is currently being submitted for any other degree, diploma or any other qualification either in the United Kingdom or overseas.

I declare that all of the above statements are true.

Gemma Louise Kerr

September 2008

# Abstract

Nanotechnology is a diverse area of research that involves the creation of new materials and tools that are able to manipulate and make contact to objects at the nanoscale. One current area of research is into carbon nanotubes, which exhibit unique electrical properties. It is hoped that one-day these nanotubes will be utilised in a variety of applications including use as interconnects in electronic devices. As these new structures have been discovered and microelectronic circuits have decreased in size and increased in complexity, the need for new techniques, capable of fabricating and characterising structures with nanometre precision at specific locations has also increased. One such technique, which is attracting considerable attention, is electron beam induced deposition, because it is a direct-write or maskless procedure with a simple manufacturing process that can be used with a wide variety of materials. However, in order for it to be accepted as a mainstream technique it is necessary to first achieve a high degree of understanding and control of the process.

Within this project electron beam deposited tungsten interconnects have been fabricated from the precursor $W(CO)_6$ to determine their suitability for use as an interconnect material. In particular, the effects of different electron sources and beam currents, as well as the lifetime of the precursor have been investigated and the electrical, structural and integrity properties of the deposits have been found to be highly dependent on each of these parameters. The resistivity of the deposits has been found to be far higher than for pure tungsten and so the use of post deposition annealing and heated substrates has been investigated to produce deposits with a lower resistivity. Furthermore, it has been found that when these deposits are exposed to currents in excess of 100 μA they undergo a structural and electrical transformation, which has been attributed to ohmic heating.

This project has also examined the electrical characteristics of suspended arc-discharge, multi-walled carbon nanotubes coated with a thin polymer layer using high precision manipulators operated within a scanning electron microscope. Their conductance-voltage characteristics have been found to be symmetric with respect to voltage and to improve with multiple cycling of the voltage. Analysis of the normalised conductance of these nanotubes, where the contribution of the contact has been factored out demonstrates that conductance's of 0.1 – 0.46 $G_0$ may be achieved.

# Contents

*Acknowledgements* II
*Authors Declaration* III
*Abstract* IV
*Contents* VI
*List of Figures, Tables and Equations* XII
*List of Commonly Used Abbreviations* XIII
*Publications and Presentations* XIV

**CHAPTER ONE** 1

**1 Introduction** 1
1.1 Introduction to Nanotechnology 1
1.2 Thesis Layout 2
1.3 References 3

**CHAPTER TWO** 4

**2 Literature Review** 4
2.1 Introduction 4
2.2 Overview of Carbon Nanotubes 4
2.2.1 Introduction to Carbon Nanotubes 4
2.2.2 The History of Carbon Nanotubes 6
2.2.3 The Production of Carbon Nanotubes 7
2.2.4 Chirality of Carbon Nanotubes 11
2.2.5 Electrical Structure of Carbon Nanotubes 12
2.2.6 Applications of Carbon Nanotubes 14
2.3 Electrical Conduction in Carbon Nanotubes 15

2.4 Overview of Electron Beam Induced Deposition (EBID) 27
2.4.1 Introduction to Electron Beam Induced Deposition 27
2.4.2 History of EBID 27
2.4.3 Experimental Equipment Used for EBID 28
2.5 Physics of EBID 29
2.5.1 Introduction to Physics of EBID 29
2.5.2 Precursor Introduction 29
2.5.3 Precursor-Substrate Interactions 30
2.5.4 Electron-Solid Interactions 33
2.6 Effects of Experimental Parameters on EBID 38
2.6.1 Effects of Beam Current 38
2.6.2 Effects of Substrate Temperature 45
2.7 Effects of Post-Deposition Processing 50
2.8 Conductance Mechanisms of EBID Interconnects 54
2.9 Summary 59
2.10 References 60

**CHAPTER THREE** 64

**3 Experimental Tools and Techniques** 64
3.1 Introduction 64
3.2 Scanning Electron Microscopy (SEM) 64
3.2.1 Cambridge Instruments Stereoscan 250 MK3 SEM 67
3.2.2 FEI Quanta 200 ESEM 67
3.2.3 FEI Nova Nanolab 600 Dual Beam Focused Ion Beam 68
3.3 Transmission Electron Microscopy (TEM) 69
3.3.1 Philips CM 200 Transmission Electron Microscope 70
3.4 Auger Electron Spectroscopy 70
3.4.1 Thermo VG Scientific MICROLAB 350 71
3.5 Atomic Force Microscopy (AFM) 72
3.5.1 Veeco, Dimension 3100 Atomic Force Microscope 73
3.6 Nanomanipulation 73
3.6.1 Zyvex S100 Nanomanipulator System 75
3.6.2 Piezo Positioners 76

3.7 National Instruments LabView Software 84
3.8 Keithley Source Measurement Units 84
3.9 Omicron Nanotechnology, Resistive Heater 85
3.10 Electron Beam Lithography (EBL) 87
3.10.1 Nanometer Pattern Generation System (NPGS) 88
3.11 Summary 88
3.12 References 89

CHAPTER FOUR 90

4 **Geometrical and Structural Characterisation of Electron Beam Deposited Tungsten Interconnects** 90
4.1 Introduction 90
4.2 Experimental Method 90
4.3 Geometrical Characterisation 93
4.3.1 Height Characterisation 95
4.3.2 Width Characterisation 98
4.3.3 Discussion 100
4.4 Structural and Compositional Characterisation 101
4.4.1 Compositional Characterisation 101
4.4.2 Structural Characterisation 105
4.4.3 Discussion 106
4.5 Analysis of System Variables 107
4.5.1 Effects of the Electron Source 108
4.5.2 Effects of the Precursor Lifetime 109
4.5.3 Discussion 112
4.6 Effects of the Substrate 114
4.7 Effects of the Substrate Temperature 117
4.8 Measurement Accuracy and Reproducibility 121
4.9 Conclusions 121
4.10 References 122

# CHAPTER FIVE 123


5 **Electrical Characterisation of Electron Beam Deposited Tungsten Interconnects** 123

5.1 Introduction 123

5.2 Experimental Method 123

5.3 Resistivity Characterisation 124

5.3.1 Effects of the Electron Beam Current 124

5.3.2 Effects of the Electron Source 134

5.3.3 Effects of the Precursor Lifetime 137

5.3.4 Discussion 140

5.4 Effects of the Substrate Temperature 142

5.4.1 Electrical Characterisation 142

5.4.2 Structural Characterisation 145

5.4.3 Discussion 149

5.5 Measurement Accuracy and Reproducibility 150

5.6 Conclusions 150

5.7 References 151


# CHAPTER SIX 152


6 **High Bias Electrical Characterisation of Electron Beam Deposited Tungsten Interconnects** 152

6.1 Introduction 152

6.2 Experimental Method 153

6.3 High Bias Electrical Measurements 153

6.3.1 Electrical Characterisation 154

6.3.2 Structural Characterisation 158

6.3.3 Breakdown Characterisation 173

6.3.4 Discussion 178

6.4 Effects of Post Deposition Annealing 179

6.4.1 Structural Characterisation 179

6.4.2 Electrical Characterisation 181

6.4.3 Discussion 187

6.5 Conclusions 188

6.6 References 188

## CHAPTER SEVEN 189

**7 Electrical Conduction of Suspended Multi-Walled Carbon Nanotubes** 189

7.1 Introduction 189

7.2 Experimental Method 190

7.3 Experimental Results 192

7.4 Analysis of I-V Characteristics 193

7.5 Conductance Analysis 197

7.6 Conclusions 211

7.7 References 211

## CHAPTER EIGHT 212

**8 Conclusions** 212

8.1 Electron Beam Deposition of Tungsten Interconnects 212

8.2 Suspended Multi-Walled Carbon Nanotubes 215

8.3 Future Work 216

# List of Figures, Tables and Equations

## Chapter 2


| Type | Number | Description | Page |
|---|---|---|---|
| Figure | 2.1 | Representation of a (a) single-walled carbon nanotube and (b) multi-walled carbon nanotube. | 5 |
| Figure | 2.2 | Experimental set-up of the arc discharger apparatus used to produce carbon nanotubes. | 8 |
| Figure | 2.3 | Schematic of the apparatus used in the laser ablation production of carbon nanotubes. | 8 |
| Figure | 2.4 | (a) Schematic of the horizontal furnace used in the CVD production of carbon nanotubes. (b) Schematic of the vertical furnace used for the mass production of CVD grown carbon nanotubes. | 9 |
| Figure | 2.5 | Diagram showing weak catalyst interaction (left) and strong catalyst interaction (right). | 10 |
| Equation | 2.1 | Chirality vector for carbon nanotubes | 11 |
| Figure | 2.6 | Schematic diagram of a two dimensional plane illustrating the roll-up vector: $C_h = na_1 + ma_2 \equiv (n, m)$. | 11 |
| Figure | 2.7 | Diagram of the band structure of a graphene sheet (top) and the first Brillouin zone (bottom). | 12 |
| Equation | 2.2 | Wave vector for carbon nanotubes | 13 |
| Equation | 2.3 | Diameter of a carbon nanotube | 13 |
| Equation | 2.4 | Chiral angle for carbon nanotubes | 13 |
| Figure | 2.8 | Diagram showing the band structure (left) and the density of states (right) of a metallic CNT. | 15 |
| Equation | 2.5 | Landauers equation | 16 |
| Figure | 2.9 | Two three-dimensional reservoirs at different chemical potentials are connected by a ballistic conductor of length L, the number of ballistic channels available between $\mu_1$ and $\mu_2$ is M. | 16 |
| Equation | 2.6 | Current in a ballistic conductor | 17 |

| | | | |
|---|---|---|---|
| Equation | 2.7 | Simplified version of equation 2.6. | 17 |
| Equation | 2.8 | Contact resistance of a ballistic conductor | 17 |
| Figure | 2.10 | Schematic diagram of the experimental setup. The nanotube fibre is connected to an SPM tip and then lowered into a liquid metal. | 18 |
| Figure | 2.11 | Graph showing the conductance of a MWNT as it is lowered in and out of a liquid metal contact as a function of time. | 18 |
| Figure | 2.12 | Graph showing the conductance of a MWNT as it is lowered into a liquid metal contact as a function of position. | 19 |
| Figure | 2.13 | TEM of a pristine MWNT (a) before and (b) after failure. | 20 |
| Figure | 2.14 | I - V curve of a MWNT from – 8 to 8 V (left hand axis) and the corresponding G – V curve (right hand axis). | 21 |
| Figure | 2.15 | Scanning electron microscope (SEM) image of a MWNT contacted by four gold fingers. | 22 |
| Figure | 2.16 | Schematic of the measurement setup. The active length L of the SWNT device can be changed by moving the AFM tip. | 23 |
| Figure | 2.17 | (a) Low-bias resistance as a function of length. (b) High-bias resistance as a function of length. | 24 |
| Equation | 2.9 | Optical phonon scattering mean free path | 24 |
| Figure | 2.18 | (a) Scanning electron microscope image taken at 45° of the nonsuspended (on nitride) and suspended (over 0.5 μm deep trench) parts of a SWNT connected. (b) A schematic of the cross section of the experimental setup. | 25 |
| Figure | 2.19 | The current versus voltage characteristics of the same length suspended and nonsuspended parts of a SWNT. | 25 |
| Figure | 2.20 | Illustration of EBID. (a) A precursor gas is injected into a high vacuum microscope where it is adsorbed onto the substrate and exposed to an electron beam. (b) The gas molecules form a non-volatile deposit and a volatile by-product that is pumped away. | 27 |
| Figure | 2.21 | Schematic of a gas injection nozzle and the parameters used to model the gas delivery. | 30 |
| Equation | 2.10 | Rate of adsorption in EBID | 30 |
| Equation | 2.11 | Sticking coefficient for adsorbed molecules | 31 |

| Equation | 2.12 | Rate of adsorption | 31 |
|---|---|---|---|
| Equation | 2.13 | Equation to model the rate of adsorption | 31 |
| Equation | 2.14 | Equilibrium condition for the number of adsorbed molecules | 31 |
| Equation | 2.15 | Layer growth rate | 31 |
| Equation | 2.16 | Equilibrium condition for the layer growth rate | 31 |
| Equation | 2.17 | Surface residence time | 32 |
| Equation | 2.18 | Distance a molecule can diffuse | 32 |
| Equation | 2.19 | Diffusion rate | 32 |
| Equation | 2.20 | Equation to model the EBID process | 32 |
| Figure | 2.22 | Energy distribution of SEs from metal and insulator surfaces. | 34 |
| Figure | 2.23 | Experimentally measured (a) height h(t) and (b) base diameter b(t) for various precursor temperatures and (c) height h(t) and (d) base diameter b(t) for various beam energies of tungsten needles as a function of deposition time. | 35 |
| Figure | 2.24 | A curve showing the evolution of the dot diameter. Three regimes can be distinguished: the nucleation stage (0 - A), an intermediate regime (A – B) and the saturation regime (B-C). | 36 |
| Equation | 2.21 | Probability of electron induced dissociation of a molecule | 36 |
| Figure | 2.25 | (a) Percentage relative contribution to vertical nanopillar growth for PE and $SE_I$. (b) Simulated ratio of the number of tungsten atoms deposited by $SE_I$s and $SE_{II}$s to the total number of tungsten atoms deposited by PEs. | 37 |
| Figure | 2.26 | (a) Tip length, tip diameter and cone length and (b) deposited volume, as a function of the beam current for a beam voltage of 30 keV and a deposition time of 2 minutes. | 39 |
| Figure | 2.27 | Platinum fibre deposited at 30 keV for 5 minutes at (a) 20,000 pA and (b) 1,500 pA. | 40 |
| Figure | 2.28 | Cobalt content as a function of tip length and beam current. The 10 % background level of carbon and oxygen measured on the substrate is also indicated. | 41 |
| Figure | 2.29 | (a) High-resolution dark field STEM image of a typical tip deposit. (b) Backscattered electron image of a cobalt tip deposited with a 3 μA beam current for 600 s. | 42 |

| | | | |
|---|---|---|---|
| Figure | 2.30 | Composition of material deposited at 20 keV from (a) $Mo(CO)_6$ and (b) CpPtMe3. | 43 |
| Figure | 2.31 | Plot of resistivity versus electron beam current for $Me_2Au$(tfac). | 44 |
| Table | 2.1 | Deposition conditions, resistivities and yield of EBID platinum wires. | 45 |
| Figure | 2.32 | The effects of different substrate temperatures on the composition of gold tips deposited from the precursor Me2Au(tfac). | 46 |
| Figure | 2.33 | Fraction of the film comprising Pt formed by electron beam deposition of $Pt(PF_3)_4$ as a function of substrate temperature. | 46 |
| Figure | 2.34 | The natural logarithm of the deposited volume versus the inverse of the substrate temperature for (a) a beam current of 140 pA and beam voltages of 5, 10, 20 and 30 keV and (b) a beam voltage of 20 keV and beam currents of 51, 403 and 3430 pA. | 47 |
| Figure | 2.35 | Variation of the desorption energy with the (a) beam energy and (b) beam current. | 48 |
| Figure | 2.36 | Variation in the deposited (a) base width and (b) height for different beam currents and (c) base width and (d) height for different beam voltages as a function of substrate temperature. | 49 |
| Figure | 2.37 | Average concentration of material in the deposit after treatment in either $N_2$ or air for (a) gold deposits and (b) platinum deposits. | 51 |
| Figure | 2.38 | Effect of annealing on material concentration for (a) gold and (b) platinum deposits. | 51 |
| Figure | 2.39 | (a) STEM-HAADF image of as-deposited gold, (b) STEM-HAADF image after annealing at 500°C in $O_2$, (c) Dark-field image after annealing at 500°C in $O_2$. | 52 |
| Figure | 2.40 | SEM image of a platinum deposit after annealing at 300°C in $O_2$. The hole on the left was milled for cross sectional analysis of the deposit. The voids are marked by the white arrows. | 52 |

| | | | |
|---|---|---|---|
| Figure | 2.41 | Resistivity and metal concentration as a function of annealing temperature in pure $O_2$ for (a) platinum and (b) gold deposits. | 53 |
| Equation | 2.22 | Poole-Frenkel Conduction | 54 |
| Equation | 2.23 | Variable range hopping conduction | 55 |
| Figure | 2.42 | (a) Conductivity of platinum deposits as a function of voltage at 155 K. (b) Logarithm of the conductivity of platinum deposits versus the inverse temperature at 3 V. | 55 |
| Equation | 2.24 | Activation energy for variable range conduction | 56 |
| Figure | 2.43 | (a) Logarithm of the conductance as a function of temperature. (b) The activation energy for conductance by variable range hopping versus temperature. | 56 |
| Figure | 2.44 | Electrical characteristics at different temperatures. (a) I-V plot and (b) ln G vs √V plot. | 57 |
| Equation | 2.25 | Temperature dependence of conductance | 58 |
| Figure | 2.45 | I-V characteristics of cobalt deposits at different temperatures. | 58 |
| Figure | 2.46 | I-V characteristics of different nanowire segments at 4.2 K. The SEM image in the inset shows the different nanowire segments used and their numbering, which is used in the main figure. | 59 |


**Chapter 3**


| Type | Number | Description | Page |
|---|---|---|---|
| Figure | 3.1 | Schematic drawing of the main components in a scanning electron microscope including the electron column, the deflection system and the electron detectors. | 65 |
| Figure | 3.2 | Image of a four-probe manipulation system that is being used for the electrical characterisation of a sub-microscale device. | 74 |
| Figure | 3.3 | Image of a two-probe manipulation system being used to lift out a TEM sample, within a scanning electron microscope. | 75 |
| Figure | 3.4 | Image of the Zyvex S100 nanomanipulation stage. | 76 |
| Figure | 3.5 | Diagram showing the slip-stick motion of an Omicron MS5 positioner. | 77 |

| Figure | 3.6 | Diagram showing the slip-stick motion of an Attocube Positioner. | 77 |
|---|---|---|---|
| Figure | 3.7 | Image of three MS 5 positioners connected together to allow for movement in the x, y and z-axis. | 78 |
| Figure | 3.8 | Image of the two-probe manipulation system mounted inside the Cambridge Instruments Stereoscan 250, MK3 SEM. | 79 |
| Figure | 3.9 | Image of three attocube positioners connected together to allow for movement in the x, y and z-axis. | 80 |
| Figure | 3.10 | Image of the Attocube Inertial Moter Driving Controller, ANC150. | 80 |
| Figure | 3.11 | Image of the Attocube positioners mounted within the FEI ESEM. | 82 |
| Figure | 3.12 | Image of the Attocube positioners mounted within the FEI ESEM. | 83 |
| Figure | 3.13 | Experimental temperature reference curve for resistive heating within the FEI ESEM. | 86 |
| Figure | 3.14 | Image of the heater and manipulation system being used together. | 86 |


**Chapter 4**


| Type | Number | Description | Page |
|---|---|---|---|
| Figure | 4.1 | AFM scan of three successive EBID tungsten interconnects. The left hand deposit was produced using 140 passes of the electron beam, the centre deposit using 120 passes and the right hand deposit was produced using 100 passes of the electron beam. | 93 |
| Figure | 4.2 | (a) Graph of the height profile of three electron beam deposited tungsten interconnects taken along green line shown in figure 4.1. The left peak is produced by a deposit made with 140 passes, the centre peak with 120 passes and the right hand peak by a deposit with 100 passes. (b) Graph of the height profile of a deposit made using 140 passes of the electron beam taken along the length of the deposit. | 94 |

| | | | |
|---|---|---|---|
| Figure | 4.3 | Graph showing how the deposited height varies with increasing number of passes for beam currents of 0.36, 1.5 and 5.9 nA. | 95 |
| Equation | 4.1 | Electron Dose | 97 |
| Figure | 4.4 | Graph showing how the deposited height varies with the total electron dose for beam currents of 0.36, 1.5 and 5.9 nA. | 97 |
| Figure | 4.5 | Graph showing how the width of the deposits increases with both number of passes or height and increasing beam current. | 98 |
| Figure | 4.6 | AES spectra for kinetic energies of 30 – 600 eV of an EBID tungsten wire deposited using 1.5 nA and 200 passes of the electron beam showing tungsten, carbon and oxygen peaks. | 102 |
| Figure | 4.7 | Thermo MICROLAB 350 SEM image of a deposit produced using an electron beam current of 1.5 nA and 200 passes of the electron beam. The marked central square shows the area of the deposit that was chosen to be analysed. | 103 |
| Figure | 4.8 | AES maps of (a) gold, (b) tungsten, (c) carbon and (d) oxygen of a deposit fabricated so as to bridge a gold four terminal contact structure using a beam current of 1.5 nA. | 104 |
| Figure | 4.9 | Bright Field TEM image of an as-deposited tungsten strip. The dark central line is the deposit which was found to consist of amorphous tungsten and carbon, while the surrounding grey area is the silicon nitride membrane. | 105 |
| Figure | 4.10 | Differential of the Auger spectrum for a tungsten deposit produced using a 1.5 nA beam current and 200 passes. | 106 |
| Figure | 4.11 | Graph showing how the total amount of material deposited is dependent on the energy of the electron source. | 108 |
| Figure | 4.12 | Graph showing how the total amount of material deposited deteriorates over time for an electron beam current of 1.5 nA. | 110 |
| Figure | 4.13 | (a) SEM image and (b) ion beam image of the capillary tube used to inject the precursor molecules during EBID. | 112 |
| Figure | 4.14 | (a) AFM image of a deposit with the top half of the deposit on the membrane frame and the bottom half of the deposit on the membrane window. (b) Height profiles of the deposit on the membrane frame and the membrane window. | 115 |

| Figure | 4.15 | Graph showing the effects of different substrate temperatures on the deposited height of tungsten interconnects. | 118 |
|---|---|---|---|
| Equation | 4.2 | Growth rate for EBID. | 118 |
| Equation | 4.3 | Residence time of adsorbed molecules. | 118 |
| Equation | 4.4 | Arrhenius rate of a chemical reaction. | 119 |
| Equation | 4.5 | Logarithm of Arrhenius rate equation. | 119 |
| Figure | 4.16 | Plot of the natural logarithm of the deposited volume as a function of the inverse of the substrate temperature. | 120 |


**Chapter 5**


| Type | Number | Description | Page |
|---|---|---|---|
| Figure | 5.1 | (a) SEM image of a four terminal gold contact structure with tungsten probes connected to each of the pads. (b) SEM image of the set-up used for the deposition and subsequent electrical characterisation of EBID tungsten interconnects using four point probe measurements. | 125 |
| Figure | 5.2 | A typical four point probe measurement of a tungsten wire produced using 100 passes of the electron beam and an electron beam current of 1.5 nA. | 127 |
| Figure | 5.3 | Graph showing the effect of electron dose and electron beam current on the resistivity of EBID tungsten interconnects. | 128 |
| Figure | 5.4 | Graph showing the effect of the deposited height and electron beam current on the resistivity of electron beam deposited tungsten interconnects. | 129 |
| Figure | 5.5 | Analysis of the elemental composition of ~52 nm high deposits produced using electron beam currents of 0.36, 1.5 and 5.9 nA. | 130 |
| Figure | 5.6 | Graphs showing the differential of the Auger spectrum given in figure 5.6 for electron beam currents of (a) 0.36 nA, (b) 1.5 nA and (c) 5.9 nA. | 131 |
| Table | 5.1 | Table showing the peak to peak heights and percentage differences with respect to an electron beam current of 0.36 nA of the differential of the Auger spectrum for tungsten, carbon and oxygen. | 132 |

| | | | |
|---|---|---|---|
| Figure | 5.7 | SEM image of a two terminal gold contact structure with electrochemically etched tungsten probes connected to each of the pads using the Attocube manipulation system. | 135 |
| Figure | 5.8 | Four point measurement of a tungsten wire produced using 50 passes of the electron beam and a beam current of 1.5 nA. | 135 |
| Figure | 5.9 | Graph showing the effects of the use of two different electron sources on the resistivity of electron beam deposited tungsten wires as a function of the deposited height. | 136 |
| Figure | 5.10 | SEM image of a EBID tungsten interconnect deposited so as to bridge two gold pads patterned using electron beam lithography that has been contacted to using two electrochemically etched tungsten probes and the Zyvex S100 Nanomanipulation system. | 137 |
| Figure | 5.11 | A typical two point probe measurement of a tungsten wire produced using 150 passes, a precursor with more than 120 hours of use and an electron beam current of 1.5 nA. | 138 |
| Figure | 5.12 | Graph showing the effect of the total electron dose and the age of the precursor source on the resistivity of electron beam deposited tungsten interconnects. | 139 |
| Figure | 5.13 | Graph showing the effect of the deposited height and the age of the precursor source on the resistivity of electron beam deposited tungsten interconnects. | 140 |
| Figure | 5.14 | The effects of substrate temperature on the resistivity of tungsten interconnects deposited using a beam current of 1.5 nA and 200 passes of the electron beam. | 143 |
| Figure | 5.15 | The effects of different substrate temperatures during the deposition of tungsten interconnects on the resistivity and height of deposits produced using 200 passes of the electron beam and a beam current of 1.5 nA. To compare the effects of the substrate temperature on the resistivity the effect of different height deposits on the resistivity is also shown. | 145 |
| Figure | 5.16 | Analysis of the elemental composition of tungsten deposits produced using an electron beam current of 1.5 nA for substrate temperatures of 25, 50, 75 and 100°C. | 145 |

| | | | |
|---|---|---|---|
| Figure | 5.17 | Graphs showing the differential of the Auger spectrum for deposits fabricated using an electron beam current of 1.5 nA and substrate temperatures of (a) 25°C, (b) 50°C, (c) 75°C and (d) 100°C. | 146 |
| Table | 5.2 | Table showing the peak to peak heights and percentage differences of the differential of the Auger spectrum for tungsten, carbon and oxygen for deposits produced using and electron beam current of 1.5 nA and substrate temperatures of 25, 50, 75 and 100°C. | 148 |


**Chapter 6**


| Type | Number | Description | Page |
|---|---|---|---|
| Figure | 6.1 | I-V characteristic of a tungsten deposit taken with a current limit of 75 μA showing the onset of non-linearity in the I-V characteristics. The deposit was produced using electron source two, an electron beam current of 1.5 nA and 25 passes. | 155 |
| Figure | 6.2 | I-V characteristics of a tungsten deposit taken with a current limit of 400 μA showing hysteresis and non-linearity in the I-V characteristics. The I-V characteristics also show how the resistivity of the deposit improves for successive voltage cycles. | 155 |
| Figure | 6.3 | I-V characteristic of a tungsten deposit for a current limit of 1 mA. The deposit was produced using electron source two, an electron beam current of 1.5 nA and 25 passes. | 156 |
| Figure | 6.4 | (a) Resistance variation and (b) logarithm of the resistance variation for a tungsten deposit produced using electron source two, an electron beam current of 1.5 nA and 25 passes. | 157 |
| Figure | 6.5 | SEM image of a tungsten wire that was deposited using an electron beam current of 1.5 nA and 50 passes of the electron beam that had been exposed to a current of 2 mA. | 158 |

| | | | |
|---|---|---|---|
| Figure | 6.6 | (a) SEM image of the set up of a tungsten wire and contact pads on a silicon nitride membrane. (b) Closer SEM image of an EBID tungsten wire contacted to ion beam deposited leads. | 160 |
| Figure | 6.7 | (a) Resistance variation and (b) logarithm of the resistance variation for a tungsten deposit produced using electron source two, an electron beam current of 1.5 nA and 100 passes on a 100 nm thick silicon nitride membrane. | 162 |
| Figure | 6.8 | STEM images (a) before electrical characterisation, (b) after an I-V sweep run with a 4.25 mA current limit. The left wire is being electrically characterised and the right wire is as deposited. | 164 |
| Figure | 6.9 | STEM images of tungsten wires taken after an I-V sweep with a current limit of (a) 5 mA and (b) 6 mA. The left wire is being electrically characterised and the right wire is as deposited. | 166 |
| Figure | 6.10 | STEM image of two tungsten interconnects taken after their electrical characterisation for current limits up to 6 mA. The left hand wire shown in the image is the one being electrically characterised while the right hand wire is unconnected. | 167 |
| Figure | 6.11 | Low magnification TEM image of an EBID tungsten wire after being exposed to currents of up to 6 mA. | 168 |
| Figure | 6.12 | EELS map of (a) tungsten and (b) carbon for an EBID wire after electrical characterisation. The tungsten and carbon show up as the brighter parts of the respective maps. | 169 |
| Figure | 6.13 | EELS map of the nitrogen in the silicon nitride membrane. The presence of nitrogen is shown by the lighter grey areas. | 170 |
| Figure | 6.14 | (a) TEM carbon EFTEM image of a tungsten wire. The carbon is graphitised (light grey area), as confirmed by filtered EELS and HREM. The dark dots are tungsten clusters. (b) HREM image of a tungsten wire showing the 002 lattice fringes with a spacing of 0.34 nm. | 171 |

| | | | |
|---|---|---|---|
| Figure | 6.15 | Image of the TEM EELS map for tungsten, carbon and nitrogen overlaid onto the AFM image for the same deposit. The blue dots in the centre of the image correspond to tungsten clusters, the red corresponds to carbon and the green, which can just be seen at the top, corresponds to nitrogen. | 172 |
| Figure | 6.16 | Resistance variation of a tungsten deposit produced using an electron beam current of 1.5 nA and 500 passes for current limits of 2.4 and 2.6 mA. | 173 |
| Figure | 6.17 | (a) Graph showing the electrical breakdown and (b) SEM image of the breakdown, of a tungsten wire produced using 1.5 nA beam current and passes of the electron beam. | 174 |
| Figure | 6.18 | Resistance variation for a tungsten deposit made using 100 passes for current limits between 3.4 and 6 mA. | 175 |
| Figure | 6.19 | SEM image of the breakdown of a tungsten wire that has been exposed to 3 mA and was deposited using electron source one, a 5.9 nA beam current and 200 passes. | 176 |
| Figure | 6.20 | SEM image of the breakdown of a tungsten wire that has been exposed to a current limit of 5 mA and was deposited using electron source one, a 5.9 nA beam current and 200 passes. This image also shows how an area of the gold pads on the left and right hand sides of the image had been damaged and removed during the breakdown process. | 177 |
| Figure | 6.21 | STEM image of two tungsten deposits that have been annealed in a high vacuum system at ~1000°C for approximately one hour. Both deposits were produced using 200 passes of the electron beam and the left hand deposit was produced using an electron beam current of 5.9 nA, while the right hand deposit was produced using and electron beam current of 1.5 nA. | 180 |
| Figure | 6.22 | Graph showing the effects of annealing temperature on the resistance of a tungsten wire produced using an electron beam current of 1.5 nA and 100 passes. | 182 |

| | | | |
|---|---|---|---|
| Figure | 6.23 | Graph showing the effects of annealing temperature on the resistance of a tungsten wire produced using an electron beam current of 1.5 nA and 100 passes. | 183 |
| Figure | 6.24 | (a) Effects of annealing temperature on the resistance. (b) Change in resistance taken at room temperature as a function of the temperature to which the sample has been annealed. | 184 |
| Figure | 6.25 | Activation energy as a function of the temperature to which the deposit has been annealed for a tungsten wire deposited using an electron beam current of 1.5 nA, 100 passes and a precursor with more than 120 hours of use. | 185 |


## Chapter 7


| Type | Number | Description | Page |
|---|---|---|---|
| Figure | 7.1 | (a) SEM image of a typical nanotube-polymer sample. (b) HREM image of a MWNT with a ~14 nm thick polymer coating. | 190 |
| Figure | 7.2 | SEM image of a protruding polymer coated MWNT, which is attached to a sharpened tungsten probe. The nanotube has been enhanced in this image for clarity. | 191 |
| Figure | 7.3 | TEM image of a MWNT with a polymer coating of up to 5 nm after electrical characterisation. | 192 |
| Figure | 7.4 | I-V characteristics of a typical undoped, polymer coated 3μm long nanotube. | 192 |
| Figure | 7.5 | Representative current - voltage characteristic showing the reference voltages for a typical polymer coated, suspended multi-walled carbon nanotube. | 193 |
| Figure | 7.6 | Current-voltage characteristics for a 5 μm long MWNT where the current limit was gradually raised from 16 μA up to 40 μA. | 194 |
| Figure | 7.7 | Variation of the average reference voltage as a function of current limit for a reference current of 1 μA for the 5 μm long MWNT given in figure 7.6. | 194 |

| | | | |
|---|---|---|---|
| Figure | 7.8 | I-V characteristics of a 10μm long MWNT at different current limits. The current limit was increased by 2 μA every four voltage cycles, from 2 to 16 μA. | 195 |
| Figure | 7.9 | Variation of the magnitude of the average reference voltage of MWNT given in figure 1.10 as a function of current limit for a reference current of 1 μA. | 195 |
| Figure | 7.10 | I-V characteristics of a 2μm polymer coated MWNT at different voltage limits. | 196 |
| Figure | 7.11 | Variation of the average reference voltage of a 2 μm long MWNT as a function of current limit for a reference current of 1 μA for voltage limits of ± 10, ± 12 and ± 14 V. | 196 |
| Figure | 7.12 | Conductance versus voltage for a 10 μm long MWNT for current limits of 2 μA (sweep 1) and 16 μA (sweep 2). | 197 |
| Figure | 7.13 | Conductance versus voltage measurement for a clean MWNT in air. | 198 |
| Figure | 7.14 | Diagram showing the band structure (left) and the density of states (right) of a metallic CNT. | 199 |
| Equation | 7.1 | The band gap between the first set of semiconducting sub-bands in a metallic carbon nanotube. | 199 |
| Equation | 7.2 | The conductance of a carbon nanotube at near zero voltage, when only the two metallic sub-bands conduct. | 199 |
| Figure | 7.15 | The predicted conductance versus bias voltage for a nanotube from the Landauer equation, assuming unit transmission for all channels. | 200 |
| Equation | 7.3 | The Landauer equation for the height of each step in the conductance as the bias voltage is increased for a CNT. | 200 |
| Equation | 7.4 | The gradient of the conductance for a carbon nanotube. | 200 |
| Figure | 7.16 | Conductance versus voltage variation for a MWNT for current limits of 14 μA (sweep 1) and 22 μA (sweep 2). | 201 |
| Figure | 7.17 | Graph showing $G_{min}$ for successive voltage cycles on a 10 μm long MWNT for different current limits. The current limit was increased by 2 μA every four voltage cycles, from an initial limit of 2 μA to a final limit of 18 μA. | 202 |

| | | | |
|---|---|---|---|
| Figure | 7.18 | Graph showing the gradient of the conductance for successive voltage cycles on a 10 μm long MWNT for different current limits. The current limit was increased by 2 μA every four voltage cycles, from an initial limit of 2 μA to a final limit of 18 μA. | 202 |
| Figure | 7.19 | The distribution of values measured for $G_{min}$ for all of the MWNTs analysed. | 203 |
| Figure | 7.20 | Graph showing the distribution of values measured for the gradient of the conductance for all of the multi-walled carbon nanotubes analysed. | 203 |
| Equation | 7.5 | Normalisation of the conductance of a carbon nanotube | 204 |
| Equation | 7.6 | Simplified equation for the normalised conductance of a carbon nanotube | 204 |
| Figure | 7.21 | Graph showing the normalised gradient of a 10μm long multi-walled carbon nanotube for different current limits over successive sweeps. | 205 |
| Figure | 7.22 | Graph showing the distribution of normalised gradients for all of the nanotubes tested. | 205 |
| Figure | 7.23 | SEM image of a MWNT, which is attached to two sharpened metal tungsten probes. The nanotube has been enhanced in this image for clarity. | 207 |
| Figure | 7.24 | The conductance of a 15.7 μm MWNT for different probe configurations. Sweep 1 shows a typical data set for the voltage cycles run between probe 1 and the substrate, sweep 2 shows a typical data set for the voltage cycles run between probe 2 and the substrate and sweep 3 shows a typical data set for the voltage cycles run between the two probes. | 208 |
| Figure | 7.25 | The variation of the normalised gradient for a 15.7 μm long, polymer coated MWNT for different probe configurations. | 209 |
| Equation | 7.7 | The band gap between the first set of conducting sub bands in a semiconducting carbon nanotube. | 210 |
| Figure | 7.26 | The conductance versus voltage characteristics of a highly resistive MWNT. | 210 |

# List of Commonly Used Abbreviations

AES - Auger Electron Spectroscopy
AFM - Atomic Force Microscopy
BSE - Backscattered Electron
CMOS - Complementary Metal Oxide Semiconductor
CNT - Carbon Nanotubes
CRT - Cathode Ray Tube
CVD - Chemical Vapour Deposition
EBID - Electron Beam Induced Deposition
EBL - Electron Beam Lithography
EDX - Energy Dispersive X-ray
EELS - Electron Energy Loss Spectroscopy
EFTEM - Energy Filtered Transmission Electron Microscopy
ESD - Electron Stimulated Desorption
ESEM - Environmental Scanning Electron Microscope
FIB - Focused Ion Beam
FWHM - Full Width at Half Maximum
$G_{min}$ - Conductance at Near Zero Voltage
HAADF - High-Angle Annular Dark Field
HREM - High Resolution Electron Microscopy
mfp - Mean Free Path
MWNT - Multi-Walled Carbon Nanotube
PE - Primary Electron
SE - Secondary Electron
$SE_I$ - Secondary Electron Generated by Scattering of the Beam Electrons
$SE_{II}$ - Secondary Electron Generated by the Entire Electron Interaction Volume
SEM - Scanning Electron Microscopy
STEM - Scanning Tunnelling Electron Microscopy
STM - Scanning Tunnelling Microscopy
STS - Scanning Tunnelling Spectroscopy
SWNT - Single-Walled Carbon Nanotube
TEM - Transmission Electron Microscopy
VRH - Variable Range Hopping
1D - One-Dimensional

# Publications and Presentations

1. Electrical conduction and transmission coefficients of suspended multiwalled carbon nanotubes, G. L. Kerr, P. R. Smith, J. D. Carey and S. R. P. Silva, Nanotechnology **18**, 295203 (2007).

2. Characterisation of electron-beam deposited tungsten interconnects, G. L. Kerr, D. C. Cox, V. Stolojan and S. R. P. Silva, poster presentation and conference proceedings, J. Phys.: Conf. Ser. **126**, 012073 (2008).

3. In-situ electrical characterisation of suspended multiwalled carbon nanotubes, G. L. Kerr, P. R. Smith, J. D. Carey and S. R. P. Silva, oral presentation and conference proceedings, J. Phys.: Conf. Ser. **126**, 012032 (2008).

4. Structural modification of electron beam deposited tungsten nanowire interconnects, G. L. Kerr, D. C. Cox, V. Stolojan, J. D. Carey and S. R. P. Silva (submitted to Appl. Phys. Lett.).

5. Electrical conduction in MWCNT, J. D. Carey, G. L. Kerr, P. R. Smith, D. C. Cox, R. D. Forrest and S. R. P. Silva, oral presentation, IVC16, Venice, June 2004.

# CHAPTER ONE

## 1 Introduction

This chapter will focus on briefly introducing the subject "Nanotechnology" and outline aspects as to why electronics research at the nanoscale is important. It shall also introduce the reader to the layout used within this thesis.

### 1.1 Introduction to Nanotechnology

Nanotechnology has emerged from the convergence of the physics, chemistry, biology, material science and electronic research fields and allows for the creation of new materials, devices and systems by controlling matter at the atomic and molecular scale. Hence, the development of the technology cuts across traditional boundaries and is aimed at providing a functional understanding of the materials whose structures exhibit novel physical, chemical, biological, structural and electronic properties and processes due to their small dimensions. Nanotechnology also aims to create, manipulate and use structures, devices and systems with these novel properties within the length scales of 1 – 100 nm and is likely to revolutionise many of the current technologies.

The introduction of powerful, yet affordable computers and the explosive growth of the Internet have meant that today, semiconductor products are one of the main drivers of the economy and are utilised in a wide range of industries. For the last three decades their performance has doubled every eighteen months following Moore's law, to make the silicon-based complementary metal-oxide semiconductor (CMOS) technology smaller, faster, more efficient and cheaper. One of the most important physical phenomena that stands in the way of the continued scaling of this technology is the power that can be

dissipated into the primary leakages: the sub-threshold channel current; the gate to channel tunnelling current through the insulator; the body to drain junction tunnelling current and the source to drain tunnelling current along the channel in short devices. [1]

Hence, electronic circuits cannot continue to shrink by orders of magnitude and provide the corresponding increases in computational power, unless radically different device materials, architectures and assembly processes are developed. Thus, alternative solutions such as nanotechnology, that operate at nanoscale dimensions are under investigation to overcome the fundamental size barrier found in the existing semiconductor technology. Some of the most promising alternatives include the use of nanotubes or organic molecules in device construction and electron beam induced deposition, electron beam lithography and multi-walled carbon nanotubes in being able to electrically connect to these smaller devices. [2]

## 1.2 Thesis Layout

This thesis is divided into two main areas. The first covers the characterisation of electron beam deposited tungsten interconnects, which may be used to electrically connect nanoscale devices, while the second covers the electrical characterisation of multi-walled carbon nanotube devices, which may also be used as interconnects. As such, Chapter Two will introduce the reader to electron beam induced deposition, the physics of the deposition process and review the relevant literature to allow for the experimental results to be characterised. It will also introduce the reader to carbon nanotubes, describe how they are produced and give some examples of applications that involve the use of this unique material. The relevant literature about the electrical properties of carbon nanotubes and the affect of the contacts on these properties shall also be reviewed to allow for the experimental work to be analysed.

The experimental tools and set-ups that are used in order to carry out each of the experiments covered in this thesis will be described in detail in Chapter Three. Chapters Four, Five and Six will examine the geometrical, electrical and high bias electrical characterisation of electron beam deposited tungsten interconnects respectively. In particular, these chapters will look at the effects of changing the deposition parameters on the characteristics of the resulting deposits and determine the optimum conditions required to use electron beam deposited tungsten as an interconnect material for nanoscale devices. It

shall also highlight the effects of several system variables including the precursor lifetime and the electron source on the properties of the interconnects with a view to gaining a greater understanding of the process. Furthermore, it will look at the high bias electrical characteristics of these deposits in order to gain an insight into its operations and an understanding of the limitations of these wires.

Chapter Seven will analyse an alternative contact geometry for suspended multi-walled carbon nanotubes, which allows for the electrical properties of the nanotubes themselves to be studied without the substrate affecting the results. This chapter will also highlight the importance of the role of the contacts in this set-up and show how they can dominate the electrical characteristics of these structures. Finally, Chapter Eight will review and draw some conclusions about the work that has been carried out in this thesis and suggests some routes through which this work could be extended as part of the future work enabled as a result of this thesis research.

## 1.3 References

[1] D. Frank, R. Dennard, E. Nowak, P. Solomon, Y. Taur & H. Wong, Device Scaling Limits of Si MOSFETs and Their Application Dependencies, Proceedings of the IEEE **89**, No 3, 259 (2001).

[2] R. Baughman, A. Zakhidov & W. de Heer, Carbon Nanotubes – The Route Toward Applications, Science **297**, 787 (2002).

# CHAPTER TWO

# 2 Literature Review

## 2.1 Introduction

This chapter will introduce carbon nanotubes (CNTs) and review the relevant literature about their electrical characteristics. In particular, it shall outline the discovery, basic electrical and structural properties, production and possible applications of CNTs. It will also discuss the results of a number of groups who have published work on the electrical characteristics of CNTs in a variety of different set-up geometries in order to aid the analysis of the experiments carried out on multi-walled carbon nanotubes (MWNTs). This chapter will then discuss electron beam induced deposition (EBID), which is another possible method of creating nanoscale wires. It will discuss some of the relevant literature to aid the characterisation and optimisation of EBID tungsten wires for use as an interconnect material.

## 2.2 Overview of Carbon Nanotubes

### 2.2.1 Introduction to Carbon Nanotubes

Carbon nanotubes are a relatively new form of carbon and are one of the most commonly discussed building blocks used in nanotechnology today. They may be thought of as being made up of a single layer of graphite (graphene) that has been rolled up to make a seamless cylinder. These structures are known as single-walled nanotubes (SWNTs) and may be thought of as the fundamental cylindrical structure. An example of the structure of a SWNT is shown in Figure 2.1(a). Another type of CNT, which is found more commonly than the SWNT is the MWNT, which consist of a number of SWNTs nested concentrically inside each other like Russian dolls as shown in Figure 2.1(b).

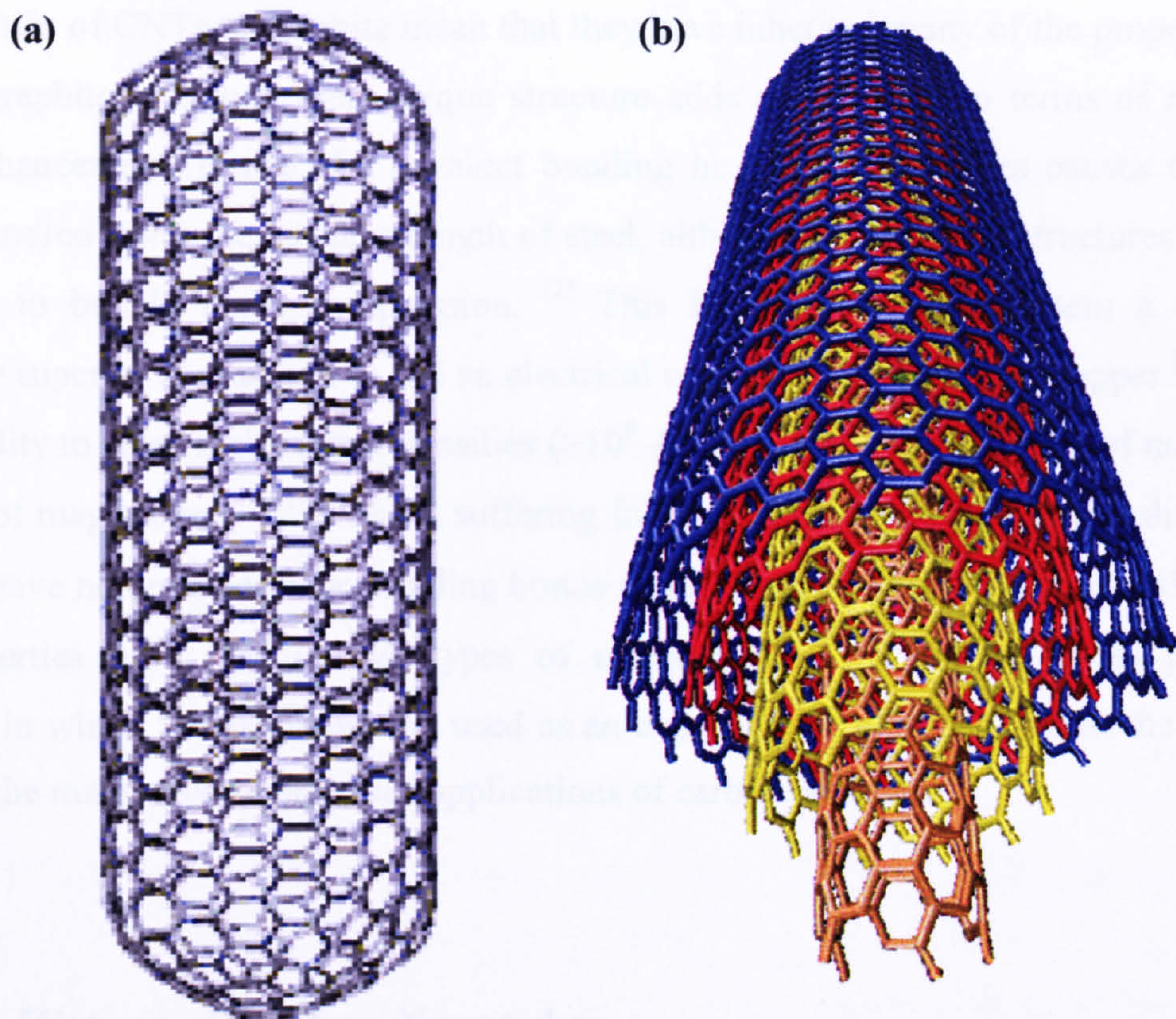


**Figure 2.1.** Representation of a **(a)** SWNT and **(b)** MWNT.

The majority of SWNTs have diameters of between 1 and 2 nm, while their lengths are typically of the order of several micrometers. This aspect ratio means that SWNTs may exhibit one-dimensional (1D) conduction. SWNTs are also more difficult to produce than MWNTs and so are grown in smaller quantities, while their quality varies greatly and slow scanning instruments are required for their observation. SWNTs also naturally form ropes, which are held together by van der Waals forces and are pliable so that they may be twisted, flattened and bent in small circles without breaking. [1]

MWNTs are much larger than SWNTs and have typical diameters of 10 – 20 nm. As stated previously, they are made up of a number of SWNTs that are nested concentrically inside each other with an interlayer spacing of 0.34 - 0.39 nm that decreases with increasing CNT diameter down to a minimum spacing of 0.34 nm, which is the interplanar separation of graphite. These shells may be uncorrelated with respect to each other and so MWNTs can exhibit the properties of turbostratic graphite. Recent experiments have also shown that if a contact is made only to the outer shell of the MWNT then the conduction is likely to only occur through the outermost shell. [1]

The similarities of CNTs to graphite mean that they have inherited many of the properties of interplane graphite, although their unique structure adds much more in terms of material property enhancement. Hence, the covalent bonding in carbon nanotubes causes them to have one hundred times the tensile strength of steel, although their hollow structures tend to cause them to buckle under compression. [2] This bonding also gives them a thermal conductivity superior to diamond [3] and an electrical conductivity better than copper [4-9], but with the ability to carry high current densities (>$10^9$ $Acm^{-2}$), which exceeds that of metals by two orders of magnitude, [10,11] without suffering from electromigration or atomic diffusion. CNTs also have no open edges or dangling bonds and so are largely inert to chemical attack. These properties have lead to two types of research; the first is into novel physical phenomena in which the nanotubes are used as an experimental platform, whilst the second area is into the many diverse proposed applications of carbon nanotubes.

### 2.2.2 The History of Carbon Nanotubes

During the 1970s M. Endo, prepared carbon filaments of nanometre dimensions using a vapour growth technique. However, the structure of these fibres was not studied and so nanotubes were not actually identified until 1991, when Iijima used a high-resolution transmission electron microscope (TEM) to study the sooty material deposited on the cathode of an arc-evaporation system. Within this system, electrical sparks were passed between two graphite rods in order to vaporise some of the graphite, which was then allowed to condense into a soot. In the centre of this deposit a number of distinct closed graphitic structures that included nanoparticles and multi-walled carbon nanotubes (MWNTs) were found. [12,13]

In 1992 Ebbesen and Ajayan developed a highly efficient way of making large quantities of MWNTs by varying the arc-evaporation conditions. Whilst in 1993, further research by Iijima's and Bethunes's groups lead to the discovery of single-walled carbon nanotubes. These nanotubes were produced through the addition of metals, such as cobalt, to the graphite electrodes within the system. In 1996, the Rice group used laser vaporisation of graphite to produce a high yield of SWNTs with fairly uniform diameters, which tended to form aligned bundles and made it possible for experiments relevant to 1D physics to be performed. [13]

### 2.2.3 The Production of Carbon Nanotubes

Carbon nanotubes may be produced using three main processes. The first two are the high temperature and short time processes known as arc discharge and laser ablation. The third is a medium temperature and relatively long time process known as chemical vapour deposition (CVD). Initial research into the properties of CNTs was carried out on nanotubes produced using either arc-discharge or laser ablation because they had a highly crystalline structure, whereas, the CVD process produced defective, spaghetti like nanotubes. More recently the CVD method has been improved so that it is now a highly controlled process, which allows for the fabrication of high quality CNTs. These nanotubes may be aligned either horizontally or vertically, have a predetermined diameter and length and be grown either directly onto a substrate ready for use in devices or as a bulk, raw material. [14]

Today the production of CNTs is through any one of these techniques, which can be tailored to suit the application that they are to be used in. The CVD process allows for large amounts of nanotubes to be synthesised at a low cost with almost no impurities, although the quality does decrease with decreasing temperature. Meanwhile arc discharge and laser ablation carbon nanotubes have less defective structures with the arc discharge grown CNTs having the straightest structures. Also, while the CVD process allows for nanotubes to be grown ready for immediate use in device applications, the other processes require the nanotubes to be produced, purified and then manipulated onto substrates before use.

The arc discharge technique is the most common, simplest and cheapest way of producing both SWNTs and MWNTs and employs the set-up shown in Figure 2.2. The process is conducted in an enclosure that is filled with an inert gas such as helium or argon, and kept at a pressure between 50 and 700 mbar. Two rods consisting of ~90% pure graphite with diameters between 5 and 20 mm are then placed end to end with a separation of ~1 mm to act as the electrodes. A direct current of 50 to 100 A driven by ~20 V is applied to the electrodes to create a high temperature discharge of ~3000°C between them. This discharge vaporises one of the carbon electrodes and forms a small rod shaped deposit on the other electrode, which contains a mixture of carbon nanotubes, fullerenes and amorphous carbon. The type and amount of nanotubes that are produced depend on the uniformity of the plasma arc and the temperature of the deposit formed on the carbon electrode. The growth of MWNTs occurs using the conditions described above, whilst SWNT growth requires the addition of a catalyst such as Fe, Co or Ni to the carbon anode. [15,16]

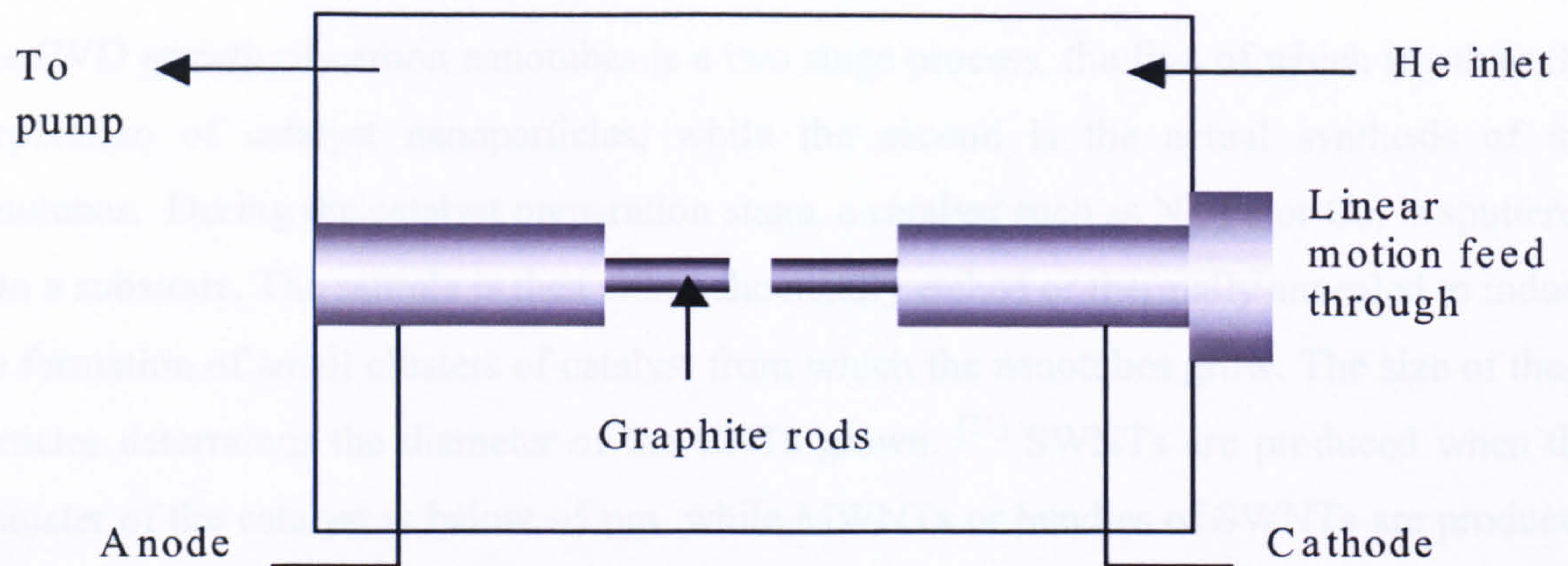


**Figure 2.2.** Experimental set-up of the arc discharger apparatus used to produce carbon nanotubes.

In 1995 Smalley's group were the first group to use laser ablation to synthesise carbon nanotubes. It now produces some of the purest nanotubes with the highest yield. For this process a graphite target is installed in the centre of a quartz pipe, which is inserted into a tubular electric furnace as shown in Figure 2.3. This furnace is heated to 1200°C and filled with an inert gas such as helium in order to maintain a constant pressure of 500-700 Torr. Two sequenced high power laser pulses are then used to irradiate and vaporise the graphite target. This vapour expands and then cools rapidly causing the small carbon molecules and atoms to condense and form larger clusters. As the catalysts also cool, they attach to the carbon clusters and CNTs are formed. As in the arc-discharge process, pure graphite produces MWNTs, whilst for SWNTs, an electrode doped with a catalyst such as Co, Fe or Ni is required. The CNTs produced using this method also have a very small diameter distribution in comparison to the other techniques, which is controlled by varying the temperature of the system. [17,18,19]

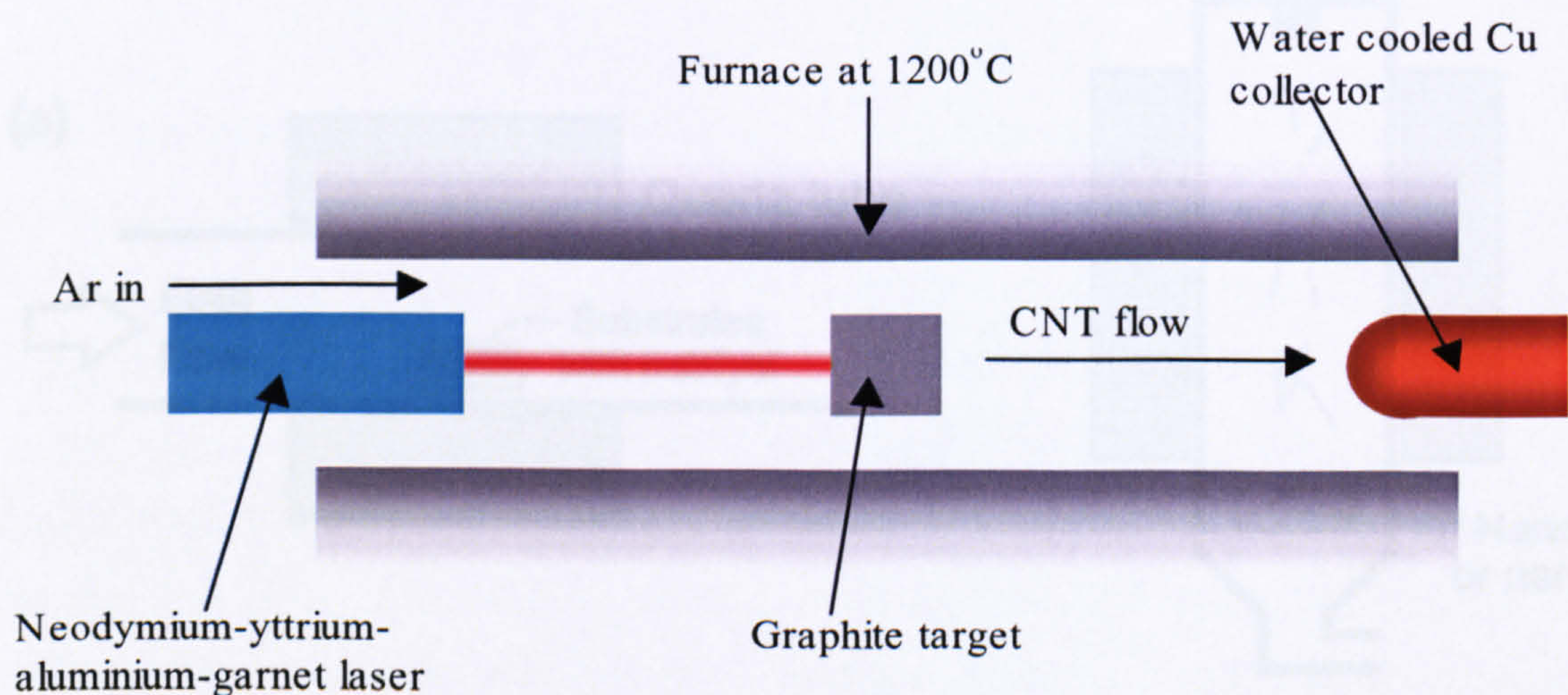


**Figure 2.3.** Schematic of the apparatus used in the laser ablation production of carbon nanotubes.

The CVD growth of carbon nanotubes is a two stage process, the first of which involves the preparation of catalyst nanoparticles, while the second is the actual synthesis of the nanotubes. During the catalyst preparation stage, a catalyst such as Ni, Fe or Co, is sputtered onto a substrate. The sample is then either chemically etched or thermally annealed to induce the formation of small clusters of catalyst from which the nanotubes grow. The size of these particles determines the diameter of the CNTs grown. [21] SWNTs are produced when the diameter of the catalyst is below ~5 nm, while MWNTs or bundles of SWNTs are produced for catalyst sizes above this. The type of catalyst used is also important as mixtures of catalysts produce SWNTs more readily than if a single catalyst is used. [20,21,22]

The prepared substrate is then placed in either a horizontal or vertical furnace, which is heated to 650 - 900°C. Horizontal furnaces are the most popular and consist of a heated quartz tube with a ceramic holder in which the substrates are placed (Figure 2.4(a)). In vertical furnaces the catalyst and carbon feedstock are injected into the top of the furnace and the nanotubes grow during their flight to the bottom of the chamber where they are collected (see Figure 2.4(b)). Once the substrate has been added to the furnace, the quartz tube is filled with an inert gas and heated. A carbon feedstock gas and an energy source, such as plasma are then added. The type of carbon source used, affects the growth of the nanotubes. Saturated carbon feedstocks such as methane produce highly graphitised nanotubes with few walls, whilst unsaturated sources such as acetylene have high yields; deposition rates and carbon content and so are used for MWNT growth. [20]

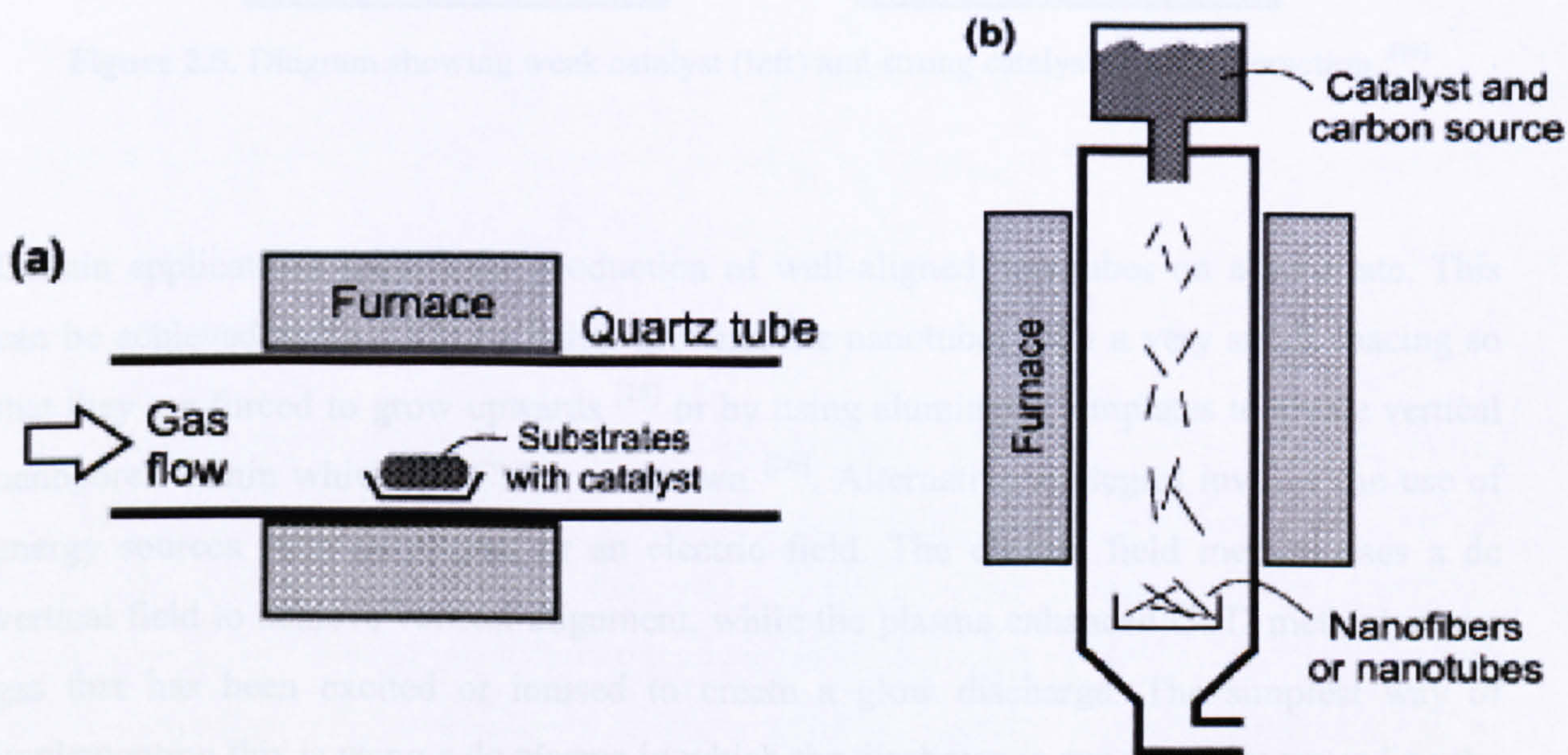


**Figure 2.4. (a)** Schematic of the horizontal furnace used in the CVD production of CNTs. **(b)** Schematic of the vertical furnace used for the mass production of CVD grown CNTs. [14]

The growth of these CNTs is generally said to be due to the decomposition of the feedstock on the catalyst surface. This process is usually exothermic and so a temperature gradient may exist across the particle in the growth direction. Carbon is then precipitated at the colder zone behind the particle until the catalyst becomes either poisoned or deactivated. [1] However, there are two issues with this method. The first is that not all hydrocarbon reactions are exothermic and yet they can still be used to grow nanotubes. The second is that because the catalyst particles are so small, it is unlikely that a temperature gradient exists. Hence, it is thought that the decomposition of the feedstock raises the temperature of the entire filament, and the growth is driven by a concentration gradient across the particle. [14] There are also two different types of growth modes, which are based upon the interaction of the catalyst with the substrate. The first is a weak interaction which causes tip growth, whilst the second is a strong interaction that causes base growth (Figure 2.5). [23,24]

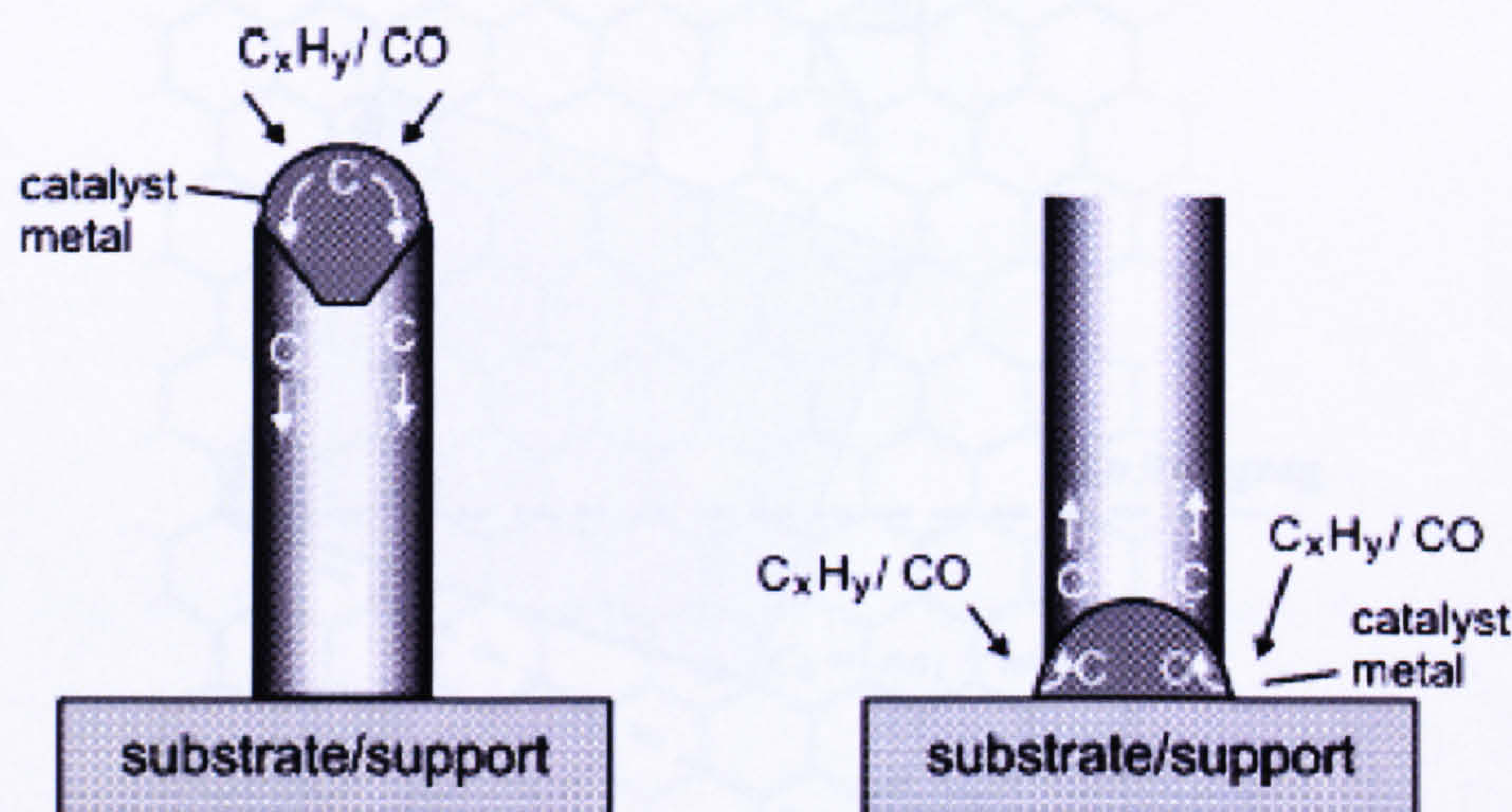


**Figure 2.5.** Diagram showing weak catalyst (left) and strong catalyst (right) interaction. [14]

Certain applications require the production of well-aligned nanotubes on a substrate. This can be achieved using CVD by either growing the nanotubes with a very small spacing so that they are forced to grow upwards [25] or by using aluminium templates to create vertical nanopores within which the CNTs are grown [26]. Alternative strategies involve the use of energy sources such as plasma or an electric field. The electric field method uses a dc vertical field to achieve vertical alignment, while the plasma enhanced CVD method uses a gas that has been excited or ionised to create a glow discharge. The simplest way of implementing this is using a dc plasma in which the discharge is generated by grounding the anode and applying between –400V and -600V to the cathode. [14]

### 2.2.4 Chirality of Carbon Nanotubes

As mentioned earlier carbon nanotubes may be thought of as being made up of a small sheet of graphene that has been rolled up to form a seamless cylinder. Depending on how this cylinder has been formed it is possible to create either a nanotube where the sides match and hexagons form circles around the diameter, or a nanotube where the sides do not match and the hexagons spiral up or down. The chirality vector, $C_h$, which connects two crystallographically equivalent points on the graphene sheet as shown in Figure 2.6, is used to describe this structure. This vector is defined as:

$$C_h = na_1 + ma_2 \equiv (n,m) \tag{2.1}$$

where $a_1$ and $a_2$ are the graphene lattice vectors and $n$ and $m$ are integers. [27,28]

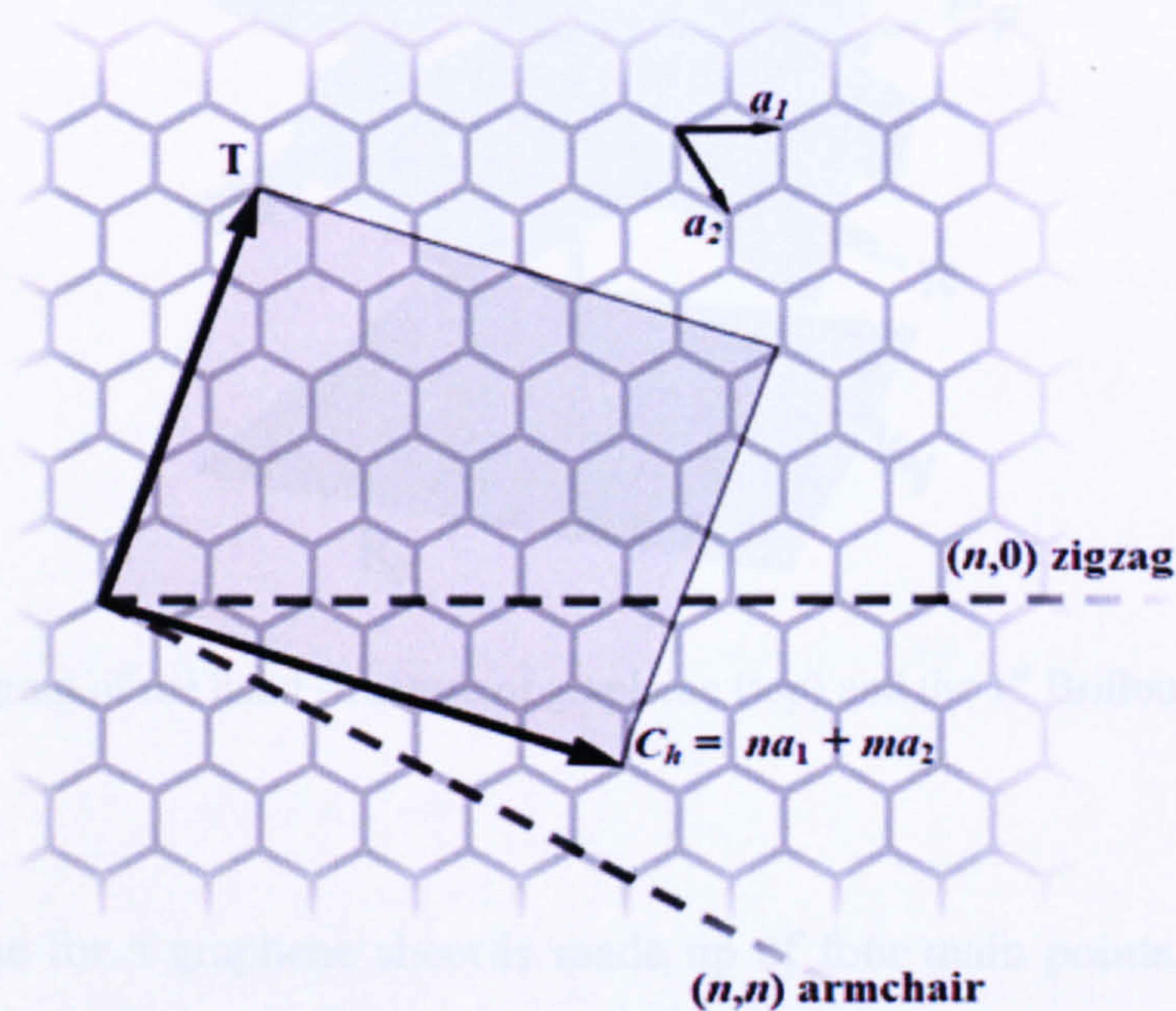


**Figure 2.6.** Schematic diagram of a two dimensional plane illustrating the roll-up vector: $C_h = na_1 + ma_2 \equiv (n, m)$.

There are three types of chirality in carbon nanotubes, which are known as armchair, zigzag and chiral. Zigzag nanotubes occur when either n or m is equal to zero and the hexagonal atoms form a zigzag pattern around the circumference of the nanotube. Armchair nanotubes occur when $C_h$ has been rotated away from n or m equal to zero by 30° and the atoms around the circumference of the nanotube form an armchair pattern. All of the other sorts of nanotubes with chiral angles between 0° and 30° have the hexagons spiralling around the nanotube axis and are known collectively as chiral nanotubes. [27,28]

## 2.2.5 Electrical Structure of Carbon Nanotubes

The fact that carbon nanotubes are essentially made up of small, rolled up sheets of graphene means that they have also inherited many of the properties of in plane graphite. It is therefore logical that the electrical properties of carbon nanotubes may be deduced from the two dimensional properties of a graphene sheet. The band structure and first Brillouin zone of the graphene sheet are given in the energy versus propagation constant or momentum, k, diagram shown in Figure 2.7. [1,13,29]

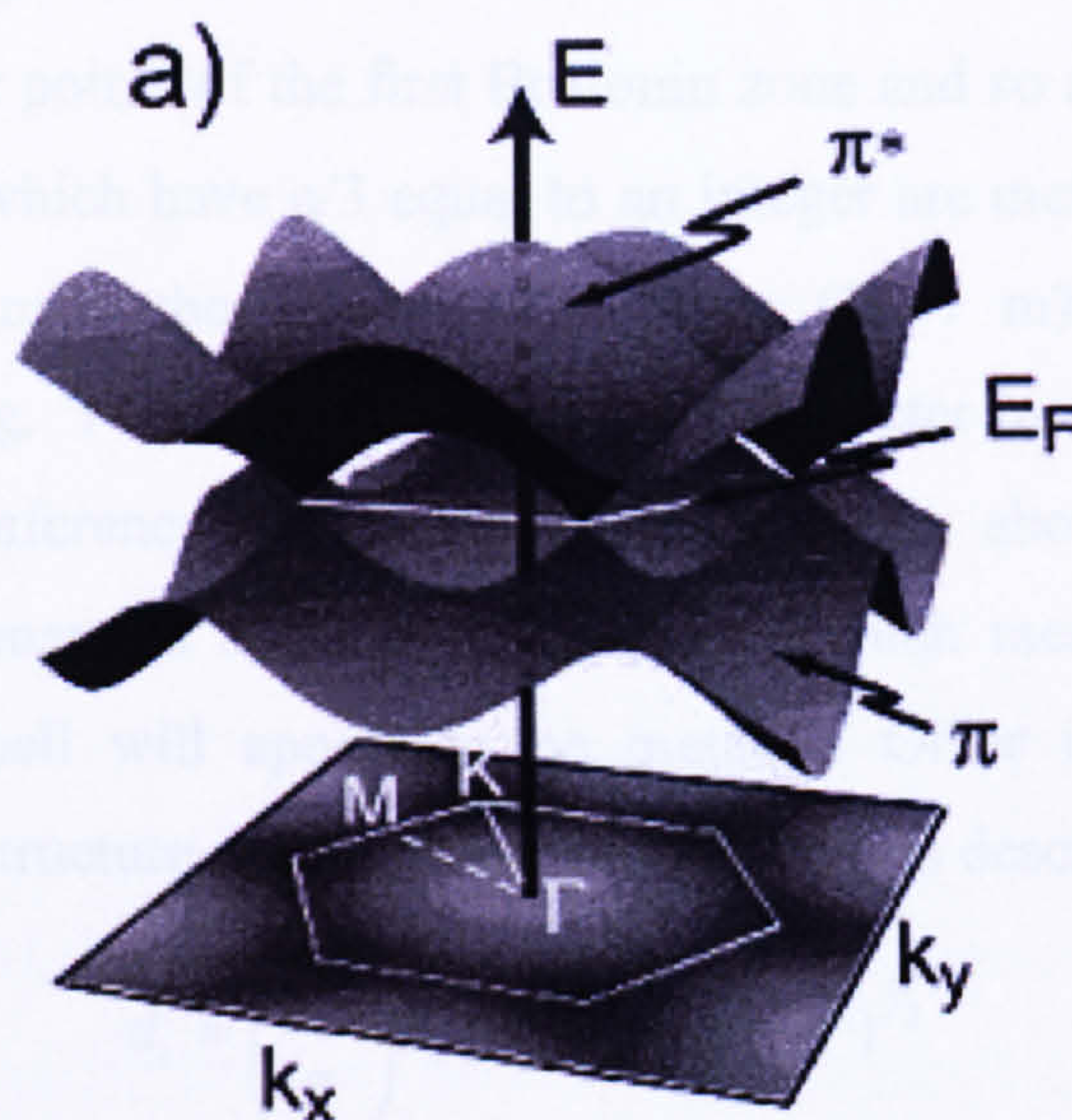


**Figure 2.7.** Diagram of the band structure of graphene (top) and the 1st Brillouin zone (bottom).

The Brillouin zone for a graphene sheet is made up of four main points, *K, Γ, M* and *K'*, where *K* and *K'* are the six equivalent Fermi points at which the conduction (π*) and the valence (π) bands touch, *Γ* is the Brillouin zone center and *M* lies equidistant between the *K* and *K'* points. In graphene, the top of the valence band has the same energy as the bottom of the conduction band, and equals the Fermi energy for one wavevector, the K-point of the two-dimensional Brillouin zone. This unusual band structure has immediate consequences for the electronic properties of graphene. While allowed states exist at the Fermi level, a vanishing density of states exists when integrating over the Fermi surface, which means that graphene is a zero-gap semiconductor. As such in most directions such as in the Γ – M direction, the electrons encounter a semiconductor like band gap. In the Γ – K directions and in five other directions, which differ by 60° and pass through the Fermi points, the electrons have free motion and the graphene behaves as a metal. In real space, these six unique directions correspond to free electron motion along the six zigzag directions of the lattice.

In CNTs, there is an additional quantisation condition that arises from the confinement of electrons around the circumference of the nanotube. This means that the circumferential component of the wave vector, $k_C$ can only take values fulfilling the condition:

$$k_c \cdot C_h = 2\pi j \qquad (2.2)$$

where $C_h$ is the chirality vector and $j$ is an integer. This allows for the set of values of $j$ to be found and used to find the dispersion relations of the CNT so that when the bands pass through a Fermi point, the CNT is metallic, and when the bands do not pass through a Fermi point it is semiconducting. This means that arm-chair CNTs, which have n = m, always have states crossing the corner points of the first Brillouin zone and so are expected to always be metallic. Zigzag CNTs, which have n/3 equal to an integer are metallic, while all others are semiconducting. Chiral nanotubes are metallic when (2n + m)/3 is an integer but are otherwise semiconducting. Furthermore, as the CNT diameter increases, more wavevectors occur around the circumference so for nanotube diameters above 3 nm, the bangap is comparable to thermal energies at room temperature, which means that MWNTs with a semiconducting outer shell will appear to be metallic. Other important parameters for describing a nanotube's structure are the diameter, $d_t$, which is described by the equation:

$$d_t = \left(\frac{\sqrt{3}}{\pi}\right) a_{c-c}(m^2 + mn - n^2)^{1/2} \qquad (2.3)$$

and the chiral angle between $C_h$ and $a_1$, which is described by the equation:

$$\angle C_h = \tan^{-1}\left(\frac{\sqrt{3}n}{2m+n}\right) \qquad (2.4)$$

where $a_{c-c}$ is the distance between carbon atoms. [1,13,29,30]

In order to verify the above predictions, that depending on the chirality, nanotubes are either semiconducting or metallic, scanning tunnelling spectroscopy (STS) may be used to experimentally determine the atomic structure and the electronic density of states of the CNT. Firstly, an ultra high vacuum (UHV) scanning tunnelling microscope (STM) is used to atomically image a selected SWNT to determine its diameter and the angle of the zigzag direction relative to the nanotube axis. These values may then be substituted into equations (2.3) and (2.4) to estimate the indices of the nanotube and predict the conduction mechanism. To verify the expected conduction mechanism STS is then used to examine the current and the normalised density of states variation with voltage. If the current increases linearly with voltage and the density of states is finite throughout the voltage range, the nanotube is metallic. Otherwise, it is semiconducting.

### 2.2.6 Applications of Carbon Nanotubes

The huge range of properties of CNTs means that they have a wide range of possible applications in a number of industries. For electronics, CNTs can produce streams of electrons that may be used as light sources in displays. They also have a strong covalent structure, which enables them to withstand current densities up to $10^9$ $Acm^{-2}$, whereas electromigration limits copper to $10^6$ $Acm^{-2}$. [2-7] This property combined with a high aspect ratio, means CNTs are ideal for use as electrical wires or interconnects in integrated circuits. This property also means that CNTs may be used as field emission tips in displays [31], X-ray tubes [32], electron sources in electron microscopy and as gas discharge tubes. [33] Another interesting application of CNTs is as electrodes in electrochemical supercapacitors, which have giant capacitances in comparison with dielectric based capacitors. [34,35]

Another electronic application for CNTs is for semiconducting SWNTs to be used as a replacement of transistor channels in today's silicon based IC technology. This is because as conventional transistors reduce in size, they present an increasing number of challenges, which must be overcome. One example of this is that as the channel size reduces, so does the required number of dopant atoms and the numbers are fast approaching the statistical limit. [36] SWNTs have the advantage that they do not require dopant atoms. Indeed in 2006 Chen et al. [37] produced the first five stage SWNT CMOS-type ring oscillator using an 18 μm CNT. Carbon nanotubes also have the advantage that they exhibit either ballistic or quasi-ballistic transport, which means that SWNT transistors may be operated at faster speeds than conventional transistors. [38] However, there are still a number of challenges that must be overcome before SWNT transistor circuits will be capable of replacing the conventional semiconductor technology. One such issue is that CNTs are currently produced as a mix of semiconducting and metallic nanotubes, with different lengths and diameters.

Another attribute of CNTs is their large surface area, which means that both the inside and outside of CNTs may be used to support reactant particles. These nanotubes may be used in catalytic conversion reactions and for the storage of elements such as hydrogen. [39,40] CNTs are also very sensitive to adsorbed molecules and may be used in chemical and biological sensors to detect dangerous gases in the atmosphere. [41] Within the mechanical industry CNTs can be used in polymer composites, mechanical deformation applications and as miniature springs. In particular, their high aspect ratio, exceptional in-axis strength and low weight mean that they can improve the strength and stiffness of a polymer and add

multifunctionality such as electrical conductivity to the system. Furthermore, they can be made to deflect under electric stimulation and so have suitable properties for use as cantilevers or actuators. Another potential application for CNTs is as electromechanical sensors because any deformation is reflected in their electrical characteristics. [42,43]

## 2.3 Electrical Conduction in Carbon Nanotubes

The conduction of CNTs has been extensively studied and been shown to be ballistic, diffusive or quasi-ballistic. This section shall discuss some of the theoretical descriptions of the ballistic transport mechanism in CNTs and outline a number of experimental studies, which have confirmed this. It will then go on to look at the experimental work of a number of groups whose results appear to be due to other types of conduction.

As described in section 2.2.5, CNTs have either a metallic or semiconducting character. In metallic nanotubes, there are two metallic 1-D sub-bands that cross at the Fermi level and a number of occupied and unoccupied semiconducting sub-bands positioned symmetrically either side of the Fermi level (Figure 2.8). As the bandgap between the occupied and unoccupied levels is much greater than kT at room temperature, for bias voltages less than this value, only the two metallic sub-bands, will contribute to the transport. These sub-bands have a pure bonding and antibonding character, which means that backscattering is significantly reduced and ballistic conduction can occur.

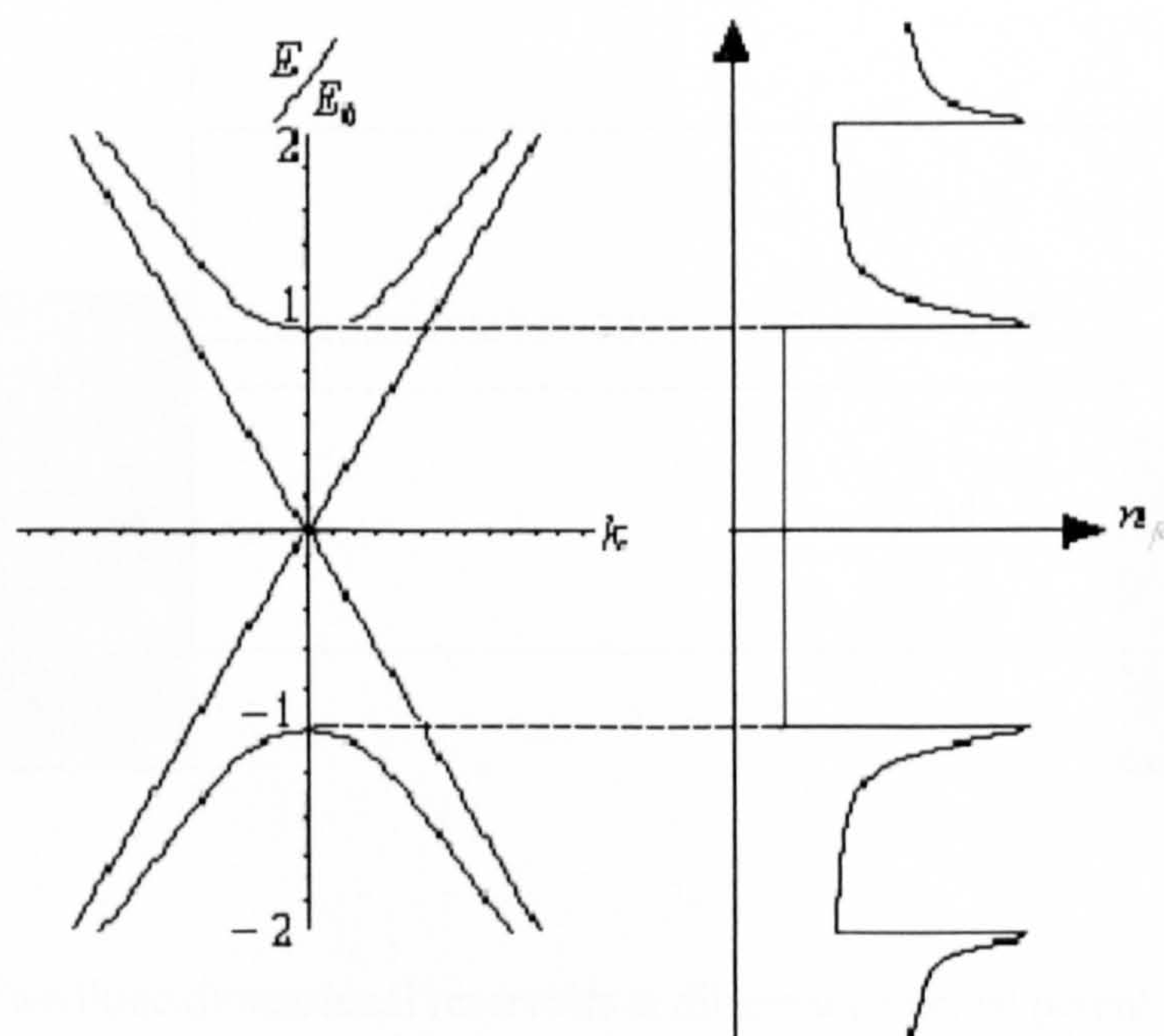


**Figure 2.8.** Diagram of the band structure (left) and the density of states (right) of a metallic CNT.

In ballistic nanotube devices, the conductance is summarised by Landauer's equation:

$$G = G_0 \sum T_i \qquad (2.5)$$

where $G_0$ is the quantum of conductance ($2e^2/h$) and $T_i$ is the transmission coefficient of each contributing sub-band. In ideal nanotubes with no scattering, $T_i = 1$ and as there are two conducting metallic sub-bands, $G = 2G_0$. This equates to a quantum mechanical contact resistance (1/G) of 6.5kΩ, which arises from the mismatch of the number of conduction channels in the nanotube and macroscopic metal leads. In non-ideal carbon nanotubes, defects or imperfect contacts will cause some elastic back scattering (reflections), which reduce the transmission coefficient and hence the final value of G. When the scattering length is much greater than the inter-contact distance, then the conductivity is independent of length, and the transport may be said to be ballistic. [44]

In order to understand how research has arrived at this result, the approach taken by Saito et al. [1] is reviewed. Figure 2.9 shows an ideal case for ballistic transport, where a wire of length, $L$ is connected to two metal electrodes, with electron chemical potentials of $\mu_1$ and $\mu_2$. This model assumes that there is no scattering at the contacts, so only electrons with wavevectors greater than zero and energies between $\mu_2$ and $\mu_1$ will contribute to the current with an initial energy, E. The electronic states are quantised perpendicular to the current and so there are several sub-bands $E_j(k)$, which have the same k value and an energy between $\mu_2$ and $\mu_1$. [1]

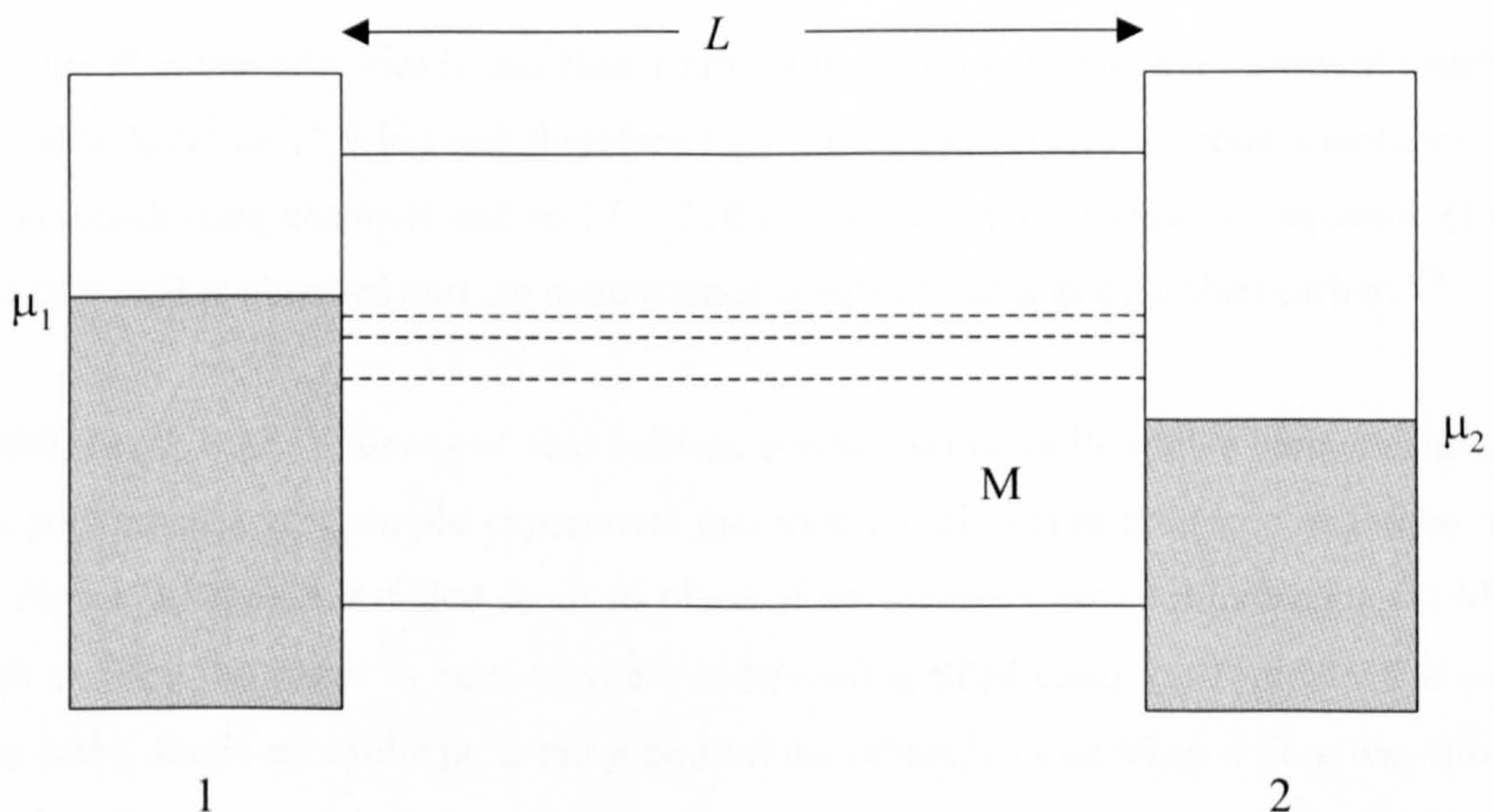


**Figure 2.9.** Two three-dimensional reservoirs at different chemical potentials are connected by a ballistic conductor of length $L$, the number of ballistic channels available between $\mu_1$ and $\mu_2$ is M. [1]

If an electron in this model has a velocity of $v = \hbar^{-1} \cdot (\partial E / \partial k) > 0$, then the total current, I may be described by the equation:

$$I = \frac{e}{L} \cdot 2 \cdot \frac{L}{2 \cdot \pi} \cdot \sum_j \int_{k>0} \frac{1}{\hbar} \cdot \frac{\partial E_j(k)}{\partial k} \cdot \left[ f(E_j - \mu_1) - f(E_j - \mu_2) \right] \cdot dk \tag{2.6}$$

where:

- the factor of two is added to account for spin degeneracy
- $L/2\pi$ is the inverse of the level spacing
- $\Sigma$ sums the contribution to I from each channel
- j is the number of contributing sub-bands
- f(E) is the Fermi-Dirac function
- $[f(E_j - \mu_1) - f(E_j - \mu_2)]$ is the probability that an electron with an energy $E_j$ at contact 1 exists with a probability smaller than an electron at contact 2 with an energy $E_j$. [1]

If the total number of conduction channels is denoted by M(E) and M is constant between $\mu_2$ and $\mu_1$ then equation (2.6) may be simplified to:

$$I = \frac{2e^2}{h} M \frac{\mu_1 - \mu_2}{e} \tag{2.7}$$

Also, as the voltage between the two electrodes is equal to $(\mu_1 - \mu_2)/e$, the contact resistance of a ballistic conductor may be written as:

$$R_c = \frac{(\mu_1 - \mu_2)/e}{I} = \frac{h}{2e^2} \cdot \frac{1}{M} \tag{2.8}$$

When the diameter of a wire is less than 1 nm, M is equal to one and the quantised resistance is equal to $h/2e^2$ or 12.9 kΩ and therefore $G_0 = 2e^2/h$. However, in carbon nanotubes there are two conducting channels and so M = 2. By substituting this value into equation (2.8), a value of 6.5kΩ is obtained and the conductance is equal to $2G_0$ as described earlier. [1]

In 1998, Frank et al. [45] demonstrated ballistic conduction in multi-walled carbon nanotubes. They performed a very simple experiment that took arc-discharge produced nanotube fibres (see Figure 2.10) and installed them in place of an scanning probe microscope (SPM) tip which enabled the fibres to be moved accurately using SPM controls. Typically the carbon fibres had a single nanotube protruding beyond the others, so that when a fibre was lowered towards a liquid metal such as mercury, a second reproducible contact was formed between the nanotube and the liquid metal. [45]

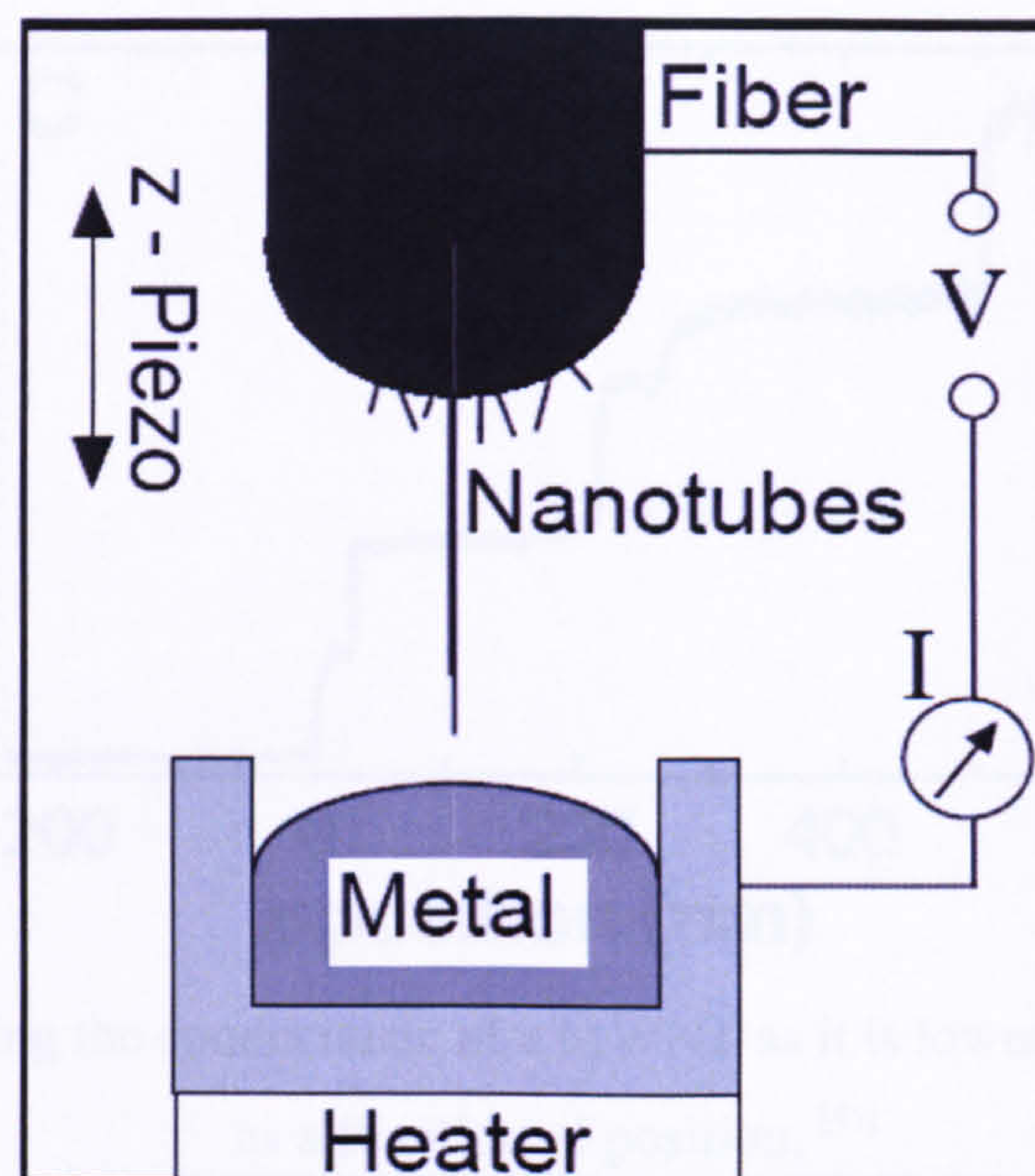


**Figure 2.10.** Schematic diagram of the experimental set up used by Frank et al. The nanotube fibre is connected to an SPM tip and then lowered into a liquid metal. [45]

The initial experiment raised and lowered the fibre into the liquid metal and the conductance was measured over a number of different depths to give a set of data such as that shown in Figure 2.11. As can be seen from the data, contact of a single nanotube to the metal produced a conductance plateau very close to $1G_0$, which is consistent with a ballistic conductor of uniform width and strongly suggests that the nanotube is a quantised conductor. Further experiments gradually lowered the fibre further into the metal so that increasing numbers of tubes came into contact with the liquid metal. The resulting data is shown in Figure 2.12 and indicates that each time another nanotube comes into contact with the metal, the conductance increases by an interval of $\sim 1G_0$. [45]

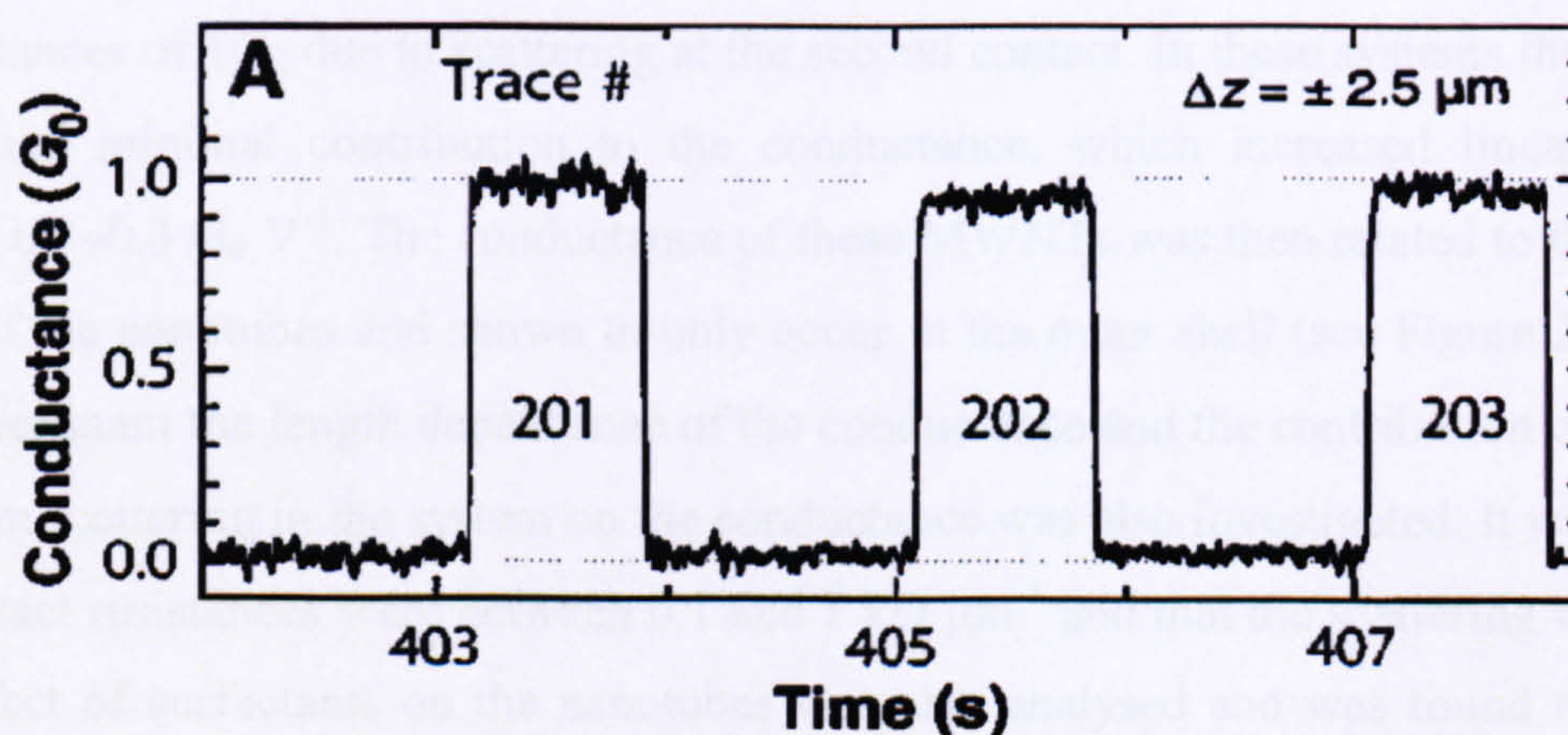


**Figure 2.11.** Graph showing the conductance of a MWNT as it is lowered in and out of a liquid metal contact as a function of time. [45]

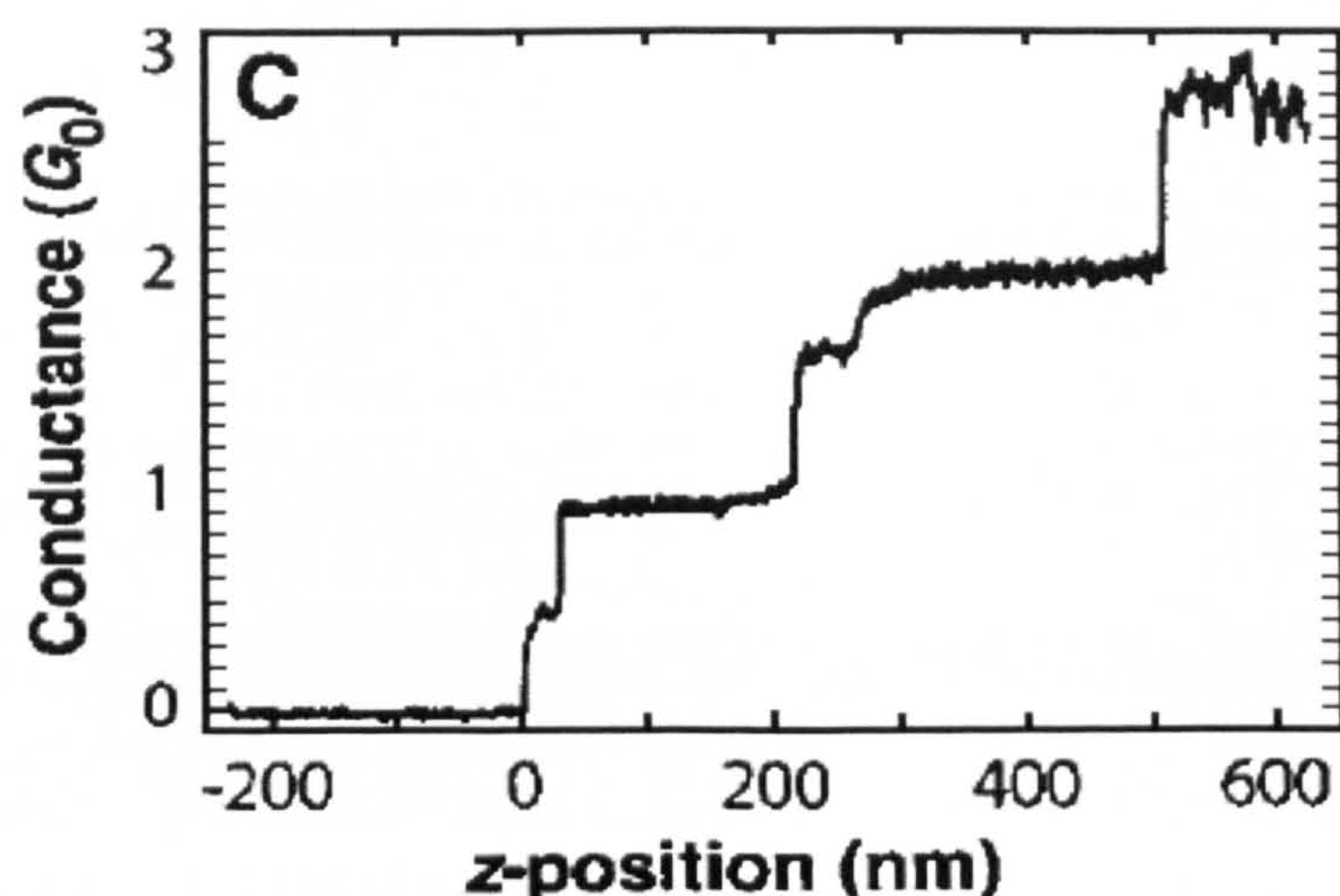


**Figure 2.12.** Graph showing the conductance of a MWNT as it is lowered into a liquid metal contact as a function of position. [45]

In summary, these results show that the nanotubes are 1D conductors, whose conductance rises approximately linearly with voltage and is symmetric with respect to voltage polarity. It was also shown that the electronic transport only occurred in the outer layer of the nanotubes and that high voltages did not damage the nanotubes as any heating of the nanotubes was dissipated into the leads. Within this experiment current densities of $\sim 10^7$ A/cm$^{-2}$ were also measured, which is greater than that of any other material other than superconductors. [45]

In 2002, Poncharal et al. [51] extended this experiment and found that nanotubes with poor contacts to the fibre had conductances of less than $0.5G_0$. These nanotubes tended to fall away from the fibre during successive dipping cycles. It was also found that when high voltages were applied to nanotubes with large defects, the MWNTs broke at the site of the defect, while nanotubes with a metallic outer layer and no defects showed lowered ballistic conductances of $1G_0$ due to scattering at the second contact. In these systems the higher sub-bands had minimal contribution to the conductance, which increased linearly with the voltage by $\sim 0.3\ G_0\ V^{-1}$. The conductance of these MWNTs was then related to the density of states of the nanotubes and shown to only occur in the outer shell (see Figure 2.13). Within this experiment the length dependence of the conductance and the contribution of the contact and from scattering in the system on the conductance was also investigated. It was found that the contact resistances were between 0.1 and 1 k$\Omega$ $\mu$m$^{-1}$ and that the scattering was minimal. The effect of surfactants on the nanotubes was also analysed and was found to reduce the conductance of the nanotubes, as well as causing the conductance to rise nonlinearly and be asymmetric with respect to the voltage. [46]

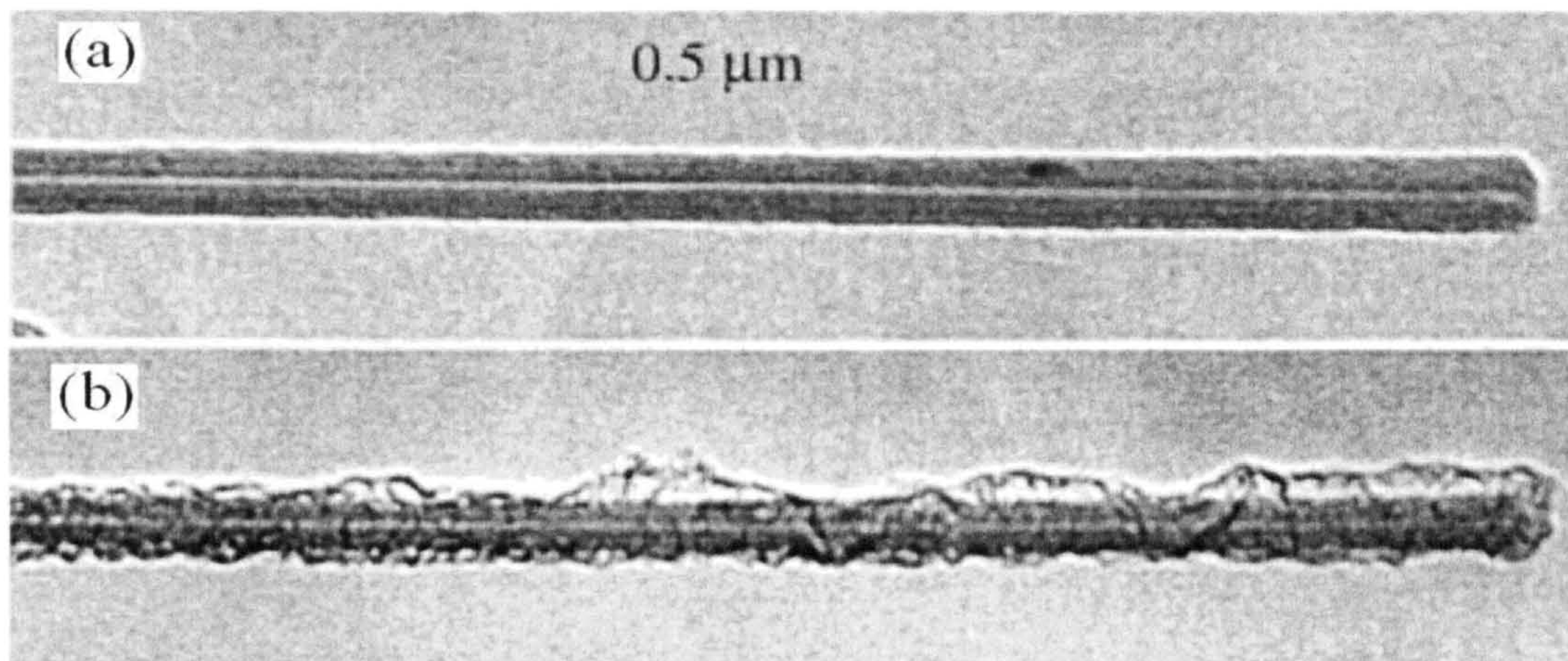


**Figure 2.13.** TEM of a pristine MWNT **(a)** before and **(b)** after failure. [46]

It should be noted here that both Frank et al. [45] and Poncharal et al. [46] did not process their CNTs in an attempt to avoid any contamination or damage to the samples and that the conductance was $G_0$ rather than the predicted $2G_0$. As the transport through the MWNTs is primarily on the surface, the purification and other processing steps that are generally carried out during the fabrication of contacts by most groups can damage and significantly alter the transport properties. Also, these devices may be affected by a number of sources of contact resistance, such as that produced by poor coupling between the nanotubes and the leads such as Schottky Barriers at the contacts and nanotube-substrate interactions. These effects may dominate and obscure the intrinsic electrical properties of the nanotubes and so not all nanotube conduction experiments will demonstrate ballistic conduction. [45,46]

In another experiment, which also showed ballistic conduction in MWNTs, Liang et al. [47] dispersed arc-discharge MWNTs over an oxidised silicon substrate that had been prepatterned with gold electrodes with a 1 μm spacing using standard optical lithography. The MWNTs were contacted to the electrodes using alternating electrical fields and then two terminal I-V measurements between – 8 V and + 8 V were run. A typical I-V measurement is shown in Figure 2.14. As can be observed from this graph, the current through the structure reached 675 μA at 8 V, and dissipated a maximum power of 5.4 mW. As the thermal conductivity of a MWNT reaches its peak at 3000 $Wm^{-1} K^{-1}$, Liang et al. [53] calculated that the centre of the MWNT should have reached a temperature in excess of 7000 K. This temperature is significantly higher than the boiling point of graphite and so it was concluded that a significant fraction of the power in the structure must have been dissipated at the contacts and that the electrical transport was ballistic. [47]

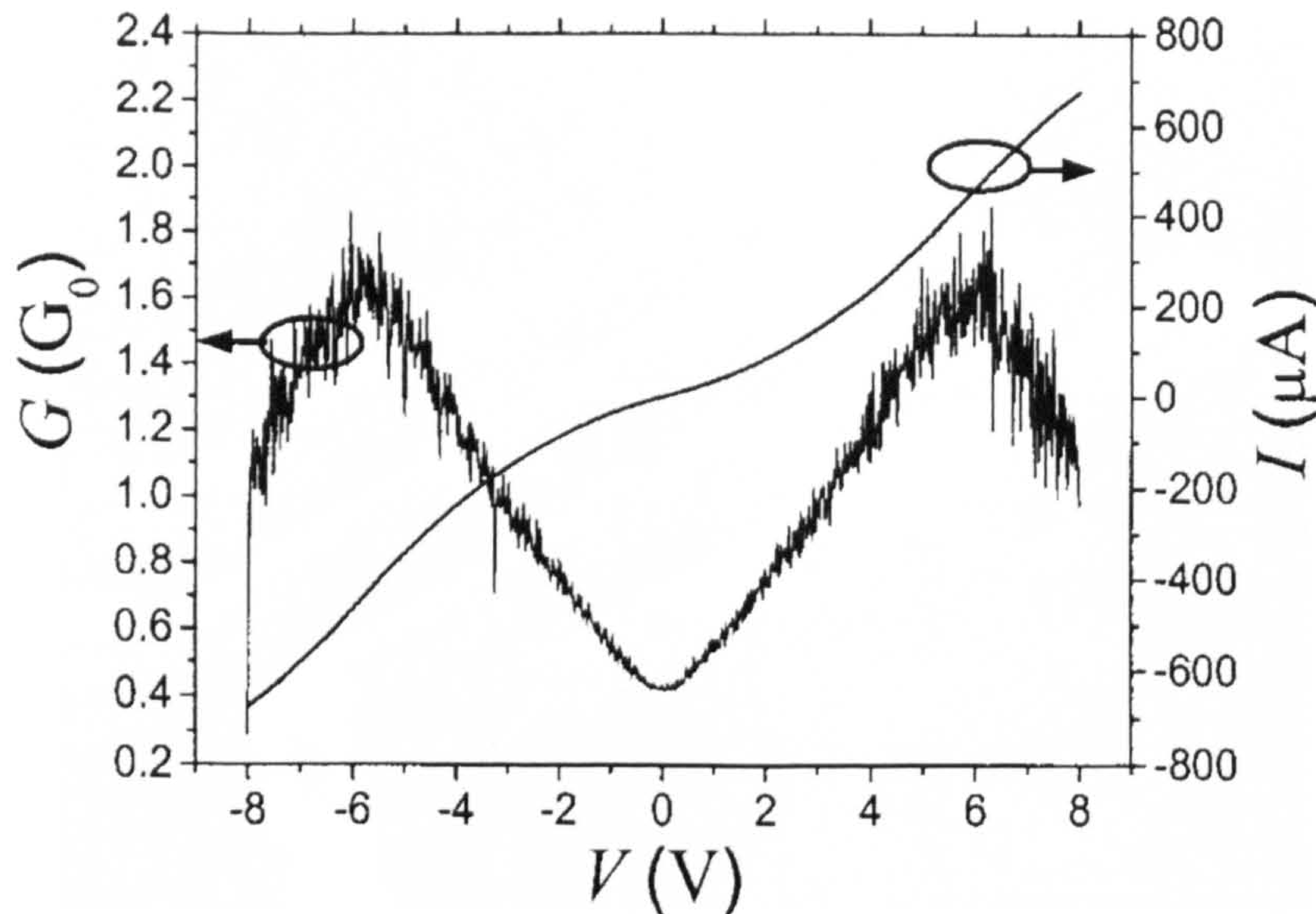


**Figure 2.14.** I - V curve of a MWNT from – 8 to 8 V (right hand axis) and the corresponding G – V curve (left hand axis). [47]

Liang et al. [47] went on to analyse the conductance versus voltage characteristics of this nanotube (see Figure 2.14). The conductance at near zero voltage was found to be 0.4 $G_0$, which is significantly lower than that seen by Frank et al. [45] and Poncharal et al. [46] This was attributed to either the contacts causing scattering at the nanotube – metal interface or to the MWNT having a semiconducting outer shell through which the conduction occurs with a very small band gap of 0.05 eV. The conductance characteristics then increased linearly with voltage with a slope of 0.2 $G_0$ $V^{-1}$ until they reached its peak at ~ 5.8 V, after which they decreased. These peaks were found to occur at $\pm$ $2\gamma_0/e$, where $\gamma_0$ is the $\pi$ bonding energy for carbon nanotubes, which again is a sign of ballistic conduction in MWNTs. [47]

One group that found that their experimental observations did not match those described previously was Schronenberger et al. [48] Within this experiment arc-produced MWNTs were dispersed onto a silicon substrate with a 400 nm thick oxide layer. A resist layer was then spun over the MWNTs and four terminal gold electrodes were fabricated using electron beam lithography and thermal evaporation of the metal (see Figure 2.15). This contact scheme relies upon chance and so its yield is low. It was also chosen in preference to the more conventional method of dispersing CNTs over prefabricated metal electrodes as it yielded lower contact resistances of ~5 kΩ. This methodology also has the disadvantage that the contacts deteriorate over a period of one to two weeks, which meant that the electrical characterisation had to be undertaken immediately after fabrication. [48]

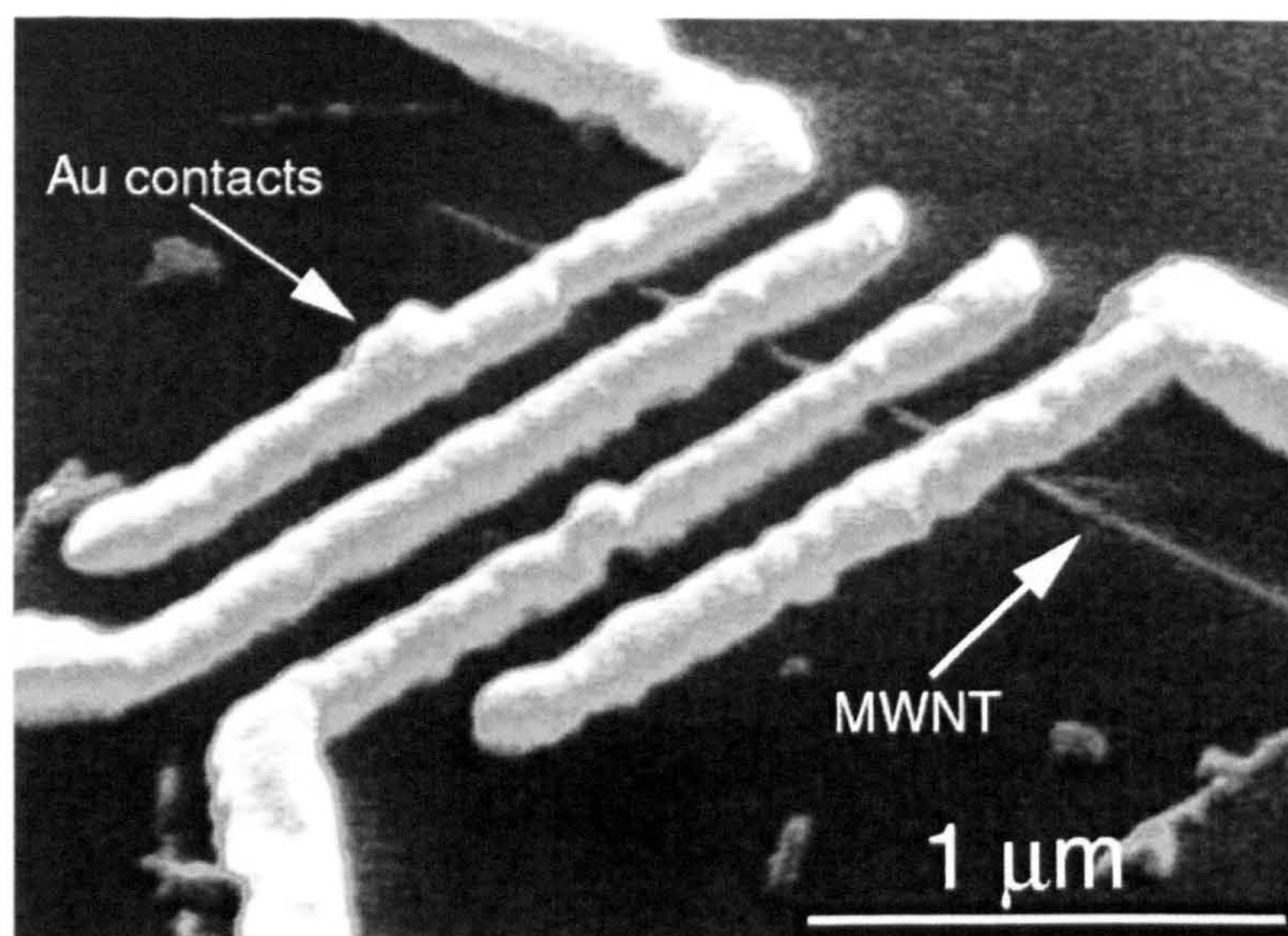


**Figure 2.15.** Scanning electron microscope image of a MWNT contacted by four gold fingers. [48]

For the electrical characterisation Schronenberger et al. [48] chose to only investigate nanotubes that had four low ohmic contacts (<10 kΩ). For these structures, they found that as the temperature of the system was decreased to ~0.3 K, the resistance increased by a factor of two to three and saturated for temperatures below 10 K. Examination of the Aharnov-Bohm effect of these samples showed that the transport in the MWNTs was diffusive at the scale of the circumference. However, the dI/dV spectrum for a 1D sub-band agreed with the tight-binding models and suggested a large elastic-scattering length. Comparison of the measured resistance of these MWNTs also compared well to a simple Drude resistance equation and again gave large elastic-scattering lengths. It was hence thought that these nanotube structures demonstrated quasi-ballistic transport. [48]

Meanwhile Javey et al. [49] also investigated the electrical transport of SWNTs and found that they exhibited quasi-ballistic transport properties at high biases. They fabricated near-ohmic palladium contacts using electron beam lithography over CVD grown SWNTs with lengths between 10 nm and 1 μm and diameters between 1.5 and 2.5 nm that were dispersed on a silicon oxide substrate that was used as a back gate. At room temperature, the SWNTs exhibited conductances in the range of 2 to 4 $e^2/h$ for low biases. Javey et al. [49] also found that upon cooling, nanotubes with lengths greater than 200 nm showed increasing conductance, while SWNTs with lengths below 100 nm were temperature independent. This result suggests that in short SWNTs (L<100 nm) electron backscattering by acoustic phonons is ineffective and in the low energy regime the transport is ballistic. [49]

Javey et al. [49] also investigated the conduction of SWNTs at higher conductances and found that for long SWNTs, optical or zone boundary phonon scattering caused the current to saturate at ~20 μA, whilst for short SWNTs (below 100 nm) the current saturated at ~60 μA. Monte Carlo simulations were then used to determine whether these results were consistent with the expected mean free paths (mfp) by solving the Boltzmann transport equation stochastically. This work gave mfps of 300 nm for phonon scattering and 15 nm for optical phonon scattering, which fitted well with the experimental data. This lead to the conclusion that at low bias, ballistic transport occurred on the nm scale and at high bias quasi-ballistic transport occurred. [49]

Park et al. [50] also calculated the electron mfp for backscattering by evaporating gold electrodes over SWNTs and using a gold coated atomic force microscope (AFM) tip as a third electrode (Figure 2.16). A bias voltage was applied to the source electrode (left electrode in Figure 2.16) and the current was measured using the AFM tip, which served as the drain electrode. The second electrode (right electrode in Figure 2.16) was then used as a probe to measure the voltage drop at the tip-nanotube drain junction. This allowed Park et al. [50] to deduce that $V = V_{SD} - V_{tt}$ and that the I-V curves corresponded to just the left contact and the SWNT between this contact and the AFM tip. By moving the AFM tip, they were able to obtain I-V measurements for different channel lengths on the same SWNT. [50]

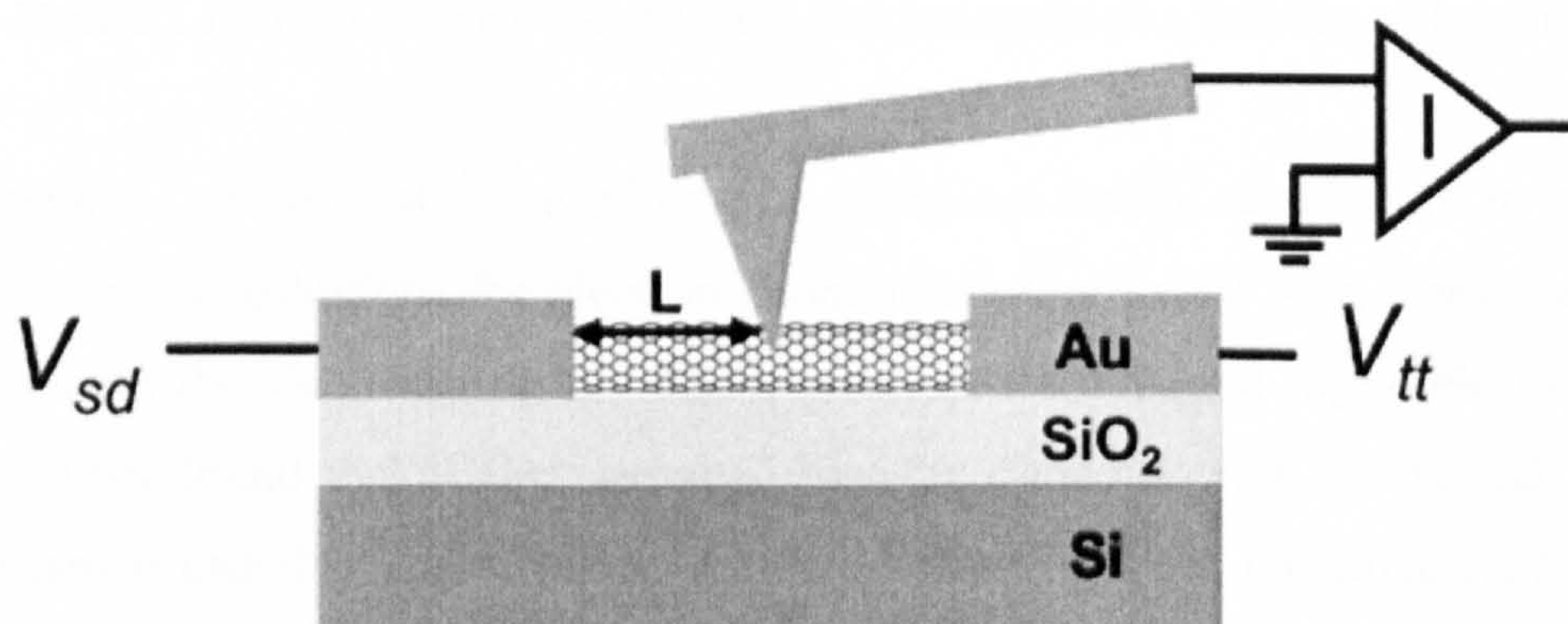


**Figure 2.16.** Schematic of the measurement setup. The active length L of the SWNT device can be changed by moving the AFM tip. [50]

At low biases, the I-V characteristics were linear and had the resistances shown in Figure 2.17(a). For lengths up to 200 nm the resistance was almost constant, whereas for lengths greater than 200 nm the resistance increased linearly with length at a rate of 4 kΩ $\mu m^{-1}$. This one-dimensional resistivity was used to estimate a low bias electron mfp for backscattering

of ~1.6 μm, which was attributed to scattering with acoustic phonons. Park et al. [50] hence concluded that for lengths below this the low field electrical transport was essentially ballistic. At high biases, the I-V slope decreased with increasing voltage and for lengths greater than 500 nm the current saturated at ~20 μA. Meanwhile, for lengths below 500 nm, the slope of the I-V curves increased at a rate lower than that measured for low biases. The resistance at high biases scaled linearly with length and the resistivity was measured to be 800 kΩ μm$^{-1}$ as shown in Figure 2.17(b). This resistivity was approximately two hundred times larger than that measured at low biases and produced a mfp of ~10 nm, which was attributed to scattering by optical and zone boundary phonons. [50]

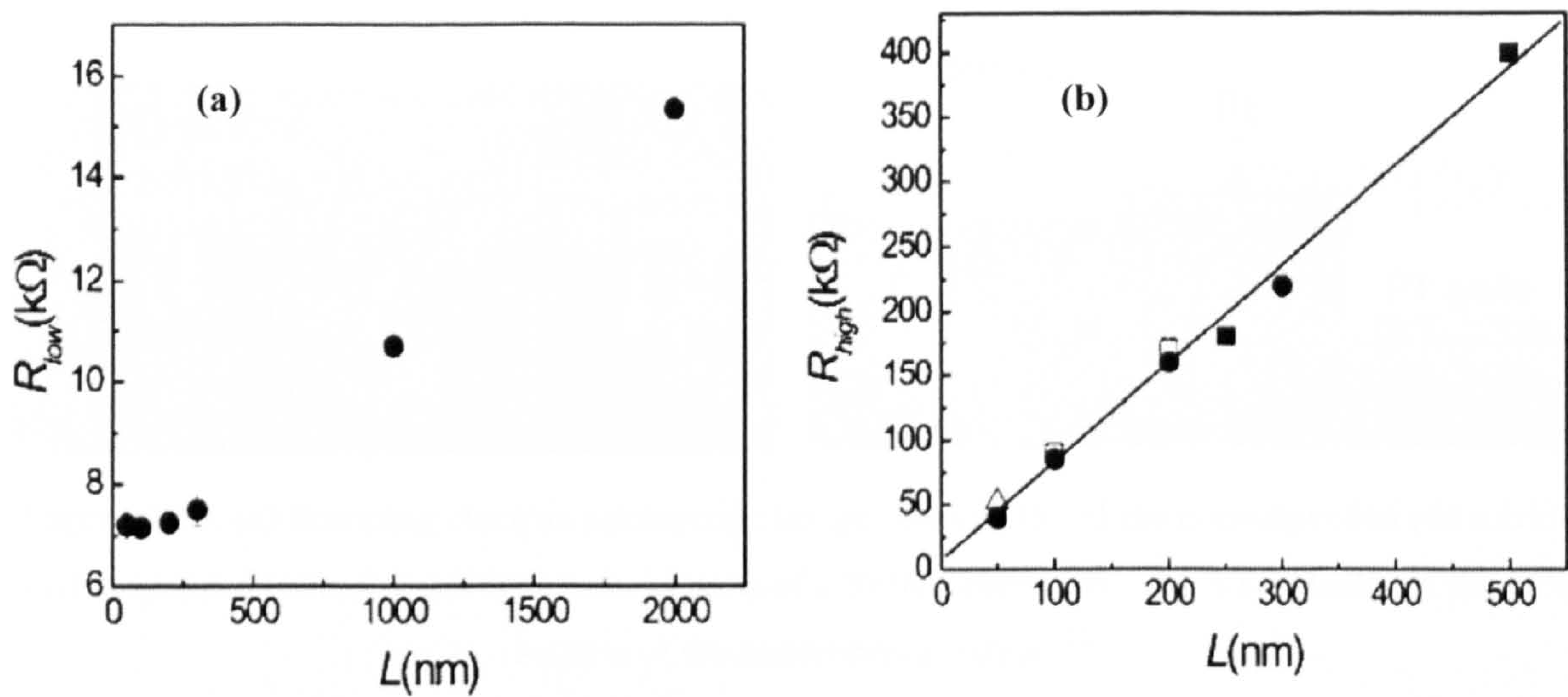


**Figure 2.17. (a)** Low-bias and **(b)** High-bias resistance as a function of length. [50]

More recently, Lazzeri et al. [51] used density functional theory calculations to calculate the optical phonon contributions for electron-phonon coupling in SWNTs. They then used this value to obtain the electron mfp for optical phonon scattering in high-field quasi-ballistic transport. They found that if they assumed that the phonons were in thermal equilibrium with the lattice and that there was no forward scattering, then the calculated mfp due to optical phonon scattering, $l_{op}$ could be calculated using the equation:

$$l_{op} = 65d \tag{2.9}$$

where, $d$ is the diameter of the nanotube being investigated. This equation produces an optical phonon mfp that is one order of magnitude larger than that seen by Javey et al. [54] and Park et al. [55] in their experimentally estimated values of ~10 nm. Lazzeri et al. [56] then went on to assume that the optical phonon mfp was ~10 nm and calculated that the corresponding temperature of the phonon bath had to be several thousand Kelvin. They hence concluded that the phonons could not be in thermal equilibrium with the lattice. [51]

The existence of a non-thermal equilibrium phonon population is consistent with the results of Pop et al. [52], who grew SWNTs over trenches so that half their length was suspended as shown in Figure 2.18. They found that the suspended and nonsuspended parts of the same metallic SWNT exhibited drastically different I-V characteristics as shown in Figure 2.19. As can be seen from this graph the nonsuspended part of the nanotube exhibited monotonic I-V characteristics similar to those seen by Park et al. [50] with the current approaching ~20 μA, while the suspended part reached a maximum current of ~ 10 μA/L, where L is the length of the nanotube with no ground plane interaction before exhibiting a negative differential conductance. [52]

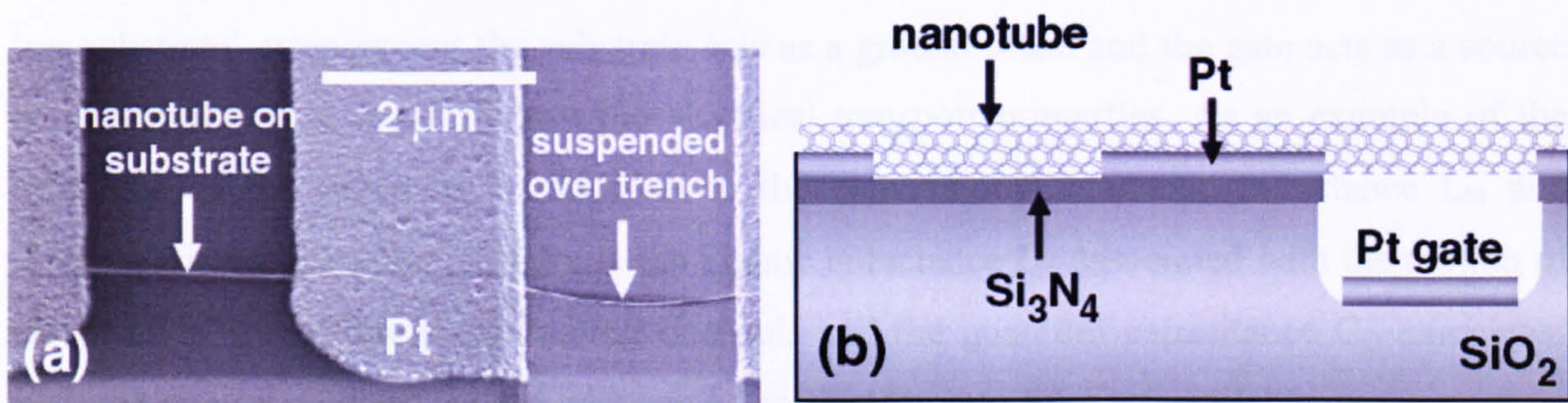


**Figure 2.18. (a)** Scanning electron microscope image taken at 45° of the nonsuspended (on nitride) and suspended (over 0.5 μm deep trench) parts of a SWNT connected. **(b)** A schematic of the cross section of the experimental setup. [52]

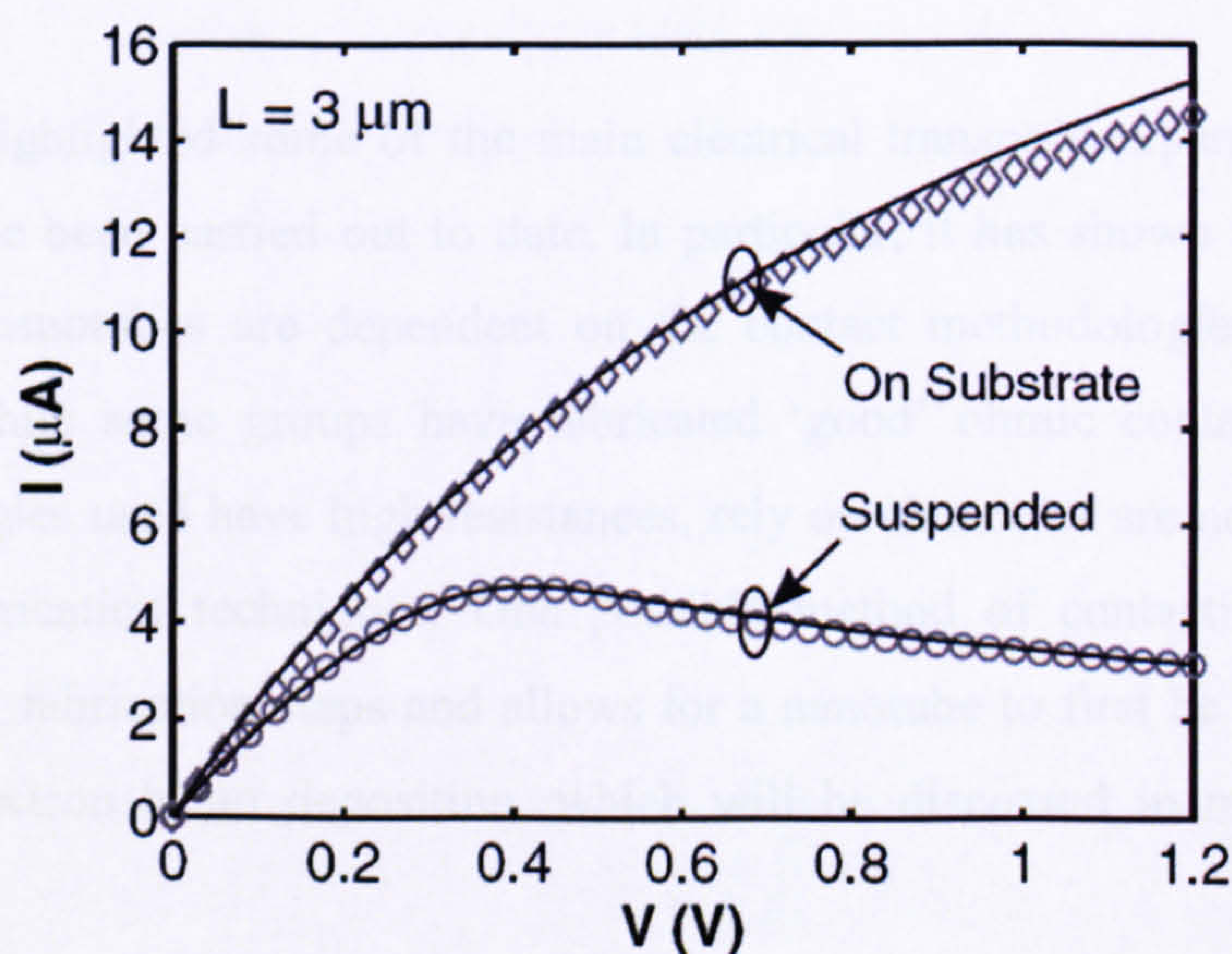


**Figure 2.19.** The current versus voltage characteristics of the same length suspended and nonsuspended parts of a SWNT. [52]

The lower current saturation level in the suspended part of the nanotube was attributed to the absence of a substrate to act as a heat sink, while the negative differential conductance was thought to be due to the existence of nonequilibrium, hot optical phonons at high bias. The higher currents observed in the nonsuspended nanotubes were hence thought to be due to the substrate-nanotube interactions that aid heat dissipation and more importantly assist in the relaxation of optical phonons emitted though electron scattering. [52]

Indeed, most investigations into the transport properties of carbon nanotubes have used a three-terminal arrangement in which the carbon nanotubes lie on a silicon dioxide gate insulator and source and drain contacts are deposited over the ends of the nanotubes. In this 'on-substrate' arrangement the substrate acts as a ground plane and the gate acts as a source of capacitance that can influence the electrical transport properties. As an example of the influence of the substrate, in addition to the conventional magnetic inductance $L_M$ and electrostatic capacitance $C_E$, there is the kinetic inductance $L_K$ associated with the motion of electrons in the different conducting channels and the quantum capacitance $C_Q$ associated with the energy required for the addition of an electron into the first available quantum state. For a SWNT with a diameter of 2 nm lying on an oxide, Burke [53] gives values of $L_M \sim 1$ pH $\mu m^{-1}$ and $C_E \sim 50$ aF $\mu m^{-1}$. These values can be compared with estimated values of $L_K \sim 16$ nH $\mu m^{-1}$ and $C_Q \sim 100$ aF $\mu m^{-1}$ and indicate that in one-dimensional systems, while the kinetic inductance dominates the total inductance, both the classical electrostatic capacitance and the quantum capacitance need to be taken into account. [53]

This section has highlighted some of the main electrical transport experiments on carbon nanotubes that have been carried out to date. In particular, it has shown that the electrical properties of the nanotubes are dependent on the contact methodologies and geometries used. However, while some groups have fabricated 'good' ohmic contacts, many of the contact methodologies used have high resistances, rely on chance or are not suitable for use in mainstream fabrication techniques. One possible method of contacting to nanotubes, which has minimal fabrication steps and allows for a nanotube to first be selected and then contacted to is electron beam deposition, which will be discussed in more detail in the following section.

## 2.4 Overview of Electron Beam Induced Deposition (EBID)

### 2.4.1 Introduction to Electron Beam Induced Deposition

Electron beam induced deposition (EBID) is a versatile, direct-write technique that allows for features to be directly patterned onto a substrate. In this process a precursor, which contains the element to be deposited, is heated and injected through a small bore needle into a high vacuum electron microscope such as a scanning electron microscope (SEM), where it is adsorbed onto the substrate (see Figure 2.20(a)). The electron beam exposes the adsorbed gas molecules causing them to undergo a series of complex beam-induced surface reactions and dissociate. This results in the formation of a non-volatile solid deposit on the substrate and a volatile by-product that is desorbed and pumped away (see Figure 2.20(b)).

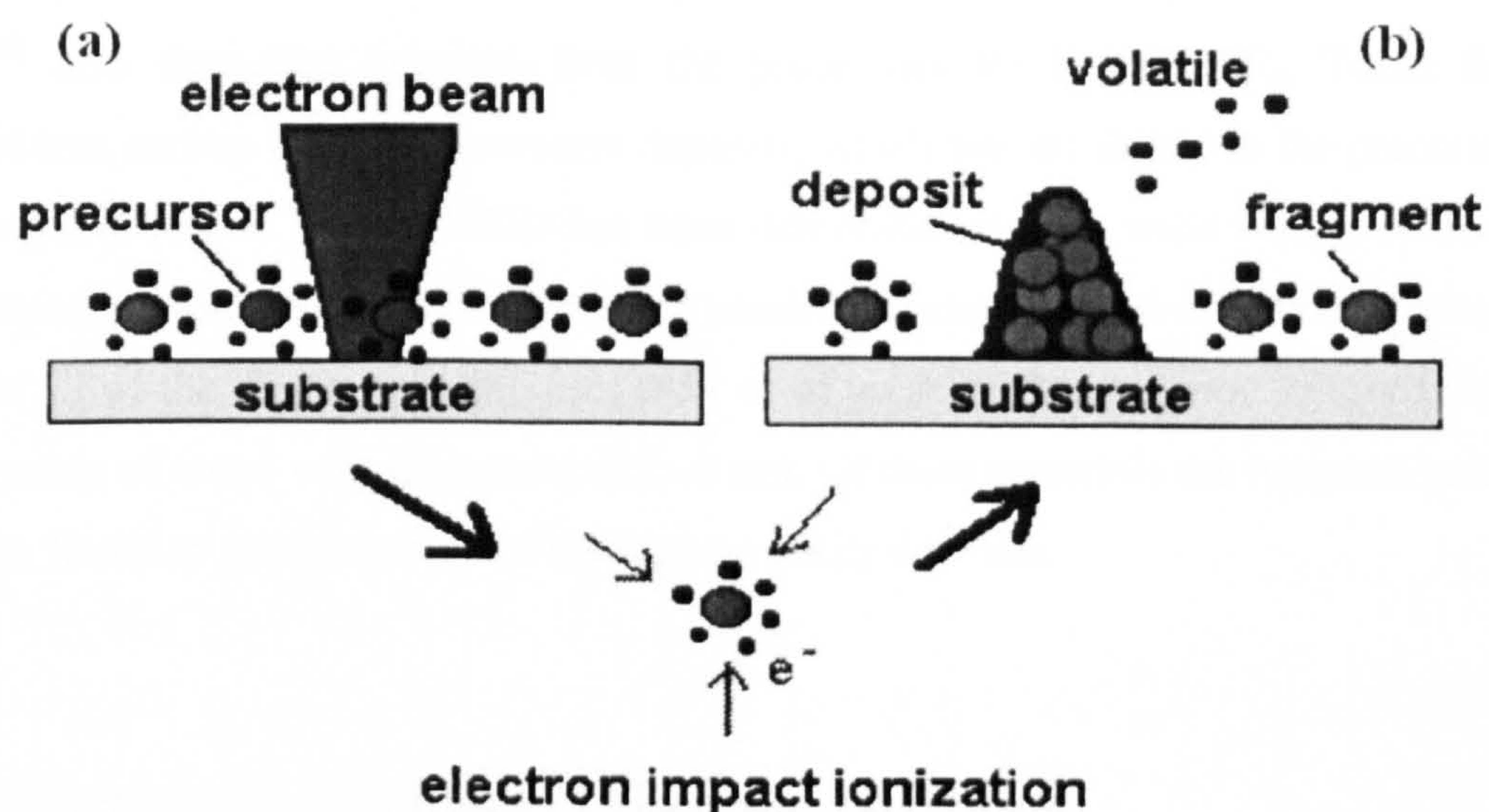


**Figure 2.20.** Illustration of EBID. (a) A precursor gas is injected into a high vacuum microscope where it is adsorbed onto the substrate and exposed to an electron beam. (b) The gas molecules form a non-volatile deposit and a volatile by-product that is pumped away.

### 2.4.2 History of EBID

The use of an electron beam to deposit material was first reported in the 1940s, when electron microscopists noticed that wherever the electron beam impinged upon the sample, a contaminating deposit was formed. [54,55] Hillier et al. [56] found that this deposit mainly consisted of amorphous carbon and attributed its formation to the ionisation and dissociation of organic molecules that had been adsorbed onto the sample's surface. In 1959 Buck et al. [57] went on to use this phenomenon to fabricate a negative resist onto a molybdenum film

that had been covered with a copper mesh to pattern it into squares. The negative resist was formed by introducing tetra-ethoxysilane into the vacuum system that held the sample and exposing it to an electron flood beam. This caused a polymer film to be deposited onto the exposed parts of the substrate. The subsequent introduction of a chlorine vapour caused the unprotected molybdenum to be etched away leaving an array of molybdenum squares.

The use of different gases to produce metal rich deposits with EBID was pioneered by Matsui et al. [58,59] In 1984, Matsui et al. [58] demonstrated that 0.5μm wide chromium lines could be deposited from the precursor $Cr(C_6H_6)_2$ using a modified SEM. Auger electron spectroscopy (AES) of the deposits showed that they contained chromium and carbon from the precursor and oxygen which was thought to have originated in the chamber. It was concluded that the choice of source was important in order to obtain pure chromium. Matsui et al. [59] also deposited tungsten from the precursors $WCl_6$ and $WF_6$. These deposits contained less carbon than the chromium deposits, which was attributed to the precursors not containing any carbon. Today, EBID has been demonstrated for a wide variety of materials, which depending on the precursor and beam conditions used, consist of either an amorphous matrix of all of the elements in the precursor or of an amorphous carbon matrix containing small crystals of metal with diameters of 2 –3 nm. Of these materials the tungsten precursors have been found to produce some of the highest purity deposits.

### 2.4.3 Experimental Equipment Used for EBID

EBID is carried out in high vacuum to minimise scattering of the electron beam and contamination of the deposit. To date, the majority of EBID has been carried out in modified SEMs that include a vapour injection system, which allows the precursor to be heated outside of the vacuum chamber before being injected into the sample chamber. These injection systems are positioned so that the vapour is injected into the path of the electron beam close to the substrate surface. However, EBID may be carried out within any type of electron microscope, which can produce a focused electron beam. Indeed van Dorp et al. [60] used a TEM to study the resolution limits of EBID because these instruments are capable of producing much finer electron beams, which should result in smaller deposits and allow for the structure of the deposit to be studied in-situ. Meanwhile, Mølhave et al. [61] used an environmental SEM (ESEM) to deposit gold needles because it allowed for the effects of adding a water vapour during the deposition on the deposit's structure to be examined.

The dynamics of the deposition process and the vapour flow in an EBID system is dependent on many variables, including the vacuum, chamber geometry, injector geometry, precursor vapour pressure and the lines connecting the precursor source to the chamber. Each of these criteria varies between systems and some such as the precursor and vacuum can vary over time within one system. This makes the accurate prediction of the deposition growth for a particular set-up very difficult. Another issue with many EBID instruments is that they can only scan simplistic patterns such as rectangles, lines and dots. To deposit more complex features a three-dimensional pattern generator such as the Nanometer Pattern Generation System, which will be described in section 3.10.1 needs to be integrated into the system. EBID also has the limitation that the deposits are produced in serial and as such take a long time to produce in comparison with conventional techniques such as UV lithography, where the whole pattern is exposed at once. In an attempt to overcome this, prototype multibeam systems that can deposit several structures in parallel are being developed. [62,63]

## 2.5 Physics of EBID

### 2.5.1 Introduction to Physics of EBID

Before being able to fully understand and analyse the results of EBID, it is necessary to gain a good grounding of the processes involved and the factors that limit EBID. In most EBID experiments the main mechanisms that need to be considered are the introduction of the gaseous precursor, the interaction of the precursor with the substrate and the interaction of the electron beam with the sample and the adsorbed precursor molecules. The following sections will discuss the physics concerned with each of these processes.

### 2.5.2 Precursor Introduction

Most EBID gas injection systems consist of a reservoir, which contains and heats the precursor and a fine capillary tube, which is used to inject the gaseous precursor into the vacuum system. The capillary tube is positioned close to the sample surface to reduce the scattering of electrons with the gas molecules before they are adsorbed and to minimise the quantity of the gas that needs to be used. Figure 2.21 shows a schematic of a typical gas injection tube and the relevant parameters for gas delivery to the deposition area.

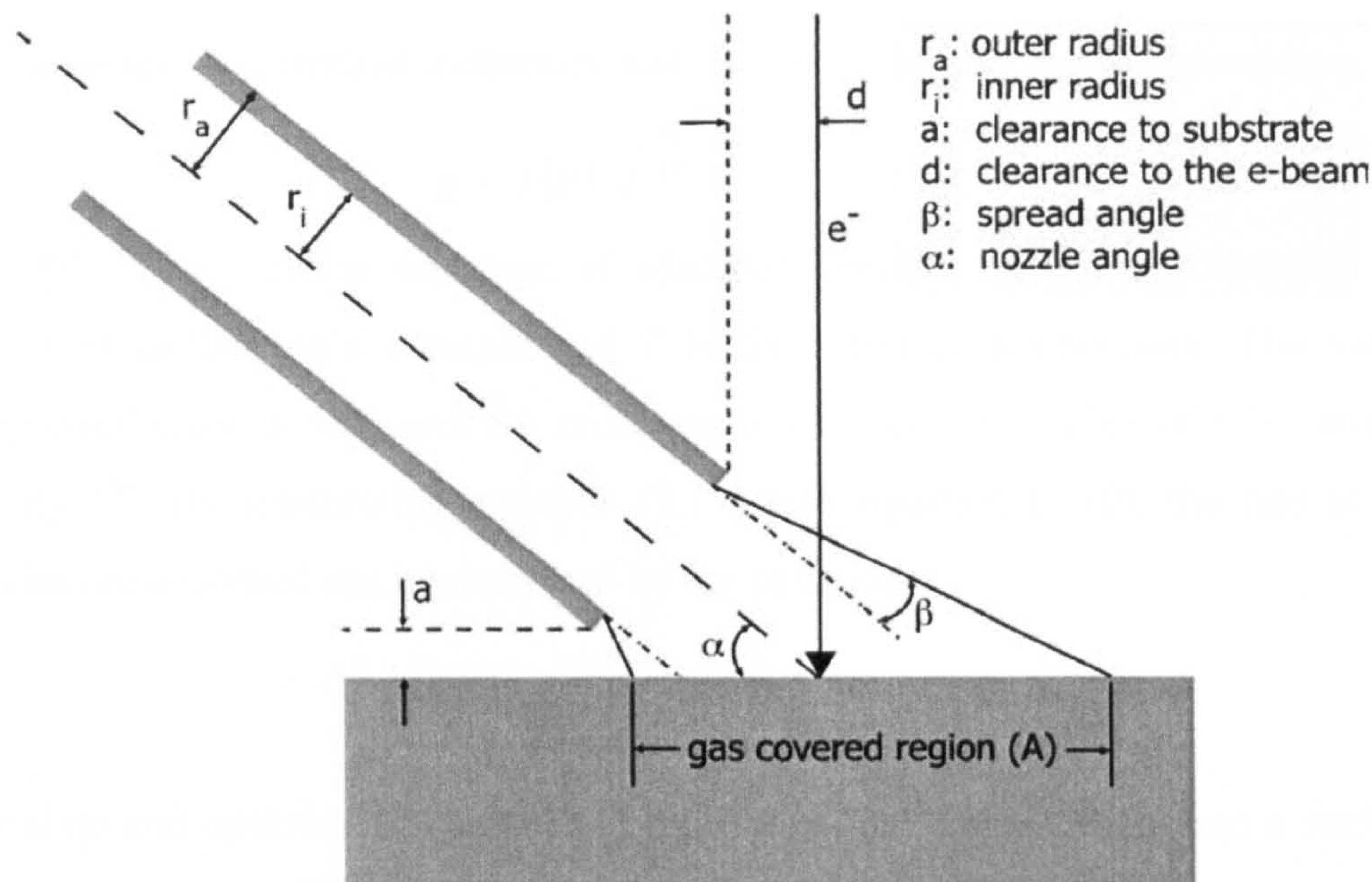


**Figure 2.21.** Schematic of a gas injection tube and the parameters used to model the gas delivery. [62]

In particular, this figure shows how the gas flux is dependent on both the dimension and orientation of the capillary tube. To optimise the gas flux, the projected gas area needs to be minimised by using a short capillary tube to substrate distance, $a$, a low spread angle, $\beta$ and a small capillary tube inner radius, $r_i$. Ideally, the capillary tube angle, $\alpha$, should also be equal to 90°. However, this is not experimentally possible, as it would cause the tube to interfere with the electron beam, which is situated at 90° to the substrate. The gas flux may also be increased by raising the temperature to which the precursor is heated, which increases the gas pressure and hence the number of molecules arriving at the sample surface. [62,64]

### 2.5.3 Precursor-Substrate Interactions

When a precursor gas is injected into the system, the molecules impinge on the surface of the substrate and absorb with a probability known as the sticking coefficient, $g$. The rate at which these molecules adsorb, $R$, varies with time and follows the equation:

$$R = \frac{dN}{dt} = g \cdot F \quad (mols / m^2 s) \tag{2.10}$$

where, $N$ is the number of adsorbed molecules, $t$ is the time and $F$ is the initial surface flux. [66,67] Depending on the system, the sticking coefficient takes a value between 0 and 1, where a value of 1 means that every molecule that impinges on the surface is adsorbed, while a value of 0 means that no molecules are adsorbed. As such the sticking coefficient depends

on the coverage of adsorbed molecules and the activation barrier for adsorption, such that:

$$g = f(\theta) \cdot e^{-\frac{E_a}{kT}} \tag{2.11}$$

where, $f(\theta)$ is the surface coverage of adsorbed species, $E_a$ is the adsorption activation energy, $k$ is Boltsmann's constant and $T$ is the interface temperature. The value of the sticking coefficient is unknown for most precursors and so a value of 1 is often used for simplicity. [64] By substituting equation (2.11) into equation (2.10), the rate at which the molecules are adsorbed can be described by the equation:

$$R = \frac{f(\theta)P}{\sqrt{2\pi mkT}} \cdot e^{-\frac{E_a}{kT}} \tag{2.12}$$

To simulate and optimise the number of molecules that are adsorbed onto a surface during EBID, Koops et al. [65] used an alternative version of this equation that followed the theoretical approach of Scheuer et al. [66], such that:

$$R = \frac{dN}{dt} = g \cdot F\left(1 - \frac{N}{N_0}\right) - \frac{N}{\tau_a} - q \cdot N \cdot f \tag{2.13}$$

where, $f$ is the electron flux density, $q$ is the dissociation cross section, $F$ is the molecular flux density arriving on the substrate, $N_0$ is the molecule density in a monolayer and $\tau_a$ is the mean lifetime of an adsorbed molecule. In this equation, the first term represents the adsorption rate, the second term represents the desorption rate and the third term represents the consumption of adsorbed molecules by the deposition process itself. [65]

The density of adsorbed molecules is in equilibrium, $N_E$, when $dN/dt = 0$, such that:

$$N_E = N_0 \cdot \frac{(g \cdot F/N_0)}{(g \cdot F/N_0) + 1/\tau_0 + q \cdot f} \tag{2.14}$$

This equation shows that $N_E$ must be less than or equal to $N_0$ for all supply and bombardment conditions and that the maximum surface coverage is one monolayer. Therefore, the layer growth rate, R, for EBID can be described using the equation:

$$R = V \cdot N \cdot q \cdot f \tag{2.15}$$

where, $V$ is the volume occupied by a dissociated molecule. For the equilibrium condition, $N = N_E$, the growth rate hence follows the equation:

$$R = V \cdot N_0 \cdot \frac{(g \cdot F/N_0 \cdot q \cdot f)}{(g \cdot F/N_0) + (1/\tau_0) + q \cdot f} \tag{2.16}$$

This equation shows how increasing either the electron or molecular flux density results in an increase in the growth rate. However, these properties are limited by system constraints

including the electron column, the gas injection system and the vacuum system. The amount of time a molecule remains on a surface before it either undergoes a chemical reaction or is desorbed is called the surface residence time, $\tau_a$ and is given by the equation:

$$\tau_a = \frac{1}{v} \cdot e^{\frac{E_{des}}{kT}} \quad (s) \tag{2.17}$$

where, $v$ is an attempt frequency and $E_{des}$ is the desorption energy of the molecules adsorbed on the substrate. This equation shows that as the temperature is lowered the residence time for each precursor molecule increases such that there is a higher concentration of adsorbed molecules on the sample and a higher deposition rate can occur. [65]

During EBID, when the electron beam reacts with the adsorbed molecules, it dissociates them and the volatile part is desorbed. This localised loss causes a concentration gradient to form such that further adsorbed molecules migrate to replenish these areas. The distance that an adsorbed molecule can diffuse in a time, t is:

$$x = \sqrt{2Dt} \tag{2.18}$$

where, $D$ is the diffusion coefficient, which is described by the equation:

$$D = a_0^2 \cdot v_d \cdot e^{-\frac{E_{diff}}{kT_s}} \quad (cm^2/s) \tag{2.19}$$

where, $a_0$ is the jump distance, $v_d$ is the jump attempt frequency and $E_{diff}$ is the activation energy for the surface diffusion. [62] The model of Koops et al. [65] did not consider the effects of surface diffusion. However, as can be seen from equation (2.18), surface diffusion can play a significant role in the deposition process. Therefore, Hoffman et al. [67] produced a more complete model of the deposition process, such that:

$$R = \frac{dN}{dt} = g \cdot F\left(1 - \frac{N}{N_0}\right) - \frac{N_0}{\tau} - q \cdot N \cdot f + D \cdot \nabla^2 \cdot N \tag{2.20}$$

where, $\nabla$ is the Laplacian operator of the number of adsorbed molecules. Within this equation the first three terms are identical to those in equation (2.13), while the fourth term includes the effects of surface diffusion. As such this equation includes both possible molecule supply mechanisms and is accepted as the most complete description of the EBID process.

In conclusion equations (2.10) to (2.20) may be used to show that in EBID, the mass transport of the precursor is controlled by the localised partial pressure, the temperature of the precursor and the sample and the desorption activation energy of the precursor.

### 2.5.4 Electron-Solid Interactions

When a primary electron beam impinges on a solid surface, it undergoes a series of complex interactions with the sample. These interactions result in either elastic or inelastic scattering events, which can alter the primary electron (PE) energy and trajectory and impart energy into the solid. In elastic scattering the PEs transfer less than 1 eV of their energy to the solid and deviate from their original path by 2° - 5°. In inelastic scattering the PEs transfer an energy up to their entire energy to the solid and deviate by ~0.1°. There are also many different types of inelastic scattering including phonon, plasmon and secondary electron (SE) excitation, continuum X-ray generation and ionisation of the inner shells of the atoms in the substrate. The overall effect of elastic and inelastic scattering is that they limit the distance that an electron beam can travel in a solid. This region is known as the interaction volume and is dependent on both the beam energy and the atomic number of the substrate.

When an electron beam scatters within a solid, a number of electrons may be scattered back out of the specimen and can play a role in the EBID process. These electrons take two forms, the first have energies below 50 eV and are known as secondary electrons, while the second type have energies greater than 50 eV and are known as backscattered electrons (BSE). BSEs are generated by multiple elastic scattering events and retain 60 to 80% of the PE beam energy, which means that they can escape from depths of up to several micrometers. The exact depth that they can escape from depends on the substrate and increases with decreasing atomic number. [62,68,69]

Secondary electrons are produced by inelastic scattering and take two forms. The first are known as $SE_I$ and are produced by scattering of the PEs, while the second type are known as $SE_{II}$ and originate from electrons in the entire interaction volume including BSEs. The energy of SEs follows the energy distribution shown in Figure 2.22, with more than 90% of SEs being emitted with energies below 10 eV. This graph also shows how the energy distribution for insulators is much smaller than it is for metals. Secondary electron emission is very sensitive on the surface layers of a substrate because the electrons are subject to inelastic scattering and energy loss during their travel through the sample. As such the probability that a SE will escape from the sample surface decreases exponentially with the depth at which it is generated. The maximum escape depth of SEs has been found to be approximately five times the mfp of SEs, which has been found to be equal to ~1 nm for metals and ~10 nm for insulators. [68, 69]

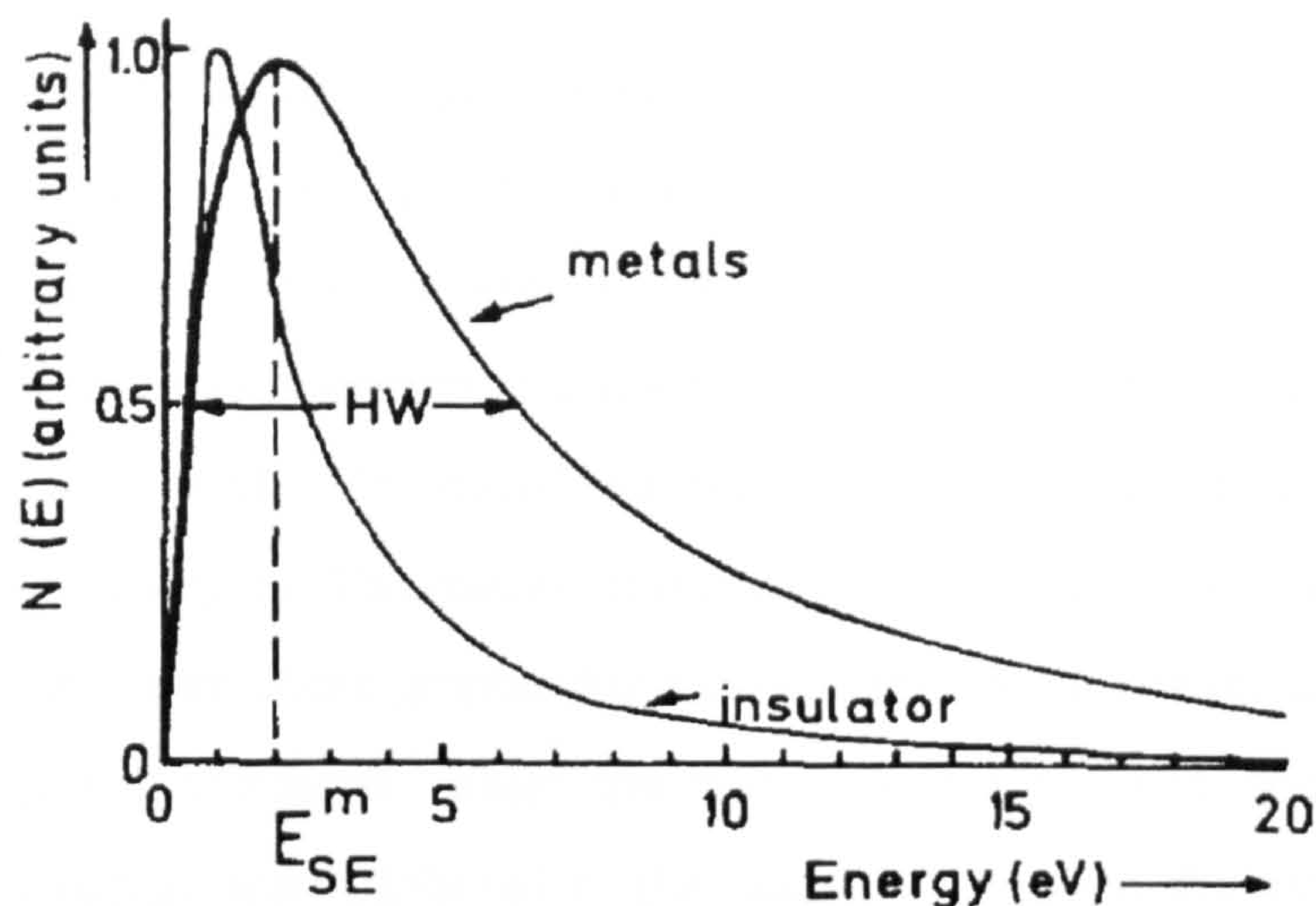


**Figure 2.22.** Energy distribution of secondary electrons from metal and insulator surfaces. [69]

The amount of $SE_I$ and $SE_{II}$ that are generated are not equal because BSEs are more efficient at generating SEs than PEs. This is because the PEs enter the sample perpendicular to its surface and travel through the region from which SEs can be emitted quickly without significant scattering. Meanwhile, BSEs approach the surface at much shallower angles so their path through the escape depth is longer. This means greater amounts of scattering and SE generation can occur. BSEs are also more efficient at generating SEs because they have a lower energy and so are more likely to transfer kinetic energy to the weakly bound sample electrons allowing them to be ejected as SEs. Typically, the ratio of $SE_{II}$ to $SE_I$ has been found to be of the order of three to four. [68,69]

In the earliest studies of EBID it was assumed that only PEs induced the deposition process. However, research into the resolution limits and growth process of EBID, in which the growth of single dots has been examined, has shown that the base diameter of the dots always exceeds that of the electron beam. Furthermore, it has been found that the diameter of these dots initially increased with time before reaching a constant diameter with a value that is approximately twice that of the mfp of SEs in the material. Therefore, it is now assumed that both PEs and SEs contribute to the EBID process. [70-73]

This research may be understood more clearly by considering the work of Kohlmann-von Platen et al. [70] who investigated the effects of deposition time, beam voltage and precursor temperature on the growth rate of tungsten needles deposited using a SEM and the precursor $W(CO)_6$. Initially, the effects of different deposition times and precursor temperatures on the

height and width of the needles was investigated. The resulting data is shown in Figure 2.23 (a) and (b) respectively. These graphs show that the growth rate is higher for short times than for long times and that the growth rate increases with precursor temperature. The increasing growth rate with precursor temperature was attributed to an increasing gas flux. Kohlmann-von Platen et al. [70] repeated this experiment for a constant precursor temperature and different beam energies. The results of this experiment are shown in Figure 2.23 (c) and (d). As can be seen from these graphs, for a given time, as the beam energy was increased the deposited height increased, while the width decreased. The decreasing width with increasing beam energy was attributed to the decreasing size of the electron beam and the fact that it is easier to focus the beam at higher energies. It can also be seen from these graphs that the width of the needles increased with time, which indicates that the growth of these needles is due to SEs produced by the PE beam within the tip of the deposit.

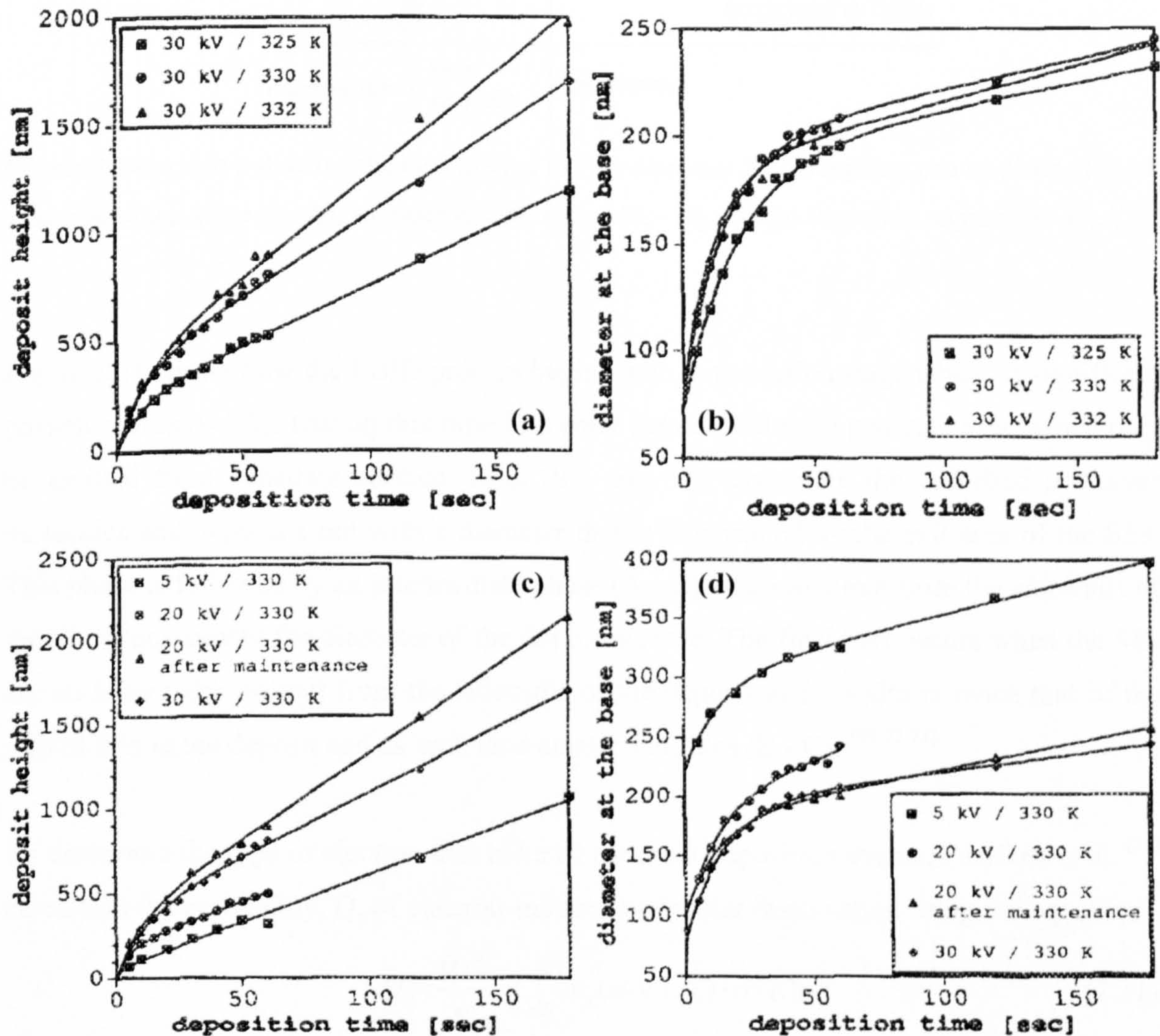


**Figure 2.23.** Experimentally measured **(a)** height h(t) and **(b)** base diameter b(t) for various precursor temperatures and (c) height h(t) and (d) base diameter b(t) for various beam energies of tungsten needles as a function of deposition time. [70]

The easiest way to separate out the contributions of primary, secondary and backscattered electrons to the EBID process is to use Monte Carlo simulations to simulate the EBID process and to then compare the results of the simulations to experimental results gained using similar conditions. As such Silvis - Cividjian et al. [72,73] developed a quantitative model to simulate the effect of SEs on the spatial resolution of EBID dots and found that the growth process could be split into three parts as shown in Figure 2.24.

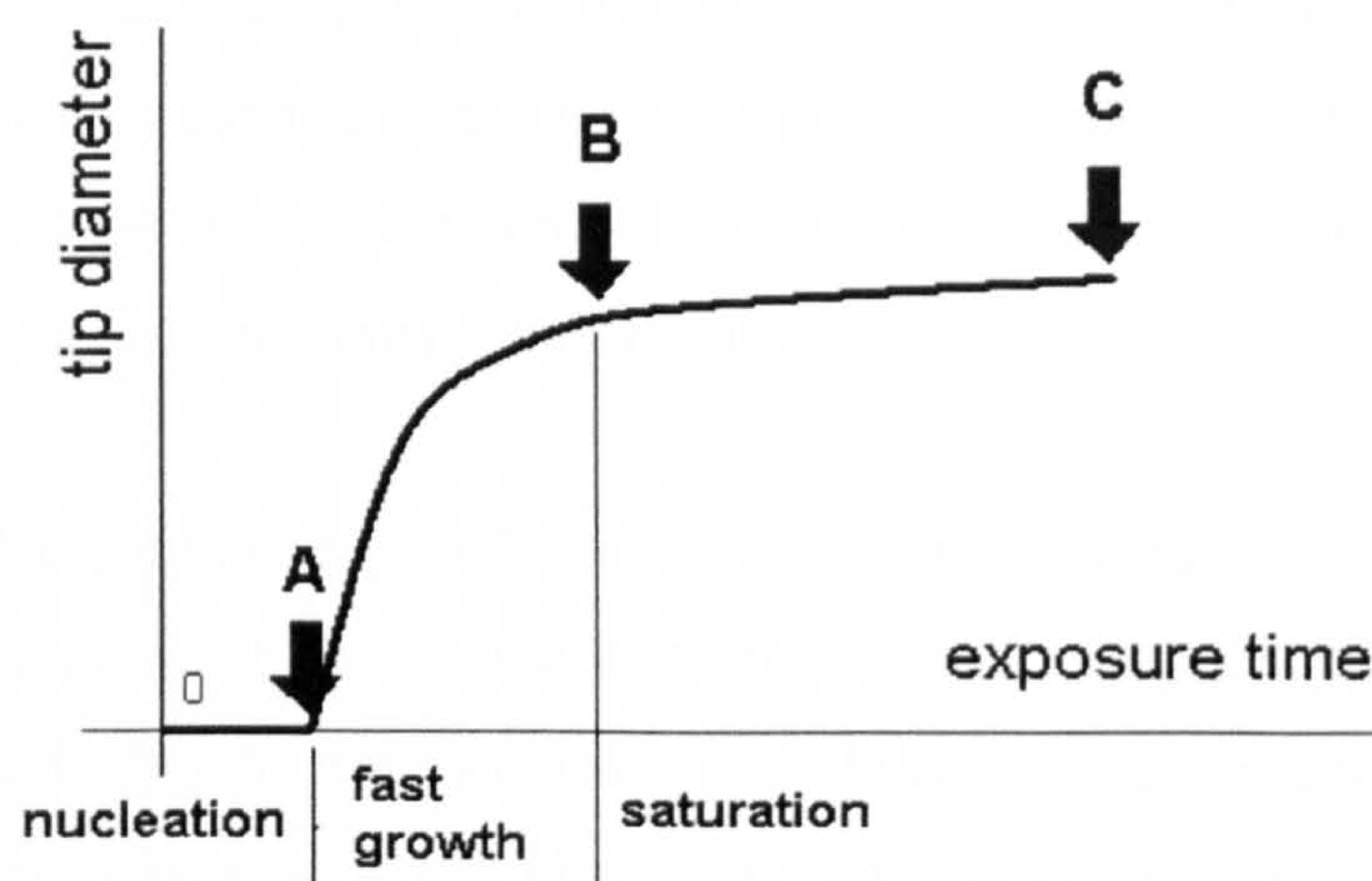


**Figure 2.24.** A curve showing the evolution of the dot diameter. Three regimes can be distinguished: the nucleation stage (0 - A), an intermediate regime (A – B) and the saturation regime (B – C). [72]

Figure 2.24 shows how the EBID process begins with a nucleation stage when no significant growth occurs (0 - A). During this time PEs enter the substrate and generate SEs, which may be emitted from substrate surface. Both PEs and SEs dissociate the adsorbed precursor molecules and deposit a dot with a diameter that is determined by the exit area of the SEs. This phase is followed by an intermediate phase (A - B) when SEs exit from the sidewalls of the tip, which causes the diameter of the dot to increase. The final part occurs when the SEs are no longer able to exit from the sidewalls of the deposit as its width is twice that of the mfp of SEs in the deposit and as such its diameter saturates (B - C). [68,72,73]

To determine the type of electron that induced the most deposition events, Fowlkes et al. [74] calculated the probability, Q, of electron-induced molecular dissociation using the equation:

$$Q = \frac{\theta \cdot S_\rho}{n_{PE}} \cdot \int_{E_i}^{E_f} n_x(x, y, t, E) \cdot \sigma(E) dE \tag{2.21}$$

where, $n_x(E)$ is the electron energy distribution of the particular electron species, $x$ = $SE_I$, $SE_{II}$, BSE or PE, $\sigma(E)$ is the dissociation cross section, $\theta$ is the percentage surface coverage

of adsorbed precursor molecules and $S_p$ is the atomic surface site density. As can be seen from this equation, the electron energy distribution of each of the types of electron species investigated are a function of nanopillar shape and size and continuously change during the growth. The results of the calculations showed that the probability for deposition was highest for the PEs (Q = 0.183) and $SE_I$s (Q = 0.155) than it was for $SE_{II}$s (Q = 0.1) and BSEs (Q = 0.019). Simulation of the growth process using these values showed that the effective current density of $SE_{II}$'s and BSEs emerging from the substrate was also much lower than it was for PEs and $SE_I$s because they emerge over a much larger area. This leads to the conclusion that both the PEs and the $SE_I$s induce the vertical growth of the pillar, while the BSEs and the $SE_{II}$s influence the radial broadening of the structures. [74]

Fowlkes et al. [74] also simulated the effects of beam energy on the deposition process and found that the contribution of PEs to the vertical growth increased with decreasing beam energy. This was attributed to the increasing probability of dissociation of the precursor molecules at low beam energies. It was also found that the PEs contributed significantly to the nanopillar growth for all beam energies, while $SE_I$s only contributed significantly for beam energies between 2 and 5 keV as shown in Figure 2.25 (a). Fowlkes et al. [77] also investigated the role of SEs with time as shown in Figure 2.25 (b) and found that the contribution of the SEs increased with time. This was attributed to the continuously increasing surface area of the deposit allowing more SEs to be emitted. [74]

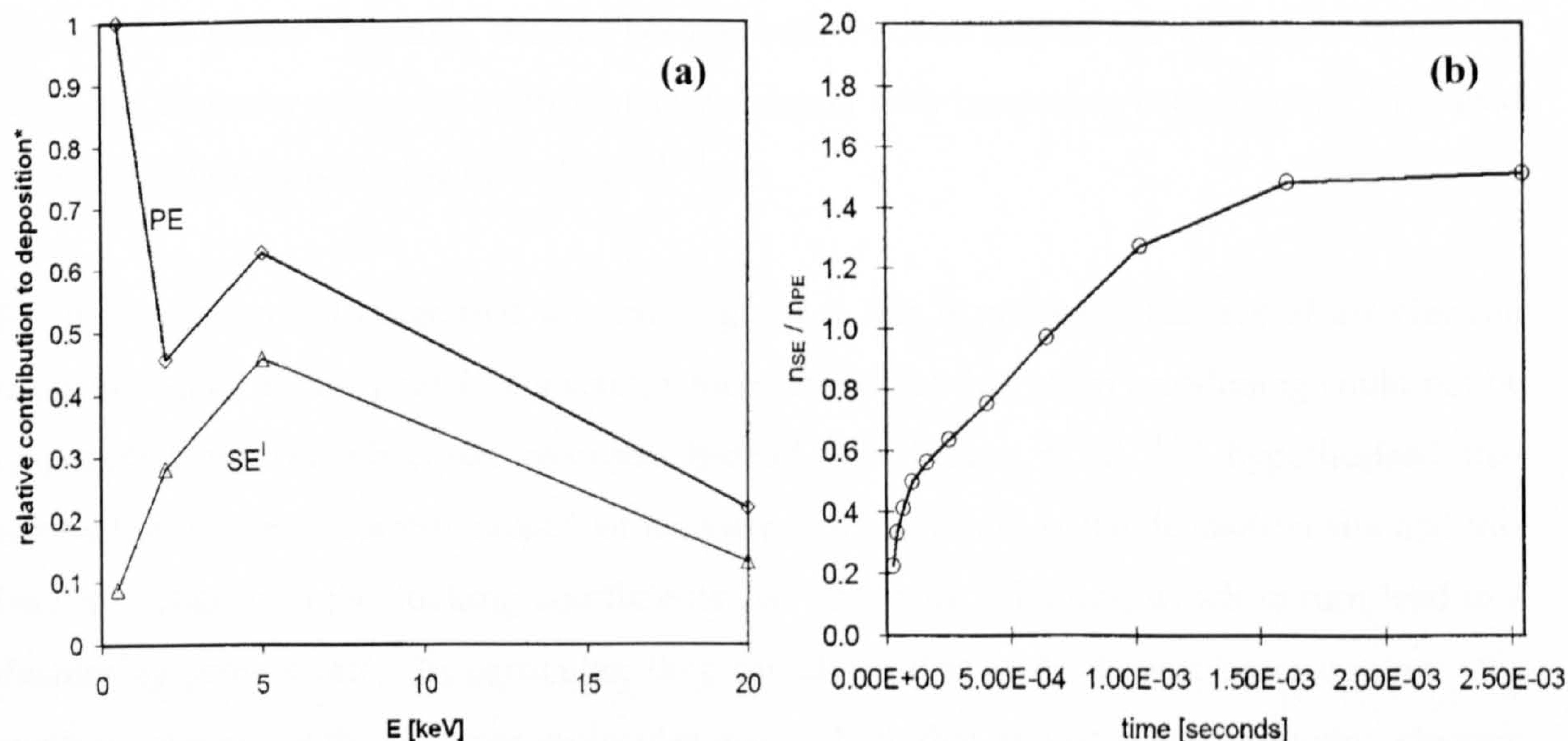


**Figure 2.25. (a)** Percentage relative contribution to vertical nanopillar growth for PE and $SE_I$. **(b)** Simulated ratio of the number of tungsten atoms deposited by $SE_I$s and $SE_{II}$s to the total number of tungsten atoms deposited by PEs. [74]

## 2.6 Effects of Experimental Parameters on EBID

The main areas of focus of EBID research are the optimisation of the growth rate and the resolution. Both of these parameters are affected by the experimental set-up, which includes the beam voltage and current, the scanning parameters, the carrier or background gas and the substrate temperature. The following sections shall review the effects of the beam current and the substrate temperature on the deposition rate, structure and resistivity of the deposits, which is relevant to the experimental work in this thesis.

### 2.6.1 Effects of Beam Current

To investigate the effect of the electron beam current on the deposition rate Shiffmann et al. [75] used the contamination in a SEM chamber, which consists of $O_2$, $H_2$, $H_2O$, CO and hydrocarbon molecules from the vacuum pumping oils to deposit a series of carbon tips for beam currents between 3 and 300 pA. The tips were deposited in spot mode using a beam energy of 30 keV for two minutes and the resulting data for tip lengths, diameter, cone lengths and deposited volume are shown in Figure 2.26. This figure shows how the dependence of the tip growth on the beam current can be split into two regimes. During the first regime, for beam currents below 30 pA, the tip length decreases, the tip diameter increases and the cone length remains constant as the beam current increases, which leads to an overall increase in the deposit volume. When the beam current was increased to values in excess of 30 pA (2$^{nd}$ regime), the tips became entirely cone shaped and the length decreased, while the diameter remained approximately constant with increasing beam current. This lead to an overall decrease in the tip volume. [75]

For the beam current range that was investigated in this experiment, the size of the electron beam remained approximately constant, which meant that that beam broadening could not be responsible for the observed changes. Instead Schiffmann et al. [75] hypothesised that increasing the beam current caused an increase in temperature at the deposition site and this lead to a change in the sticking coefficients and adsorbate lifetimes, which in turn lead to a decreasing growth rate. In particular, they calculated that at the lowest beam currents, the surface coverage with precursor molecules was so high that almost every impinging electron caused the deposition of one carbon atom, while at the highest currents, the value for thermal desorption increased such that one carbon atom was deposited for every 250 PEs. [75]

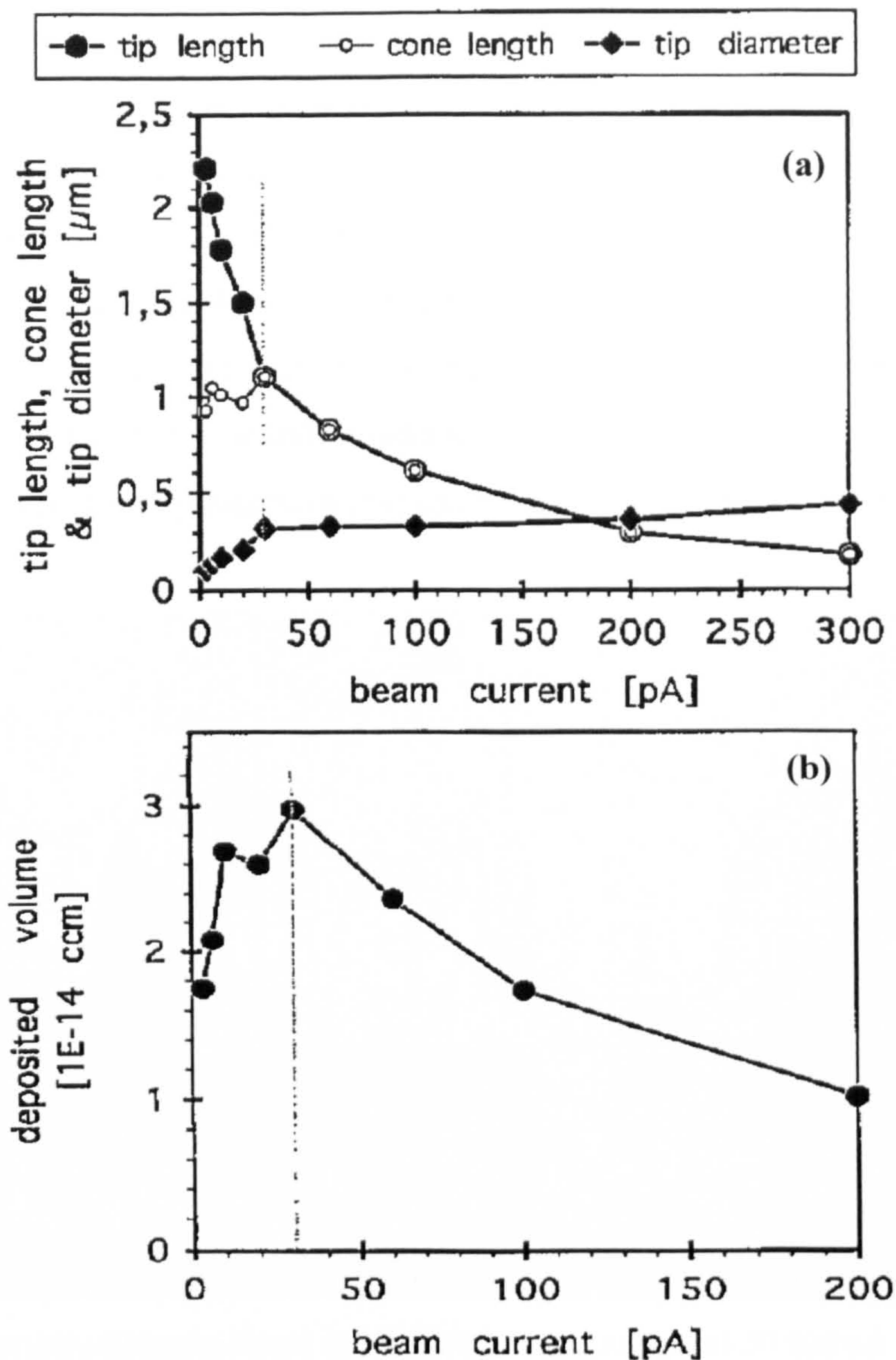


**Figure 2.26. (a)** Tip length, tip diameter and cone length and **(b)** deposited volume, as a function of the beam current for a beam voltage of 30 keV and a deposition time of 2 minutes. [75]

A more comprehensive investigation into the effects of the electron beam current on the deposition rate and resolution of EBID structures was carried out by Beaulieu et al. [76] In this experiment an ESEM was used to deposit platinum fibres and lines on a p-type silicon substrate using the precursor $C_2H_5Pt(CH_3)_3$ for an electron beam energy of 30 keV and beam currents of 60 - 20,000 pA. Once the structures had been fabricated, they were analysed by taking SEM images at 90° to the substrate and measuring the height and base diameter of the fibres and the height and base width of the lines at their mid-point. The growth rate was then calculated by dividing each of these values by the total deposition time. This analysis showed that the growth rate increased significantly with the beam current such that

increasing the current from 100 to 5400 pA caused the growth rate to increase from 0.07 to 0.55 μm/minute. This result is the opposite of that found by Schiffmann et al. [75] Within this experiment it was also found that increasing the beam current caused the base diameter of the fibres and the linewidth of the line deposits to increase less significantly (Figure 2.27). This behaviour was attributed to the higher beam currents having a larger beam diameter so that the SEs, which can contribute to the deposition process, are produced from a larger substrate area and result in a lateral broadening of the structure. Increasing the beam current also produces more primary electrons that can be involved in the deposition process. [76]

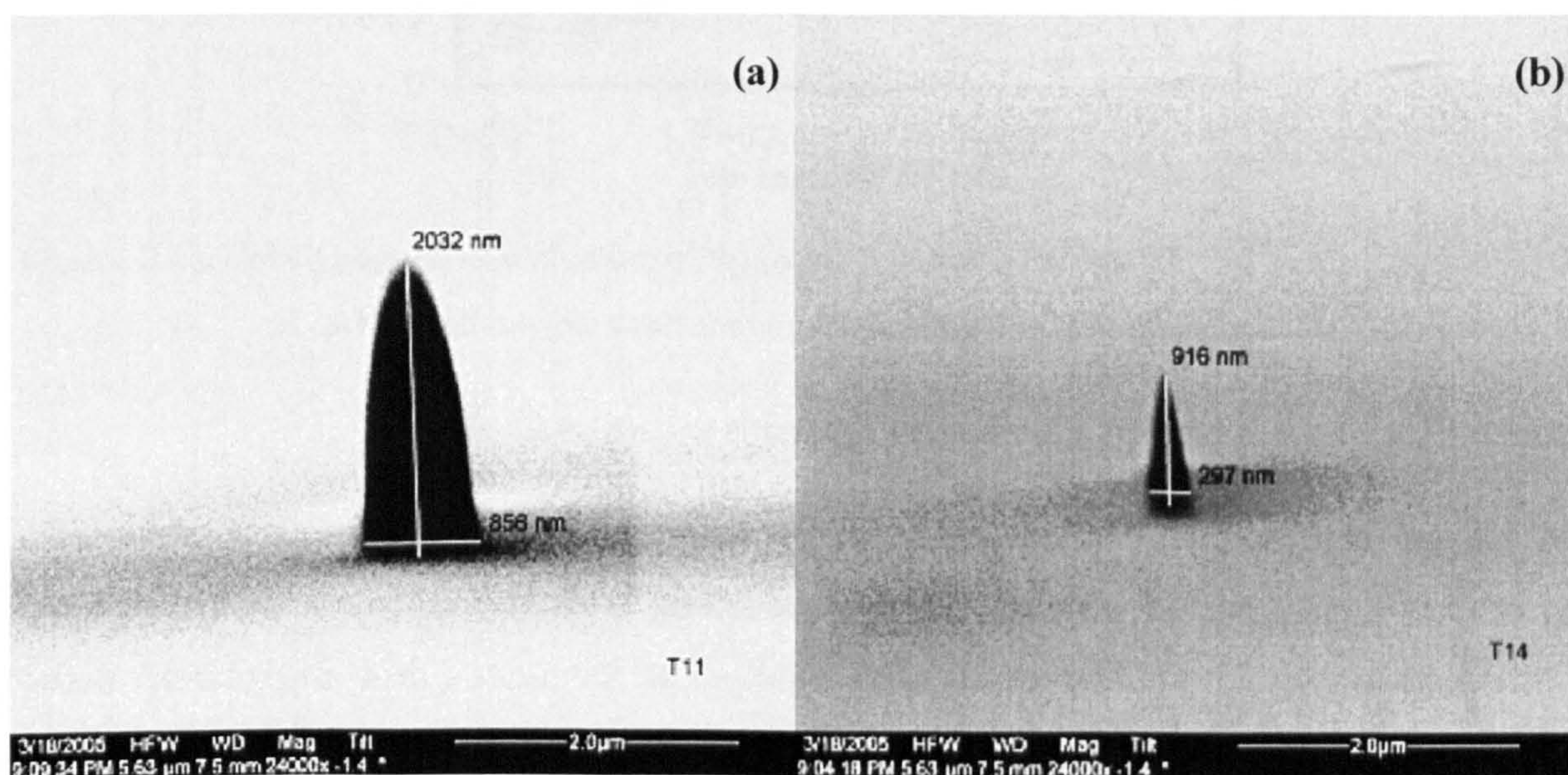


**Figure 2.27.** Platinum fibre deposited at 30 keV for 5 minutes at **(a)** 20,000 pA and **(b)** 1,500 pA.[76]

To investigate the effects of the beam current on the structure of EBID tips, Utke et al. [77,78] deposited cobalt tips from the precursor $Co_2(CO)_8$ in a SEM for an electron beam energy of 25 keV and electron beam currents between 20 pA and 3 μA. The tips were deposited onto silicon oxide wafers to allow for the resulting structures to be analysed using energy dispersive X-ray (EDX) spectroscopy in a SEM and standard copper TEM grids to allow for the resulting structures to be analysed using selected area electron diffraction and bright and dark field imaging in a TEM. The results of the EDX measurements as a function of different tip lengths are shown in Figure 2.28. As can be seen from this graph the amount of cobalt in the deposits increased from 12 at. % (atomic percentage) at 20 pA (lower than the metallic content of the precursor), with increasing beam current and tip length up to a maximum of 80 at. %, which is equal to the cobalt content of the precursor. [77,78]

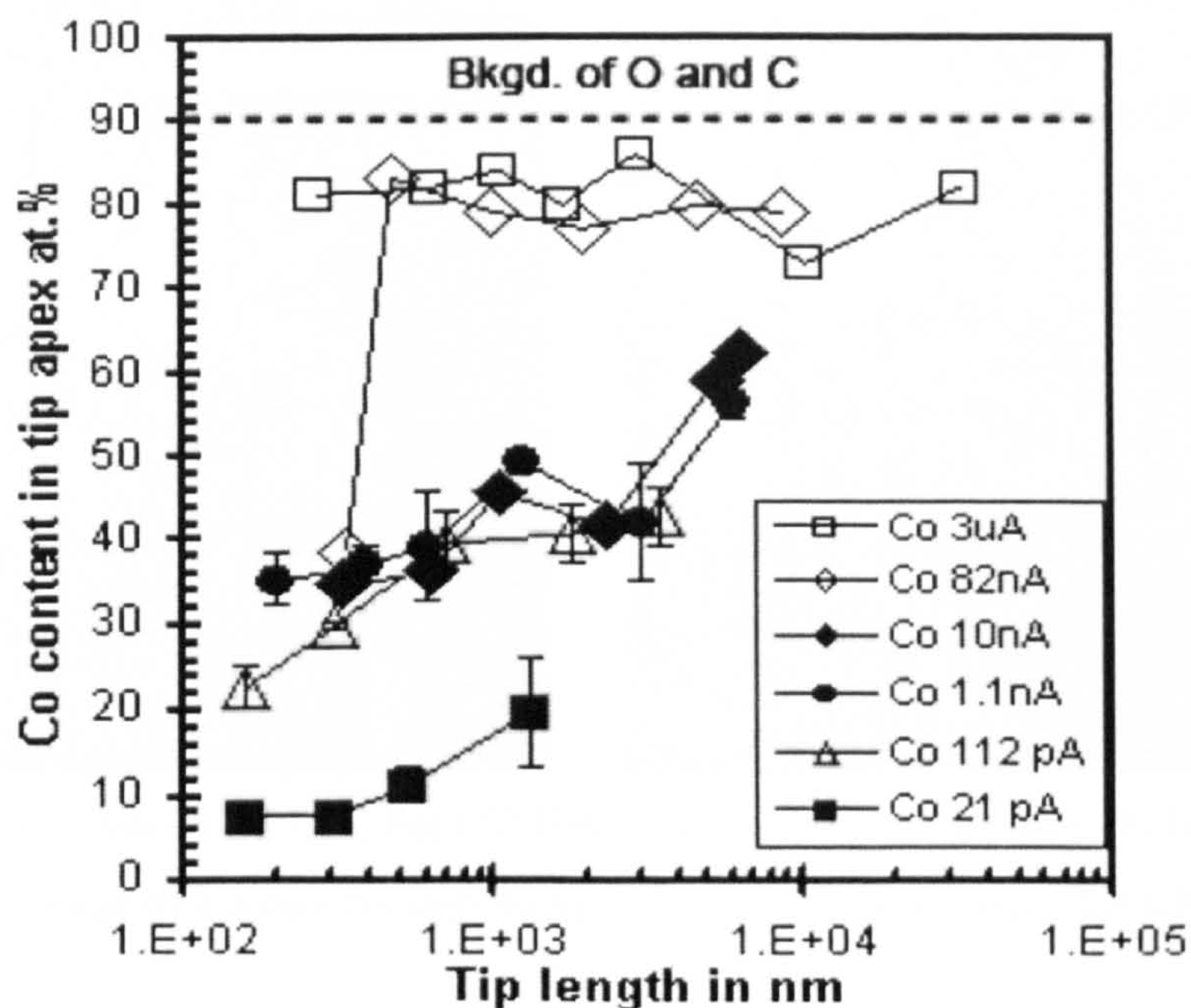


**Figure 2.28.** Cobalt content as a function of tip length and beam current. The 10 % background level of carbon and oxygen measured on the substrate is also indicated. [77]

TEM of the tips showed that their structure was dependent on both the beam current and the deposition time. The tips that were deposited for beam currents below 1 nA consisted of cobalt nanocrystals with a diameter of 1 –2 nm embedded in an amorphous carbon matrix, while the tips deposited using greater beam currents with lengths in excess of 1 μm consisted of a carbon and oxygen rich base core with cobalt crystals and a cobalt rich crust with a textured whisker like structure. As the beam current was increased the cobalt crystals in the base core increased up to 40 nm in size, while the whiskers in the crust also increased and caused the surface to become corrugated. The base core was also found to orientate towards the precursor source, while the crust remained symmetrical around the electron beam axis as shown in Figure 2.29 (a). As the beam current was increased to values in excess of 82 nA, voids formed within the structure and were attributed to the growing tip stopping the precursor from being adsorbed behind the tip. Finally, it was found that the tips deposited with a beam current of 3 μA had a whisker like structure that grew towards the precursor source. These deposits also had a flat top, which was attributed to a precursor-limited regime as shown in Figure 2.29 (b). During these investigations it was also found that for beam currents greater than or equal to 10 nA, the apex of the tips became larger than the electron beam diameter, which indicates that an additional decomposition mechanism to the one induced by electrons was present. [77,78]

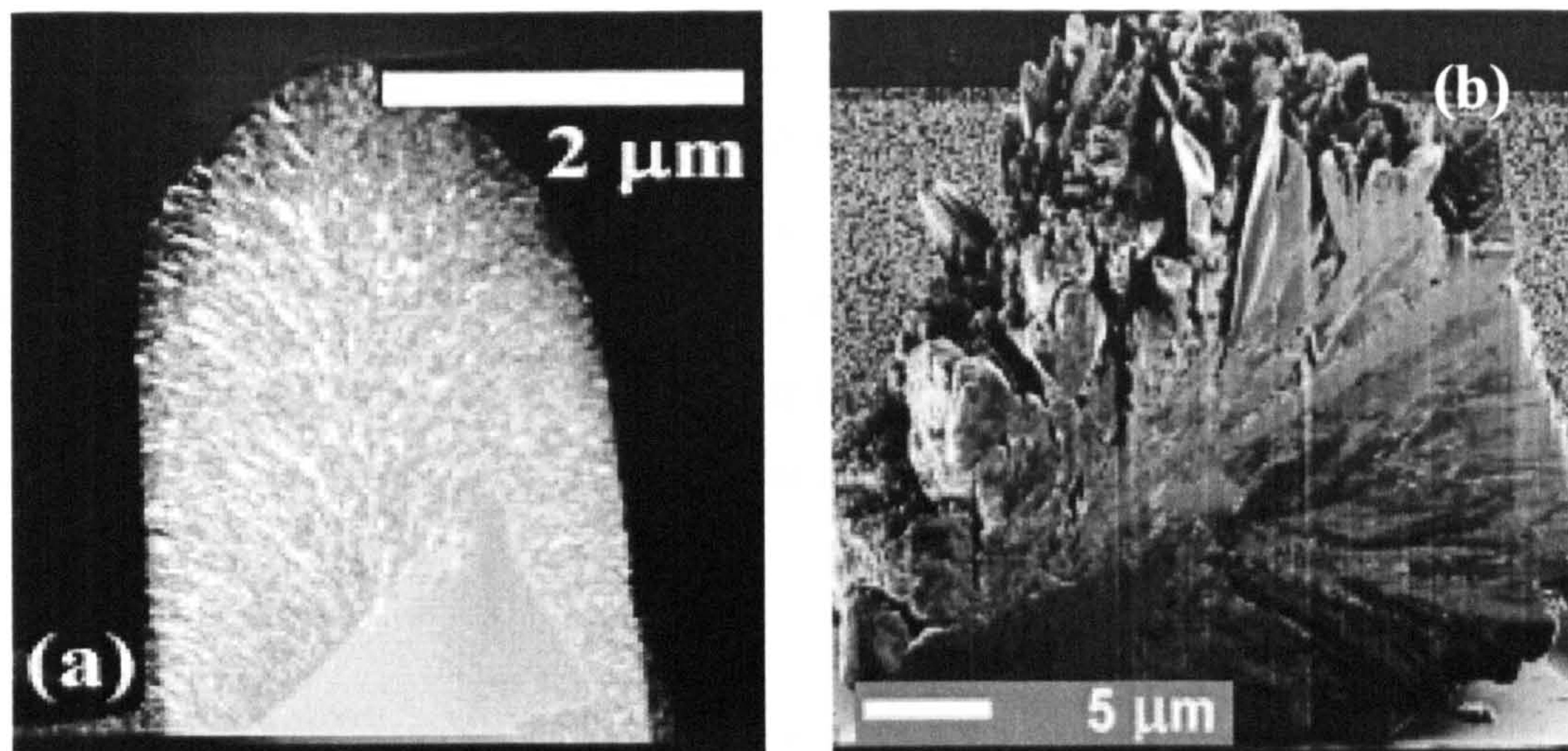


**Figure 2.29. (a)** High-resolution dark field STEM image of a typical tip deposit. **(b)** Backscattered electron image of a cobalt tip deposited with a 3 μA beam current for 600 s. [77]

These results lead Utke et al. [77,78] to propose that heating of the substrate and the tip by the electron beam influenced the deposition process. It was found that initially substrate heating was important and the cobalt content of tips increased as the beam current and hence the substrate temperature increased. The temperature rise for beam currents below 100 nA was found to be insignificant and the deposition process was said to be electron flux limited, while a beam current of 3 μA was predicted to raise the substrate temperature by 23°C so that an auto-catalytic deposition process occurred resulting in a higher cobalt content. As the tips increased in length, Utke et al. [77,78] suggested that the observed changes were due to the heating from the electron beam becoming confined within the tips so that the precursor molecules changed from electron flux limited to thermally activated. [77, 78]

Weber et al. [79] investigated the effects of beam currents between 1 and 2,000 pA on the structure of EBID tips deposited in a SEM using the precursors $Me_2Au(acac)$, $Me_2Au(tfac)$, $Me_2Au(hfac)$, $Cu(hfac)_2$, $Mo(CO)_6$ and $CpPtMe_3$. To allow for high resolution TEM examination of the structures, the tips were deposited at 45° on standard copper grids, while to allow for EDX analysis, arrays of 20 x 20 tips were deposited in a 1 $\mu m^2$ area so that scattering of the electrons caused the tips to merge and form a solid block of deposited material. High resolution TEM, showed that tips deposited using beam currents below 20 pA had a completely amorphous structure and a smooth surface, while tips deposited using beam currents in excess of 60 pA had an irregular shape and a polycrystalline structure with metal crystallites up to 4 nm in diameter embedded in an amorphous matrix. The tips

deposited with the higher beam current were also found to have a bright core region embedded in a faint material. EDX showed that increasing the beam current caused the metal content to increase and the carbon content to decrease. This behaviour is shown for the $Mo(CO)_6$ precursor in Figure 2.30 (a) and for the $CpPtMe_3$ precursor in Figure 2.30 (b). For all of the precursors investigated it was found that the percentage of metal in the deposit increased until it was equal to the amount of metal in the precursor. [79]

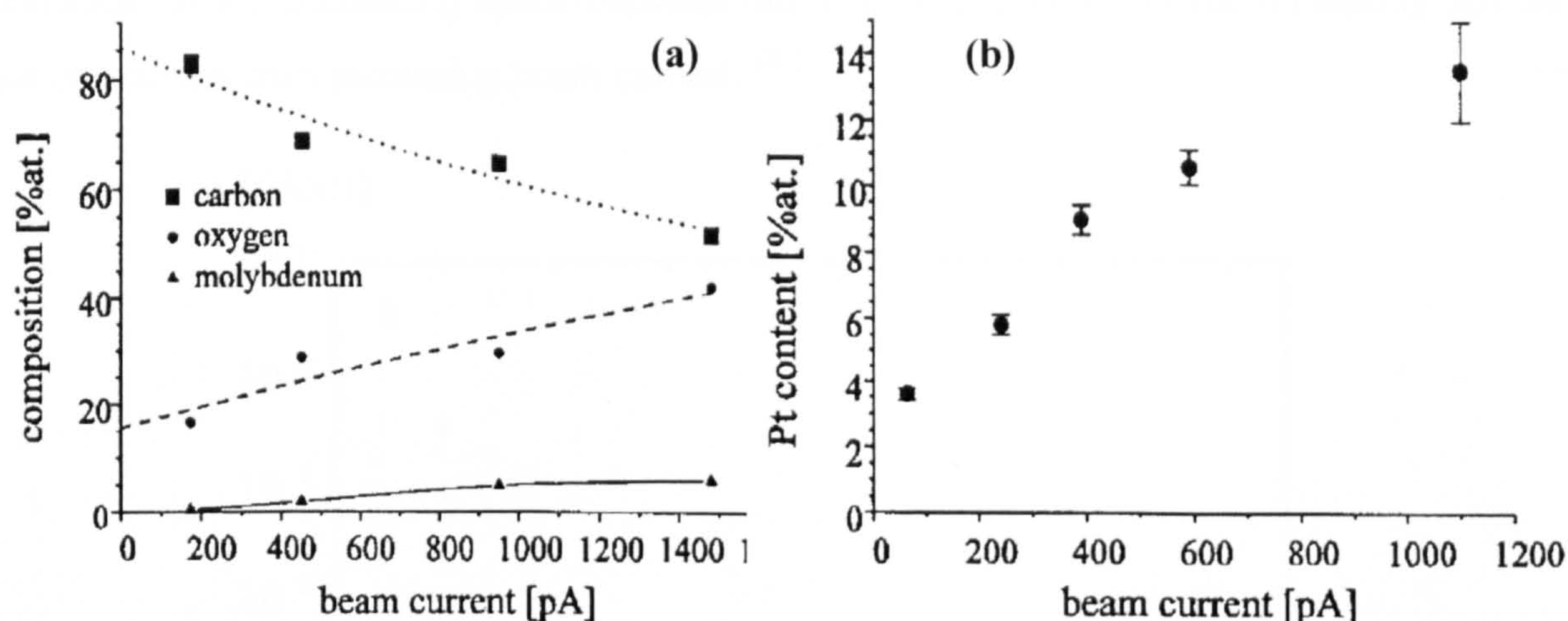


**Figure 2.30.** Composition of material deposited at 20 keV from **(a)** $Mo(CO)_6$ and **(b)** CpPtMe3. [79]

Koops et al. [80] also studied the effects of beam current on the structure of deposits made using the precursors $Me_2Au(acac)$ and $Me_2Au(tfac)$ in a SEM. TEM of tips deposited onto copper grids showed that in agreement with the results of Weber et al. [79] the deposits consisted of nanometer sized crystallites embedded in an amorphous matrix. The diffraction patterns of the crystallites showed that they had an elementary lattice cell size of 0.401 nm, which suggests that the crystallites consisted of gold that had been compressed slightly by surface tension forces. It was also found that the amorphous matrix in which the crystallites were embedded in was mainly carbon. Furthermore, this analysis showed that as the beam current was increased the crystallites became more closely packed and increased in size. [80]

The chemical composition of these structures were analysed using EDX and it was found that increasing the beam current caused the gold content to increase until it was equal to the gold content in the precursor. This indicates that at high beam currents, the electron beam decomposes and excites a high number of adsorbed molecules. The thermal conductivity of the substrate means that the substrate then quickly cools these molecules so that they don't have time to form stable agglomerates. The increasing gold content was attributed to the

increasing beam current being able to separate out increasing amounts of the volatile methyl groups from the deposit, so that there was less carbon incorporated into the deposit. During this experiment Koops et al. [80] also investigated the effects of beam current on the conductivity of the deposits using two point electrical measurements. It was found that increasing the beam current by one order of magnitude caused the resistivity of the deposits to improve by five orders of magnitude as shown in Figure 2.31. This improvement was attributed to the decreasing space between the metal crystallites and the increasing size of the crystallites with increasing beam current. [80]

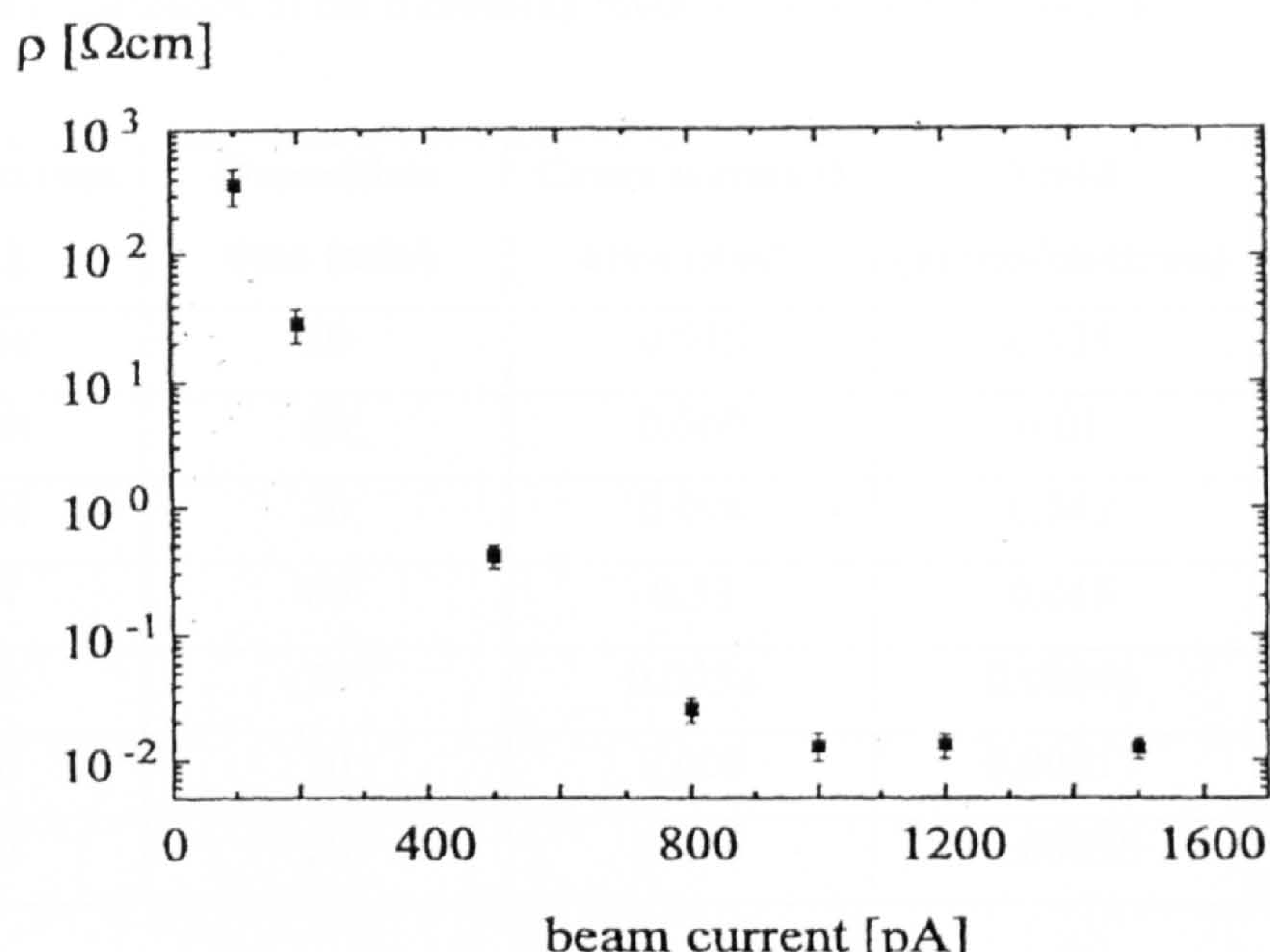


**Figure 2.31.** Plot of resistivity versus electron beam current for $Me_2Au(tfac)$. [80]

Weber et al. [80] also investigated the effects of beam current on the resistivity of their deposits which were described earlier. The deposition was carried out on $SiO_2$ substrates that had been prepatterned with a four-point measurement structure using UV lithography. The measurements showed that the conductivity increased with the beam current and was attributed to the increasing metallic content of the deposits. These measurements also showed that the deposits made with high beam currents had linear I-V characteristics and could withstand current densities up to $2 \times 10^6$ A/cm$^2$. Meanwhile, the deposits made with low beam currents had nonlinear I-V characteristics, which may be attributed to either Poole-Frenkel conduction or activated tunnelling. To determine which of these mechanisms is responsible for the observed characteristics it is necessary to carry out resistivity versus temperature measurements, which will be covered in section 2.6.5. [80]

Barry et al. [81] also used four point measurements to characterise platinum EBID wires. In this experiment the precursor $Pt(PF_3)_4$ was used to deposit a range of wires for beam currents between 0.6 and 46 nA onto a $SiO_2$ substrate at 10 keV in a dual beam focused ion beam (FIB) system. To accurately measure the size of the deposits FIB sectioning of the deposit was used to expose the cross sectional area midway along the deposits. Current-voltage measurements were taken on other deposits by passing a fixed current through the outer two contacts and measuring the voltage between the inner two contacts using a probe station. As shown in Table 2.1, the resistivity of the deposits decreased with increasing beam current and was again attributed to the increasing metal content of the deposits. [81]

| Beam current (nA) | Deposition time (min) | Cross sectional area ($\mu m^2$) | Yield (atoms/electron) | Resistivity ($\mu\Omega$ cm) |
|---|---|---|---|---|
| 0.604 | 20 | 0.045 | 0.038 | 113850 |
| 0.828 | 60 | 0.069 | 0.01 | 436 |
| 0.884 | 20 | 0.094 | 0.042 | 3600 |
| 2.84 | 60 | 0.38 | 0.016 | 641 |
| 3.00 | 20 | 0.0038 | 0.00046 | 178 |
| 13.0 | 20 | 0.006 | 0.00017 | 26 |
| 46.0 | 20 | 0.045 | 0.00036 | 33.3 |

**Table 2.1.** Deposition conditions, resistivities and yield of EBID platinum wires. [81]

### 2.6.2 Effects of Substrate Temperature

In 1995 Weber et al. [79] carried out the first investigation into the effect of substrate temperature on EBID by depositing a series of gold and molybdenum tips for substrate temperatures between 20 and 50°C from the precursors $Me_2Au(tfac)$ and $Mo(CO)_6$ respectively. The subsequent analysis showed that for both types of deposit the growth rate remained almost constant, while EDX showed that the chemical composition of the tips varied with temperature. In particular, the metal content of the gold tips increased with increasing temperature and reached approximately 70 at. % at 45°C, while the carbon content decreased to zero by 40°C as shown in Figure 2.32. In contrast, the metal content of the molybdenum tips actually decreased with increasing temperature. [79]

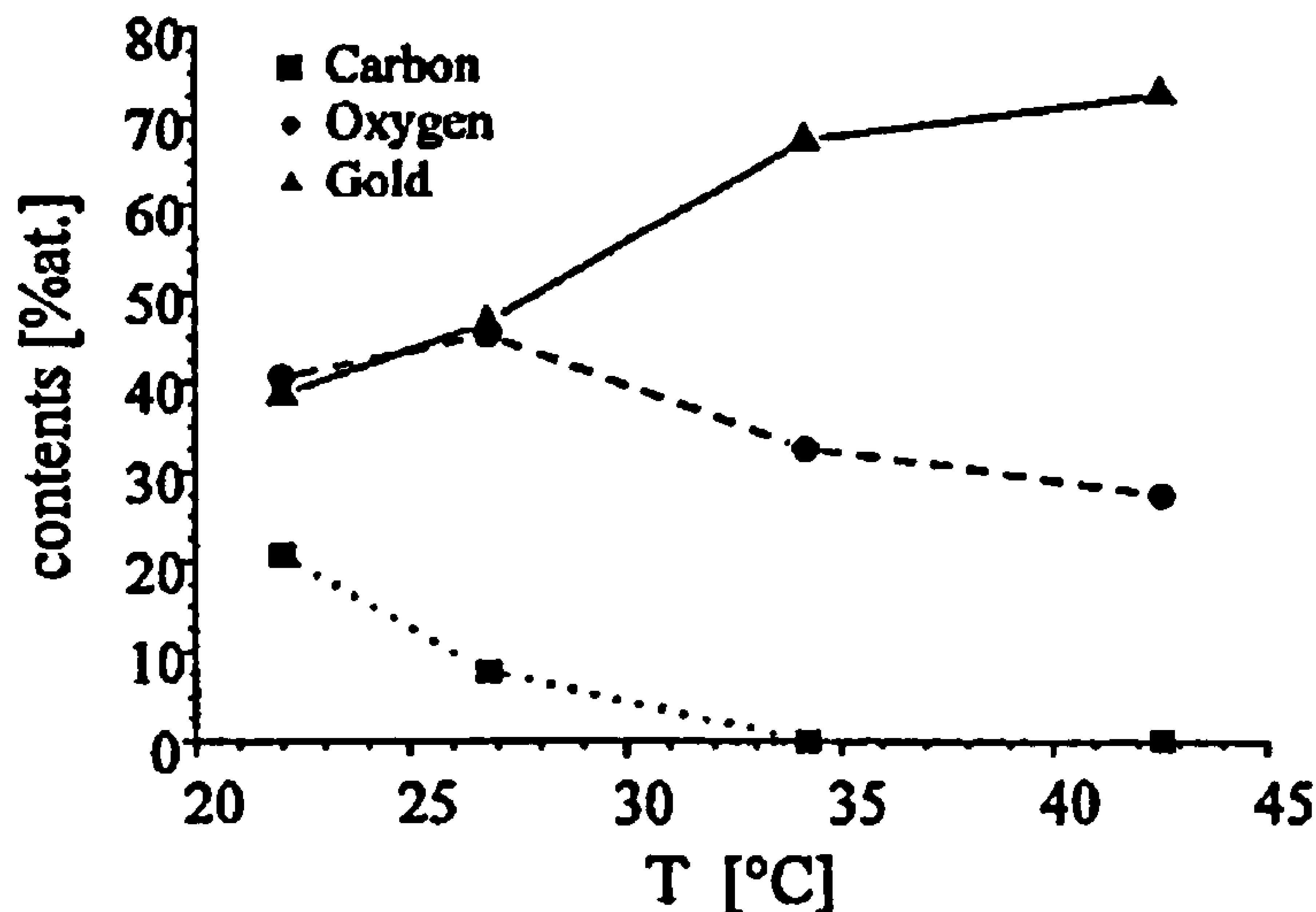


**Figure 2.32.** The effects of different substrate temperatures on the composition of gold tips deposited from the precursor Me2Au(tfac). [79]

Wang et al. [82] also studied the effects of substrate temperature on the growth of EBID platinum structures deposited using the precursor $Pt(PF_3)_4$. The deposits were made and analysed using AES in a custom designed vacuum system that was operated at 3 keV. Increasing the substrate temperature reduced the amount of phosphorous incorporated in the structures significantly, such that, as shown in Figure 2.33, the Pt/(Pt + P) ratio rose until at 120°C it reached Pt/P = 3. This Figure also shows how increasing the substrate temperature from 25 to 40°C nearly doubled the ratio. As the thermal decomposition of $PF_3$ from Pt occurs for temperatures above 80°C, this was attributed to local heating of the deposit by the electron beam in the irradiated region. [82]

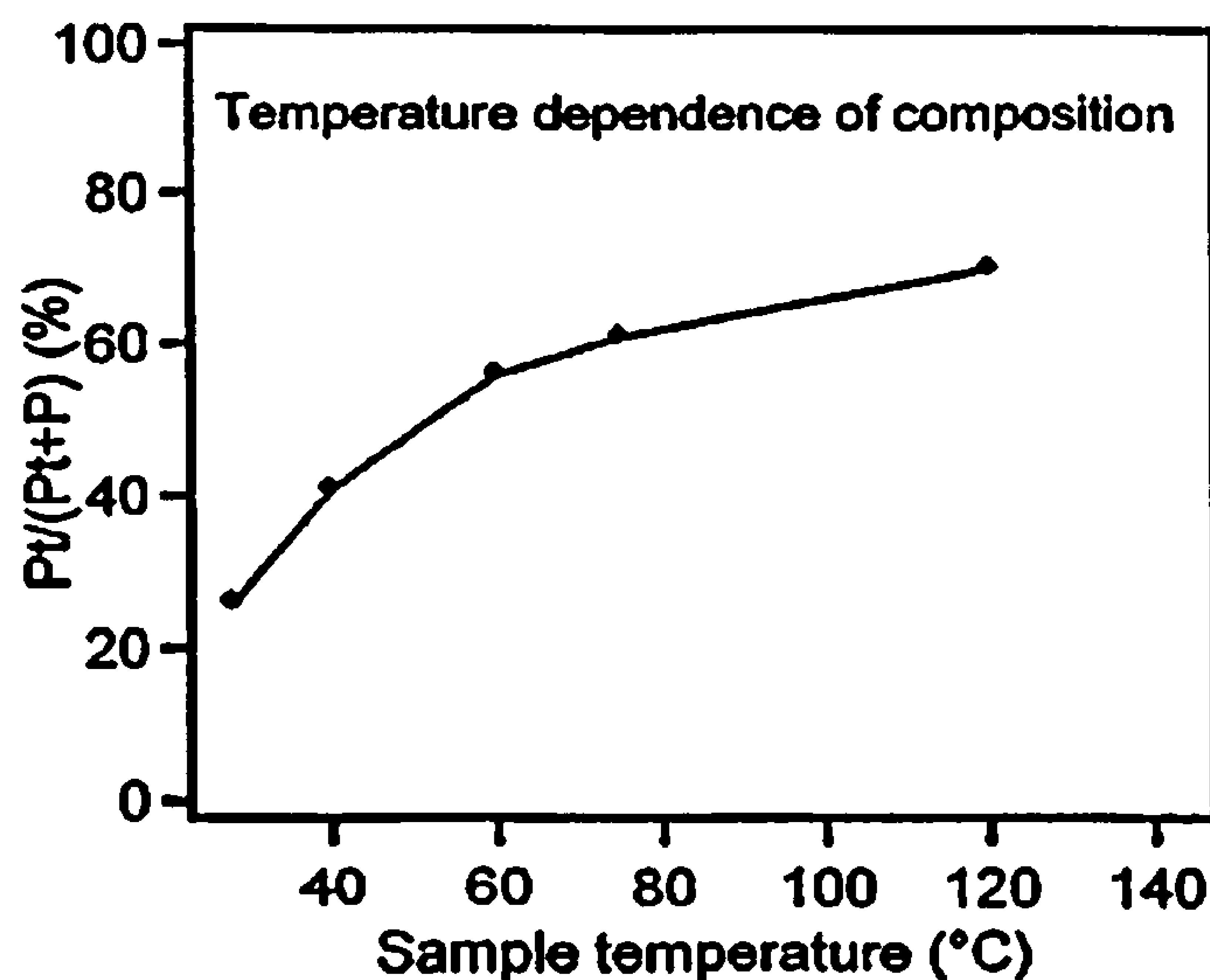


**Figure 2.33.** Fraction of the film comprising Pt formed by electron beam deposition of $Pt(PF_3)_4$ as a function of substrate temperature. [82]

Li et al. [83] carried out a more thorough investigation into the effects of substrate temperature on the growth rate and size of EBID dots in an attempt to explain the physical processes involved in EBID. The experiments were carried out using the precursor $WF_6$ in a SEM, which was equipped with a Peltier cooling stage that allowed for the temperature of the substrate to be varied between -30°C and +75°C. Initially Li et al. [83] carried out depositions for a range of different beam voltages, beam currents and substrate temperatures for a fixed deposition time of 60 s. The effects of changing the beam voltage and substrate temperature for a fixed beam current of 140 pA on the deposited volume are shown in Figure 2.34 (a) and the effects of changing the beam current and substrate temperature for a beam voltage of 20 keV on the deposited volume are shown in Figure 2.34 (b). These figures show how the growth rate increases with decreasing substrate temperature for all of the beam voltages and currents investigated. This result shows that the EBID process involves the dissociation of molecules adsorbed onto the surface of the substrate and is a function of the residence time of the adsorbed molecules, which follows an Arrhenius relationship. [83]

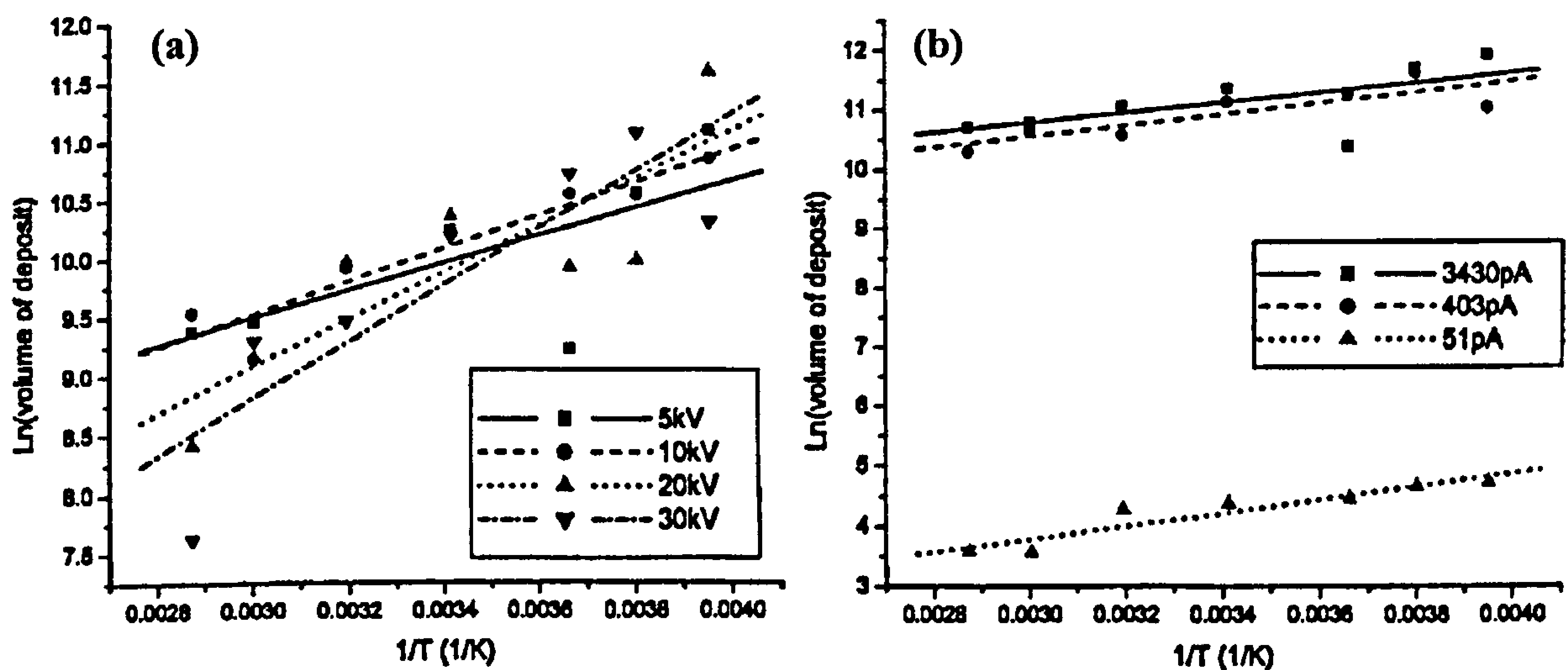


**Figure 2.34.** The natural logarithm of the deposited volume versus the inverse of the substrate temperature for **(a)** a beam current of 140 pA and beam voltages of 5, 10, 20 and 30 keV and **(b)** a beam voltage of 20 keV and beam currents of 51, 403 and 3430 pA. [83]

Li et al. [83] went on to calculate the desorption energies of the deposits using the slope of the Arrhenius plots in Figure 2.34 (a) and (b) and equations (2.16) and (2.18). The results of this analysis as a function of the different beam energies and beam currents investigated are shown in Figure 2.35 (a) and (b) respectively. As can be seen from these graphs, the desorption energies are in the range between physisorption (~0.01 eV) and chemisorption (~1 eV). This result shows that the adsorption – desorption process plays a significant role in

EBID and also supports the earlier assumption that the dissociation of the precursor occurs with the layer of the molecules adsorbed on the substrate rather than in the gas phase. [83]

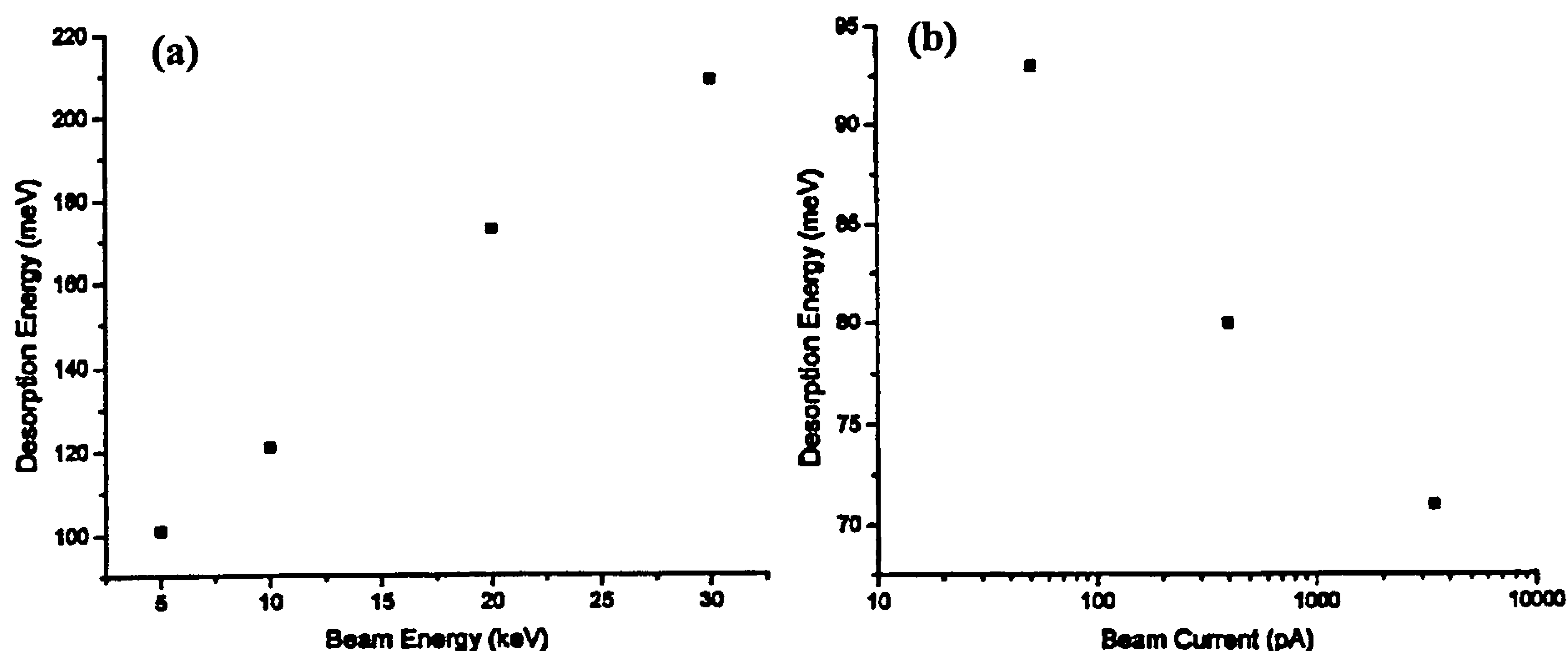


**Figure 2.35.** Variation of the desorption energy with the **(a)** beam energy and **(b)** beam current. [83]

To explain these results Li et al. [83] considered the role that the SEs play in the EBID process. As described in section 2.5.3 and 2.5.4, the SEs can both remove the adsorbed molecules, which is unfavourable to the deposition process and dissociate them, which is favourable. Therefore Li et al. [83] thought that there must be a competition between the desorption and dissociation processes and used this to explain why the activation energy for EBID decreases with the beam current and increases with the beam energy. In particular, it was found that when the SE yield was low, which occurs for small beam currents or high beam voltages, electron stimulated desorption (ESD) has little effect on determining the mean lifetime of the adsorbed precursor molecules and thermal desorption dominates the EBID process. When the SE yield is high (i.e. low beam voltage and high beam current) ESD becomes more dominant than thermal desorption. [83]

During this experiment Li et al. [83] also measured the size of each deposit. Figures 2.36 (a) and (b) show the variation in the base width and height respectively for different beam currents and substrate temperatures, while Figures 2.36 (c) and (d) show the variation in width and height for different beam voltages and substrate temperatures. These results show how for varying beam current, the base width for all beam currents and the height for a low beam current increases with decreasing temperature, while for higher beam currents, the height initially increases and then falls with decreasing temperature. The results for the different beam voltages show a similar behaviour. [83]

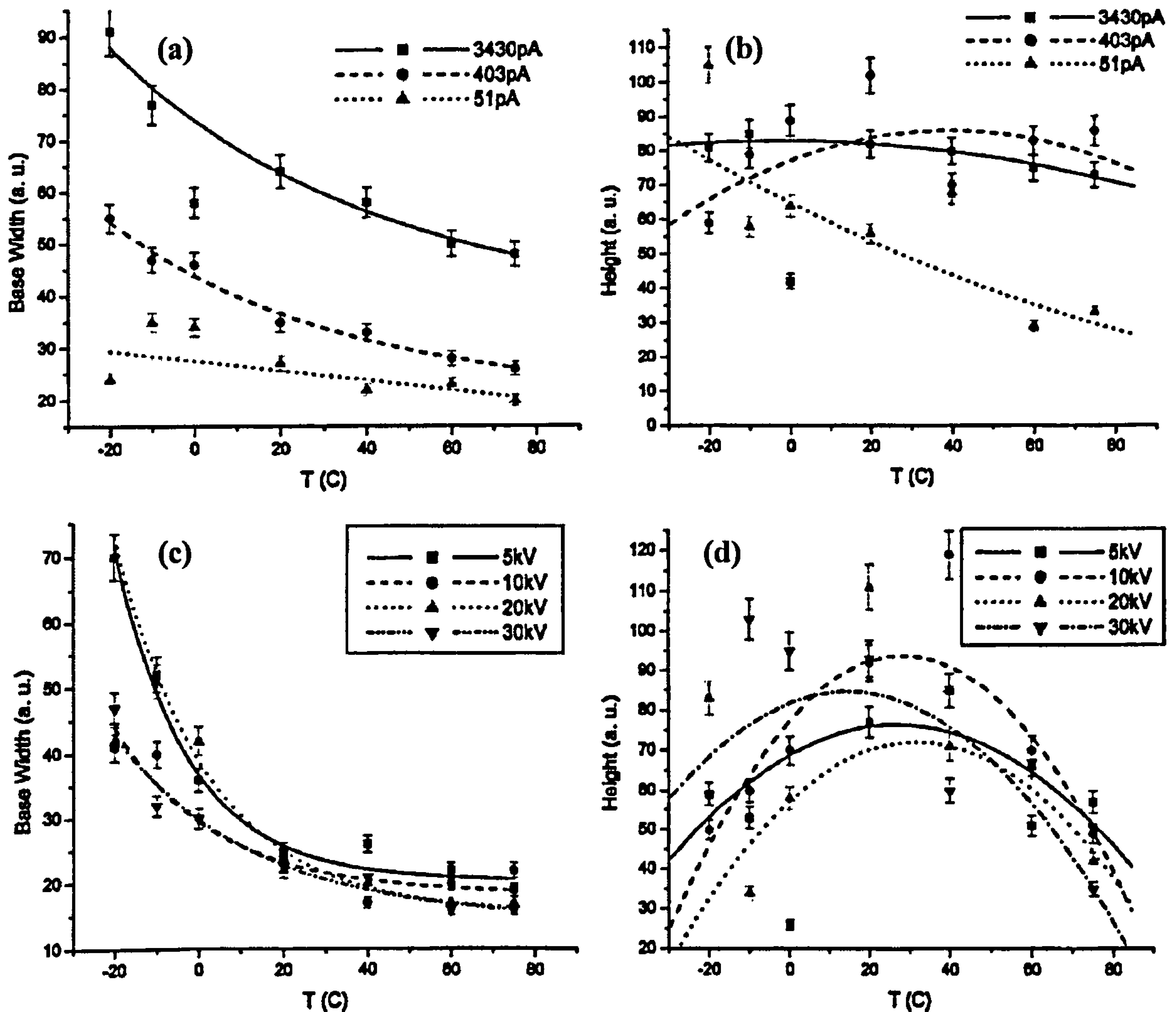


**Figure 2.36.** Variation in the deposited **(a)** base width and **(b)** height for different beam currents and **(c)** base width and **(d)** height for different beam voltages as a function of substrate temperature. [83]

Li et al. [83] explained this result by considering the diffusion rate of the adsorbed molecules, which decreases with the temperature. As the temperature decreases toward 0°C, the diffusion rate decreases, but is still high enough to allow molecules to diffuse up the sidewalls of the deposits. The molecules also spend more time on the substrate surface so their chance of being dissociated increases and the growth rate also increases. As the temperature is reduced below 0°C, the diffusion becomes so slow, that the molecules can no longer reach the top of the deposit. This means that fewer molecules are deposited on the top of the structures, while more molecules are dissociated on the sidewalls. Hence, the height of the deposits started to decline while the base width increased. Li et al. [83] attributed the different growth rate of the deposits produced using low beam currents, to the far lower numbers of SEs. As such, at low beam currents, the growth is dominated by the SE flux rather than by the decomposition and dissociation of the adsorbed precursor molecules. [83]

## 2.7 Effects of Post-Deposition Processing

The experimental results of the EBID research that has been presented so far has shown that one of the downfalls of EBID as a fabrication technique for interconnect applications is the low electrical conductance of the deposits. One method of improving their resistance is to anneal them after the deposition process has been completed. Frabboni et al. [84] investigated the effects of annealing platinum nanowires in vacuum and oxygen. The wires were deposited from the precursor $(CH_3)_3CH_3C_5H_4Pt$ in a dual beam FIB using a beam current of 90 pA and a beam voltage of 15 keV. The as-deposited samples were analysed in a TEM and found to consist of an amorphous carbon matrix containing ~2 nm wide platinum grains. The samples were then annealed at 550°C for 30 minutes in a furnace in either a vacuum or reactive ($O_2$) environment. The vacuum annealed deposits were found to consist of platinum crystals surrounded by an amorphous carbon matrix, while the oxygen annealed deposits no longer contained any carbon such that they only consisted of polycrystalline platinum. [84]

In another experiment Liu et al. [85] fabricated tungsten wires onto a molybdenum substrate using $W(CO)_6$, a beam energy of 20 keV and a scan speed of ~2 nm/s. The microstructure of the deposits was analysed in a TEM before and after the annealing, which was carried out in-situ at 900°C for 15 minutes. Bright field TEM and high-resolution electron microscopy (HREM) of the deposits prior to annealing showed that they consisted of 2 - 4 nm crystallites embedded in an amorphous matrix. After the annealing the deposits had shrunk slightly and consisted of polycrystalline grains of tungsten, tungsten carbide and tungsten oxide with diameters of up to tens of nanometers. The shrinkage was attributed to the crystallisation of the structure, which changed the volume and thermal expansion coefficient of the deposit. Liu et al. [85] predicted that this change would improve properties such as the conductance and field emission of the deposit. [85]

Botman et al. [86] also investigated the effects of post deposition processing by annealing deposits produced from $MeCpPtMe_3$ and $Me_2Au$-acac in $N_2$ and $O_2$. The depositions were carried out in a Dual Beam FIB operated at a beam energy of 20 keV and beam current of 620 pA. To allow for the composition of the deposits to be analysed using EDX, 1.8 x 1.8 μm structures were fabricated on a $SiO_2$ substrate for 400 s. These samples were then annealed using a quartz tube oven at temperatures between 50 and 500 °C in either $N_2$ (1 ppm $O_2$) or air (~20% $O_2$) for 10 minutes. This annealing had no effect on the chemical composition of the gold deposits as shown in Figure 2.37 (a), while the ratio of platinum to

carbon in the platinum deposits increased with temperature and was higher after annealing in air than in $N_2$ as shown in Figure 2.37 (b). [86]

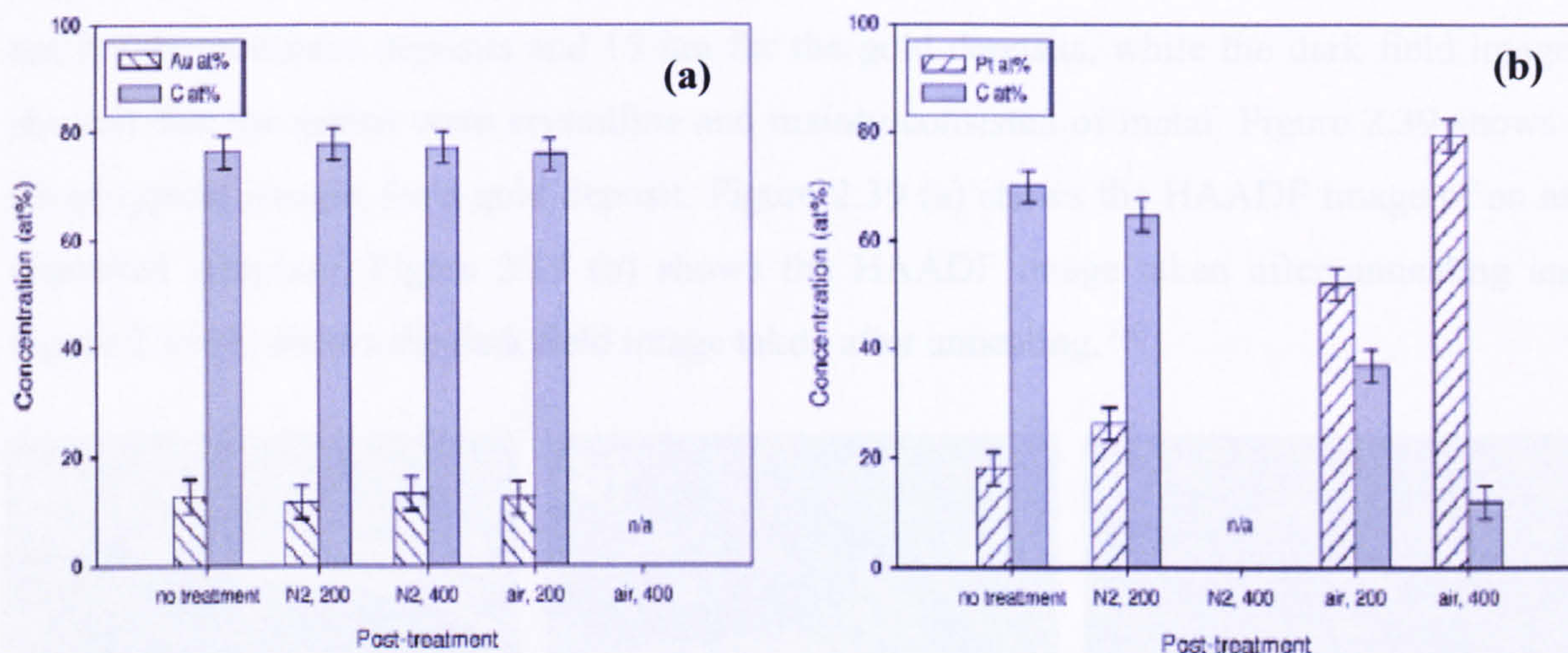


**Figure 2.37.** Average concentration of material in the deposit after treatment in either N2 or air for **(a)** gold deposits and **(b)** platinum deposits. [86]

Another batch of samples were annealed in pure $O_2$ for 10 minutes and it was found that they underwent a thermal activation process, which reduced the carbon content for temperatures in excess of 250°C. This was attributed to the formation of either CO or $CO_2$. The results of this experiment for the gold and platinum deposits are shown in Figure 2.38 (a) and (b) respectively. These graphs show how the gold content increased from 8 at. % to nearly 60 at. %, while the platinum content increased from 15 at. % to nearly 70 at. %. [86]

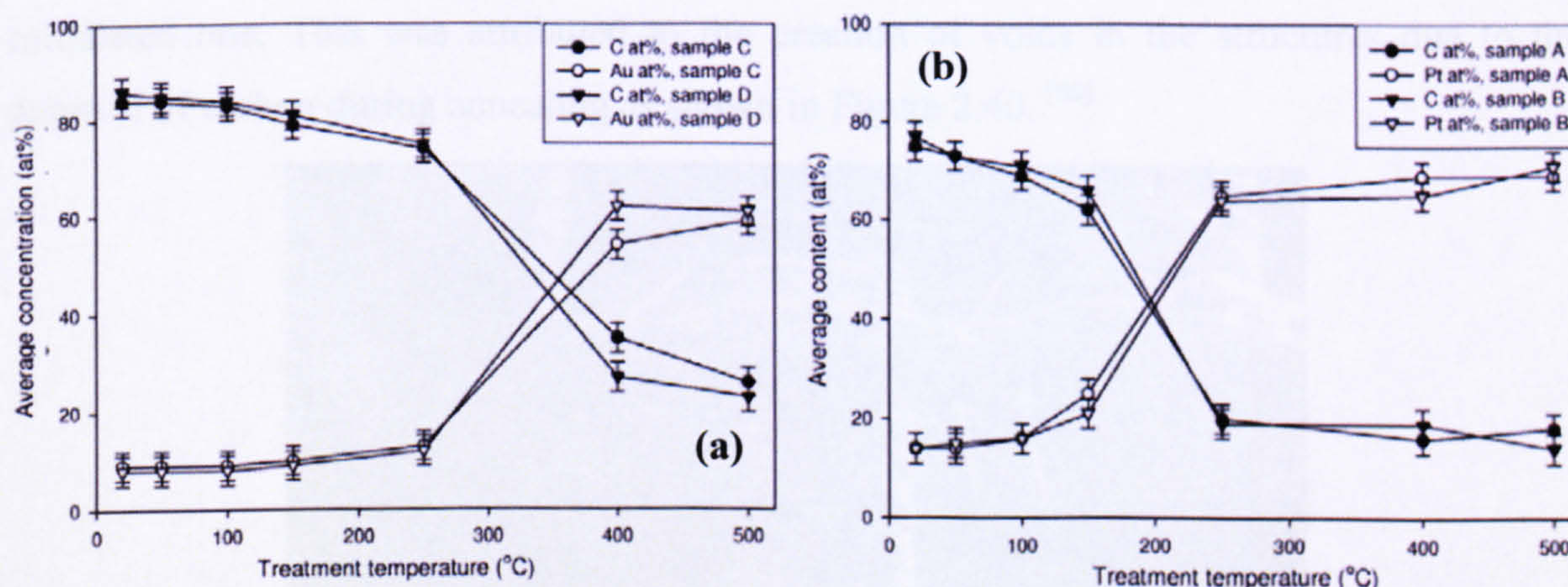


**Figure 2.38.** Effect of annealing on material concentration for **(a)** gold and **(b)** platinum deposits. [86]

Botman et al. [86] also analysed the structure of several cross sections of the deposits in a STEM. Both high-angle annular dark field (HAADF) and dark field images of the deposits

as-deposited and after annealing in pure $O_2$ at 500°C were taken. The HAADF images showed that the annealing caused the deposits to form grains with an average diameter of 98 nm for the platinum deposits and 15 nm for the gold deposits, while the dark field images showed that the grains were crystalline and mainly consisted of metal. Figure 2.39 shows a set of typical images for a gold deposit. Figure 2.39 (a) shows the HAADF image of an as-deposited structure, Figure 2.39 (b) shows the HAADF image taken after annealing and Figure 2.39 (c) shows the dark field image taken after annealing. [86]

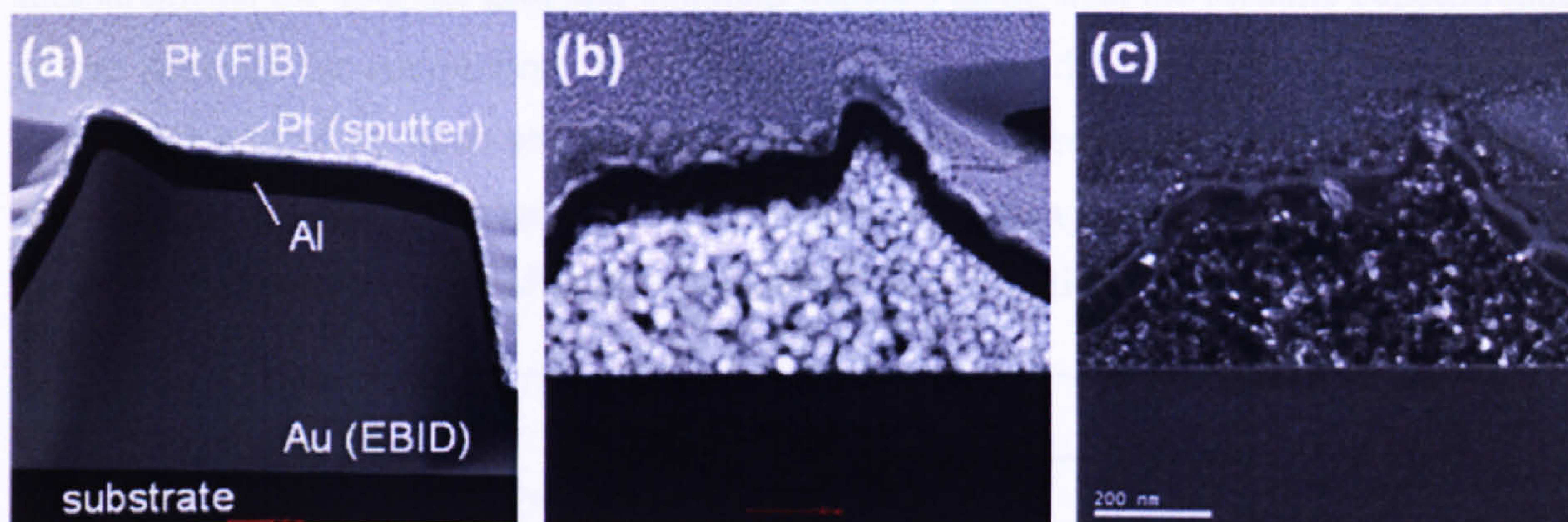


**Figure 2.39. (a)** STEM-HAADF image of as-deposited gold, **(b)** STEM-HAADF image after annealing at 500°C in $O_2$, **(c)** Dark-field image after annealing at 500°C in $O_2$. [86]

During this analysis Botman et al. [86] also found that the height of the deposits decreased with annealing. They attempted to calculate the reduction in height using the average atomic composition and found that the actual reduction in height was always less severe than the calculated one. This was attributed to the creation of voids in the structures due to the removal of carbon during annealing as shown in Figure 2.40. [86]

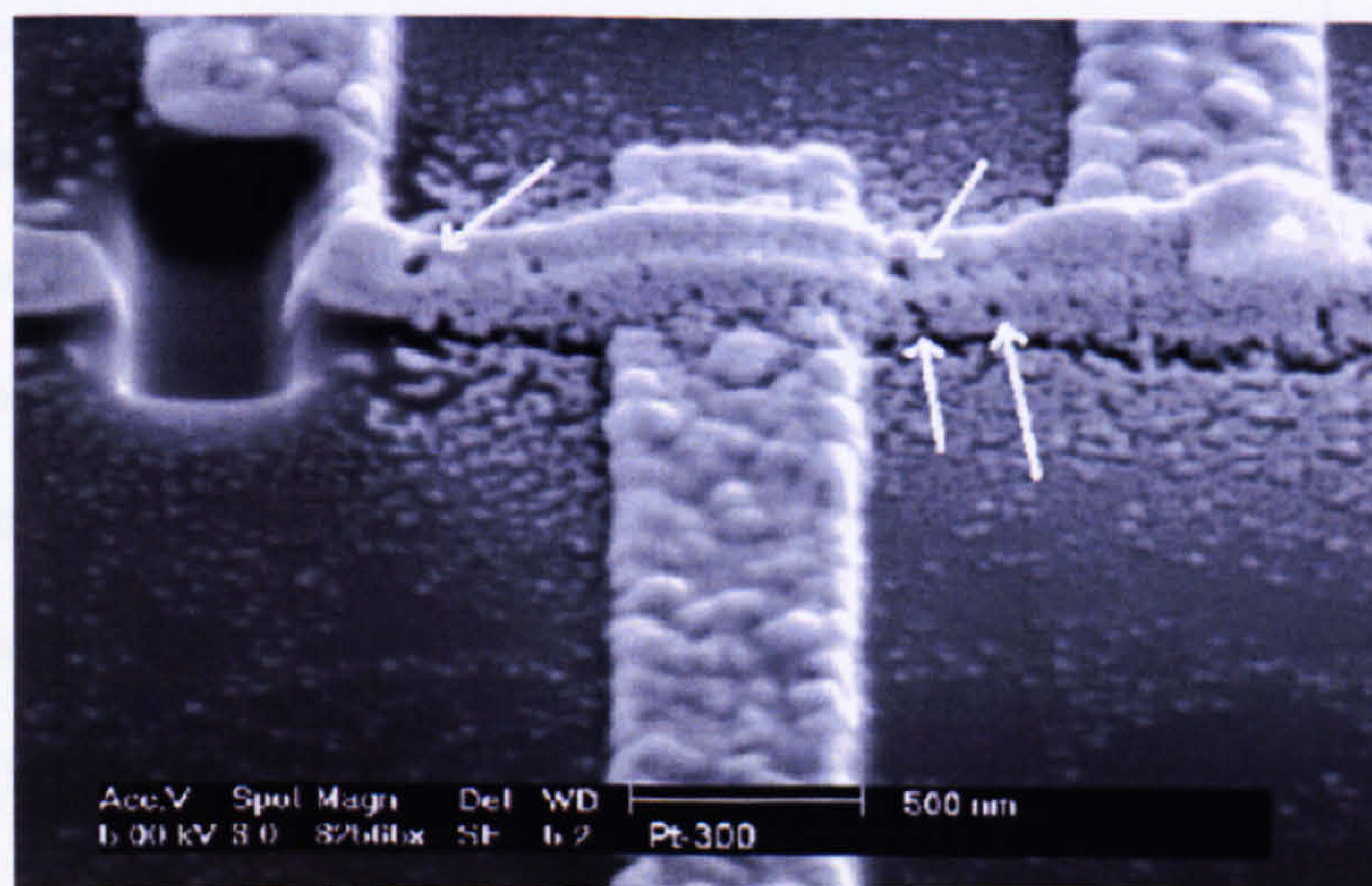


**Figure 2.40.** SEM image of a platinum deposit after annealing at 300°C in $O_2$. The hole on the left was milled for cross sectional analysis of the deposit. The voids are marked by the white arrows. [86]

As part of this experiment Botman et al. [86] also investigated the effects of annealing in pure $O_2$ on the resistivity of the deposited structures. In order to be able to make four point electrical measurements of the deposits, 300 nm by 4 μm depositions were made onto a $SiO_2$ wafer that had been prepatterned with gold electrodes. The resistance was measured for the as-deposited wires, for those annealed to the temperature just before the metal concentration changed significantly and for those annealed to the temperature at which the metal concentration saturated after changing. Figure 2.41 shows the results of the resistivity measurements for both the gold and platinum deposits along with the metallic concentration of the deposits for comparison. These Figures show how the resistivity of the platinum deposits improved by three orders of magnitude, while the resistivity of the gold deposits improved by one order of magnitude. These Figures also show how the resistivity changes at the same temperatures as the change in the metallic concentration. [86]

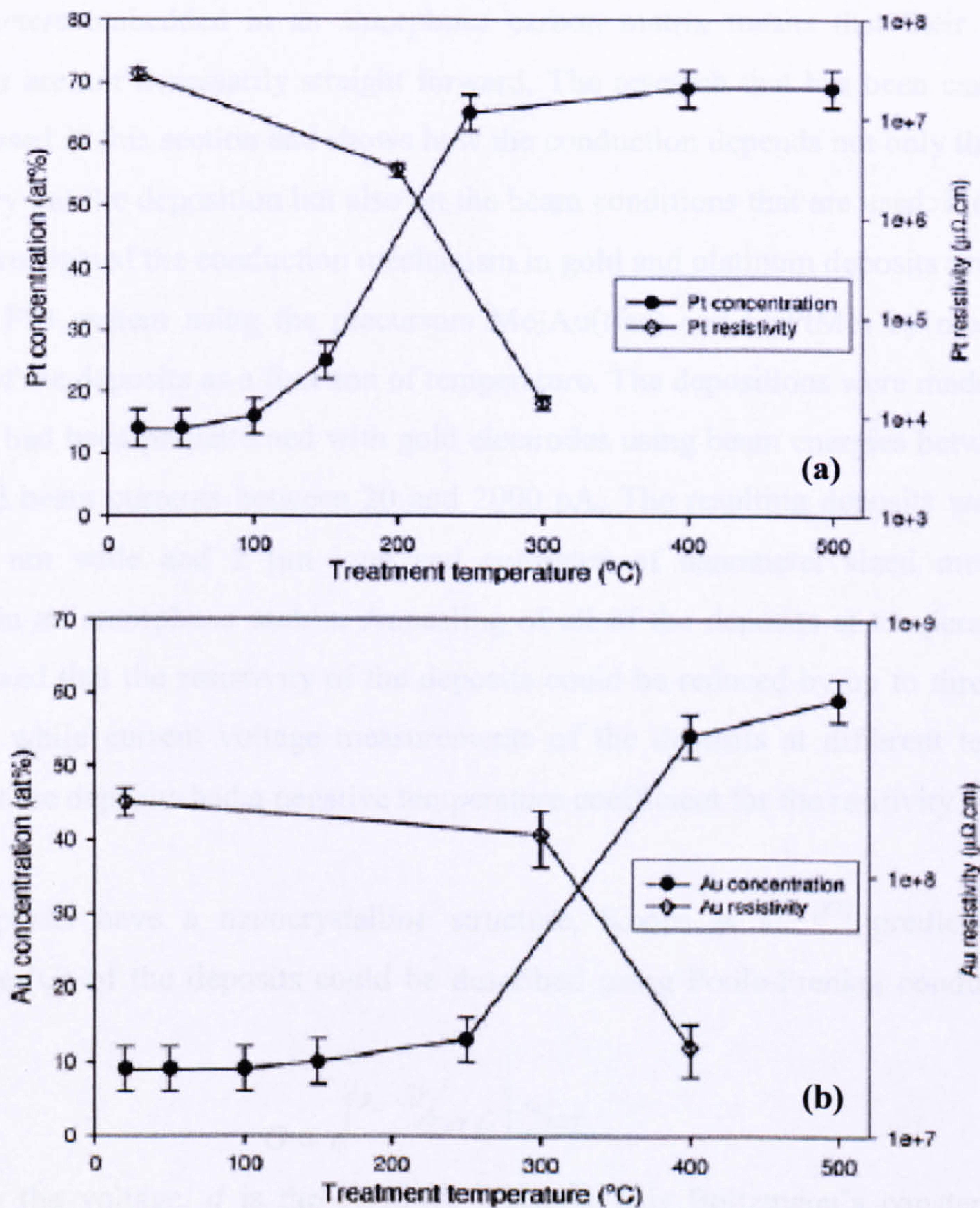


**Figure 2.41.** Resistivity and metal concentration as a function of annealing temperature in pure $O_2$ for **(a)** platinum and **(b)** gold deposits. [86]

While Figure 2.41 shows that the conductance improves with the metallic concentration and increasing size of the metallic grains within the structures, it still remains low and doesn't approach the bulk values for resistivity. Botman et al. [86] attributed this low conductance to a percolation mechanism for the transport of electrons from one grain to the next. During these measurements it was also found that if the resistance of the deposits was measured using currents in excess of 1 μA then the resistance of each subsequent measurement decreased. This effect was attributed to current-induced annealing or self-heating improving the conductivity of the wires. [86]

## 2.8 Conductance Mechanisms of EBID Interconnects

The fact that EBID interconnects are typically made up of crystallites with a diameter of a few nanometers embedded in an amorphous carbon matrix means that their conduction mechanisms are not necessarily straight forward. The research that has been carried out so far is discussed in this section and shows how the conduction depends not only the precursor used to carry out the deposition but also on the beam conditions that are used. Indeed Koops et al. [87] investigated the conduction mechanism in gold and platinum deposits produced in a dual beam FIB system using the precursors $Me_2Au(tfac)$ and $CpPtMe_3$ by measuring the resistance of the deposits as a function of temperature. The depositions were made onto $SiO_2$ wafers that had been prepatterned with gold electrodes using beam energies between 20 and 30 keV and beam currents between 20 and 2000 pA. The resulting deposits were 200 nm thick, 200 nm wide and 2 μm long and consisted of nanometer sized metal crystals embedded in an amorphous matrix. Annealing of all of the deposits at temperatures up to 180°C showed that the resistivity of the deposits could be reduced by up to three orders of magnitude, while current voltage measurements of the deposits at different temperatures showed that the deposits had a negative temperature coefficient for the resitivity. [87]

As the deposits have a nanocrystalline structure, Koops et al. [87] predicted that the conductance (G) of the deposits could be described using Poole-Frenkel conduction, such that:

$$G \propto e^{\left(\beta_{PF}\sqrt{U} / 2KT\sqrt{d}\right) - \Phi / 2KT} \tag{2.22}$$

where $U$ is the voltage, $d$ is the electrode distance, $k$ is Boltzmann's constant, $T$ is the temperature, $\Phi$ is the activation energy for Poole-Frenkel conductivity and $\beta_{PF}$ is the Poole-

Frenkel constant. Koops et al. [87] began by plotting the logarithm of the conductivity (ln G) against √U as shown in Figure 2.42 (a) for a platinum deposit produced using a beam energy of 30 keV and beam current of 120 pA. This graph shows how the conductivity follows two different behaviours. Below 2.25 V Koops et al. [87] attributed the conductance behaviour to variable range hopping (VRH), which shows the temperature and conductance dependency:

$$\ln G \sim \left( T_0 / T \right)^{\gamma} \tag{2.23}$$

where $\gamma$ = ½ for temperatures between 160 and 300 K and $T_0$ is Mott's characteristic temperature. Above 2.25 V the conductance follows Poole-Frenkel conduction and has a linear dependence of ln G on √U. Figure 2.42 (b) shows how ln G is also inversely proportional to the temperature for an applied voltage of 3 V, which is in agreement with Poole-Frenkel conductivity. From this graph an activation energy of 0.23 eV was also found. For the gold deposits ln G did not show a linear dependence on the inverse temperature and so the conductivity was attributed to VRH. [87]

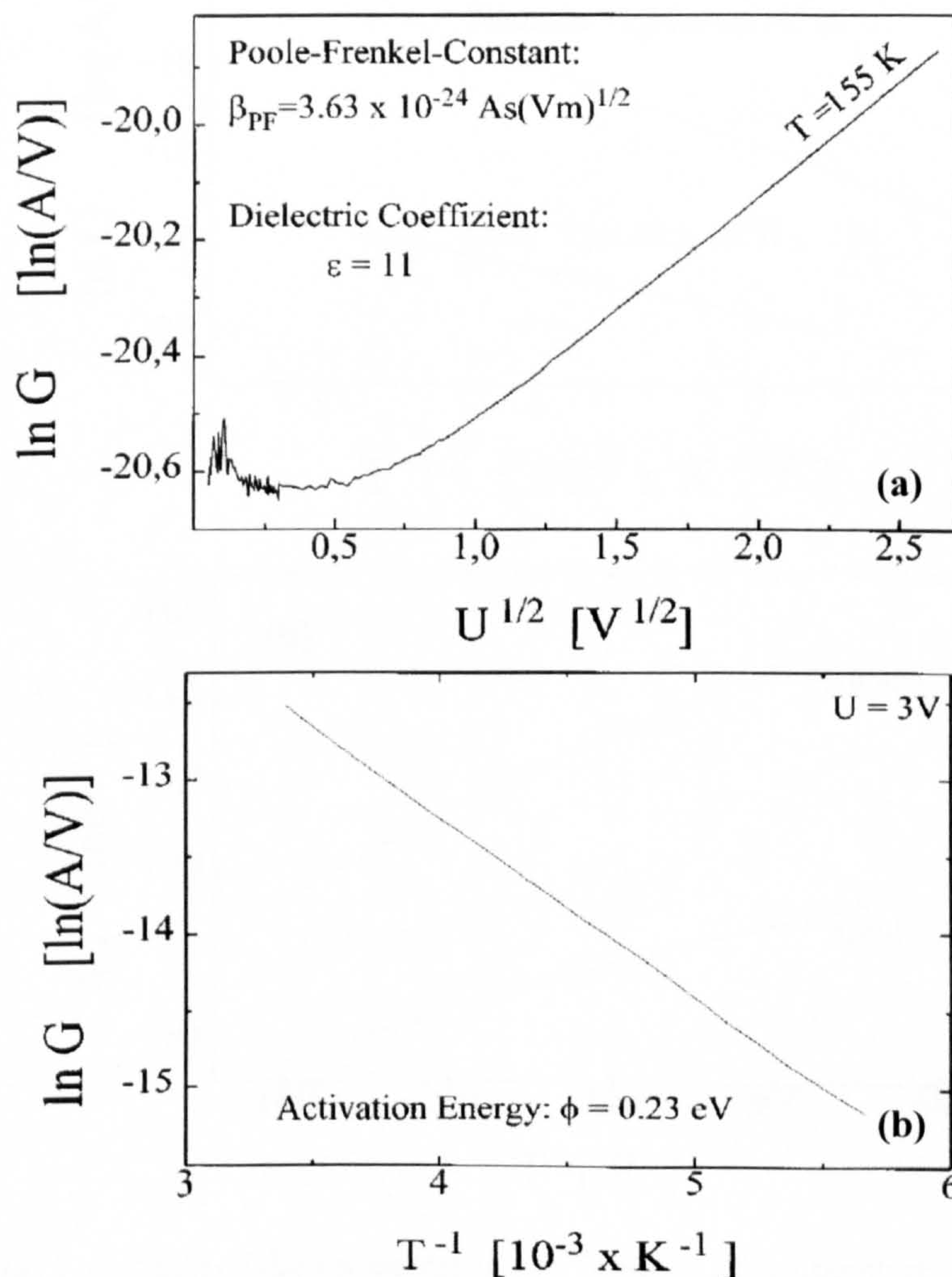


**Figure 2.42. (a)** Conductivity of platinum deposits as a function of voltage at 155 K. **(b)** Logarithm of the conductivity of platinum deposits versus the inverse temperature at 3 V. [87]

Koops et al. [87] also determined the activation energy for VRH conduction ($W_A$) for both the gold and platinum deposits, where:

$$W_A = \frac{k\sqrt{T}\sqrt{T_0}}{2} \tag{2.24}$$

Initially, the conductance versus temperature was measured at 50 mV for the gold wires deposited at 80°C and platinum wires deposited at room temperature. The results of this experiment are shown in Figure 2.43 (a). The activation energy was then calculated using equation (2.24) and plotted as a function of temperature as shown in Figure 2.43 (b). As can be seen from this figure, the activation energy for VRH conduction of the EBID gold studied here varied between 0.055 to 0.09 eV, while for the EBID platinum deposits the activation energy for VRH conduction varied between 0.092 and 0.16 eV. [87]

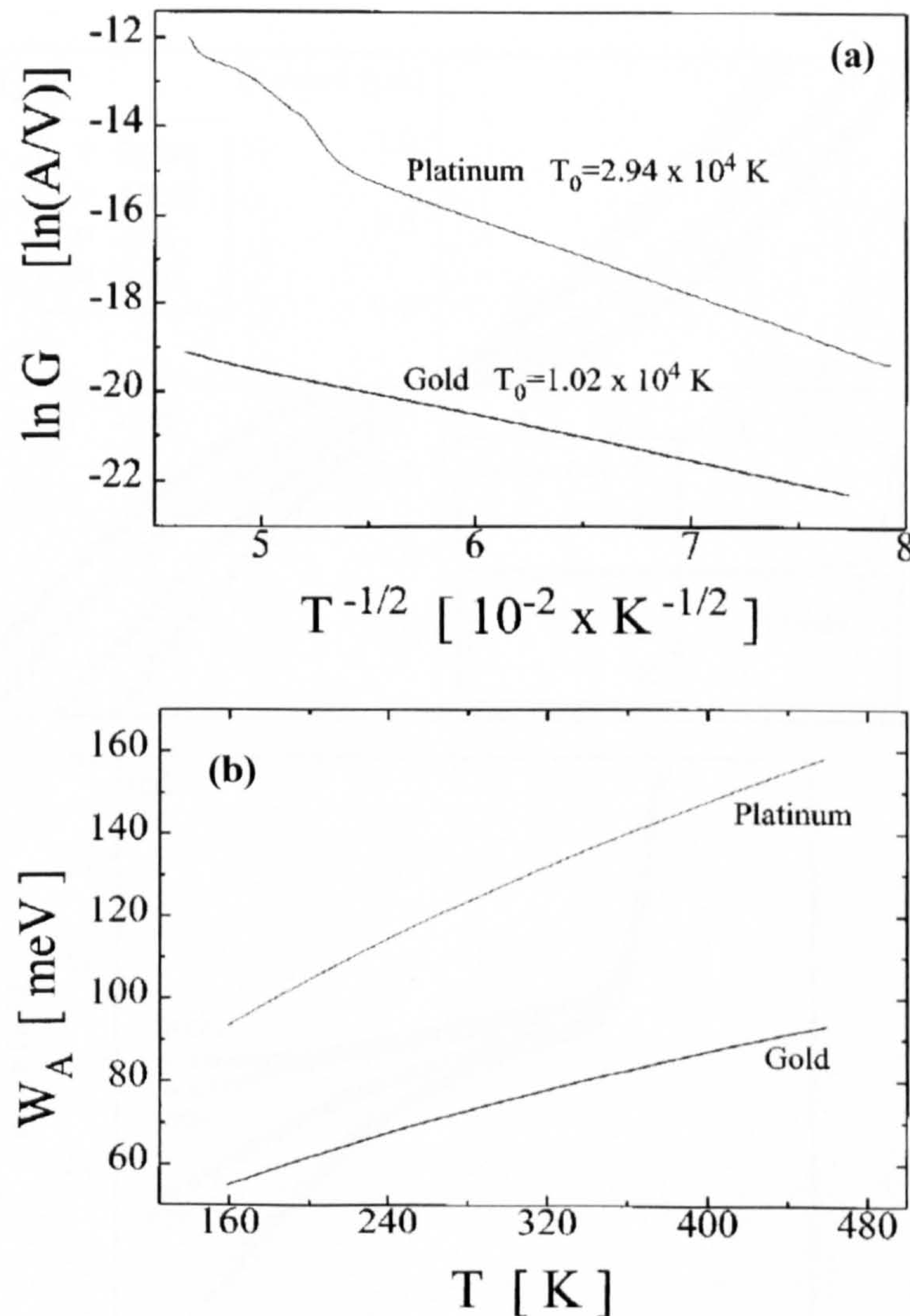


**Figure 2.43. (a)** Logarithm of the conductance as a function of temperature. (b) The activation energy for conductance by variable range hopping versus temperature. [87]

In another experiment that investigated the conduction mechanisms of EBID interconnects, Lau et al. [88] investigated the effects of temperature on the conductance of cobalt arches deposited from the precursor $Co_2(CO)_8$ in an ESEM. The arches consisted of small crystallites of cobalt embedded in an amorphous carbon matrix and had a negative temperature coefficient of resistivity for temperatures between 25 and 80°C, which suggests that the conduction path is not a metallic network. To further understand the conduction mechanism in these deposits, I-V measurements were made for temperatures between 20 and 200 K as shown in Figure 2.44 (a). As part of this experiment Lau et al. [88] followed the experimental analysis of Koops et al. [87] and plotted ln G versus √V for these I-V characteristics to determine whether the conduction mechanism followed Poole-Frenkel conduction. As can be seen from Figure 2.44 (b) the plot is not linear so Poole-Frenkel conduction cannot be used to explain the electrical characteristics of these structures. [88]

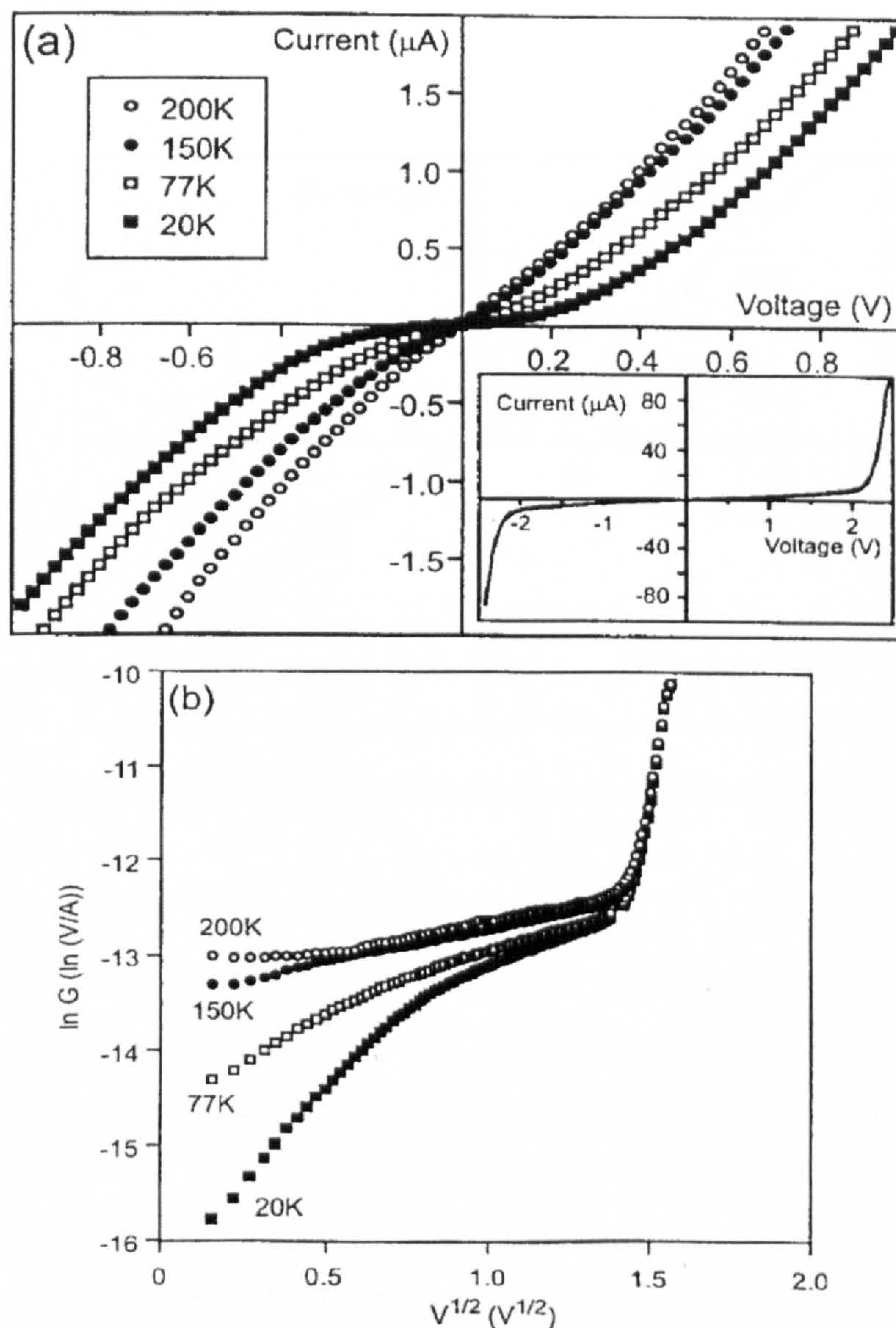


**Figure 2.44.** Electrical characteristics at different temperatures. **(a)** I-V and **(b)** ln G vs √V plot. [88]

Figure 2.45 shows how for these deposits there are three distinct conduction regimes. At low bias voltages below 0.7 V, Lau et al. [88] found that the conductance showed a temperature dependence at a fixed voltage bias of:

$$\ln G \propto \frac{1}{T^{\gamma}} \tag{2.25}$$

where, $\gamma$ = 0.087. This value of $\gamma$ is too small for VRH to be the dominant mechanism. A more detailed current-voltage sweep between +/- 25 mV (Figure 2.45) showed that at low temperatures, some step like features were present in the I-V characteristics and that the steps became more pronounced with decreasing temperature. Lau et al. [88] attributed these steps to the presence of Coulomb blockade effects in the conduction mechanism and suggested that the steps were not distinctive because the large size of the structures allowed for a high number of conduction paths to exist and smear the effect out. It was concluded that it was more likely that there were a number of different conduction mechanisms occurring in parallel. [88]

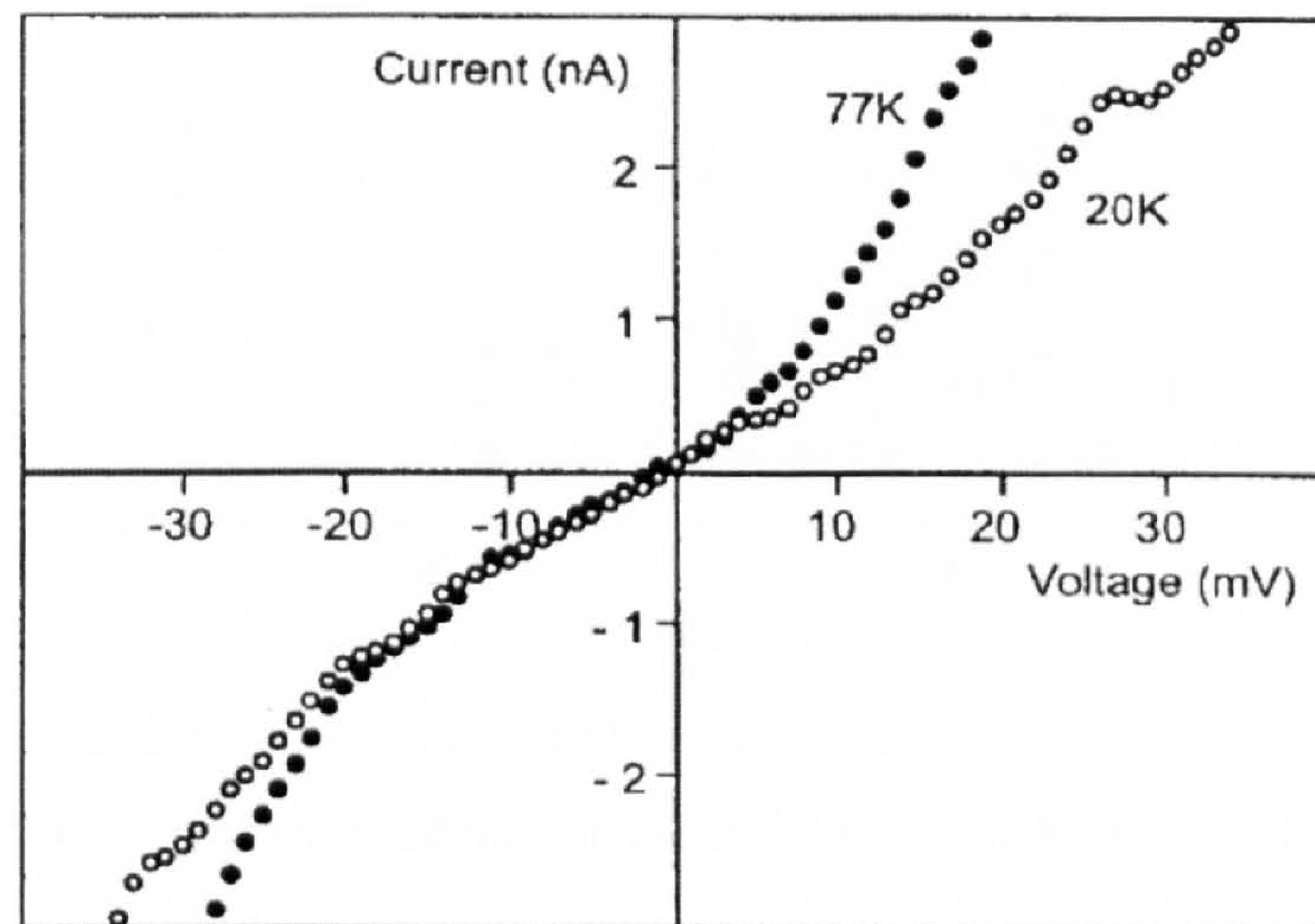


**Figure 2.45.** I-V characteristics of cobalt deposits at different temperatures. [88]

Rotkina et al. [89] also investigated the conduction mechanisms of EBID structures and attributed the conduction of platinum wires deposited using $(C_2H_5)Pt(CH_3)_3$ to Coulomb blockade conduction. For this experiment they deposited the wires on a 60 nm $Si_3N_4$ layer on a p-type silicon substrate so as to bridge prepatterned electrodes and allow for four-point current-voltage measurements to be taken using currents below 1 pA. They found that the current-voltage measurements of different platinum wires (see inset of Figure 2.46) at 4.2K were symmetric around zero bias voltage, highly non-linear and had a voltage gap of the

order of 0.1 to 0.2 V. They attributed this voltage gap to Coulomb blockade conduction, which arises from single electron tunnelling of electrons between the platinum nanocrystals that exist in the wires. As such Rotkina et al. [89] estimated the capacitance of a single 2 nm platinum metal grain to be 2 x $10^{-19}$ F and found that this value correlates to a charging energy of ~0.4 eV. This energy is in reasonable agreement with the size of the voltage gap seen in the I-V characteristics at 4.2 K and reinforces the idea that the conduction is due to Coulomb blockade conduction. [89]

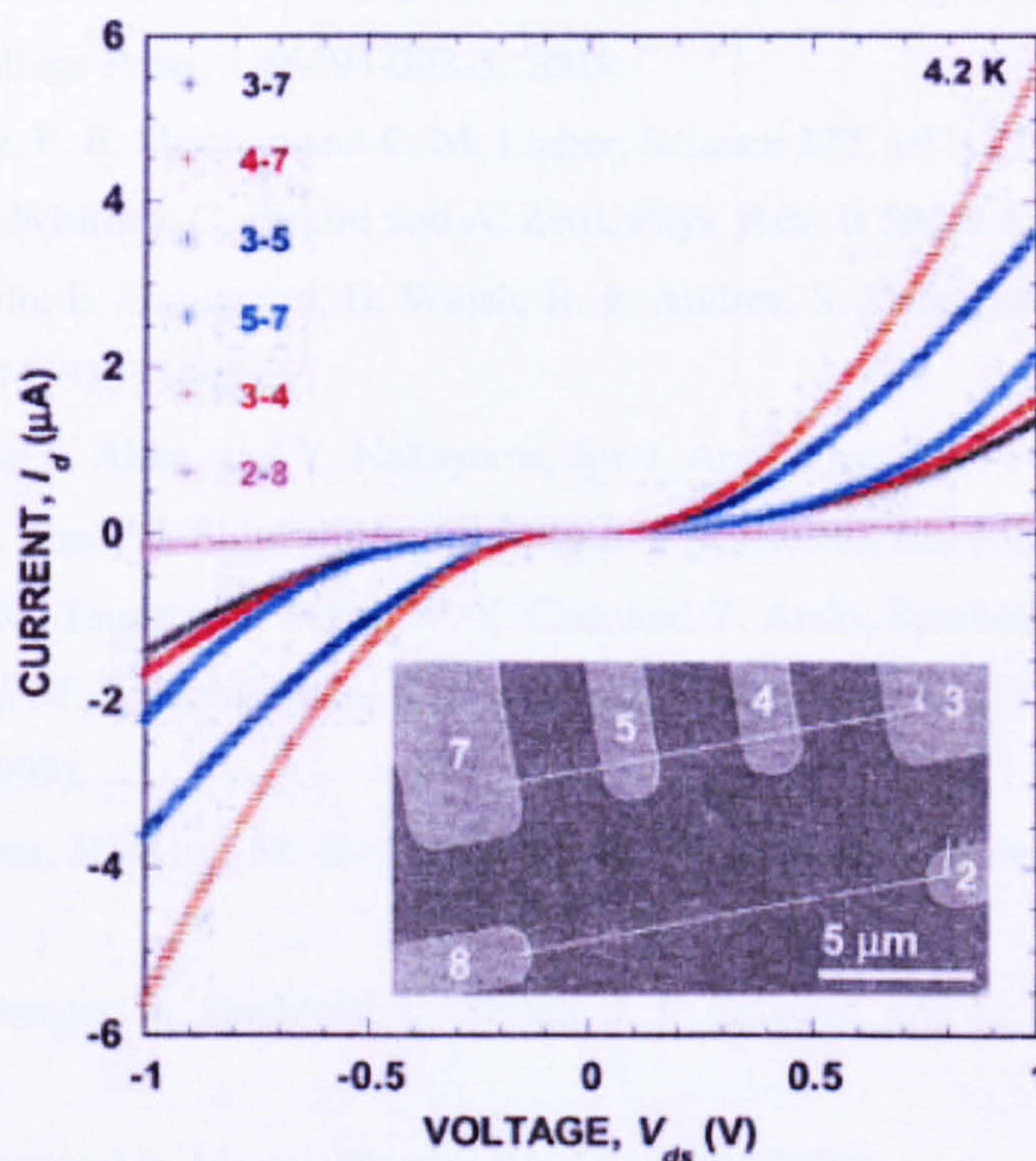


**Figure 2.46.** The I-V characteristics of different nanowire segments at 4.2 K. The SEM image in the inset shows the different nanowire segments used and their numbering, which is used in the main figure. [89]

## 2.9 Summary

This chapter has highlighted some of the main research efforts that have been carried out to gain a greater understanding of carbon nanotubes and electron beam induced deposition. This chapter has paid particular attention to describing the electronic band structure of carbon nanotubes and the effects of this band structure on the electrical characteristics of the nanotubes. It has also shown that the electrical characteristics of the carbon nanotubes depend on the type and amount of processing that the nanotubes have undergone during the

device fabrication and the contact geometry used to carry out the characterisation. This chapter has also discussed the main physical processes involved in the EBID process and the effects of the different set-up parameters on the structure, growth rate and electrical characteristics of EBID tips and nanowires.

## 2.10 References


[1] R. Saito, G. Dresselhaus & M. S. Dresselhaus, Physical Properties of Carbon Nanotubes, Imperial College Press, 1-86094-093-5, 2003.

[2] E. W. Wong, P. E. Sheehan and C. M. Lieber, Science **277**, 1971 (1997).

[3] J. Hone, M. Whitney, C. Piskoti and A. Zettl, Phys. Rev. B **59**, R2514 (1999).

[4] P. J. de Pablo, E. Graugnard, B. Walsh, R. P. Andres, S. Datta, and R. Reifenberger, Appl. Phys. Lett. **74**, 323 (1999).

[5] H. Nishijima, S. Akita, and Y. Nakayama, Jpn J. Appl. Phys. Part 1 **38**, 7247 (1999).

[6] Y. Ando, X. Zhao, H. Shimoyama, G. Sakai and K. Kaneto, Int. J. Inorg. Mat. **1**, 77 (1999).

[7] K. Kaneto, M. Tsuruta, G. Sakai, W. Y. Cho, and Y. Ando, Synthetic Met. **103**, 2543 (1999).

[8] S. L. Huang, M. R. Koblischka, K. Fossheim, T. W. Ebesen, and T. H. Johansen, Physica C **311**, 172 (1999).

[9] D. H. Galvan, H. Kim, M. B. Maple, G. A. Hirata, and E. Adem, Physica C **341**, 1269 (2000).

[10] C. Schonenberger, A. Bachtold, C. Strunk, J. P. Salvetat, and L. Forro, Appl. Phys. A **69**, 283 (1999).

[11] W. A. de Heer and R. Martel, Physics World **13**, 49 (2000).

[12] S. Iijima, Nature **354**, 56 (1991).

[13] Special Issue on Carbon Nanotubes, Physics World, **13**, 6 (2000).

[14] K. Teo, C. Singh, M. Chhowalla and W. Milne, Encyclopedia of Nanoscience & Nanotechnology 1 - 22 (2003).

[15] C. Journet, W. K. Maser, P. Bernier, A. Loiseau, M. Lamyde la Chapelle, S. Lefrant, P. Deniard, R. Lee and J. E. Fischer, Nature **388**, 756 (1997).

[16] T. W. Ebbesen and P. M. Ajayan, Nature **358**, 220 (1992).

[17] A. Thess, R. Lee, P. Nikolaev, H. Dai, P. Petit, J. Robert, C. Xu, Y. H. Lee, S. Kim, A. G. Rinzler, D. T. Colbert, G. E. Scuseria, D. Tomanek, J. E. Fischer and R. E. Smalley, Science **273**, 483 (1996).

[18] T. Guo, P. Nikolaev, A. Thess, D.T. Colbert and R.E. Smalley, Chem. Phys. Lett. **243**, 49 (1995).

[19] M M. Yudasaka, T. Komatsu, T. Ichihashi and S. Iijima, Chem. Phys. Lett. **278**, 102 (1997)

[20] M. Endo, Chemtech **18**, 568 (1988).

[21] C. L. Cheung, A. Kurtz, H. Park and C. Lieber, J. Phys. Chem. B **106**, 2429 (2002).

[22] Y Y. Li, J. Liu, Y. Wang and Z. L. Wang, Chem. Mat. **13**, 1008 (2001).

[23] R. T. K. Baker, Carbon **27**, 315 (1989).

[24] N. M. Rodriquez, J. Mat. Res. **8**, 3233 (1993).

[25] W. Z. Li, S. S. Xie, L. X. Qian, B. H. Chang, B. S. Zou, W. Y. Zhou, R. A. Zhao and G. Wang, Science **272**, 1701 (1996).

[26] T. Kyotani, L. Tsai, and A. Tomita, Chem. Mat. **7**, 1427 (1995).

[27] T. Odom, J. Huang, P. Kim and C. Lieber, Nature **391**, 62 (1998).

[28] J. Wildoer, L. Venema, A. Rinzler, R. Smalley and C. Dekker, Nature **391**, 59 (1998).

[29] M. S. Dresselhaus, G. Dresselhaus and R. Saito, Phys. Rev. B **45**, 6234 (1992).

[30] J J. W. Mintmire, B. I. Dunlap and C. T. White, Phys. Rev. Lett. **68**, 631 (1992).

[31] N.S. Lee, D.S. Chung, I.T. Han, J.H. Kang, Y.S. Choi, H.Y. Kim, S.H. Park, Y.W. Jin, W.K. Yi, M.J. Yun, J.E. Jung, C.J. Lee, J.H, You, S.H. Jo, C.G. Lee and J.M. Kim, Diam. Relat. Mat. **10**, 265 (1999).

[32] H. Sugie, M. Tanemura, V. Filip, K. Iwata, K. Takahashi and F. Okuyama, Appl. Phys. Lett. **78**, 2578 (2001).

[33] R. Rosen, W. Simendinger, C. Debbault, H. Shimoda, L. Fleming, B. Stoner, and O. Zhou, Appl. Phys. Lett. **76**, 1668 (2000).

[34] K. H. An, W. S. Kim, Y. S. Park, J.-M. Moon, D. J. Bae, S. C. Lim, Y. S. Lee and Y. H. Lee, Adv. Funct. Mat. **11**, 387 (2001).

[35] C. Niu, E. K. Sickel, R. Hoch, D. Moy, H. Tennent, Appl. Phys. Lett. **70**, 1480 (1997).

[36] D. J. Frank, R. H. Dennard, E. Nowak, P. M. Solomon, Y. Taur and H.-S. P. Wong, Proc. IEEE **89**, 259 (2001).

[37] Z. Chen, J. Appenzeller, Y.-M. J. Lin, J. Sippel-Oakley, A. G. Rinzler, J. Tang, S. J. Wind, P. M. Solomon and Ph. Avouris, Science **311**, 1735 (2006).

[38] Y.-M. Lin, J. Appenzeller, Z. Chen, Z.-G. Chen, H.-M. Cheng and P. Avouris, IEEE Electr. Dev. Lett. **26**, 823 (2005).

[39] G. G. Tibbetts, G. P. Meisner and C. H. Olk, Carbon **39**, 2291 (2001).

[40] Y. Ye, C. C. Ahn, C. Witham, B. Fultz, J. Liu, A. G. Rinzler, D. Colbert, K. A. Smith and R. E. Smallery, Appl. Phys. Lett. **74**, 2307 (1999).

[41] J. Kong, N. Franklin, C. Zhou, M. Chapline, S. Peng, K. Cho and H. Dai, Science **287**, 622 (2000).

[42] M. J. Biercuk, M. C. Llaguno, M. Radosavljevic, J. K. Hyun, A. T. Johnson and J. E. Fischer, Appl. Phys. Lett. **80**, 2767 (2002).

[43] D. Qian, E. C. Dickey, R. Andrews and T. Rantell, Appl. Phys. Lett. **76**, 2868 (2000).

[44] R. Landauer, J Phys-Condens Mat. **1**, 8099 (1989).

[45] S. Frank, P. Poncharal, Z. L. Wang and W. de Heer, Science **280**, 1744 (1998).

[46] P. Poncharal, C. Berger, Y. Yi, Z. Wang and W. de heer, J. Phys. Chem. B **106**, 12104 (2002).

[47] Y. X. Liang, Q. H. Li and T. H. Wang, Appl. Phys. Lett. **84**, 3379 (2004).

[48] C. Schonenberger, A. Bachtold, C. Strunk, J. Salvetat and L. Forro, Appl. Phys. A **69**, 283 (1999).

[49] A. Javey, J. Guo, M. Paulsson, Q. Wang, D. Mann, M. Lundstrom and H. Dai, Phys. Rev. Lett. **92**, 106804-1 (2004).

[50] J.-Y. Park, S. Rosenblatt, Y. Yaish, V. Sazonova, H. ÜstUnel, S. Braig, T. A. Arias, P. W. Brouwer and P. L. McEuen, Nano Lett. **4**, 517 (2004).

[51] M. Lazzeri, S. Piscanec, F. Mauri, A. C. Ferrari and J. Robertson, Phys. Rev. Lett. **95**, 236802-1 (2005).

[52] E. Pop, D. Mann, J. Cao, Q. Wang, K. Goodson and H. Dai, Phys. Rev. Lett. **95**, 155505-1 (2005).

[53] P. J. Burke, IEEE Trans. Nanotechnol. **2**, 55 (2003).

[54] A. Ennos, Brit. J. Appl. Phys. **4**, 101 (1953).

[55] J. H. L. Watson, J. Appl. Phys. **18**, 153 (1947).

[56] J. Hillier, J. Appl. Phys. **19**, 226 (1948).

[57] D. A. Buck and K. R. Shoulders, Proceedings of the Eastern Joint Computer Conference, 55 – 59 (1959).

[58] S. Matsui and K. Mori, Jpn. J. Appl. Phys. **23**, L706 (1984).

[59] S. Matsui and K. Mori, J. Vac. Sci. Technol. B **4**, 299 (1986).

[60] W. F. van Dorp, B. van Someren, C. W. Hagen and P. Kruit, Nano Lett. **5**, 1303 (2005).

[61] K. Mølhave, D. N. Madsen, A. M. Rasmussen, A. Carlsson, C. C. Appel, M. Brorson, C. J. H. Jacobsen and P. Bøggild, Nano Lett. **3**, 1499 (2003).

[62] S. J. Randolph, J. D. Fowlkes and P. D. Rack, Crit. Rev. Solid State **31**, 55 (2006).

[63] M. J. van Bruggen, B. van Bruggen and P. Kruit, J. Vac. Sci. Technol. B **23**, 2833 (2005).

[64] www.chem.qmul.ac.uk/surfaces/scc/scat2-3.htm

[65] H. W. P. Koops, R. Weiel, D. Kern and T. Baum, J. Vac. Sci. Technol. B **6**, 477 (1988).

[66] V. Scheuer, H. Koops and T. Tschudi, Microelectron. Eng. **5**, 423 (1986).

[67] K. Mitsuishi, T. Noda, T. Mano, M. Tanaka, K. Furuya and N. Koguchi, Jpn. J. Appl. Phys. **46**, 6277 (2007).

[68] J. I. Goldstein, D. E. Newbury, P. Echlin, D. C. Joy, A. D. Romig, Jr., C. E. Lyman, C. Fiori and E. Lifshin, Scanning Electron Microscopy and X-Ray Microanalysis: A Text for Biologists, Materials Scientists and Geologists, Second Edition, Plenum Press, New York and London, 0-306-44175-6, 1992.

[69] H. Seiler, J. Appl. Phys. **54**, R1 (1983).

[70] K. T. Kohlmann-von Platen, J. Chiebek, M. Weiss, K. Reimer, H. Oertel and W. H. Brünger, J. Vac. Sci. Technol. B **11**, 2219 (1993).

[71] K. Lee and M. Hatzakis, J. Vac. Sci. Technol. B **7**, 1941 (1989).

[72] N. Silvis-Cividjian, C. Hagen, L. Leunissen & P. Kruit, Microelectron. Eng. **61**, 693 (2002)

[73] N. Silvis-Cividjian, C. W. Hagen, P. Kruit, M. A. J. v.d. Stam and H. B. Groen, Appl. Phys. Lett. **82**, 3514 (2003).

[74] J. D. Fowlkes, S. J. Randolph and P. D. Rack, J. Vac. Sci. Technol. B **23**, 2825 (2005).

[75] K. I. Schiffmann, Nanotechnology 4, 163 (1993).

[76] D. Beaulieu, Y. Dong, Z. Wang and W. Lackey, J. Vac. Sci. Technol. B **23**, 2151 (2005).

[77] I. Utke, J. Michler, P. Gasser, C. Santschi, D. Laub, M. Cantoni, P. A. Buffat, C. Jiao and P. Hoffmann, Adv. Eng. Mat. **7**, 323 (2005).

[78] I. Utke, T. Bret, D. Laub, Ph. Buffat, L. Scandella and P. Hoffmann, Microelectron. Eng. **73**, 553 (2004).

[79] M. Weber, H. Koops, M. Rudolph and J. Kretz, J. Vac. Sci. Technol. B **13**, 1364 (1995).

[80] H. W. P. Koops, J. Kretz, M. Rudolph, M. Weber, G. Dahm and K. L. Lee, Jpn. J. Appl. Phys. **33**, 7099 (1994).

[81] J. D. Barry, M. Ervin, J. Molstad, A. Wickenden, T. Brintlinger, P. Hoffman and J. Meingailis, J. Vac. Sci. Technol. B **24**, 3165 (2006).

[82] S. Wang, Y.-M. Sun, Q. Wang and J. M. White, J. Vac. Sci. Technol. B **22**, 1803 (2004).

[83] W. Li and D. C. Joy, J. Vac. Sci. Technol. A **23**, 431 (2006).

[84] S. Frabboni, G. C. Gazzadi and A. Spessot, Physica E **37**, 265 (2007).

[85] Z.-Q. Liu, K. Mitsuishi and K. Furuya, Jpn. J. Appl. Phys. **45**, 5548 (2006).

[86] A. Botman, J. J. L. Mulders, R. Weemaes and S. Mentink, Nanotechnol. **17**, 3779 (2006).

[87] H. W. P. Koops, C. Schössler, A. Kaya and M. Weber, J. Vac. Sci. Technol. B **14**, 4105 (1996).

[88] Y. M. Lau, P. C. Chee, J. T. L. Thong and V. Ng, J. Vac. Sci. Technol. A **20**, 1295 (2002).

[89] L. Rotkina, J.-F. Lin and J. P. Bird, Appl. Phys. Lett. **83**, 4426 (2003).

# CHAPTER THREE

# 3 Experimental Tools and Techniques

## 3.1 Introduction

This chapter will focus on describing the instruments that are used to carry out the experimental work and the basic techniques that will be used in order to fabricate the devices to be investigated. In particular, it will focus on the microscopes that are used to image and analyse the samples, the manipulation systems that are used to electrically characterise the samples and the processes that are used to fabricate contacts. It will also describe the fabrication of a two terminal manipulation system that will allow for samples to be electrically characterised within a scanning electron microscope and the modification of a resistive heater to work with the manipulation system to allow for samples to be simultaneously heated and electrically characterised.

## 3.2 Scanning Electron Microscopy (SEM)

SEMs are part of a family of microscopes that use electromagnetic lenses and fast moving electrons to irradiate and image a sample in a high vacuum (HV) environment. They are generally used in applications similar to those employed in optical microscopy and give simulated, three-dimensional images of a material's surface on either the macrometer or micrometer scale. A number of more advanced SEMs exist and may contain facilities to heat and/or cool the sample, gather chemical data about the elemental composition of a sample or allow for electronic measurements of a sample to be taken. There are also specialist types of SEM such as the ESEM, which is designed to work under a variety of pressures and atmospheres and the dual beam focused ion beam (FIB) system, which utilises both an electron beam and an ion beam to image a sample's surface. A number of combined systems

such as the SEM/SPM or SEM/STM have also been manufactured for use in multi-technique analysis of samples.

A typical electron microscope consists of an electron column that is made up of an electron gun and electromagnetic lenses, a sample chamber, an operating and display consol or computer and a remote unit that supplies the power (see Figure 3.1). The electron gun consists of a tungsten wire filament, which is resistively heated using a high voltage supply so that it emits electrons and a grid cap and anode, which direct electrons down the column. The electromagnetic condenser lenses are then used to focus the electron beam into the specimen chamber with a spot size of 1-10 nm. Within the specimen chamber is the stage, which has the ability to move up to 25 mm in the x-y directions and the electron detectors. [1]

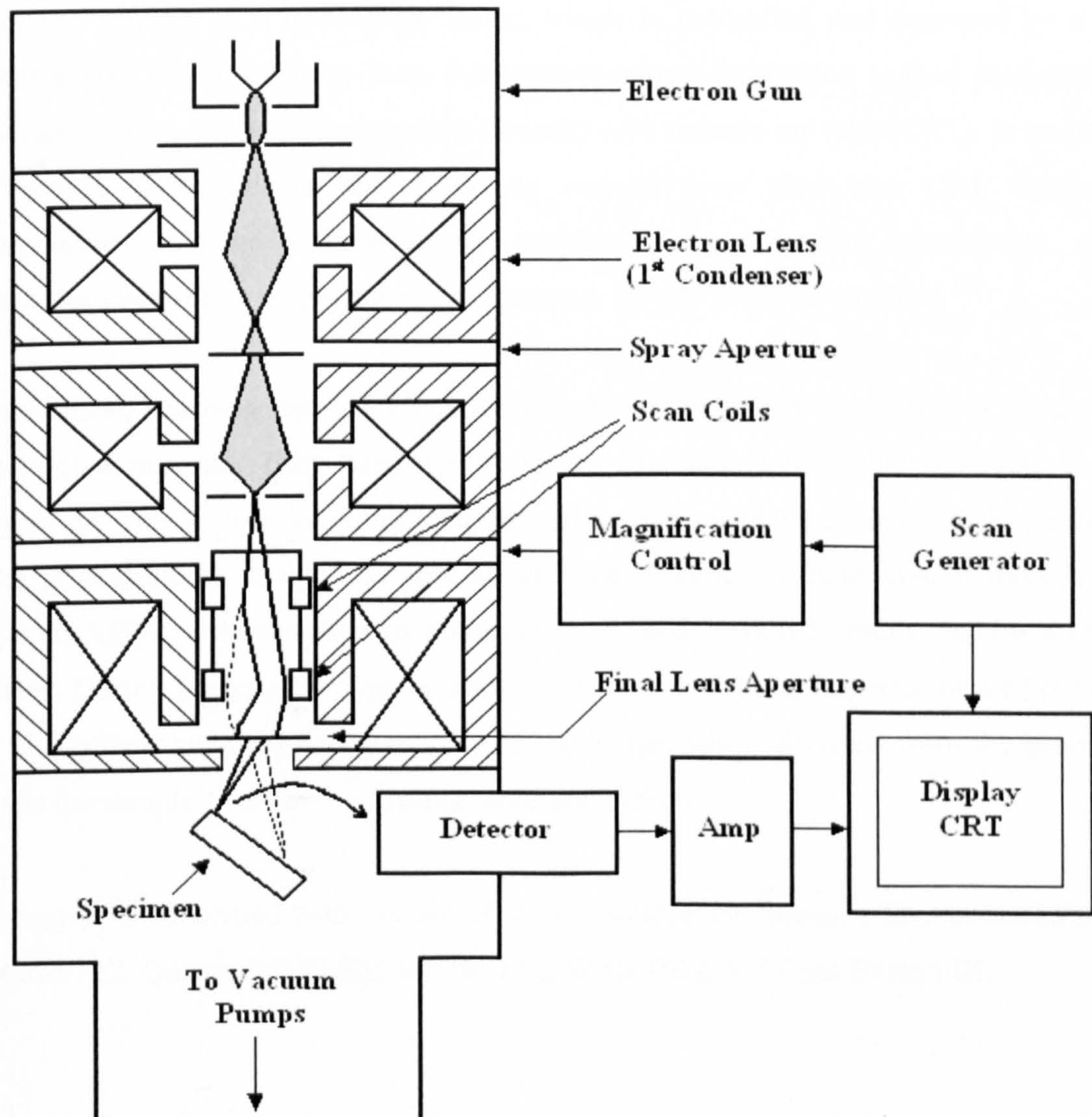


**Figure 3.1.** Schematic drawing of the main components in a scanning electron microscope including the electron column, the deflection system and the electron detectors. [1]

Most of the imaging that is carried out in these microscopes is concerned with the back-scattered and secondary electron signals. Secondary electrons loose a fair quantity of energy and are collected by a detector that is situated at the side of the stage. This detector uses a wire mesh screen held at +300 V to attract the secondary electrons, so that they are accelerated toward the scintillator and produce light when they impinge upon it. This signal is passed to the photomultiplier, where it is converted into an amplified electrical signal that creates the image. The back-scattered electrons loose less energy, and so are not affected by the electrostatic collection fields of the secondary electron detector. As such, a backscattered electron detector uses a semiconductor or scintillator-photomultiplier detector placed above the stage. [1]

In order to produce a three-dimensional image of a sample, the electron beam is scanned across the sample in a rectangular raster, which is controlled and powered by a scan generator. The signal intensity from the beam-specimen interaction is then measured and shown as a bright spot of corresponding intensity on a cathode ray tube (CRT). In traditional microscopes, these images are shown on one or more slow-scan CRT displays, a photographic CRT and a television-rate display. In more modern microscopes, digital images that consist of a numerical matrix array are viewed using a computer. [1]

In conclusion, scanning electron microscopes are a quick and easy method of imaging the surface of a material. They have the advantage that their images are relatively easy to interpret as well as a large, continuous magnification range of 10-200,000 times, which makes it possible to image a sample at all magnifications without system modification. However, SEMs are expensive to purchase, and good, detailed results require a trained operator. During imaging the type of sample being analysed and imperfections of the beam may also affect the quality and accuracy of the image, while electrons from the beam may damage the sample's surface by causing structural defects.

This project is concerned with the use of the Cambridge Instruments, Stereoscan 250 MK3 SEM, the FEI, Quanta 200 ESEM and the FEI, Strata DB235M Dual Beam FIB.

### 3.2.1 Cambridge Instruments Stereoscan 250 MK3 SEM

This instrument is a traditional SEM that follows the conventional structure described above. The electron-optical column consists of a conventional triode electron gun with a fixed tungsten hairpin filament, two condenser lenses and one objective lens. The gun has an accelerating potential that can be varied from 500 V to 40 kV and produces beam currents of up to 400 μA. The specimen chamber contains a stage that has the ability to move in the x, y and z directions as well as being tilted or rotated and an Everhart-Thornley secondary electron detector. This allows the microscope to produce three-dimensional images on a CRT display with a sub-six nm resolution and a magnitude range of x20 to x100000. [2]

### 3.2.2 FEI Quanta 200 ESEM

This is a much more modern microscope which has been engineered to provide the maximum data for the imaging and microanalysis of both prepared and unprepared samples. What makes this microscope different from traditional SEMs is its ability to switch between three different types of vacuum, whilst detecting secondary and/or backscattered electrons and producing high-resolution images. The first type of vacuum that it may be operated in is the standard SEM HV environment. This mode is used to image and analyse conductive and conventionally prepared samples at a pressure of ~$10^{-5}$ mbar with a standard Everhart-Thornley secondary electron detector. Scanning electron microscopes are traditionally operated in this environment in an attempt to minimise the interference of molecules in air with the electron beam and the reflected secondary electrons. [3]

This microscope may also be operated in both low vacuum and ESEM modes. In these modes the vacuum is poor and gases may be introduced into the specimen chamber at a pressure of up to 26 mbar. The gas molecules collide with the secondary electrons and produce gaseous secondary electrons and positively charged gas ions. The gaseous electrons continue to collide with the gas molecules and produce an amplified signal at the detector, whilst the positive ions are attracted to the surface of the material and neutralise the negative charge caused by the electron beam. In low vacuum mode at pressures below 1.3 mbar this allows for non-conductive, unprepared samples to be imaged and analysed using a large field gaseous secondary electron detector without charging. In ESEM mode, samples that are not compatible with high vacuum conditions may be imaged at pressures up to 26 mbar, using a gaseous secondary electron detector. [3]

Although this system is a specialist type of SEM and has a number of different types of detectors it still maintains a traditional SEM structure. The electron optical column uses a tetrode gun with a tungsten hairpin filament to produce high quality images with up to 50 times more beam current than in traditional designs. The electron gun has an accelerating voltage of 200 V to 30 kV and a beam current greater than 2 mA. The stage is motorised and is able to move 50 mm in the x, y and z directions, rotate 360° and tilt up to 75°. It is also able to take either single or multiple samples and hold single wafers of up to six-inches. A computer running MS-Windows 2000 is used to operate the microscope and view images of the sample and chamber using an in chamber CCD camera. These features allow the microscope to have a resolution of 3.5 nm in the high vacuum and ESEM modes and a resolution better than 15 nm in low vacuum. This microscope also has a magnification of x6 to x 1,000,000 and the stage may be operated at temperatures between -15°C and +75°C. This instrument also has a solid-state scanning TEM detector for the analysis of thinned samples and a Peltier stage, which is capable of heating samples up to 1000 °C. [3]

### 3.2.3 FEI Nova Nanolab 600 Dual Beam Focused Ion Beam (FIB)

This instrument is another specialist type of SEM, which combines a SEM and a FIB to analyse and modify samples. It uses a Magnum ion column with a liquid gallium ion source to produce an ion beam voltage of 5 - 30 kV and beam current of 1 pA to 20 nA. The final ion spot size is 6 nm at 1 pA and produces a resolution of 7 nm. The SEM column uses a Schottky emitter and an immersion final lens with in-lens detector, where the specimen is immersed in the magnetic field and aberrations are minimal. This allows the lens to produce a smaller final probe size and have a higher resolution. As the secondary electrons spiral upward in this set-up the detector is placed above the lens. This allows for the column to have smaller than usual working distances and a higher resolution of 2 nm at 5 kV. [4]

The two columns share a single chamber so that both the SEM and FIB can be used simultaneously. This instrument also has a solid-state scanning TEM detector for the analysis of thinned samples, an in-situ lift out system to transfer a section of a sample to a TEM grid and a variety of patterning tools including the J. C. Nabity Lithography Systems, Nanometer Pattern Generation System, which will be described in section 3.10.1. A computer is used to operate the microscope and controls any milling or deposition work that is carried out using a high degree of automation. [4]

## 3.3 Transmission Electron Microscopy (TEM)

Like the SEM, TEMs use an electron gun and electromagnetic lenses to produce a fine beam of electrons that are used to image a sample. However unlike the SEM, which uses reflected electrons to produce topographical images, the TEM uses electrons, which are transmitted through a sample to image its internal microstructure. These microscopes can be operated in a number of different modes and fitted with a variety of different detectors, which make them a powerful and versatile analytical tool. In particular an electron cryomicroscope is a TEM that is able to cool samples to liquid nitrogen temperatures, while an analytical TEM uses a number of different types of detectors to determine the elemental composition of a sample. Modern TEMs are capable of analysing sub nanometer features at magnifications in excess of fifty million times. [5]

When the electron beam interacts with a crystalline sample, the electrons are diffracted. The amount that the electrons are diffracted depends on the density of the material and the orientation of the atoms relative to the electron beam. This means that at certain incident beam angles the electrons are strongly diffracted, whilst at other angles, they are mainly transmitted. By varying the angle of the sample, it is possible to use either only the scattered or the unscattered electrons to produce the images. Images formed using unscattered electrons are known as bright field images and contain information about the structure of the material being imaged. These images are particularly sensitive to crystal lattice defects in an otherwise ordered material. Images formed using the scattered electrons are known as dark field images. In the most powerful TEMs, high-resolution transmission electron microscopy (HRTEM) or phase contrast imaging may also be used to investigate the crystal structure of a sample by comparing the differences in the phase of the electron waves. [5]

One of the main advantages of TEM are that they are capable of achieving information about the internal structure of a sample, which instruments such as the SEM are not. However, their field of view is relatively small and most samples require extensive preparation in order to make them thin enough to be electron transparent. This makes TEM analysis a relatively time consuming process in comparison with SEM analysis. Another disadvantage of TEM is that these microscopes use relatively high electron beam voltages, which may change the internal structure of the samples while they are being imaged.

This project uses a Philips CM 200 Transmission Electron Microscope.

### 3.3.1 Philips CM 200 Transmission Electron Microscope

This microscope can produce accelerating voltages of up to 200 kV and is capable of imaging very thin samples with a resolution of 0.19 nm at 200 kV. The images are taken digitally using a Gatan Imaging Filter (GIF 2000 with a $1k$ x $1k$ Charge Couple Device) that is situated below the viewing chamber.

## 3.4 Auger Electron Spectroscopy (AES)

AES is a surface spectrometry technique that is based on the Auger process. It is carried out in an ultra high vacuum (UHV) system that is equipped with an electron-optical column for both imaging and electron excitation with beam energies between 5 and 25 keV and an electron energy analyser and detector, which is used to measure the emitted Auger electrons. The process that makes up AES can be split into three main steps. Initially, a PE from the electron beam ionises a substrate atom by removing a core electron. This atom is in an excited state and tries to relax back to a lower energy state by either X-ray fluorescence or Auger emission. In Auger emission, an electron falls from a higher level to fill the core hole and transfers some of its energy to a second electron. The remaining energy is emitted as kinetic energy by an Auger electron. The final part of AES includes the collection of the emitted electrons and the measurement of their kinetic energy, which is characteristic of the element that emitted it and can thus be used to identify the element. Auger electrons typically have energies between 50 eV and 3 keV and as such have a short mean free path in a solid, which means that AES is also a highly surface sensitive technique. [6,7]

AES is a highly surface sensitive technique that is only concerned with the top few layers of atoms so it is crucial that any hydrocarbons adsorbed on the sample surface, while the sample has been exposed to an air environment are removed. Therefore, prior to carrying out AES the sample is typically cleaned using a diffuse ion beam such as an argon beam with an energy between 50 eV and 5 keV. This process will sputter off the top layer of atoms, which will consist mainly of carbon and oxygen and will prevent these elements from dominating the Auger spectra. The fact that AES is so highly sensitive to the surface atoms and contaminants means that it is typically carried out in an UHV environment in order to avoid the formation of a thin gas adsorbate layer on the sample as it is being analysed. By carrying out this process in UHV it is also possible to ensure that any scattering of the low energy Auger electrons on residual gas atoms can also be minimised. [6,7]

During the collection of the Auger electrons, the electron beam is held at a fixed, focused point of less than 12 nm on the sample surface and the voltage in the analyser is varied so that Auger electrons with the full range of kinetic energies can be detected. The resulting data is plotted as a function of kinetic energy versus the intensity of the Auger signal against the broad SE background spectrum. The peak values of the Auger electrons are difficult to interpret because of background intensity variations. Therefore, conventionally Auger spectra are differentiated and peak-to-peak measurements of the differentiated data are made. By stepping the electron beam across the sample surface and repeating this analysis for each point, a two-dimensional map of the different elements can be built up. [6,7]

AES has a number of unique advantages in that it is able to detect all elements apart from hydrogen and helium with a rapid acquisition time, good surface sensitivity of ~1 nm and a high lateral resolution of ~10 nm. It has high magnification imaging in SEM mode, which allows for perfect correlation between the SE image and the point at which the Auger analysis is carried out. Furthermore, AES can be combined with ion sputtering for depth profiling. However, it also has a number of disadvantages in that some of the analysis peaks can overlap and it has a low signal to noise ratio. Specimen damage can occur both as the sample is cleaned using the ion beam and during the analysis. This is because as the sample is hit by ions and high-energy electrons the substrate molecules can be dissociated such that structural transformations can occur. AES also has the disadvantage that as with conventional SEM imaging only conductive samples can be analysed because the charging effects that occur in non-conducting samples severely alter the yield of electrons emitted from the sample and can distort the measured Auger peaks. Finally, there are currently significant difficulties in the proper, absolute quantification of AES such that in order to quantify AES data some kind of calibration experiment must first be performed. [6,7]

This project is concerned with the use of the Thermo MICROLAB 350 Auger Electron Spectroscopy instrument.

### 3.4.1 Thermo VG Scientific MICROLAB 350

This instrument is a high performance scanning Auger electron spectrometer with a spherical sector analyser that allows for simultaneous scanning Auger and energy dispersive X-ray analysis to be carried out in UHV. The SEM imaging on this instrument has a resolution better than 7 nm, while the AES can be carried out with a resolution of less than 12 nm. [8]

## 3.5 Atomic Force Microscopy (AFM)

Unlike optical or electron microscopy, AFMs do not depend on the interactions between photons or electrons and a sample. Instead they measure the local forces between a small tip and the surface as the tip is scanned across the sample. As such the AFM is a member of the SPM family and is capable of producing true three-dimensional images of a sample with nanometer resolution unlike electron microscopes, which can only produce true two-dimensional images. AFMs are also capable of being operated in both air and vacuum. [9]

Atomic force microscopes consist of a microscale cantilever with a sharp tip mounted perpendicularly at one end of the cantilever that is used to scan the surface of the sample. The other end of the cantilever is connected to a tip holder in the AFM head. When the tip is brought close to the surface of a sample, forces between the tip and the sample deflect the cantilever. This deflection is measured using a laser spot that is reflected from the top of the cantilever onto an array of photodiodes. In order to be able to adjust the height of the sample and hence the deflection of the cantilever and to scan the sample, most AFMs use a sample stage which is controlled using piezo-electric tubes. [9]

The first AFM technique to be developed was contact mode AFM. In this mode the tip is in contact with the sample and the force between the tip and the surface is kept constant by maintaining a constant cantilever deflection. The changes in the cantilever's height are then measured and used to produce the images. Whilst this technique has enabled atomic force microscopy to be used to produce atomic resolution images on a wide variety of samples, it has also been found that it can damage or alter the surface of more sensitive samples, while rough surfaces can break the tip. For this reason non-contact and tapping mode AFM have been developed. In both of these modes the cantilever is vibrated close to its resonant frequency and tip-sample interaction forces affect the amplitude, phase and resonance frequency of the oscillations. These changes are measured with respect to the external reference oscillation. In tapping mode, the cantilever is oscillated such that the tip comes into contact with the sample periodically and then a restoring force is supplied by the cantilever in order to detach the tip from the sample surface and attempt to keep the oscillation amplitude constant. Typically, this technique has a lower resolution than contact mode, however it does reduce the damage caused to the sample and increases the lifetime of the tips. In non-contact mode, the cantilever is held further away from the sample's surface so that the inter-molecular forces of the sample do not affect the tip and the system detects

the vicinity of the surface. This form of AFM has the poorest resolution and is incompatible with rough surfaces as the tip can loose its interaction with the substrate surface easily. [9]

In conclusion, AFMs are very useful tools in determining the phase and topography of a substrate's surface and unlike electron microscopes they can produce true three-dimensional images of a surface. They also have the advantage over electron microscopes in that they can image both conducting and insulating samples, whereas electron microscopes have difficulty in imaging insulating samples. However, for high resolution analysis AFM images take much longer to be gathered than electron microscope images.

This project is concerned with the use of a Veeco, Dimension 3100 AFM.

### 3.5.1 Veeco, Dimension 3100 Atomic Force Microscope

This AFM is capable of being operated in contact, tapping, non-contact and lateral modes, as well as being modified for use in magnetic force microscopy and scanning capacitance microscopy. The instrument is operated using a Nanoscope IV controller which controls the AFM head and communicates data to the control PC and a Dimension 3100 controller which monitors secondary functions such as the optical microscope and sample stage. In normal operating conditions this instrument can scan areas between 500 x 500 $nm^2$ and 60 x 60 $\mu m^2$ in the XY plane and detect features between 1 and 500 nm in the Z plane. It also has a resolution of 20 nm in the XY plane and 0.1 nm in the Z plane. [9]

## 3.6 NanoManipulation

Manipulation is a fast growing area of research, which allows for objects being imaged in an electron microscope to be contacted to and/or moved. This technique has enabled the electrical characterisation of sub micro-scale devices as shown in Figure 3.2, surface science experimentation, assembly and manipulation of nano-scale devices as shown in Figures 3.3 and nanowelding to be investigated. The tools currently available for manipulation, take one of two forms. The first, involves the use of dedicated manipulation systems, whilst the second utilises a number of SPM coarse approach piezo's in-home built systems. Examples of commercial manipulation systems include the Zyvex S100 Nanomanipulator system from Zyvex [11] and the Nanoprobe from Omicron NanoTechnology. [12]

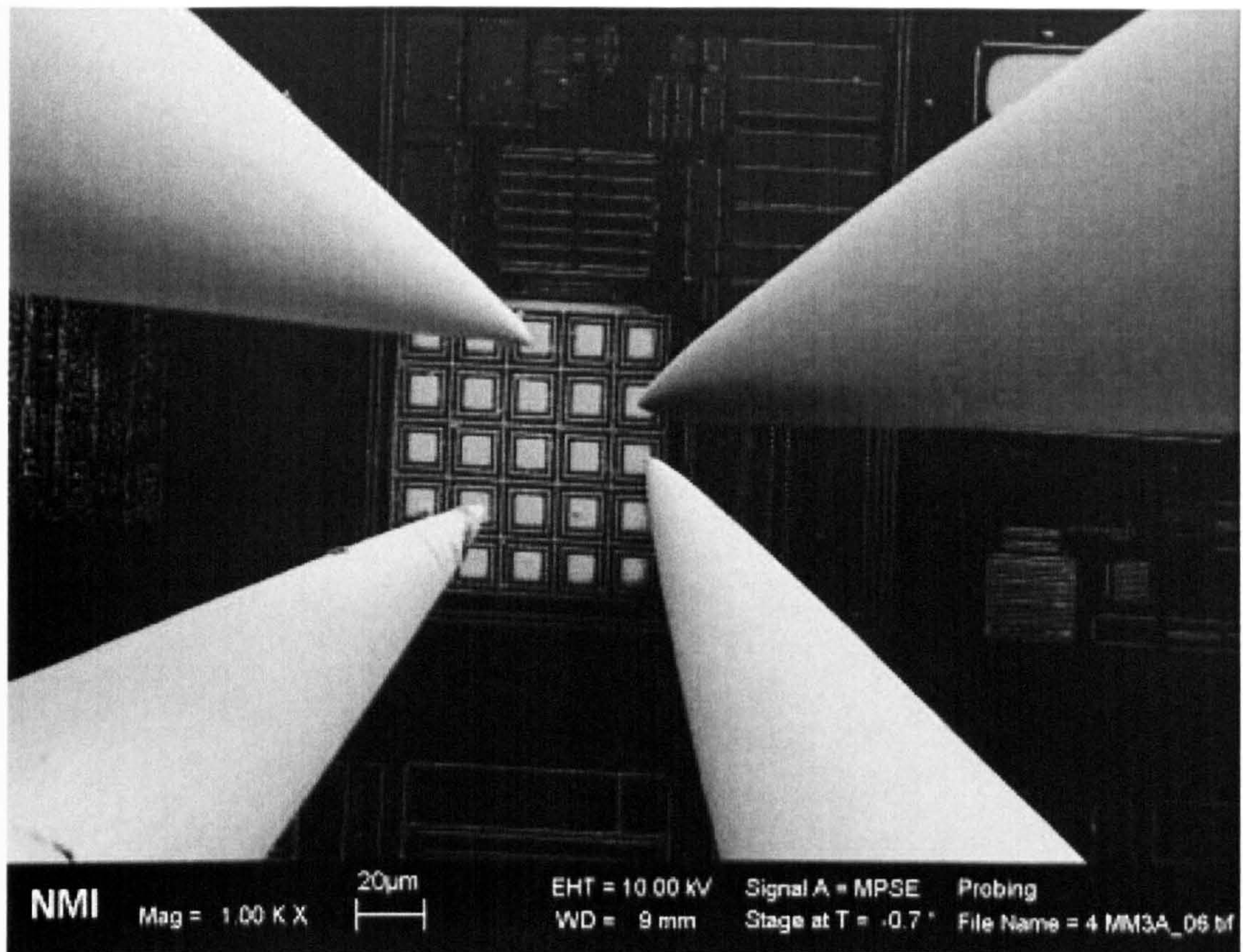


**Figure 3.2.** Image of a four-probe manipulation system that is being used for the electrical characterisation of a sub-microscale device. [10]

The Zyvex S100 manipulator consists of a four-probe manipulation system mounted on a plate than can be installed quickly and easily into an existing SEM system enabling the operator to upgrade any existing High Vacuum SEM. The Omicron Nanoprobe comprises of a 4 probe manipulation head, which is capable of atomic resolution STM and is mounted within its own Ultra High Vacuum system that includes an SEM column for navigation. Examples of the coarse approach piezo positioners include the Attocubes from Attocube Systems and the MS5 from Omicron Nanotechnology, which may be used for sample position in SPMs and SEMs, beam and device alignment and sample rotation in high magnetic fields at low temperatures. Each device is a linear positioner, which through the application of voltage may travel forwards and backwards on one axis. To travel in more than one direction, multiple units may be combined. [12, 13]

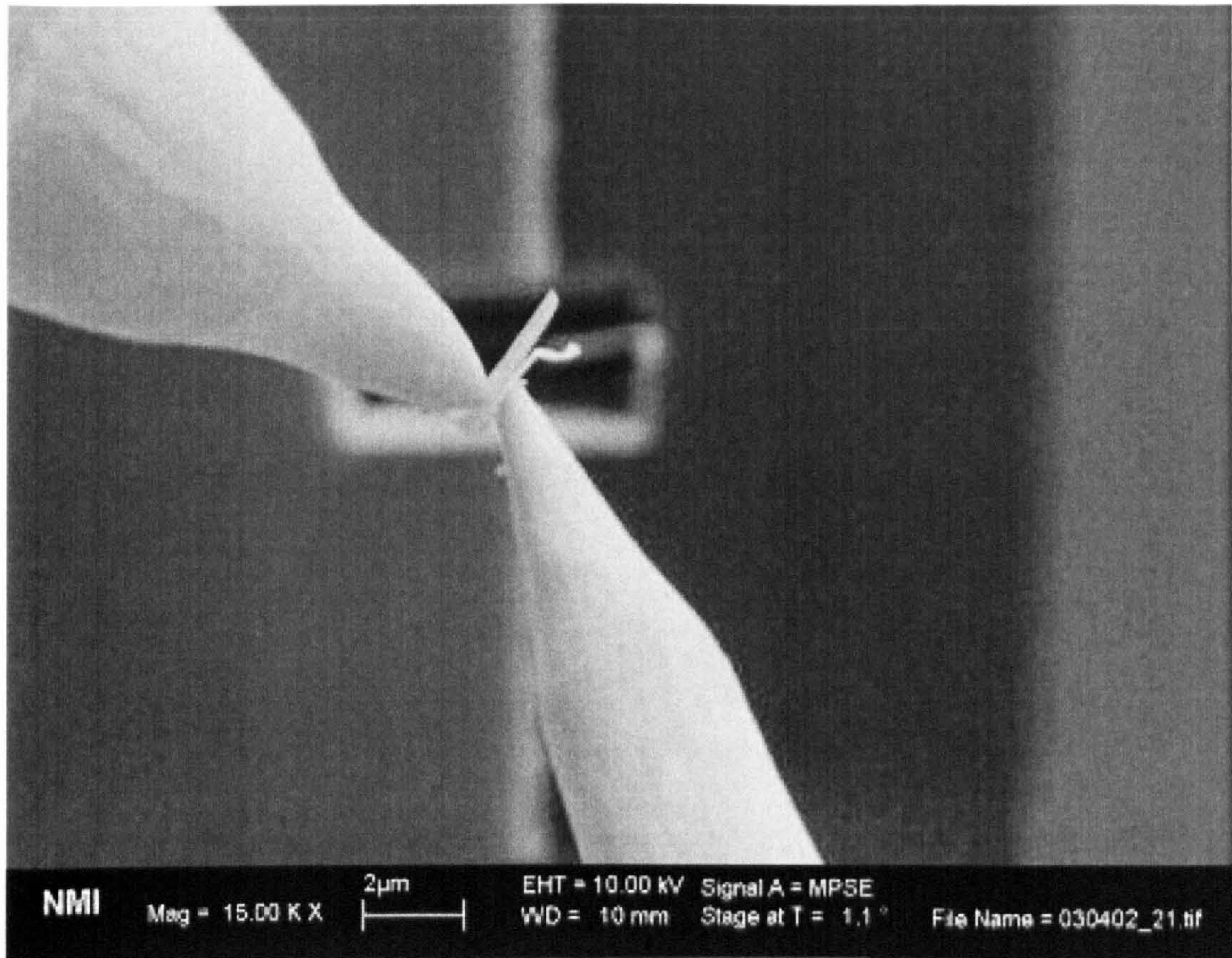


**Figure 3.3.** Image of a two-probe manipulation system being used to lift out a TEM sample, within a scanning electron microscope. [10]

## 3.6.1 Zyvex S100 Nanomanipulator System

This system is a versatile research platform that provides unique solutions to problems faced by micro- and nanotechnology researchers. It allows the user to combine their existing SEM imaging power with four positioners for precision manipulation, characterisation and testing of samples while viewing them in real time. The system consists of four positioners and a sample stage, which are mounted onto a single plate (see Figure 3.4) that can be easily installed onto the existing SEM stage using an adaptor plate. A single wire connecter is then used to connect the positioners directly to the system's control unit using a single electrical feed-through port in the sample chamber. The positioners are manipulated using a user-friendly joystick and keypad interface that is also connected to the control unit. To allow for the electrical characterisation of nanoscale devices, simple electrical connections have been included in each of the positioners. This allows for each of the probes to be connected to a wide range of test and measurement equipment using low noise BNC connections within the S100 control unit. [11]

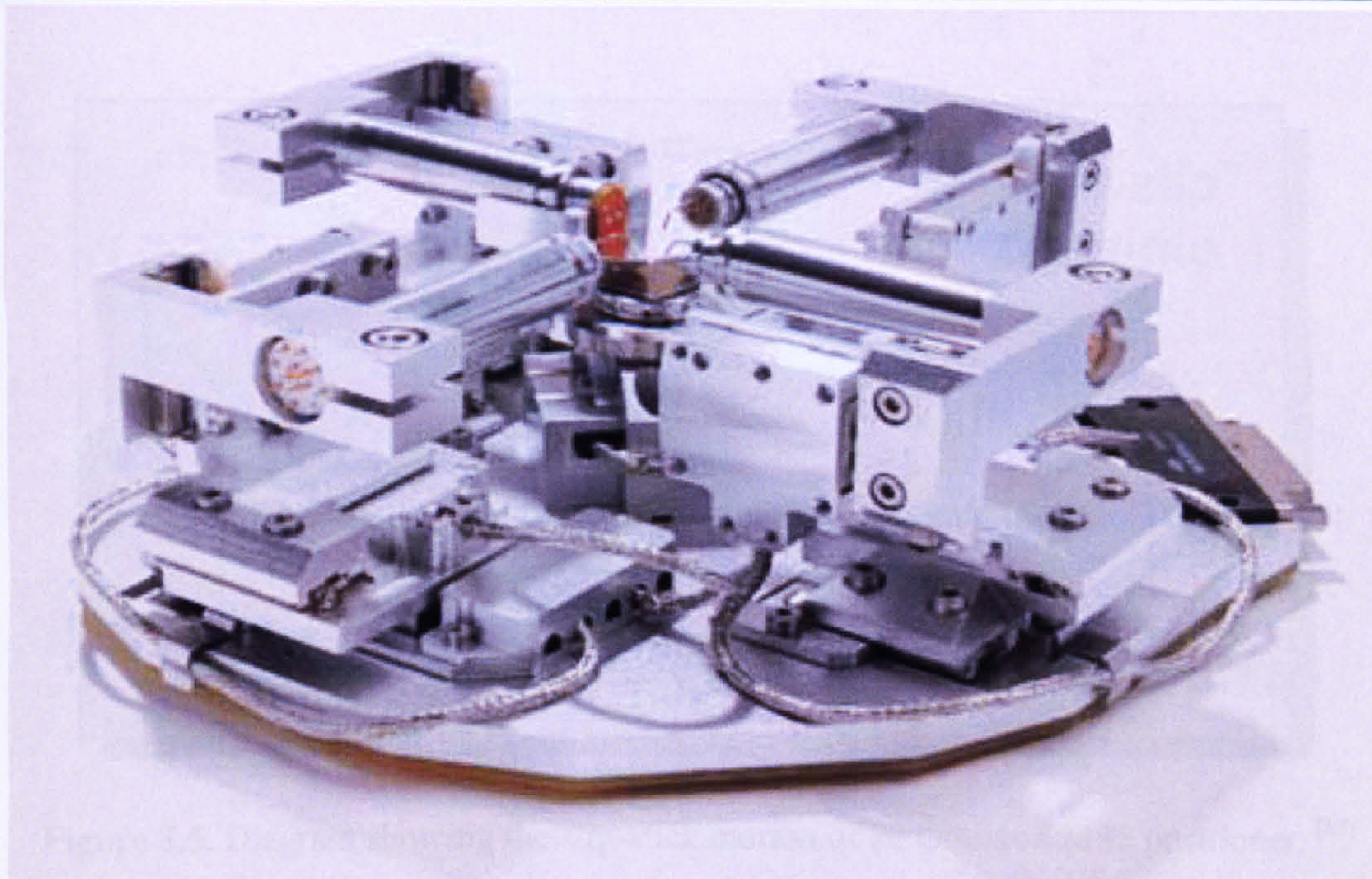

**Figure 3.4.** Image of the Zyvex S100 nanomanipulation stage. [11]

The Zyvex S100 nanomanipulation system uses both coarse and fine positioners to allow for the maximum possible range and the best resolution possible. The coarse positioners have a total range of 12 mm in each of the three orthogonal directions, whilst the fine positioners have a total range of 100 μm in the z and x directions and a range of 10 μm in the y direction. The coarse positioners also have a movement resolution of 100 nm whilst the fine positioners have a resolution of less than 5 nm in each of the axes. The central sample stage has an 360° rotation capability and is able to only be moved in the z direction. [11]

### 3.6.2 Piezo Positioners

Piezo positioners are devices, which through the application of a voltage may travel forwards and backwards on one axis. The movement of these positioners is controlled using slip-stick motion, which converts electrical impulses into a movement by controlling the inertia of a sliding block as it slips along a guide. Normally, the block is stuck to the guide in frictional arrangement. When the positioner needs to be moved, the guide is accelerated very rapidly so that the inertia of the block overcomes the frictional forces and remains almost stationary. When the guide moves back, the block sticks to it and hence makes a small step. This movement is demonstrated through the use of a guided groove in an MS5 (Figure 3.5) and the use of a guided rod in an Attocube positioner (Figure 3.6) [12, 13]

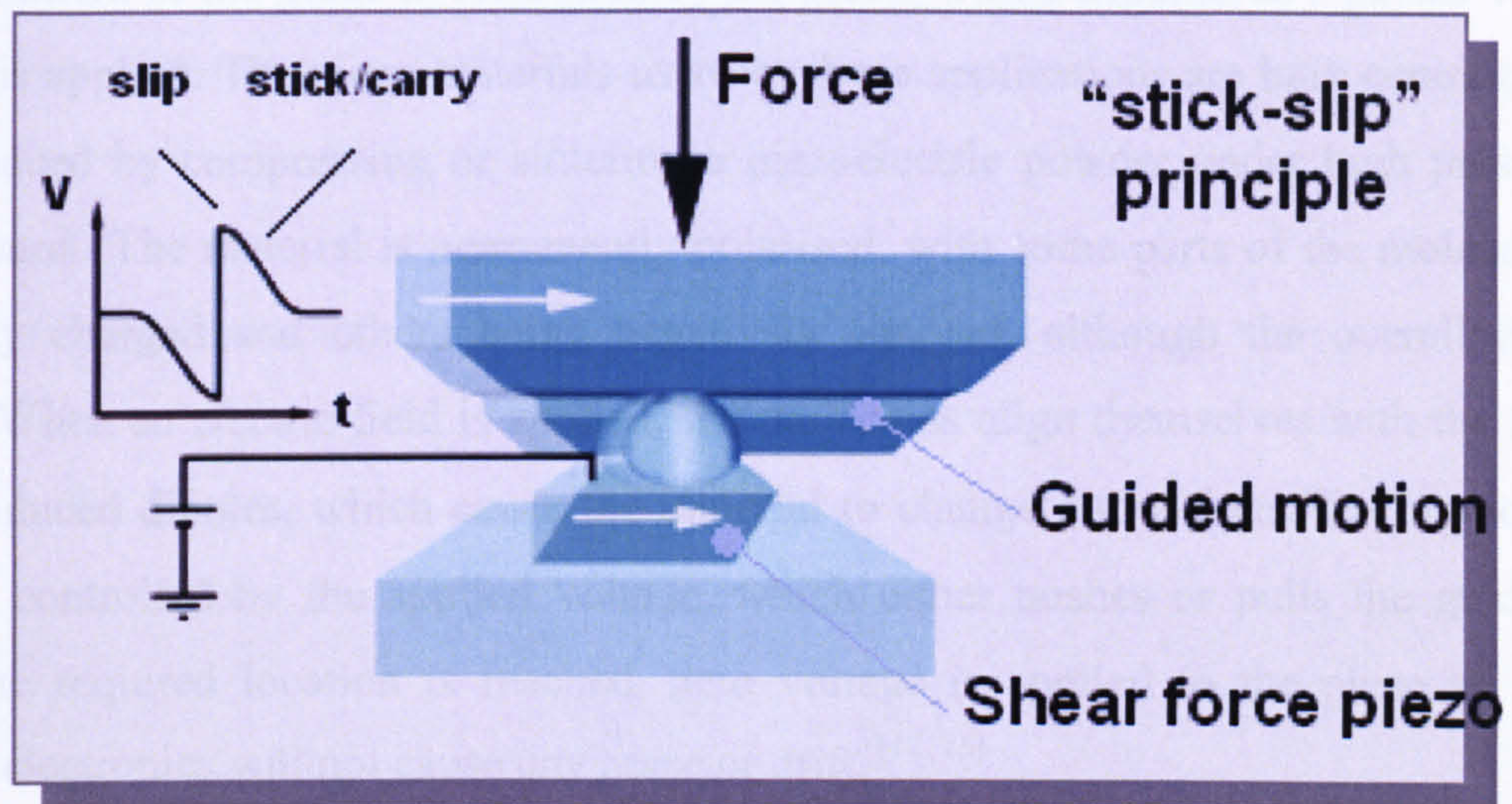


**Figure 3.5.** Diagram showing the slip-stick motion of an Omicron MS5 positioner. [12]

Piezoelectric Actuator
Sliding Block
Guiding Block
Fixed Frame
AT REST
Voltage Piezo
Time
SLIP
Voltage Piezo
Time
Δx
STICK
Voltage Piezo
Time
Δx
Net step is completed

**Figure 3.6.** Diagram showing the slip-stick motion of an Attocube Positioner. [13]

The movement of the guide is controlled by the piezo, which expands as a pulsed voltage of ~150 V is applied. The piezo materials used for these applications are bulk ceramics, which are produced by compressing or sintering a piezoelectric powder under high pressure and temperature. The material is permanently polarised, with some parts of the molecule being positively charged and others being negatively charged, although the overall charge is neutral. When an electric field is applied, the molecules align themselves with the field and create induced dipoles, which cause the material to change dimensions. The motion of the piezo is controlled by the applied voltage, which either pushes or pulls the guide along. When the required location is reached, zero voltage is applied to the piezo so that any external electronics will not cause any noise or drift. [12, 13]

One of the example of the piezo positioners that are used in this project are the Omicron Nanotechnology MS5's (Figure 3.7). These devices are versatile positioning tools that may be used under ultra-high vacuum, high vacuum and air. They have been shown to be precise and backlash free and are capable of repeatable positioning in any orientation. The step size can be varied between 40 and 400 nm with a maximum travel of 5 mm. They are also controlled using an electronic control unit, MSCU, which allows for the operation of up to three-axis movement. [12]

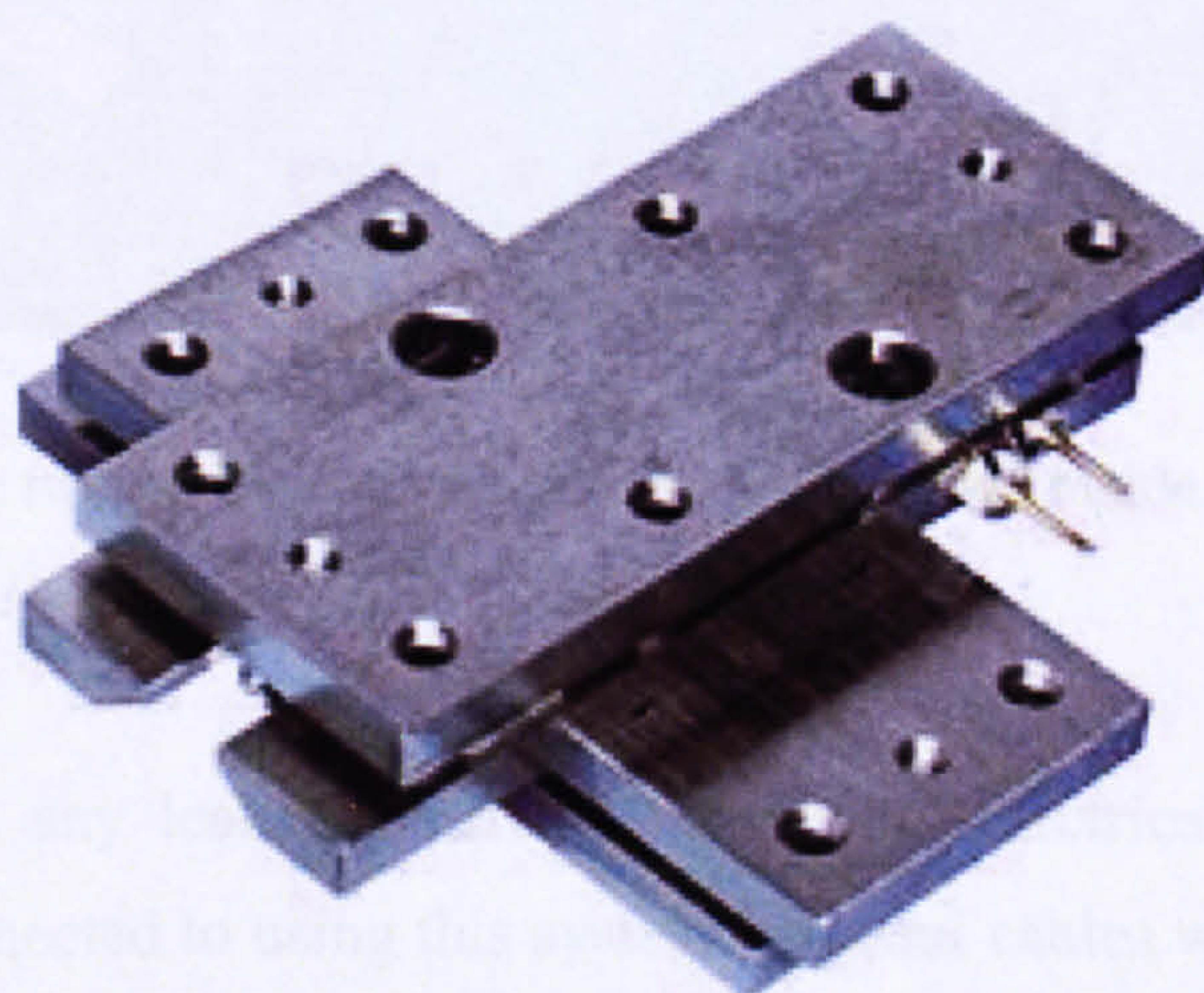

**Figure 3.7.** Image of three MS 5 positioners connected together to allow for movement in the x, y and z-axis. [12]

For this project two sets of three of these Omicron Nanotechnology MS'5s were combined and then each set of three was mounted to one of the platforms that were situated on either side of Cambridge Instruments Stereoscan 250 MK3 SEM chamber that was described in section 3.2.1. Electrochemically-etched tungsten probes, with tip radii between 25 and 400

nm were attached to each of the sets of piezo-sliders using stiff sections of wire. This allowed for the probes to be situated and moved about underneath the final pole piece of the SEM where they could be imaged. An electrical feedthrough was also used to allow for suitable electrical source-measurement units to be connected to each of the probes as well as to the SEM stage to allow for samples examined within the microscope to be electrically characterised using up to three terminals. An image of the set-up that was used in this project is shown in Figure 3.8.

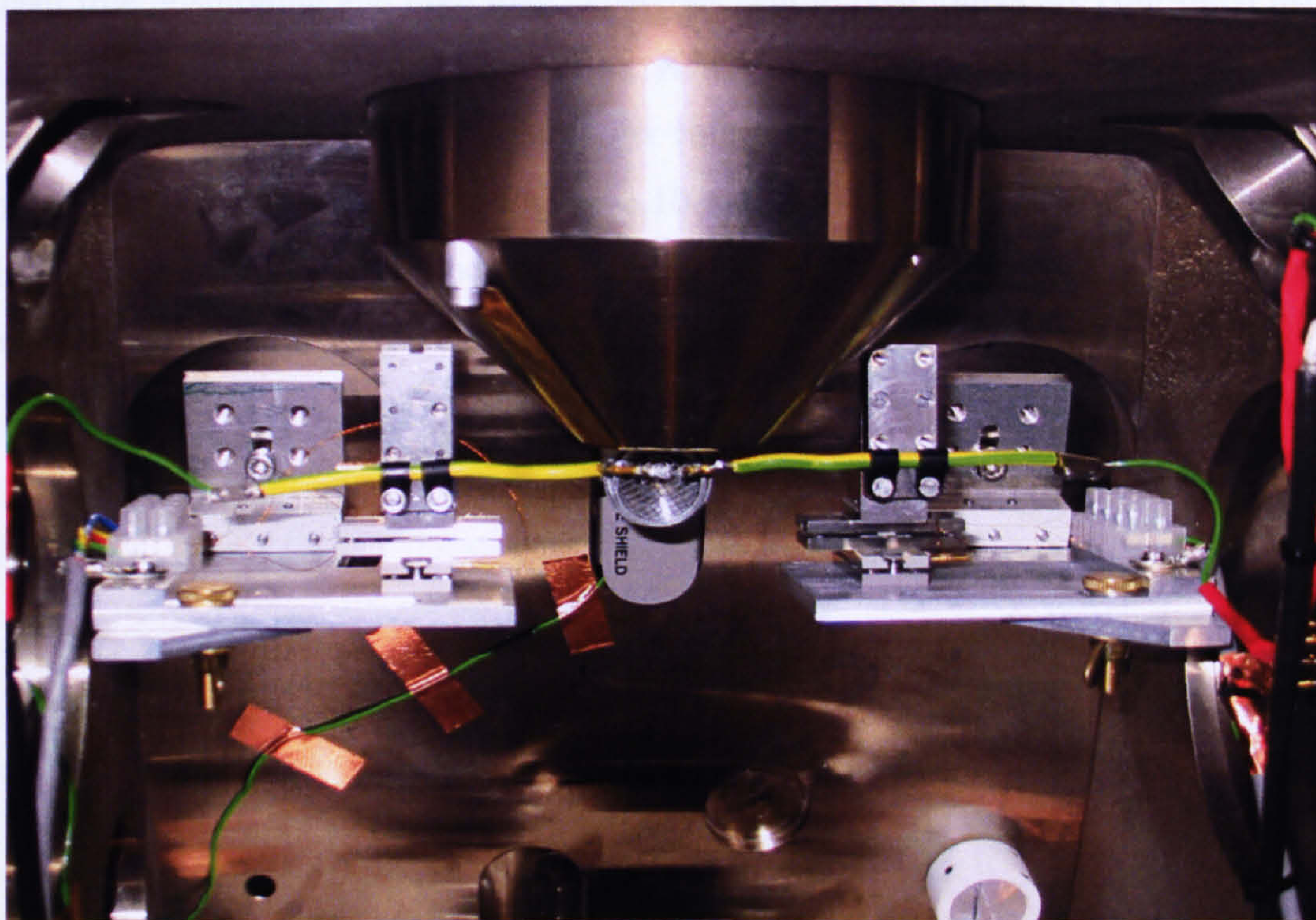


**Figure 3.8.** Image of the two-probe manipulation system mounted inside the Cambridge Instruments Stereoscan 250, MK3 SEM.

In order to minimise any leakage currents during the electrical characterisation of the samples that were connected to using this system, co-axial cables were used to connect from the electrical feedthrough to as near to the probes as possible. The use of these cables means that during the electrical measurements, the guard lead within the cables can be maintained at the same voltage as the inner lead and as a result will minimise the measurement of any leakage currents within the cables as the leakage and capacitive charging currents will only flow from the guard lead to the outer ground shield. However, using this set-up, the probes themselves will still have some capacitance charging to ground. This can be minimised by taking the measurements at a slow speed.

Another example of coarse approach piezo positioners that were used within this project are the Attocubes from Attocube Systems. Like the Omicron Nanotechnology MS5's, these positioners can be combined to produce a stack capable of movement in the three orthogonal directions. An example of three positioners that have been combined is shown in Figure 3.9. Attocube positioners can be used in both air and high vacuum, at temperatures down to 10 mK, have a maximum travel of 3 to 7 mm and a minimum step size of 1.5 nm. Furthermore, their design enables reliable positioning, low driving voltages and power consumption, backlash free positioning and high load capacities. These positioners are controlled using an Attocube Inertial Moter Driving Controller, ANC150, which applies voltage pulses to the positioners either manually or under computer control using a program such as LabView. An example of this unit is shown in Figure 3.10 and allows for the frequency and voltage amplitude applied to the positioners to be adjusted and for the selected driver to either be driven continuously or in single step mode. [13]

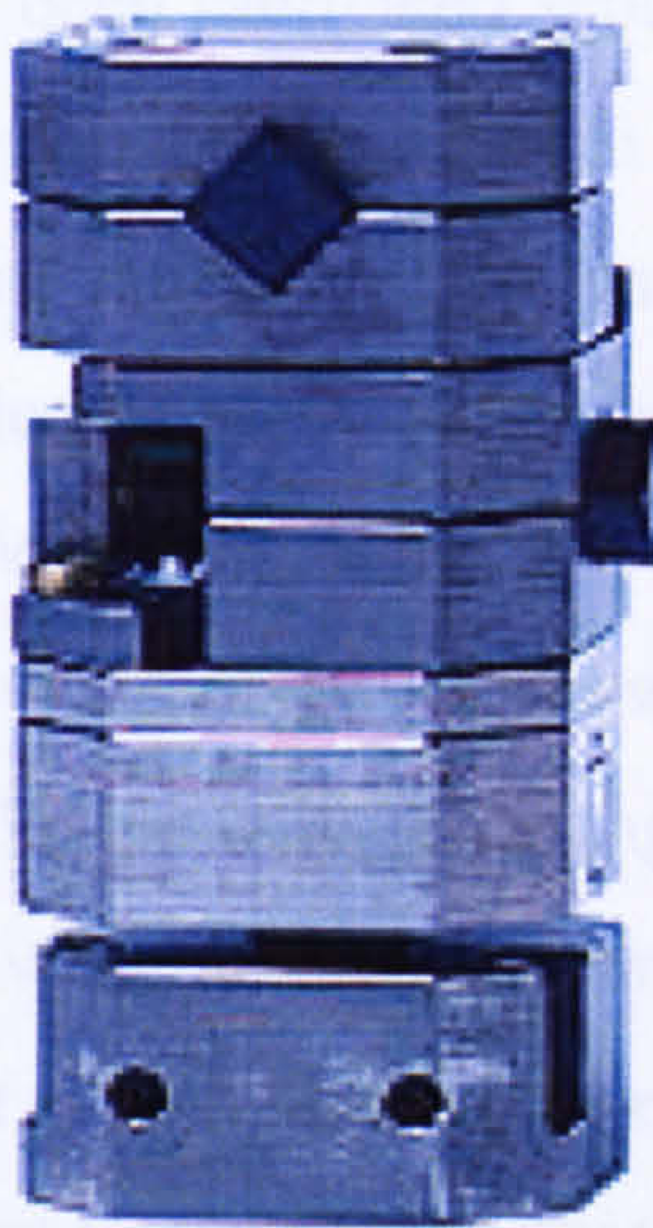

**Figure 3.9.** Image of three attocube positioners connected together to allow for movement in the x, y and z-axis. [13]

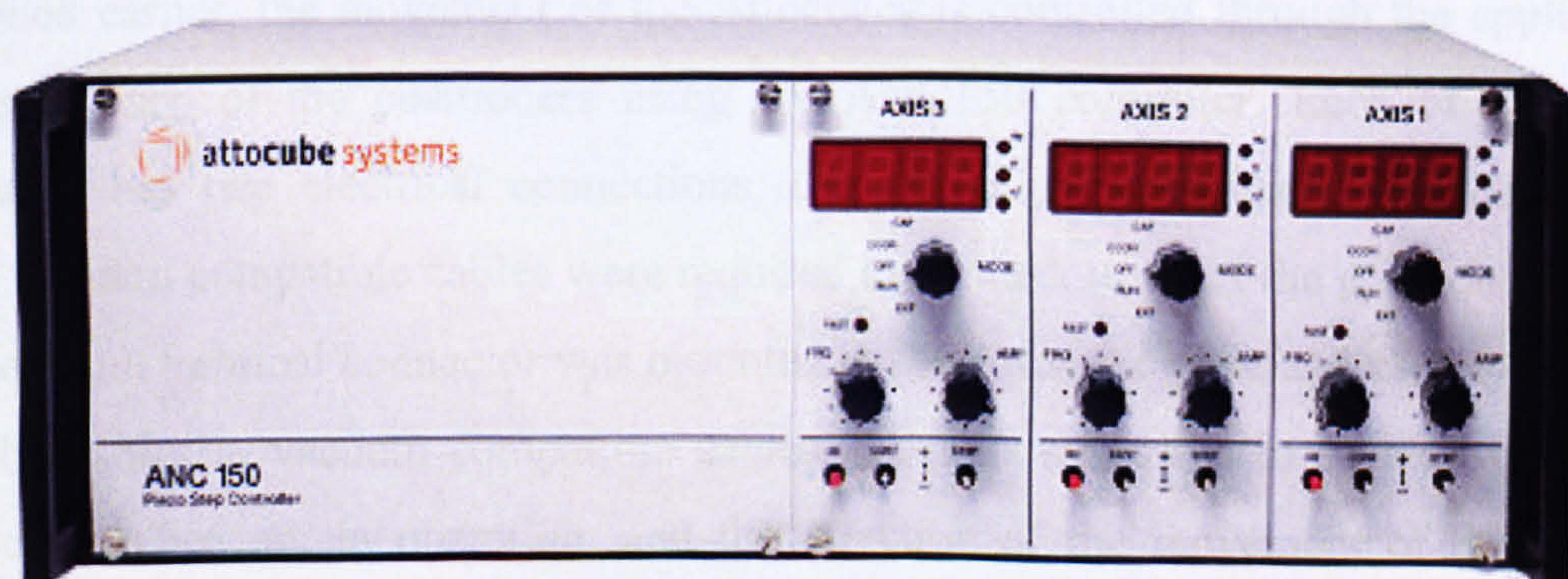


**Figure 3.10.** Image of the Attocube Inertial Moter Driving Controller, ANC150. [13]

In order to be able to operate the Attocube positioners within the FEI ESEM, a suitable method of attaching the positioners to the sample plate as well as electrically connecting to them had to be developed. The design that was produced for this, involved the manufacture of a number of specialist components, which included: -

- A plate that would mount to the stage without interfering with its movement during imaging and also hold the Attocubes.
- Two probe holders that could be mounted to the top of the Attocube stacks.
- A feedthrough for the Attocube positioner electronics.
- A feedthrough to allow for an electrical measurement system to be connected to the probes.
- Vacuum suitable cables.
- An electrically isolated sample holder.

Once each of these components had been fabricated separately, the system was installed and developed. Initially, the two-feedthrough plates were connected to the microscope and checked to ensure that the vacuum could still be maintained. Next the two stacks of Attocubes were attached to the fabricated plate, which was then attached to the actual stage. To allow for this system to be removed easily when not in use, this plate was designed to be mounted onto the microscope stage using only two screws. A probe holder was then fixed to the top of each of the stacks and its height adjusted using plastic spacers. The height was set so that when the Attocube stacks were at their maximum height, the probes would not interfere with the pole piece, from which the electron beam emerges into the chamber. However, the height had to also be set to a suitable value to allow for the probes to be moved about above the surface of the sample.

Once the Attocubes were in a suitable position, the electrical cables were connected. As mentioned earlier, the movement of the Attocubes is controlled through the application of voltage to each of the positioners using the ANC150 controller. Each of the Attocube positioners has two electrical connections, one of which is grounded. Hence, a total of twelve vacuum compatible cables were required to connect to all of the positioners. Initially, a fourteen pin terminal connector was mounted to the Attocube plate and used to connect the Attocube cables to vacuum compatible cables. As this system is to be removed from the microscope when not in operation, and the direction of the movement of the positioners depends on the way round the wires are connected, the wires were splits into two groups of

six (one for each stack). A six-way connector was then added to each group so that only two contacts have to be taken apart and reconnected when removing and replacing the system. Each of these wires was then connected to the inside of an electrical feedthrough. On the outside of the electrical feedthrough co-axial cables were used to connect each pair of the wires to the ANC150 controller.

As this system was designed to allow for the probes to be used to carry out electrical measurements, the electrical wiring used to connect the probes to the measurement system was designed to minimise any leakage and capacitive charging currents. As such, the feedthrough for the electrical wiring was designed to have four tri-axial connectors on the outside to allow for up to four connections to be made. On the inside of this feedthrough tri-axial connectors were again used with vacuum compatible tri-axial cables to connect from the feedthrough to the probe holders and the electrically isolated sample holder. To connect to the probe holders, co-axial connectors were used, as they are smaller and lighter and so would not affect the Attocubes movement.

Finally, two hollow steel wires that hold the tungsten probes were mounted on top of the probe holders, both electrically and physically to allow for the sample to be electrically connected to. The final set-up of the Attocube positioners within the ESEM is shown from the side in Figure 3.11 and from the top in Figure 3.12.

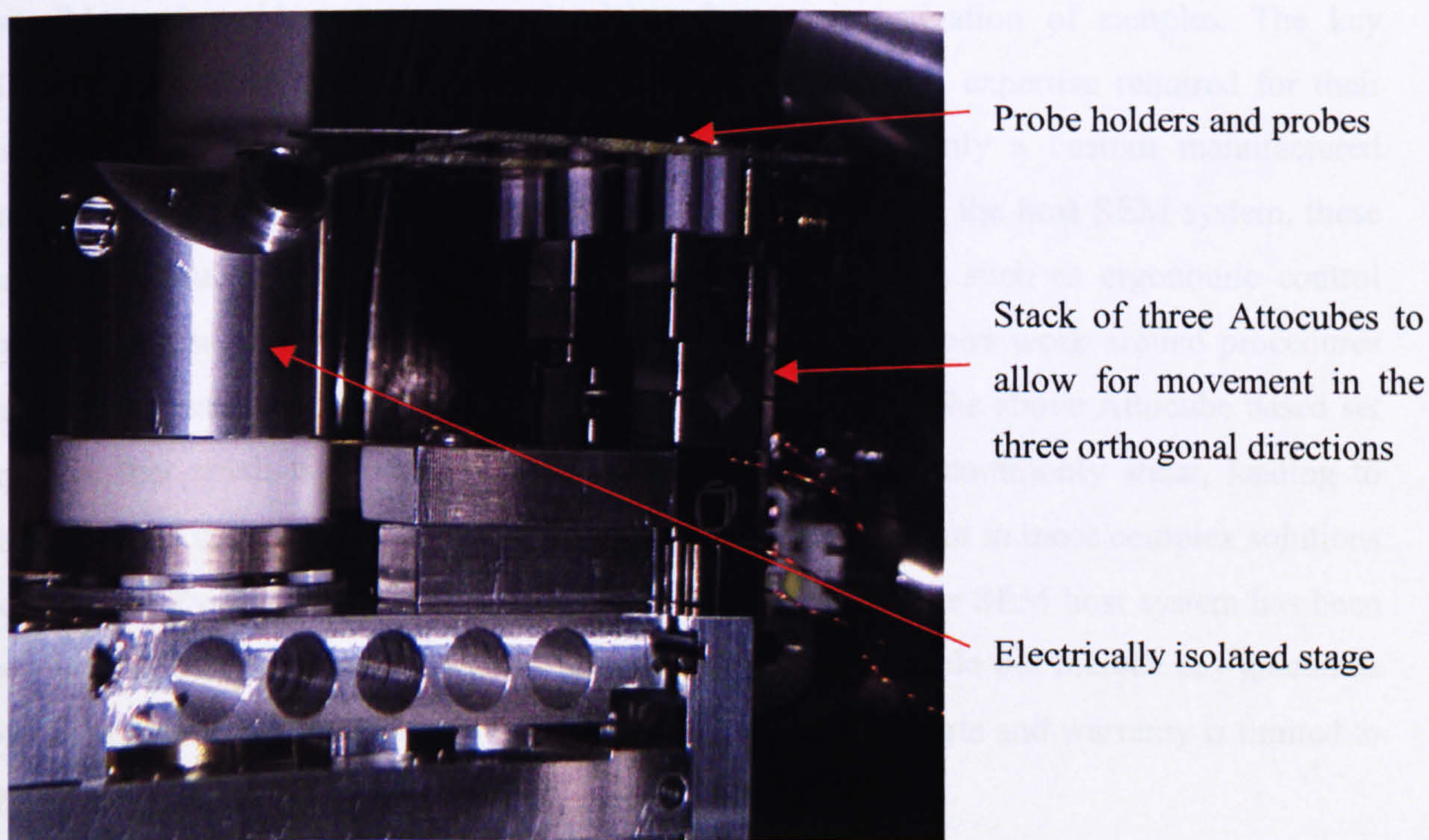


**Figure 3.11.** Image of the Attocube positioners mounted within the FEI ESEM.

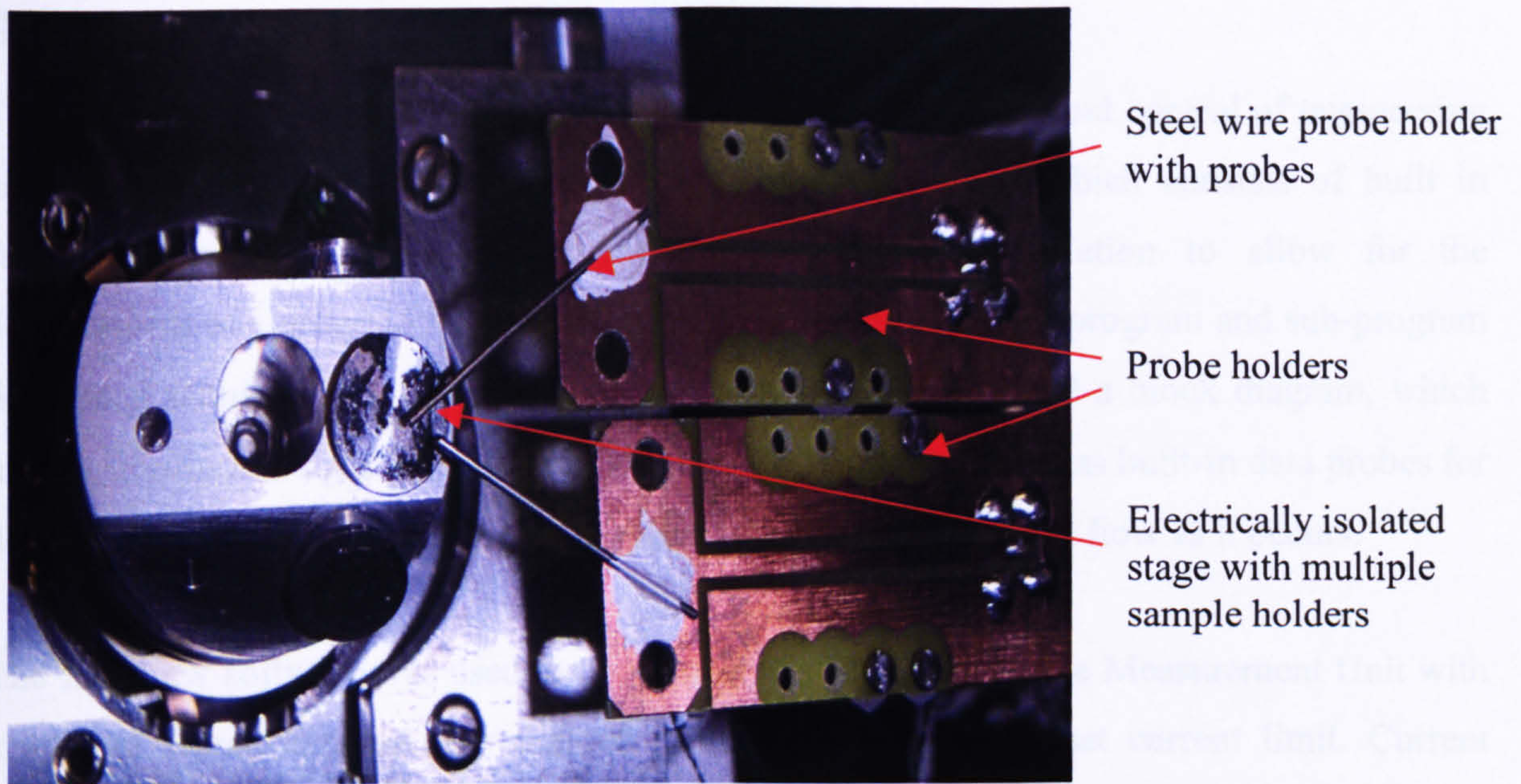


**Figure 3.12.** Image of the Attocube positioners mounted within the FEI ESEM.

The advantage of such a home-built manipulation system is that they can be specifically manufactured for each application or experiment. The availability of a wide "tool-box" of modular component parts from a variety of suppliers mean that any type of manipulation is available to meet various budgets and host SEM system internal geometries. In addition the integration of specialist modules such as rotation mean that one-off experiments are also possible and rapid prototyping and trial and error investigation of samples. The key disadvantage of such systems is the high degree of technical expertise required for their assembly and the time taken for their assembly. Commonly a custom manufactured mounting plate is required for mounting of all the parts within the host SEM system, these can be difficult and costly to obtain. User-friendly features such as ergonomic control systems and safety systems are often missing and as such require work around procedures and risk of instrument damage. A common issue found with the above Attocube based set up was that small electrical voltage connection pins would commonly shear, leading to failure of the unit. This simple failure mechanism does not occur in more complex solutions such as the Zyvex manipulator in which disconnection from the SEM host system has been considered in the design of the entire unit. Finally, these units do not include any guarantee of final operational performance, only that of the constituent parts and warranty is limited to the single parts not the unit as a whole.

## 3.7 National Instruments LabView Software

This software tool has been developed for the test, measurement and control of engineering and scientific systems. It uses a graphically based language, which consists of built in functions for input/output control, analysis and data presentation to allow for the development of a program in a similar way to flow-charting. Each program and sub-program developed within this software consists of both a front panel and a block diagram, which may be configured for a particular application. This software also has built-in data probes for debugging and a highlighted execution mode, which shows the data flow as it occurs. [14]

The LabView software was used to program a Keithley 238 Source Measurement Unit with a voltage sweep between two defined voltage limits, up to a set current limit. Current measurements were taken for each voltage step, with a defined step size that allowed for the Keithley 238's maximum of one thousand points to be taken. Further options included a user delay to be added to the machine delay and an average number of current measurements to be taken for each voltage step.

## 3.8 Keithley Source Measurement Units

Two types Keithley Source measurement units are used within this project. The first is the Keithley 238 High-Current Source Measure Unit, which was used to carry out voltage sweeps on devices situated in the Cambridge Instruments SEM and to power a resistive heater within either the FEI ESEM or the Dual Beam FIB (see section 3.8). The second is Keithley 4200 Semiconductor Characterisation System, which was used to carry out measurements within the FEI ESEM and the FEI Dual Beam FIB. [15]

The Keithley 238 High-Current Source Measure Unit consists of four instruments in one: a voltage source, a voltage measure, a current source and a current measure unit. It is able to take 1000 measurements in a sweep, source and measure voltage or current simultaneously and has a measurement sensitivity of 10 fA and 10 μV. For the Cambridge Instruments system, this instrument was programmed using the LabView software described in section 3.7 to undertake a staircase sweep with an initial bias of 0 V that gradually stepped up the voltage a set value at a time. The instrument simultaneously took current measurements, which were stored in a buffer until the end of the sweep when they were passed back to the LabView software. [9] As a power source for the resistive heater, this instrument was used to

apply a constant voltage to the heater and the current was recorded once the temperature had stabilised. This allowed for the power that was being supplied to the heater to be calculated and for the heater to be calibrated.

The Keithley 4200 Semiconductor Characterisation System has four source-measure units, which include pre-amps that may be used to characterise electronic devices with sub-femtoamp measurement sensitivity. The instrument is run using Windows, which allows for both interactive and automated tests to be carried out whilst simultaneously acquiring the data, plotting graphs and analysing the data. This system also has a number of programs, which are able to carry out up to four terminal measurements of devices. [15]

## 3.9 Omicron Nanotechnology, Resistive Heater

In order to be able to electrically characterise samples, whilst they are being annealed, an Omicron Nanotechnology Resistive Heater was modified so that it could be operated within either the FEI ESEM or the Dual Beam FIB. The heater consists of a solid-state pyrolytic boron nitride (PBN) heating element mounted on a standard Omicron Nanotechnology sample plate so that the sample can be placed in front of the heating element. The heating element is operated using a low noise current regulated power supply, which is connected to the heater using a standard BNC feedthrough. During operation it is possible to achieve temperatures in excess of 750 K, however the power supply must not exceed 7.5 W. [12]

In order to determine the actual sample temperature during its heating in a high vacuum environment, a k-type thermocouple was mounted as close to the sample as possible (less than 1 mm). To calibrate the device, the voltage and the subsequent current that the heater sourced was gradually increased and monitored to calculate the power that the heater was using. The temperature that the sample was being heated to was simultaneously measured and recorded for each power once the temperature had stabilised. These measurements resulted in the calibration curve shown in Figure 3.13. This experiment was repeated several times and the results were found to be reproducible. To test the reliability of the heater and to determine whether it would overshoot, a selection of different powers were also applied to the heater and the temperature was monitored over a time period of 20 – 30 minutes. It was found that the heater met the temperatures given on the calibration curve and in the time period investigated the heater did not overshoot and exceed the required temperature.

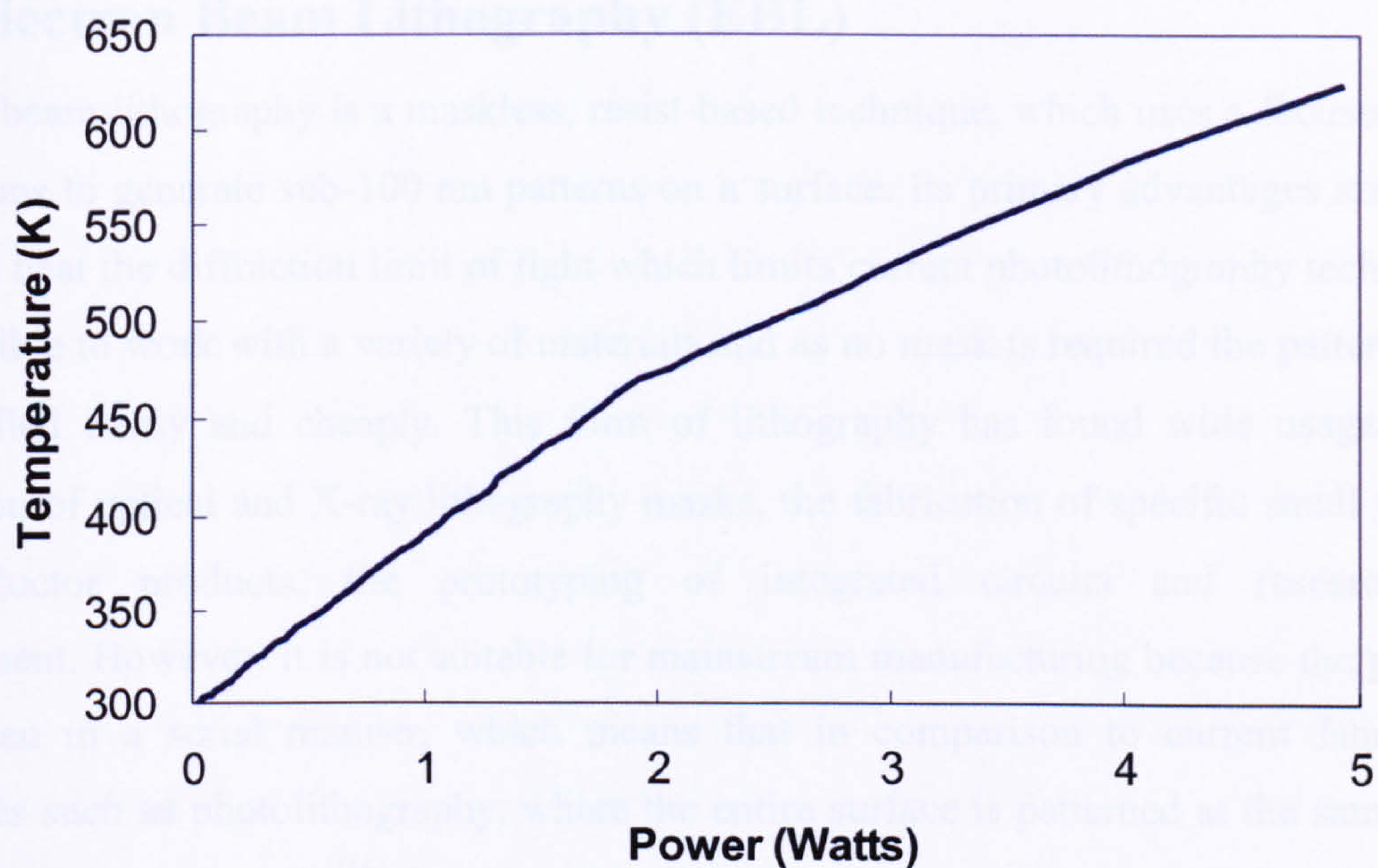


**Figure 3.13.** Experimental temperature reference curve for resistive heating within the FEI ESEM.

The modification of the heater's design also included opening the heater up so that the Attocube Manipulation system could be used in parallel with the heater and allow for electrical measurements to be taken during heating as shown in Figure 3.14.

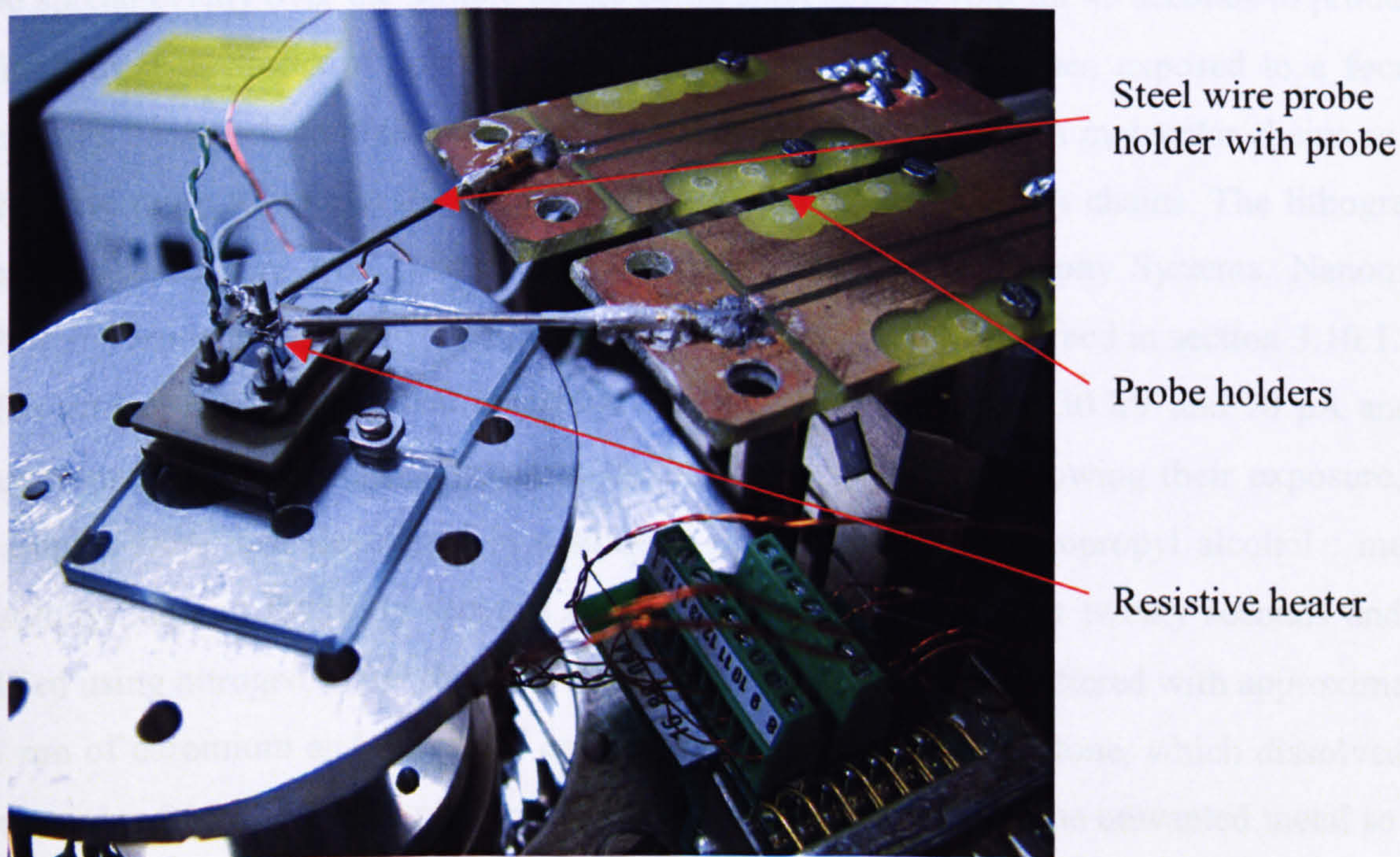


**Figure 3.14.** Image of the heater and manipulation system being used together.

## 3.10 Electron Beam Lithography (EBL)

Electron beam lithography is a maskless, resist-based technique, which uses a focused beam of electrons to generate sub-100 nm patterns on a surface. Its primary advantages are that it is able to beat the diffraction limit of light which limits current photolithography techniques, it is possible to work with a variety of materials and as no mask is required the patterns may be modified easily and cheaply. This form of lithography has found wide usage in the fabrication of optical and X-ray lithography masks, the fabrication of specific small volume semiconductor products, the prototyping of integrated circuits and research and development. However, it is not suitable for mainstream manufacturing because the patterns are written in a serial manner, which means that in comparison to current fabrication techniques such as photolithography, where the entire surface is patterned at the same time, this technique is very slow. [16]

Electron beam lithography works in a similar way to photolithography. Initially, a thin film of positive photoresist, which is sensitive to light, is spun onto the substrate onto which the pattern is to be written. For this project poly(methyl-methacrylate) (PMMA) with a concentration of 7% in anisole was first dispersed onto the samples using disposable glass pipettes. The samples were then pre-spun at 500 rpm for 15 seconds to allow for the resist to be spread evenly over the sample before being spun at 2500 rpm for 45 seconds to produce a final resist thickness of approximately 1 μm. The samples are then exposed to a focused electron beam, which breaks many of the bonds in the large PMMA molecular chains so that they are more soluble in the developer than the unexposed PMMA chains. The lithography patterns used here were written using the J. C. Nabity Lithography Systems, Nanometer Pattern Generation System within the FEI Dual Beam FIB as described in section 3.10.1. For this project it was found that using the electron beam conditions 30 kV and 70 pA and an area dose of 250 $\mu C/cm^2$ resulted in the best final patterns. Following their exposure, the samples were then developed in a solution of 1:1 IPA:MIBK (isopropyl alcohol : methyl isobutyl ketone) for thirty seconds before being rinsed in IPA for twenty seconds and the dried using nitrogen. After their development the samples were sputtered with approximately 5 nm of chromium and 30 nm of gold before being soaked in acetone, which dissolved the remaining PMMA. As the photoresist is removed it also removes the unwanted metal so that only the required metal pattern is left on the sample's surface. [16]

### 3.10.1 Nanometer Pattern Generation System (NPGS)

This system is a user-friendly program, which has been designed to allow for complex patterns to be written in virtually any electron microscope. There are three main parts to the system, the first is the pattern design program, the second is the parameter run file editor and the third is pattern writing controller. The pattern designs are created using DesignCAD, which has many powerful layout and editing features, including being able to draw either lines or filled elements such as circles, arcs and rectangles and text in a range of fonts. The program also allows for the pattern elements within one file to be written with different exposure conditions and controlled separately to each other. Once the pattern design has been completed, the run file editor is used to set the exposure conditions for each of the types of elements within the pattern. This editor also has a range of options, which allow the writer to carry out more complex commands such as writing a number of arrays, writing at different magnifications and at different exposures. Once the run file has been created, the patterns may be processed and run. The NPGS controls the writing of the pattern within the microscope by simultaneously controlling the x-y scan coils and the beam blanking. [16]

## 3.11 Summary

This chapter has highlighted the experimental tools and techniques used in the research presented in this thesis. It has outlined how each of the instruments works and discussed some of the advantages and disadvantages of each of the instruments. It has also explained the development of a two-probe manipulation system that was built as part of this work using Attocube piezo positioners that can be used to carry out two or three terminal electrical measurements of various samples. Two other manipulation systems that will be used in this work have also been introduced as well as the modification of a resistive heater to work in conjunction with the Attocube manipulation system. Where appropriate, further details of specific procedures will be explained within the relevant chapter.

## 3.12 References

[1] Goldsteing, J., Scanning Electron Microscopy and X-Ray Microanalysis: A Text for Biologists, Materials Scientist and Geologists, Kluwer Academic, Plenum Press, 2nd Edition, May 1992

[2] Cambridge Instruments S250 MK3 Scanning Electron Microscope Manual

[3] FEI, Quanta 200 Manual

[4] FEI, Strata DB 235M Manual

[5] Transmission Electron Microscopy of Materials, G. Thomas and M. J. Goringe, A Wiley-Interscience Publication (1999)

[6] The Casa Cookbook, Part 1: Recipes for XPS Data Processing. The CasaXPS User's Manual, Neal Fairley and Alan Carrick, Acolyte Science, 0-9549533-0-4 (2005).

[7] Modern Techniques of Surface Science, D. P. Woodruff and T. A. Delchar, Cambridge Solid State Science Series, 2nd Edition, 0-521-42498-4 (1999).

[8] www.thermo.com

[9] Digital Instruments, Veeco Metrology Group Scanning Probe Microscopy Training Notebook, Version 3.0 (1998)

[10] www.nanotechnik.com

[11] Zyvex S100 Nanomanipulation System Manual

[12] www.omicron-instruments.com

[13] www.attocube.com

[14] www.ni.com

[15] www.keithley.com

[16] J. C. Nabity Lithography Systems Nanometer Pattern Generation System Users Manual for NPGS v8 and v9, Released 08/2004

# CHAPTER FOUR

# 4 Geometrical and Structural Characterisation of Electron Beam Deposited Tungsten Interconnects

## 4.1 Introduction

This chapter will focus on describing the geometrical and structural characterisation of tungsten interconnects that have been fabricated from the precursor $W(CO)_6$ using EBID. The geometrical characterisation shall be carried out using an atomic force microscope, while the structural characterisation shall be carried out using a transmission electron microscope. In particular, it shall be shown that the growth rate of the deposits increase with increasing beam current and decrease as the lifetime of the precursor increases. It shall also be shown that the growth rate of the deposits is highly dependent on the electron source and the type of substrate used. The structural analysis shows that the as-deposited structures consist of a mix of amorphous carbon and tungsten, with more carbon than tungsten in the deposits. The effects of heating the substrate during the deposition are also investigated and it is found that the growth rate decreases with increasing substrate temperature.

## 4.2 Experimental Method

The depositions were carried out using the FEI Dual Beam FIB that was described in section 3.2.3 using $W(CO)_6$ as a precursor. As this work has been undertaken with a view to being able to use these deposits to contact to nanostructures such as nanowires or carbon nanotubes. The deposition parameters have been chosen to cause minimal damage to the nanostructures while still achieving a reasonable deposition rate.

When nanostructures, such as CNTs, are imaged within a SEM, they are prone to heating and damage by the electron beam. It has also been shown that when CNTs are imaged and contacted to in a SEM, the exposed areas of the sample become covered in a carbonaceous material, which is a result of the ubiquitous hydrocarbons adsorbed on the walls of the SEM chamber being deposited on the sample by the electron beam. Both the amount of damage and the thickness of the carbonaceous layer increase with increasing electron beam voltage and result in an increase in the resistance of the devices. Therefore, nanostructures are generally imaged using relatively low electron beam energies of between 5 and 10 keV. [1,2]

The effects of changing the electron beam voltage on the deposition rate and resistivity of EBID structures has also been investigated by a number of researchers [3-5], notably Gopal et al. [5] As the electron beam voltage is increased the deposition rate decreases, with the most significant changes in the growth rate occurring for beam energies below 10 keV. [3,4] The resistivity of the deposits has also been found to decrease with increasing beam voltage for beam energies below 5 keV, while for electron beam voltages above this, the resistivity has been found to remain approximately constant. [5] During this study Gopal et al. [5] also measured the leakage currents between closely spaced EBID interconnects and found that the leakage current increased exponentially with electron beam voltage and decreased exponentially with increasing distance between the wires. These results indicate that a trade off needs to be made between achieving the maximum growth rate, which is attractive for making EBID a mainstream technique, and the minimum resistivity and leakage between closely spaced wires, which is crucial for interconnect application needs. As this project is concerned with the use of EBID to connect to CNTs, an electron beam energy of 10 keV was chosen as it yields a reasonable growth rate and resisitivity, which is important for electrical applications but will cause minimal damage and contamination growth on the CNTs.

When selecting the electron beam current, a similar trade off has to be made as for the selection of the electron beam energy. This is because when the electron beam current is increased, it results in a beam with a larger diameter with more electrons of the same energy. When imaging nanostructures this has the effect of allowing increased heating and damage of the structures to occur, while for EBID it has the effect of reducing the resolution of the process. However, recent studies into the effects of the electron beam current on the growth rate and resolution of EBID has shown that the growth rate increases with increasing beam current [4], while the resistivity initially decreases as the beam current is increased up to 1 nA

and then remains constant [6]. These results mean that a trade off between the growth rate, resolution and the resistivity of EBID interconnects again needs to be made. As the deposits produced here are characterised with a view to being used as an interconnect material for nanostructures, the deposits will be characterised for electron beam currents of 0.36, 1.5 and 5.9 nA to determine the most suitable deposition parameters.

The properties of EBID interconnects are not only dependent on the electron beam conditions, but also on the exact manner in which the electron beam is scanned. There are two main parameters that are used to control the scan of the electron beam:

1. The dwell time - the amount of time that the electron beam spends on each pixel of the deposition area.
2. The pitch - the distance between each point that the electron beam makes.

The effect of increasing the dwell time on the deposition growth rate has been shown to cause the deposition rate to decrease. [7,8] This has been attributed to the electron beam dissociating more of the adsorbed precursor molecules during the dwell time than are replaced during the beam off time so that the process becomes gas flux limited. However, it has also been shown that the resistivity decreases with increasing dwell time as a greater number of dissociation events can occur and remove a greater quantity of volatile by-products from the deposits. [8] As such, to produce deposits with a reasonable growth rate and resistivity, a dwell time of 200 μs was chosen. Changing the pitch that is used to carry out the depositions can also affect the shape and the resistivity of the deposited structures. If the pitch is increased to large enough values, it will produce a deposit that is not uniform and is made up of a series of dots rather than a continuous structure. As the structure becomes less continuous the resistivity of the deposit will also increase. If the pitch is reduced to very small values it will increase the time required to produce the deposit. Therefore, a pitch of 10 nm was chosen in accordance with the size of the focused electron beam.

The base pressure in the chamber of the FEI Dual Beam FIB that was used in this study was measured using a cold cathode ion gauge and was found to be better than $4 \times 10^{-6}$ mbar before any of the depositions were carried out. When the GIS needle was opened in order to carry out any of the depositions this pressure was found to rise to $\sim 4 \times 10^{-5}$ mbar. For all of the following characterisation work, rectangular deposits were made onto either silicon dioxide substrates with a 300 nm thick oxide layer or onto standard 100 nm thick silicon nitride TEM membranes with a 3 $mm^2$ silicon frame and a 500 $\mu m^2$ $Si_3N_4$ window.

## 4.3 Geometrical Characterisation

In order to determine how varying the number of the passes that the electron beam made on the size of the deposits, deposits 200 nm by 3 μm were made onto a silicon dioxide substrate with a 300 nm oxide layer. The number of passes was varied from 20 up to 200 passes in 20 pass steps and was carried out using the electron beam conditions described previously. After the deposition, the samples were transferred to the Digital Instruments 3100 AFM described in section 3.5.1 and accurate height measurements were made using the AFM operated in tapping mode with Nanosensor silicon cantilevers. Figure 4.1 shows a typical AFM scan for three successive deposits made using an electron beam current of 1.5 nA. The left hand deposit was made using 140 passes, the centre deposits made using 120 passes and the right hand deposit made using 100 passes of the electron beam.

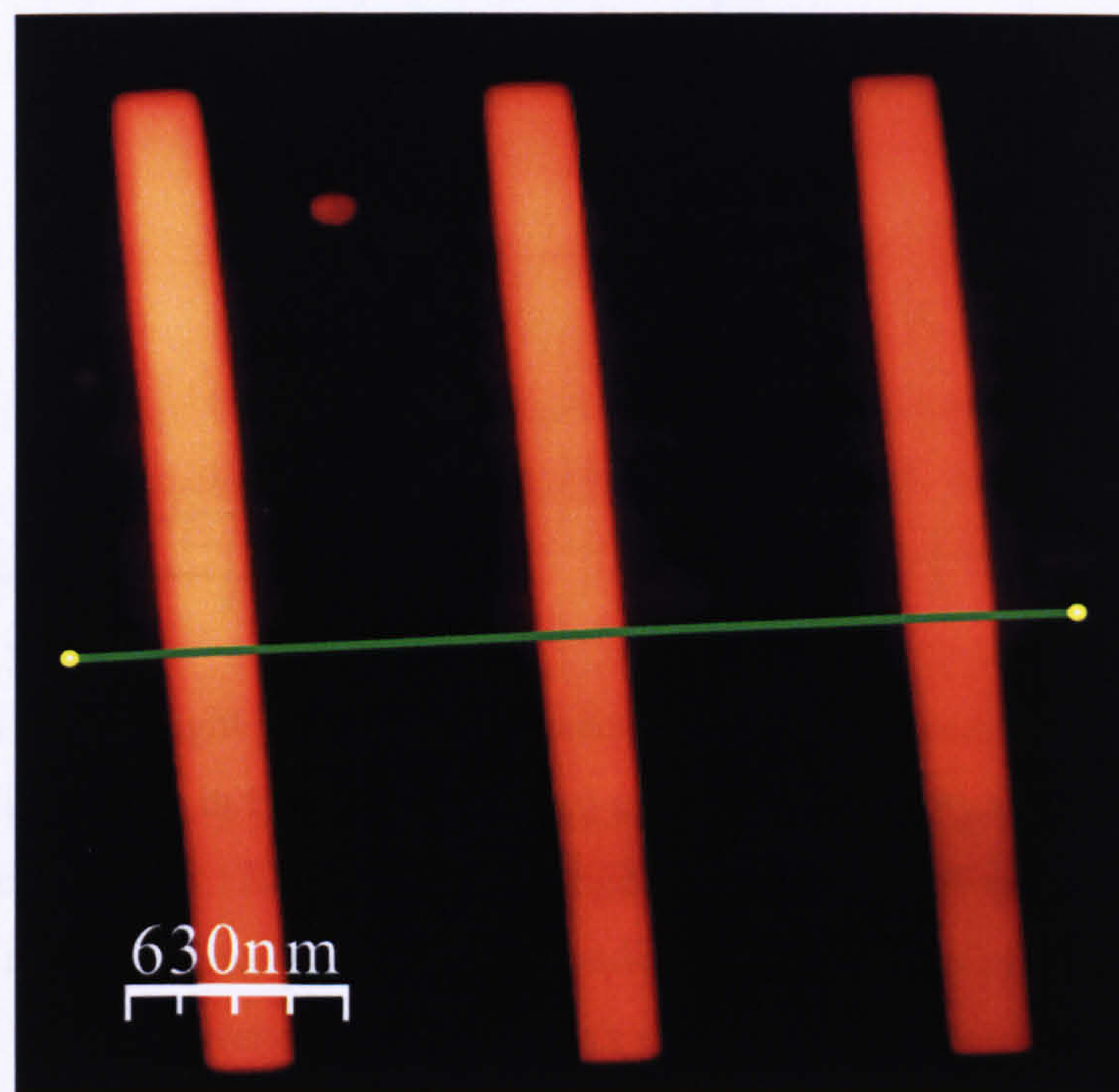


**Figure 4.1.** AFM scan of three successive EBID tungsten interconnects. The left hand deposit was produced using 140 passes of the electron beam, the centre deposit using 120 passes and the right hand deposit was produced using 100 passes of the electron beam.

The effect of changing the number of passes made by the electron beam and the actual geometry of the deposits may be seen more clearly and analysed through the examination of the height and length profiles of the deposits. The resulting profiles for the deposits shown in Figure 4.1 are shown in Figure 4.2. In particular Figure 4.2 (a) shows the height profile for

the three deposits along the section line that is shown in Figure 4.1, while Figure 4.2 (b) shows the length profile for the left hand deposit shown in Figure 4.1, which was deposited using 140 passes of the electron beam. As can be seen from Figure 4.2 (a), the height of the deposits increases linearly with the number of passes made by the electron beam. Meanwhile, Figure 4.2 (b) shows how the height of the deposits remains approximately constant along their length. In both Figures 4.2 (a) and (b) the height profiles of the deposits show that the sidewalls of the deposits are not completely vertical. This may be due to secondary electrons emitted from the sidewalls of the deposits during the deposition dissociating the precursor molecules adsorbed there as was described in section 2.5.4.

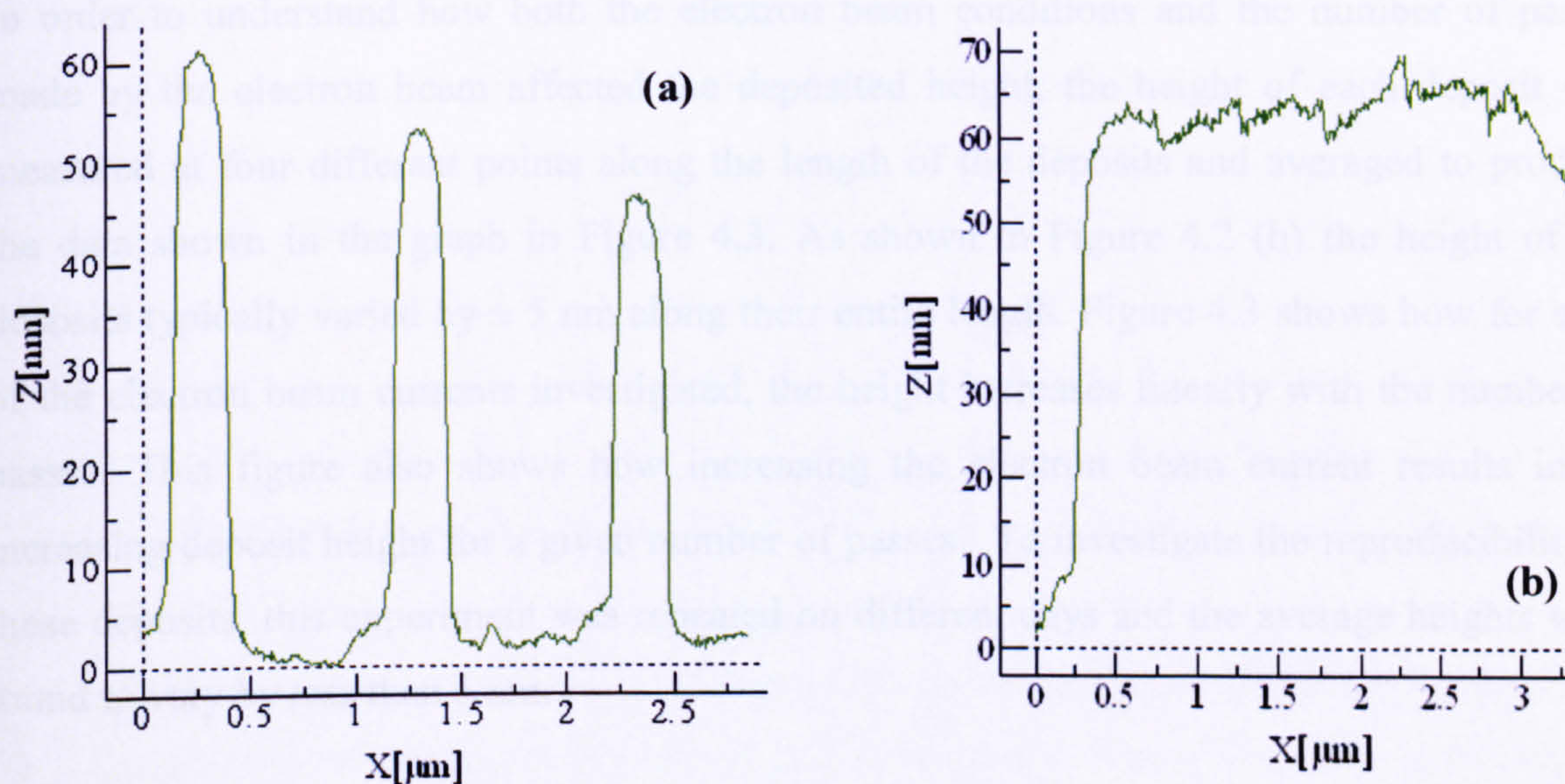


**Figure 4.2. (a)** Graph of the height profile of three electron beam deposited tungsten interconnects taken along green line shown in Figure 4.1. The left peak is produced by a deposit made with 140 passes, the centre peak with 120 passes and the right hand peak by a deposit with 100 passes. **(b)** Graph of the height profile of a deposit made using 140 passes of the electron beam taken along the length of the deposit.

Furthermore, both the measured width and length of the deposits were found to be greater than the defined deposition area, with the three deposits measured in Figure 4.2 having FWHM widths of ~290 nm and FWHM lengths of ~3.09 μm. These values support the idea that secondary electrons are emitted from the sidewalls of the deposits where they dissociate any precursor molecules. The measured FWHM widths and lengths of these deposits were also found to remain approximately constant with the number of passes made by the electron beam so it can be concluded that the size of the deposits over that of the defined deposition area has become greater than that of the mean free path of secondary electrons in the

deposited material. This idea is also supported by the fact that both the width and the length of the deposits is ~ 90 nm greater than the defined deposition area and suggests that the mean free path of secondary electrons in tungsten deposits produced using EBID of $W(CO)_6$ is ~ 45 nm. From this result it may also be expected that for deposits produced with a low number of passes of the electron beam there would be some variation in the measured width and length of the deposits.

### 4.3.1 Height Characterisation

In order to understand how both the electron beam conditions and the number of passes made by the electron beam affected the deposited height, the height of each deposit was measured at four different points along the length of the deposits and averaged to produce the data shown in the graph in Figure 4.3. As shown in Figure 4.2 (b) the height of the deposits typically varied by ± 5 nm along their entire length. Figure 4.3 shows how for each of the electron beam currents investigated, the height increases linearly with the number of passes. This figure also shows how increasing the electron beam current results in an increasing deposit height for a given number of passes. To investigate the reproducibility of these deposits, this experiment was repeated on different days and the average heights were found to vary by less than 5 nm.

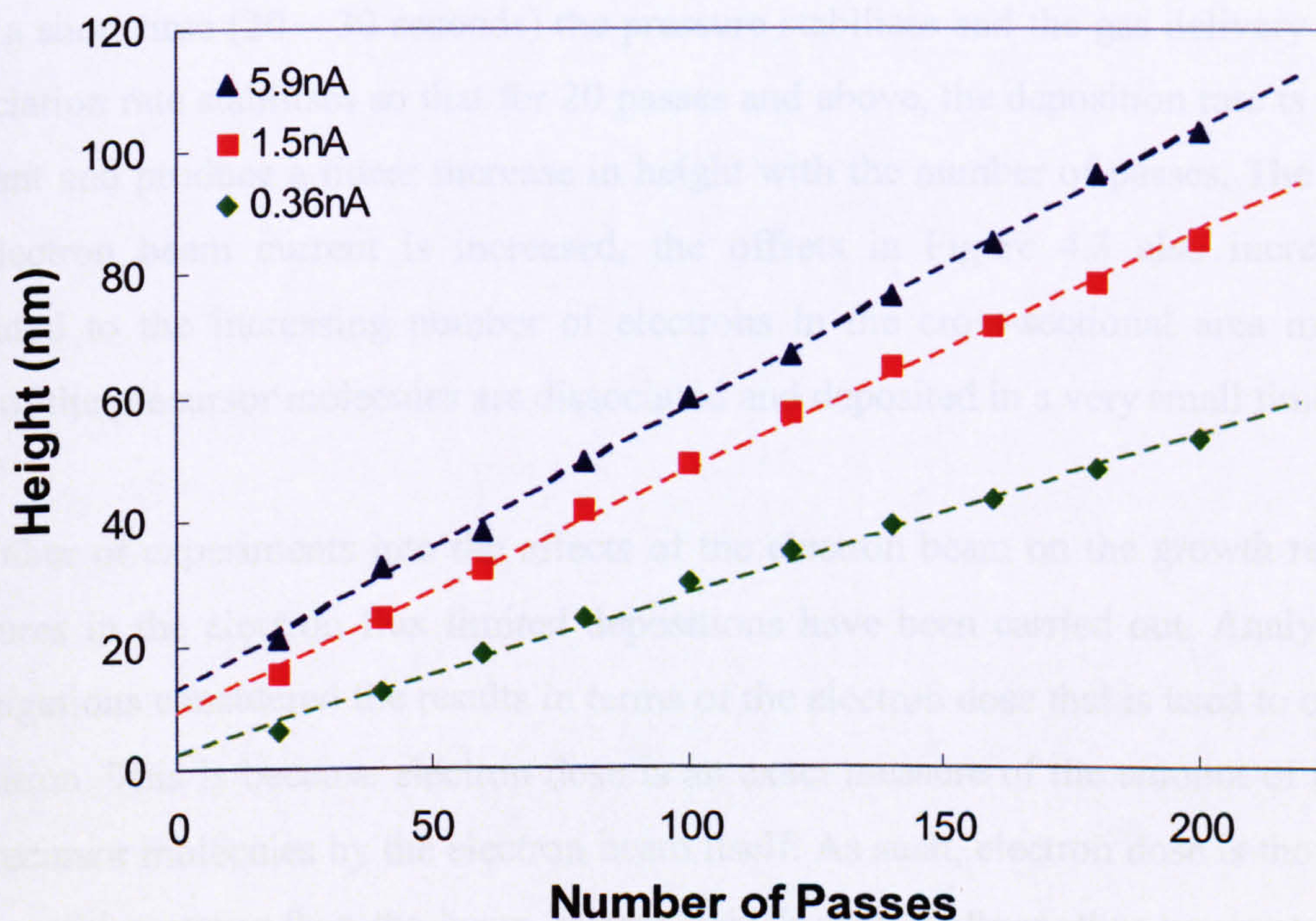


**Figure 4.3.** Graph showing how the deposited height varies with increasing number of passes for beam currents of 0.36, 1.5 and 5.9 nA.

In order to be able to estimate the deposited height for a given number of passes at each electron beam current, lines of best fit were fitted to the data as shown in Figure 4.3. The gradients of these lines were found to increase with the beam current and be equal to 0.26, 0.39 and 0.46 nm per pass for electron beam currents of 0.36, 1.5 and 5.9 nA respectively. The increasing gradient with deposited height may be understood by considering the effect of changing the beam current on the electron beam itself. As the electron beam current is increased the diameter of the electron beam also increases and has diameter of 1.7, 3.4 and 6.7 nm for electron beam currents of 0.36, 1.5 and 5.9 nA respectively. This means that as the beam current is increased the number of electrons also increases. Each of these electrons is capable of being involved in the deposition process and so the increased electron beam current means that the probability of a precursor molecule being dissociated also increases.

Figure 4.3 also shows how extrapolation of the lines of best fit of the data for each of the electron beam currents does not extend through the origin but rather through 2.6, 9.2 and 12.7 nm for beam currents of 0.39, 1.5 and 5.9 nA respectively. This result suggests that the growth of EBID deposits is not constant throughout the deposition time and that a faster deposition rate occurs during the very early stages. This behaviour may be explained by considering the start of the deposition process. Indeed, at the start of the deposition process, the injection needle is opened and a large pressure surge is observed. This gas surge allows for a slightly higher than normal deposition rate to occur and causes the offsets in Figure 4.3. After a short time (20 – 30 seconds) the pressure stabilises and the gas delivery – precursor dissociation rate stabilises so that for 20 passes and above, the deposition rate is found to be constant and produce a linear increase in height with the number of passes. The fact that as the electron beam current is increased, the offsets in Figure 4.3 also increase can be attributed to the increasing number of electrons in the cross-sectional area meaning that more of the precursor molecules are dissociated and deposited in a very small time.

A number of experiments into the effects of the electron beam on the growth rate of EBID structures in the electron flux limited depositions have been carried out. Analysis of these investigations considered the results in terms of the electron dose that is used to carry out the deposition. This is because electron dose is an exact measure of the amount of exposure of the precursor molecules by the electron beam itself. As such, electron dose is thought to be a more useful measure than the beam current, which should allow other groups to replicate a set of results exactly in another system. In order to calculate the electron dose it is necessary

to first measure the beam current accurately using a Faraday cup. The actual beam specimen currents were hence found to be 130 pA for the 0.36 nA electron beam current, 700 pA for the 1.5 nA electron beam current and 1870 pA for the 5.9 nA electron beam current.

These beam currents and the other deposition parameters, as given in section 4.2, may then be substituted into the following equation for dose:

$$Dose = \frac{I_p \cdot t}{pitch\ x \cdot pitch\ y}\left(\frac{\mu C}{cm^2}\right) \tag{4.1}$$

where $I_p$ is the primary electron beam current, $t$ is the time in seconds, *pitch x* is the step size of the electron beam in the x direction and *pitch y* is the step size of the electron beam in the y direction. From this equation the electron doses for a single pass of the electron beam at each of the beam currents studied were found to be 25000 μC/cm$^2$ for a beam current of 0.36 nA, 134000 μC/cm$^2$ for a beam current of 1.5 nA and 358000 μC/cm$^2$ for a beam current of 5.9 nA. To calculate the corresponding dose for each height deposited, the number of passes used was then multiplied by the electron dose for one pass. The results of this analysis are shown in Figure 4.4. As can be seen from this figure, the higher the electron beam current that is used, the higher the electron dose that is required to deposit a given height. However, it should also be noted that the higher the electron beam current, the more quickly an electron dose is given. Therefore these results demonstrate that both the electron beam current and the deposition time affect the deposition growth rate.

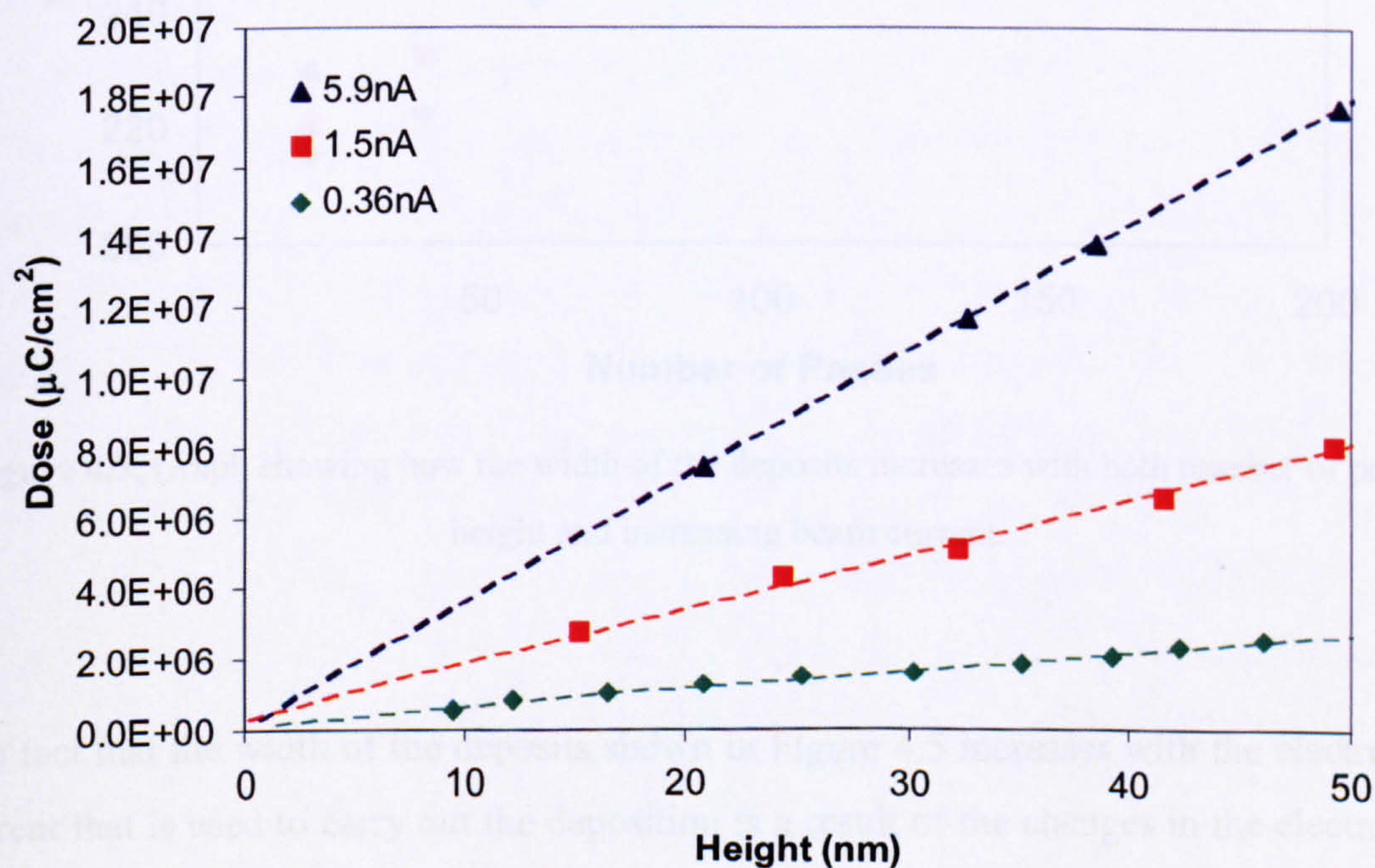


**Figure 4.4.** Graph showing how the deposited height varies with the total electron dose for beam currents of 0.36, 1.5 and 5.9 nA.

### 4.3.2 Width Characterisation

For more detailed examination of how the width of the deposits varied with the number of passes, the width of each deposit investigated in Figure 4.3 was measured at FWHM for four different points along the length of the deposit and averaged to produce the graph in Figure 4.5. As can be noted from this graph, at each of the electron beam currents investigated, the width of the deposits increases with the total number of passes made by the electron beam before saturating for all of the beam currents after ~120 passes. In particular the width was found to saturate at 261 nm for the 0.36 nA beam current, 287 nm for the 1.5 nA beam current and 300 nm for the 5.9 nA beam current. This figure also shows how increasing the electron beam current results in an increasing deposited width for a given number of passes of the electron beam. To investigate the reproducibility of these deposits, this experiment was repeated on different days and the average widths were found to vary by less than 5 nm.

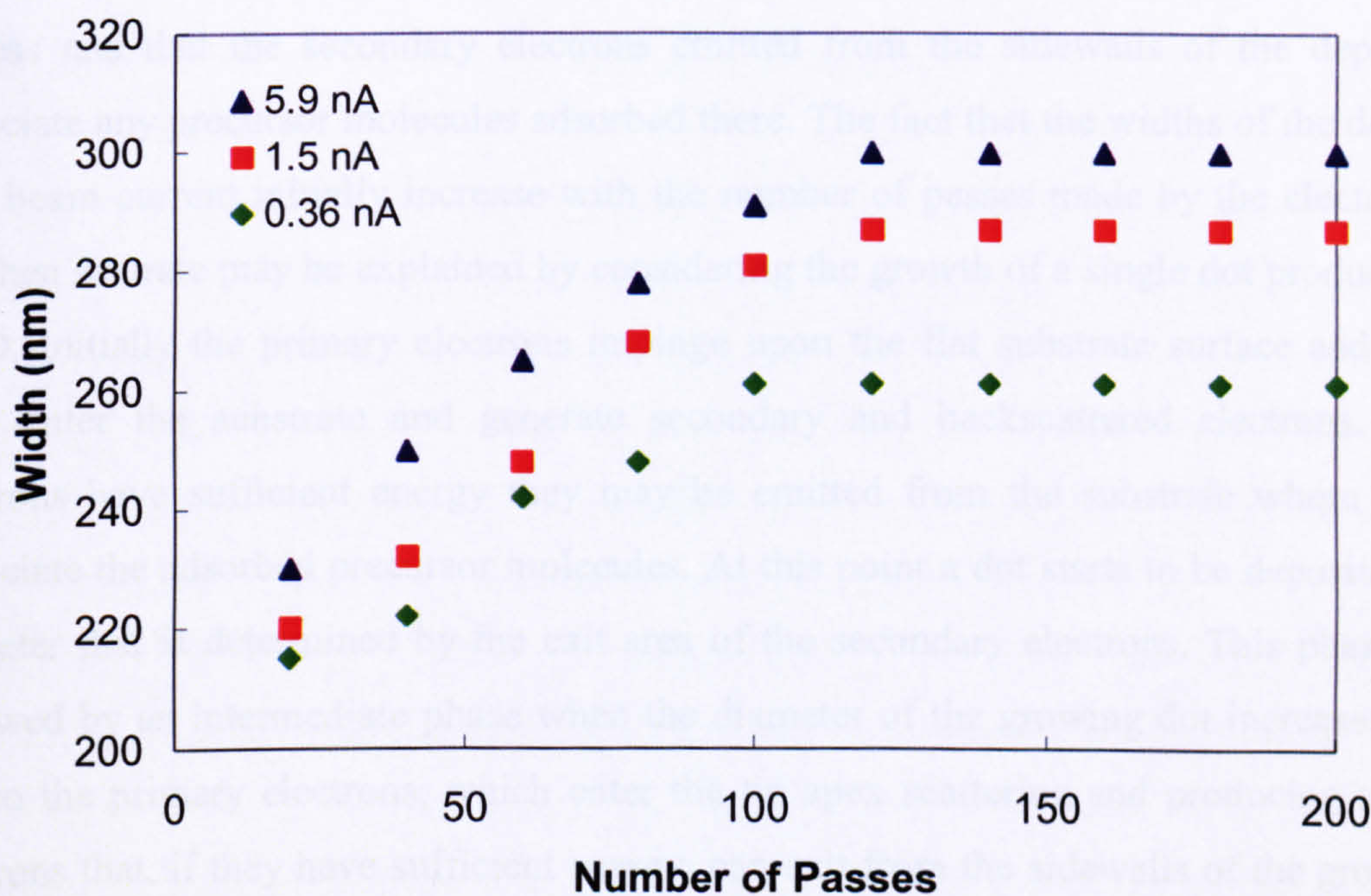


**Figure 4.5.** Graph showing how the width of the deposits increases with both number of passes or height and increasing beam current.

The fact that the width of the deposits shown in Figure 4.5 increases with the electron beam current that is used to carry out the deposition is a result of the changes in the electron beam as the beam current is changed. When the electron beam current is increased the diameter or cross-sectional area of the electron beam also increases. This means that as the electron

beam current is increased, the primary electrons impinge upon the substrate surface over an increasing surface area. Each of these electrons is capable of being involved in the deposition process and so the area over which the dissociation occurs is also increased. Furthermore, a number of the primary electrons may enter the substrate where they can generate both secondary and backscattered electrons. A proportion of these electrons are then scattered back out of the substrate where they can contribute to the radial broadening of EBID structures by dissociating the precursor molecules adsorbed there. As the diameter of the electron beam is increased the interaction volume in which the secondary and backscattered electrons are generated also increases and hence the dissociation and deposition of the precursor occurs over a larger area.

Figure 4.5 also shows how the measured width of the deposits is greater than the defined deposition area for all of the deposits. This result supports the theory described in section 2.5.4 that primary, secondary and backscattered electrons are all involved in the deposition process and that the secondary electrons emitted from the sidewalls of the deposits can dissociate any precursor molecules adsorbed there. The fact that the widths of the deposits at each beam current initially increase with the number of passes made by the electron beam and then saturate may be explained by considering the growth of a single dot produced using EBID. Initially the primary electrons impinge upon the flat substrate surface and some of them enter the substrate and generate secondary and backscattered electrons. If these electrons have sufficient energy they may be emitted from the substrate where they can dissociate the adsorbed precursor molecules. At this point a dot starts to be deposited with a diameter that is determined by the exit area of the secondary electrons. This phase is then followed by an intermediate phase when the diameter of the growing dot increases. This is due to the primary electrons, which enter the tip apex scattering and producing secondary electrons that, if they have sufficient energy, can exit from the sidewalls of the growing tip. These secondary electrons may induce deposition events on the sidewalls of the deposit and hence increase the width of the structure. The final part of the growth process is characterised by the width of the structure reaching an almost constant value. This saturation occurs when the secondary electrons are no longer able to exit from the sidewalls of the deposit as its width over the defined deposition width is more than twice that of the inelastic mean free path of secondary electrons in the deposit.

### 4.3.3 Discussion

The results that have been presented in this section show that the beam currents and the number of passes that are used to produce a deposit need to be selected for the particular application for which the deposit is to be used. For example, in an application where the resolution of a deposit is critical it is best to use the lowest possible beam current and number of passes. However, these deposits will also have a small thickness, which if post deposition processing is required can be undesirable as the material can easily be removed or destroyed. However, for applications which require structures with a large surface area and a significant height, where the accuracy of the defined deposition area is less critical, it is more suitable to use the highest possible beam currents and a large number of passes. However, this set-up is unsuitable when in use with substrates that are highly sensitive to the electron beam, as the electron beam can damage the sample through heating. The time taken to produce deposits with large numbers of passes is also much longer than those produced with a low number of passes and so a trade off between the resolution, the deposited height and the time taken to produce the deposits needs to be made.

The height measurements also showed that in the initial stages of deposition (as shown by the presence of an offset), the increase in the height with the number of passes made by the electron beam is non-linear. This means that the height of all deposits increases linearly with the number of passes or the total electron dose plus some fixed offset. For very thin deposits made with less than ten passes of the electron beam, this behaviour can be undesirable and if possible it should be removed. One possible method of reducing this offset would be to open the capillary tube through which the precursor is injected into the system before turning on the electron beam and allowing the gas flux on the surface of the sample to stabilise before commencing the actual deposition process. It may also be desirable to carry out a short deposition on a non-critical part of the substrate before moving to the required location to carry out the deposition. If the precursor flow were allowed to continue during this stage then it would be possible to carry out all of the deposition with the gas delivery – precursor dissociation rate being constant.

## 4.4 Structural and Compositional Characterisation

This section will characterise the structure and composition of the EBID tungsten wires. For this work deposits are fabricated onto both 100 nm thick silicon nitride membranes with a 500 $\mu m^2$ window and a 3 $mm^2$ silicon frame and silicon substrates with a 300 nm thick oxide layer that have been prepatterned with gold contact pads. The deposits were then produced using an electron beam current of 1.5 nA and 200 passes of the electron beam as well as the scanning conditions described in section 4.2 to produce a reasonable thickness of deposit. The deposits also had a width of 200 nm and a length of 8 µm, which allowed for them to be easily found, imaged and analysed. The resulting structures and compositions of the deposits are then analysed using both the Philips CM 200 TEM described in section 3.3.1 and the Thermo MICROLAB 350 described in section 3.4.1.

For this experimental work the TEM was operated using an accelerating voltage of 200 kV. This instrument was fitted with a Gatan Imaging Filter (GIF 2000 with a $1k$ x $1k$ Charge Couple Device), which allowed for the elemental composition of the structures to be analysed using electron energy loss spectroscopy (EELS). The MICROLAB 350 was used to carry out AES to determine the composition of the samples and was operated using an electron beam energy of 10 keV. The AES was carried out for a limited kinetic energy range of 30 to 600 eV because tungsten, carbon and oxygen, which are expected to be present in the deposits, have Auger peaks below 600 eV. Before carrying out the AES, the sample was also sputtered using a diffuse argon ion beam operated with a ~1 mm beam diameter at 1 keV for approximately thirty seconds to remove any carbon, oxygen and water that had been adsorbed on the surface of the substrate when the sample was exposed to an air environment. Although this process may cause some damage to the sample surface and remove the top layer of the deposits, it is assumed that the composition of the deposits is uniform throughout the structure and that the large beam diameter means that the damage is minimal.

### 4.4.1 Compositional Characterisation

A preliminary examination of the elemental composition of the deposits was carried out using EELS within the TEM. As the tungsten hexacarbonyl precursor contains a mix of tungsten, carbon and oxygen, the EELS was carried out for each of these elements. The results of this examination for the deposits fabricated on the silicon nitride membranes showed that they consisted of a mix of carbon and tungsten and that there was a greater

amount of carbon than tungsten in the structures. This analysis also showed that there was a negligible amount of oxygen incorporated in the structures. To analyse the composition of these deposits more thoroughly AES was carried out on the deposits fabricated on the silicon substrates with a 300 nm oxide layer using spot analysis. A typical AES spectrum is shown in Figure 4.6. This spectra shows a first set of peaks at 160 – 180 eV, which correspond to the Auger transitions for tungsten W NO2 and W NO1 respectively, a second peak at ~ 260 – 270 eV, which corresponds to the Auger transition for carbon C KL1 and a third set of peaks between 460 and 510 eV, which correspond to the Auger transitions for oxygen, O KL3, O KL2 and O KL1 respectively.

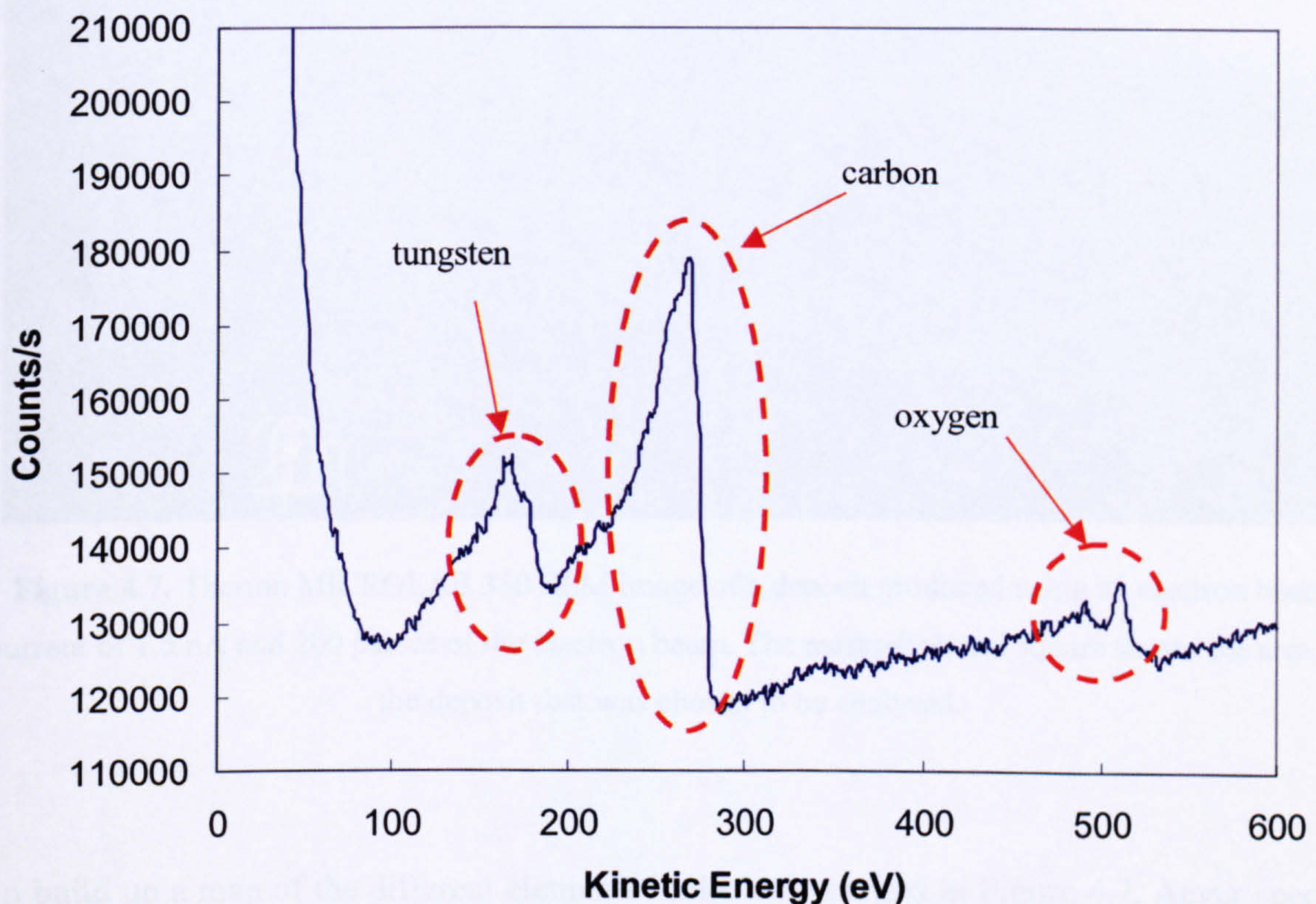


**Figure 4.6.** AES spectra for kinetic energies of 30 – 600 eV of an EBID tungsten wire deposited using 1.5 nA and 200 passes of the electron beam showing tungsten, carbon and oxygen peaks.

To investigate the elemental composition of the deposit further an AES map of the same deposit as the one shown in Figure 4.6 was produced. Figure 4.7 shows an SEM image of the deposit, which was fabricated so as to bridge a gold four terminal contact structure, as well as the area of the sample on which the map was chosen to be carried out. The map was selected to include part of the gold pads, the silicon substrate and the tungsten deposit.

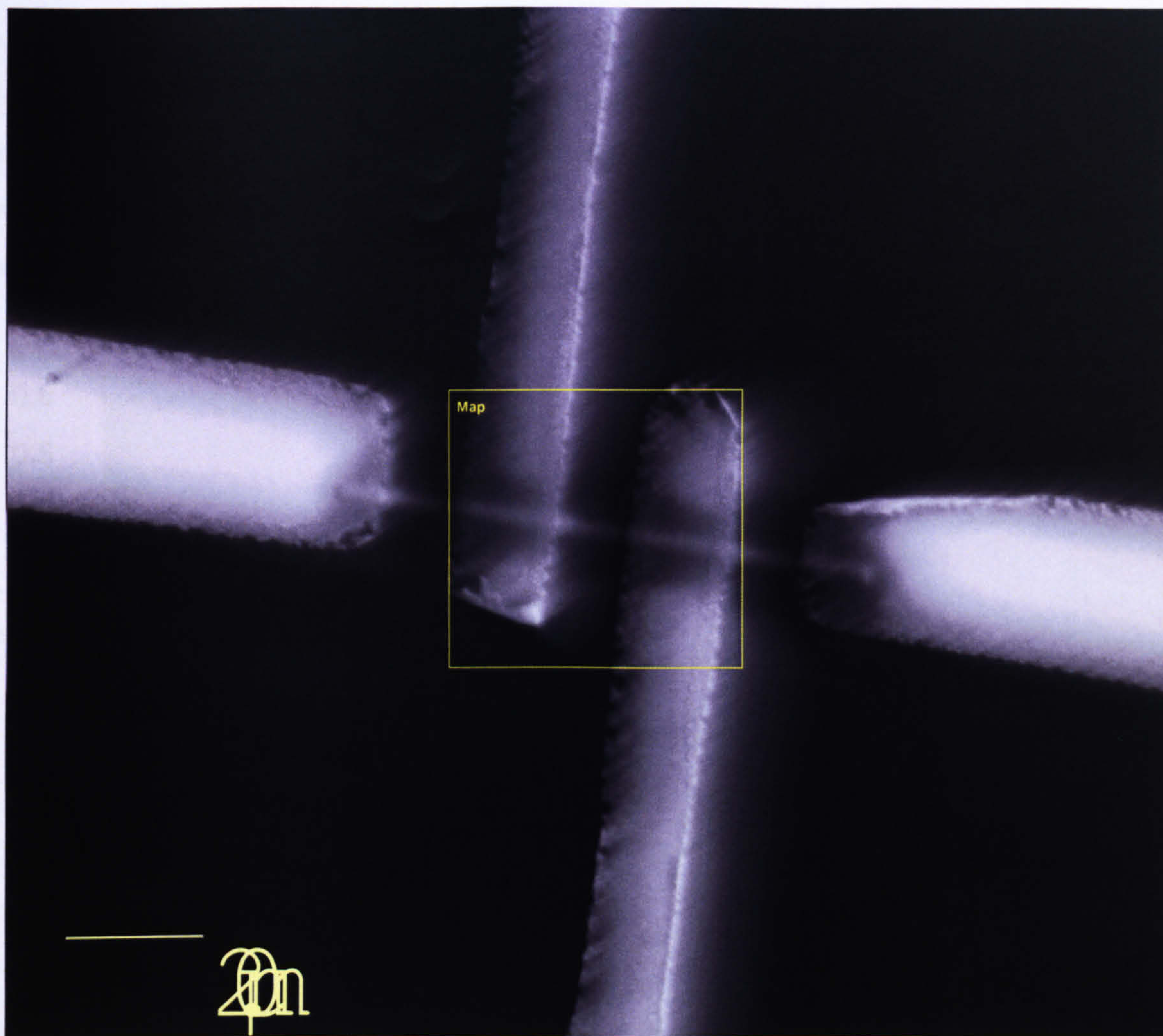


**Figure 4.7.** Thermo MICROLAB 350 SEM image of a deposit produced using an electron beam current of 1.5 nA and 200 passes of the electron beam. The marked central square shows the area of the deposit that was chosen to be analysed.

To build up a map of the different elements in the area marked in Figure 4.7, Auger spectra similar to the one shown in Figure 4.6 were taken for each pixel in the image. The output of this experiment is presented in Figure 4.8 as images showing the intensities of the Auger signals for each of the elements that are present as a function of the location at which they occur. In particular, Figure 4.8 (a) shows the gold from the contact pads that is found in the map area, Figure 4.8 (b) shows the location of the tungsten in the deposit, Figure 4.8 (c) shows the carbon map for the deposit and Figure 4.9 (d) shows the oxygen map. As can be seen from these images, tungsten appears mainly in the defined deposition area, whereas the carbon extends over a much wider area, with a more intense signal in the area surrounding the main part of the deposit. The width of the carbon in the deposit also extends over a larger area than the width of the deposits that were measured using the AFM. This suggests that the

backscattered and $SE_{II}$ electrons that occur within the substrate and escape can cause some deposition of the precursor over a much larger area than that which has been defined. The oxygen map shows a very weak signal intensity within the deposit itself and that the oxygen is also spread throughout the deposit. These results are also in agreement with the EELS that was carried out in the TEM.

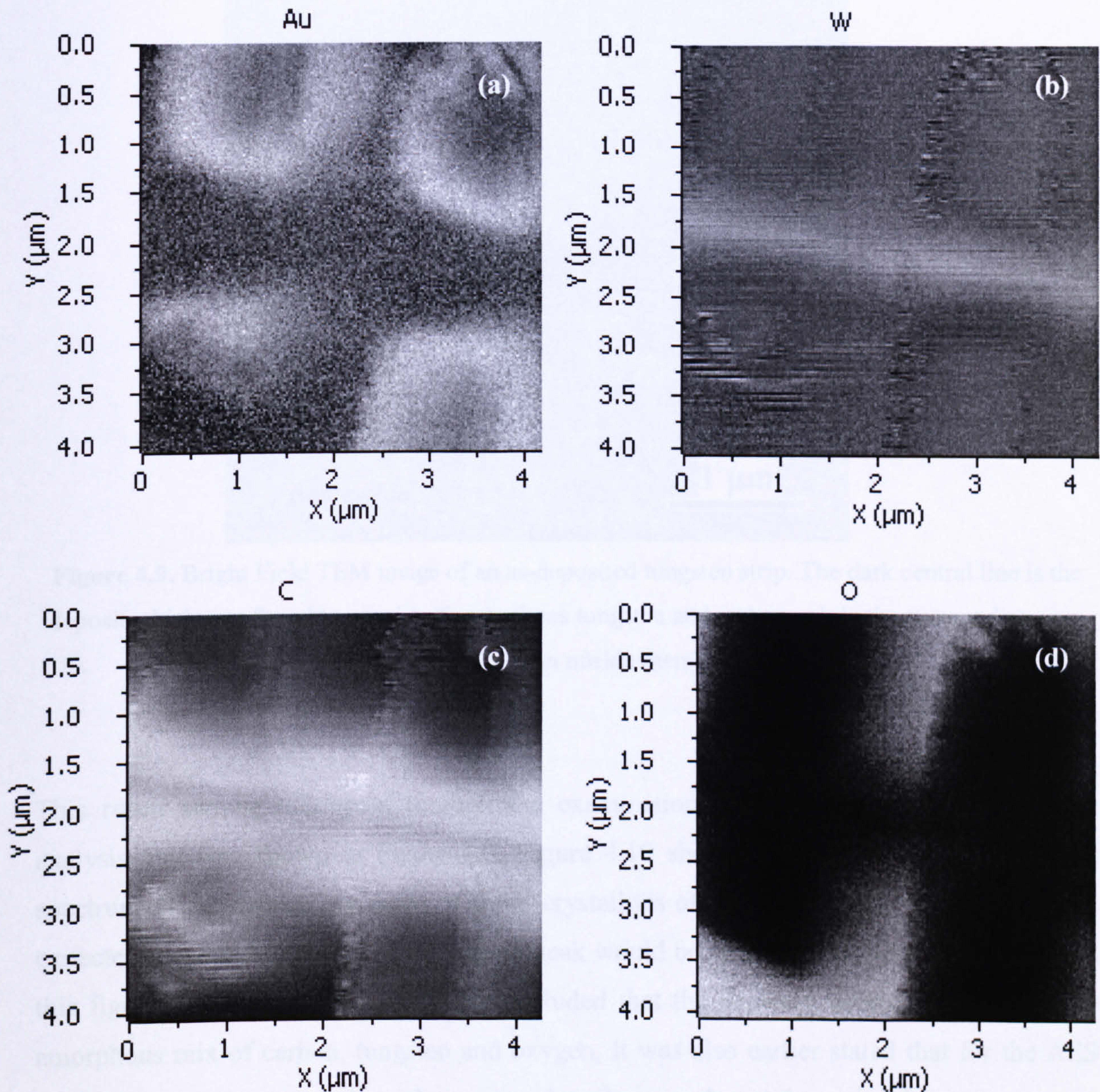


**Figure 4.8.** AES maps of **(a)** gold, **(b)** tungsten, **(c)** carbon and **(d)** oxygen of a deposit fabricated so as to bridge a gold four terminal contact structure using a beam current of 1.5 nA.

### 4.4.2 Structural Characterisation

The structure of the deposits on the silicon nitride membranes was investigated using high-resolution electron microscopy (HREM) within the TEM. It was found that the structures were completely amorphous in character. An example of this structure is shown in the bright field image in Figure 4.9.

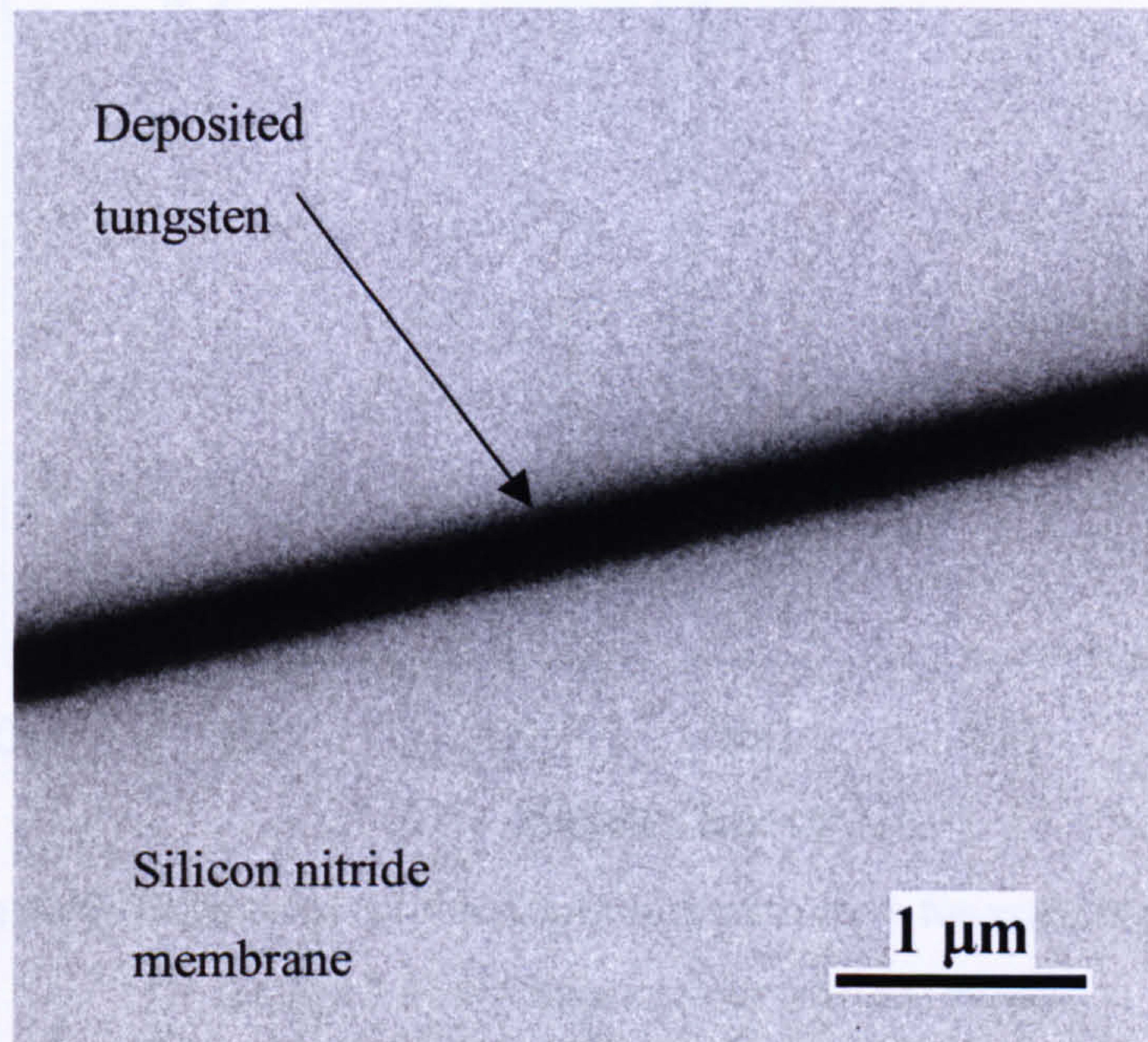


**Figure 4.9.** Bright Field TEM image of an as-deposited tungsten strip. The dark central line is the deposit which was found to consist of amorphous tungsten and carbon, while the surrounding grey area is the silicon nitride membrane.

This result can be reinforced through the examination of the differential of the Auger analysis that was shown in Figure 4.6. Figure 4.10 shows the differential of this Auger spectrum. If the deposit consisted of small crystallites of tungsten carbide then it would be expected that the differential of the carbon peak would be symmetrical. As can be seen from this figure it is not and so it may be concluded that the deposits consist of a completely amorphous mix of carbon, tungsten and oxygen. It was also earlier stated that for the AES analysis it was assumed that when sputtering the samples with an ion beam to remove ubiquitous hydrocarbons that the deposits were not damaged. However, it is well known that during the sputtering process some of the carbon may become implanted in the deposits and can cause the formation of carbides within the structures themselves. Therefore, the lack of any carbides in the Auger spectrum suggests that the ion beam did not damage the samples in this experiment and influence the results.

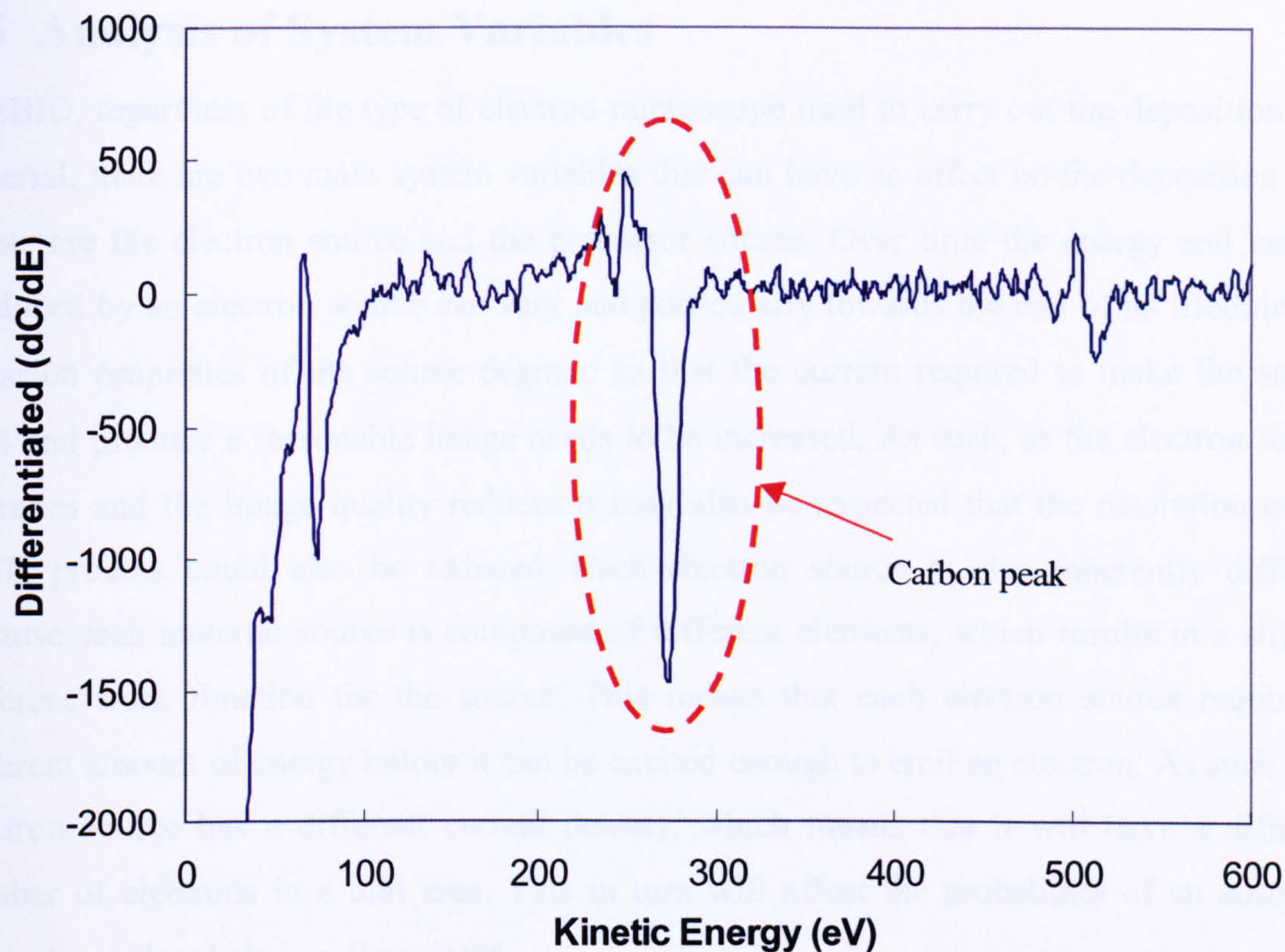


**Figure 4.10.** Differential of the Auger spectrum for a tungsten deposit produced using a 1.5 nA beam current and 200 passes.

### 4.4.3 Discussion

The fact that the deposits studied here are predominantly made up of carbon may be attributed to the composition of the precursor, which has six carbon and oxygen atoms for every tungsten atom. Meanwhile, the lack of a crystalline structure in the deposits may be attributed to the fact that the deposits were produced using a relatively low electron beam energy and electron dose per scan. When a low electron dose per scan is used in EBID, the adsorbed precursor molecules are dissociated before they can migrate to regular sites and they remain in the same position after they are dissociated. If a high dose per scan were used, then the electrons would repeatedly bombard the dissociated precursor molecules and transfer energy to them in the form of heat. The molecules would then be able to move to lower energy sites and transfer their energy to the substrate, which would result in a crystallite structure. By using a high dose per scan, it may also be possible to improve the tungsten to carbon ratio because a greater quantity of the precursor would be dissociated and more of the volatile parts of the deposit would have a chance to escape before they are covered with the next layer of deposited molecules.

## 4.5 Analysis of System Variables

In EBID, regardless of the type of electron microscope used to carry out the deposition of a material, there are two main system variables that can have an effect on the deposition rate. These are the electron source and the precursor source. Over time the energy and current produced by an electron source can vary and particularly towards the end of its lifetime, the emission properties of the source degrade so that the current required to make the source emit and produce a reasonable image needs to be increased. As such, as the electron source degrades and the image quality reduces it may also be expected that the resolution of the EBID process could also be reduced. Each electron source is also inherently different because each material source is composed of different elements, which results in a slightly different work function for the source. This means that each electron source requires a different amount of energy before it can be excited enough to emit an electron. As such each electron source has a different current density, which means that it will have a different number of electrons in a unit area. This in turn will affect the probability of an adsorbed precursor molecule being dissociated.

There are also a number of variations in the precursor source that can influence the growth rate of EBID structures. Each different type of precursor needs to be heated to a different temperature before it will turn into a gas and as such each type of precursor tends to have a different gas flux. The different composition of each type of precursor also means that certain precursors are more easily dissociated and deposited by the electron beam than others. Also it may be expected that as the life of a particular precursor source proceeds, there becomes less material available to be used in the deposition process and as such the gas flux on the surface of the sample will decrease. This in turn means that there are fewer molecules available to be used in the deposition of a structure and the growth rate decreases.

Both of these variations mean that it is possible that deposits produced using different electron sources or even at different times in an electron sources or a precursor's lifetime will have slightly different growth rates. To investigate the effects of this the following sections will compare and discuss the effects of two different electrons sources and a precursor at the beginning and end of its lifetime on the deposition rate of tungsten interconnects deposited using $W(CO)_6$ as a precursor.

### 4.5.1 Effects of the Electron Source

The effect of the energy of an electron source on the deposition rate can be seen by examining the height of interconnects deposited using two different electron sources within the same system. For this experiment two different electron sources were compared. The first electron source is denoted electron source 1 and is the electron source that has been used to create the deposits examined thus far. The second electron source is denoted electron source 2 and is a brighter electron source, which was installed in the system when it was delivered. Within this experiment, the precursor source has been used for less than twenty hours and the beam current is set using spot three, which results in a quoted current of 1.5 nA for the first electron source and a current of 2.1 nA for the second electron source. All of the other deposition parameters were kept the same as those described in section 4.2. The resulting data for this experiment is shown in Figure 4.11.

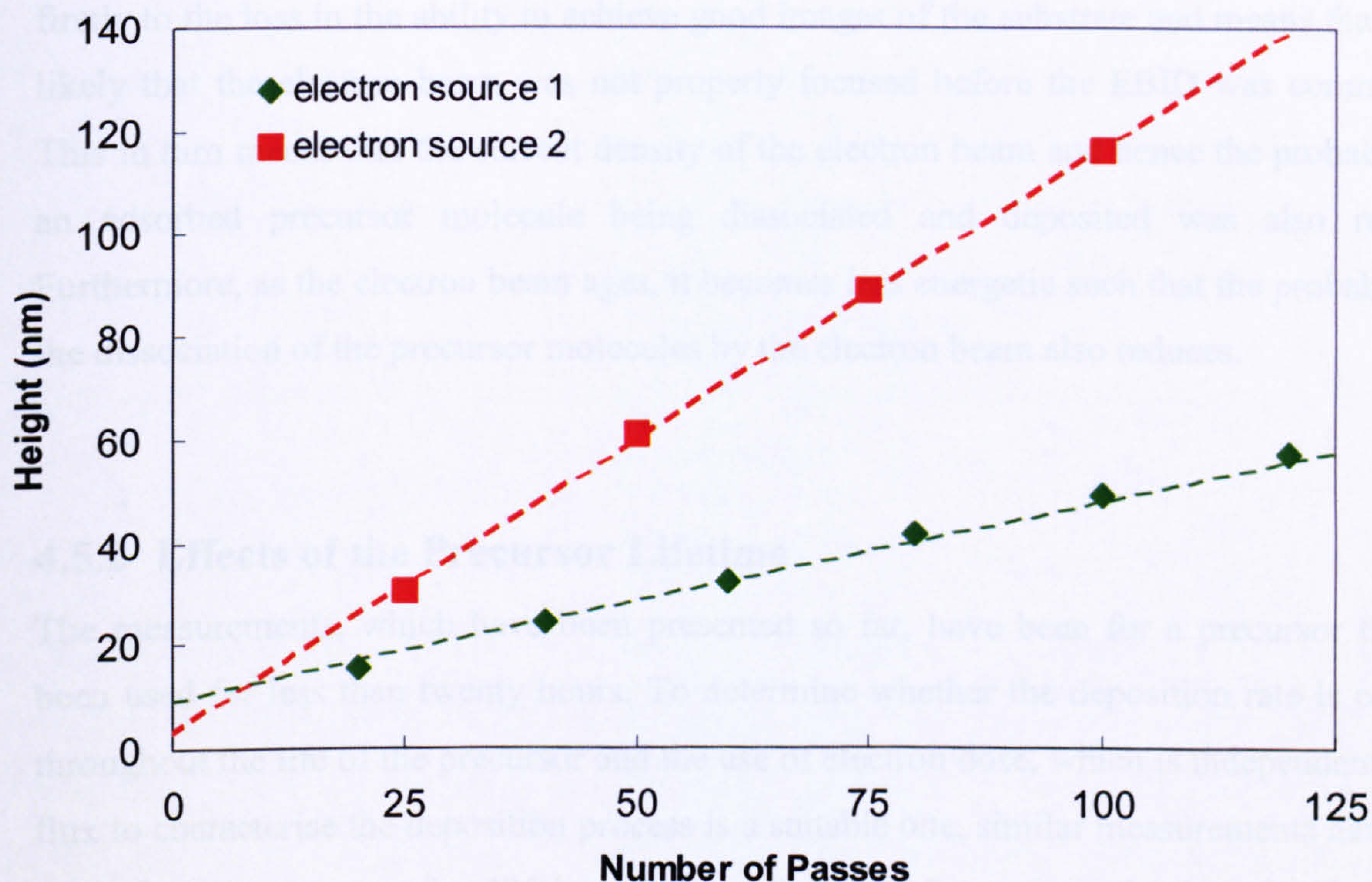


**Figure 4.11.** Graph showing how the total amount of material deposited is dependent on the energy of the electron source.

Figure 4.11 shows how the deposits made with electron source two had a much higher growth rate than those made with electron source one. The reasons for this difference may be understood by comparing the differences in the electron sources and the resulting effects that they have on EBID. In particular, the second electron source had a higher beam current for a

spot size of three than the first electron source. This higher current results in a higher current density, which means that there are more electrons per unit area for this electron source. The greater the number of electrons, the higher the probability that an adsorbed precursor molecule will be dissociated and deposited. Therefore, a higher growth rate may be expected. This result also demonstrates that there is an inherent variability between electron sources, which makes the accurate comparison of deposits, produced using different instruments and different electron sources very difficult.

During this work it has also been attempted to produce EBID interconnects with an electron source that is very near the end of its lifetime. While it was possible to produce some kind of deposit, it was found that the deposits were less well defined such that there was a loss in the resolution of the process and that far less material was deposited. This can be attributed firstly to the loss in the ability to achieve good images of the substrate and means that it was likely that the electron beam was not properly focused before the EBID was commenced. This in turn means that the current density of the electron beam and hence the probability of an adsorbed precursor molecule being dissociated and deposited was also reduced. Furthermore, as the electron beam ages, it becomes less energetic such that the probability of the dissociation of the precursor molecules by the electron beam also reduces.

### 4.5.2 Effects of the Precursor Lifetime

The measurements, which have been presented so far, have been for a precursor that has been used for less than twenty hours. To determine whether the deposition rate is constant throughout the life of the precursor and the use of electron dose, which is independent of gas flux to characterise the deposition process is a suitable one, similar measurements have been made for the precursor after 120 hours of use. Figure 4.12 compares the deposited height for a set number of passes for a beam current of 1.5 nA at the beginning and end of a precursor's life. As can be seen from this figure, the amount of material that is deposited is reduced significantly at the end of the precursors life such that the line of best fit for zero passes deteriorates from 9.2 to 4.2 nm and the gradient reduces from 0.39 to 0.22. To analyse these differences more accurately, the differences in the deposited heights were calculated and it was found that for all of the deposits investigated, the deposits made using the precursor with more than 120 hours of use were 47 % ± 2 % of the size of the deposits made using the precursor with less than 20 hours of use. These changes imply that as the time that the

precursor has been used for increases, the amount of material that is heated into a gas decreases. This results in a decreasing gas flux, which means that there is less material available for deposition. After the precursor has been used for more than 120 hours the amount of material that is deposited has been found to reduce even more significantly.

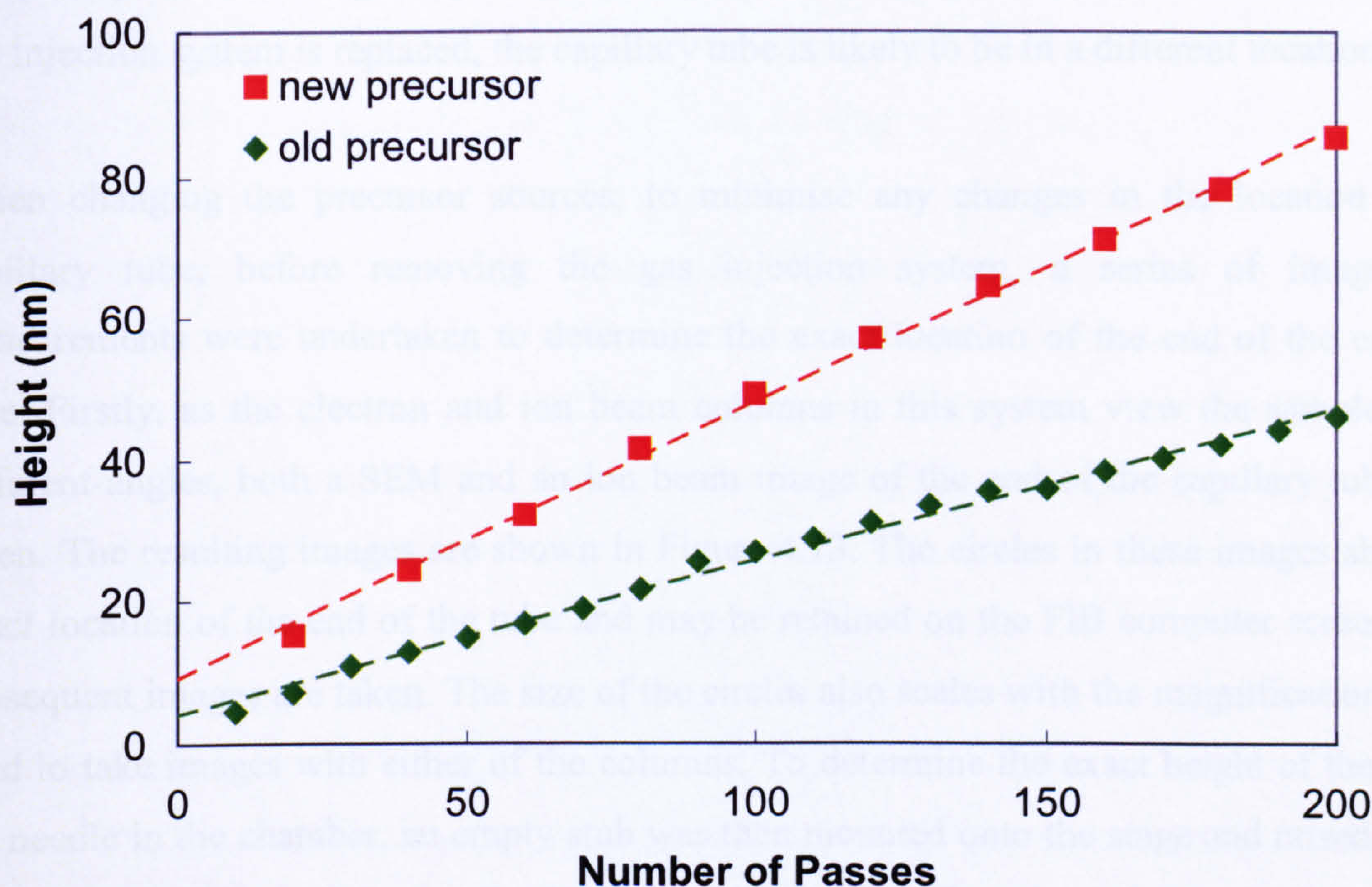


**Figure 4.12.** Graph showing how the total amount of material deposited deteriorates over time for an electron beam current of 1.5 nA.

This result may be reinforced by considering the differences in the precursor morphology at the beginning and end of its lifetime. Indeed, before the tungsten hexacarbonyl precursor has been used it is found to consist of a fine white powder with a table salt like texture, while after more than 150 hours of use, it is found to have formed large agglomerates with diameters of approximately 5 mm. This change in the materials structure means that over time the surface area of the precursor decreases and hence the amount of precursor that is heated into the gas phase is reduced. This results in the gas flux decreasing with time.

The results shown in Figure 4.12 could also be considered in terms of dose, which according to equation (4.1) is constant throughout the life of the precursor. However, as can be seen from this graph, the deposition rate does decrease with the amount of time that it has been used. This result implies that using just the total electron dose to predict the deposition rate of EBID in either different systems or at different times is unsuitable.

Another effect that was also noticed was that the deposition rate depended on the exact location of the precursor injection needle. As described in section 2.5.2, the gas flux on the surface of the substrate depends partly upon the orientation of the capillary tube through which the precursor gas is delivered. In order to change the precursor it is necessary to completely remove the gas injection system and then replace it. This means that when the gas injection system is replaced, the capillary tube is likely to be in a different location.

When changing the precursor sources, to minimise any changes in the location of the capillary tube, before removing the gas injection system, a series of images and measurements were undertaken to determine the exact location of the end of the capillary tube. Firstly, as the electron and ion beam columns in this system view the samples from different angles, both a SEM and an ion beam image of the end of the capillary tube were taken. The resulting images are shown in Figure 4.13. The circles in these images show the exact location of the end of the tube and may be retained on the FIB computer screen when subsequent images are taken. The size of the circles also scales with the magnification that is used to take images with either of the columns. To determine the exact height of the end of the needle in the chamber, an empty stub was then mounted onto the stage and raised until it just touched the end of the needle. It was possible to tell when the stub was in contact with the end of the capillary tube because the capillary tube was seen to move slightly when the contact was made. The height of the stage at which this was seen to occur was recorded.

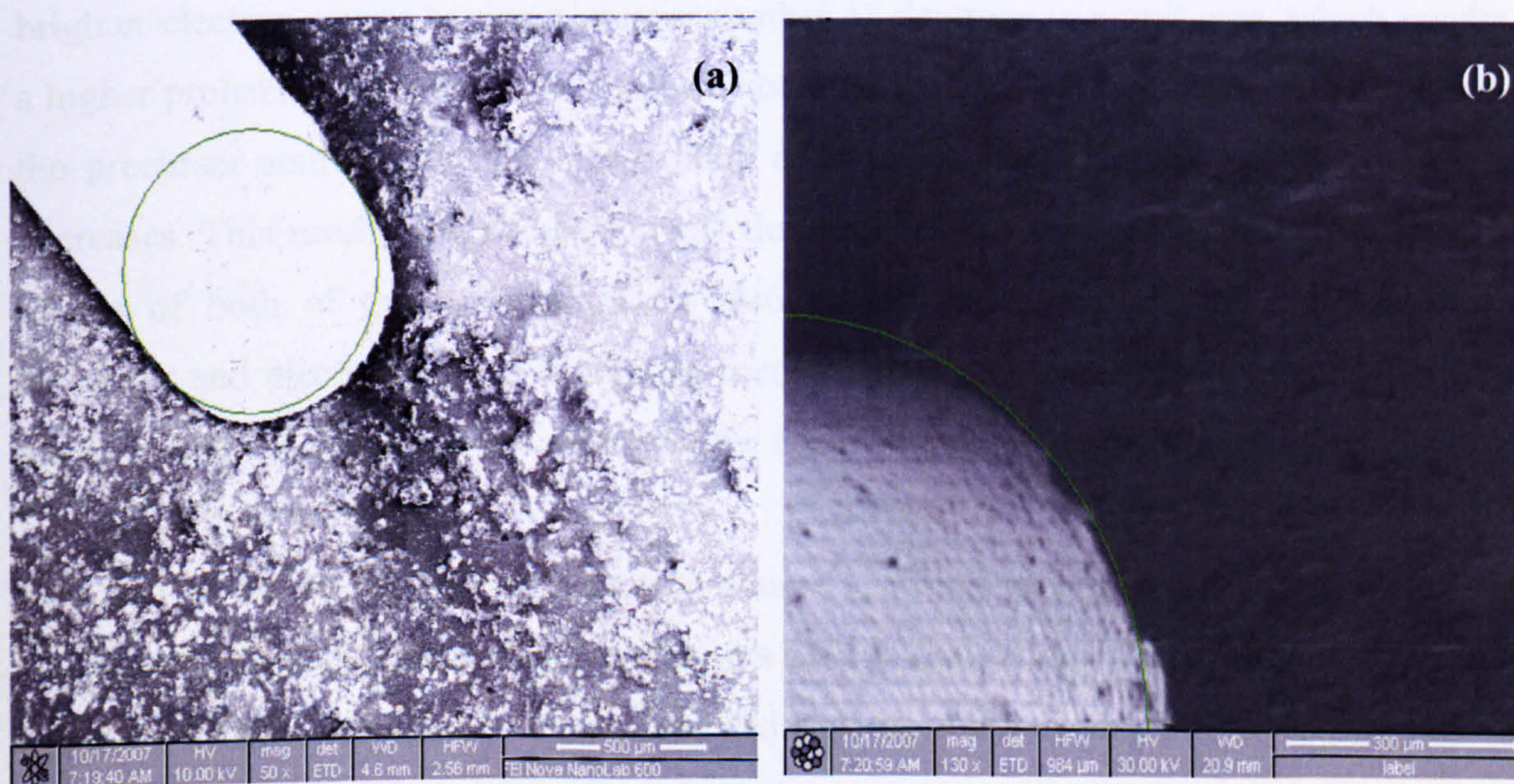


**Figure 4.13. (a)** SEM image and **(b)** ion beam image of the capillary tube used to inject the precursor molecules during EBID.

Once the precursor source had been changed and the gas injection system replaced, both electron and ion beam images were taken as the placement of the injection system was varied. The marker circles shown in Figure 4.13 were retained so that it could be seen when the capillary tube matched its original location. The height of the capillary tube was determined by again raising the height of the stage until an empty stub made contact with the end of the tube. The height of the stage when the contact was made was noted and the capillary tube height adjusted until it matched its original height. Once the gas injection system had been reinstalled correctly a series of test deposits were made using both the electron and the ion beam. Initially the growth rate was found to be lower than it had been before the precursor was changed. By making very small adjustments to the location of the capillary tube, the growth rate was enhanced significantly. This result shows that the deposition rate for EBID is highly dependent on the location of the gas injection system and the subsequent gas flux on the surface of a substrate.

### 4.5.3 Discussion

The experiments and analysis that has been carried out in this section has shown that the deposition rate of EBID structures is highly dependent on changes in both the electron source and the precursor. In particular, it has been found that when brighter electron sources with higher current densities are used for EBID they produce structures with a greater deposited height for a given number of passes. This has been explained in terms of the brighter electron source having a greater number of electrons in a unit area, which results in a higher probability of a precursor molecule being dissociated. It has also been shown that as the precursor source ages, the morphology of the precursor changes and its surface area decreases. This results in a decreasing gas flux and hence a decreasing deposition rate. The results of both of these investigations also suggest that ideally both a relatively new precursor and electron source should be used where possible and that the selection of the most energetic electron sources necessary for achieving a high deposition rate.

It is also worth noting here that electron source 2, which was investigated in section 4.5.1 was actually the first electron source that was used in the system. Therefore, the system with a precursor with less than 20 hours of use and electron source 2 was the set-up that was used when the system was first delivered to the university. It is generally accepted that during the factory acceptance tests of a new instrument, the performance of the system is optimised

such that the upper levels of performance of the instrument are achieved. It is also possible for additional performance of the instrument to be gained within its first year of use. However, after this time both the instrument itself and its consumable parts such as the filaments start to deteriorate due to wear and tear and can affect the overall performance. On site replacement of consumable parts will improve the performance. However, it is generally accepted that such replacements do not involve the same degree of instrument tuning as would occur in the factory. Therefore, performance after the exchange and service of various parts of the instrument are often found to be lower. While each new electron source has a different level of performance and it can be accepted that some of the differences between the two sources may be due to the filaments having different qualities. It is also possible that part of the reason that electron source 1 does not meet the performance of electron source 2, is that the set-up of the electron column on site by the service department did not reach the same standard as that which was achieved within the factory. If the electron beam is less focused it will have a lower current density and less precursor molecules will be dissociated.

The observed differences in the electron sources highlight one of the main difficulties in making EBID suitable as a mainstream fabrication technique as industry would require more precise control of the deposition rate between different instruments and would not accept having to recalibrate the instruments every time an electron source was changed. Therefore, to be able to improve the reproducibility of EBID with different electron sources it would be necessary to have the ability to calibrate and modify the deposition rate produced by each electron source in each system.

As discussed in section 4.5.2, the precursor gas flux on the substrate is highly dependent on the way that the system has been set up. This means that part of the reason that the deposition rate was much higher for electron source 2 with a precursor with less than 20 hours of use than it was for electron source 1, again with a precursor that has been used for less than 20 hours (section 4.5.1) may be due in part to the precursor that was used with electron source 2 having been optimised as part of the factory acceptance tests. Meanwhile, the precursor used with electron source 1 was installed at the University and so the location of the capillary tube may not have been optimised as well. Also, the two precursors were sourced from different suppliers and so may have a slightly different chemical compositions or grain size, which can affect the deposition rate. It is also likely that a different amount of the precursor material would have been used, which could again affect the deposition rate.

## 4.6 Effect of the Substrate

As described in section 2.5.4, there has been considerable controversy about the factors that control the deposition accuracy and the growth rate of EBID. This has lead to much discussion about the types of electrons that contribute to the deposition process. If, as discussed by Fowlkes et al. [9], the deposition rate is influenced by the contribution of both secondary and backscattered electrons, then the choice of substrate on which the deposition is carried out should play an important role in influencing the final deposited structure. This is because the number of BSEs, which are created by scattering of the primary electrons in a substrate, is dependent on the atomic number of the substrate material. Meanwhile the number of SEs that are generated will remain almost constant because their generation is largely independent of the substrate material used.

To investigate the effects of this, a series of deposits 200 nm wide and 8 μm long were deposited onto a 100 nm thick silicon nitride membrane, which had a 500 $\mu m^2$ window with a 3 $mm^2$ silicon frame for the electron beam currents of 0.39, 1.5 and 5.9 nA. Half of the structures were deposited onto the membrane itself and the other half deposited onto the membrane frame. The membrane window appears transparent to an electron beam so the number of BSEs produced will be approximately zero until the deposit has reached a reasonable thickness, which is greater than the mean free path of the secondary electrons. Once the deposit is thick enough, the BSEs are produced by scattering of the electron beam within the deposit rather than in the substrate. Meanwhile the membrane frame acts as an infinitely thick substrate and as such when the electron beam interacts with it, it will produce a much larger number of BSEs. This means that if the BSEs play a significant role in the deposition process then the part of the deposit on the membrane frame will be different to the part deposited on the membrane itself.

Figure 4.14 (a) shows the AFM image for this deposit, which was made using the parameters described earlier and an electron beam current of 1.5 nA. As can be seen from the image, the deposition on the infinitely thick substrate has a halo around it, while the deposition on the electron transparent part of the substrate has a much less significant halo. The height profile of the deposit on both the membrane window and the membrane frame was also measured and is shown in Figure 4.14 (b). This figure shows how both the width at FWHM and the height on the membrane window (electron transparent substrate) and the membrane frame (infinitely thick substrate) were approximately the same. This measurement also shows that

the base width of the deposit on the membrane frame is slightly larger than it is on the membrane window and is produced by the formation of the halo that can be seen in Figure 4.14 (a). Similar characteristics were seen for the other electron beam currents investigated.

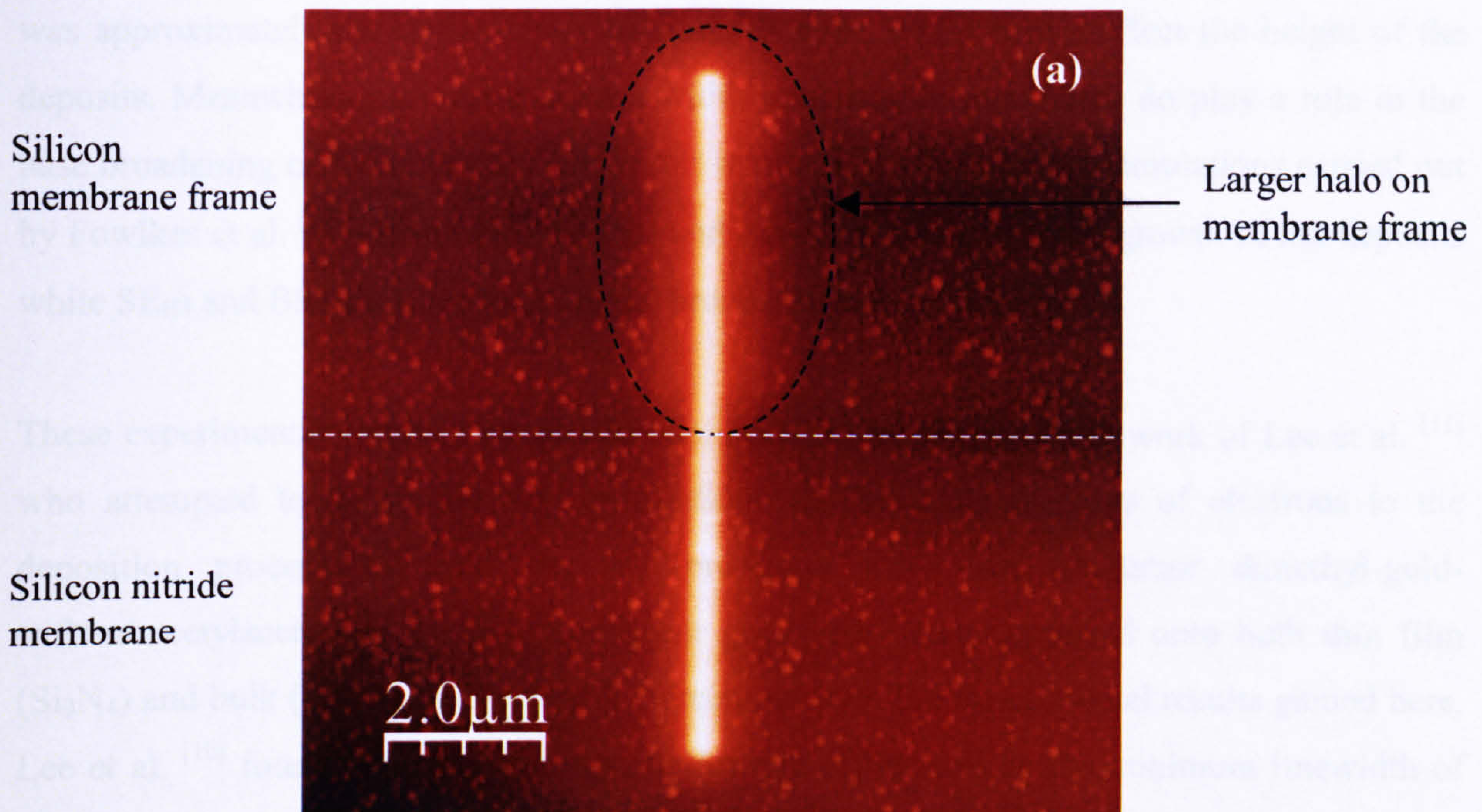


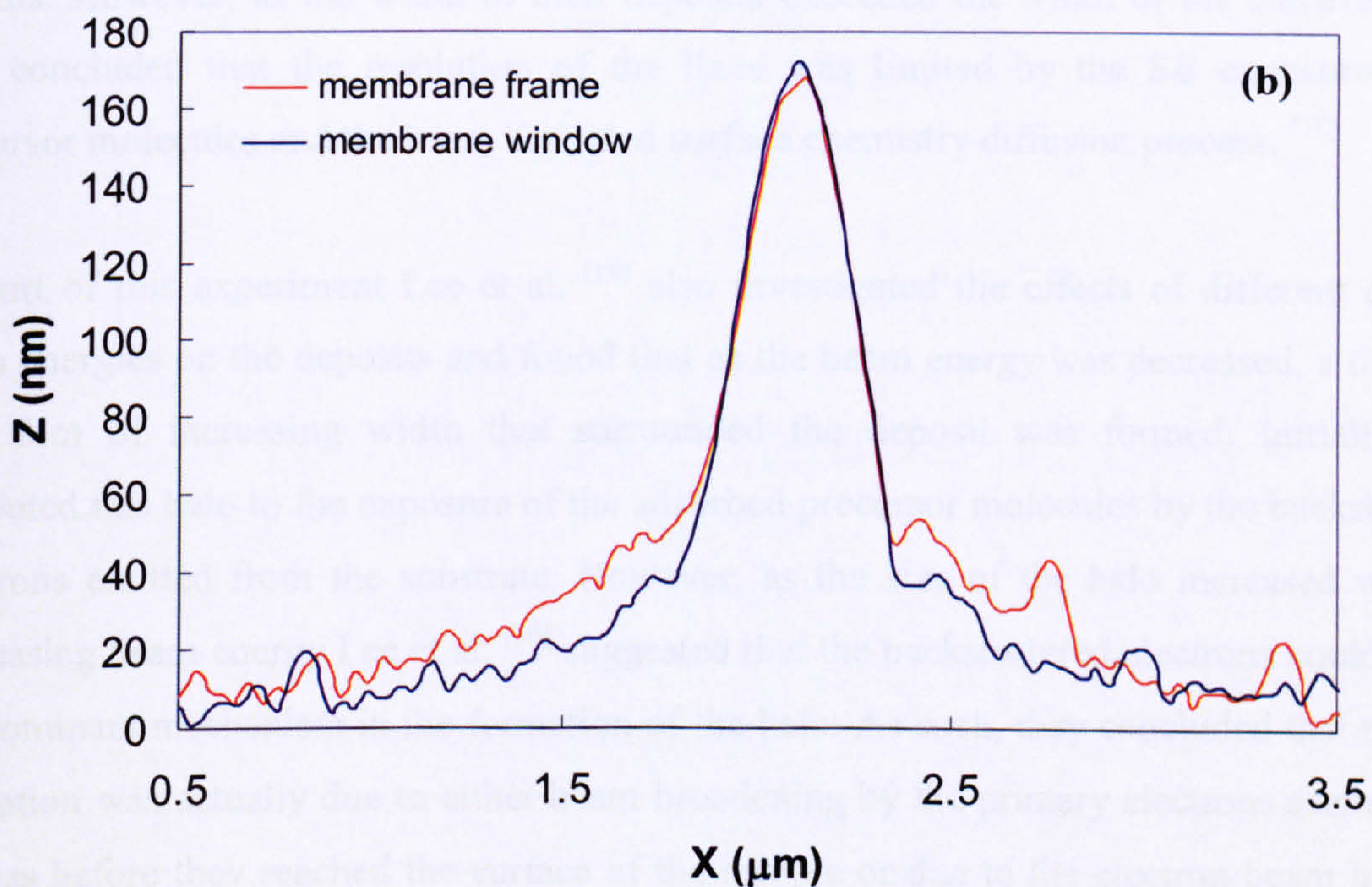


**Figure 4.14. (a)** AFM image of a deposit with the top half of the deposit on the membrane frame and the bottom half of the deposit on the membrane window. (b) Height profiles of the deposit on the membrane frame and the membrane window. This profile shows that while the height and the FWHM of the width were the same for both parts of the deposit, the deposit on the membrane frame had a larger base width than the deposit on the membrane window.

The fact that the images in Figure 4.14 show a more substantial halo on the infinitely thick part of the substrate than on the electron transparent part suggests that BSEs do play a role in EBID. In particular, it was found that the height of the deposit on both parts of the substrate was approximately the same, which suggests that the BSEs do not affect the height of the deposits. Meanwhile the increased base width suggests that the BSEs do play a role in the base broadening of the deposits. This result is in agreement with the simulations carried out by Fowlkes et al. [10] who found that PEs and $SE_I$s induce the vertical growth of the deposits while $SE_{II}$s and BSEs influence the radial broadening of the deposits.

These experimental results may also be compared to the experimental work of Lee et al. [11] who attempted to determine the contributions of the different types of electrons to the deposition process of gold deposits produced using the precursor dimethyl-gold-trifluoroacetylacetonate. In this experiment gold lines were deposited onto both thin film ($Si_3N_4$) and bulk (silicon) substrates. In agreement with the experimental results gained here, Lee et al. [10] found that there were no noticeable differences in the minimum linewidth of the deposits and so concluded that the BSEs do not play a dominant role in the EBID process. However, as the width of their deposits exceeded the width of the electron beam, they concluded that the resolution of the lines was limited by the SE exposure of the precursor molecules and the beam activated surface chemistry diffusion process. [10]

As part of this experiment Lee et al. [10] also investigated the effects of different electron beam energies on the deposits and found that as the beam energy was decreased, a thin halo type film of increasing width that surrounded the deposit was formed. Initially, they attributed this halo to the exposure of the adsorbed precursor molecules by the backscattered electrons emitted from the substrate. However, as the size of the halo increased with the decreasing beam energy Lee et al. [10] suggested that the backscattered electrons could not be the dominant mechanism in the formation of the halo. As such, they concluded that the halo formation was actually due to either beam broadening by the primary electrons scattering in the gas before they reached the surface of the sample or due to the electron beam having a non-Gaussian intensity distribution. [10] If this conclusion were correct then it would be expected that the experimental work carried out here would have a significant halo on both parts of the deposits. However, Figure 4.14 (b) shows that there was a much smaller halo on the electron transparent part of the substrate than on the infinitely thick part, which suggests that the halo formation is due at least in part to backscattered electrons.

This experimental work also indicates that in EBID applications where the resolution of the deposits is crucial and the leakage between closely spaced interconnects needs to be minimised it is better to use thin, electron transparent substrates as it allows for deposits with smaller halos to be produced without sacrificing the vertical growth rate. However, thin substrates are more difficult to handle and can be easily broken, which means that a trade off between the horizontal resolution and ease of sample handling needs to be made.

## 4.7 Effect of the Substrate Temperature

As described in section 2.6.2 heating or cooling the substrate while the deposition is being carried out can have an effect of the growth rate of the process. To investigate the effects of changing the substrate temperature on the deposition of tungsten from the precursor $W(CO)_6$, the modified Omicron Nanotechnology Resistive Heater described in section 3.9 was mounted on a modified sample stage in the FEI Dual Beam FIB. To insulate the heater from the stage, several glass slides were placed between the base of the heater and the sample stage. The heater was then connected to the Keithley 238 Source Measurement Unit that had been used to carry out its calibration using a co-axial electrical feedthrough. This experimental set-up meant that the depositions could be carried out using the same method as for all of the other depositions characterised in this chapter.

Before carrying out any of the depositions with a heated substrate, the temperature of the heater was raised to the required temperature and allowed to saturate for at least thirty minutes. The depositions were made using electron source 1 with a beam current of 1.5 nA and a new precursor for substrate temperatures of 25, 50, 75 and 100°C. Each of the deposits was also produced using 200 passes of the electron beam. The sizes of the resulting deposits were then examined using the same AFM methodology as before. The results were repeated on different days and were found to be reproducible. Analysis of the AFM images showed that the width of the deposits were independent of the substrate temperature, while the height of the deposits was found to vary with substrate temperature. A typical set of data, which shows the effects of the temperature on the deposited height, is shown in Figure 4.15.

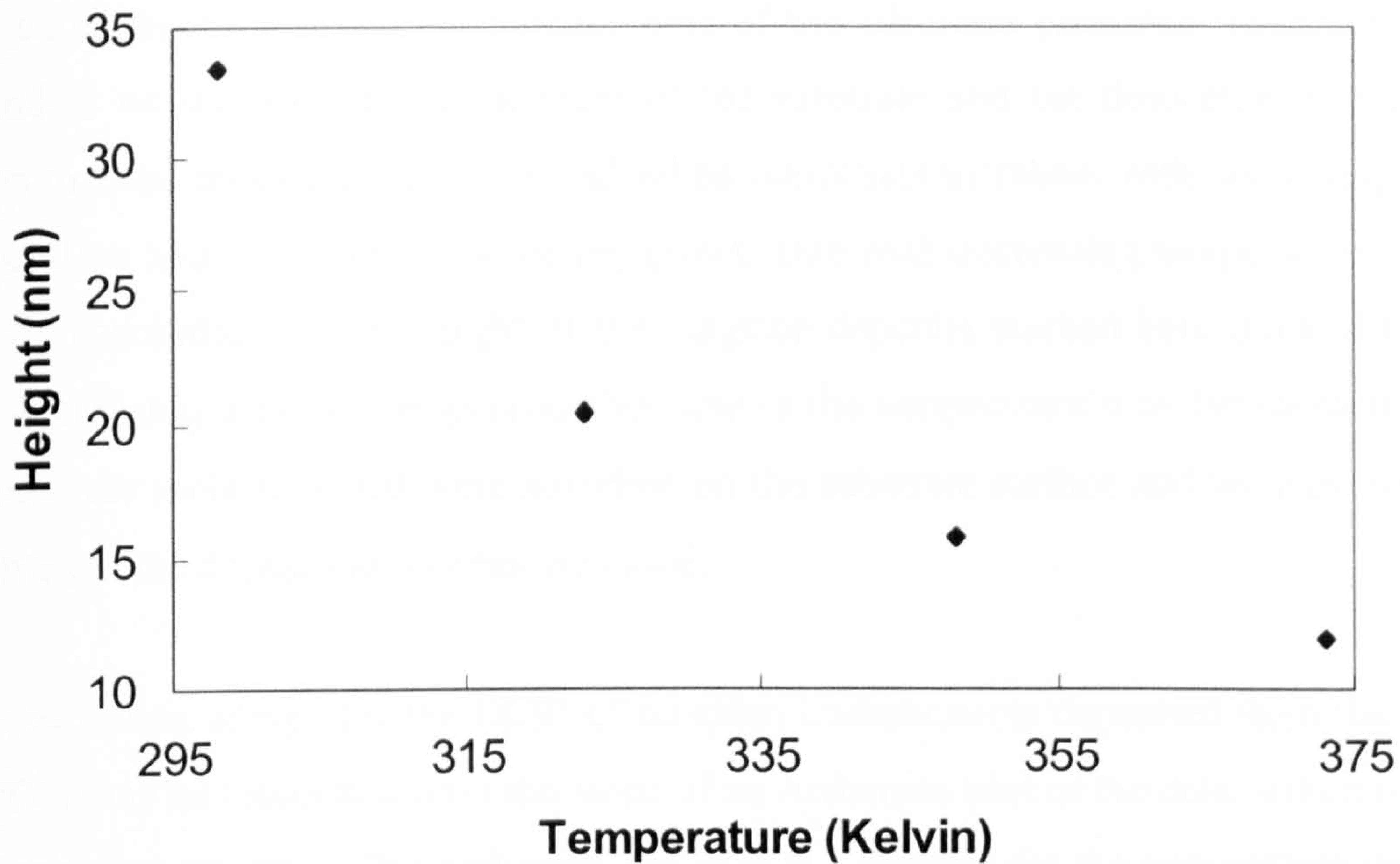


**Figure 4.15.** Graph showing the effects of substrate temperature on the deposited height.

Figure 4.15 shows how the growth rate of tungsten deposits decreases with increasing substrate temperature. This result follows the same trend as that found by Li et al. [11] in their experimental work, which studied the effects of substrate temperature on the growth rate of EBID tips deposited using the precursor $WF_6$. The fact that the growth rate decreases with increasing substrate temperature indicates that the precursor molecules are dissociated on the substrate surface rather than in the gas phase, because if the process occurred in the gas phase, then the growth rate would be independent of the substrate temperature. This idea is also in agreement with the explanation of the precursor-substrate interactions that was given in section 2.5.3 and reinforces the use of equations (2.11), (2.15) and (2.17). In particular, equation (2.15) described the growth rate of EBID using the equation:

$$R = (N\tau)\sigma f \tag{4.2}$$

where $N$ is the flux of the precursor molecules, $\tau$ is the residence time of the adsorbed precursor molecules, $\sigma$ is the dissociation cross section and $f$ is the electron flux density. The residence time of the adsorbed molecules given in this equation was then described by equation (2.17), such that:

$$\tau = \frac{1}{\nu} e^{\frac{E_{des}}{kT}} \tag{4.3}$$

where $\nu$ is the vibrational frequency, $E_{des}$ is the desorption energy, $k$ is Boltzmann's constant and $T$ is the temperature in Kelvin.

This equation shows that the residence time of the adsorbed precursor molecules is highly dependent on the both the temperature of the substrate and the desorption energy. It also shows that the residence time of the adsorbed molecules increases with decreasing substrate temperature and results in an increasing growth rate with decreasing temperature. As such it may be concluded that the height of the tungsten deposits studied here increased in height with decreasing substrate temperature because as the temperature was decreased the amount of precursor molecules that were adsorbed on the substrate surface and were available to be involved in the deposition process increased.

The desorption energy for the EBID of tungsten interconnects deposited from the precursor $W(CO)_6$ may be calculated from the slope of an Arrhenius plot of the data, which is based on the Arrhenius equation. The Arrhenius equation is a formula for the temperature dependence of the rate constant and therefore the rate of a chemical reaction, k, such that:

$$k = Ae^{\frac{-E_A}{RT}} \tag{4.4}$$

where $A$ is the pre-exponential factor, $E_a$ is the activation energy, which is the energy required for a thermally activated physical or chemical process to occur, $R$ is the gas constant and $T$ is the temperature in Kelvin. To determine whether a chemical process follows the Arrhenius equation and is a single rate limited thermally activated process then a plot of ln(k) versus 1/T is fabricated. If the plot yields a straight line it follows the Arrhenius equation such that:

$$\ln(k) = -\frac{E_A}{R} \cdot \frac{1}{T} + \ln(A). \tag{4.5}$$

As can be seen from this equation, an Arrhenius plot that yields a straight line and follows this equation can then be used to calculate both the activation energy from the gradient of the line and the pre-exponential factor from the y-intercept.

To determine whether the deposits studied here follow this behaviour, the volume of each of the deposits studied in Figure 4.15 were plotted as a function of the inverse of the substrate temperature. For this calculation the lengths of the deposits were 8 μm, while their widths were of the order of 250 nm. The results of this analysis are shown in Figure 4.16.

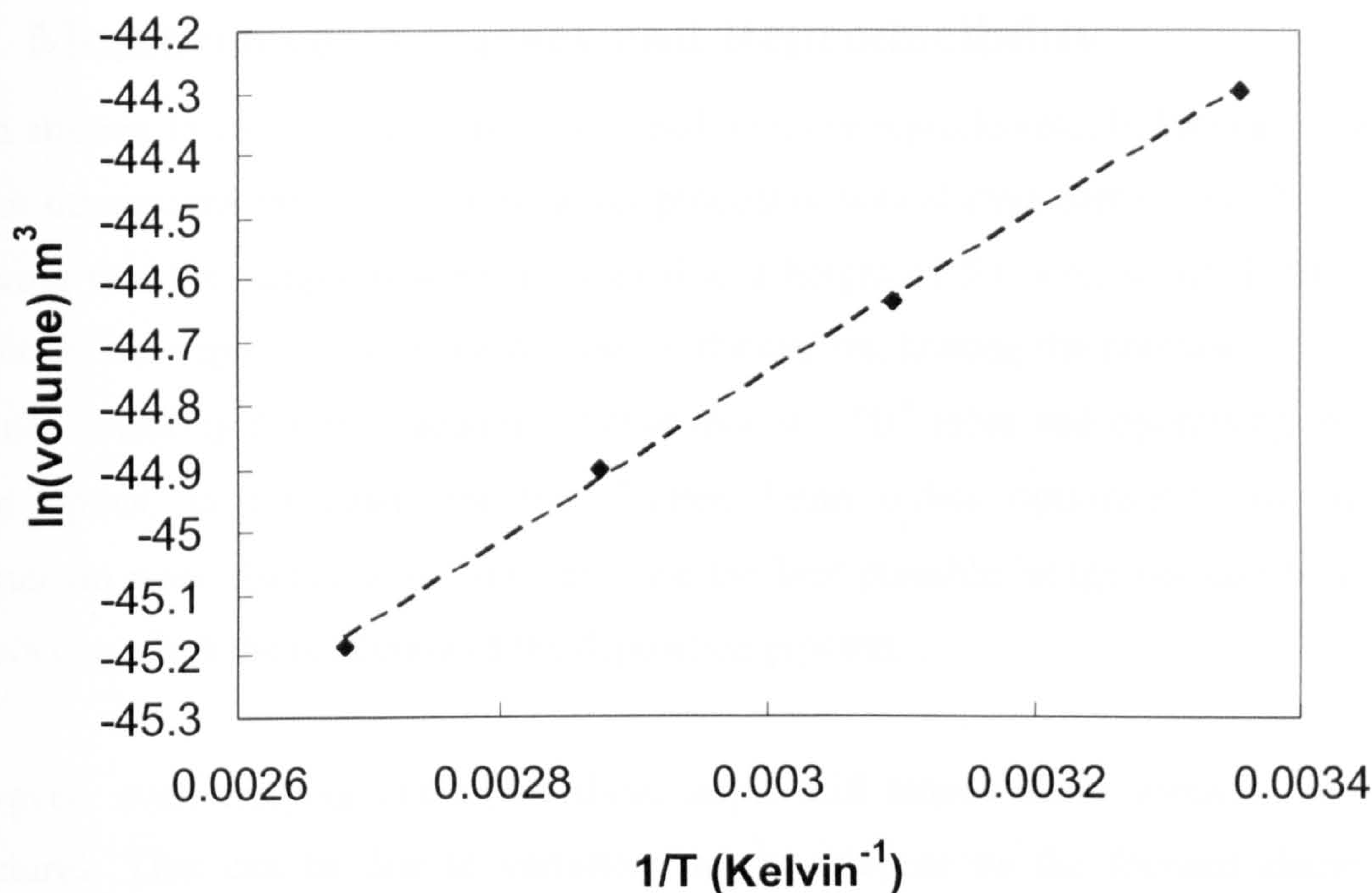


**Figure 4.16.** Plot of the natural logarithm of the deposited volume as a function of the inverse of the substrate temperature.

As can be seen from Figure 4.16, the deposited volume of tungsten interconnects produced from the precursor $W(CO)_6$ follows an Arrhenius behaviour. The gradient of the line of best fit produced in this figure has a value of 1302.4 and is equal to $-E_A/R$, while this line intercepts the y-axis at -48.663 and is equal to ln(A). From these values the pre-exponential factor can be calculated to be $7.1 \times 10^{-22}$, while the activation energy can be calculated to be 107 meV by using a gas constant value of $8.21 \times 10^{-5}$ $m^3 \cdot atm \cdot K^{-1} \cdot mol^{-1}$. This value for the activation energy for an electron beam voltage of 10 keV and an electron beam current of 1.5 nA is within the range of desorption energies found by Li et al. [11] who calculated a desorption energy of ~120 meV for a beam energy of 10 keV and a beam current of 140 pA. This result suggests that the reaction rate of deposits made using the EBID of $W(CO)_6$ is similar to that of EBID tips produced from the precursor $WF_6$. This value for the activation energy is also found to be in the range between physisorption (~0.01 eV) and chemisorption (~1 eV) and as such suggests that the adsorption-desorption process plays a significant role in EBID.

## 4.8 Measurement Accuracy and Reproducibility

In an attempt to ensure that the results gained here are reproducible, before carrying out any of the depositions the same optimisation procedure was always carried out. This included ensuring that the sample was always raised to a height of 5.1 mm, which is the optimum height for the deposition to be carried out in the system, heating the precursor for at least 30 minutes, ensuring that the vacuum is better than 4 x $10^{-6}$ mbar and optimising the electron beam optics. In particular, for the electron beam optics optimisation the focus and stigmatism were always adjusted to produce the best possible image because both of these factors can affect the resolution of the deposition process.

However, even carrying out all of these steps, still leaves some variation in the final structures. This can be due to variations in the vacuum or the focused electron beam including its emission current and small operator based errors in alignment. Each of these factors result in a change in the gas flux at the sample surface and in the focused electron beam at the point at which it impinges on the substrate. In particular producing the same deposits on different days produced a height variation of ~ 5 nm. This is not too large a value and is within the realm of experimental error when considering the thicker deposits. Although in the smallest structures this can cause significant variations and may affect the use of this technique in mainstream fabrication techniques.

## 4.9 Conclusions

This section has shown that for a constant electron beam current, the height of the deposits increases linearly with the number of passes made by the electron beam or the total electron dose that has been delivered. It has also been shown that the width of the deposits initially increases with the number of passes made by the electron beam and then saturates. This behaviour has been attributed to scattering of the primary electrons within the deposit and the subsequent generation of secondary electrons, which can be emitted out of the sidewalls of the deposit where they can be involved in the deposition process. This section has also shown how the deposited width and height of the structures increases with increasing beam current. This effect has been explained in terms of the increasing diameter of the electron beam and the increasing numbers of electrons (both primary and secondary) that are available to be involved in the deposition process.

This section has also highlighted some of the system variables, which can cause significant variations in the deposition growth rate. In particular, it shows how difficult it is for EBID researchers to accurately characterise the process and produce results, which may be accurately reproduced by other groups. As such this section has highlighted some of the main issues with making EBID suitable for mainstream fabrication techniques where the amount of material deposited is crucial.

### 4.9.1 References

[1] Q. Chen, S. Wang and L.-M. Peng, Nanotechnol. **17**, 1087 (2006).

[2] R. Gupta, R. E. Stallcup II and M. in het Panhuis, Nanotechnol. **16**, 1707 (2005).

[3] H. Fujioka, K. Nakamae, M. Hirota, K. Ura, N. Tamura and T. Takagi, J. Physics D: Appl. Phys. **23**, 266 (1990).

[4] D. Beaulieu, Y. Dong, Z. Wang and W. Lackey, J. Vac. Sci. Technol. B **23**, 2151 (2005).

[5] V. Gopal, E. A. Stach, V. R. Radmilovic and I. A. Mowat, Appl. Phys. Lett. **85**, 49 (2004).

[6] H. W. P. Koops, J. Kretz, M. Rudolph, M. Weber, G. Dahm and K. L. Lee, Jpn. J. Appl. Phys. **33**, 7099 (1994).

[7] K. T. Kohlmann-von Platen, L.-M. Buchmann, H.-C. Petzold and W. H. Brünger, J. Vac Sci. Technol. B **10**, 2690 (1992).

[8] P. C. Hoyle, J. R. A. Cleaver and H. Ahmed, J. Vac. Sci. Technol. B **14**, 662 (1996).

[9] J. D. Fowlkes, S. J. Randolph and P. D. Rack, J. Vac. Sci. Technol. B **23**, 2825 (2005).

[10] K. Lee and M. Hatzakis, J. Vac. Sci. Technol. B **7**, 1941 (1989).

[11] W. Li and D. C. Joy, J. Vac. Sci. Technol. A **23**, 431 (2006).

# CHAPTER FIVE

# 5 Electrical Characterisation of Electron Beam Deposited Tungsten Interconnects

## 5.1 Introduction

This chapter will describe the electrical characterisation of EBID tungsten interconnects fabricated from the precursor $W(CO)_6$ using either two or four probe measurements. It is found that the current-voltage characteristics are symmetric with respect to voltage polarity and that the resistance decreases with increasing interconnect height as expected due to the larger cross section available for conduction. It is also possible that the thicker deposits have a higher metallic content. The effects of various system variables including the electron beam current, the electron source, the lifetime of the precursor and the substrate temperature on the resistivity of the deposits is investigated and it is found that resistance of these deposits is highly dependent on the deposition parameters used.

## 5.2 Experimental Method

The depositions were carried out using the FEI Nanolab 600 Dual Beam FIB system described in section 3.2.3 and the precursor $W(CO)_6$. This work builds upon the work undertaken in chapter four and so the same conditions have been used to produce the deposits. As such a beam energy of 10 keV, a dwell time of 200 μs and a pitch of 10 nm were used for all of the depositions. The beam current, electron sources and the amount of time that the precursor had been used for were then varied as described in chapter four.

To allow for these deposits to be electrically characterised, rectangular deposits were made onto silicon dioxide substrates with a 300 nm thick oxide layer that had been prepatterned with gold contact pads so that each of the deposits bridged the gold contact pads in either a two or four point measurement set up. Contacts were made to these pads within a SEM using one of the manipulation systems described in section 3.6. These manipulation systems allowed for electrochemically etched tungsten probes, with tip radii between 25 and 400 nm to be moved separately in each of the three orthogonal directions and be brought into contact with the gold pads. All of the electrical measurements were made using the Keithley 4200 Semiconductor Characterisation System described in section 3.8.

## 5.3 Resistivity Characterisation

In chapter four it was shown that by varying several different EBID parameters including the electron beam current, the electron source and the age of the precursor it was possible to change the deposition rate. In particular it was found that increasing the electron beam current and changing the electron source to a brighter source caused the deposition rate to increase. This work also showed that as the amount of time that the precursor had been used for was increased, the deposition rate decreased. These results imply that as the deposition parameters are varied so does the actual deposition process and that it is possible that these changes result in deposits with different resistivities. The following sections shall examine the effects of changing these parameters on the resistivity of the nanowires and analyse the results with a view to determining the most suitable parameters for use in producing interconnects with a low resistivity and high resolution to nanostructures such as CNTs.

### 5.3.1 Effects of the Electron Beam Current

The electron beam deposition and the subsequent electrical characterisation that is carried out in this section was conducted in the FEI Dual Beam FIB. For the electrical characterisation, four electrically etched tungsten probes were fitted into the Zyvex manipulation system described in section 3.6.1, which was subsequently mounted on the sample stage. This system allowed for the four tungsten probes to be used to contact to the samples to be characterised. The Keithley 4200 Semiconductor Characterisation System was also connected to the Zyvex manipulation system to allow for the samples to be electrically characterised without exposing the deposits to air.

The deposits were made onto a silicon substrate with a 300 nm oxide layer that had been pre-patterned with gold contact pads in a four terminal geometry using conventional electron beam lithography as described in section 3.9. An example of one of the four terminal contact structures is shown in Figure 5.1(a). As can be seen from this image each structure consisted of four larger 25 x 25 $\mu m^2$ gold pads to which the tungsten probes were connected and four gold leads which ran from each of the gold pads towards the centre of the structure. The gold leads that were connected to the top and bottom pads had a width of ~2 μm and a length of ~12 μm, while the gold leads that were connected to the left and right pads had a width of ~1.4 μm and a length of ~10 μm. The depositions were made so that they bridged all four of the gold contact leads and had a length of 8.5 μm and a width of 200 nm.

Before starting the deposition, the sample and beam conditions were optimised and the four tungsten probes were brought into contact with the gold pads using careful manipulation as shown in Figure 5.1(a). It was possible to see when the tungsten probes were in contact with the pads, as the pads appeared darker when contacted to. The capillary tube through which the precursor is delivered was then injected into the system as shown in Figure 5.1(b). This set up allowed for the effect of increasing the height of a deposit in increments on the resistivity of deposit at each of the electron beam currents investigated to be examined.

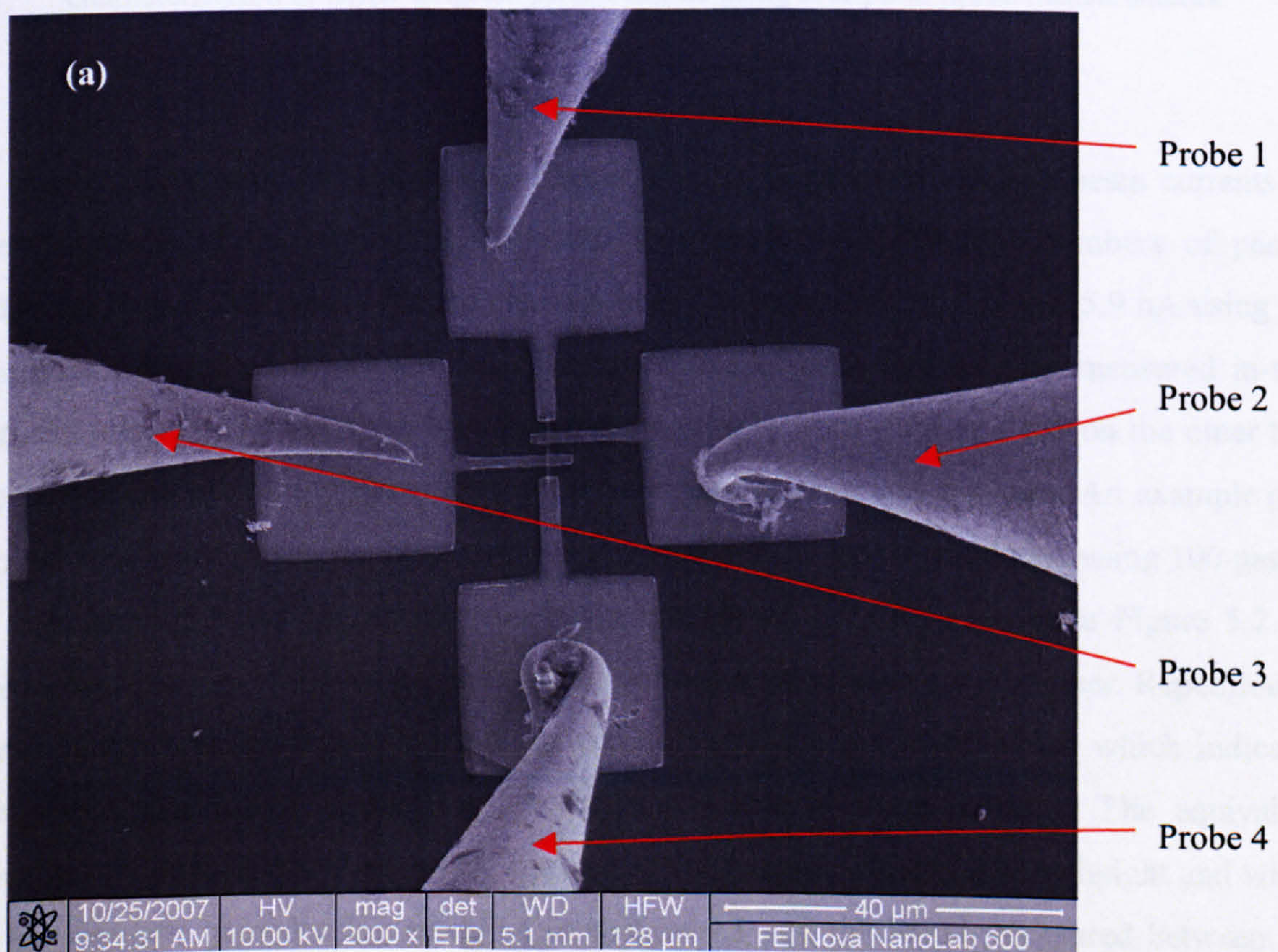

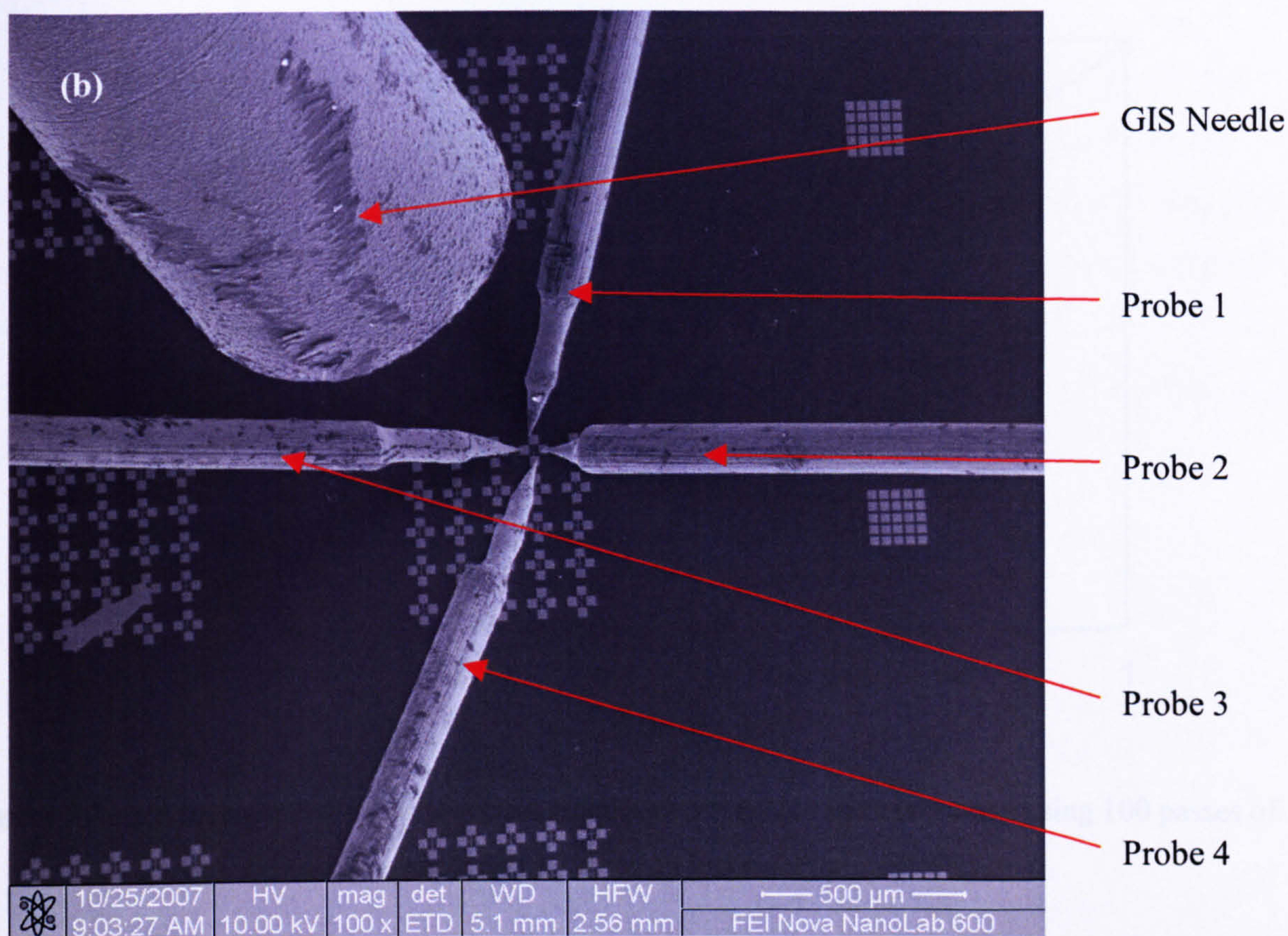


**Figure 5.1. (a)** SEM image of a four terminal gold contact structure with tungsten probes connected to each of the pads. **(b)** SEM image of the set-up used for the deposition and subsequent electrical characterisation of EBID tungsten interconnects using four point probe measurements.

In order to determine the effects of different deposit heights and electron beam currents on the resistance of the nanowires, deposits were made with different numbers of passes between 20 and 200 passes for the electron beam currents of 0.36, 1.5 and 5.9 nA using the conditions described in section 5.2. The resistance of each deposit was measured in-situ between each deposition stage by sweeping the current from 0 up to 1 μA on the outer two electrodes and measuring the voltage drop between the inner two contacts. An example of a typical four point probe measurement that was made for a deposit produced using 100 passes of the electron beam for an electron beam current of 1.5 nA is given in Figure 5.2. In particular, this figure shows that the current-voltage measurements were linear. Repetition of these current-voltage measurements showed no variation in the resistance which indicates that the resistivity of all of the deposits was stable at these currents. The equivalent resistivity was then calculated using the geometrical measurements for the height and width of the deposits gained using an AFM in section 4.3 and the length measured between the inner two contacts within the SEM.

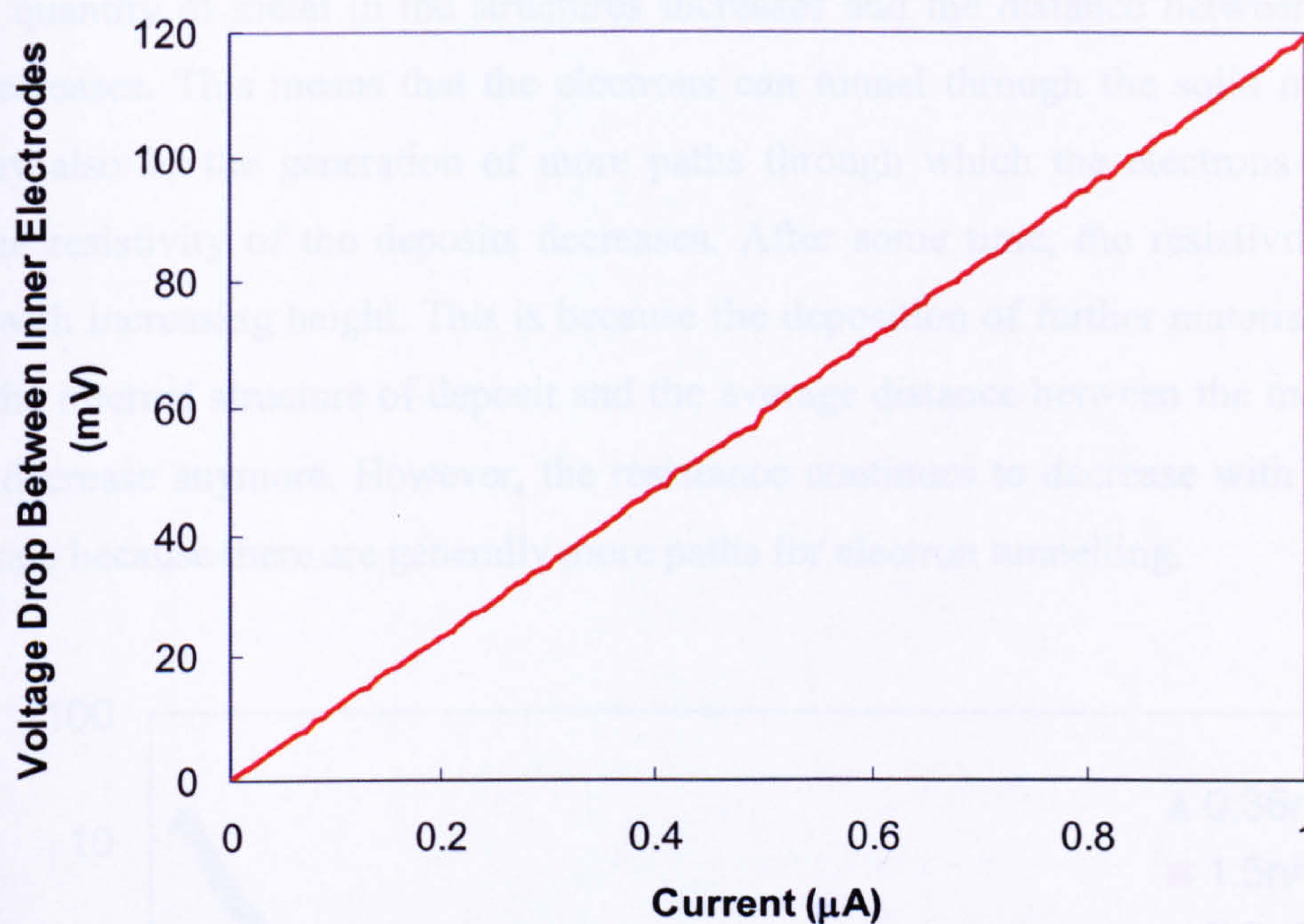


**Figure 5.2.** A typical four point probe measurement of a tungsten wire produced using 100 passes of the electron beam and an electron beam current of 1.5 nA.

As discussed in section 4.3.1, EBID results are typically presented in terms of the electron dose. Therefore, the resulting data of this experiment as a function of the total electron dose is shown in Figure 5.3. This data shows how the resistivity of EBID tungsten deposits decreases as the total amount of electron exposure that has been used and hence the height is increased. This graph also shows how initially the resistivity drops rapidly for each of the electron beam currents investigated before starting to saturate for electron beam doses in excess of 2 x $10^7$ μC/cm$^2$ for the beam currents of 1.5 and 5.9 nA. For the 0.36 nA it would take a very long time to build up this electron dose and so it was not investigated.

The decreasing resistivity with increasing total electron dose shown in Figure 5.3 may also be influenced by the morphology of the deposits, which consist of a mix of amorphous carbon and tungsten as described in section 4.4. This structure means that the conductivity mechanism in these deposits is not straightforward and as described in section 2.8, may occur through the tunnelling of electrons from one metal island to next. Therefore, the lowest height deposits have the lowest metal content and may be said to be discontinuous. This means that there is little or no path for electron tunnelling to occur and hence these deposits have a high resistivity. As the height of the deposits increases with the total electron

dose, the quantity of metal in the structures increases and the distance between the metal islands decreases. This means that the electrons can tunnel through the solid more easily. There may also be the generation of more paths through which the electrons can travel. Hence, the resistivity of the deposits decreases. After some time, the resistivity becomes constant with increasing height. This is because the deposition of further material no longer changes the internal structure of deposit and the average distance between the metal islands does not decrease anymore. However, the resistance continues to decrease with height at a constant rate because there are generally more paths for electron tunnelling.

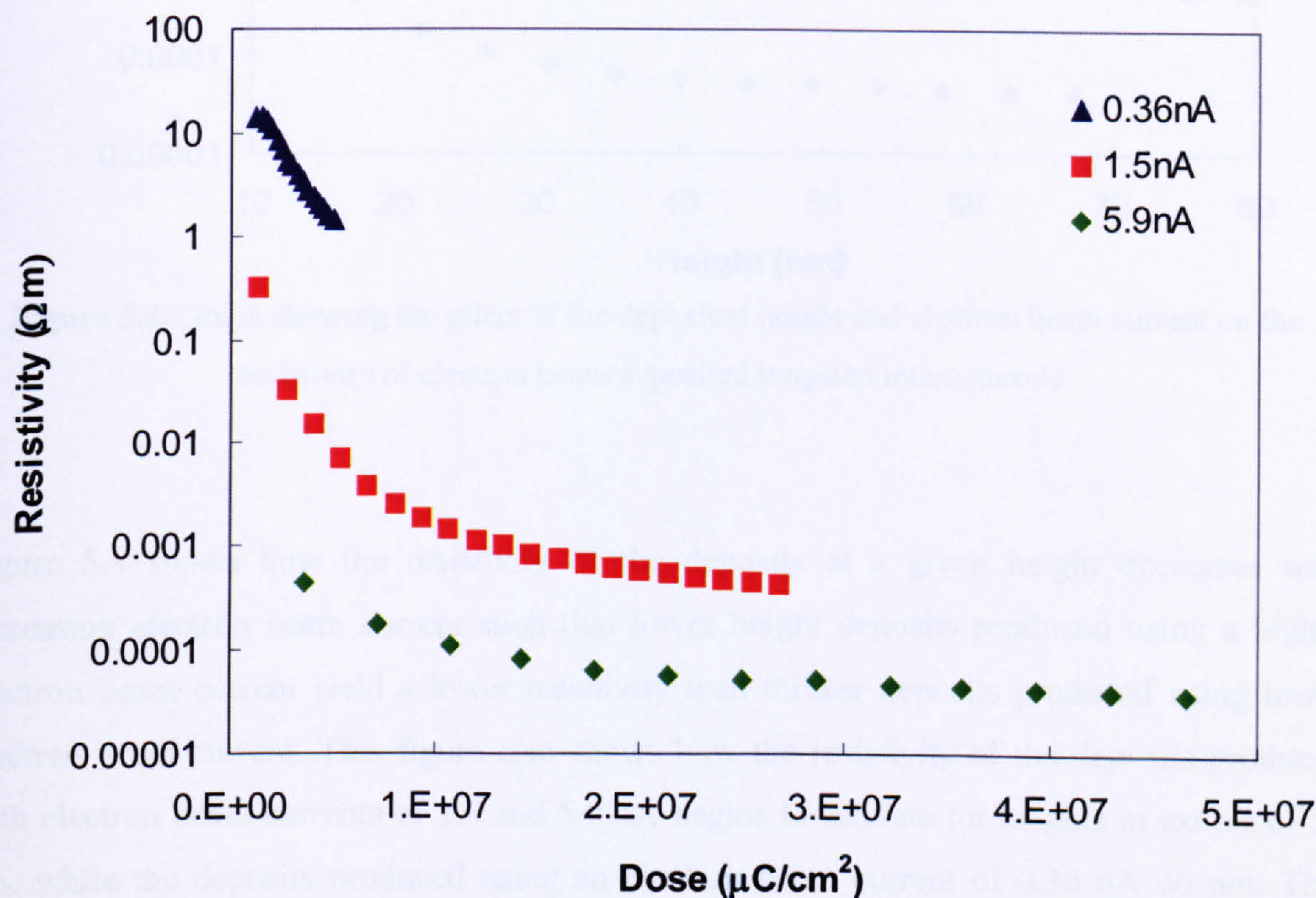


**Figure 5.3.** Graph showing the effect of electron dose and electron beam current on the resistivity of EBID tungsten interconnects.

If the above explanation for the change in resistivity with height or electron dose is correct it may also be expected that the decreasing resistivity with increasing electron beam current may be due in part to the increasing growth rate with increasing beam current that was observed in section 4.3.1. To investigate the effects of the change in deposited height with electron beam current the resistivity has also been plotted as a function of deposited height as shown in Figure 5.4.

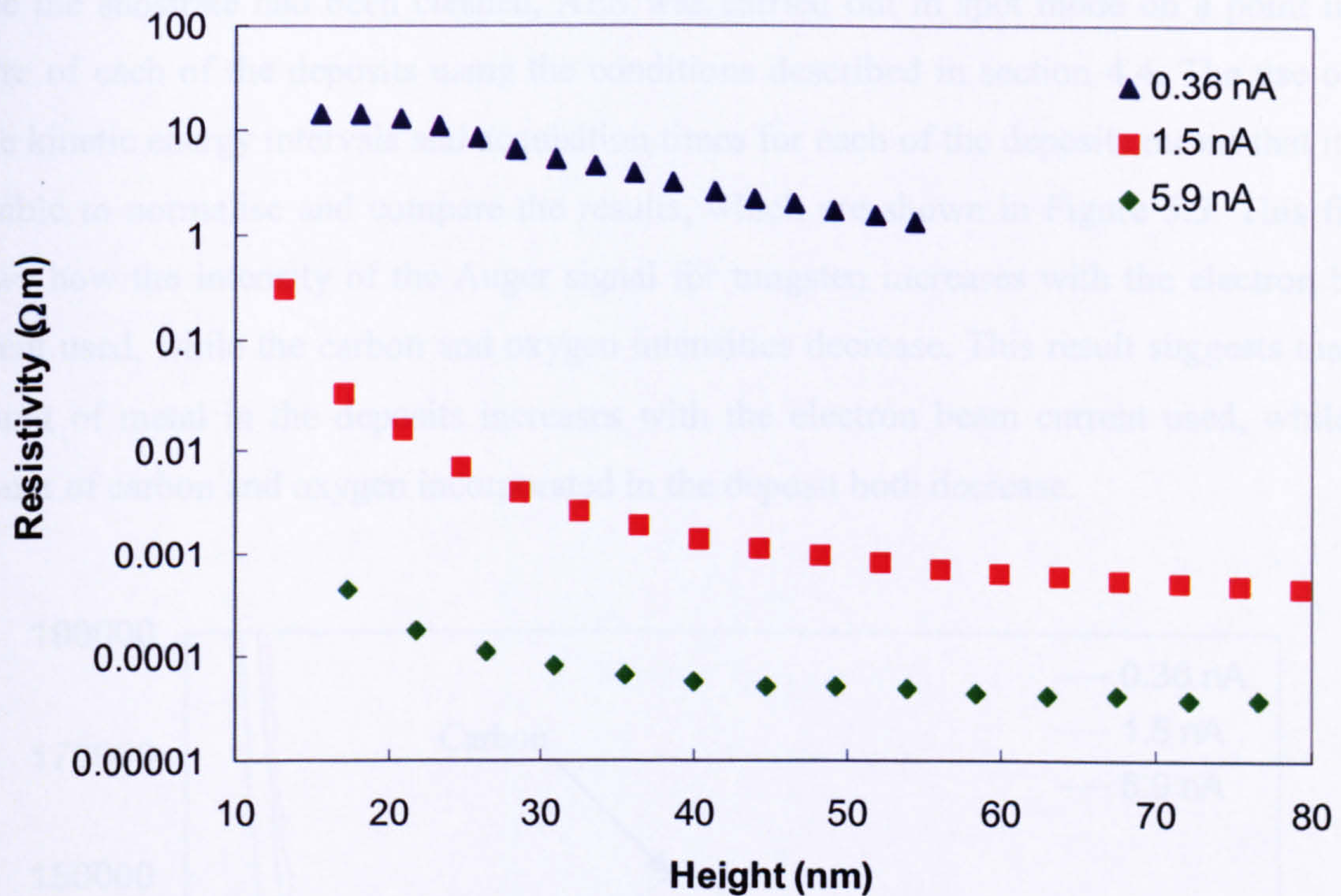


**Figure 5.4.** Graph showing the effect of the deposited height and electron beam current on the resistivity of electron beam deposited tungsten interconnects.

Figure 5.4 shows how the resistivity of the deposits at a given height decreases with increasing electron beam current such that lower height deposits produced using a higher electron beam current yield a lower resistivity than thicker deposits produced using lower electron beam current. This figure also shows how the resistivity of the deposits produced with electron beam currents of 1.5 and 5.9 nA begins to saturate for heights in excess of 50 nm, while the deposits produced using an electron beam current of 0.36 nA do not. This result is in agreement with the result shown in Figure 5.3. Therefore, it may be concluded that while the deposited height does have an affect on the resistivity of the deposits, the electron beam current that is used has a more significant effect.

The effect of the different beam currents on the resistivity of the deposits may be analysed further by examining the effects of the different beam currents on the elemental composition of the deposits. For this experiment ~52 nm high deposits were produced on a silicon substrate with a 300 nm thick oxide layer for each of the electron beam currents investigated. The elemental composition of the deposits was then examined using AES within the Thermo MICROLAB 350 that was described in section 3.4.1. Before commencing the analysis, the substrate was cleaned using the methodology described in section 4.4.

Once the substrate had been cleaned, AES was carried out in spot mode on a point in the centre of each of the deposits using the conditions described in section 4.4. The use of the same kinetic energy intervals and acquisition times for each of the deposits meant that it was possible to normalise and compare the results, which are shown in Figure 5.5. This figure shows how the intensity of the Auger signal for tungsten increases with the electron beam current used, while the carbon and oxygen intensities decrease. This result suggests that the amount of metal in the deposits increases with the electron beam current used, while the amount of carbon and oxygen incorporated in the deposit both decrease.

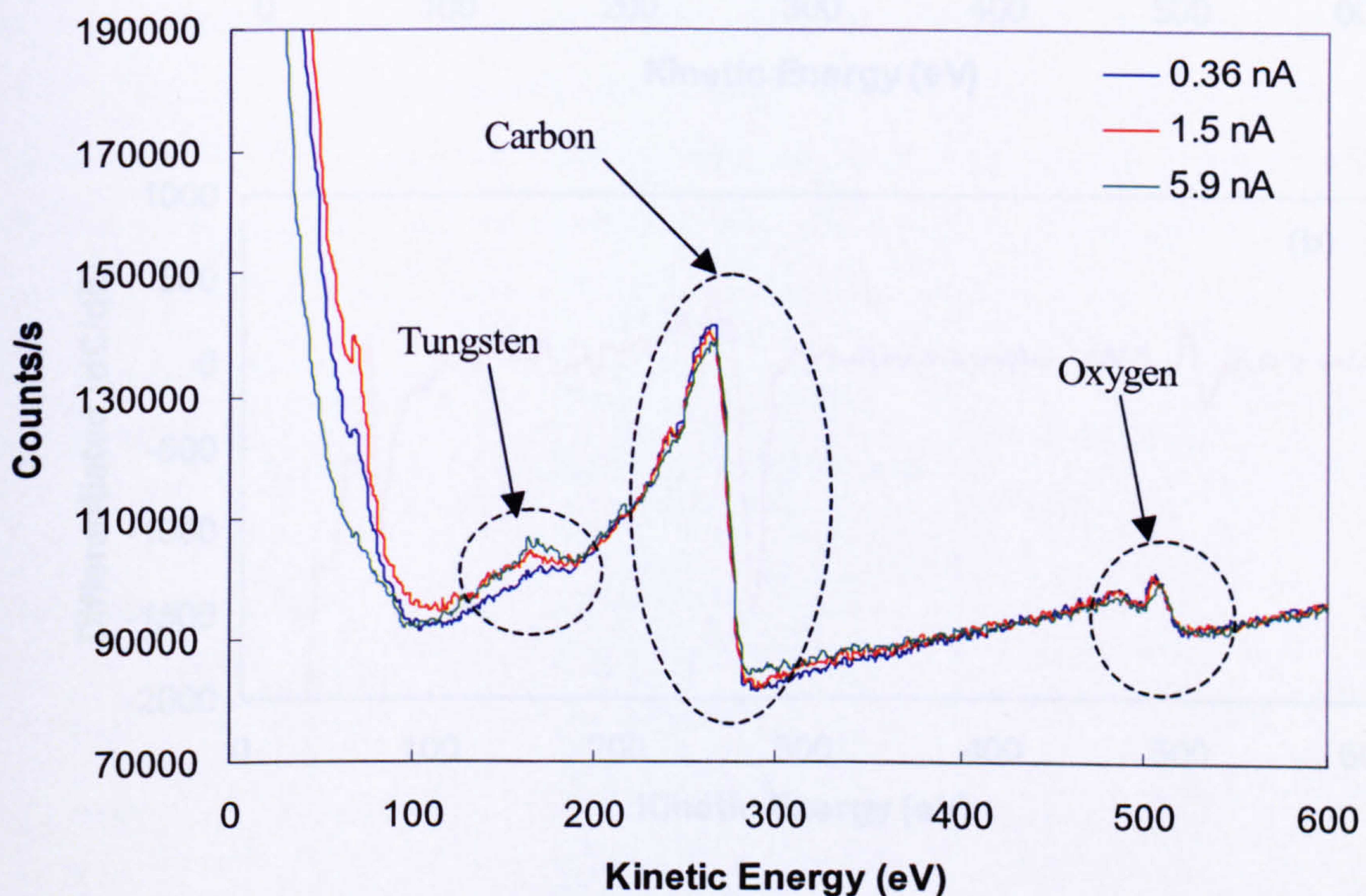


**Figure 5.5.** Analysis of the elemental composition of ~52 nm high deposits produced using electron beam currents of 0.36, 1.5 and 5.9 nA.

The changes in the elemental composition with the electron beam current can be quantified by comparing the peak-to-peak height of the intensities for the differential of the Auger spectrum without the need to normalise to the background noise. As such Figure 5.6 (a), (b) and (c) show the differential of the Auger spectrum for 0.36, 1.5 and 5.9 nA. These spectra do not show any signs of a carbide, which suggests that increasing the beam current from 0.36 to 5.9 nA for a beam energy of 10 keV, dwell time of 200 μs and a pitch of 10 nm has no effect on the local structure of the deposits. Therefore, it may be concluded that all of these deposits consist of an amorphous mix of tungsten, carbon and oxygen atoms.

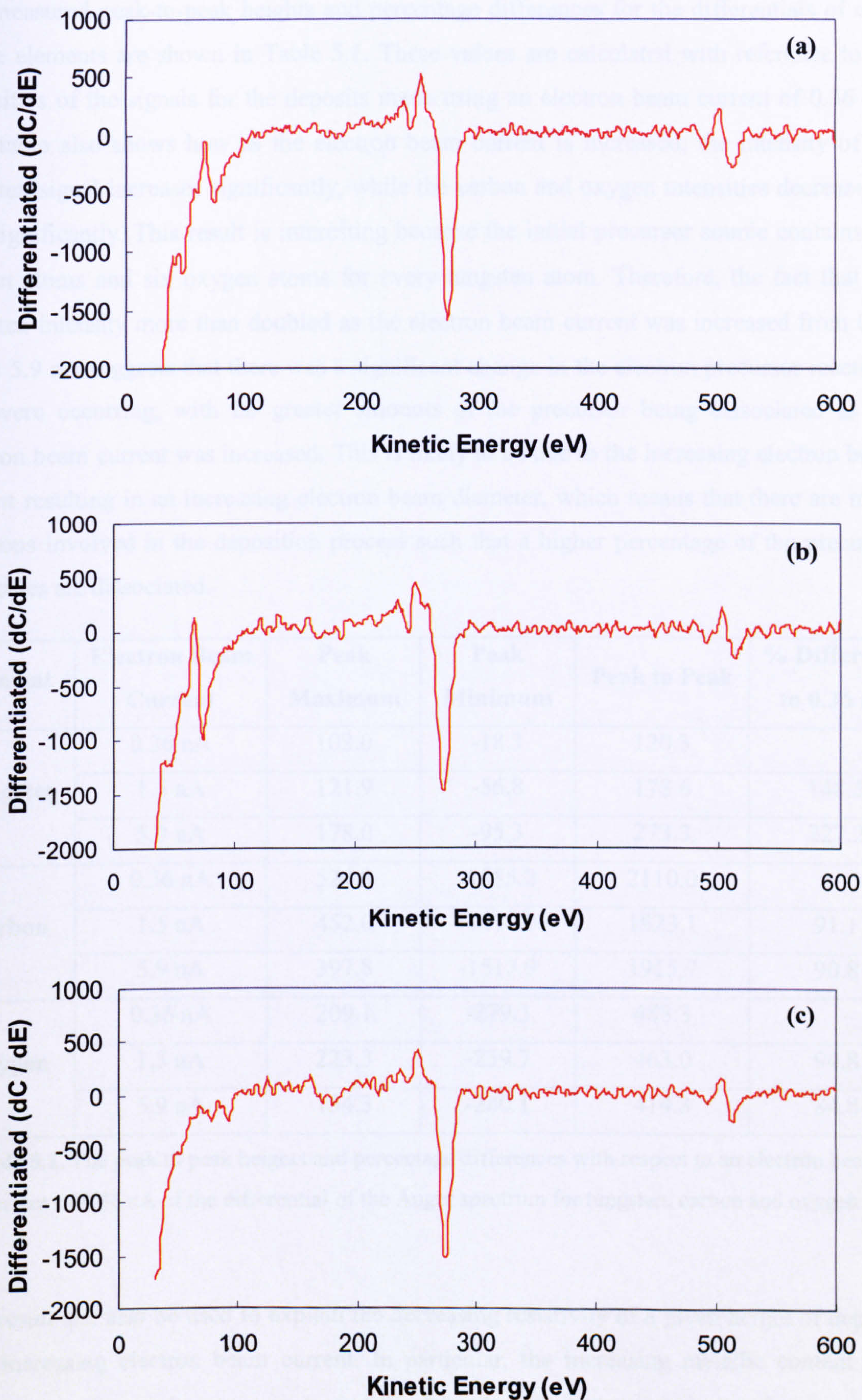


**Figure 5.6.** Graphs showing the differential of the Auger spectrum given in Figure 5.6 for electron beam currents of **(a)** 0.36 nA, **(b)** 1.5 nA and **(c)** 5.9 nA.

The measured peak-to-peak heights and percentage differences for the differentials of each of the elements are shown in Table 5.1. These values are calculated with reference to the intensities of the signals for the deposits made using an electron beam current of 0.36 nA. This table also shows how as the electron beam current is increased, the intensity of the tungsten signal increases significantly, while the carbon and oxygen intensities decrease far less significantly. This result is interesting because the initial precursor source contains six carbon atoms and six oxygen atoms for every tungsten atom. Therefore, the fact that the tungsten intensity more than doubled as the electron beam current was increased from 0.36 nA to 5.9 nA suggests that there was a significant change in the electron precursor reactions that were occurring, with far greater amounts of the precursor being dissociated as the electron beam current was increased. This is likely to be due to the increasing electron beam current resulting in an increasing electron beam diameter, which means that there are more electrons involved in the deposition process such that a higher percentage of the precursor molecules are dissociated.

| Element | Electron Beam Current | Peak Maximum | Peak Minimum | Peak to Peak | % Difference to 0.36 nA |
|---|---|---|---|---|---|
| Tungsten | 0.36 nA | 102.0 | -18.3 | 120.3 | |
| | 1.5 nA | 121.9 | -56.8 | 178.6 | 148.5 |
| | 5.9 nA | 178.0 | -95.3 | 273.3 | 227.2 |
| Carbon | 0.36 nA | 524.8 | -1585.2 | 2110.0 | |
| | 1.5 nA | 452.0 | -1471.0 | 1923.1 | 91.1 |
| | 5.9 nA | 397.8 | -1517.9 | 1915.7 | 90.8 |
| Oxygen | 0.36 nA | 209.1 | -279.3 | 488.3 | |
| | 1.5 nA | 223.3 | -239.7 | 463.0 | 94.8 |
| | 5.9 nA | 154.3 | -260.1 | 414.3 | 84.8 |

**Table 5.1.** The peak to peak heights and percentage differences with respect to an electron beam current of 0.36 nA of the differential of the Auger spectrum for tungsten, carbon and oxygen.

This result can also be used to explain the decreasing resistivity of a given height of deposit with increasing electron beam current. In particular, the increasing metallic content and decreasing carbon and oxygen content of the deposits with increasing electron beam current means that as the electron beam current is increased, an increasing percentage of the deposits' consist of the metal.

As each of these deposits have the same size it can therefore be concluded that as the electron beam current is increased, the distance between the metal islands in the deposit decreases. This in turn means that as the distance between the metal islands decreases, the conduction electrons can travel from one metal island to the next more easily and as such the resistivity of the deposit would be expected to decrease. Therefore it may be concluded that the decreasing resistivity with increasing electron beam current for a given height deposit, that was observed in Figure 5.4, is due to the increasing metallic content of the deposits.

This result is also in agreement with the experimental work of Weber et al. [1] and Koops et al. [2] In these experiments EDX and electrical measurements were used to determine the effects of changing the electron beam current on the properties of gold, molybdenum and platinum deposits and it was found that as the electron beam current was increased, the quantity of metal incorporated in the deposits increased, while the resistivity decreased. In particular Koops et al. [2] found that the percentage of the gold metal in the deposits increased with the beam current until it was equal to the amount of metal contained in the precursor, which occurred for an electron beam current of 800 pA and thereafter remained constant. Meanwhile, the resistivity of the deposits was found to decrease with increasing beam current up to a beam current of 800 pA and thereafter to also remain constant, which may be expected from the constant metal content at these high beam currents.

For the entire range of electron beam currents used in the experimental work, both the tungsten metal content and the resistivity were found to vary with increasing beam current. By comparing this result with the experimental results gained by Koops et al. [2] it may be assumed that the percentage of the metal that was incorporated in any of these deposits remained lower than that in the precursor source. This result also suggests that much higher electron beam currents are required to achieve the optimal deposition of interconnects from the precursor $W(CO)_6$ than for deposits produced from the precursor $Me_2Au(tfac)$.

### 5.3.2 Effects of the Electron Source

To investigate the effects of the electron source used on the resistivity of EBID deposits, the resistivity of deposits produced using two different electron sources were investigated. The first electron source that is investigated, is the source used to create the deposits examined in section 5.3.1 and the second electron source is another brighter source. For both sets of data the precursor was within the first twenty hours of its life and the beam current was set using spot three, which gives a current of 1.5 nA for electron source one and 2.1 nA for electron source two. The resistivity of the deposits made with electron source one were determined using the four probe methodology described in section 5.3.1, while for electron source two, two point measurements were undertaken. It was not expected that the different contact set up would make a significant difference to the electrical measurements as the contact resistances were found to be low in comparison to the resistance of the deposits themselves.

In order to undertake the two terminal measurements, a range of deposits 200 nm by 8 μm with different total electron doses were fabricated within the FEI Dual Beam FIB so as to bridge gold pads and leads with an ~5.5 μm separation that had been prepatterned using conventional UV lithography. Once all of the depositions had been completed the sample was transferred into the FEI Quanta 200 ESEM that had been fitted with the Attocube manipulation system described in section 3.6.2. Two electrochemically etched tungsten probes were then bought into contact with the gold pads connecting one of the structures so that electrical characterisation of the deposit could be undertaken. Figure 5.7 shows a typical tungsten interconnect deposited across two gold pads that has been contacted to using the Attocube manipulation system.

Once the tungsten probes had been brought into contact with the gold leads, electrical measurements of the deposits were carried out using the Keithley 4200 Semiconductor Characterisation System described in section 3.7. For these measurements a voltage sweep was run from 0 V up to a fixed positive voltage before being decreased to the equivalent negative voltage and then increased back to 0 V and the current was measured for each voltage point. For these measurements a current limit of less than 10 μA was also set in order to avoid premature destruction of the interconnects. An example of a typical current-voltage measurement for a tungsten wire produced using 50 passes of the electron beam is shown in Figure 5.8. This figure shows how the electrical characteristics of this deposit are linear and symmetrical with respect to zero voltage.

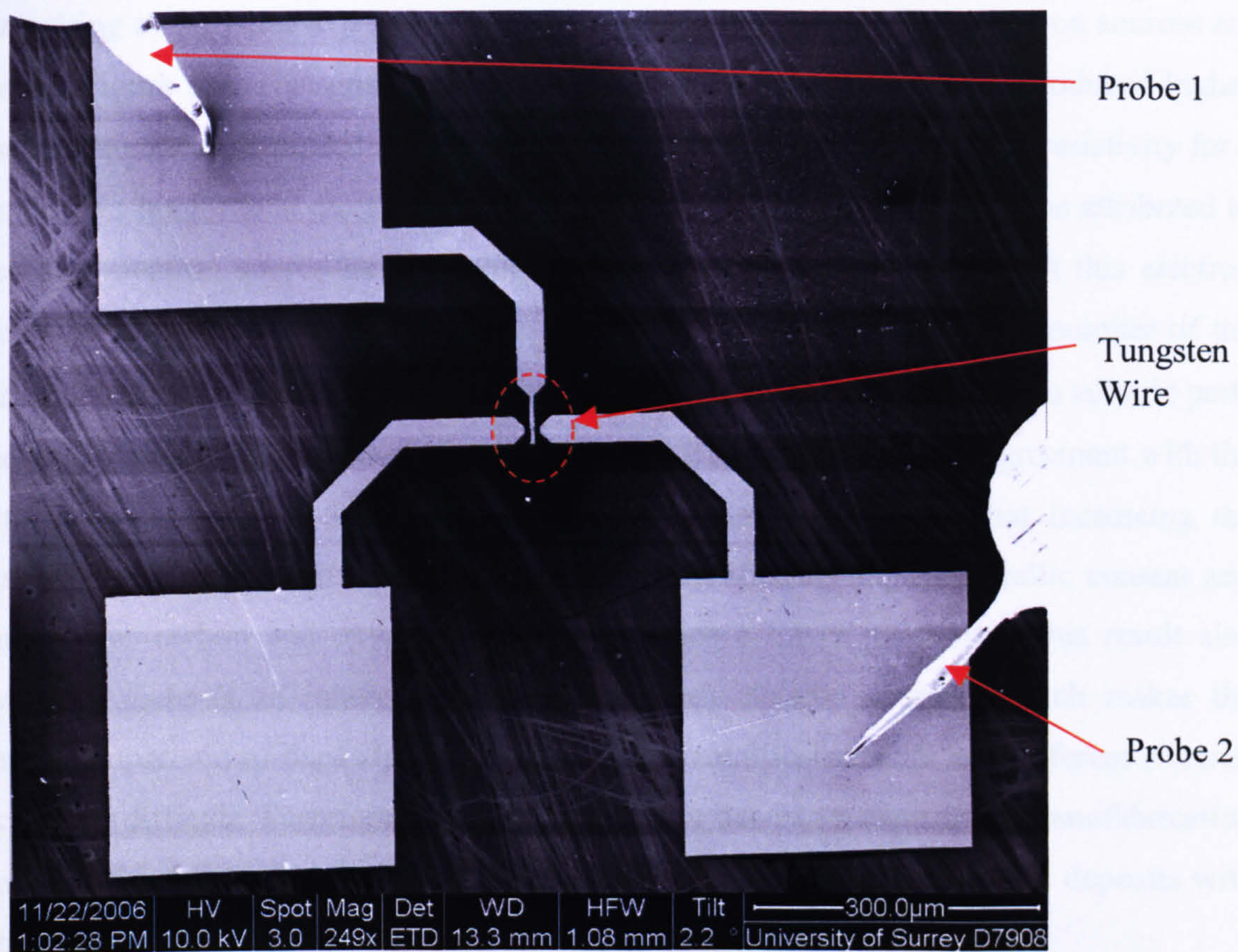


**Figure 5.7.** SEM image of a two terminal gold contact structure with electrochemically etched tungsten probes connected to each of the pads using the Attocube manipulation system.

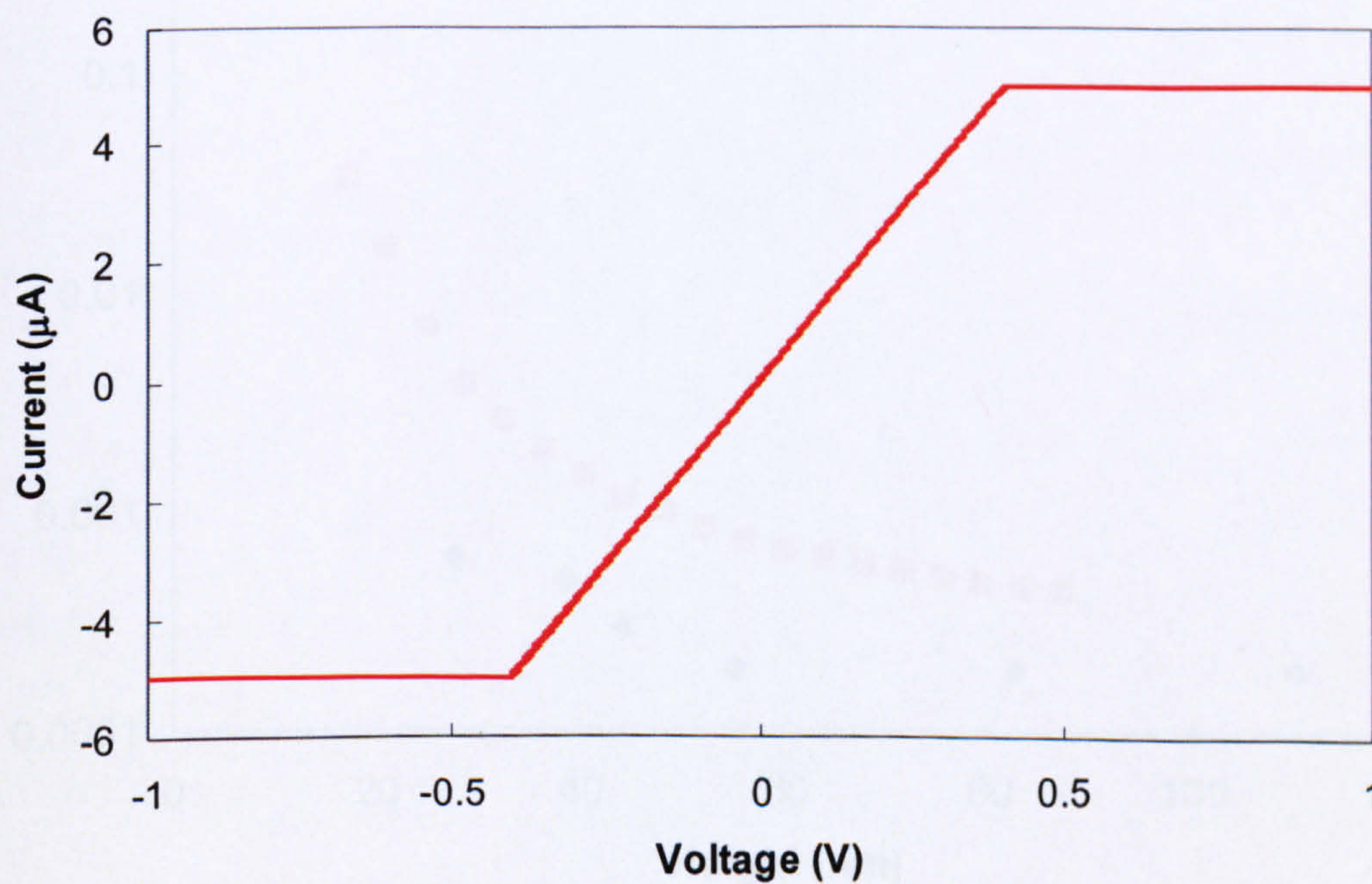


**Figure 5.8.** Four point probe measurement of a tungsten wire produced using 50 passes of the electron beam and a beam current of 1.5 nA.

The resulting resistivities as a function of deposit height, for each of the electron sources are shown in Figure 5.9. This graph shows how electron source two not only produced higher deposits, which was discussed in section 4.5.1, but also deposits with a lower resistivity for a given deposit height than electron source one. These lower resistivities may be attributed to the second electron source having a higher beam current, which means that this electron source also had a higher current density. This in turn means that a greater number of the adsorbed precursor molecules could be dissociated at one time and more of the volatile parts of the precursor could be removed from the deposit. This result is also in agreement with the results gained in section 5.3.1, where AES of the deposits showed that increasing the electron beam current resulted in deposits with a significantly higher metallic content and slightly lower carbon and oxygen content and hence a lower resistivity. This result also shows how there is an inherent variability between electron sources, which makes the accurate comparison of deposits produced using different instruments and different electron sources very difficult. Therefore, in order for EBID to become a mainstream nanofabrication technique it is necessary to be able to adjust each electron source to produce deposits with identical growth rates and resistivities in different systems.

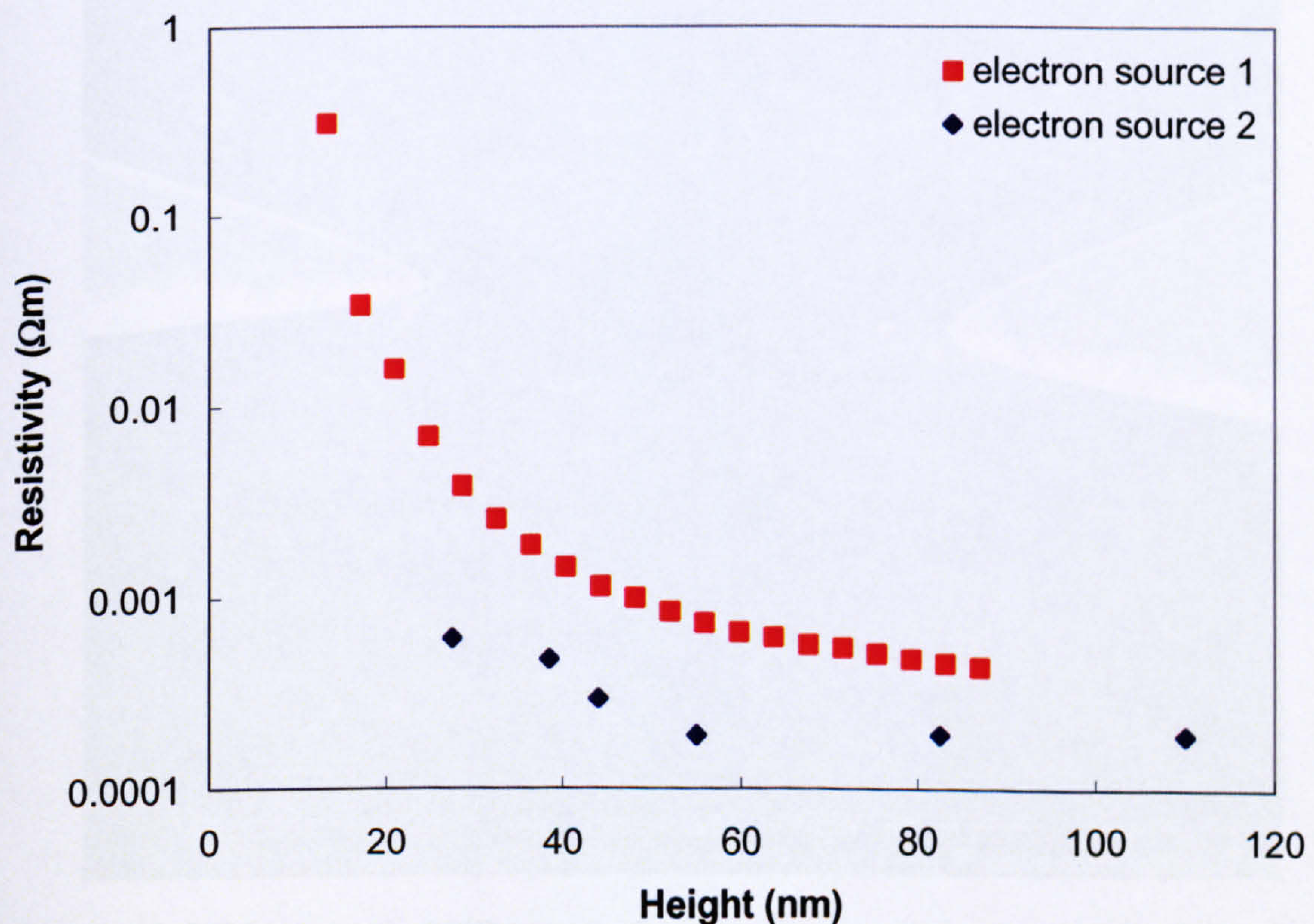


**Figure 5.9.** Graph showing the effects of the use of two different electron sources on the resistivity of electron beam deposited tungsten wires as a function of the deposited height.

### 5.3.3 Effects of the Precursor Lifetime

To investigate the effects of the precursor lifetime on the resistivity of EBID tungsten interconnects, the resistivity of deposits made using a new precursor with less than twenty hours of use were compared to those made using a precursor with more than 120 hours of use. The deposits produced using both of the precursors were fabricated with an electron beam current of 1.5 nA and had a width of 200 nm. For the precursor with less than 20 hours of use, the resistivity was measured using the four point probe measurement set-up described in section 5.3.1. For the precursor with more than 120 hours of use, two point probe measurements were undertaken on a silicon substrate with a 300 nm thick oxide layer that had been prepatterned with 20 by 20 μm gold pads with a ~6 μm separation using electron beam lithography as described in section 3.9 and shown in Figure 5.10. This substrate was mounted in the Zyvex nanomanipulation system described in section 3.5.1 within the FEI Dual Beam FIB so that the deposits could be simultaneously fabricated and electrically characterised using the same method as the one used in section 5.3.1.

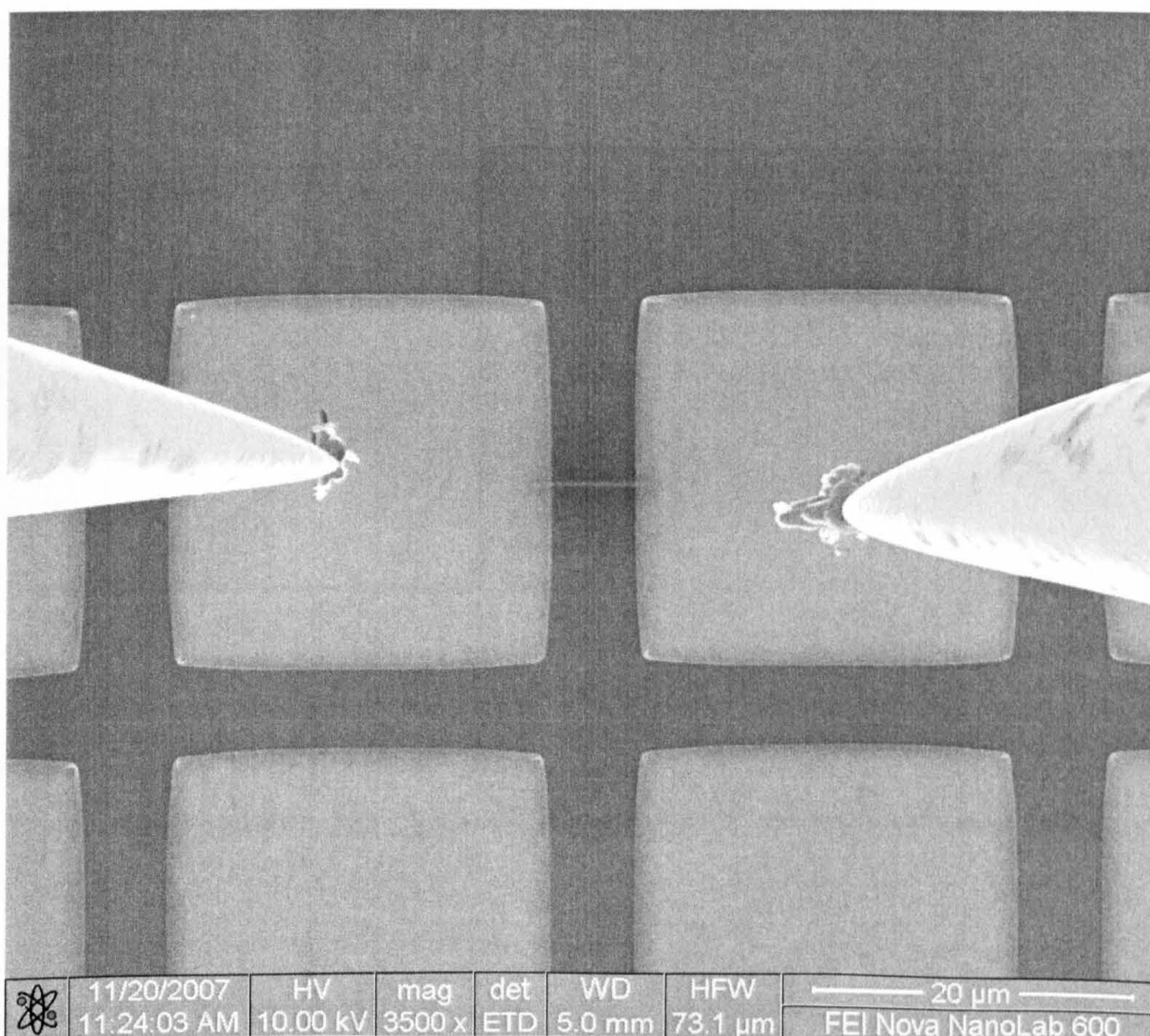


**Figure 5.10.** SEM image of a EBID tungsten interconnect deposited so as to bridge two gold pads patterned using electron beam lithography that has been contacted to using two electrochemically etched tungsten probes and the Zyvex S100 Nanomanipulation system.

Initially, a deposit was produced using 20 passes of the electron beam and its resistance was measured in-situ by sweeping the voltage from 0 V up to 2 V and then back to 0 V and measuring the current for each voltage point. The height of this deposit was then increased in twenty pass steps up to 200 passes and the resistance was measured in-situ between each deposition stage using the same voltage sweep. For all of these electrical measurements a current limit of 5 μA was set in order to avoid premature destruction of the deposits. An example of a typical two point probe measurement that was taken for a nanowire made using 150 passes of the electron beam is given in Figure 5.11 and shows how the current voltage measurements were linear. Repetition of the current-voltage measurements also showed no variation in the resistance and indicated that the electrical characteristics of all of the deposits were stable at these currents. The equivalent resistivity was then calculated using the geometrical measurements for the height and width of the deposits gained using an AFM in section 4.5.2 and the length measured between the contacts with the SEM.

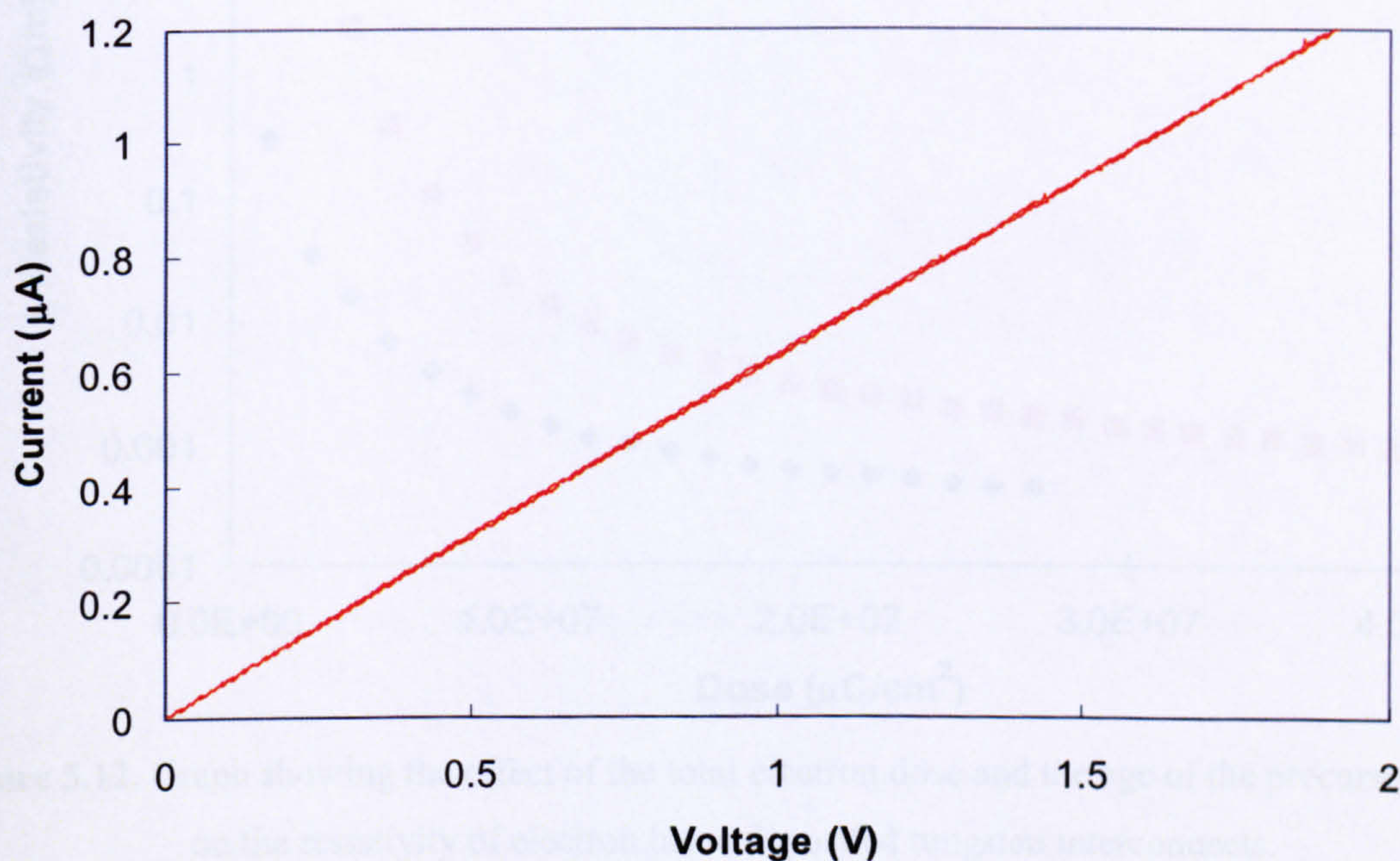


**Figure 5.11.** A typical two point probe measurement of a tungsten wire produced using 150 passes, a precursor with more than 120 hours of use and an electron beam current of 1.5 nA.

In accordance with the data analysed so far, the resistivity measurements for the new and the old precursors were plotted as a function of the electron dose that was used to produce the deposits. The results of this investigation are shown in Figure 5.12. As can be seen from this figure, the resistivity of the deposits for a given total electron dose increases with the amount

of time that the precursor has been used. In particular it was found in section 4.5.2, that as the precursor aged, it formed agglomerates, which means that less of the precursor is heated into the gas phase and as such the gas flux on the substrate surface and the deposition rate both decrease. As the deposited height decreases the quantity of metal within the structures also decreases and causes the resistivity of the deposits to increase as the conduction electrons have to travel greater distances between the metal islands. Therefore, the decreasing gas flux as the precursor ages may result in the reduced resistivity for the old precursor. Alternatively, as the precursor is repeatedly heated and cooled its elemental composition may change and result in a deposit with a lower metallic content.

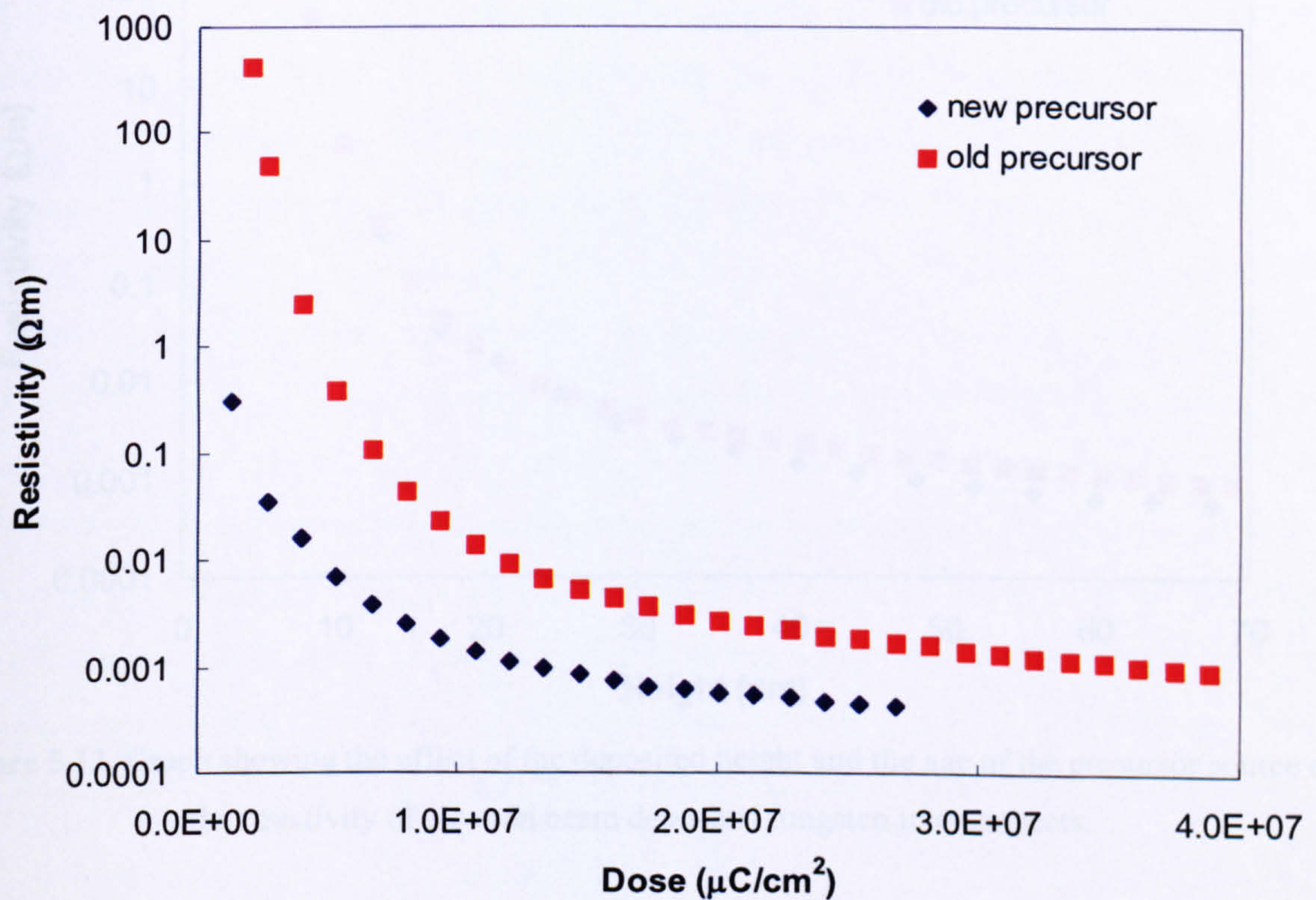


**Figure 5.12.** Graph showing the effect of the total electron dose and the age of the precursor source on the resistivity of electron beam deposited tungsten interconnects.

To examine which of these is responsible for the changes seen in the resistivity, this data can also be examined in terms of the deposited height. The resulting analysis is given in Figure 5.13, which shows that the resistivity of the deposits using the new and the old precursor sources is quite similar. This result implies that over time the elemental composition of the precursor remains the same and that it is just the gas flux on the substrate surface that decreases as the precursor forms agglomerates. The small differences that can be seen in the

two sets of data may be attributed to the use of two point probe measurements for the old precursor versus four point probe measurements for the new precursor and to inaccuracies in the measurement of the deposit sizes that are incorporated into the resistivity calculations. From this result it may also be concluded that when characterising and comparing the experimental results of EBID structures, it is not suitable to just be concerned with the electron dose used to produce the deposits but that the gas flux on the surface of the substrate also needs to be taken into account.

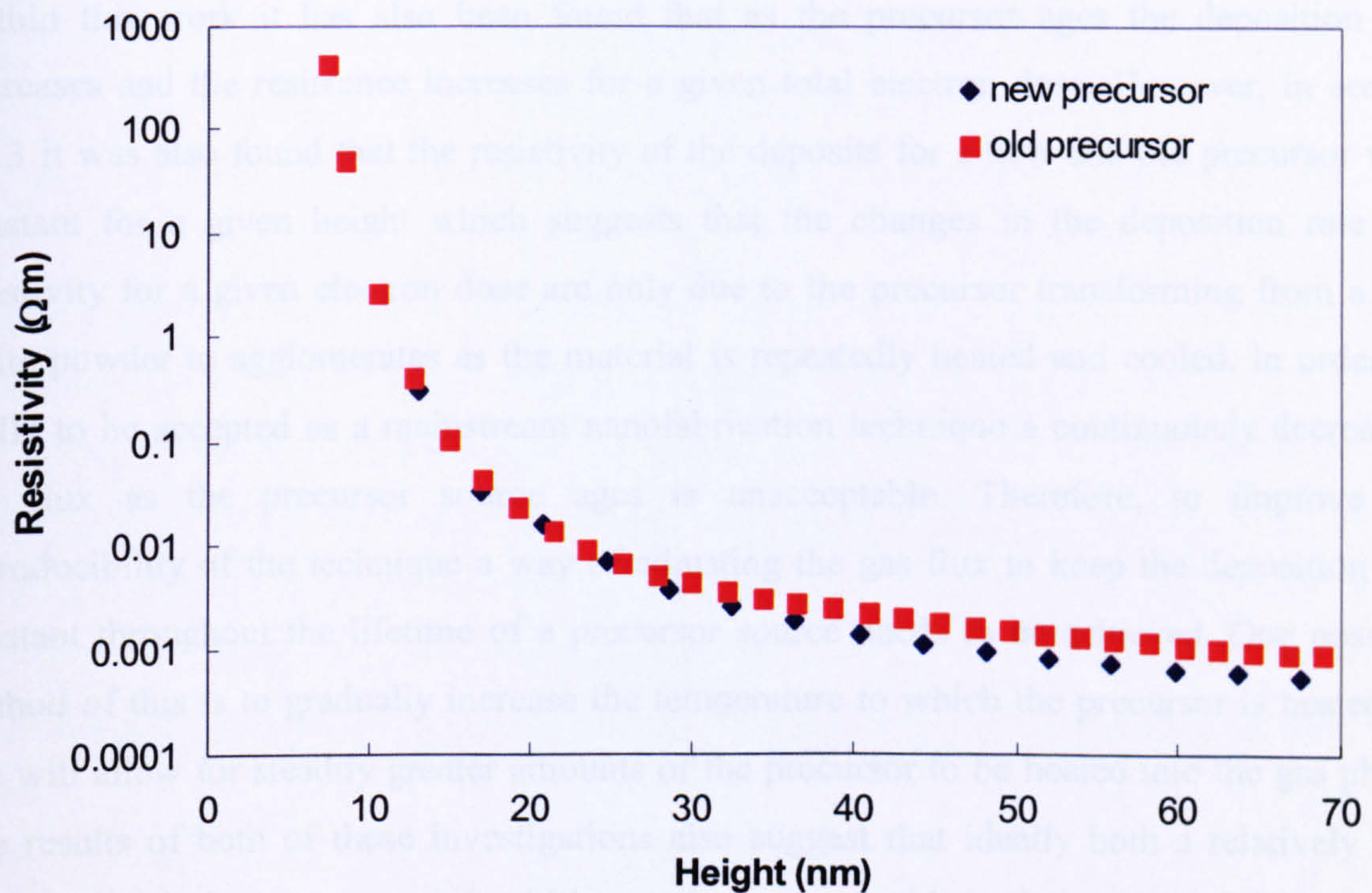


**Figure 5.13.** Graph showing the effect of the deposited height and the age of the precursor source on the resistivity of electron beam deposited tungsten interconnects.

### 5.3.4 Discussion

The results that have been presented in this section show that for electronic interconnect applications of EBID it is necessary to use high electron beam currents and high total electron doses in order to achieve low resistivity wires. However, in chapter four it was found that as the electron beam current was increased the resolution of the process decreased and so in electronic applications where the resolution of the interconnects is also critical it is necessary to trade off resistivity against resolution. As such a mid electron beam current of 1.5 nA may be the most suitable choice.

The work that has been carried out in this section and in chapter four also shows that the deposition rate and resistivity of EBID structures is highly dependent on changes in both the electron source and the precursor age. In particular, it has been shown that when brighter electron sources with higher current densities are used for EBID they produce structures with a greater deposited height and a lower resistivity for a given total electron dose. This has been attributed to the brighter electron source having a greater number of electrons in a unit area, which means that a greater number of the precursor molecules will be dissociated.

Within this work it has also been found that as the precursor ages the deposition rate decreases and the resistance increases for a given total electron dose. However, in section 5.3.3 it was also found that the resistivity of the deposits for a new and old precursor were constant for a given height which suggests that the changes in the deposition rate and resistivity for a given electron dose are only due to the precursor transforming from a fine white powder to agglomerates as the material is repeatedly heated and cooled. In order for EBID to be accepted as a mainstream nanofabrication technique a continuously decreasing gas flux as the precursor source ages is unacceptable. Therefore, to improve the reproducibility of the technique a way of adjusting the gas flux to keep the deposition rate constant throughout the lifetime of a precursor source needs to be achieved. One possible method of this is to gradually increase the temperature to which the precursor is heated, as this will allow for steadily greater amounts of the precursor to be heated into the gas phase. The results of both of these investigations also suggest that ideally both a relatively new precursor and electron source should be used where possible and that the selection of the most energetic electron sources is ideal for achieving a high deposition rate.

In conclusion, the work carried out in this section and in sections 4.5 and 4.3 has highlighted the importance of the need for greater control and characterisation of the EBID process. It has been demonstrated that before EBID can become a mainstream nanofabrication technique, a suitable method of achieving greater control of the gas flux and the electron source needs to be gained. It has also been shown that using just the electron dose to describe the deposition parameters is insufficient as the deposition rate is also very dependent on the gas flux as well as other factors including the vacuum and the type of substrate used.

## 5.4 Effects of the Substrate Temperature

In section 4.7 it was found that as substrate temperature was increased for the deposition of tungsten interconnects, the deposition rate decreased. This section will investigate whether the changes in substrate temperature also have an effect on the resistivity and composition of the deposits. To carry out this experiment the Omicron Nanotechnology Resistive Heater described in section 3.8 was mounted on a modified sample stage in the FEI Dual Beam FIB. The heater was then connected to a Keithley 238 Source Measurement Unit using a co-axial feedthrough situated within the microscope chamber. A silicon oxide substrate that had been prepatterned with gold contact pads as described in section 5.3.3 was then mounted in the heater. This experimental set-up meant that that the depositions could be carried out using the same method as for all of the other depositions that are characterised in this chapter.

To investigate the effects of a heated substrate on the electrical and structural properties of the deposits, all of the deposits were produced using an electron beam current of 1.5 nA and 200 passes of the electron beam. The depositions were then made so as to bridge the gold contact pads for substrate temperatures of approximately 100, 75, 50 and 25°C. Before carrying out any of these depositions, the temperature of the heater on which the substrate was mounted was raised to the required temperature and then allowed to stabilise for at least thirty minutes to minimise any sample drift and inconsistencies in the substrate temperature.

### 5.4.1 Electrical Characterisation

In order to electrically characterise these deposits, the sample was transferred into the Zyvex Nanomanipulation System that was described in section 3.5.1, which was in turn mounted in the FEI Dual Beam FIB described in section 3.2.3. Two electrochemically etched tungsten probes were then brought into contact with the gold contact pads connecting one of the deposits. The resistance of the deposits were determined by running current-voltage cycles from 0 V up to a fixed positive voltage and then back to 0 V. A current limit of 1 μA was also set in order to prevent premature destruction of the structures. The corresponding resistivity of each of these deposits was then calculated by combining these values with the geometrical values that were gained using an AFM in section 4.7. The resulting resistivities are presented as a function of the substrate temperature at which the deposition was carried out in Figure 5.14.

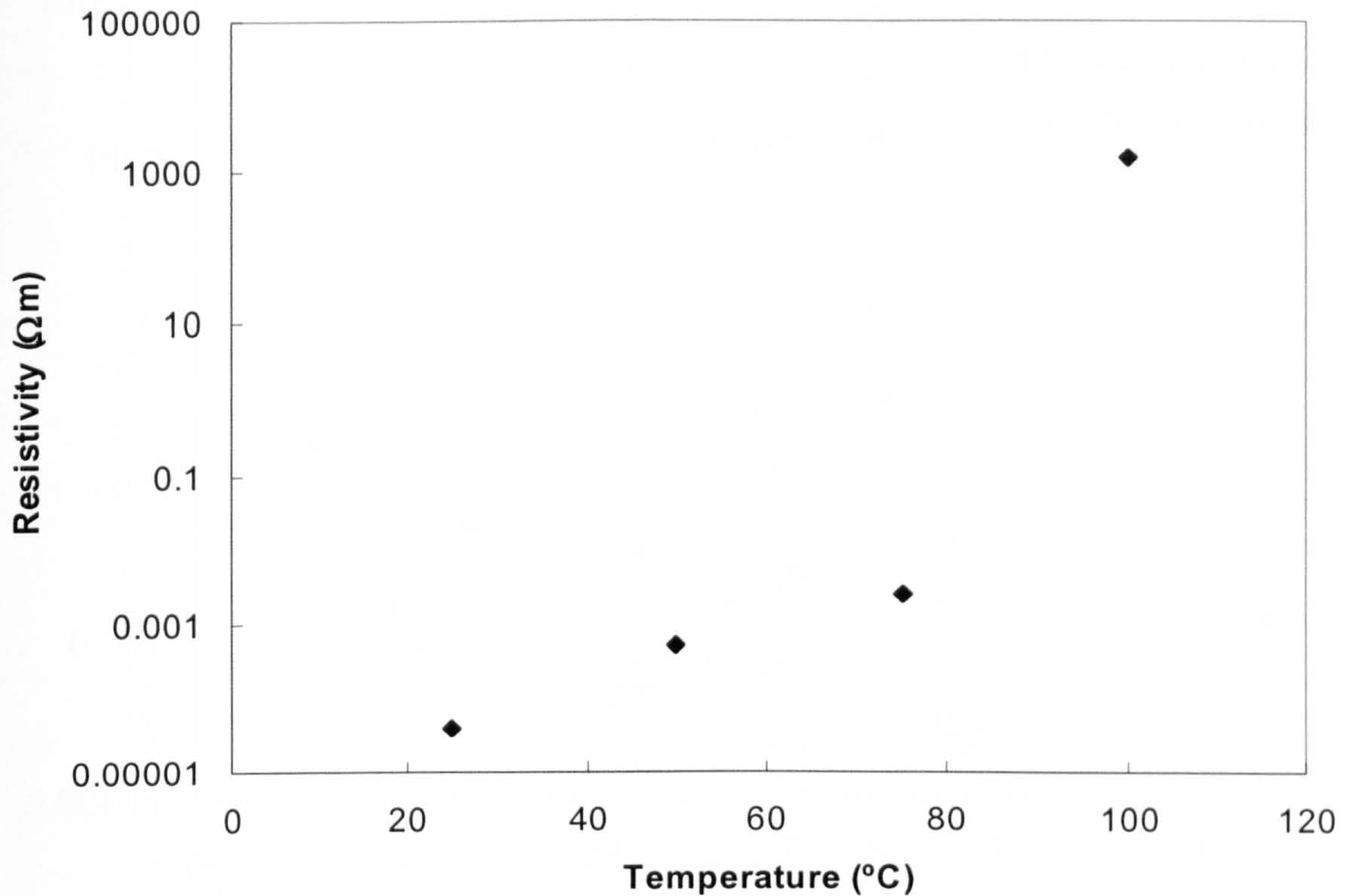


**Figure 5.14.** The effects of substrate temperature on the resistivity of tungsten interconnects deposited using a beam current of 1.5 nA and 200 passes of the electron beam.

Figure 5.14 shows how as the substrate temperature is increased, the resistivity of the deposits also increases. For substrate temperatures up to 75°C the resistivity increases at a constant rate, while for the substrate temperature of 100°C, the deposit is much more resistive. This result suggests that a different chemical reaction occurs for this substrate temperature. In section 4.7 it was also shown that as the substrate temperature for which the deposition was carried out was increased the deposit height decreased. Therefore, the increasing resistivity with increasing substrate temperature may be attributed to the increasing distance that the electrons have to travel between the metal islands in the deposit as the height of the deposits decreases. To examine the effect of the height of the deposits on the resistivity and to determine whether the increased substrate temperature also affects the resistivity deposits or whether the change in resistivity is just due to the changing height, this data is also plotted as a function of deposit height (see Figure 5.15). For comparison the data set for different height deposits produced at room temperature is also given in this figure.

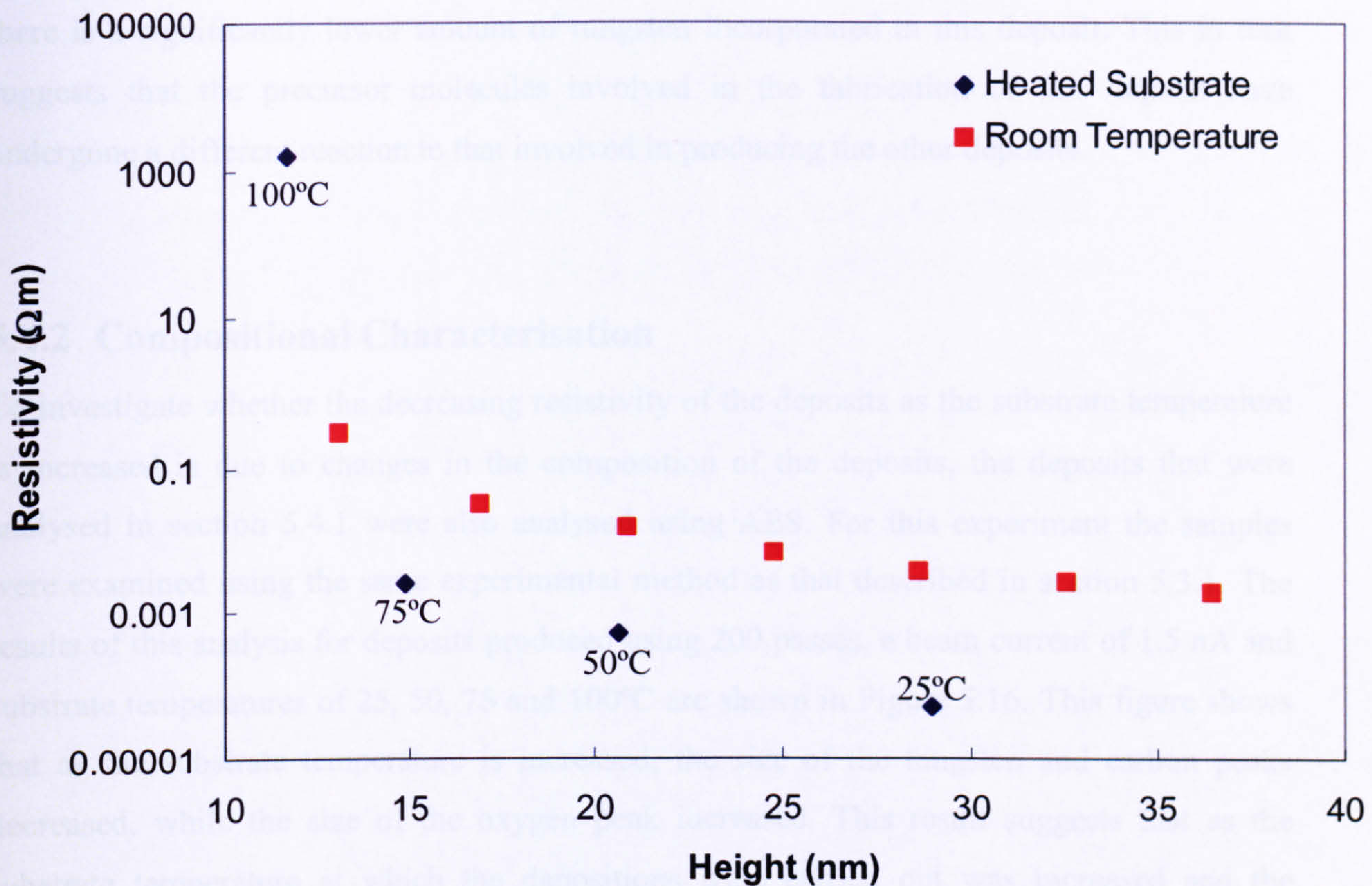


**Figure 5.15.** The effects of different substrate temperatures during the deposition on the resistivity and height of deposits produced using 200 passes and a beam current of 1.5 nA. The effect of different height deposits on the resistivity is also shown for comparison.

Initially, Figure 5.15 shows an unexpected result in that the deposit produced at 25°C has a lower resistivity than other deposits produced at room temperature with the same height. This may be due to the fact that when carrying out the depositions on the heated substrate, a deposit was first made at 100°C and then the temperature of the substrate was decreased for each subsequent deposit down to 25°C. It is well known that in vacuum, convective and radiative loses are very low and so the substrate will take much longer to cool, than it would in air. This means that it is possible that the deposit produced at 25°C was actually deposited at a temperature slightly above this. Therefore, this result along with the resistivity values of deposits produced at 50°C and 75°C shows that the resistivity of a given height deposit can be improved in comparison to the same height deposit produced at room temperature. This result also suggests that more of the undissociated molecules leave the sample surface as the temperature is increased leaving behind only the more stable dissociated molecules. This can result in an increasing metallic content for the deposits, which means that they will have a lower resistivity. The fact that the deposit produced using a substrate temperature of 100°C is much higher than an equivalent height deposit produced at room temperature suggests that

there is a significantly lower amount of tungsten incorporated in this deposit. This in turn suggests that the precursor molecules involved in the fabrication of this deposit have undergone a different reaction to that involved in producing the other deposits.

## 5.4.2 Compositional Characterisation

To investigate whether the decreasing resistivity of the deposits as the substrate temperature is increased is due to changes in the composition of the deposits, the deposits that were analysed in section 5.4.1 were also analysed using AES. For this experiment the samples were examined using the same experimental method as that described in section 5.3.1. The results of this analysis for deposits produced using 200 passes, a beam current of 1.5 nA and substrate temperatures of 25, 50, 75 and 100°C are shown in Figure 5.16. This figure shows that as the substrate temperature is increased, the size of the tungsten and carbon peaks decreased, while the size of the oxygen peak increased. This result suggests that as the substrate temperature at which the depositions were carried out was increased and the mobility of the precursor molecules on the substrate surface also increased, the amount of the precursor molecules that were dissociated decreased.

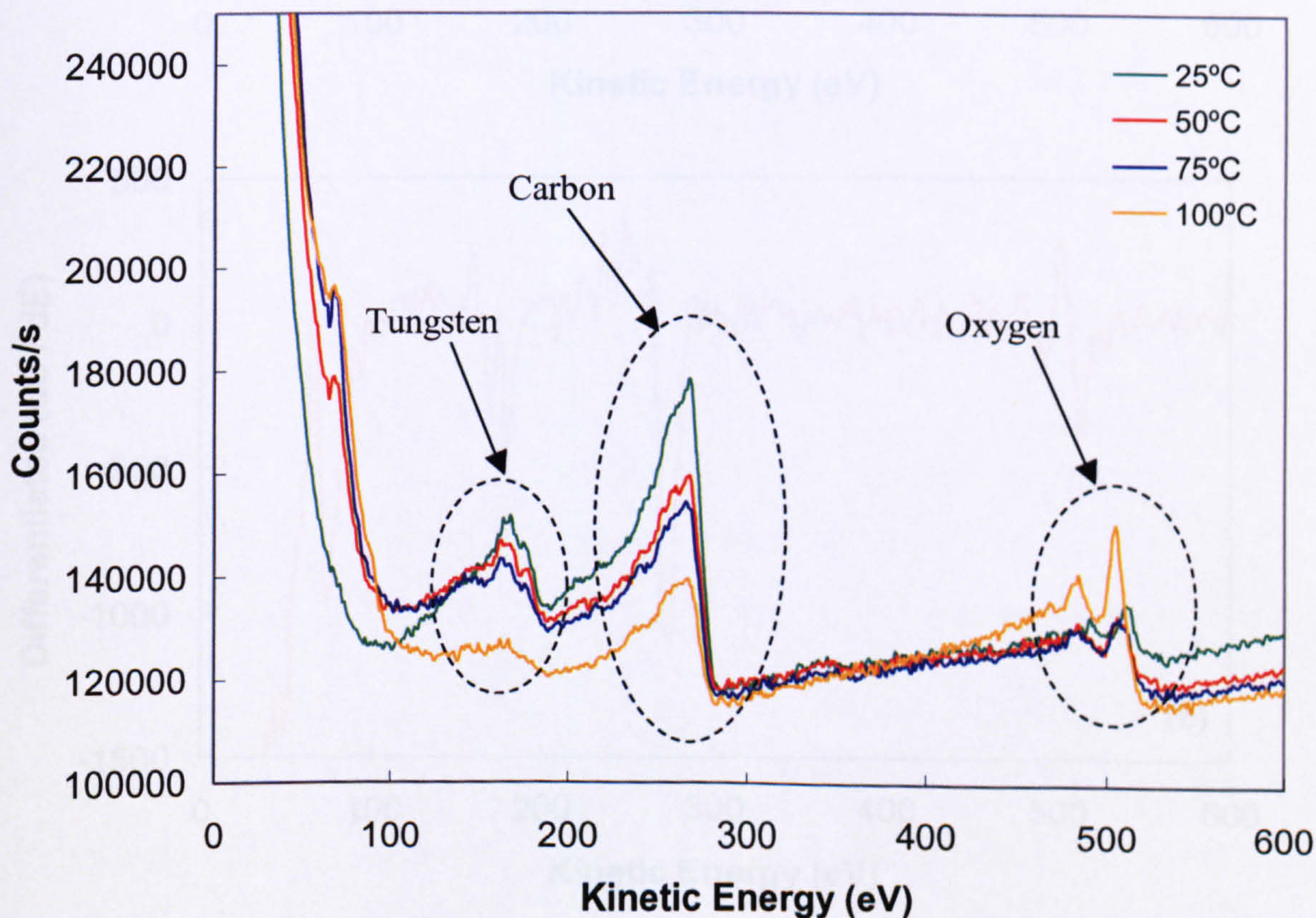


**Figure 5.16.** Analysis of the elemental composition of tungsten deposits produced using an electron beam current of 1.5 nA for substrate temperatures of 25, 50, 75 and 100°C.

In order to understand the effects of changing the substrate temperature on the elemental composition of the deposits more fully and to characterise the data it is necessary to quantify these results by comparing the peak-to-peak height of the intensities for the differential of the Auger spectrum for each of the elements in the deposits. The differential of the data in Figure 5.16 is given for the substrate temperatures 25°C, 50°C, 75°C and 100°C in Figure 5.18 (a), (b), (c) and (d) respectively.

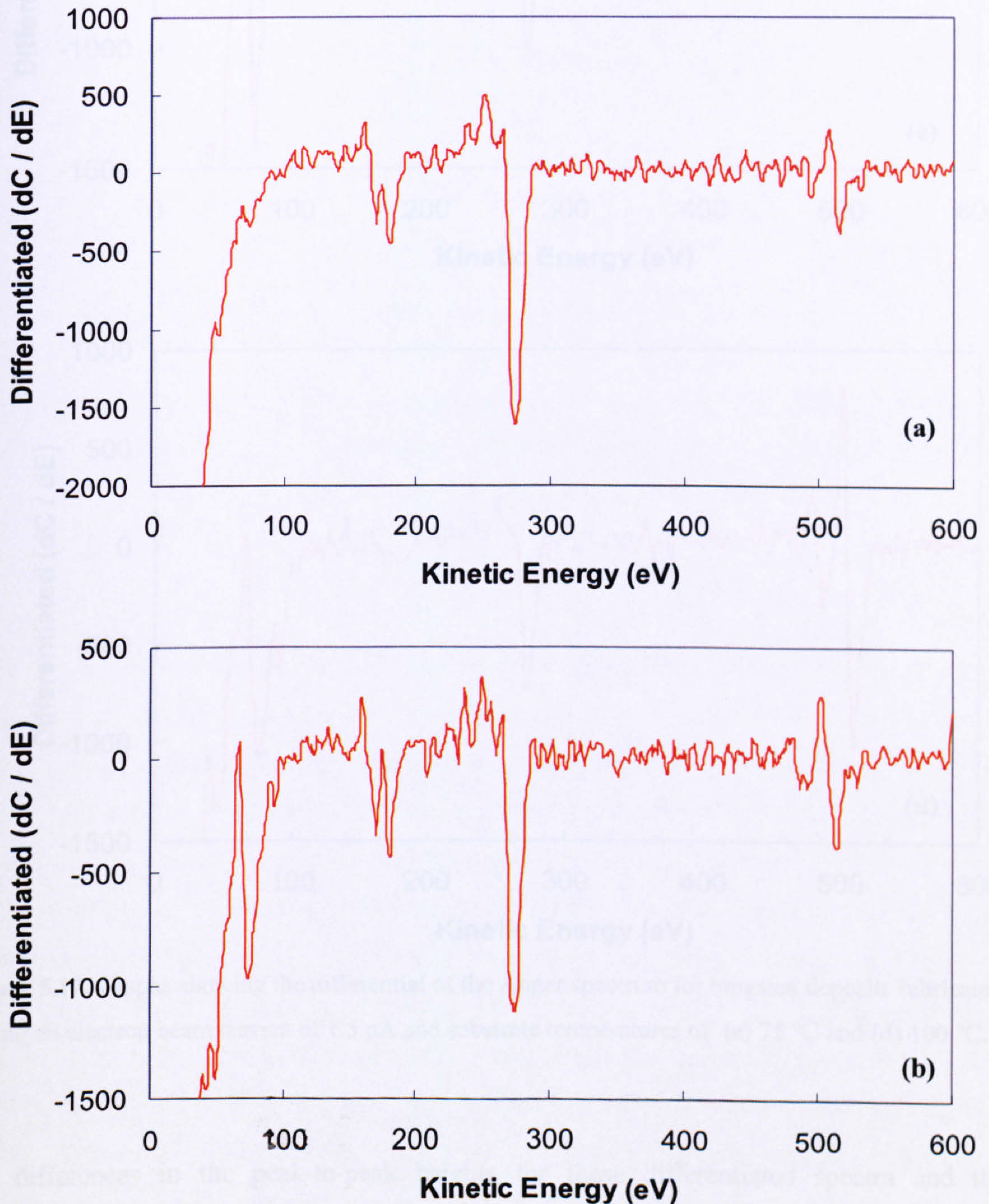


**Figure 5.17.** Graphs showing the differential of the Auger spectrum for tungsten deposits fabricated using an electron beam current of 1.5 nA and substrate temperatures of **(a)** 25 °C, **(b)** 50 °C.

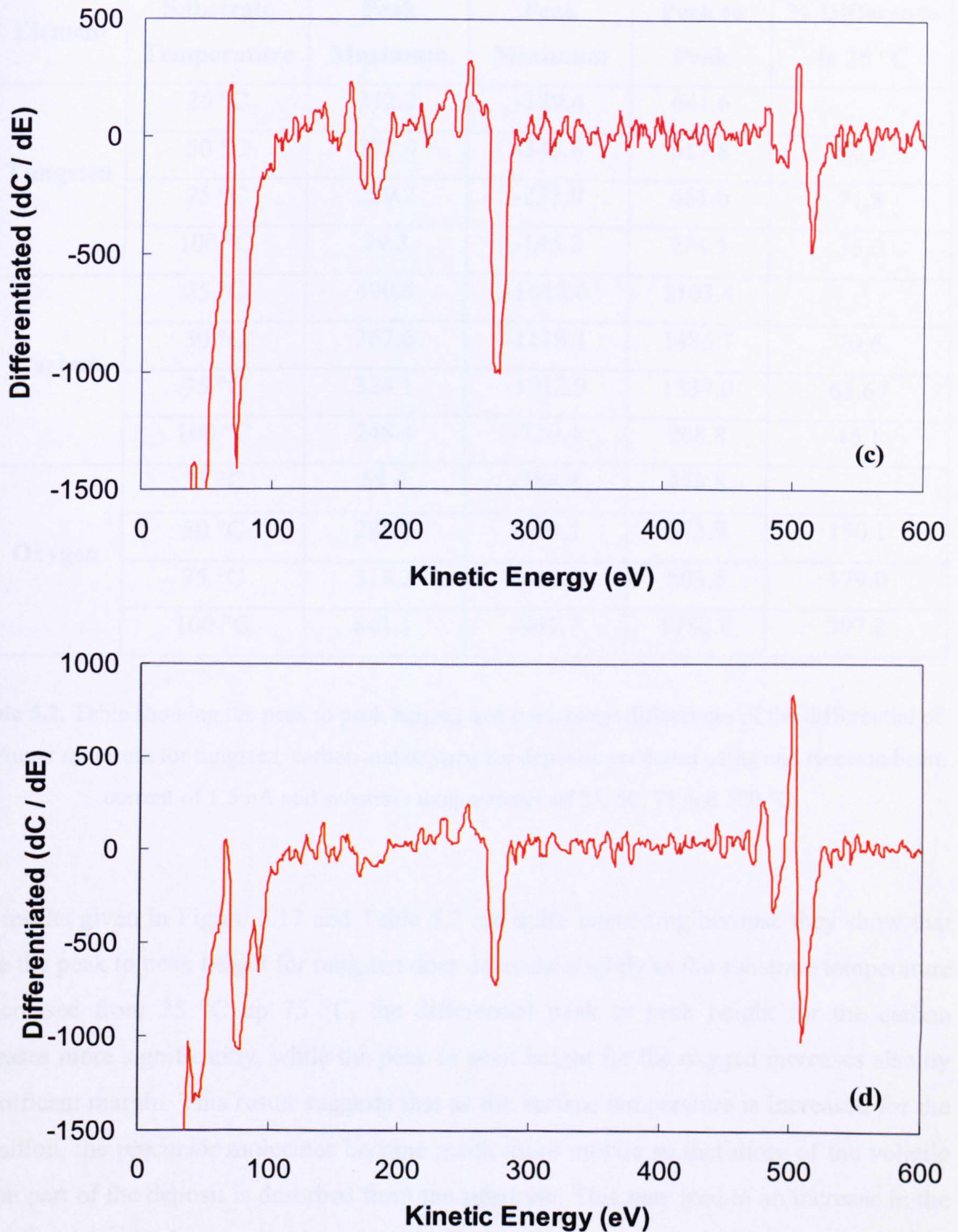


**Figure 5.17.** Graphs showing the differential of the Auger spectrum for tungsten deposits fabricated using an electron beam current of 1.5 nA and substrate temperatures of **(c)** 75 °C and **(d)** 100 °C.

The differences in the peak-to-peak heights for these differentiated spectra and the percentage difference in the intensities with respect to the deposit that was carried out at room temperature are given in Table 5.2.

| Element | Substrate Temperature | Peak Maximum | Peak Minimum | Peak to Peak | % Difference to 25 °C |
|---|---|---|---|---|---|
| Tungsten | 25 °C | 312.2 | -329.4 | 641.6 | |
| | 50 °C | 272.0 | -345.8 | 617.8 | 96.3 |
| | 75 °C | 229.2 | -231.8 | 461.0 | 71.8 |
| | 100 °C | 79.3 | -145.2 | 224.5 | 35.0 |
| Carbon | 25 °C | 490.8 | -1612.6 | 2103.4 | |
| | 50 °C | 367.6 | -1118.1 | 1485.7 | 70.6 |
| | 75 °C | 324.1 | -1012.9 | 1337.0 | 63.67 |
| | 100 °C | 248.4 | -720.4 | 968.8 | 46.1 |
| Oxygen | 25 °C | 64.4 | -384.4 | 448.8 | |
| | 50 °C | 284.7 | -389.2 | 673.9 | 150.1 |
| | 75 °C | 318.2 | -485.4 | 803.5 | 179.0 |
| | 100 °C | 841.1 | -941.7 | 1782.8 | 397.2 |

**Table 5.2.** Table showing the peak to peak heights and percentage differences of the differential of the Auger spectrum for tungsten, carbon and oxygen for deposits produced using and electron beam current of 1.5 nA and substrate temperatures of 25, 50, 75 and 100 °C.

The results given in Figure 5.17 and Table 5.2 are quite interesting because they show that while the peak to peak height for tungsten does decrease slightly as the substrate temperature is increased from 25 °C up 75 °C, the differential peak to peak height for the carbon decreases more significantly, while the peak to peak height for the oxygen increases also by a significant margin. This result suggests that as the surface temperature is increased for the deposition, the precursor molecules become much more mobile so that more of the volatile carbon part of the deposit is desorbed from the substrate. This may lead to an increase in the ratio of metal to carbon in the deposit even though the quantities of both do decrease. As such if the percentage of metal in the deposit has increased then it may also be expected that the metal islands are closer together and that the electrons can tunnel from one metal island to another more easily. This would lead to a decrease in the resistivity of the deposits as was seen in Figure 5.15. The idea that there is an increase in the percentage of metal in the deposit with increasing substrate temperature is in agreement with the experimental results of Weber et al. [1] and Wang et al. [3] In these experiments they found that the metal content in deposits produced from $Me_2Au(tfac)$ and $Pt(PF_3)^4$ increased with temperature.

The fact that when the temperature is increased further to 100 °C, the resistivity of the deposit increases may then be attributed to the fact that at this temperature the amount of tungsten incorporated in the deposit reduces far more significantly than the reduction in carbon. It may also be partly due to the fact that at this temperature a much larger increase in the intensity of the Auger signal for oxygen was seen. This result suggests that when the substrate is heated to this high temperature, the physical reaction that is occurring has changed and as such the deposit may have a different chemistry.

### 5.4.3 Discussion

The work undertaken in this section has shown that heating the substrate to temperatures in the range of 25 – 75°C while depositing EBID nanowires is a suitable method of producing interconnects with a lower resistivity from the precursor $W(CO)_6$. This may be attributed to the precursor molecules having increased mobility at higher temperatures such that only the dissociated molecules remain on the substrate surface. This result is particularly attractive for electronic applications, where the resistivity of the deposited interconnects is crucial. However, as the temperature of the substrate is increased, the deposition rate also decreases and so to achieve a reasonable height deposit the number of passes made by the electron beam or the total electron dose used to produce the deposit must also be increased. This has the downside that it requires increasing amounts of time to produce the interconnects, which is undesirable when making EBID suitable as a mainstream nanofabrication technique.

Another issue with depositing structures at increased substrate temperatures is that, as the sample is heated thermal drift of the sample becomes an increasing problem. This can be minimised by ensuring that the temperature of the substrate has saturated before commencing the set-up of the electron beam and subsequent deposition, however it will still result in a decreased resolution of the process that may be critical in certain applications. Within this work it has also been shown that using higher substrate temperatures in the range of 100°C causes the resistivity, deposited height and the metallic composition of the deposits to be lower than for deposits produced at room temperature. This result suggests that there must be an optimal temperature, when the residence time of the precursor molecules is long enough for the majority of the molecules to be dissociated such that a reasonable growth rate and resistivity can be achieved, but short enough that the volatile parts of the deposits are desorbed before they are covered by a further dissociated layer of molecules.

## 5.5 Measurement Accuracy and Reproducibility

In an attempt to ensure that the results gained here are reproducible as possible, before carrying out any of the depositions, the same optimisation procedure was always carried out. This included following the procedure that was carried out for the deposits produced for the geometrical and structural characterisation of EBID tungsten interconnects and was described in section 4.8. However, even after carrying out all of these steps, it was found that there was still some variation in the deposited size and resistivity of the final deposited structures. This may be attributed to variations in the vacuum, the electron beam optics and the gas flux at the sample surface.

## 5.6 Conclusions

This section has shown that for a constant electron beam current, the resistivity of the deposits initially decreases rapidly before reaching a constant value as the height or the total dose used to produce the deposits was increased. This has been attributed to the deposits transforming from a discontinuous structure to a more continuous one. It has also been found that the resistivity of the tungsten deposits decreases as the electron beam current is increased. This is due to the increasing metallic content of the deposits as shown by AES, which results from an increasing number of electrons being involved in the deposition process such that a greater number of the precursor molecules can be dissociated.

Within this chapter some of the system variables, which can also cause significant variations in the resistivity of EBID deposits have been investigated. In particular, it has been shown that as the precursor ages, the gas flux and hence the deposition rate decreases. However, the resistivity for a given height of deposit remains constant, which means that the composition of the deposited material remains constant. This result suggests that when describing the parameters used to produce EBID interconnects it is necessary to include some kind of reference to the gas flux. The effect of changing the electron source was also investigated and it was found that it produced deposits with quite different characteristics. Both of these results highlight how difficult it is for the people researching EBID to be able to accurately characterise the process and produce results, which may be accurately reproduced by other groups. As such better control of the electron beam and the gas flux of the precursor must be gained in order to be able to produce reproducible deposits in different systems.

Within this section, the use of a heated substrate during the depositions was also investigated to determine whether it could be used to improve the resistivity of the deposited material. The results of this work showed that heating the substrate to temperatures in the range of 25°C to 75°C during the deposition process produced deposits with a lower resistivity, which is desirable for electronic applications. However, whilst this does improve the resistivity of the deposited wires, it also involves more a complicated process, which is undesirable as it increases the cost, complexity and fabrication time of EBID devices.

## 5.7 References

[1] M. Weber, H. W. P. Koops, M. Rudolph and J. Kretz, , J. Vac. Sci. Technol. B **13**, 1364 (1995).

[2] H. W. P. Koops, J. Kretz, M. Rudolph, M. Weber, G. Dahm and K. L. Lee, Jpn. J. Appl. Phys. **33**, 7099 (1994).

[3] S. Wang, Y.-M. Sun, Q. Wang and J. M. White, J. Vac. Sci. Technol. B **22**, 1803 (2004).

# CHAPTER SIX

# 6 High Bias Electrical Characterisation of Electron Beam Deposited Tungsten Interconnects

## 6.1 Introduction

For the electrical characterisation that was carried out in chapter five, current limits of less than 10 μA were set in order to avoid premature destruction of the EBID tungsten wires. However, in order for EBID to be accepted as a mainstream fabrication technique for the production of interconnects, it is necessary to also gain an understanding of the current carrying capacity of the wires and characterise their limits. As such this chapter shall focus on the effects of exposing the wires to high currents in order to determine their current carrying capability and breakdown characteristics. As such it is shown that when the deposits are exposed to currents in excess of 100 μA, the resistance decreases with increasing current limit and multiple cycling of the voltage. Structural analysis of these deposits using a TEM has been undertaken to gain an understanding of this behaviour and shows that ohmic heating within the deposits induces high enough temperatures within the structures themselves to be able to cause the structure of the material to change permanently. Electrical measurements of the breakdown of these structures for high current limits has also been undertaken and shows that before the actual breaking of the structure, the resistance increases as the conduction path is reduced. In an attempt to prove that these changes are due to ohmic heating of the deposits, the effects of annealing on the resistance and structure of the deposits is also examined and it is shown that by annealing at temperatures of ~350°C, the resistivity of deposits produced with 100 passes of the electron beam and an electron beam current of 1.5 nA can be improved by two orders of magnitude.

## 6.2 Experimental Method

The depositions were carried out using the FEI Dual Beam FIB described in section 3.2.3 and $W(CO)_6$ as a precursor. As this work builds upon the work undertaken in chapters four and five, the same deposition conditions have been used to produce the deposits to be characterised. To allow for these deposits to be electrically characterised, rectangular deposits were made so as to bridge either gold or platinum contact pads onto silicon substrates with a 300 nm thick oxide layer that had been prepatterned using conventional UV lithography. To allow for several deposits to also be examined in a TEM after their electrical characterisation, a number deposits were also produced on standard 100 nm thick silicon nitride TEM membranes with a 3 $mm^2$ silicon frame and a 500 $\mu m^2$ $Si_3N_4$ window. These membranes were prepatterned with ion beam deposited tungsten contact pads for the electrical characterisation. This allowed for the samples to be transferred straight into the Philips CM 200 Transmission Electron Microscope described in section 3.3.1 for structural analysis after the electrical characterisation.

Once the deposits had been made the samples were transferred into the FEI ESEM that was described in section 3.2.2 that had been fitted with the Attocube manipulation system described in section 3.6.2. This manipulation system allowed for two electrochemically etched tungsten probes to be brought into contact with the contact pads and for the electrical characterisation to be carried out using the Keithley 4200 Semiconductor Characterisation System described in section 3.8. For the post deposition annealing of several deposits, the Omicron Nanotechnology Resistive Heater described in section 3.9 was also installed into the ESEM to allow for simultaneous annealing and electrical characterisation.

## 6.3 High Bias Electrical Measurements

This section shall investigate the stability of the EBID tungsten interconnects when they are exposed to high current biases. In particular, it shall examine the effects of increasing the current that the deposits are exposed to on the electrical and structural properties of the deposits by running multiple voltage cycles. For the deposits that are analysed in the following sections, electron source two with an electron beam current of 2.1 nA and a precursor that had been used for less than 20 hours was used, unless otherwise stated.

### 6.3.1 Electrical Characterisation

For this investigation, deposits were produced using a range of different total electron doses as well as a width of 200 nm and length of 8 μm, so that they bridged gold contact pads and leads with an ~5.5 μm separation. The deposits were then characterised in the FEI Quanta 200 ESEM using the Attocube manipulation system and the Keithley 4200 Semiconductor Characterisation System. The set-up of these deposits is the same as that described in section 5.3.2 and shown in Figure 5.8. To characterise the current carrying capability of each of the deposits a sequence of current-voltage cycles were run by increasing the voltage from 0 V up to a fixed positive voltage, then decreasing the voltage to the equivalent negative voltage before increasing it back to 0 V. The current was measured for each voltage point and plotted as a function of voltage. A current limit, which was steadily increased for successive voltage cycles, was also set for each voltage sweeps. Initially, as described in section 5.3.2, the current-voltage sweeps were found to be linear and symmetrical with respect to zero voltage. Repeated voltage cycles showed no variation in the electrical characteristics.

As the current limit was increased towards 100 μA, the I-V characteristics for all of the deposits investigated gradually became non-linear but remained symmetric with respect to zero voltage and showed no hysteresis. Repeated voltage cycles at these current limits also showed that there was no variation in the electrical characteristics. An example of this type of I-V characteristic, which was taken using a current limit of 75 μA for a deposit produced using 25 passes of the electron beam, is shown in Figure 6.1. This onset of non-linearity in the I-V characteristics may be attributed to heating within the deposits themselves, which is caused by the high resistivity and non-crystalline structure of the deposits.

When the current limit for the voltage cycles was increased further to values in excess of 100 μA, the I-V characteristics showed some hysteresis. This hysteresis was particularly significant in the first voltage cycle after the current limit was increased. Repeated voltage cycles at the same current limit then caused the amount of hysteresis to decrease and the resistance to improve until the I-V characteristics regained a similar shape to that shown in Figure 6.1. An example of the I-V characteristics is shown in Figure 6.2. This data was taken for the same deposit as the one shown in Figure 6.1 but with a current limit of 400 μA. The change in the resistance that was seen in these measurements may be attributed to structural changes in the deposit, which were induced by the heating of the deposit, while the non-linearity may be attributed to the heating itself.

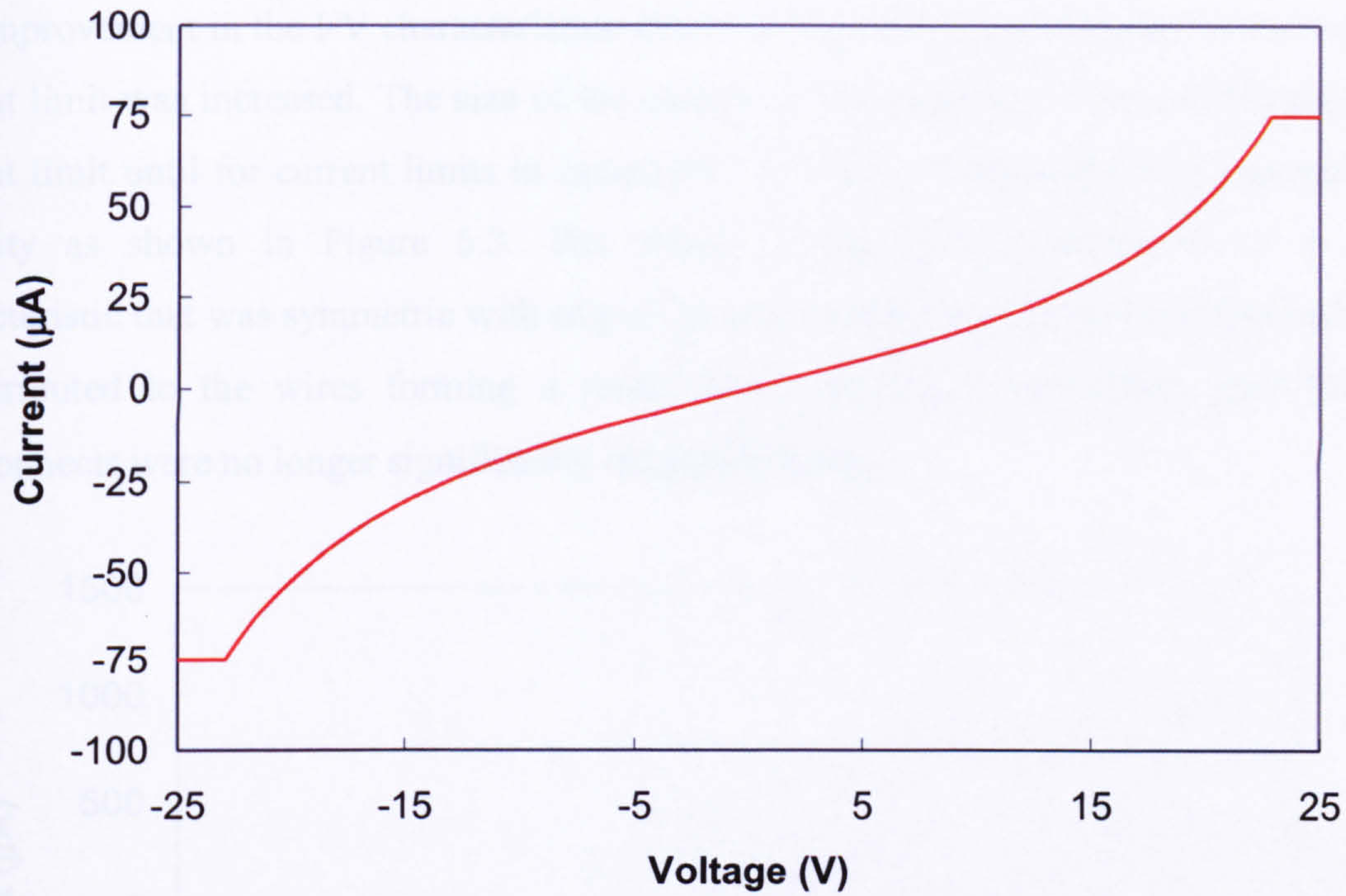


**Figure 6.1.** I-V characteristic of a tungsten deposit taken with a current limit of 75 μA showing the onset of non-linearity in the I-V characteristics. The deposit was produced using electron source two, an electron beam current of 1.5 nA and 25 passes.

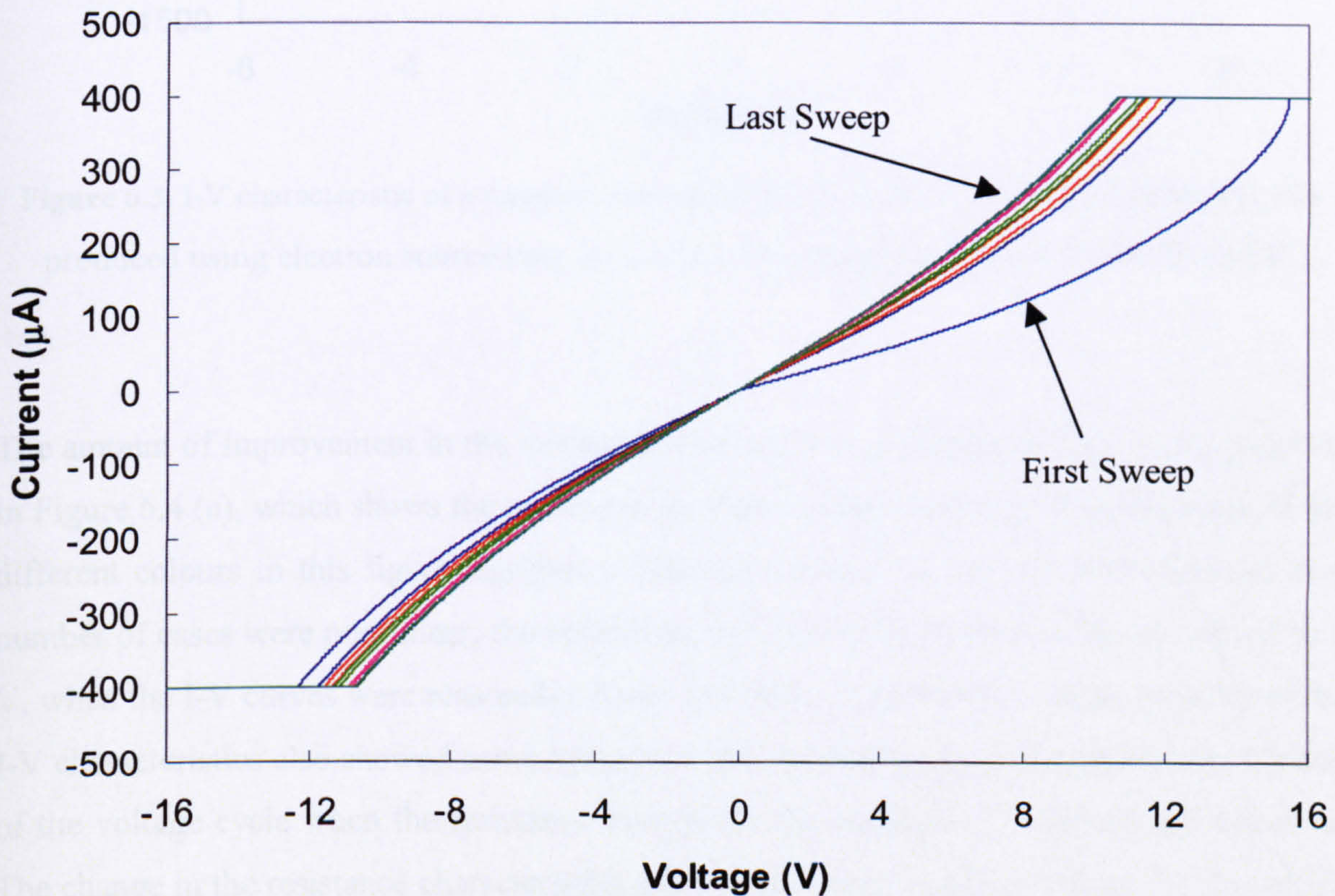


**Figure 6.2.** I-V characteristics of a tungsten deposit taken with a current limit of 400 μA showing hysteresis and non-linearity in the I-V characteristics. The I-V characteristics also show how the resistivity of the deposit improves for successive voltage cycles.

The improvement in the I-V characteristics shown in Figure 6.2 was observed every time the current limit was increased. The size of the change in the resistance decreased for each new current limit until for current limits in excess of 1 mA the I-V characteristics regained their linearity as shown in Figure 6.3. The return of the I-V characteristics to a linear characteristic that was symmetric with respect to zero voltage and showed no hysteresis may be attributed to the wires forming a more robust metallic cross-section such that the interconnects were no longer significantly ohmically heated.

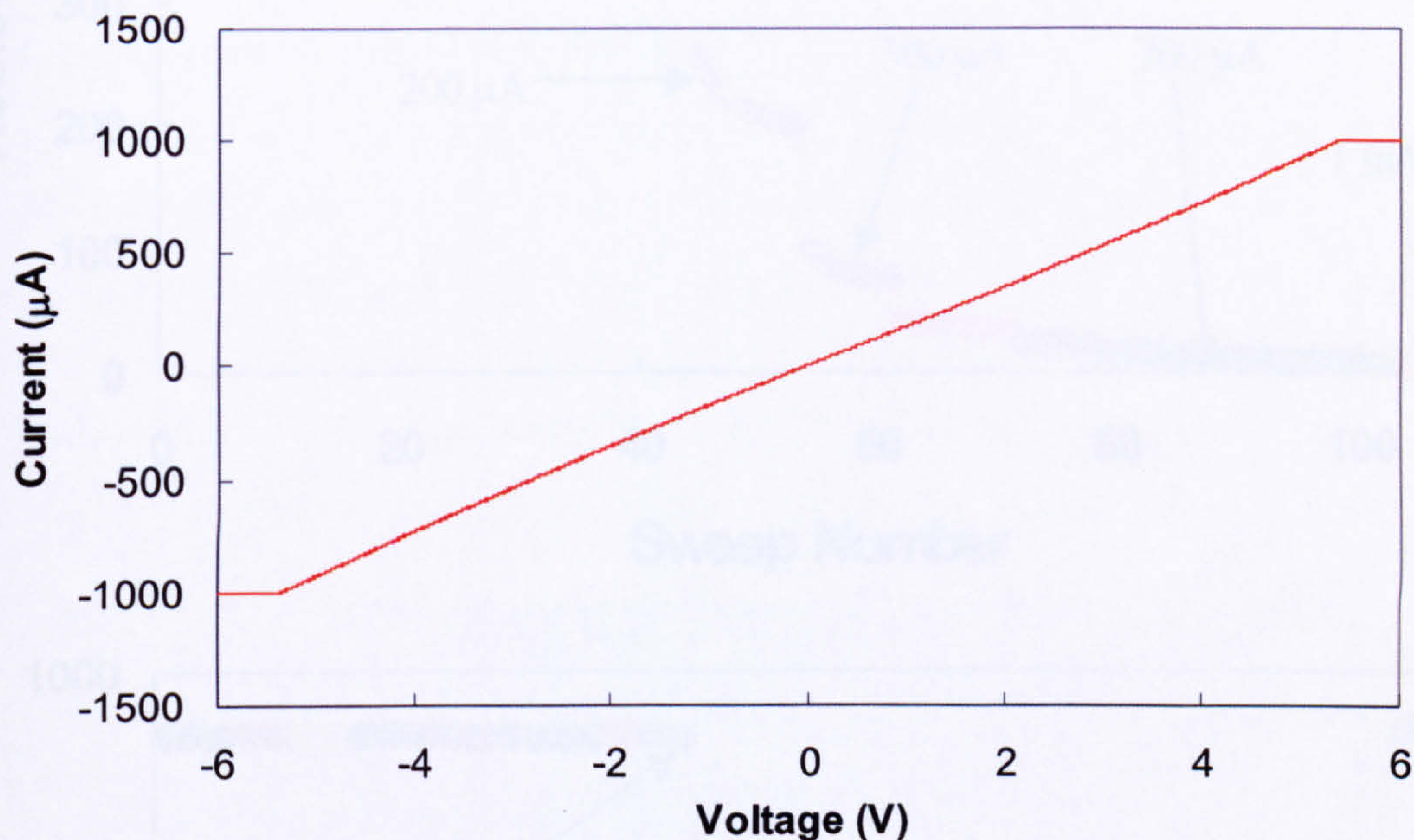


**Figure 6.3.** I-V characteristic of a tungsten deposit for a current limit of 1 mA. The deposit was produced using electron source two, an electron beam current of 1.5 nA and 25 passes.

The amount of improvement in the resistance that has been presented in this section is given in Figure 6.4 (a), which shows the resistance for each voltage cycle that was run. Each of the different colours in this figure signifies a different current. As the I-V characteristics in a number of cases were non-linear, the resistance was calculated by measuring the current at 3 V, when the I-V curves were reasonably linear for each of the voltage cycles. As some of the I-V characteristics also showed some hysteresis, the resistance was also calculated at the end of the voltage cycle when the resistance change for the particular I-V sweep had occurred. The change in the resistance characteristics can be seen more clearly in Figure 6.4 (b), which shows the logarithm of the resistance. This figure also shows how for the highest current limits there is some variation in the resistance. This may be due to some instability in the structure of the deposit.

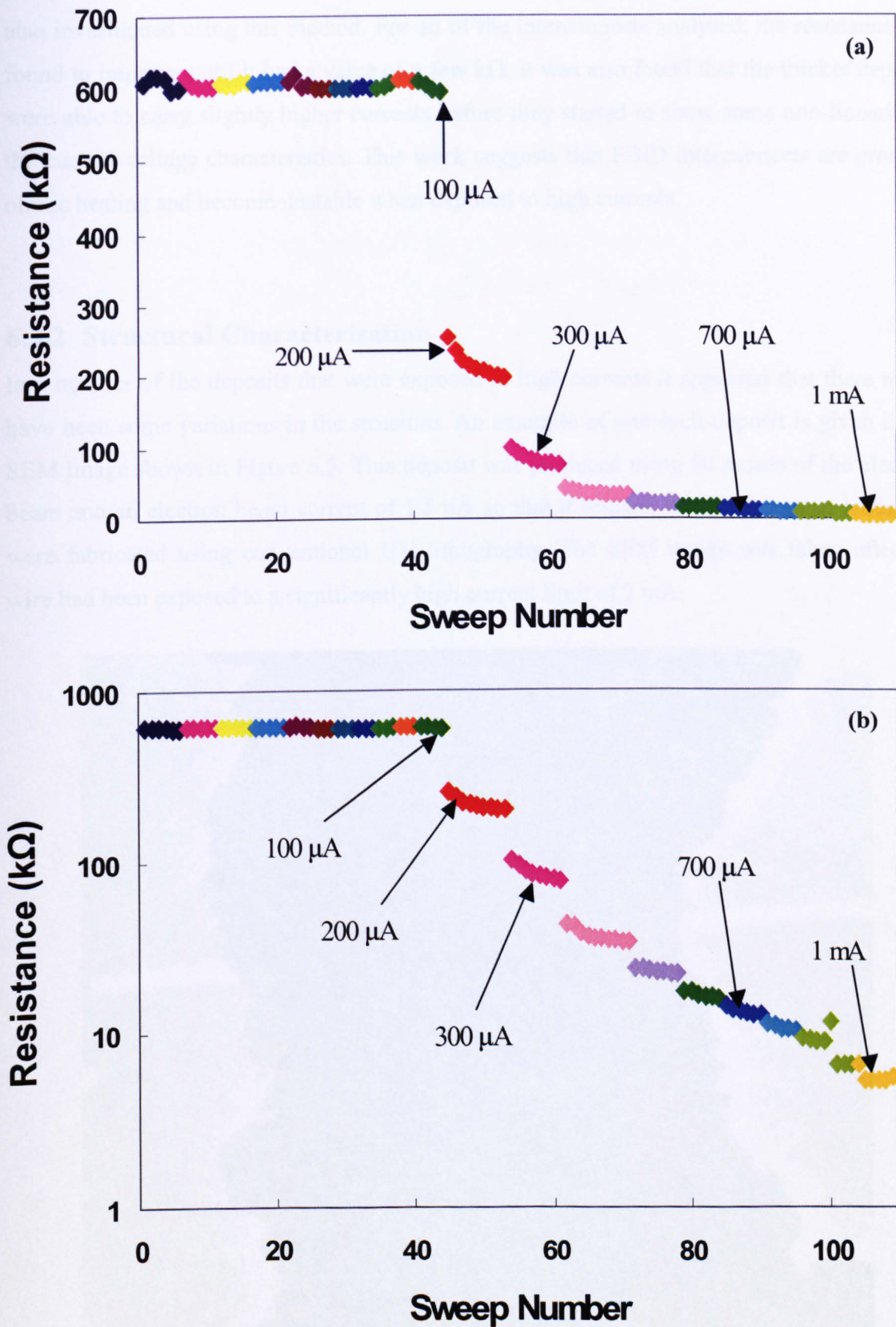


**Figure 6.4.** **(a)** Resistance variation and **(b)** logarithm of the resistance variation for a tungsten wire produced using electron source two, an electron beam current of 1.5 nA and 25 passes.

The effects of high currents on the resistance of a range of different height deposits were also investigated using this method. For all of the interconnects analysed, the resistance was found to improve until it had a value of a few kΩ. It was also found that the thicker deposits were able to carry slightly higher currents before they started to show some non-linearity in the current-voltage characteristics. This work suggests that EBID interconnects are prone to ohmic heating and become unstable when exposed to high currents.

### 6.3.2 Structural Characterisation

In a number of the deposits that were exposed to high currents it appeared that there might have been some variations in the structure. An example of one such deposit is given in the SEM image shown in Figure 6.5. This deposit was produced using 50 passes of the electron beam and an electron beam current of 1.5 nA so that it bridged two gold contact leads that were fabricated using conventional UV lithography. The SEM image was taken after the wire had been exposed to a significantly high current limit of 2 mA.

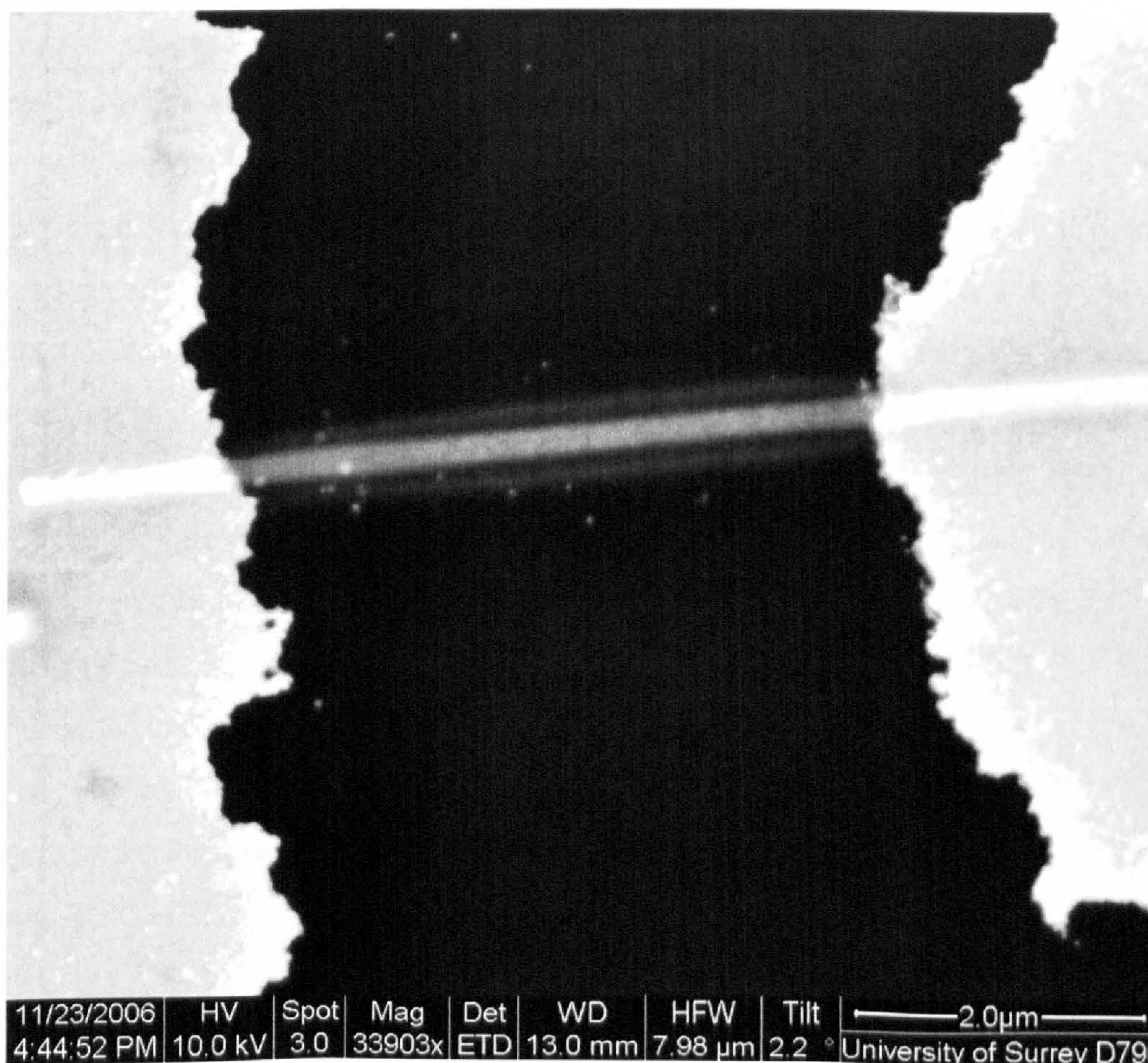


**Figure 6.5.** SEM image of a tungsten wire that was deposited using an electron beam current of 1.5 nA and 50 passes of the electron beam that had been exposed to a current of 2 mA.

While it is not possible to see a significant change in the structure of the deposit shown in Figure 6.5, it does appear that along the length of the wire, the structure of the deposit has changed from being smooth to being made up of a series of small particle like structures. These particles also appear brighter in the image than the rest of the deposit, which suggests that the particles have a higher metallic content than the rest of the deposited structure.

In order to determine whether the changes seen in the resistance of the deposits at high currents and in the SEM image shown in Figure 6.5 was indeed due to structural changes, it is necessary to analyse the structure of one of these deposits using a TEM. As the silicon substrates, which have been used so far for the electrical characterisations are not suitable for TEM analysis, the experimental work carried out in section 6.3.1 was repeated for a deposit that was made on a TEM compatible silicon nitride membrane. The use of this substrate also has the benefit that it can be imaged using a STEM detector within the ESEM. This allows for more structural details to be seen than would normally be possible using the SEM in a standard imaging mode.

To allow for electrical measurements to be undertaken on a deposit fabricated on this substrate two contact pads and leads were fabricated using ion beam deposited tungsten so that the pads were on the membrane frame and the leads ran onto the membrane window. Ion beam deposition has a much higher deposition rate than electron beam deposition and produces structures with a lower resistivity and so the use of this deposition method allowed for large contact pads with a reasonable resistivity to be produced. An electron beam deposited tungsten wire was then fabricated between the contact leads using an electron beam current of 1.5 nA and 100 passes of the electron beam. Figure 6.6 (a) shows an SEM image of the overall device set up, while Figure 6.6 (b) closer SEM image of the electron beam deposited wire connected to ion beam deposited contact leads. This image also shows how the ion beam deposited material had a much more significant height than the electron beam deposited material. In both of these figures the presence of a second electron beam deposited tungsten wire can also be seen. This wire was fabricated close to the connected wire to allow for the structure of a characterised wire to be compared to an as-deposited wire during the TEM analysis.

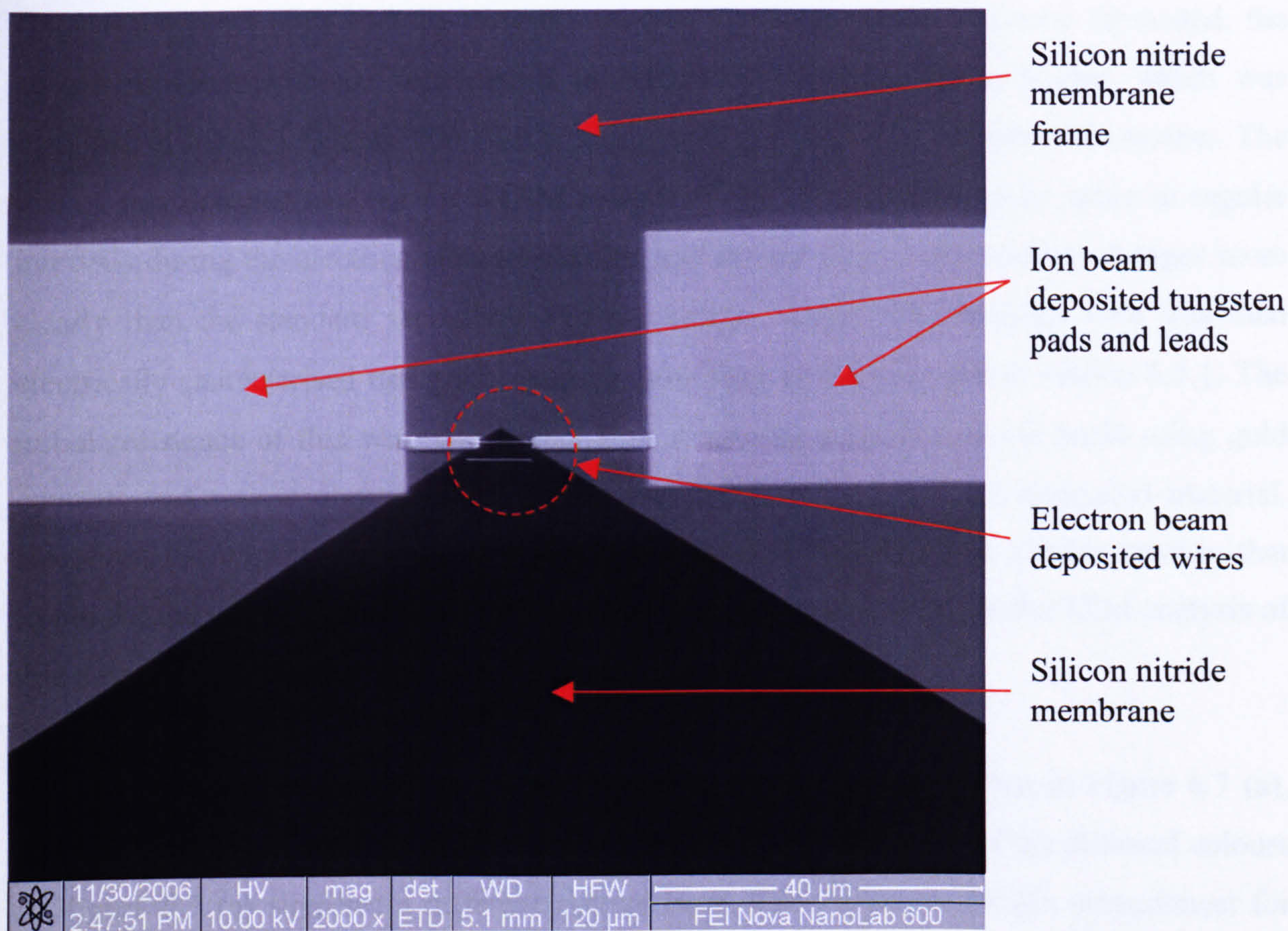


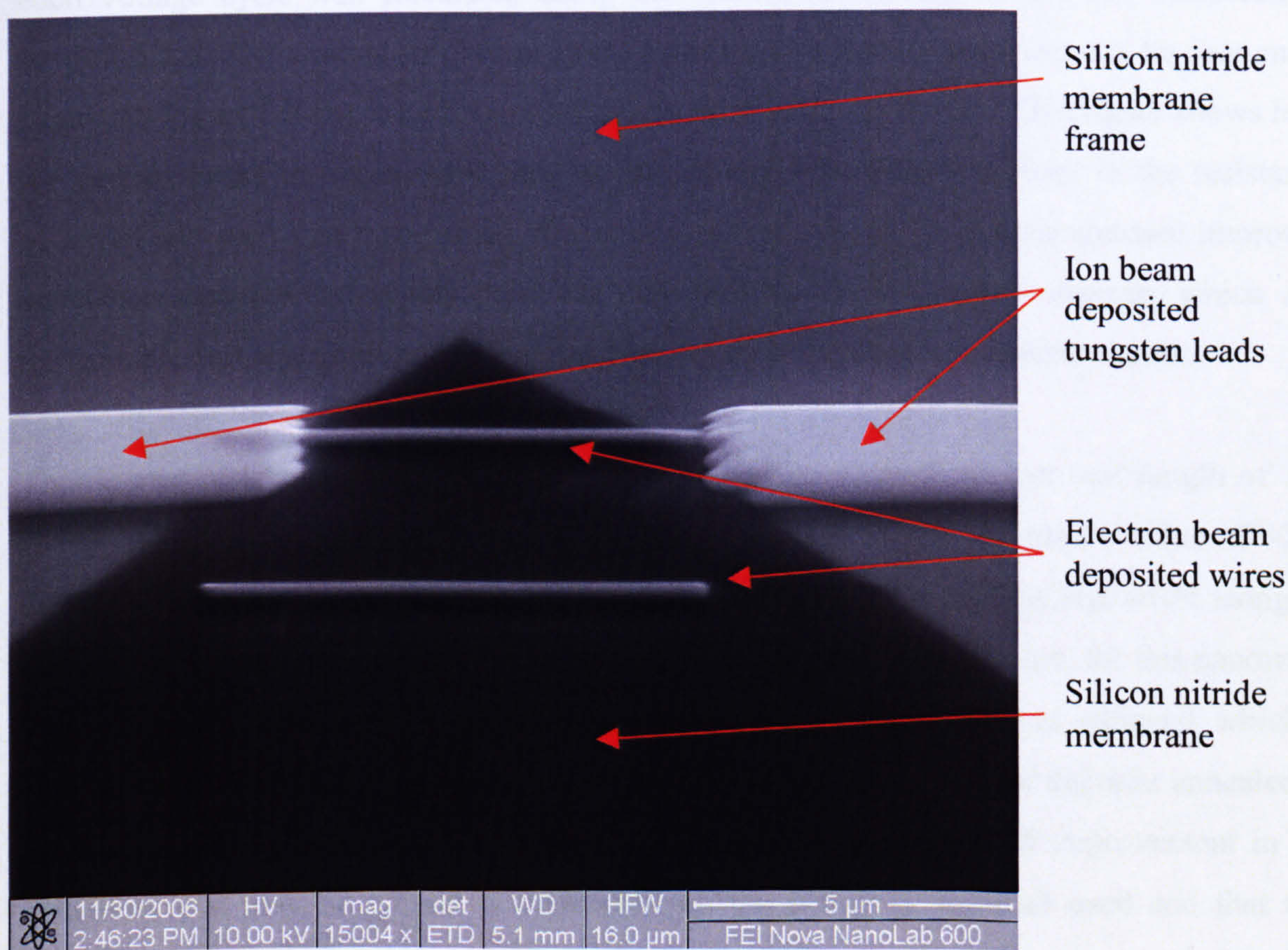


**Figure 6.6. (a)** SEM image of the set up of a tungsten wire and contact pads on a silicon nitride membrane. **(b)** Closer SEM image of an EBID tungsten wire contacted to ion beam deposited leads.

Once the contact pads and the tungsten wire to be characterised had been fabricated, the silicon nitride membrane was placed in the STEM detector device holder, which was installed in the FEI Quanta 200 ESEM along with the Attocube manipulation system. The use of this detector enables for STEM images of the interconnects to be taken at regular intervals during the electrical characterisation and should show any structural changes more clearly than the standard secondary electron images would. The tungsten wire was then electrically characterised using the same methodology as the one used in section 6.3.1. The initial resistance of this wire was higher than it was for a similar device made using gold contacts and was attributed to the higher resistivity of the ion beam deposited material. However, the improvement in the resistance of the device followed a similar trend to that found for the other devices and so it is assumed that it is suitable to use the TEM analysis of this device to explain the structural changes for all of the deposits.

The amount of improvement in the resistance of this nanowire is given in Figure 6.7 (a), which shows the resistance for each voltage cycle that was run. Each of the different colours in Figure 6.7 (a) signifies a different current limit. The resistance of this interconnect for each voltage cycle was calculated using the same methodology as the one described in section 6.3.1. The amount of change in the resistance of this interconnect can be seen more clearly in Figure 6.7 (b), which shows the logarithm of the resistance. This figure shows how for current limits in excess of 4 mA, no further significant improvement in the resistance occurred and such that it remained almost constant at 1.1 kΩ. This more constant improved resistance suggests that at this point the nanowire had formed a new structure which was more stable and was unaffected by ohmic heating during further I-V measurements.

This lowest resistance value of 1.1 kΩ is equivalent to a resistance per unit length of 172 Ω/μm, which is comparable to that of Gopal et al. [2] who also reported a value of ~200 Ω/μm for a platinum interconnect deposited from the precursor $(CH_3)_3CH_3C_5H_4Pt$ using an electron beam energy of 10 keV and a beam current of 2 nA. Furthermore, for this nanowire, an overall improvement in the resistivity of two orders of magnitude was achieved, which is similar to the amount of improvement gained by Botman et al. [12] for deposits annealed in a pure oxygen environment. These results suggest that the amount of improvement in the resistivity that may be gained is dependent on the precursor material used and that this method is a suitable alternative to improving the resistivity of EBID interconnects when it is undesirable to anneal the whole sample.

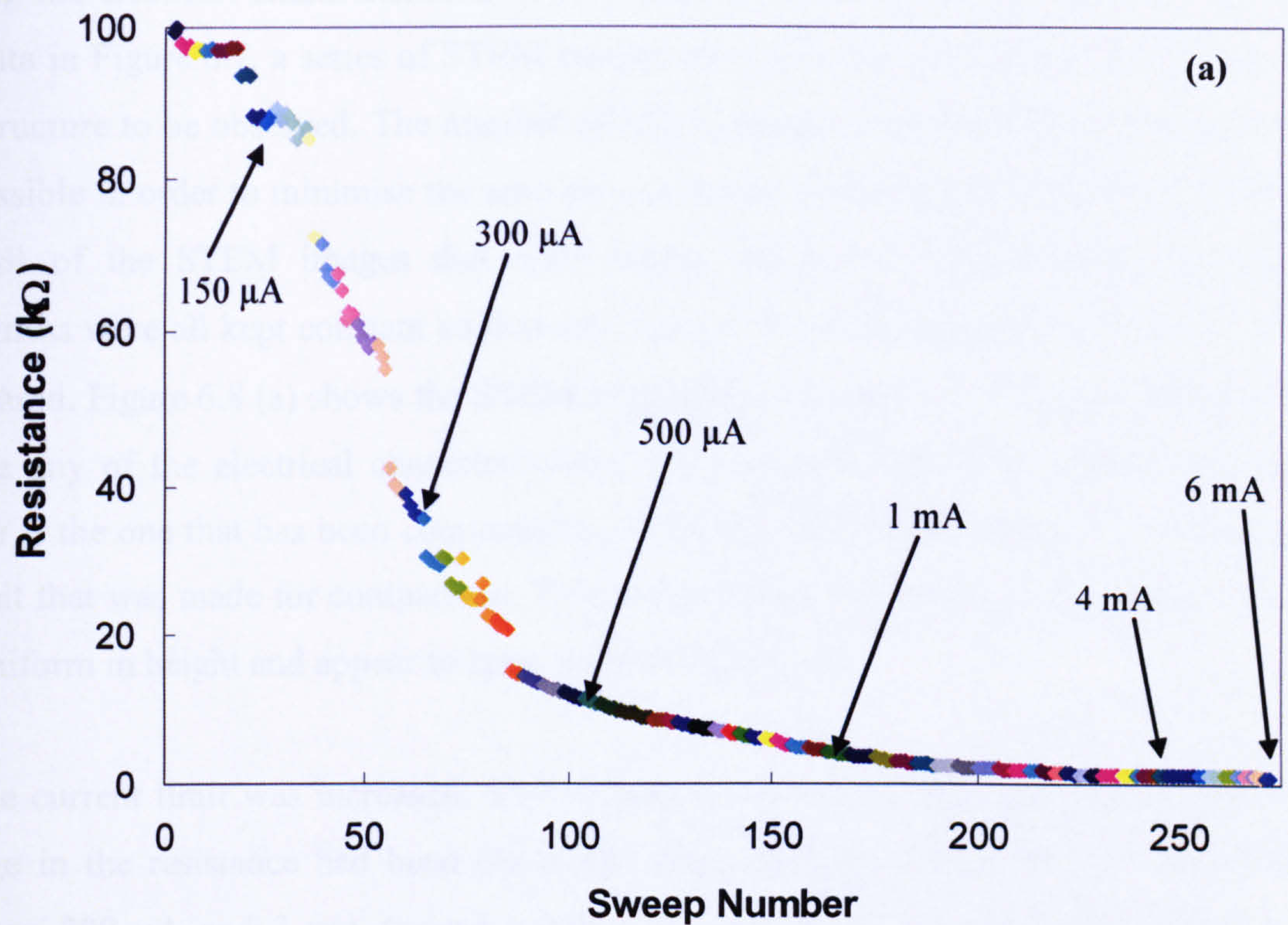


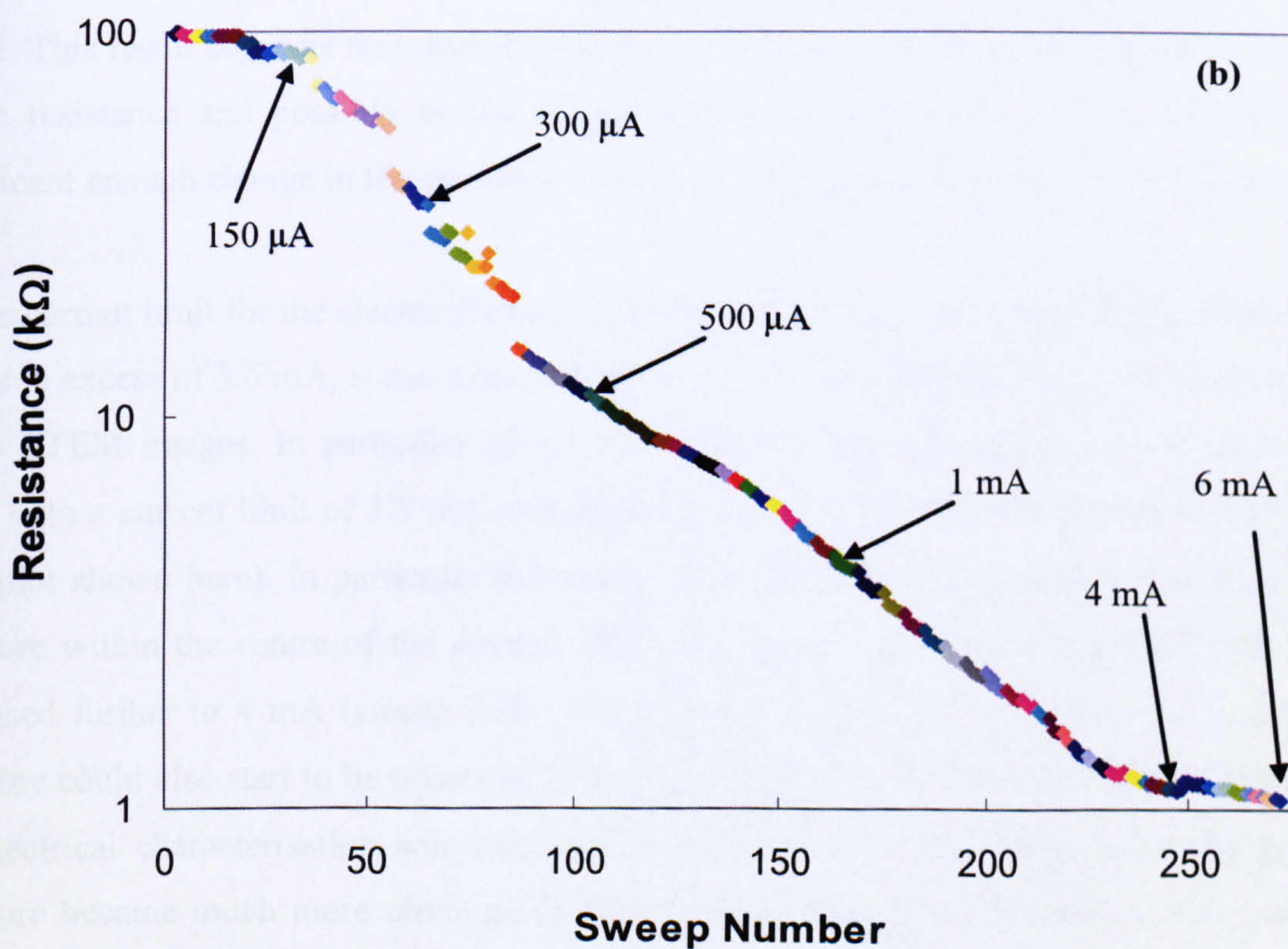


**Figure 6.7. (a)** Resistance variation and **(b)** logarithm of the resistance variation for a tungsten deposit produced using electron source two, an electron beam current of 1.5 nA and 100 passes on a 100 nm thick silicon nitride membrane.

During the electrical characterisation of the tungsten interconnect that was used to produce the data in Figure 6.7, a series of STEM images were also taken to allow for any changes in the structure to be observed. The number of STEM images that were taken was kept as low as possible in order to minimise the amount of electron beam exposure that the deposit saw. For all of the STEM images that were taken, the focus, magnification, contrast and brightness were all kept constant so that any changes in the images and the deposit could be compared. Figure 6.8 (a) shows the STEM image that was taken of the tungsten interconnect before any of the electrical characterisation. The tungsten deposit on the left side of the image is the one that has been connected to, while the right hand deposit is an unconnected deposit that was made for comparison. This image shows how both of the tungsten deposits are uniform in height and appear to have a smooth structure.

As the current limit was increased, STEM images were taken after each time a significant change in the resistance had been observed. These images showed that for current limits between 200 µA and 3 mA (sweep number 230) there was no significant change in the structure of the deposit, which can be determined from changes in the grey scale of the image. This result suggests that even though there has been some kind of permanent change in the resistance and possibly in the microstructure of the deposit, it has not caused a significant enough change in the structure to be observed using STEM within the ESEM.

As the current limit for the electrical characterisation of this deposit was increased further, to values in excess of 3.6 mA, some structural changes in the deposit could start to be observed in the STEM images. In particular after sweep number 242, the second I-V sweep to be taken with a current limit of 3.8 mA a small change in the structure of the deposit could be seen (not shown here). In particular this image showed that some kind of grainy line type structure within the centre of the deposit started to appear. Then, as the current limit was increased further to 4 mA (sweep 243), this structure became more obvious and a similar structure could also start to be observed in the right hand deposit. When the current limit for the electrical characterisation was increased further to 4.25 mA (sweep 245), the grainy structure became much more obvious, especially in the right hand deposit. At this current limit the silicon nitride membrane also started to show a brighter spot between the two deposits and have some kind grainy structure. This is shown in Figure 6.8 (b) and indicates that the two deposits are connected in some way. The bright spot in this image may be attributed to some kind of heating of the membrane.

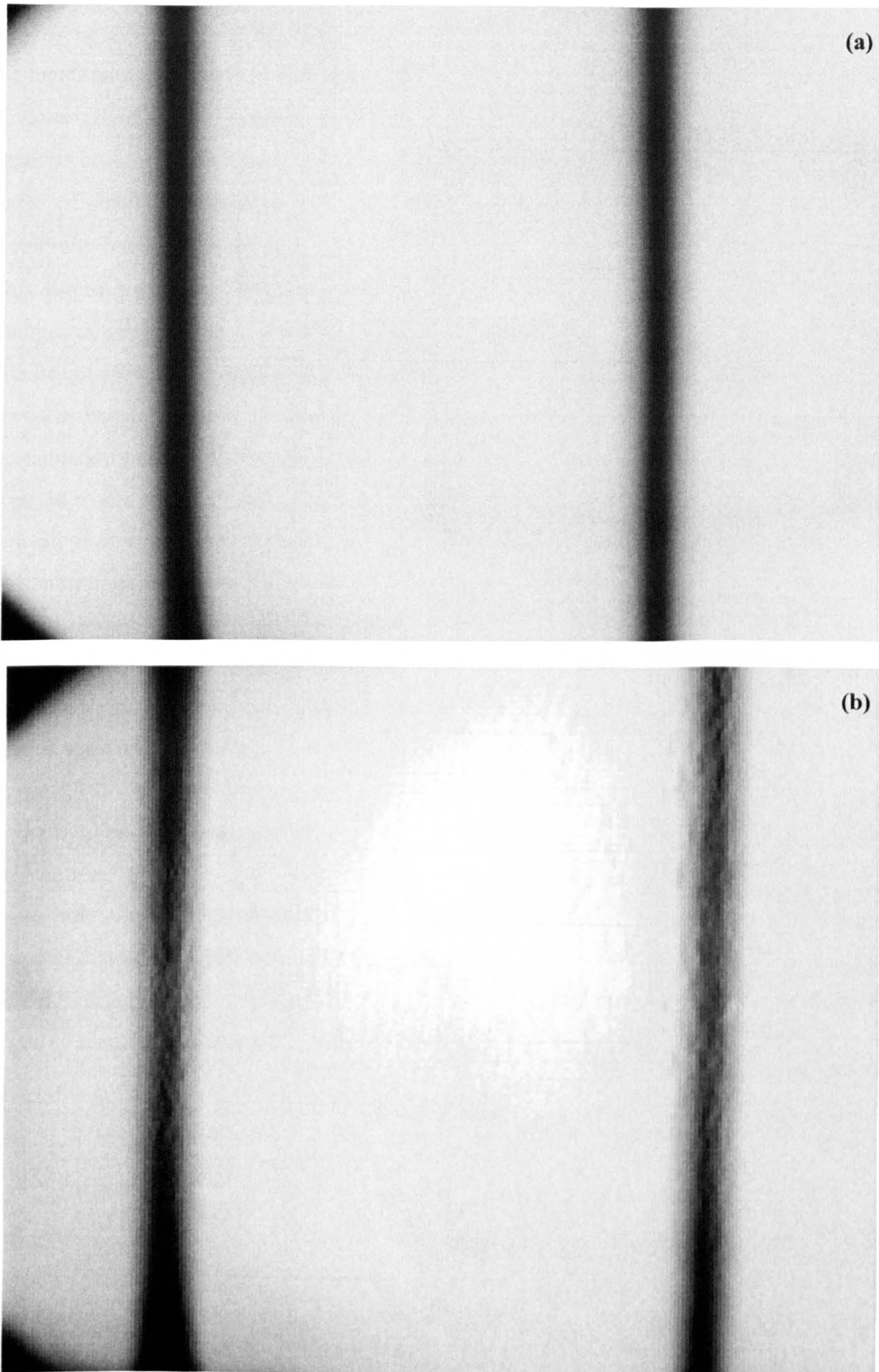


**Figure 6.8.** STEM images **(a)** before electrical characterisation, **(b)** after an I-V sweep with a 4.25 mA current limit. The left wire is being electrically characterised and the right wire is as deposited.

Subsequent I-V sweeps at this and further current limits caused the size of the bright spot on the membrane to increase in size and for the grainy structure of the deposits to become more obvious. Then, as the current limit was increased to 5 mA, the grainy structure in the deposits became much more significant such that the deposits appeared to be made up of a series of small islands rather than one continuous structure, while the bright spot on the membrane itself continued to increase in size. This behaviour is shown in Figure 6.9 (a). This figure also shows how the change in grey scale for the deposits which reflects the changes in height of the structure as well as the material also became much more significant. The bright spot on the membrane may be attributed to increasing amounts of heating by the deposits themselves. It is not thought to be due to the electron beam heating and damaging the substrate because the bright spot does not match the area of the sample that has been exposed to the electron beam. This image also suggests that at this point the structure of the deposits is starting to break down. However, examination of the I-V characteristics and the resistance measurements that are shown in Figure 6.7 suggests that this is not the case because the resistance continues to decrease rather than increase as this structure develops.

As the current limit was increased further and multiple I-V sweeps were run, the STEM images showed that the structure of the deposits continued to be similar to that shown in Figure 6.9 (a), with the island type structure becoming more pronounced and the bright area on the membrane increasing in size. Figure 6.9 (b) shows the STEM image of the tungsten interconnects after the final current-voltage sweep had been carried out. In particular it shows how almost all of the electron beam deposited material has transformed to this new island like structure. This image also shows how the whole of the membrane surrounding these deposits has become brighter than it was in the original images and also has some kind of grainy features, which were not observed before the structural changes started to occur.

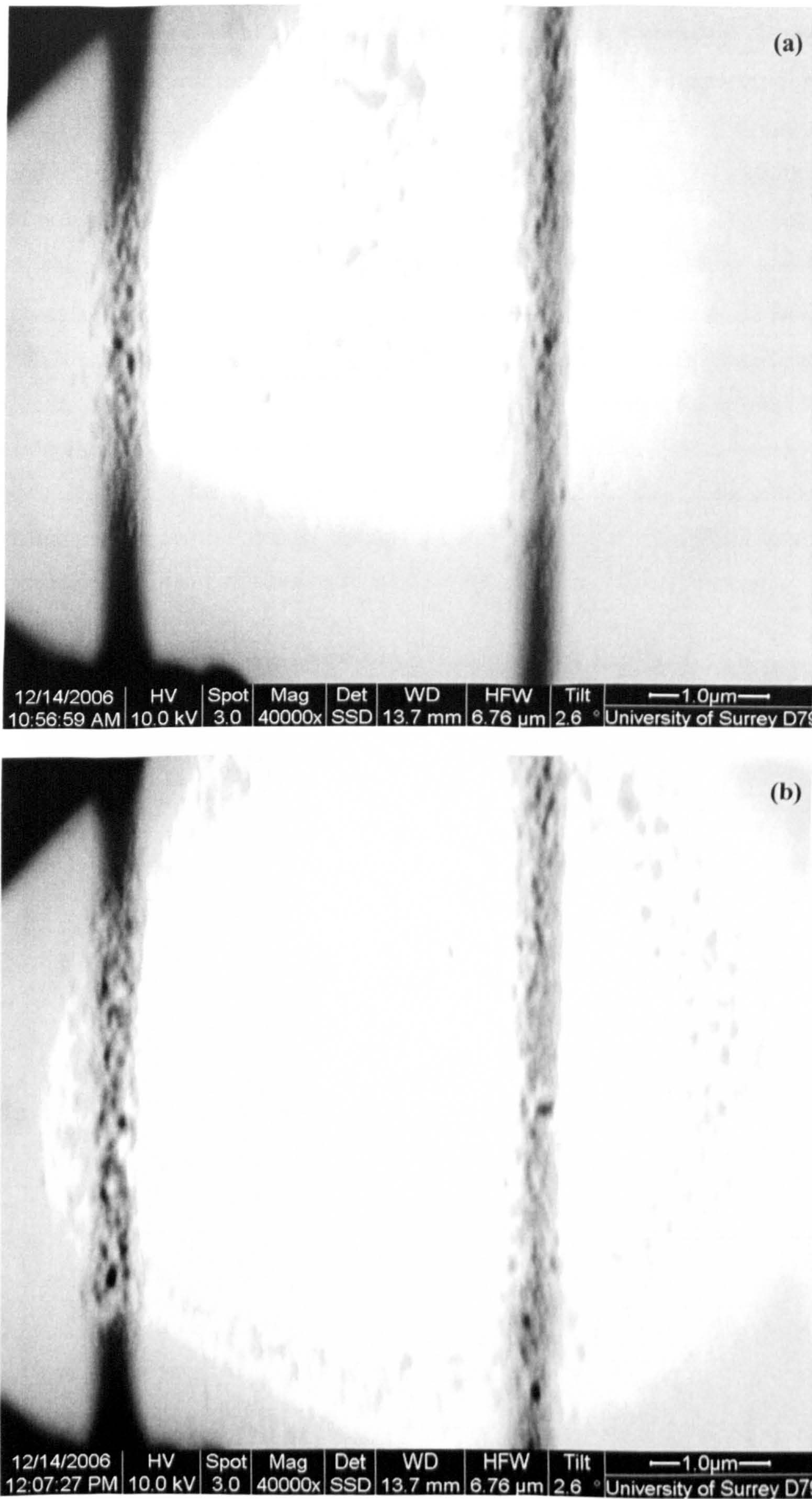


**Figure 6.9.** STEM images of tungsten wires taken after an I-V sweep with a current limit of **(a)** 5 mA and **(b)** 6 mA. The left wire is being electrically characterised and the right wire is as deposited.

Figure 6.10 shows another image of the interconnects after their electrical characterisation that was taken at a lower magnification and using a slightly different amount of brightness and contrast. In this image the amount of the silicon nitride membrane that has undergone some kind of transformation is more apparent. It can also be seen from this figure, that the damaged area of the membrane did not exactly match that of the area being imaged during the electrical characterisation. In particular, some of the altered membrane area is outside that of the imaged area, which suggests that the change in the membrane is due to some kind of reaction such as ohmic heating occurring during the electrical characterisation and not due to damage by electron beam irradiation. These images also show that this deposit appears to have undergone some kind of structural transformation, which is similar to the one shown in Figure 6.5. This result hence indicates that the assumption that carrying out transmission electron microscopy on this deposit to analyse and explain the changes observed for the deposits made on a silicon substrate with a 300 nm thick oxide is a suitable one.

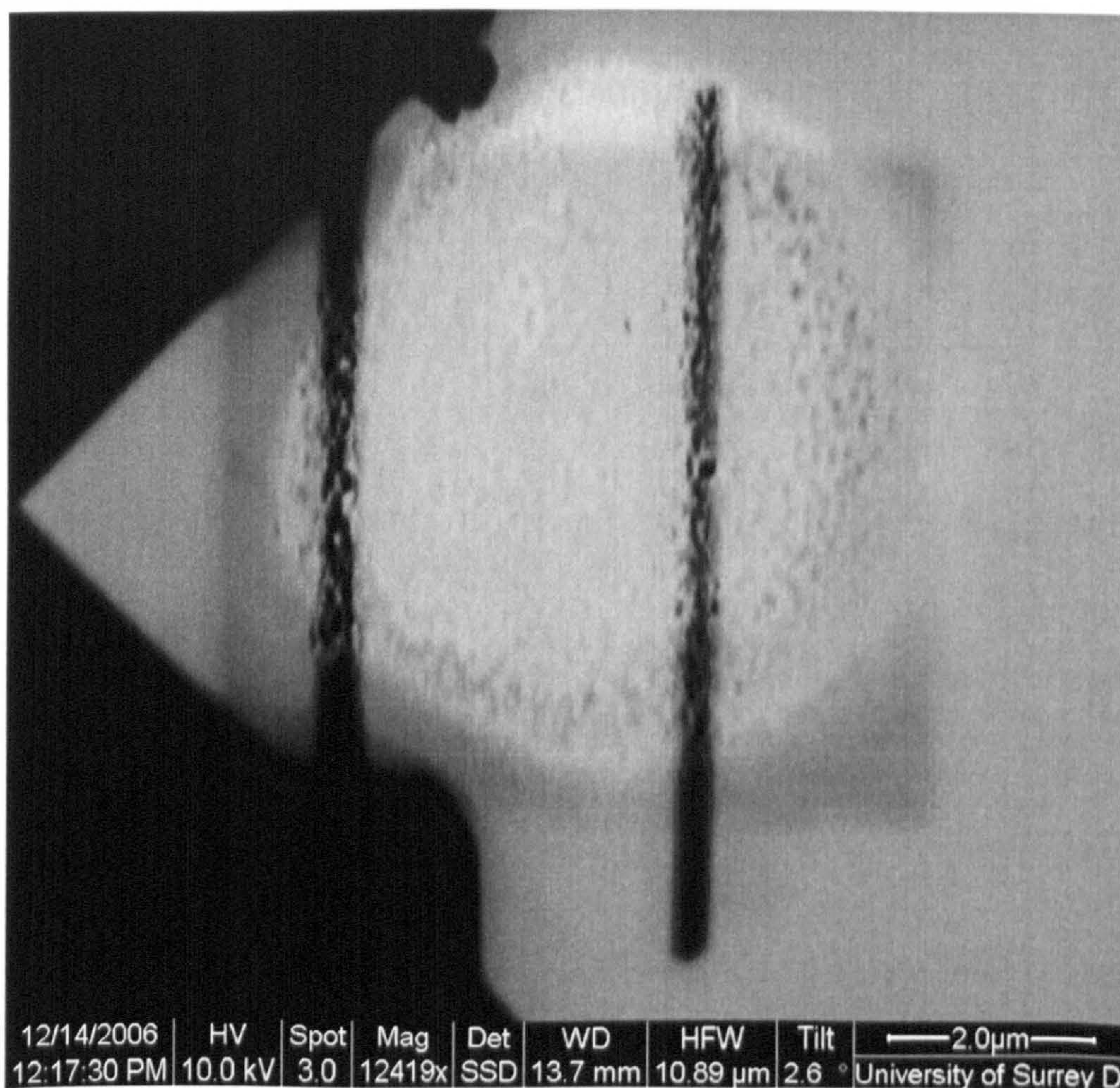


**Figure 6.10.** STEM image of two tungsten interconnects taken after their electrical characterisation for current limits up to 6 mA. The left hand wire shown in the image is the one being electrically characterised while the right hand wire is unconnected.

The effects of the electrical characterisation and the change in the resistance on the structure of this interconnect may be analysed more thoroughly using the TEM that was described in section 3.3.1. For this analysis this sample was transferred from the ESEM straight into the TEM so that the structure and elemental composition of the deposit could be analysed using HREM and EELS. Initially, a low magnification image of the deposit was taken as shown in Figure 6.11. As can be seen from this image the tungsten deposit appeared to consist of a series of clusters that do not appear to be electrically connected. This image also shows how the membrane surrounding the deposit is covered with some kind of material and has a textured appearance, which suggests that it may have been damaged during the electrical characterisation.

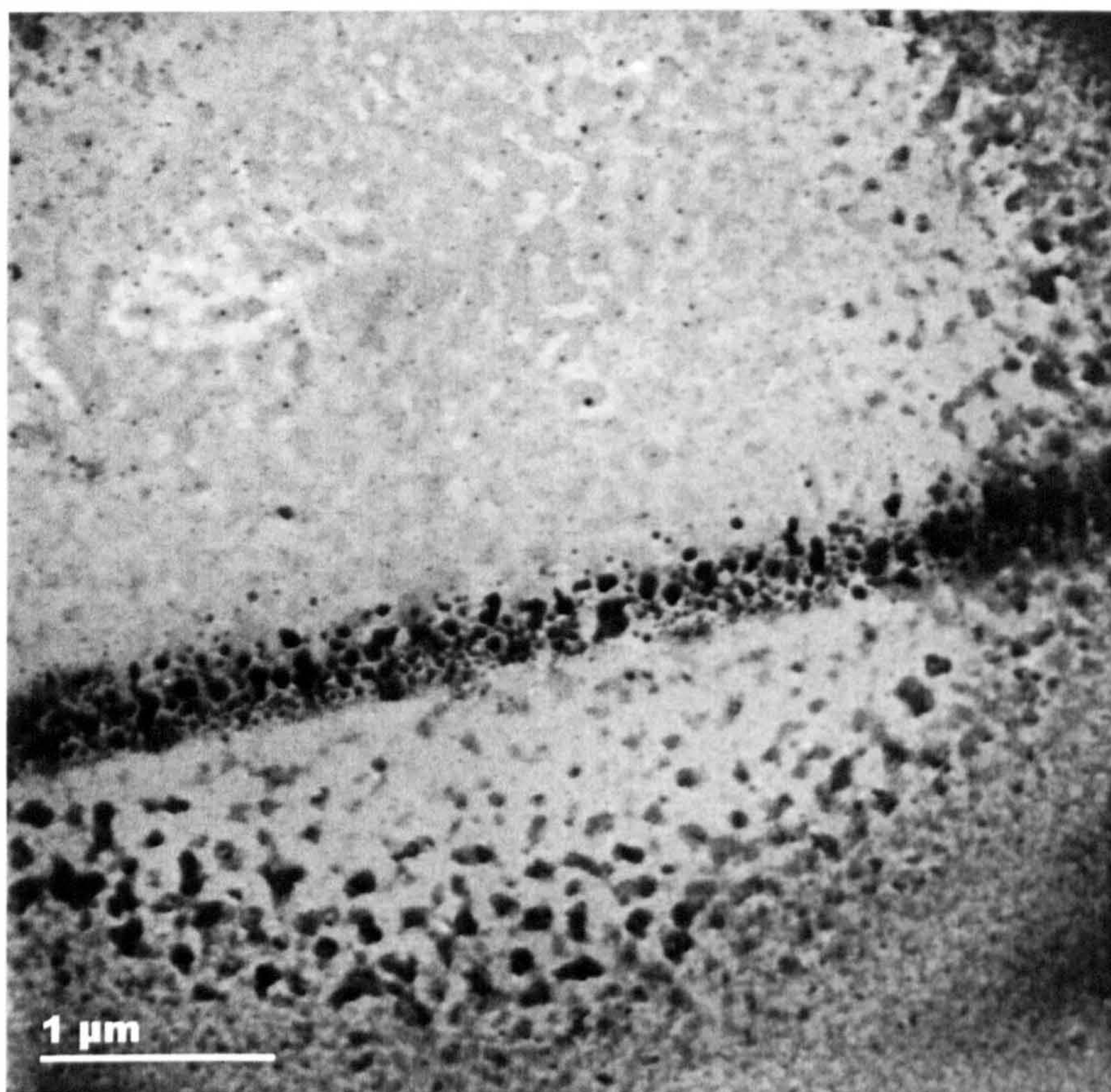


**Figure 6.11.** Low magnification TEM image of an EBID tungsten wire after being exposed to currents of up to 6 mA.

As the deposits are known to contain tungsten, carbon and oxygen, EELS was carried out to determine, which of these elements remained in the deposit and their exact location. The oxygen EELS map (not shown here) showed that there was very little oxygen present anywhere on the sample. The tungsten and carbon EELS maps are shown in Figure 6.12 (a) and (b) respectively. As can be seen from these figures, the as-deposited amorphous

structure of the deposit, which was discussed in section 4.4 had transformed significantly. In particular, as shown in Figure 6.12 (a), the tungsten was found to have formed a series of individual tungsten clusters, which occurred in the defined deposition area. Meanwhile Figure 6.12 (b) shows how the carbon occurred both within the defined deposition area and on the substrate surrounding the deposit. The carbon outside of the deposition area may be attributed to the formation of a halo during the electron beam deposition process.

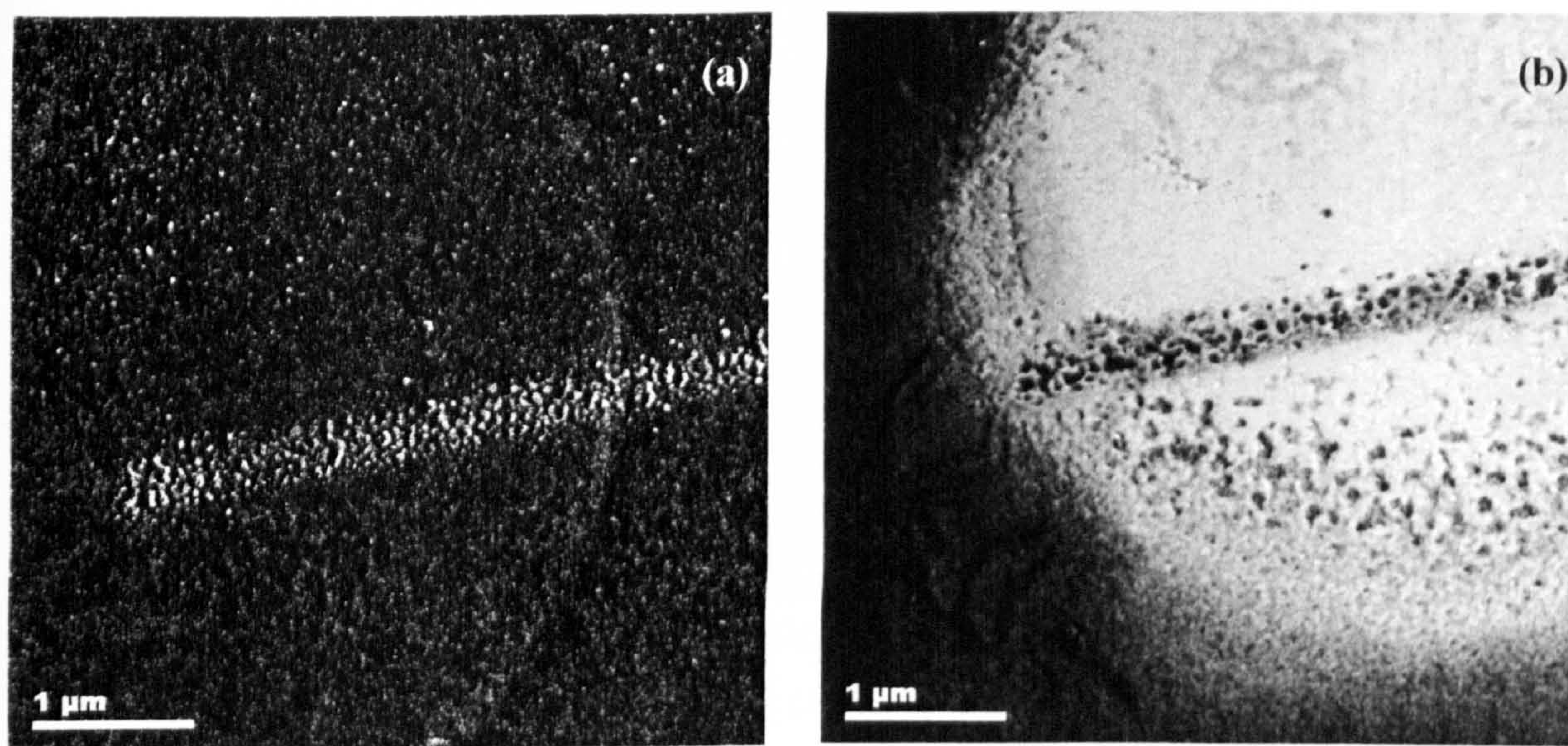


**Figure 6.12.** EELS map of **(a)** tungsten and **(b)** carbon for an EBID wire after electrical characterisation. The tungsten and carbon show up as the brighter parts of the respective maps.

To investigate whether the silicon nitride membrane had been damaged during the electrical characterisation as was suggested by the STEM images of the deposit. EELS was also used to image the nitrogen within the membrane to determine whether there were any variations in its composition. The resulting EELS map for this investigation is shown in Figure 6.13. As can be seen from this image, in the area surrounding the tungsten deposits there is no presence of any nitrogen. This suggests that the membrane had been damaged so that in this area the nitrogen had been burnt away. Silicon nitride membranes are known to be stable to temperatures in excess of 1000°C. Therefore this result suggests that during the electrical characterisation, the deposit and the area surrounding the deposit must have reached temperatures in excess of 1000°C in order for the membrane to become damaged in this way. From this temperature it is also possible to estimate that the thermal conductivity of this material is in the range of 30 – 40 $Wm^{-1}K^{-1}$. Using an effective medium theory of materials this value of thermal conductivity is within the expected range of values for tungsten and amorphous carbon.

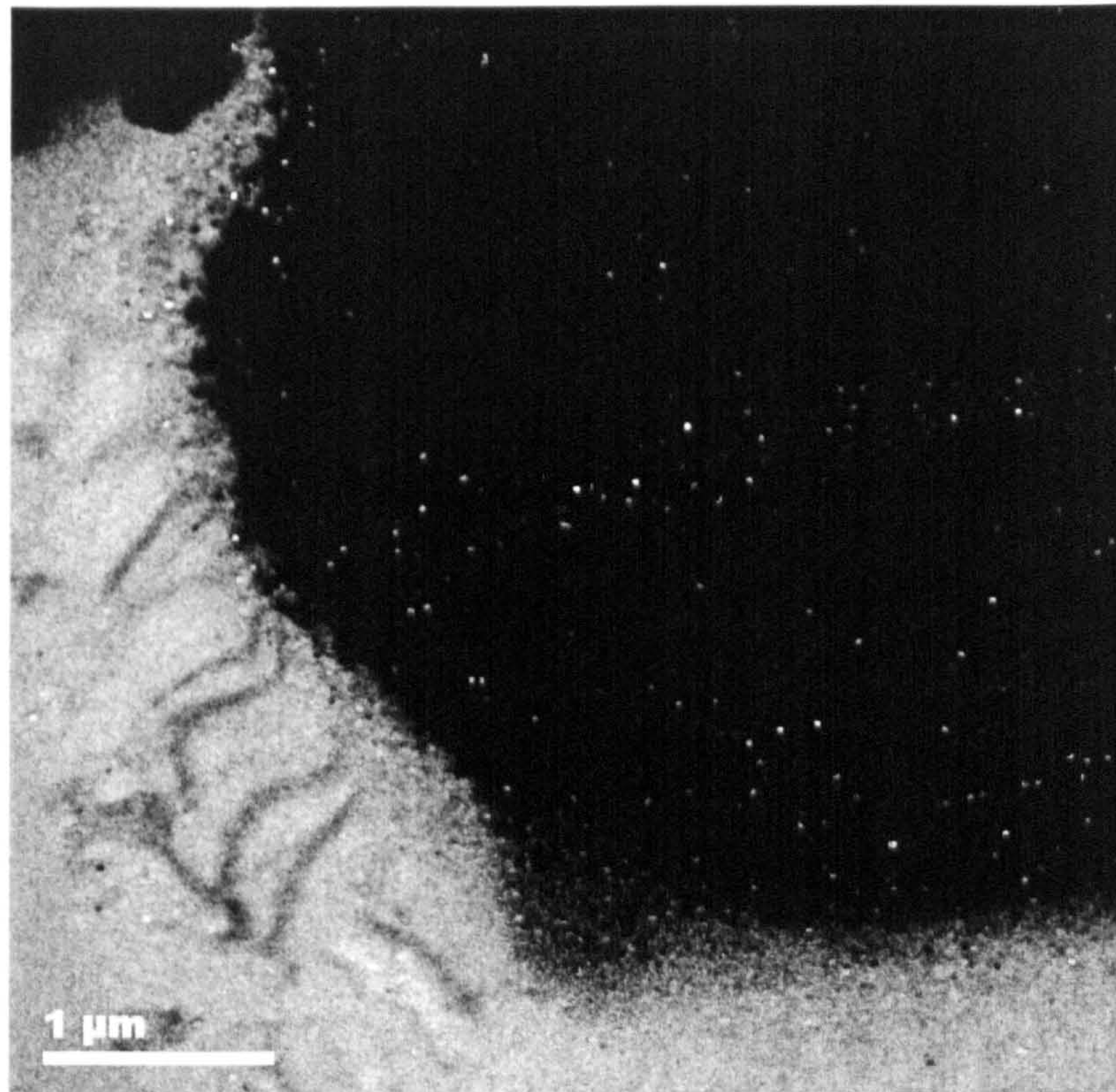


**Figure 6.13.** EELS map of the nitrogen in the silicon nitride membrane. The presence of nitrogen is shown by the lighter grey areas.

To analyse the effects of the electrical characterisation on the structure of these deposits further, HREM images of the deposits were also taken. An example of a typical high resolution EFTEM image of the centre of the tungsten deposit that had been connected to is shown in Figure 6.14 (a). This image shows more clearly how the amorphous as-deposited structure of the deposit had transformed to contain tungsten clusters (dark areas) embedded in a carbon graphitised network (light grey areas). The fact that the carbon had become graphitised was known from examination of the carbon K-edge that was gained using the EELS analysis using Fourier transforms. The graphitisation of the carbon could also be detected in the HREM images, which showed 002 fringes with a spacing of approximately 0.34 nm. An example of these fringes is shown in the HREM image of the centre of the tungsten deposit in Figure 6.14 (b). As can be seen from this image the graphitised carbon lattice fringes extended under the tungsten clusters. From this analysis it was not possible to determine whether the tungsten clusters consisted purely of tungsten or whether they were made up of some type of tungsten carbide.

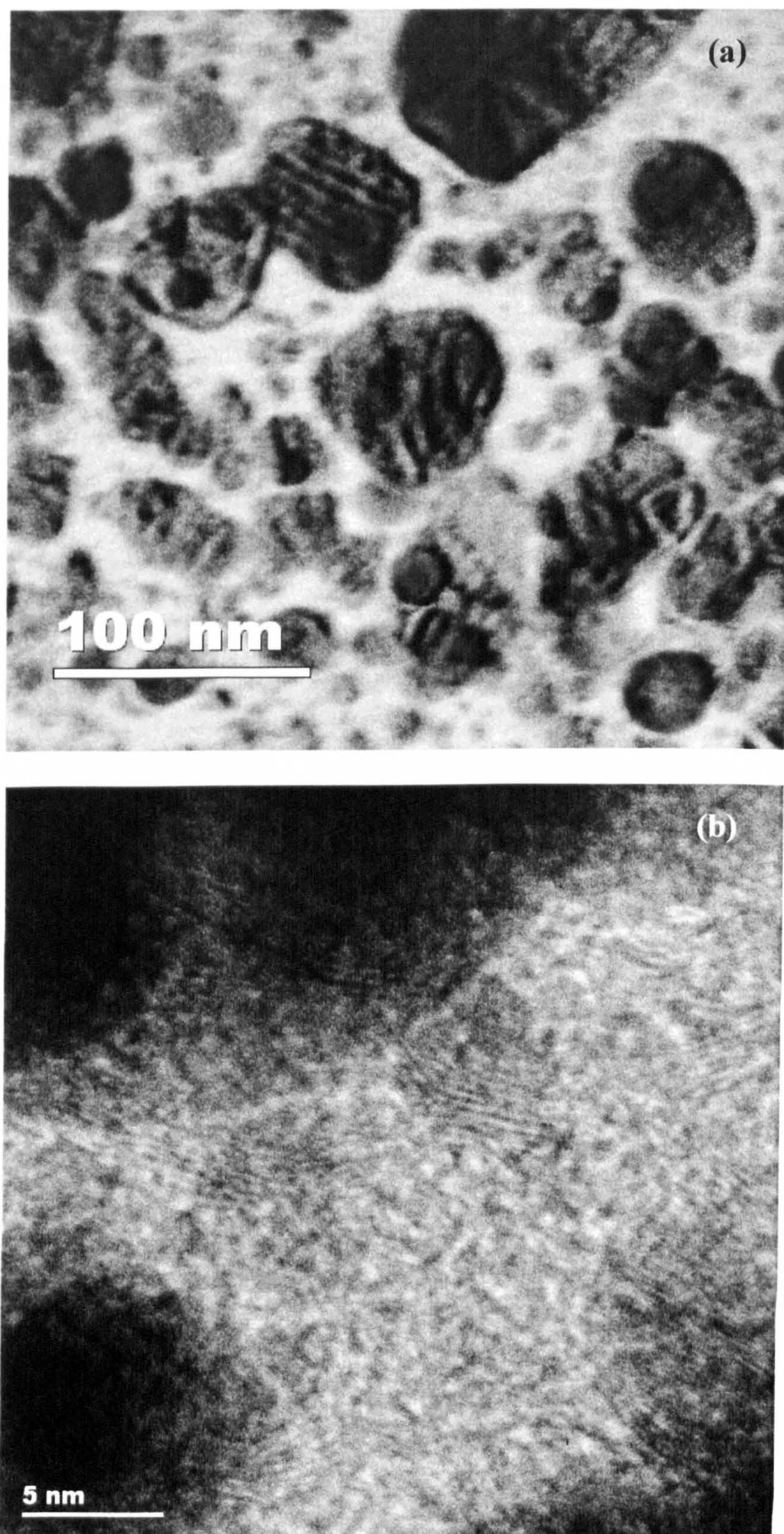


**Figure 6.14. (a)** TEM carbon EFTEM image of a tungsten wire. The carbon is graphitised (light grey area), as confirmed by filtered EELS and HREM. The dark dots are tungsten clusters. **(b)** HREM image of a tungsten wire showing the 002 lattice fringes with a spacing of 0.34 nm.

To reinforce the observation that the tungsten clusters only occurred in the defined deposition area, whereas the carbon extended beyond this the TEM EELS image for tungsten, carbon and nitrogen was overlayed onto the equivalent AFM image for the deposit. The resulting image is shown in Figure 6.15 and shows how the tungsten clusters occur in only the defined deposition area, while the carbon extends some way beyond this. This result is also in agreement with the AES map of the as deposited tungsten wire that was examined in section 4.4. Furthermore, this result may be used to explain the structure seen in the STEM images in Figure 6.9. It indicates that the dark particle like features in the deposits correlates to the tungsten clusters, while the lighter grey area surrounding the tungsten clusters correlates to graphitised carbon. This result also suggests that the reason that the deposit in Figure 6.9 (b) appears discontinuous but conducts with an improved resistance in comparison to a deposit that has not been exposed to high currents is due to the fact that the tungsten clusters with a significant height are embedded in graphitised carbon which is conducting but not easily observed in these images.

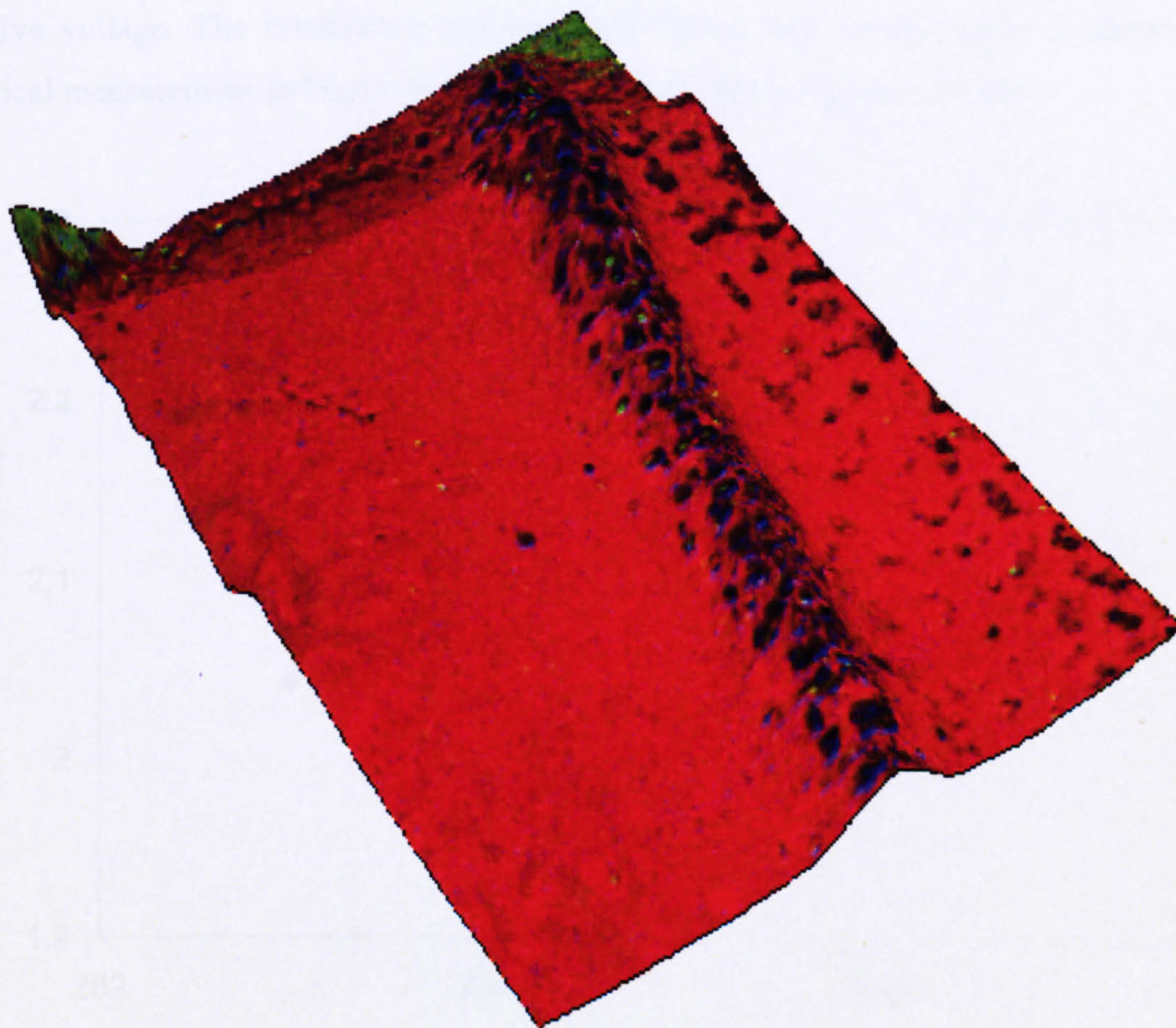

**Figure 6.15.** Image of the TEM EELS map for tungsten, carbon and nitrogen overlaid onto the AFM image for the same deposit. The blue dots in the centre of the image correspond to tungsten clusters, the red corresponds to carbon and the green to nitrogen.

### 6.3.3 Breakdown Characterisation

For all of the electrical characterisation that has been carried out, it has been found that for current limits below 10 μA, the electrical properties of the electron beam deposited tungsten wires are stable and do not appear to breakdown. Then as the current passed through the wires was increased, their resistance decreased until for currents in excess of 1 mA, the resistance measurements showed some instability and in some cases increased before the wires broke down. An example of the increase in resistance and the subsequent breakdown that occurred for a wire that was produced using 50 passes of the electron beam is shown in Figure 6.16 and Figure 6.17 (a) respectively. The SEM image that confirms that the wire did break during this I-V sweep is then shown in Figure 6.17 (b). In particular Figure 6.16 shows how for a current limit of 2.4 mA the resistance of the deposit decreased steadily. Then as the current limit was increased to 2.6 mA the resistance was found to remain constant for the first current – voltage sweep that was run and then to increase for the subsequent sweep. On the following I-V sweep, which is not shown here the wire then broke near to the contact at which the voltage was applied as the voltage was swept from zero up to a maximum negative voltage. The breakdown that occurred during this voltage cycle is shown as an electrical measurement in Figure 6.17 (a) and as an image in Figure 6.17 (b).

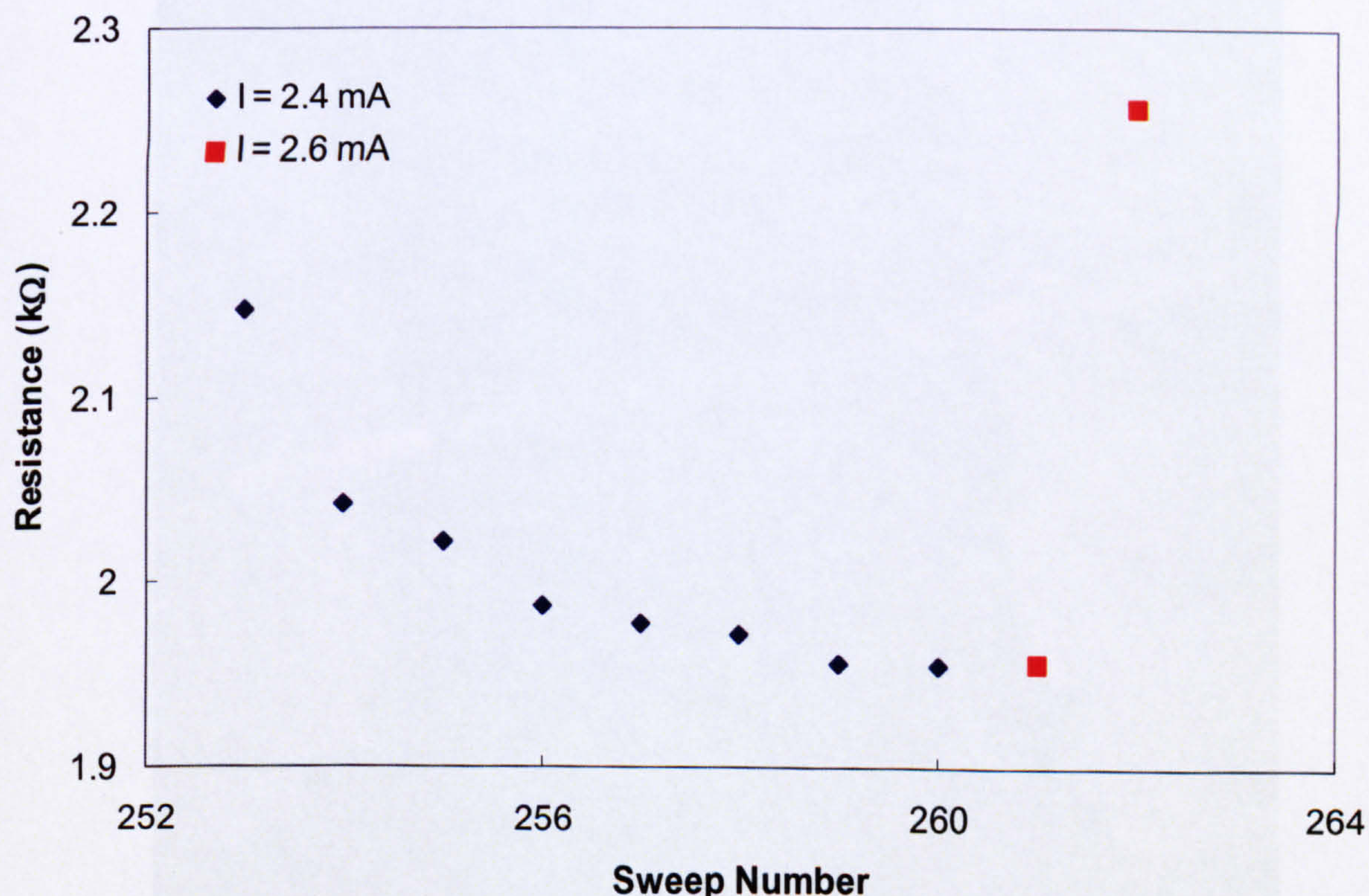


**Figure 6.16.** Resistance variation of a tungsten deposit produced using an electron beam current of 1.5 nA and 500 passes for current limits of 2.4 and 2.6 mA.

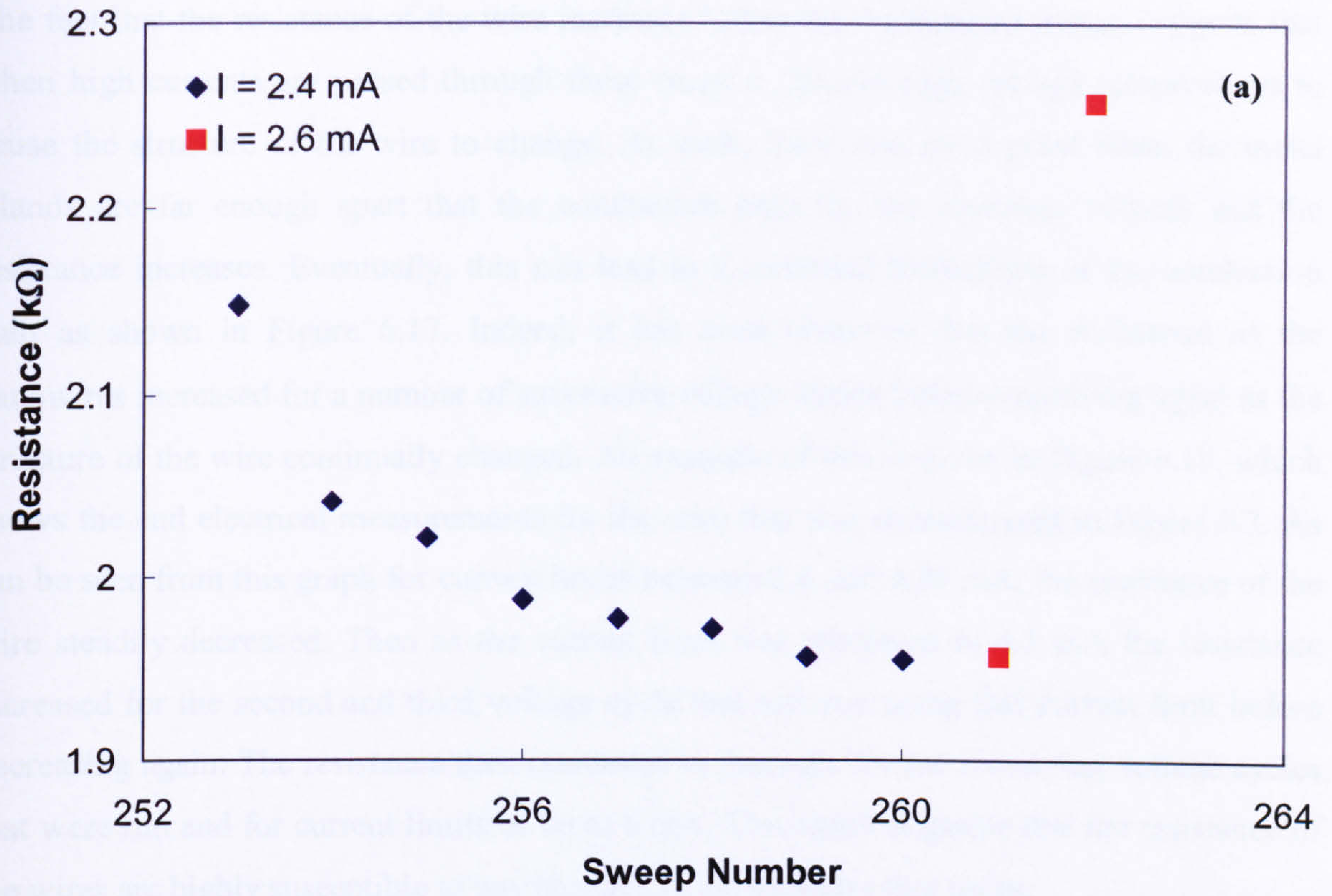


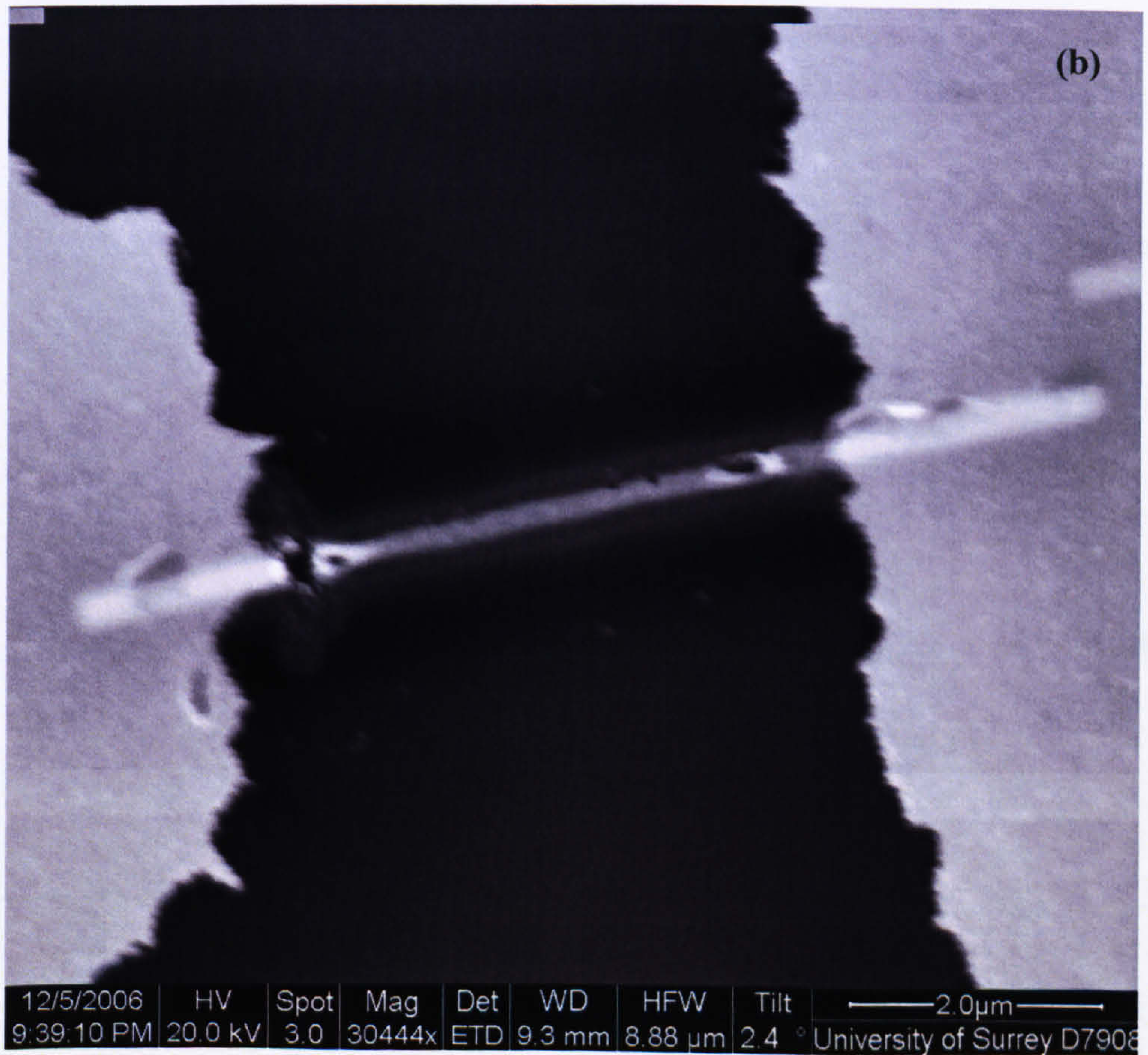


**Figure 6.17. (a)** Graph showing the electrical breakdown and **(b)** SEM image of the breakdown, of a tungsten wire produced using 1.5 nA beam current and passes of the electron beam.

The fact that the resistance of the wire increases before the breakdown occurs suggests that when high currents are passed through these wires it induces high enough temperatures to cause the structure of the wire to change. As such, there may be a point when the metal islands are far enough apart that the conduction path for the electrons reduces and the resistance increases. Eventually, this can lead to a complete breakdown of the conduction path as shown in Figure 6.17. Indeed, it has been observed that the resistance of the nanowires increased for a number of successive voltage cycles before improving again as the structure of the wire continually changed. An example of this is given in Figure 6.18, which shows the end electrical measurements for the wire that was characterised in Figure 6.7. As can be seen from this graph for current limits between 3.4 and 4.25 mA, the resistance of the wire steadily decreased. Then as the current limit was increased to 4.5 mA the resistance increased for the second and third voltage cycle that was run using this current limit before decreasing again. The resistance then continued to decrease for the remaining voltage cycles that were run and for current limits of up to 6 mA. This result suggests that the resistance of the wires are highly susceptible to any changes in the structure that occur.

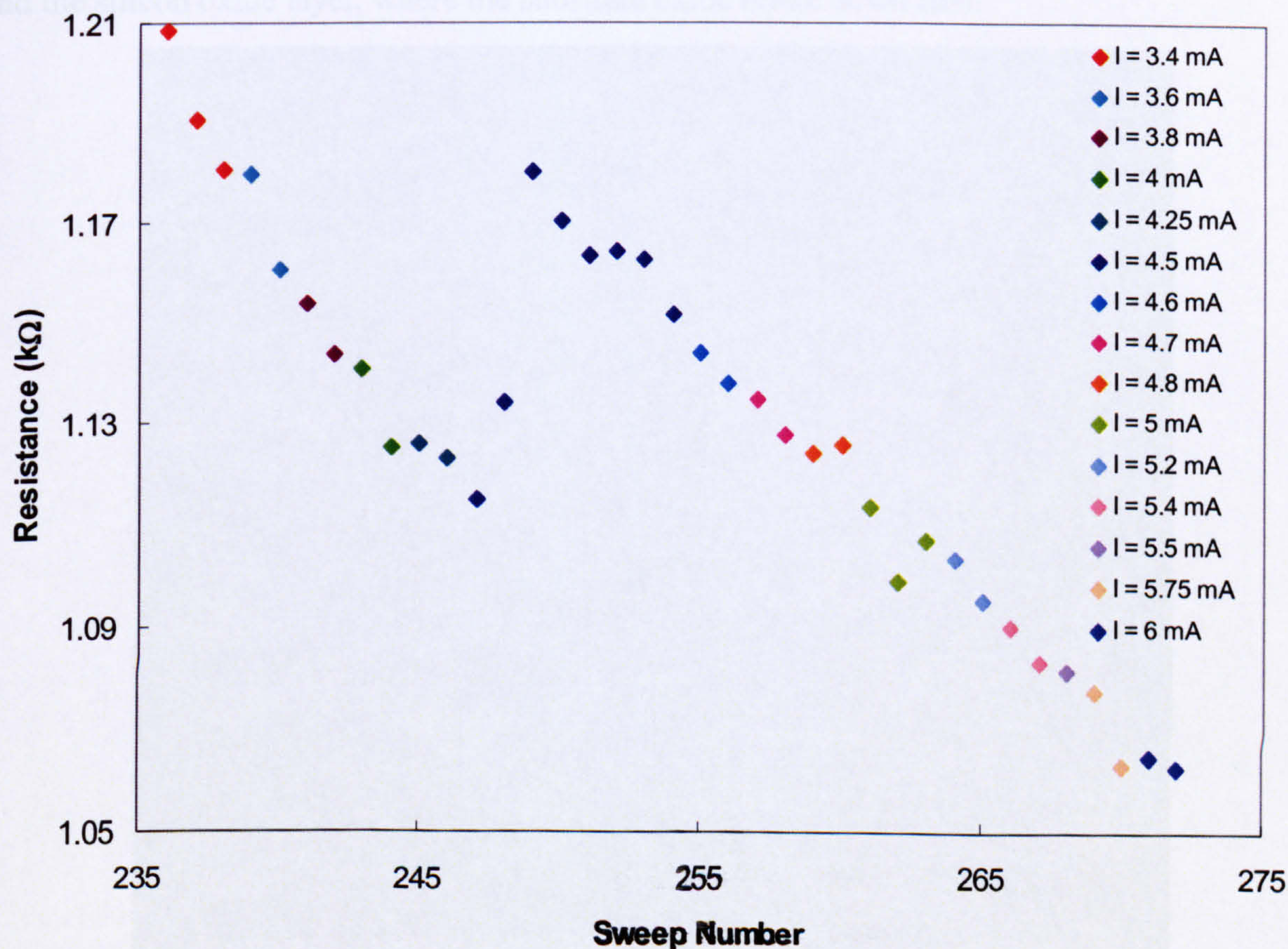


**Figure 6.18.** Resistance variation for a tungsten deposit made using 100 passes for current limits between 3.4 and 6 mA.

The manner in which these nanowires broke down appears to be dependent on the exact way that the current-voltage measurements have been made leading up to the breakdown as well as on the deposition parameters. Figure 6.19 shows the breakdown of a deposit that was fabricated using electron source one, an electron beam current of 5.9 nA and 200 passes. These parameters mean that a much more significant deposit was built up than those investigated to date and that its original resistance was also much lower. The device was conditioned using similar current limit intervals to those analysed previously and was found to break down when exposed to a current of 3 mA for the first time. As can be seen from the image in this figure, the structure of the deposit seems to have changed from its original structure, although it has not formed the discontinuous structure that was seen in section 6.3.2. Also, unlike the other deposits that have been examined, this deposit has broken near the centre in a much more extreme manner although there does also appear to be some damage at either end of the wire. As this breakdown took place it also caused some damage to the substrate oxide layer which again suggests that significant ohmic heating of the deposit has occurred. It is also possible that in this case the interconnect breakdown was caused by dissimilar thermal expansion coefficient mismatch between the silicon substrate and the silicon oxide layer, where the substrate oxide broke down first.

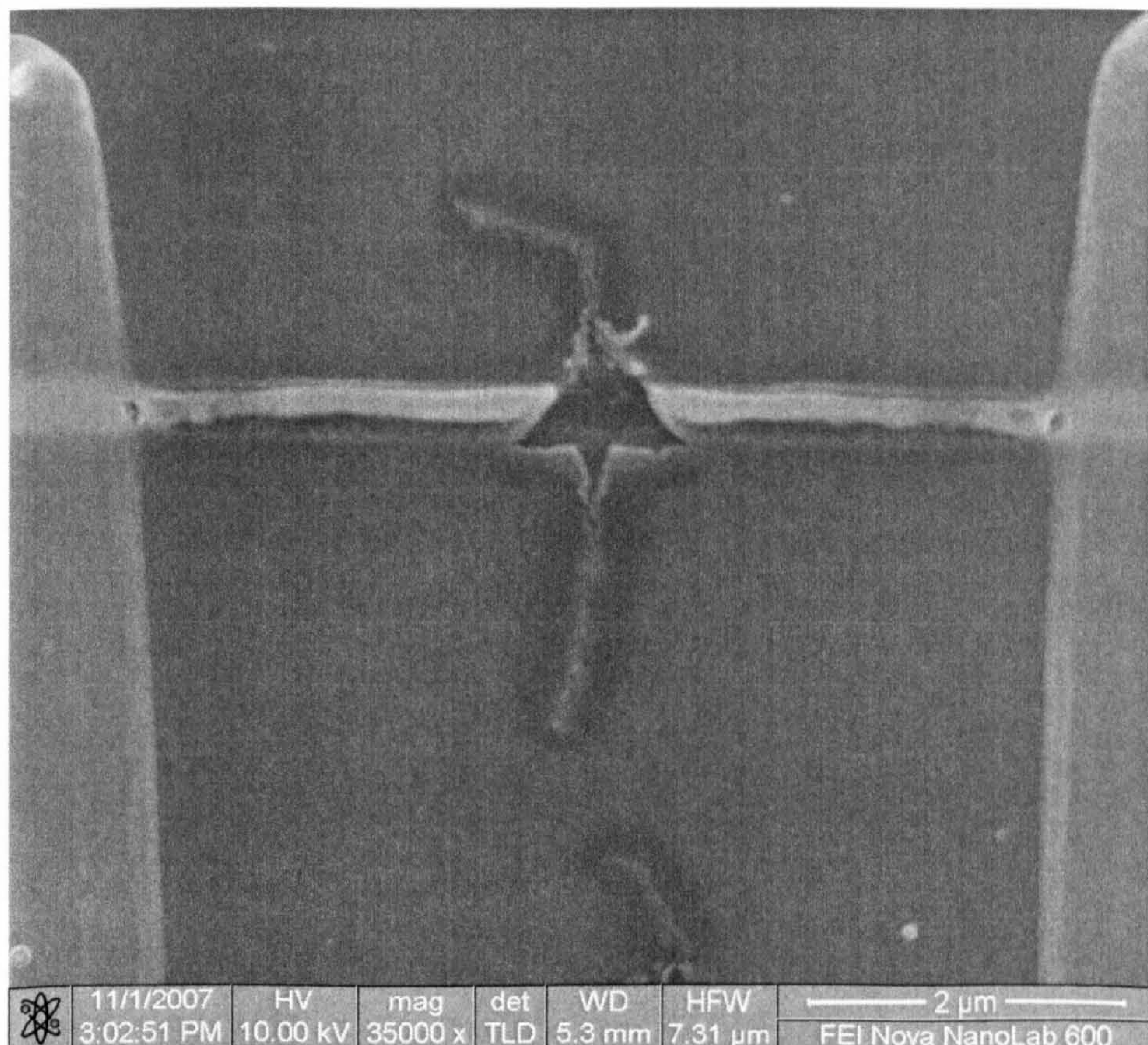


**Figure 6.19.** SEM image of the breakdown of a nanowire that has been exposed to 3 mA and was deposited using electron source one, a 5.9 nA beam current and 200 passes.

For another electron beam deposited tungsten wire that was deposited using the same conditions as those used for the previous device which is shown in Figure 6.19, the current limit carrying capacity of the wire was investigated by slowly increasing the current through the device, rather than running voltage sweeps. The resistance of the wire was again found to decrease steadily as the current the wire was exposed to increased. The wire broke at a current of 5 mA as shown in Figure 6.20. As can be seen from this image the structure of the wire had again transformed to some kind of discontinuous structure. This image also shows how during the breakdown of the wire the gold contact pads in the area surrounding the deposit had been removed. This result again suggests that the wire had become ohmically heated to a significant temperature during the electrical characterisation.

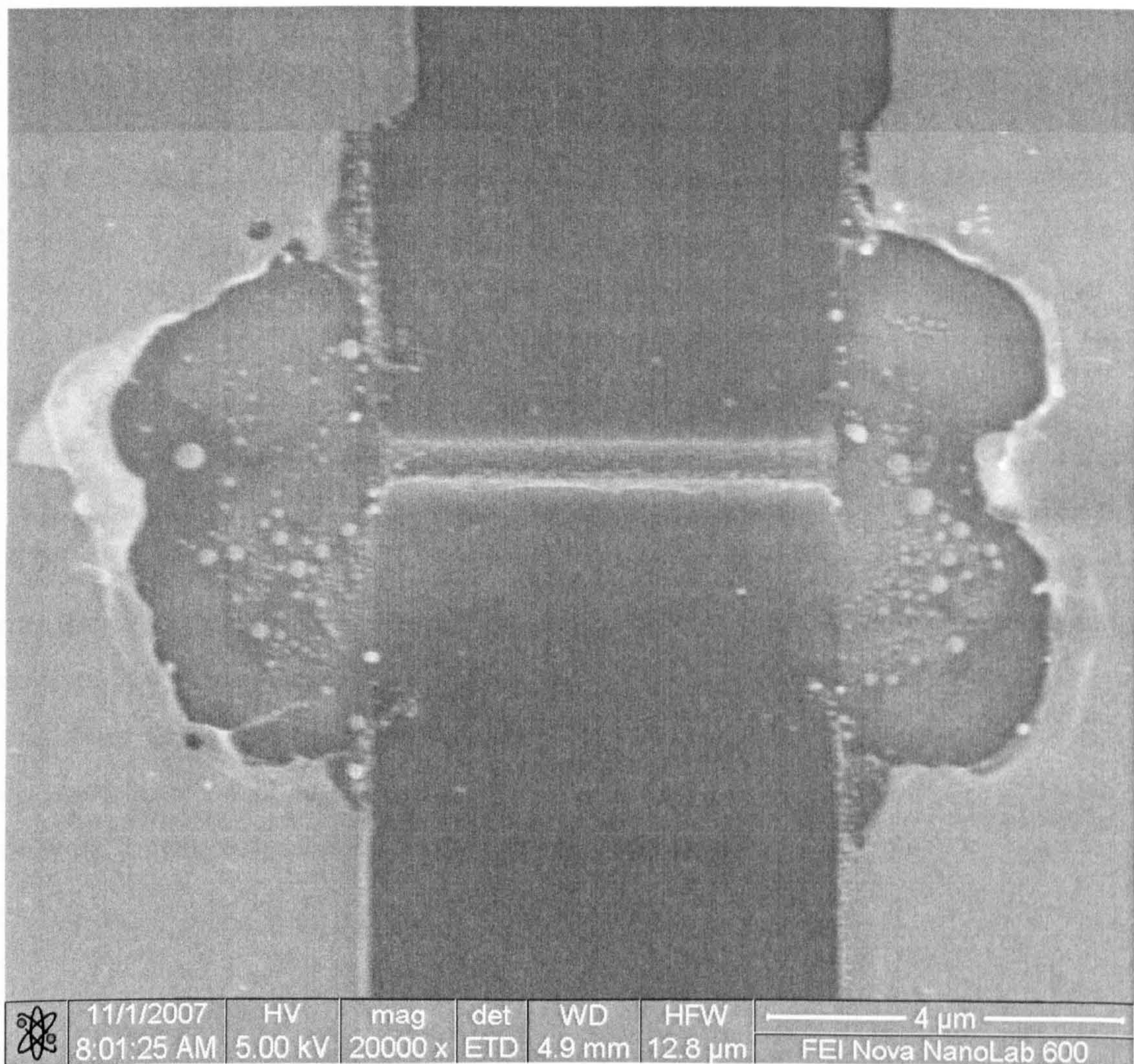


**Figure 6.20.** SEM image of the breakdown of a tungsten wire that has been exposed to a current limit of 5 mA and was deposited using electron source one, a 5.9 nA beam current and 200 passes. This image also shows how an area of the gold pads on the left and right hand sides of the image had been damaged and removed during the breakdown process.

### 6.3.4 Discussion

In this section it has been shown that when electron beam deposited tungsten wires are exposed to currents in excess of 100 μA, they undergo a change, which results in a transformation in the structure and the electrical characteristics of the deposits. In particular, it has been found that by continually exposing the wires to high currents the resistance of the wires could be improved by several orders of magnitude. This has been explained in terms of ohmic heating of the deposits themselves, which results in the structure of the deposits becoming more ordered and transforming from their original amorphous structure to a more stable one which contains tungsten clusters embedded in an amorphous matrix. When the wires are then exposed to currents in excess of 1 mA, their structure becomes unstable and in a number of cases the resistance of the deposits increases before the structures breakdown both electrically and structurally.

Of particular interest are the results of the two deposits, which were made onto a silicon nitride membrane, as described in section 6.3.2. During the electrical characterisation and the subsequent structural characterisation of these deposits it was found that both deposits underwent the same transformation even though only one of the deposits had been electrically connected. The TEM analysis showed that the area between the two deposits was covered with a thin carbon layer that may have been partly responsible for the connection between the two deposits. Although it is more likely that the second deposit underwent the same transformation as the first, when the substrate underneath the deposit reached a high enough temperature. The source of this carbon was attributed to the formation of a halo during the deposition of the deposits. This result suggests that the carbon halo layer is much more significant than has been expected and can play a crucial role in determining the suitability of EBID as a mainstream fabrication process. Therefore, in order to make EBID more suitable as a fabrication process for the production of closely spaced interconnects, some work to reduce this halo layer needs to be carried out.

## 6.4 Effects of Post Deposition Annealing

In section 2.7 it was shown that the post deposition annealing of EBID nanowires resulted in an improved conductance. In section 6.3, the improvement in the resistance of the electron beam deposited tungsten wires was also attributed the ohmic heating of the wires. Therefore, this section shall look at the effect of post deposition annealing of the tungsten wires produced here on the structure and the electronic properties of the wires.

### 6.4.1 Structural Characterisation

In section 6.3.2 it was found that during the electrical characterisation of tungsten wires that had been fabricated onto a 100 nm thick silicon nitride membrane, the membrane had been damaged such that the nitrogen in the membrane had been burnt away. Silicon nitride membranes are stable to temperatures in excess of 1000°C and so it was hypothesised that during the electrical characterisation the deposit and the area surrounding it had been exposed to temperatures in excess of this. To determine whether the structural changes that were observed in these deposits were simply due to ohmic heating at high temperature, two deposits were produced with electron beam currents of 1.5 and 5.9 nA and 200 passes on a silicon nitride membrane and annealed at ~1000°C in a high vacuum system for approximately one hour. After the annealing the sample was placed into the STEM detector within the FEI Quanta 200 ESEM that was described in section 3.2.2 for structural analysis.

The resulting STEM image for these deposits is shown in Figure 6.21. The left hand deposit was made with a beam current of 5.9 nA, while the right hand deposit was made with a beam current of 1.5 nA. This image does not show the same structure as that for the deposit that was electrically characterised in section 6.3.2. However, it does show some features, which were not observable on the sample before the annealing was carried out. In particular, it can be seen that some brighter spots have occurred on the membrane in the area surrounding the deposits that may be due to some changes in the carbon halo present there. It is also possible to some brighter spots in the deposits themselves, particularly in the right hand deposit, which was produced using the 1.5 nA beam current. This result suggests that parts of the deposits have undergone some kind of structural transformation and have a higher metallic content than the rest of the deposits. The fact that less features can be seen in the deposit made with a 5.9 nA beam current may be also due to the fact that this deposit is thicker than the 1.5 nA deposit and it also has a higher initial metallic content.

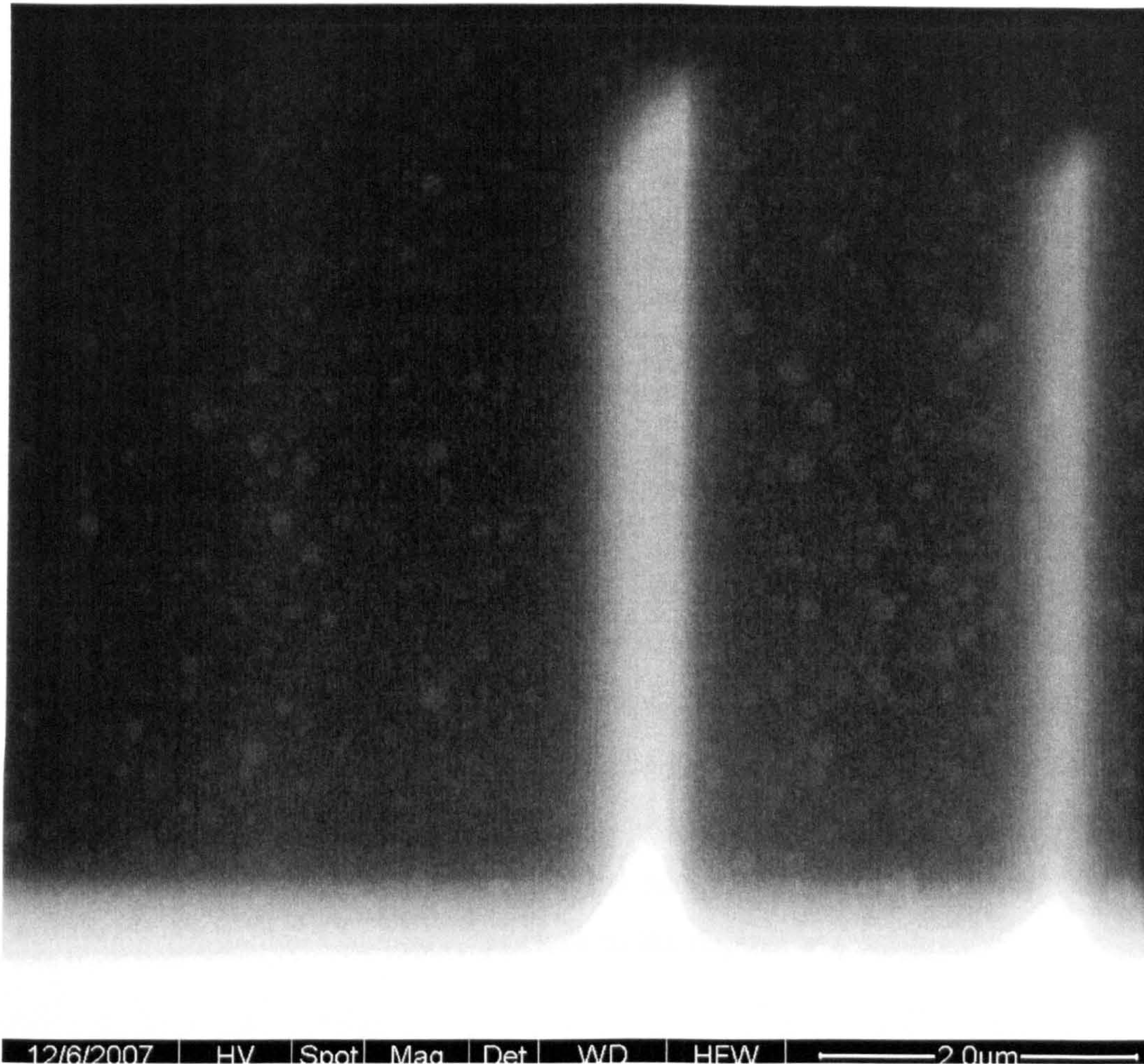


**Figure 6.21.** STEM image of two tungsten deposits that have been annealed in a high vacuum system at ~1000°C for approximately one hour. Both deposits were produced using 200 passes of the electron beam and the left hand deposit was produced using an electron beam current of 5.9 nA, while the right hand deposit was produced using and electron beam current of 1.5 nA.

The results of post deposition annealing at ~1000°C shown in Figure 6.21 suggest that during the electrical characterisation which caused the deposits to form tungsten clusters embedded in a graphitised carbon matrix that the deposits were either exposed to temperatures in excess of 1000°C or that ohmic heating was not the only mechanism responsible for the transformation. However, the fact that the STEM images of an annealed sample show some structural changes and similarities to the electrically characterised samples suggests that ohmic heating does play at least a small role.

### 6.4.2 Electrical Characterisation

In order to determine the effects of post deposition annealing on the electrical properties of EBID tungsten interconnects, a number of deposits were simultaneously annealed and electrically characterised. For this experiment a tungsten deposit was fabricated so as to bridge two palladium contacts that had been prepatterned on a silicon dioxide substrate using conventional UV lithography. The deposit was fabricated using a precursor with more than 120 hours of use, electron source one, an electron beam current of 1.5 nA and 100 passes of the electron beam. It also had a length of ~10 μm and a width of 200 nm. Once the wire had been deposited, the substrate was mounted in the modified Omicron Nanotechnology Resistive Heater described in section 3.9, which was installed within the FEI Quanta 200 ESEM described in section 3.2.2 along with the Attocube manipulation system described in section 3.6.2 and shown in Figure 3.14. The heater was powered by the Keithley 238 Source Measurement Unit that was used to calibrate the heater and the electrical measurements were carried out using the Keithley 4200 Semiconductor Characterisation system that was described in section 3.7. The temperature that the substrate reached was then measured using a k-type thermocouple that was placed as close to the deposit as possible.

To carry out the electrical characterisation, during the annealing, the deposited wire was first contacted to using the Attocube manipulation system. A constant bias of 50 mV was then applied and the changes in the current were measured as a function of time as the temperature of the heater was increased and measured using the thermocouple also as a function of time. This allowed for the change in resistance of the deposit to be calculated and plotted as a function of the change in temperature. Initially, the temperature of the heater was raised to 32°C and the resistance of the deposit was measured as a function of temperature. The resistance was allowed to reach a constant value at the maximum temperature and then the substrate was allowed to cool back to room temperature before being reheated to the same temperature, while the resistance was again measured. The resulting data for this temperature increase is shown in Figure 6.22. In this figure sweep 1 corresponds to the first time the heater was raised to 32°C, while sweep 2 corresponds to the second time that the heater was raised to this temperature. This figure shows how as the temperature was increased to 32°C the resistance of the deposit decreased with temperature for both temperature increases. It also shows how the second time that the temperature was increased, the resistance of the structure was less than it was for the first, implying that some kind of change had occurred even for this low annealing temperature.

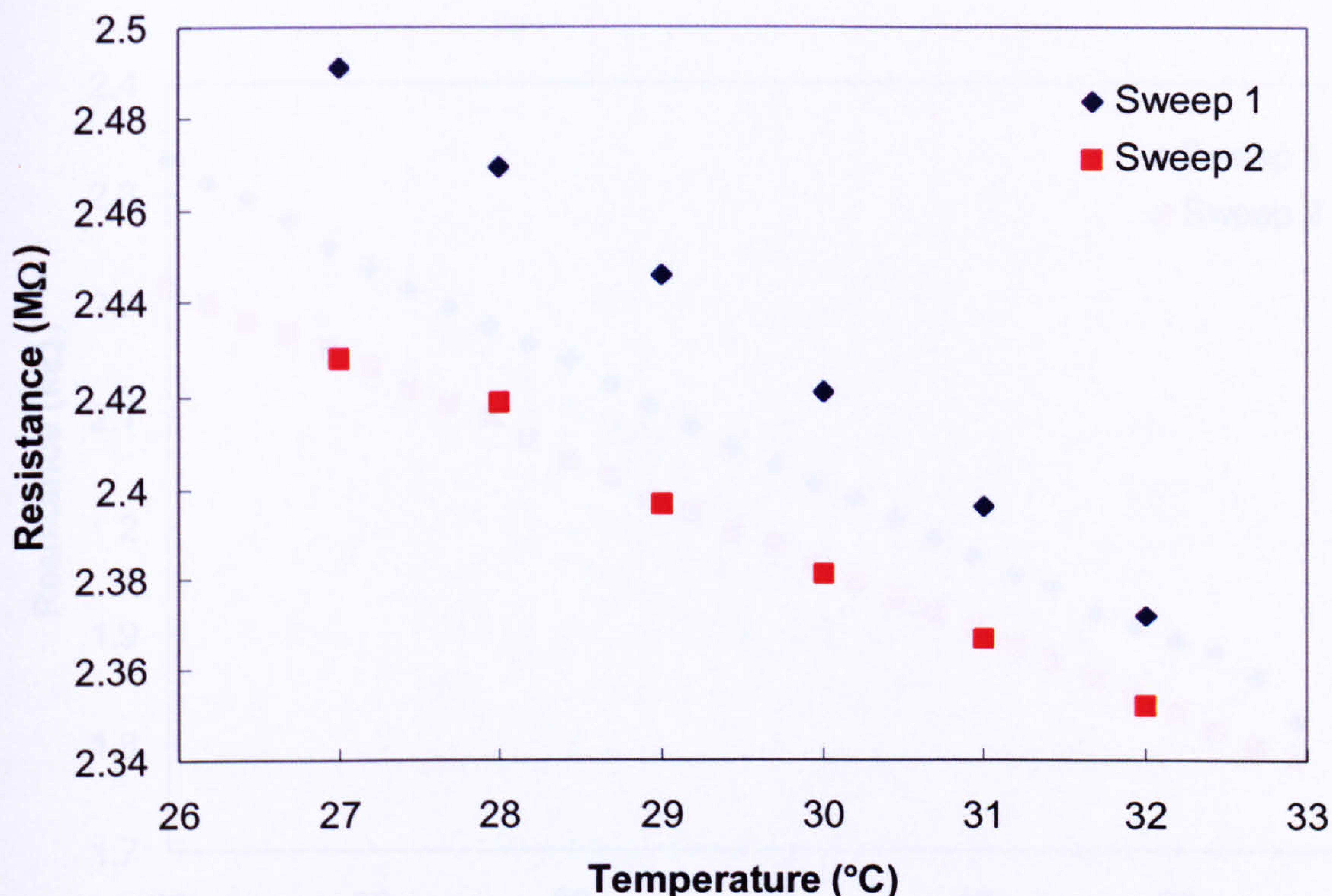


**Figure 6.22.** Graph showing the effects of annealing temperature on the resistance of a tungsten wire produced using an electron beam current of 1.5 nA and 100 passes.

This experiment was repeated using the same methodology for annealing temperatures of 41, and 51°C and a similar behaviour was observed. When the annealing temperature was increased to 56°C a more significant decrease in the resistance was observed for temperatures above 51°C as shown Figure 6.23, where sweep 1 corresponds to the first time the heater was raised to this temperature and sweep 2 corresponds to the second time that the heater was raised to this temperature. This figure also shows how for the first time the heater is raised to 56°C the resistance decreases linearly with increasing temperature for temperatures below that to which it has been annealed to previously, and then decreases at a much faster rate for temperatures above this. It also shows how the second time the heater is raised to this temperature the resistance again decreases linearly and reaches the same resistance value to the one that had been reached the previous time. This result suggests that the second time the heater is raised to this temperature no further changes in the structure occur. This result is also particularly interesting because the precursor $W(CO)_6$ sublimes in vacuum at ~52°C. Therefore, it may be concluded that as the annealing temperature is increased to temperatures in excess of 52°C some kind of different transformation is occurring to the one that occurs for temperatures below this.

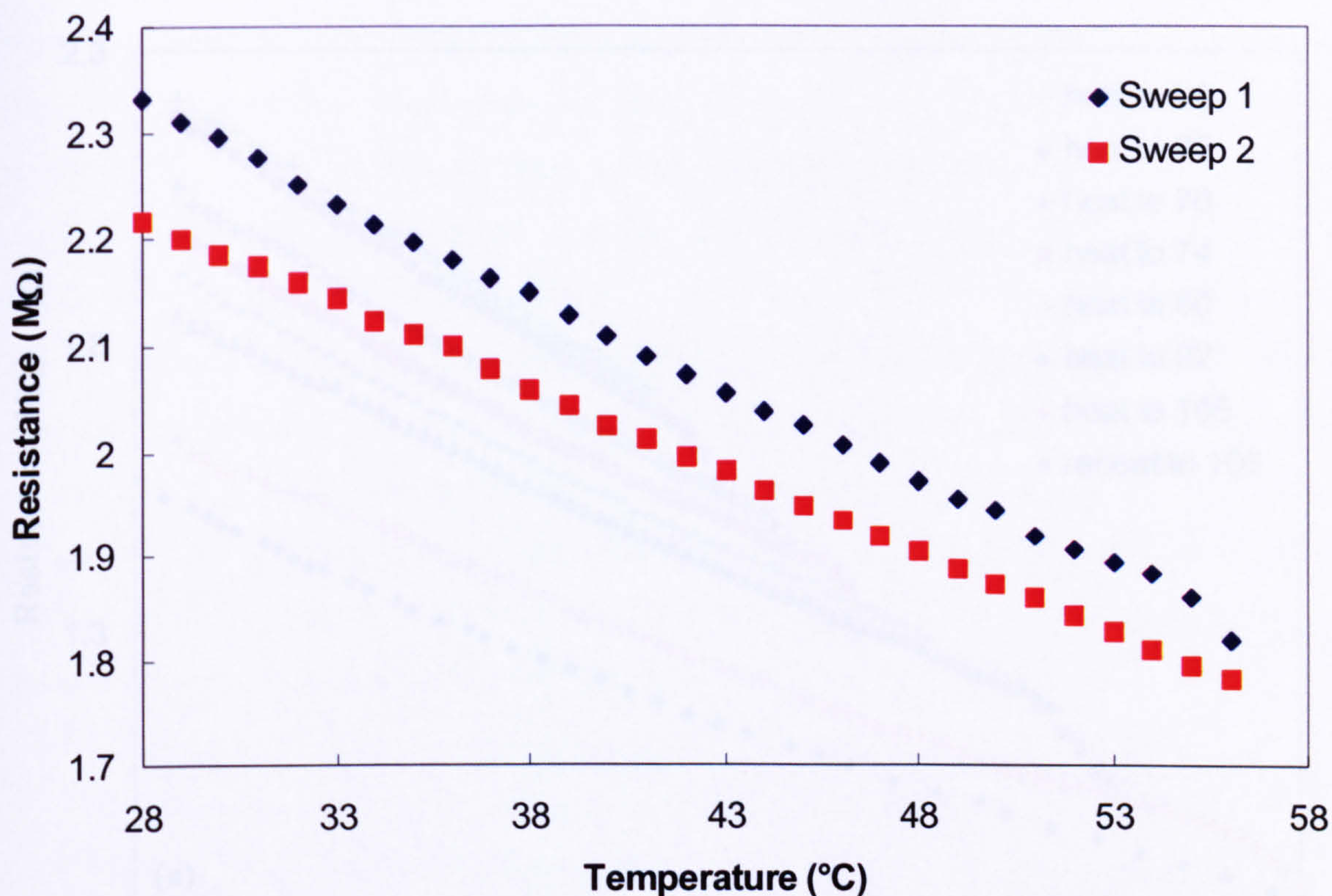


**Figure 6.23.** Graph showing the effects of annealing temperature on the resistance of a tungsten wire produced using an electron beam current of 1.5 nA and 100 passes.

A similar behaviour was observed in the resistance versus temperature characteristics each time the annealing temperature was increased up to a maximum annealing temperature of 105°C. This behaviour is summarised in Figure 6.24 (a), where the temperatures that the deposits were annealed to were 60, 65, 70, 74, 80, 92 and 105°C. The resistance of the deposit after it had been annealed at each temperature and then cooled to room temperature was also measured and the resulting data is shown in Figure 6.24 (b). This graph shows how the resistance of the deposit decreased as the temperature it had been annealed to was increased. It also shows two different regimes with the resistance of the deposit with annealing temperatures up to 51°C decreasing more slowly than it did for annealing temperatures above this. The fact that all of these changes in resistance were found to be permanent and that the rate of change in the resistance with increasing temperature suggests that there were two different structural reactions occurring. The higher decrease in resistance with increasing annealing temperature for temperatures above 51°C may also be attributed to the fact that the precursor sublimes in vacuum at 52°C and so any structural changes that occur for temperatures above this may be expected to be able to occur more easily.

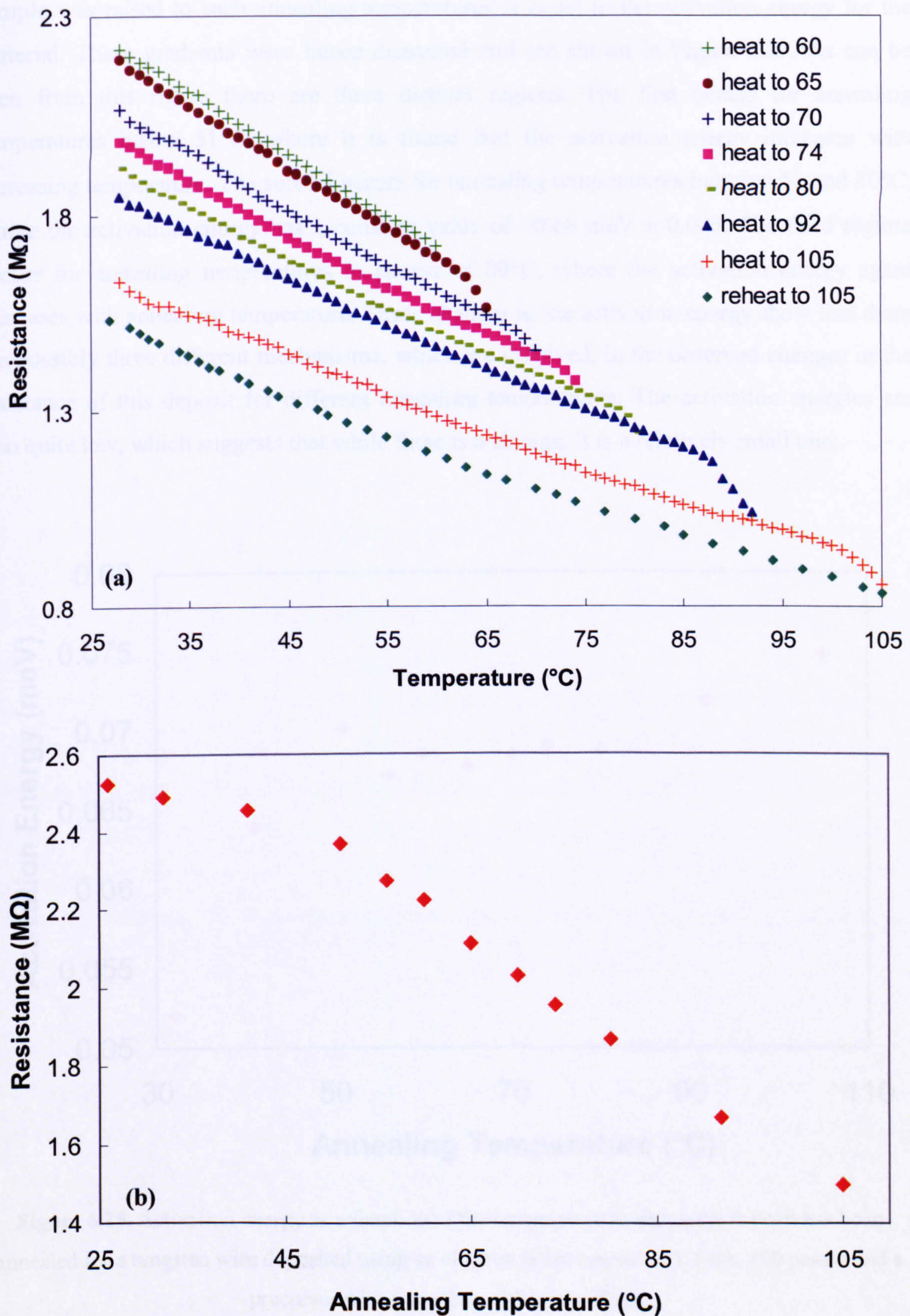


**Figure 6.24. (a)** Effects of annealing temperature on the resistance. **(b)** Change in resistance taken at room temperature as a function of the temperature to which the sample has been annealed.

The gradient of each of the resistance versus temperature plots for the second time the sample was raised to each annealing temperatures is equal to the activation energy for the material. These gradients were hence measured and are shown in Figure 6.25. As can be seen from this figure there are three distinct regions. The first occurs for annealing temperatures below 51°C, where it is found that the activation energy increases with increasing temperature. The second occurs for annealing temperatures between 52 and 80°C, where the activation energy has a constant value of ~0.68 meV ± 0.005. The third regime occurs for annealing temperatures in excess of 80°C, where the activation energy again increases with annealing temperature. These changes in the activation energy show that there are possibly three different mechanisms, which are involved, in the observed changes in the resistance of this deposit for different annealing temperatures. The activation energies are also quite low, which suggests that while there is a change, it is a relatively small one.

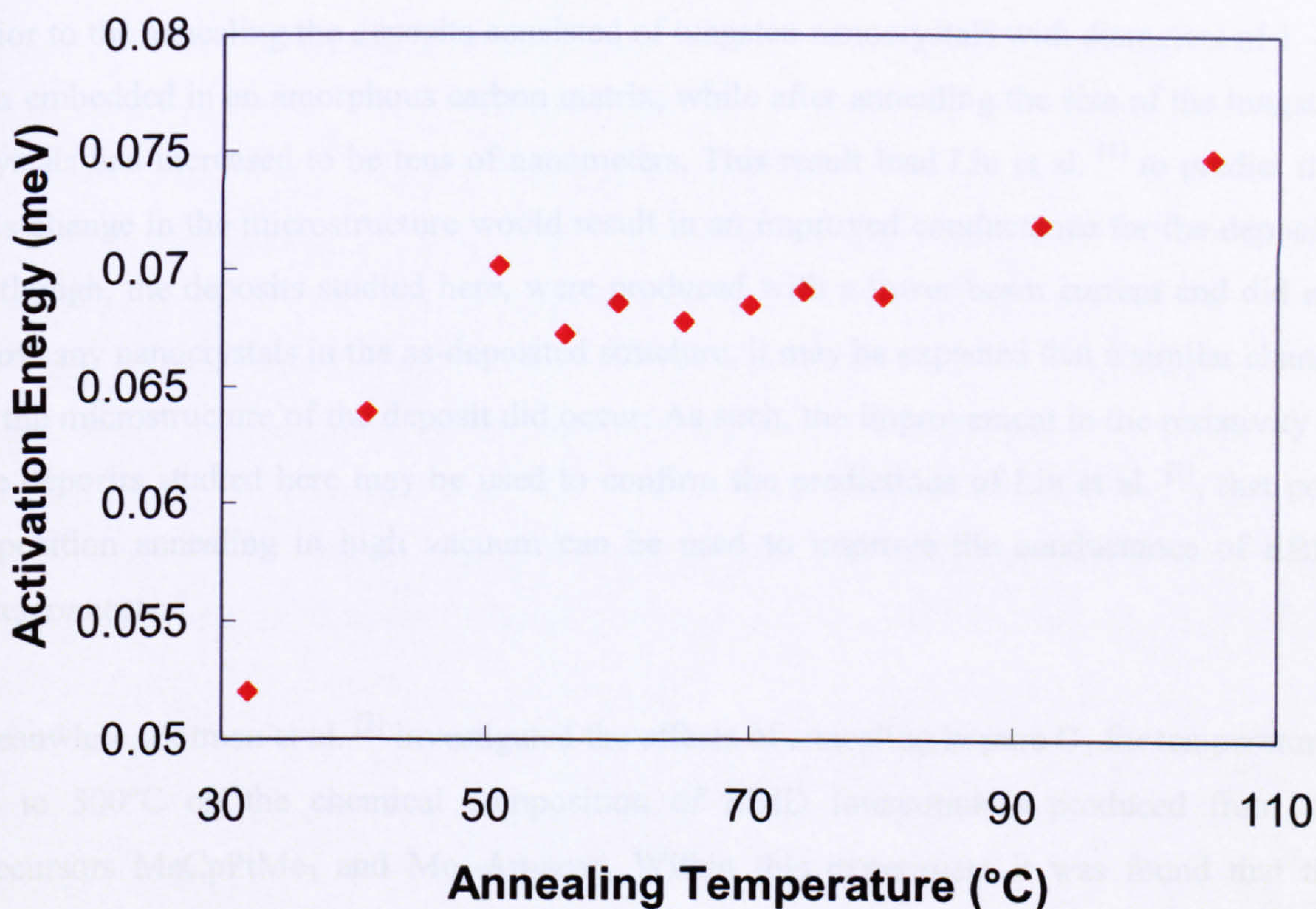


**Figure 6.25.** Activation energy as a function of the temperature to which the deposit has been annealed for a tungsten wire deposited using an electron beam current of 1.5 nA, 100 passes and a precursor with more than 120 hours of use.

To determine whether by annealing at higher temperatures the resistance of the deposits could be improved further, this experiment was repeated for another deposit that was produced using the same deposition parameters. This deposit had a higher initial resistance of 13.8 MΩ and was annealed for temperatures of up to 367°C using the same method as before. The final resistance of this deposit after it had been cooled back to room temperature was 90.9 kΩ. This result shows that by increasing the annealing temperature to 367°C, the amount of resistance improvement could also be increased such that the improvement in resistance for this deposit was two orders of magnitude.

For completeness these results may be compared to the experimental results of *Liu et al.* [1] and Botman et al. [3], who also investigated the effects of post deposition annealing on the EBID wires. In the experimental work of Liu et al. [1] tungsten deposits were fabricated from the precursor $W(CO)_6$ using a beam energy of 20 keV and were then annealed in a high vacuum environment at 900°C for fifteen minutes. TEM analysis of the deposits showed that prior to the annealing the deposits consisted of tungsten nanocrystals with diameters of 1 – 2 nm embedded in an amorphous carbon matrix, while after annealing the size of the tungsten crystals had increased to be tens of nanometers. This result lead Liu et al. [1] to predict that this change in the microstructure would result in an improved conductance for the deposits. Although, the deposits studied here, were produced with a lower beam current and did not show any nanocrystals in the as-deposited structure, it may be expected that a similar change in the microstructure of the deposit did occur. As such, the improvement in the resistivity of the deposits studied here may be used to confirm the predictions of Liu et al. [1], that post deposition annealing in high vacuum can be used to improve the conductance of EBID interconnects.

Meanwhile, Botman et al. [3] investigated the effects of annealing in pure $O_2$ for temperatures up to 500°C on the chemical composition of EBID interconnects produced from the precursors $MeCpPtMe_3$ and $Me_2$-Au-acac. Within this experiment it was found that the annealing caused the amount of carbon incorporated in the structures to be reduced and for nanometer sized metal grains to be formed in the deposits. Furthermore, it was found that as the annealing temperature was increased, the concentration of metal in the deposits increased, with significant changes occurring for the platinum deposits for temperatures between 100 and 300°C and for the gold deposits for temperatures between 250 and 500°C. The resistivity of these deposits was also measured and it was found that the resistivity

decreased with increasing annealing temperature, with the most significant changes occurring for the same temperatures as for the most significant changes in the elemental composition of the deposits. This result suggests that the more significant change in the resistivity of the deposits studied here for temperatures in excess of 50°C is due to the material subliming and a thermal activation process, which allows for some of the carbon within the deposits to be removed. Botman et al. [3] also found that for this temperature range, the resistivity of the platinum deposits improved by three orders of magnitude, which is in agreement with the amount of improvement in the resistivity that was seen for the deposits studied here.

### 6.4.3 Discussion

The experimental work that has been reviewed in this section has shown that the resistance of electron beam deposited tungsten interconnects can be improved by post deposition annealing. In particular it has been found that while annealing at temperatures of up to 367°C, the resistance of a deposit produced using an electron beam current of 1.5 nA and 100 passes can be improved by two orders of magnitude. This is particularly useful because as shown in section 5.3 the resistivity of electron beam deposited tungsten interconnects is high and needs to be improved in order to make EBID useful as a mainstream fabrication technique for the production of interconnects. In this section the effects of annealing at temperatures up to 105°C have also been investigated in more detail and it has been shown that the amount of resistance change that can be gained is dependent on the temperature. This has been attributed to the different structural changes that can occur as the annealing temperature has been changed.

In this work the effects of annealing on the structure of the deposits has also been investigated and it has been found that even annealing at temperatures near 1000°C, it was not possible to cause significant structural transformations to occur. Therefore, this work suggests that if the structural changes that were seen in section 6.3 were due to ohmic heating of the deposits, then the temperature to which the deposits were heated must have been higher than this.

## 6.5 Conclusions

Within this section it has been shown that deposits exposed to currents below 100 μA have stable electrical characteristics, while deposits exposed to currents in excess of this show significant changes in their resistivity. This has been attributed to structural changes in the deposits, which occur as a result of ohmic heating of the deposited material. When these deposits are then exposed to currents in excess of 1 mA, the structure of the deposits has been found to break down. These results demonstrate that electron beam deposited wires are suitable for applications in which high resistivities are acceptable and when only low currents are going to be used.

Within this section, several methods of being able to improve the resistivity of the deposited material have been investigated. In particular, it has been found that heating the substrate to temperatures in the range of 30 to 75°C during the deposition process can result in deposits with a lower resistivity. Also the post deposition annealing of the deposits has been investigated and it has been found that by annealing at 367°C the resistivity of the deposits could be improved by two orders of magnitude. These results have been found to be in good agreement with the experimental results of others, who have carried out similar investigations. However, while this process does improve the resistivity of the deposited wires, it also involves more a complicated process, which is undesirable as it increases the cost, complexity and fabrication time of EBID devices.

## 6.6 References

[1] Z.-Q. Liu, K. Mitsuishi and K. Furuya, Jpn. J. Appl. Phys. **45**, 5548 (2006).

[2] V. Gopal, V. Radmilovic, C. Daraio, S. Jin, P. Yang and E. A. Stach, Nano Lett. **4**, 2059 (2004).

[3] A. Botman, J. J. L. Mulders, R. Weemaes and S. Mentink, Nanotechnol. **17**, 3779 (2006).

# CHAPTER SEVEN

## 7 Electrical Conduction of Suspended Multi-Walled Carbon Nanotubes

### 7.1 Introduction

In Chapters Four, Five and Six, the use of electron beam deposited tungsten nanowires as an interconnect material for nanoscale applications was investigated. The results of this work show that while this approach allows for nanowires to be fabricated with nanometer accuracy at specific locations, the nanowires had a high resistivity which is unsuitable for many electronic applications. As such this chapter investigates another of the most common types of nanoscale interconnect, which are known as multi-walled carbon nanotubes. This type of nanowire has much lower resistances and so may be suitable for use in interconnect applications where the power dissipation and the resistance is crucial. Therefore, in this chapter the electrical transport measurements of suspended arc-discharge MWNTs coated with a thin polymer layer are investigated using high precision manipulators within a scanning electron microscope. This experimental set-up has been chosen as it allows for the MWNTs themselves to be electrically characterised without the influence of substrate-nanotube interactions. Furthermore, the nanotubes have undergone minimal processing, which may alter the electrical properties of the nanotubes. The resulting experimental work shows that the conductance-voltage characteristics of the MWNTs are symmetric with respect to voltage and that the conductance improves with multiple cycling of the voltage. Estimates of the transmission coefficients associated with the semiconducting sub-bands and the contacts of the nanotubes have also been made.

## 7.2 Experimental Method

The experimental work carried out in this chapter was conducted using the Cambridge Instruments Stereoscan 250, MK3 SEM that was described in section 3.2.1 and the custom manufactured, remote controlled manipulation system made using Omicron MS5 piezo-sliders as described in section 3.6.2. This manipulation system allowed for two electrochemically etched tungsten probes, with tip radii between 25 and 400 nm to be moved separately in each of the three orthogonal directions so that they could be used to contact to the carbon nanotubes. An electrical feedthrough was also used to connect a Keithley 238 Source-Measurement Unit to each of the probes and to the SEM stage to allow for samples examined within the microscope to be electrically characterised using up to three terminals.

The MWNTs were synthesised using an arc-discharge process and purified using a micro-filtering process. The resulting nanotube rich powder was dispersed into a polystyrene–toluene solution and as-cast composite films were pressed at 150-200 °C for thirty minutes as described in reference [1]. The resulting composites had a nanotube to polymer ratio of 1:3 and were cleaved to expose the nanotubes. Figure 7.1 (a) shows a typical SEM image of a cleaved nanotube-polymer sample. HRTEM images of the MWNTs used in this study showed that the nanotubes were of high quality as may be expected of MWNTs produced by the arc discharge method and were covered in a thin polymer layer. The images also showed that the nanotubes had an exposed length of 2 - 12 μm, an average outer diameter of ~13 nm and a polymer coating of up to 30 nm. Figure 7.1 (b) shows a high-resolution image of a typical MWNT that was imaged using the Philips CM 200 TEM described in section 3.3.1.

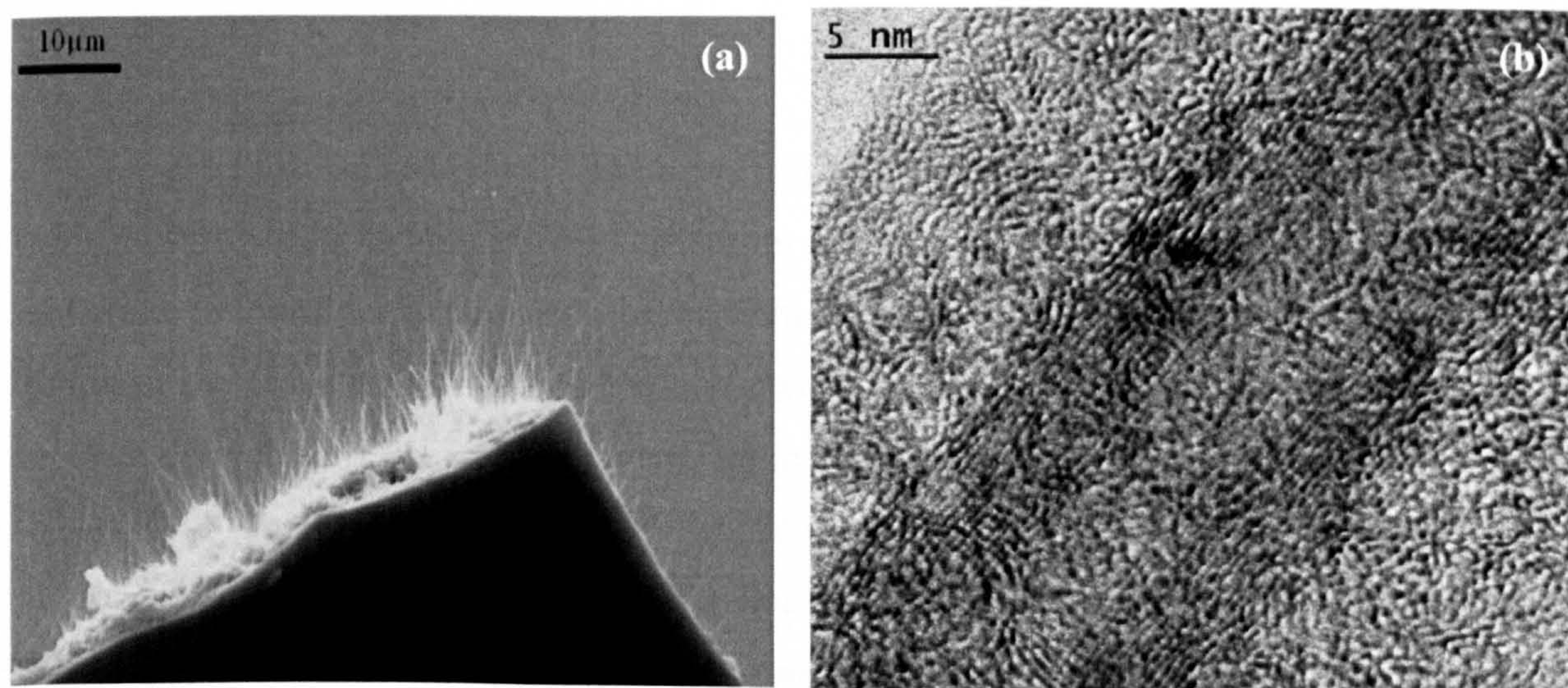


**Figure 7.1. (a)** SEM image of a typical nanotube-polymer sample. **(b)** HREM image of a MWNT with a ~14 nm thick polymer coating.

This set-up allowed for a single suitable nanotube to be first located using the SEM and then for one of the probes to be brought into contact with the nanotube using careful manipulation as shown in Figure 7.2. In order to help achieve this a positive bias was applied to the tungsten tip being manipulated using a Keithley 238 source-measurement unit. This creates an electrostatic attraction between the tip and nanotube and helps to form good electrical and mechanical contacts.

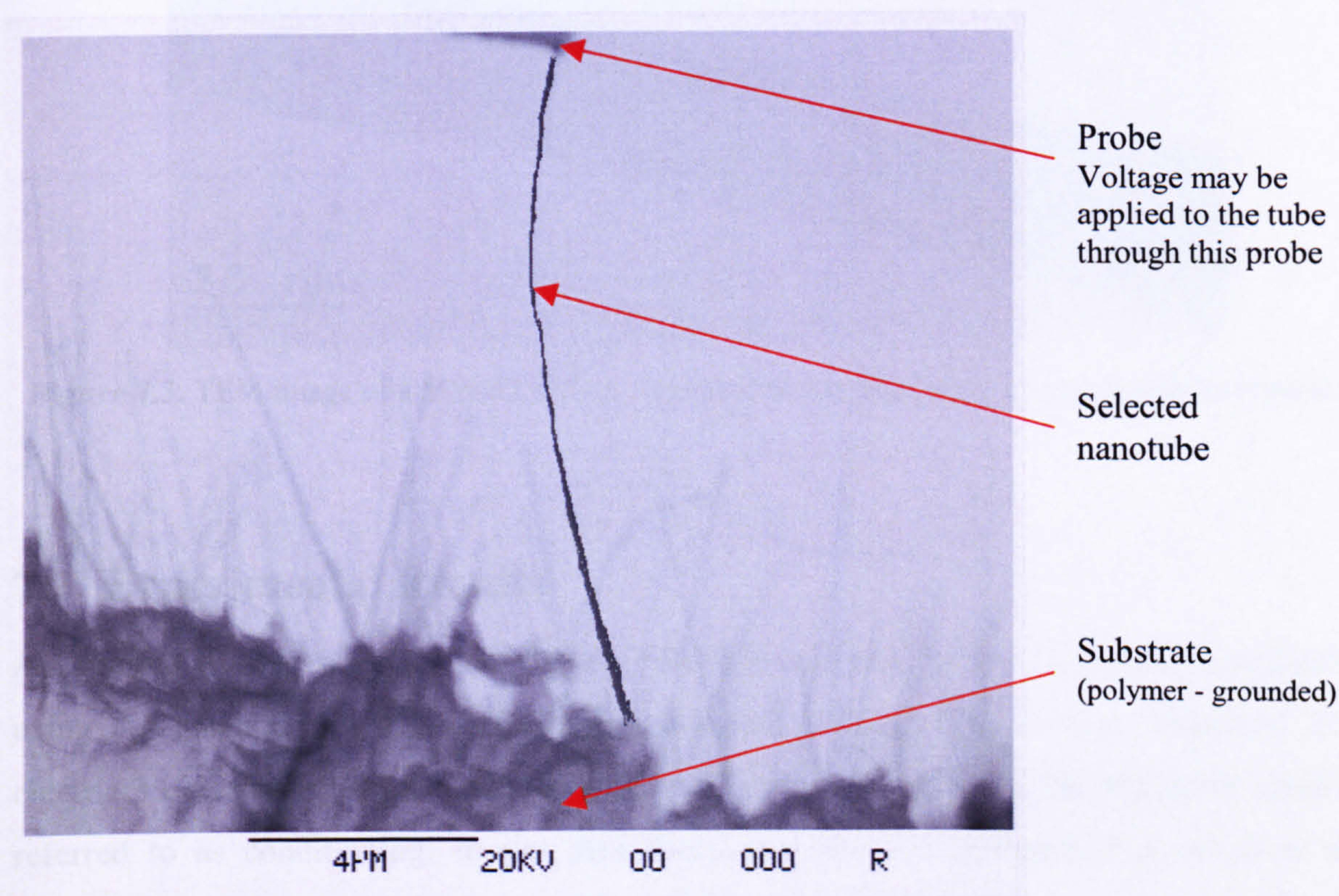


**Figure 7.2.** SEM image of a protruding polymer coated MWNT, which is attached to a sharpened tungsten probe. The nanotube has been enhanced in this image for clarity.

Once a good mechanical contact had been achieved, the electron beam within the SEM was turned off in order to minimize its affect on the properties of the nanotubes. A LabView software program was then used to perform conventional current-voltage measurements between the probe and the sample, which was grounded, over an appropriate voltage range up to a defined current limit, which was set in order to prevent premature destruction of the nanotubes. The voltage cycles were initialised at 0 V, then increased to a maximum positive voltage, before being decreased to a maximum negative voltage and then finally increased back to 0 V. In a perfectly stable I-V measurement this allows for the residual capacitance in the measurement system to be averaged out. After the electrical characterisation of several

MWNTs, the nanotubes were broken near to the polymer composite and the resulting nanotube-probe structures were placed onto standard copper TEM grids. TEM images of these structures were then taken and showed that the electron beam caused no noticible damage to the MWNTs during their imaging (see Figure 7.3).

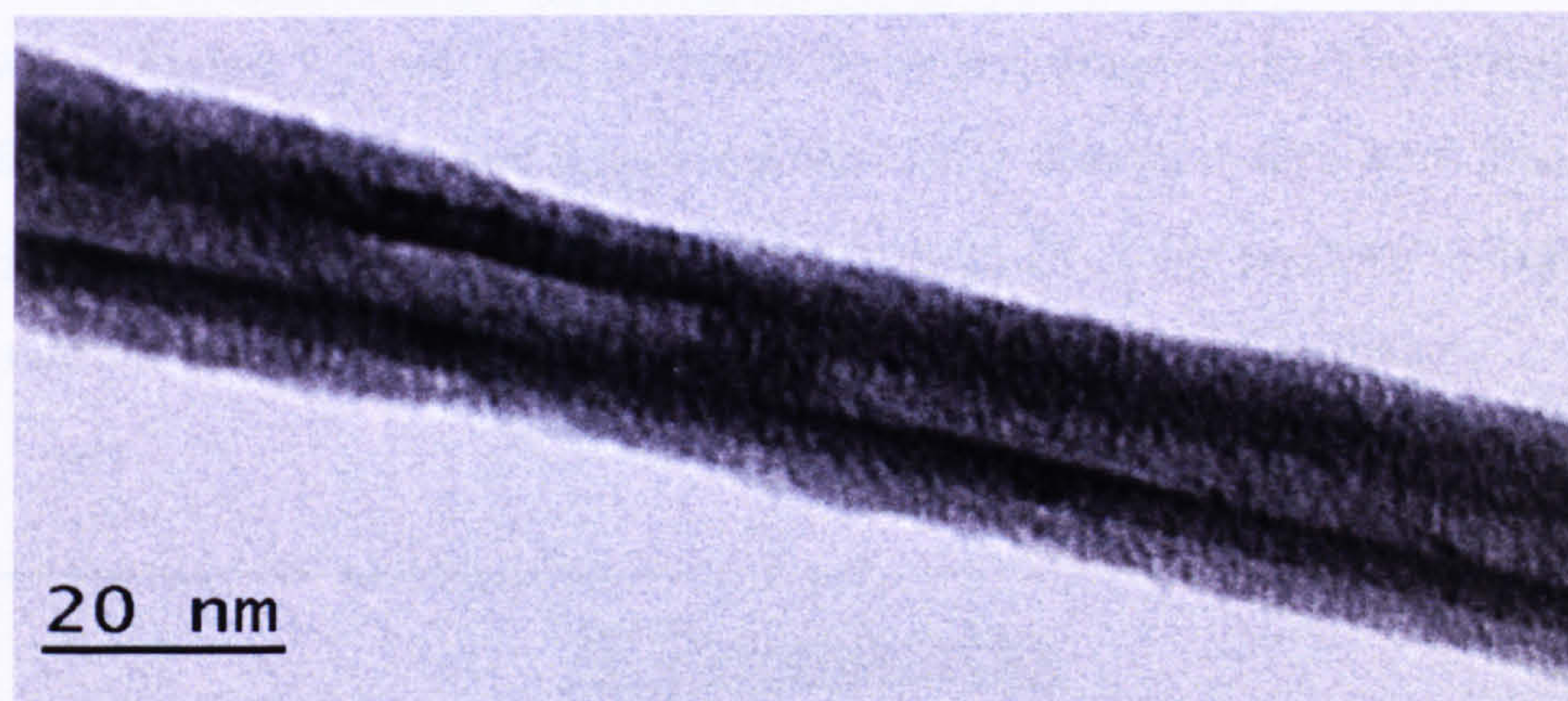


**Figure 7.3.** TEM image of a MWNT with a 5 nm polymer coating after electrical characterisation.

## 7.3 Experimental Results

Approximately fifty nanotube devices with lengths between 2 and 12 μm were investigated using this method and it was found that repeated cycling of the voltage improved their electrical characteristics as shown in Figure 7.4. From here on this improvement shall be referred to as conditioning. It was also found that the I-V characteristics of all of the nanotubes studied were highly symmetric with respect to zero voltage.

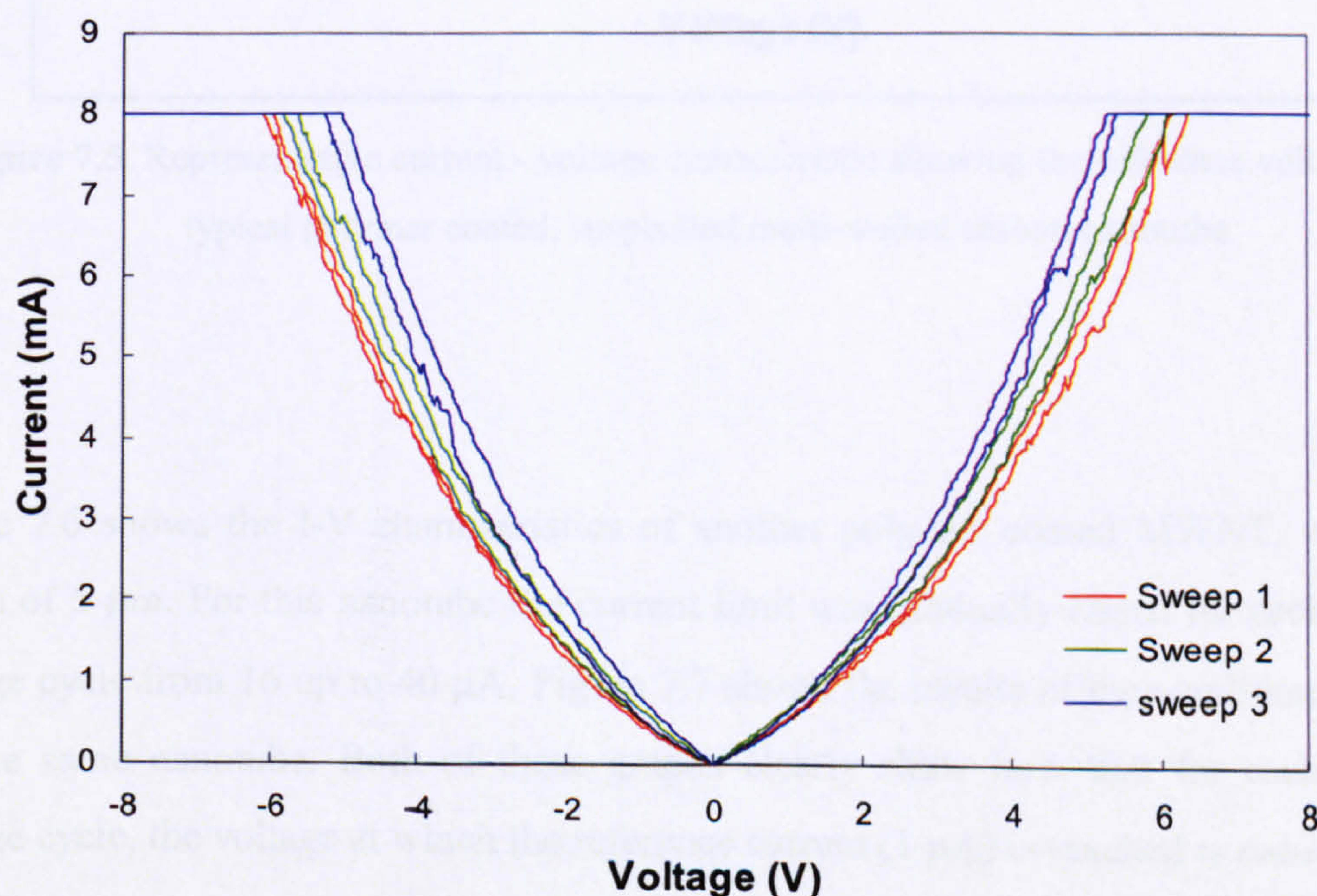


**Figure 7.4.** I-V characteristics of a typical undoped, polymer coated 3μm long nanotube.

## 7.4 Analysis of I-V Characteristics

In order to quantify the amount of conditioning that occured for each of the devices tested, a reference current (typically 1 μA) was defined for each device and the voltage was measured each time it equaled this current. These voltages were defined as the reference voltages ($V_{1-4}$) as shown in Figure 7.5 and were averaged for each voltage cycle. The average reference voltages for both the positive and negative parts of the voltage cycles were then calculated, where $V_{12}$ was defined as the average reference voltage ($V_{ref}$) for positive voltages at the set reference current and $V_{34}$, the average reference voltage for negative voltages.

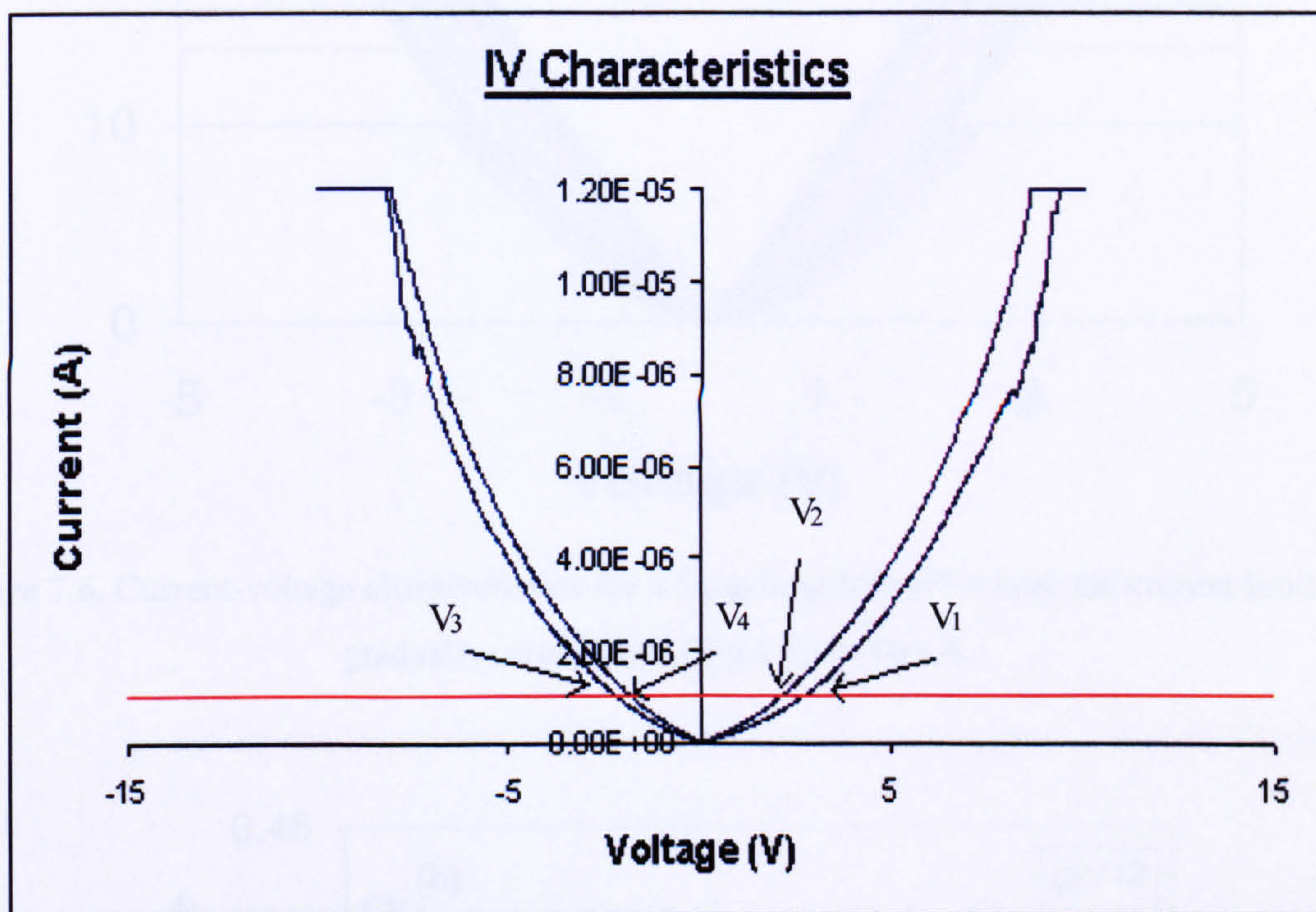


**Figure 7.5.** Representative current - voltage characteristic showing the reference voltages for a typical polymer coated, suspended multi-walled carbon nanotube.

Figure 7.6 shows the I-V characteristics of another polymer coated MWNT, which had a length of 5 μm. For this nanotube the current limit was gradually raised for each successive voltage cycle from 16 up to 40 μA. Figure 7.7 shows the results of the conditioning analysis for the same nanotube. Both of these graphs clearly show how that for each successive voltage cycle, the voltage at which the reference current (1 μA) is reached is reduced.

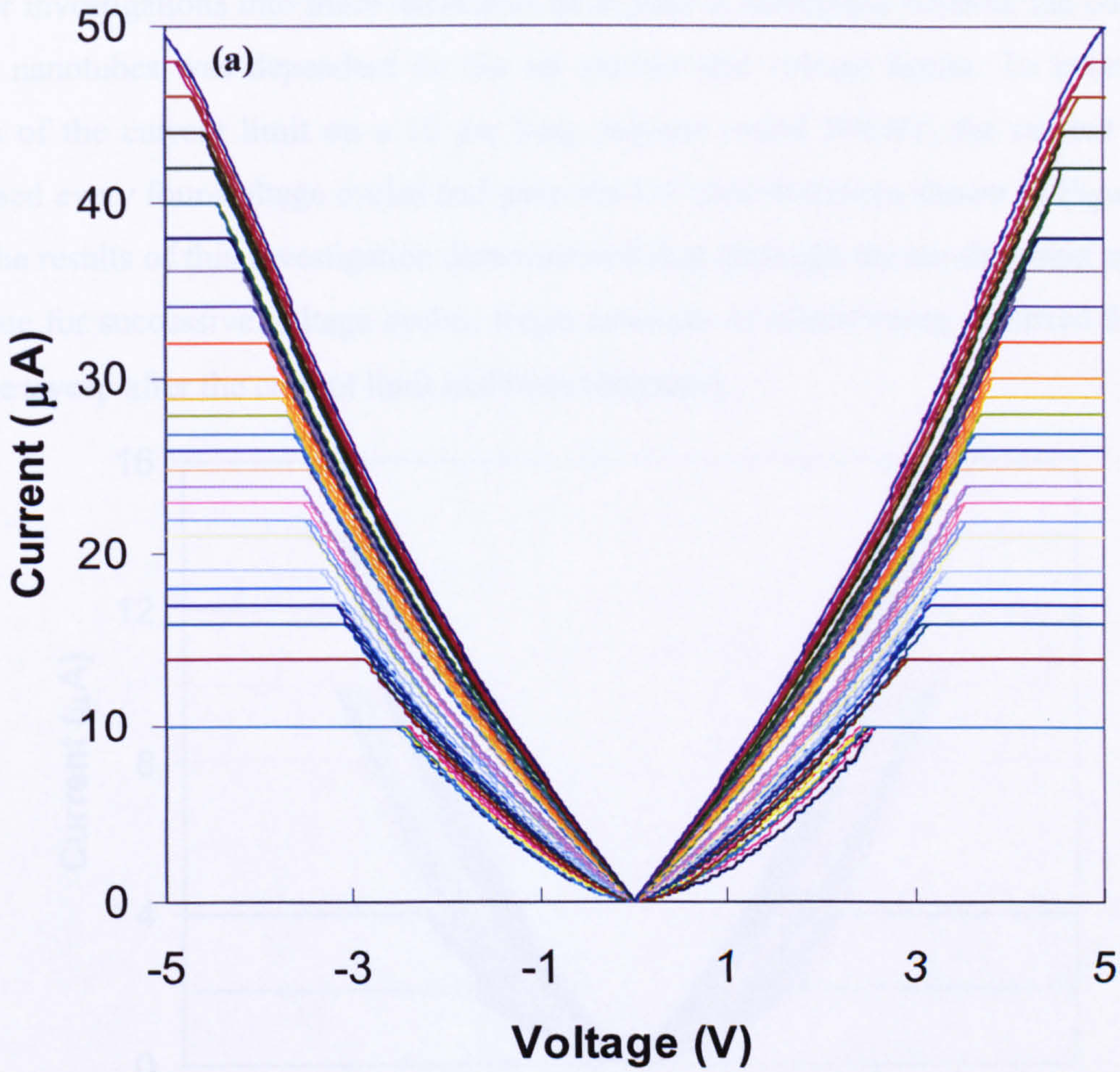


**Figure 7.6.** Current-voltage characteristics for a 5 μm long MWNT where the current limit was gradually raised from 16 μA up to 40 μA.

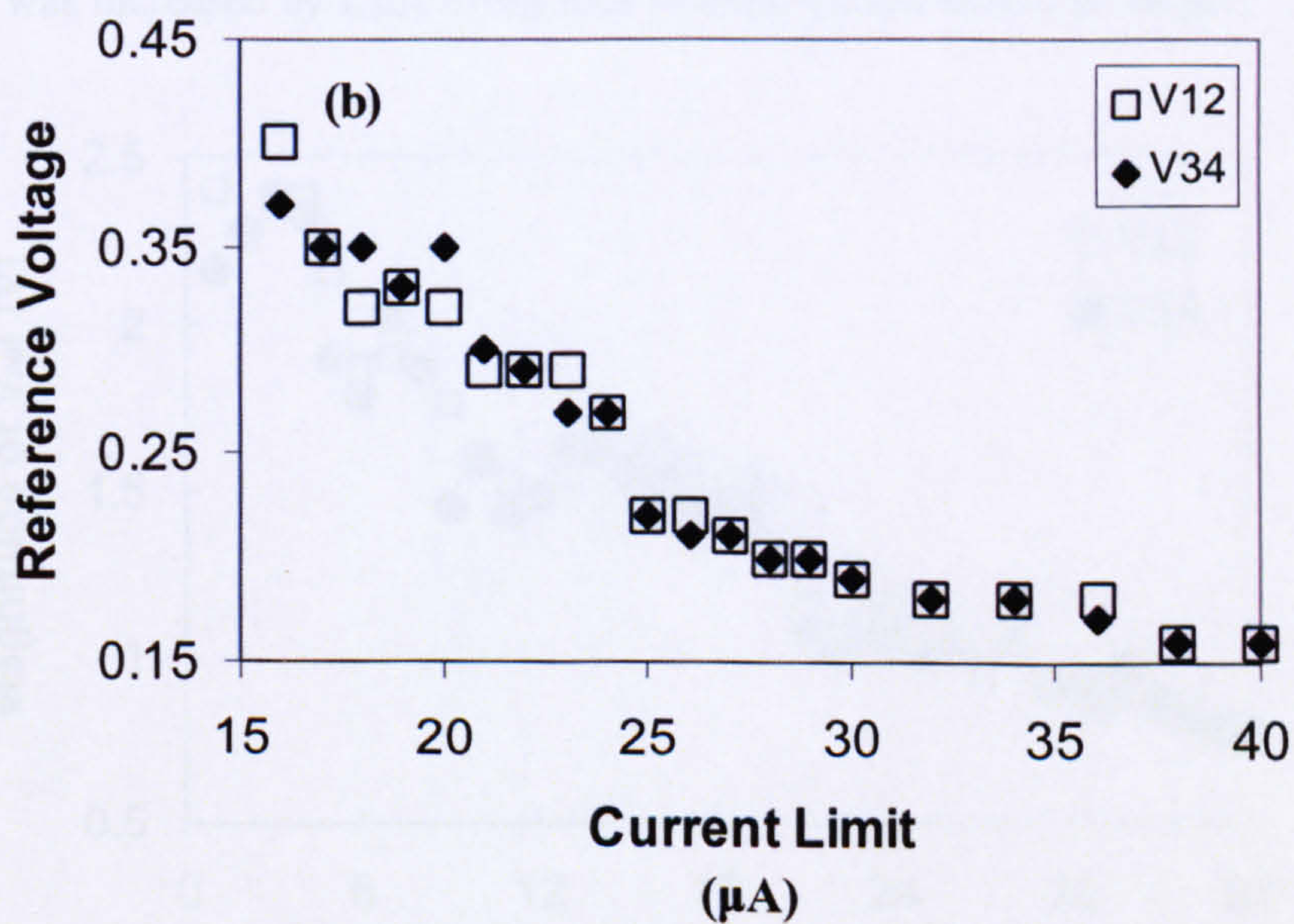


**Figure 7.7.** Variation of the average reference voltage as a function of current limit for a reference current of 1 μA for the 5 μm long MWNT given in Figure 7.6.

Further investigations into these nanotubes attempted to determine whether the conditioning of the nanotubes was dependent on the set current and voltage limits. To investigate the effects of the current limit on a 10 μm long, polymer coated MWNT, the current limit was increased every four-voltage cycles and gave the I-V characteristics shown in Figure 7.8 and 7.9. The results of this investigation demonstrated that although the conditioning appeared to continue for successive voltage cycles, larger amounts of conditioning occurred for the first voltage sweep after the current limit had been increased.

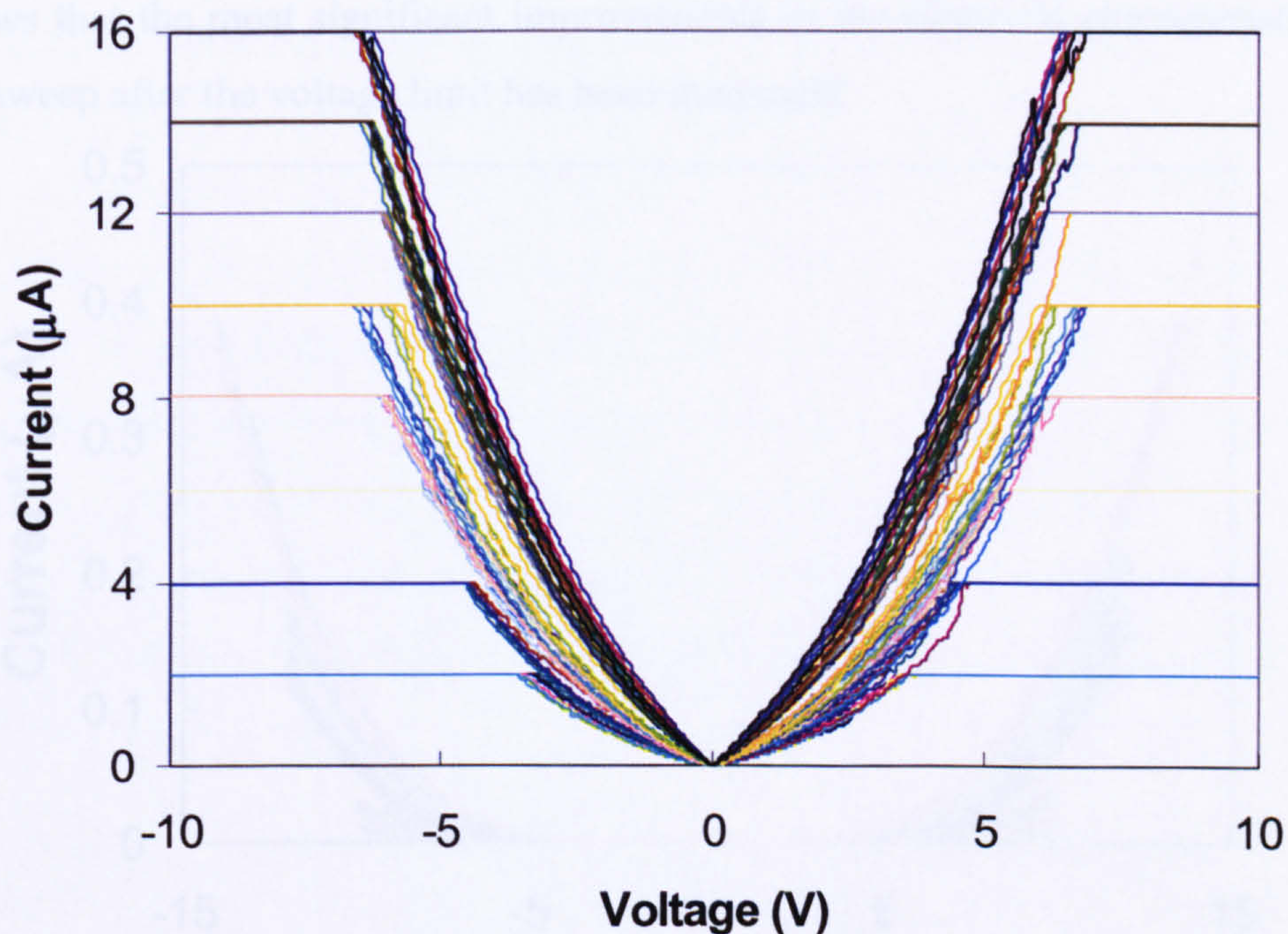


**Figure 7.8.** I-V characteristics of a 10μm long MWNT at different current limits. The current limit was increased by 2 μA every four voltage cycles, from 2 to 16 μA.

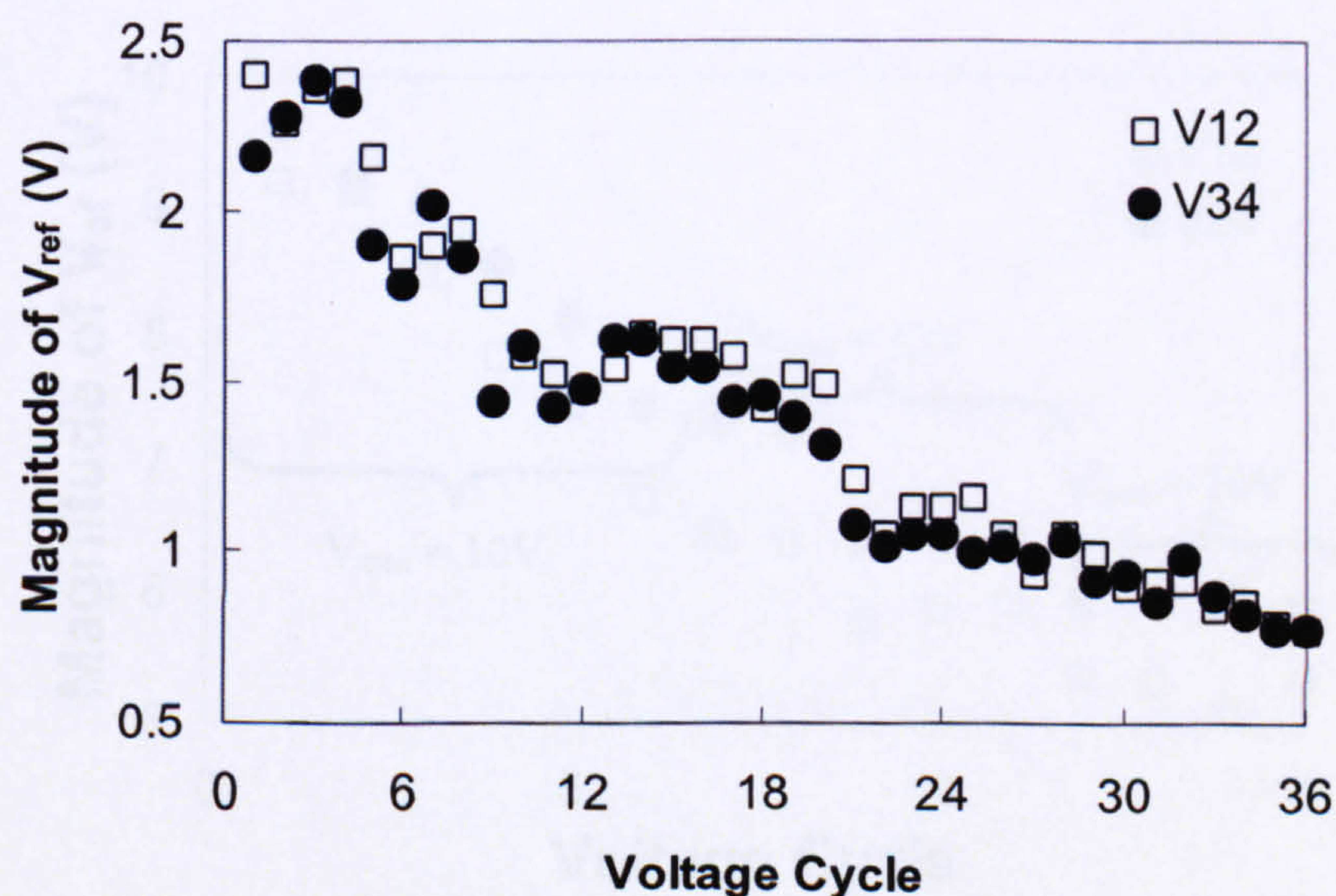


**Figure 7.9.** Variation of the magnitude of the average reference voltage of MWNT given in Figure 7.8 as a function of current limit for a reference current of 1 μA.

To investigate the dependency of the voltage on the conditioning of a nanotube, the voltage limit was increased from 10V to 12V after the first five cycles and then to 14V after the next six cycles, whilst the current limit was kept constant. This gave the results shown in Figure 7.10 and 7.11. Figure 7.10 shows how for the lower voltage limits, the voltage sweep does not reach high current values. It also shows that as the voltage limit is increased the amount of current that flows for a given voltage increases by a considerable amount and hence the electrical characteristics of this nanotube improve. Again, careful analysis of Figure 7.11 also shows that the most significant improvements in the electrical characteristics occur in the first sweep after the voltage limit has been increased.

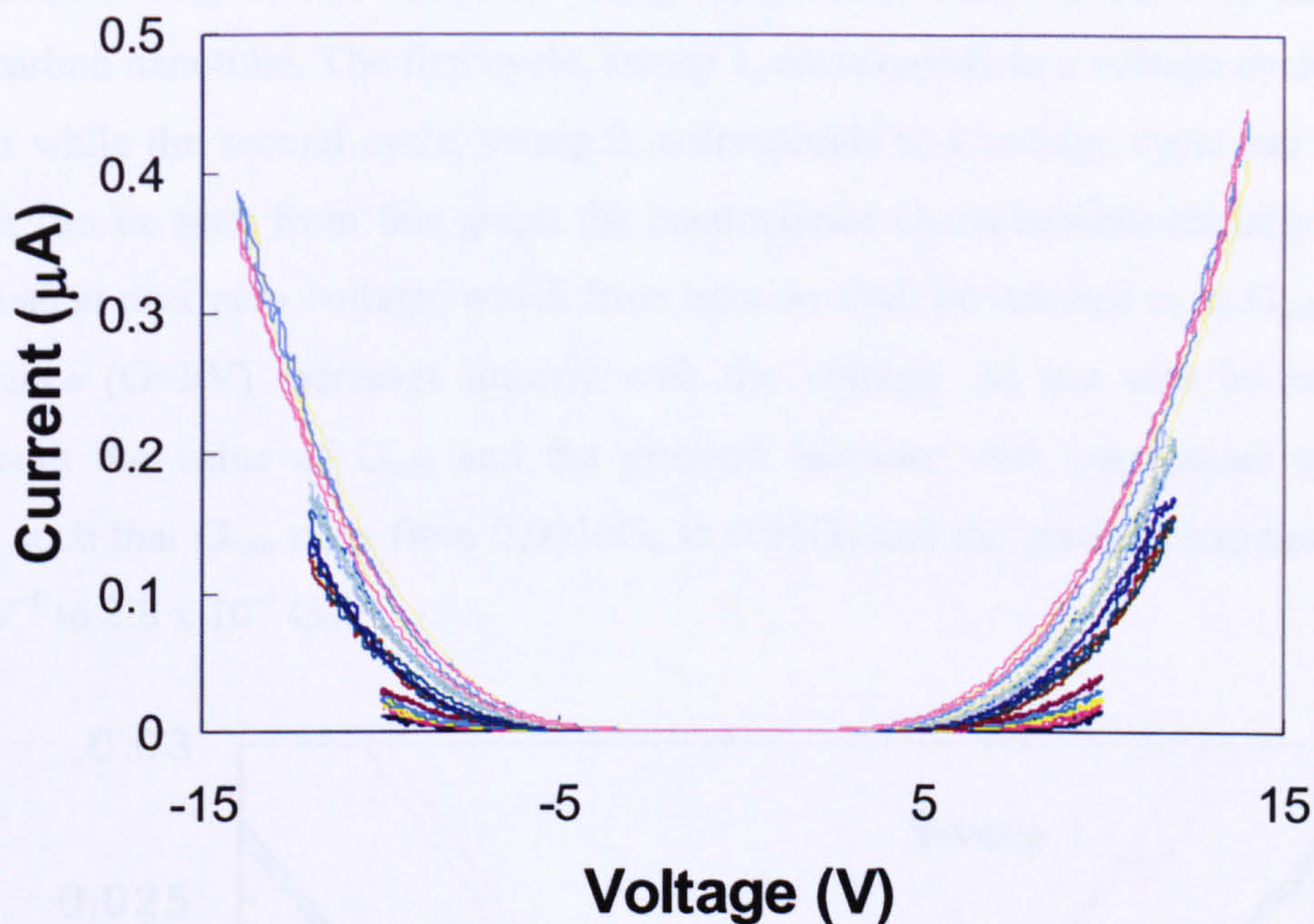


**Figure 7.10.** I-V characteristics of a 2μm polymer coated MWNT at different voltage limits.

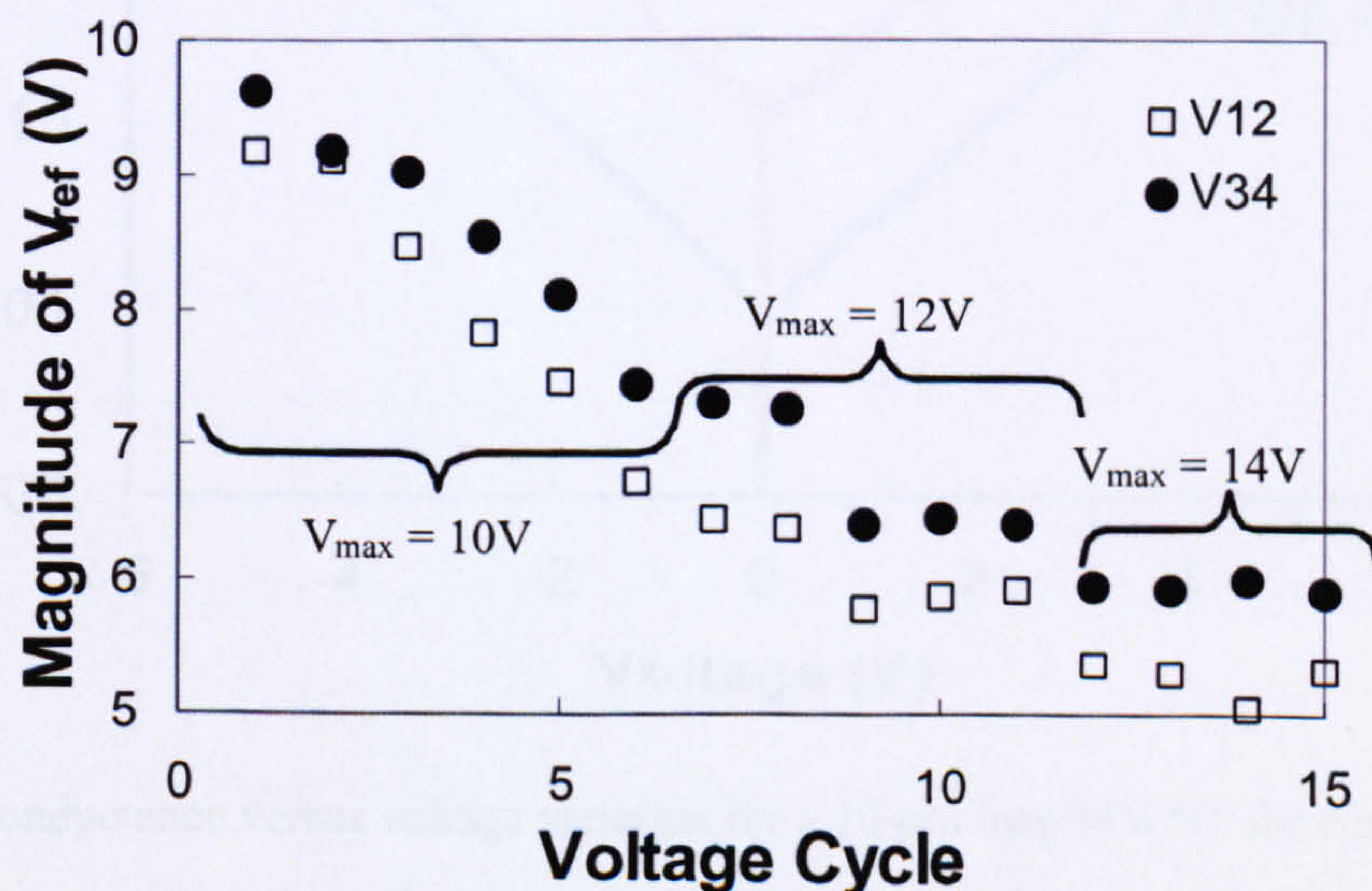


**Figure 7.11.** Variation of the average reference voltage of a 2 μm long MWNT as a function of current limit for a reference current of 1 μA for voltage limits of ± 10, ± 12 and ± 14 V.

These figures indicate that while the resistance of the nanotube devices improves for successive voltage cycles, increasing either the current or the voltage limit results in a greater improvement than average for the following voltage cycle.

## 7.5 Conductance Analysis

The current - voltage characteristics described above may be analyzed further by considering the conductance versus voltage characteristics of the nanotubes. Figure 7.12 shows the conductance ($G/G_0$) of two different voltage cycles that were run on a 10 μm long multi-walled carbon nanotube. The first cycle, sweep 1, corresponds to a voltage cycle run with a 2 μA limit while the second cycle, sweep 2, corresponds to a voltage cycle run with a 16 μA limit. As can be seen from this graph the conductance characteristics initially have a small flat plateau at near zero voltage, which from here on shall be referred to as $G_{min}$ and then the conductance ($G=I/V$) increases linearly with the voltage. As can also be seen from this graph, both the value of $G_{min}$ and the gradient increase with continuous cycling of the voltage, such that $G_{min}$ rises from $0.0036G_0$ to $0.01G_0$ and the gradient increases from $1.5 \times 10^{-3}\ G_0V^{-1}$ to $2.8 \times 10^{-3}\ G_0V^{-1}$.

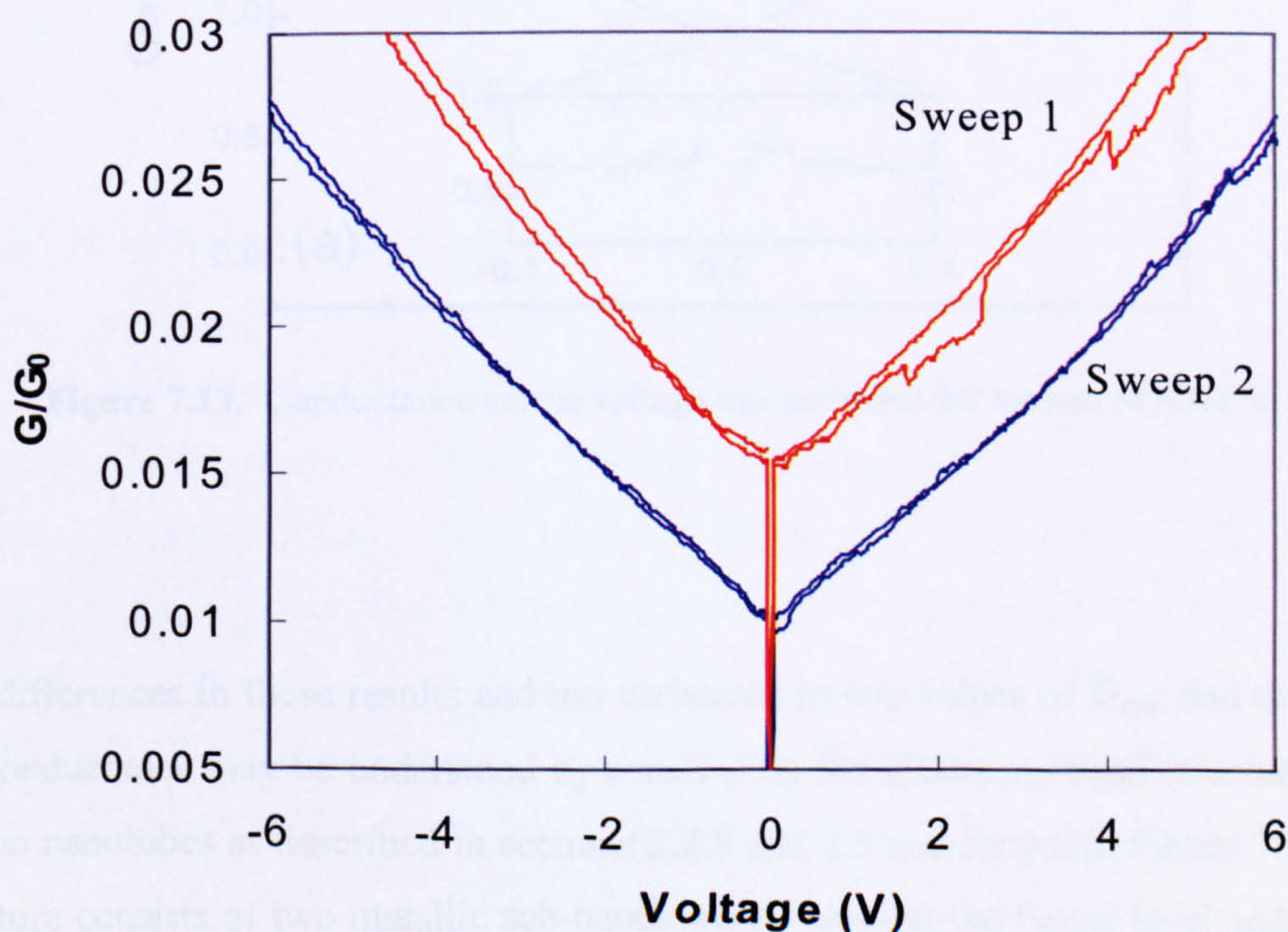


**Figure 7.12.** Conductance versus voltage variation for a 10 μm long MWNT for current limits of 2 μA (sweep 1) and 16 μA (sweep 2).

These conductance characteristics have a similar shape to those observed by Poncharal et al. [2] as shown in Figure 7.13 and Liang et al. [3], who both observed ballistic conduction in multi-walled carbon nanotubes. They are also similar to those observed by Tsutsui et al. [4], who concluded that their conductance characteristics were either due to ballistic conduction with a sub-band contribution increasing with voltage bias or due to diffusive conduction with an inner shell contribution also increasing with voltage bias. Indeed Poncharal et al. [2] achieved a minimum conductance value at near zero voltage of $0.9G_0$ as can be seen in Figure 7.13, while Liang et al. [3] measured their $G_{min}$ value as $0.4G_0$. Meanwhile Tsutsui et al. [4] observed minimum conductance's in the range of $0.3G_0$ to $1.6G_0$.

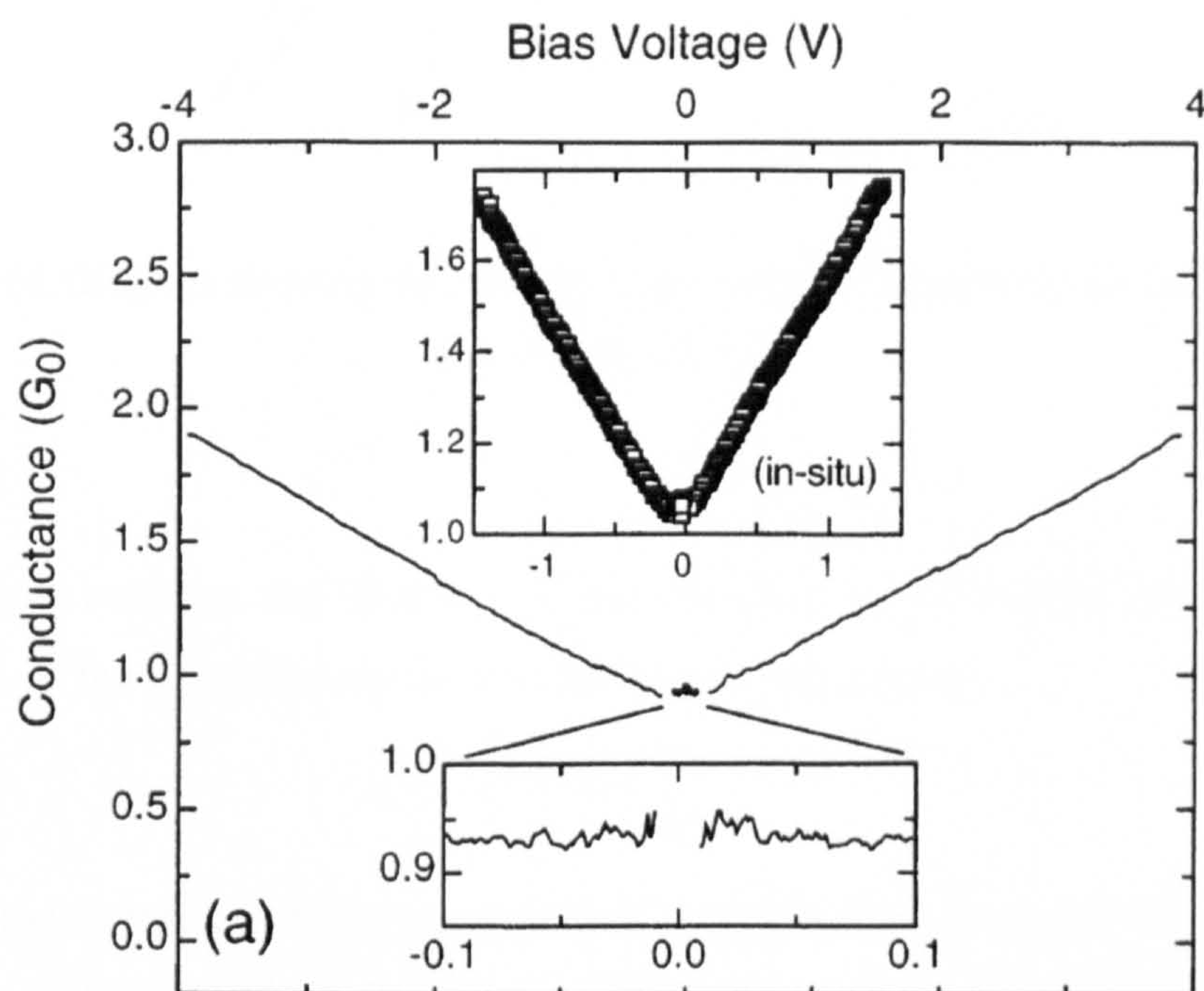


**Figure 7.13.** Conductance versus voltage measurement for a clean MWNT in air. [2]

The differences in these results and the variations in our values of $G_{min}$ and the gradient of the conductance may be understood by considering the electronic band structure of metallic carbon nanotubes as described in sections 2.2.8 and 2.3 and shown in Figure 7.14. The band structure consists of two metallic sub-bands which cross at the Fermi level and a number of occupied and unoccupied sub-bands, which are positioned above and below the Fermi level with semiconducting characteristics. The corresponding density of states diagram shows that each time the energy required to enter a new sub-band is reached, a sharp peak occurs.

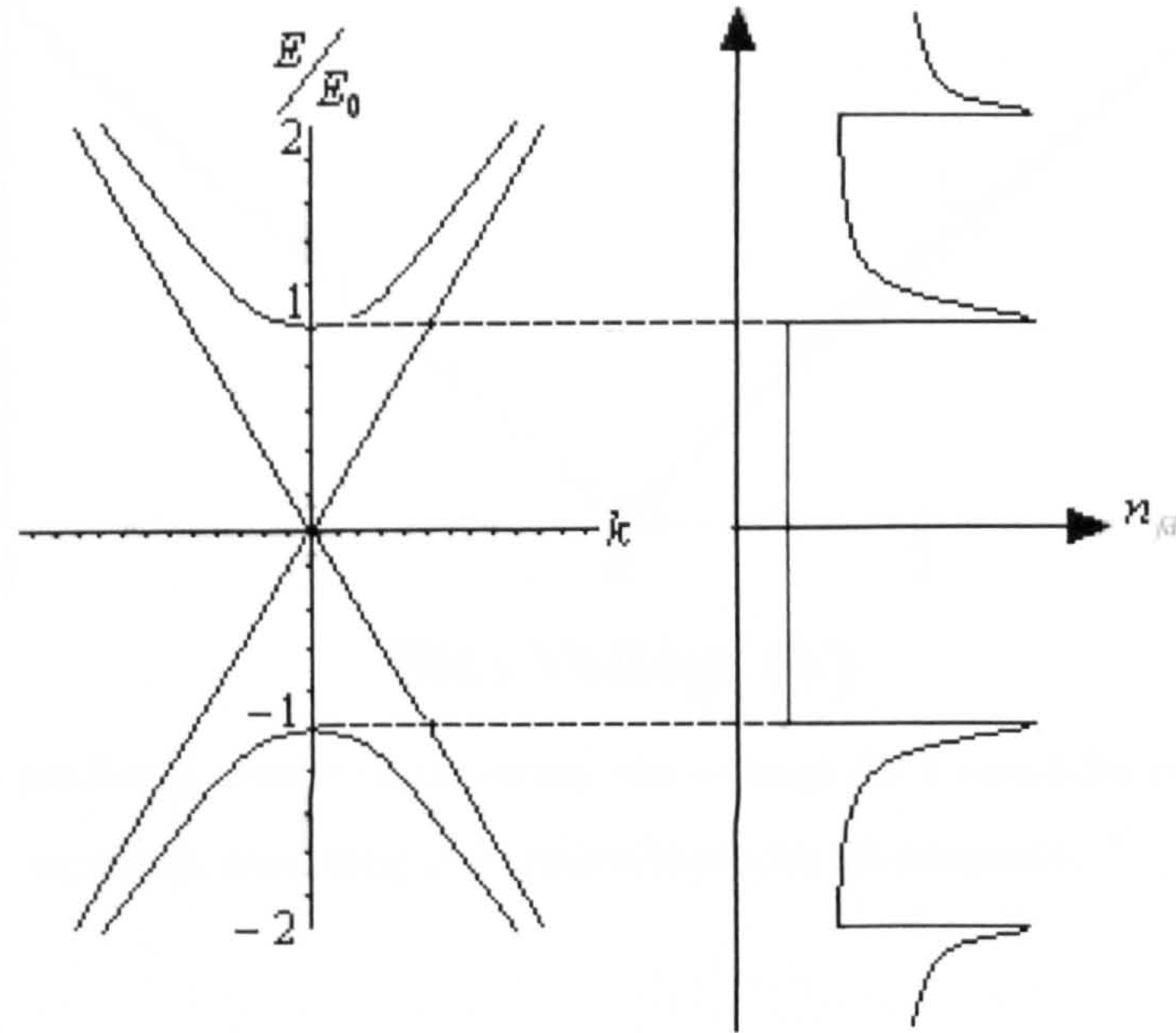


**Figure 7.14.** Diagram showing the band structure (left) and the density of states (right) of a metallic CNT.

The band gap between the first set of semiconducting sub-bands is proportional to the diameter, D, of the nanotube and is described by the equation:

$$\Delta E = \frac{6\gamma_0 a}{D_{CNT}} \propto \frac{1}{D_{CNT}} \tag{7.1}$$

where $\gamma_0$ is the energy overlap integral, which is approximately equal to 3 eV, $a$ is the carbon – carbon bond length, which is equal to 0.14 nm and $D_{CNT}$ is the diameter of the carbon nanotube being investigated in nanometers. [5] High-resolution TEM images of the MWNTs used in this study showed a typical nanotube diameter of 13 nm, which means that if the nanotube is metallic it has a semiconducting energy band separation of ΔE = 0.19 eV. As this value is much greater than kT at room temperature, at voltages below this value only the two metallic sub-bands will contribute to the transport and produce the flat plateau near V = 0 in Figure 7.14. This plateau is determined by Landauer's equation and takes into account the contributions of scattering at the contacts and from the two conducting sub-bands, such that:

$$G_{\min}(V = 0) = 2G_0 T_m T_c \tag{7.2}$$

where, $G_0 = 2e^2/h$, $T_m$ is the transmission coefficient of the metallic sub-bands and $T_c$ is the transmission coefficient of the contacts.

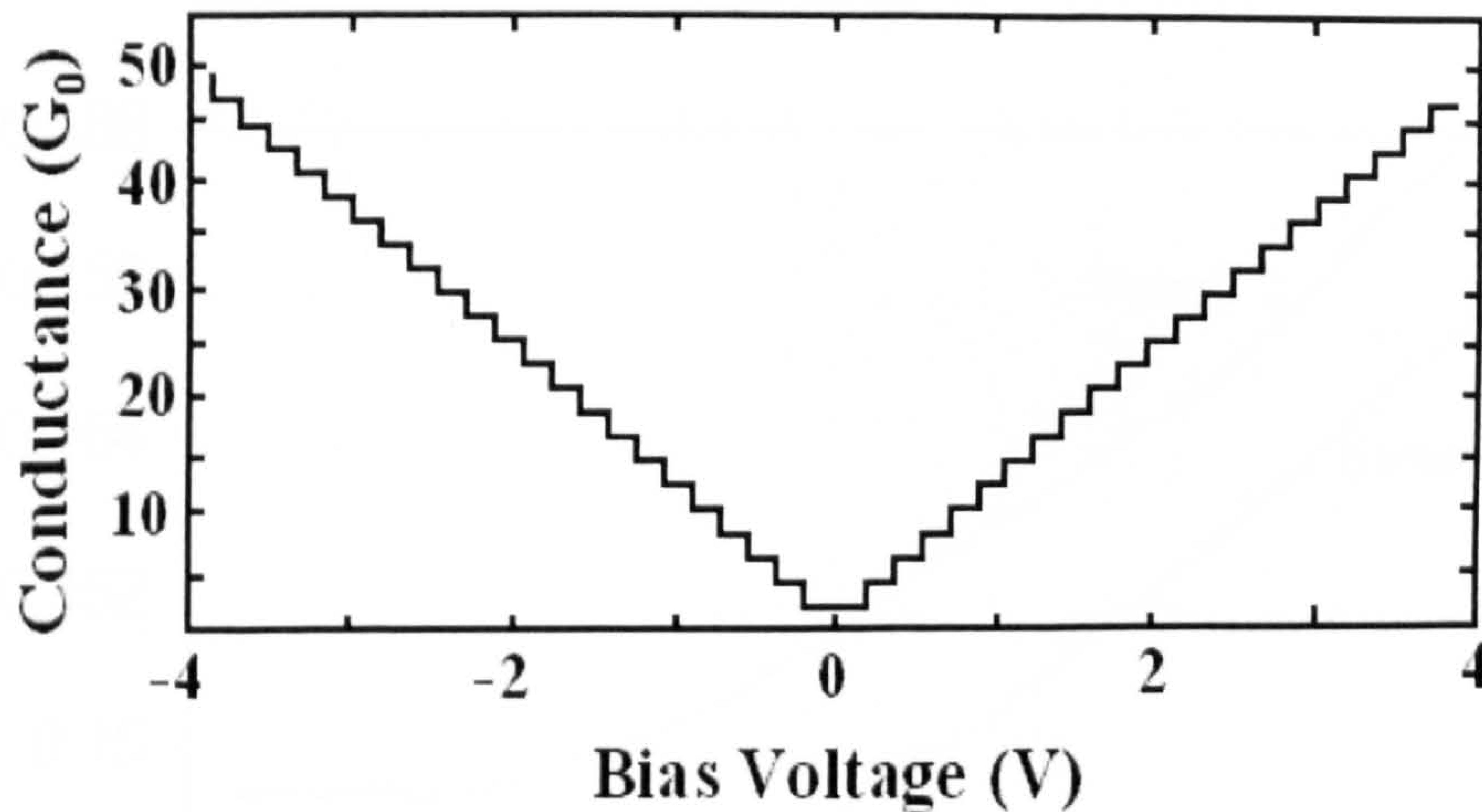


**Figure 7.15.** The predicted conductance versus bias voltage for a nanotube from the Landauer equation, assuming unit transmission for all channels. [2]

When the bias voltage is increased above ΔE, the conductance also increases in a stepwise manner as shown in Figure 7.15. Each of these steps corresponds to one of the peaks shown in the density of states diagram in Figure 7.14, which occur as the bias voltage is increased above the value necessary to make the next semiconducting sub-band conduct. The width of these steps is equal to half the value of the sub-band separation ΔE [5], while the height of the steps is set by Landauer's equation, which is dependent on the amount of scattering at the contacts and in the semiconducting sub-bands, such that:

$$Height\ of\ step\ (dG) = 2G_0T_sT_c \tag{7.3}$$

where $T_s$ is the transmission coefficient of the semiconducting sub-band. Hence the gradient of the conductance can be described by the equation:

$$\begin{aligned}\frac{dG}{dV} &= \frac{height\ of\ step}{width\ of\ step} \\ &= \frac{2G_0T_sT_c}{0.5\Delta E}\end{aligned} \tag{7.4}$$

In order to understand the effects of conditioning on the conductance, the conductance plateau at near zero bias voltages, $G_{min}$, and the gradient of the conductance were measured for each voltage cycle for all of the nanotubes tested. Detailed examination of the conductance at near zero bias voltages shows that the conductance plateaus occur for the majority of polymer coated, multi-walled carbon nanotubes investigated. Figure 7.16 shows two examples of near zero bias conductance plateaus that were seen for a typical MWNT at current limits of 14 μA (sweep 1) and 22 μA (sweep 2).

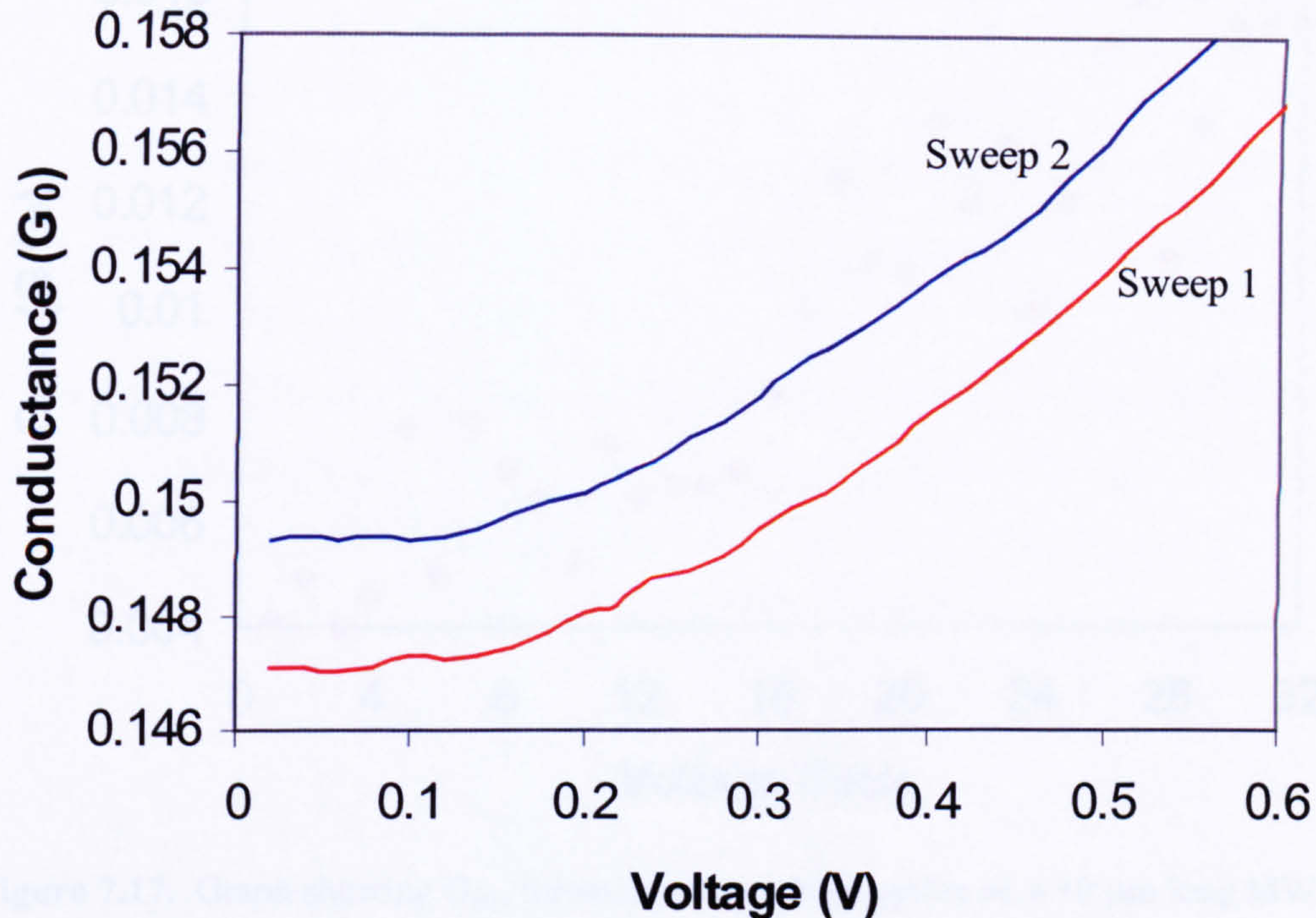


**Figure 7.16.** Conductance versus voltage variation for a multi-walled carbon nanotube for current limits of 14 μA (sweep 1) and 22 μA (sweep 2).

As can be seen from this graph the conductance plateaus extend up to 0.15 V and do not vary with the number of voltage cycles run. By referring back to equation (7.1), which gives the energy band separation between the first set of semiconducting sub-bands, it is possible to calculate that a conductance plateau of 0.15 V corresponds to a nanotube diameter of 9 nm. This value qualitatively agrees with the TEM measurements of 13 nm.

To help compare the results gained here to those of other groups, the values of $G_{min}$ and the gradient were measured and plotted for each voltage cycle for all of the nanotubes studied. Figure 7.17 shows the values of $G_{min}$ and Figure 7.18 shows the values of the gradient for the 10 μm long nanotube studied in Figures 7.8 and 7.9. For this particular nanotube, the current limit was increased from 4 μA to 18 μA in 4 μA steps every four voltage cycles.

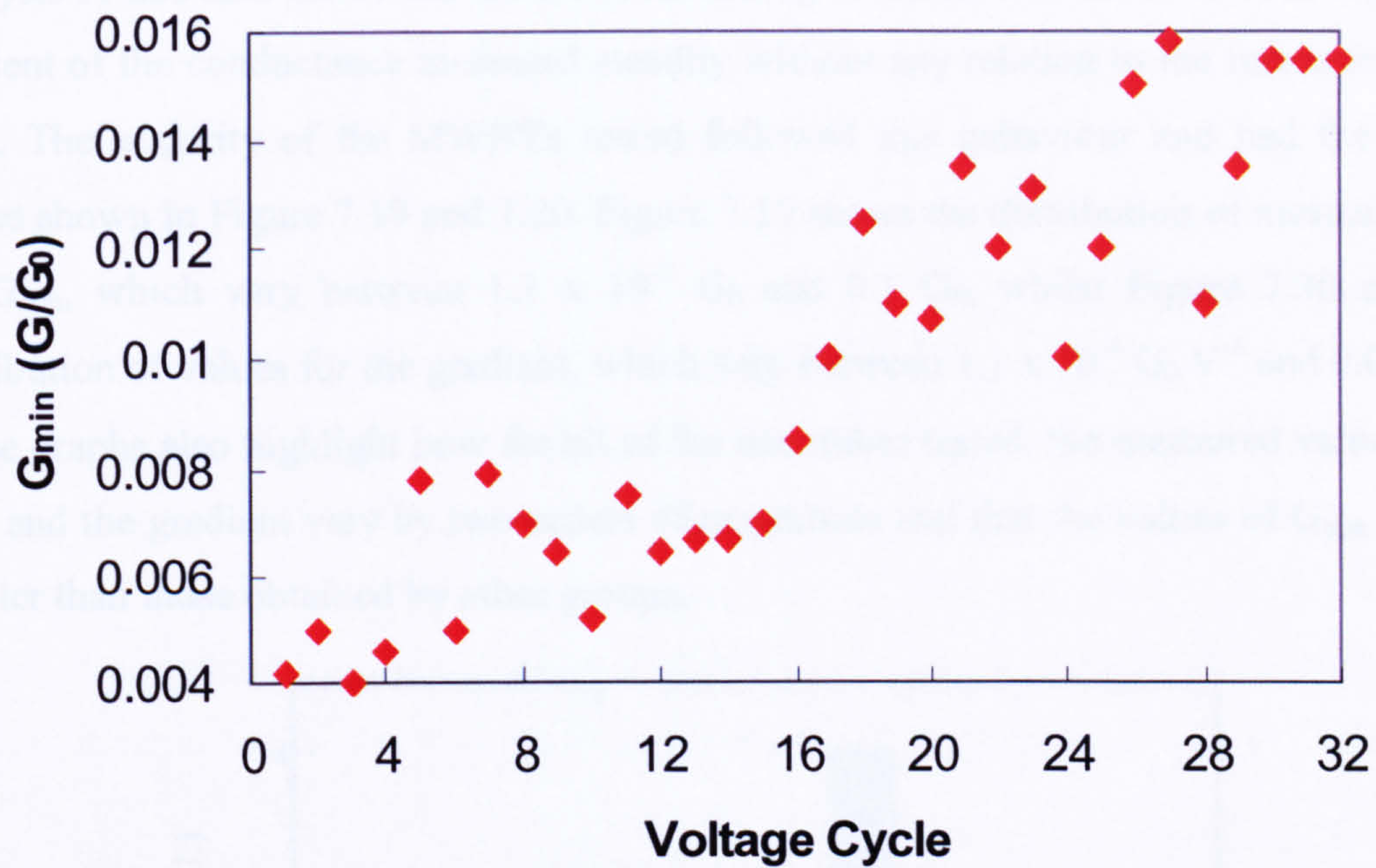


**Figure 7.17.** Graph showing $G_{min}$ for successive voltage cycles on a 10 μm long MWNT for different current limits. The current limit was increased by 2 μA every four voltage cycles, from an initial limit of 2 μA to a final limit of 18 μA.

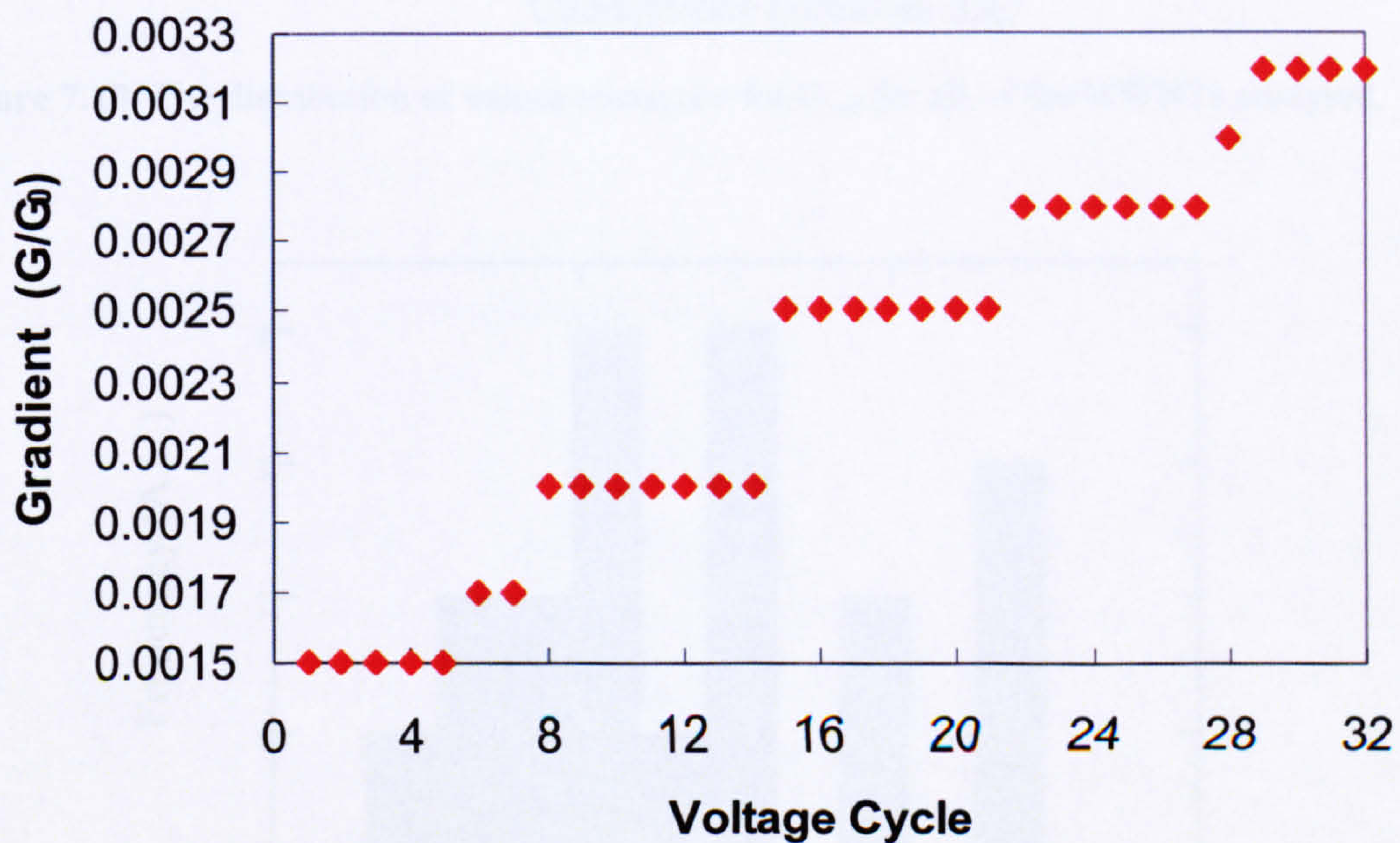


**Figure 7.18.** Graph showing the gradient of the conductance for successive voltage cycles on a 10 μm long MWNT for different current limits. The current limit was increased by 2 μA every four voltage cycles, from an initial limit of 2 μA to a final limit of 18 μA.

Analysis of this data shows that as the conditioning occurred, the values of both $G_{min}$ and the gradient of the conductance increased steadily without any relation to the increasing current limit. The majority of the MWNTs tested followed this behaviour and had the range of values shown in Figure 7.19 and 7.20. Figure 7.19 shows the distribution of measured values for $G_{min}$, which vary between 1.1 x $10^{-3}$ $G_0$ and 0.1 $G_0$, whilst Figure 7.20 shows the distribution of values for the gradient, which vary between 1.1 x $10^{-4}$ $G_0$ $V^{-1}$ and 0.05 $G_0$ $V^{-1}$. These graphs also highlight how for all of the nanotubes tested, the measured values of both $G_{min}$ and the gradient vary by two orders of magnitude and that the values of $G_{min}$ are much smaller than those obtained by other groups.

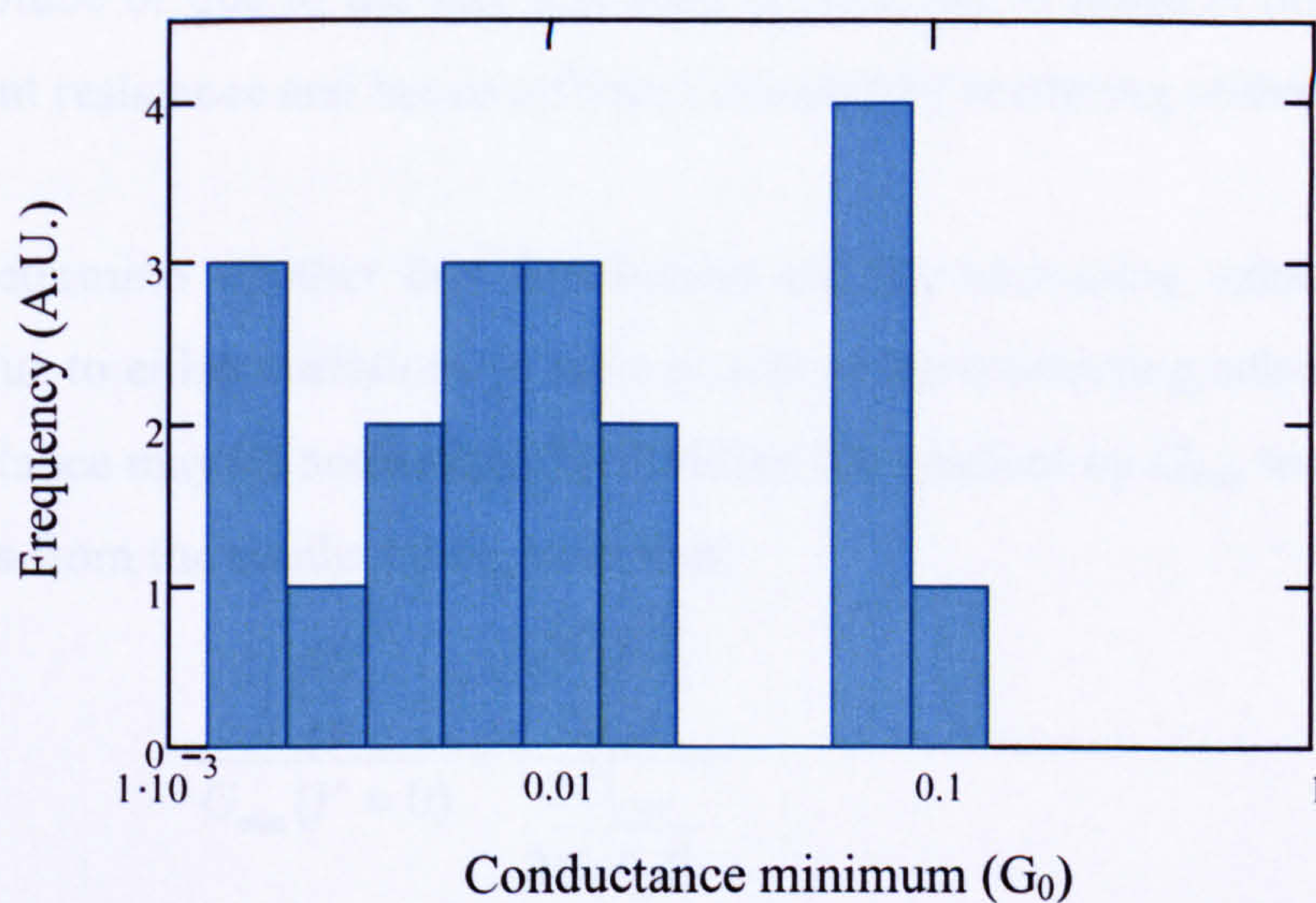


**Figure 7.19.** The distribution of values measured for $G_{min}$ for all of the MWNTs analysed.

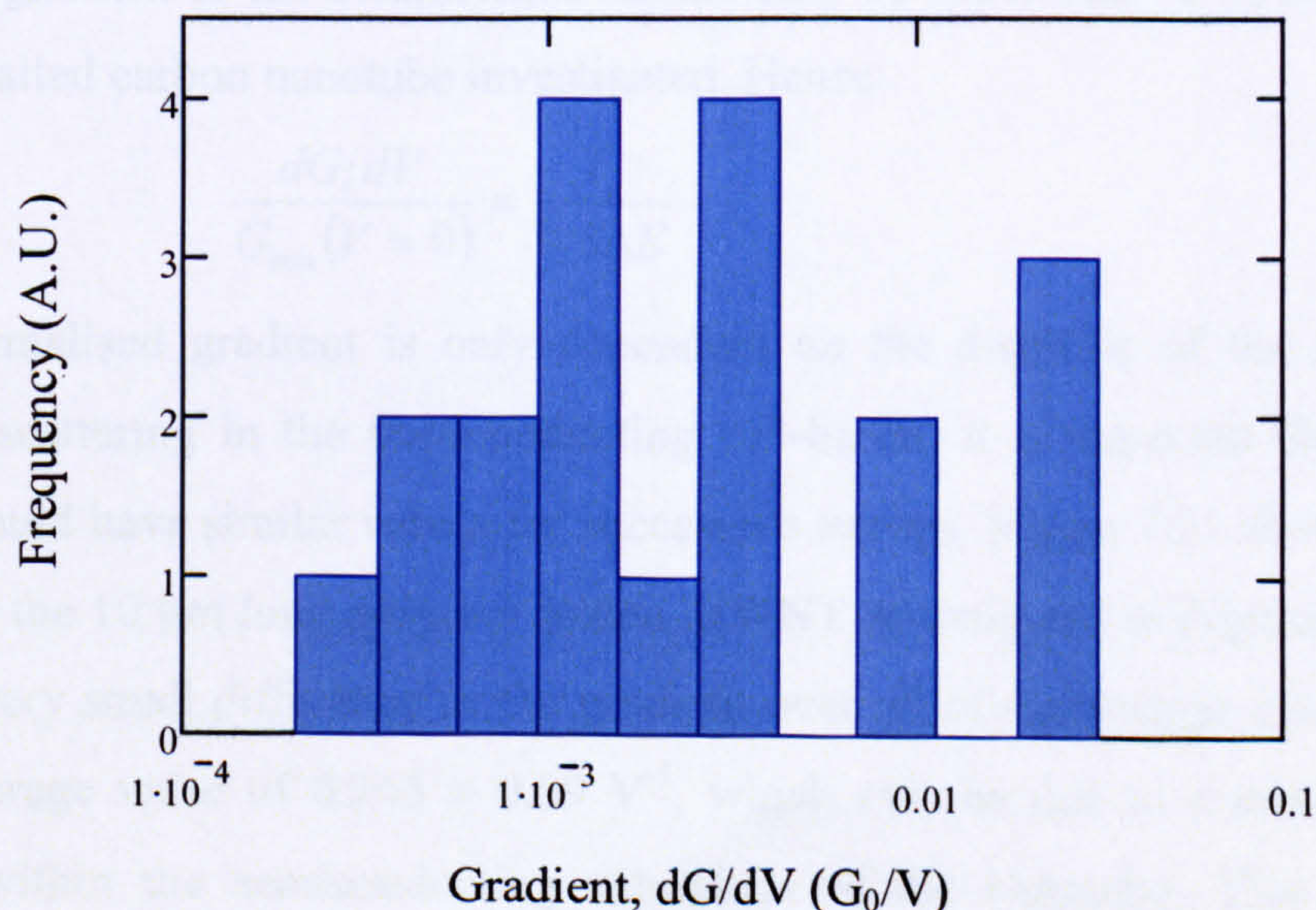


**Figure 7.20.** Graph showing the distribution of values measured for the gradient of the conductance for all of the multi-walled carbon nanotubes analysed.

By referring back to the explanation for the conductance of metallic carbon nanotubes it is possible to understand the variations in the measured values for $G_{min}$ and the gradient, which are shown in Figures 7.17 to 7.20. The increase in $G_{min}$ (Figure 7.17) which occurs over successive voltage cycles may be due to either changes in the contact or in the amount of scattering that is occurring in the metallic sub-bands, whilst the increase in the gradient (Figure 7.18) may be put down to either changes in the contact or in the amount of scattering that is occurring in the contributing semiconducting sub-bands. The wide variation in the distributions of $G_{min}$ and the gradient shown in Figure 7.19 and 7.20 may also be put down to the different amounts of scattering that occur in the conducting sub-bands for each different nanotube or due to the fact that each contact that is made is different and so may have a different resistance and hence different amounts of scattering within it.

In order to determine whether this distribution and the increasing values of $G_{min}$ and the gradient are due to either variations in the contacts or the conducting sub-bands, the gradient of the conductance may be normalised by dividing the gradient by $G_{min}$ to remove the effects of the contacts from the conductance, such that:

$$\frac{\frac{dG}{dV}}{G_{\min}(V=0)} = \frac{\frac{2G_0 T_s T_c}{6\gamma_0 a}}{\frac{2D_{CNT}}{2G_0 T_m T_c}} \tag{7.5}$$

As can be seen from this equation the effects of $G_0$ and $T_c$ cancel out. If $T_m$ is also assumed to be one, as only minimal scattering can occur in the metallic sub-bands, then the normalised gradient of the conductance should only be dependent on $T_s$ and the diameter of the multi-walled carbon nanotube investigated. Hence:

$$\frac{dG/dV}{G_{\min}(V=0)} = \frac{T_s}{0.5\Delta E} \tag{7.6}$$

As this normalised gradient is only dependent on the diameter of the nanotube and the amount of scattering in the semiconducting sub-bands, it is expected that the normalised gradient should have similar values for successive sweeps. Figure 7.21 shows the normalised gradient for the 10 μm long polymer coated MWNT investigated in Figures 7.17 and 7.18. It exhibits a very small difference in the gradient over all of the voltage cycles that were run, with an average value of 0.265 ± 0.09 $V^{-1}$, which may be due to a small variation in the scattering within the semiconducting sub-bands of the nanotube. This means that it is reasonable to conclude that by normalising the conductance this work has removed effects of the contacts on the results so that the observed characteristics are only that of the MWNT.

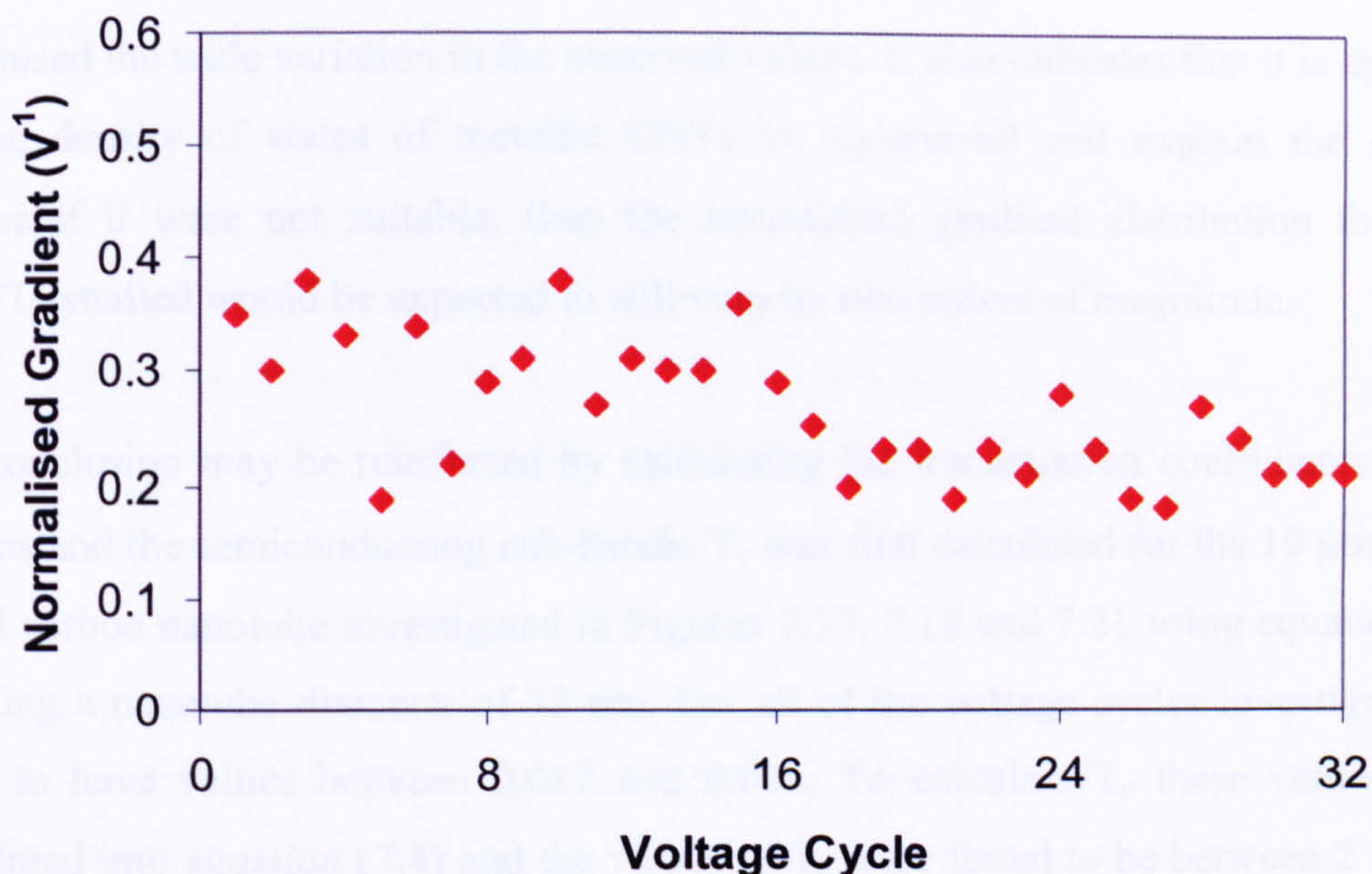


**Figure 7.21.** Graph showing the normalised gradient of a 10μm long multi-walled carbon nanotube for different current limits over successive sweeps.

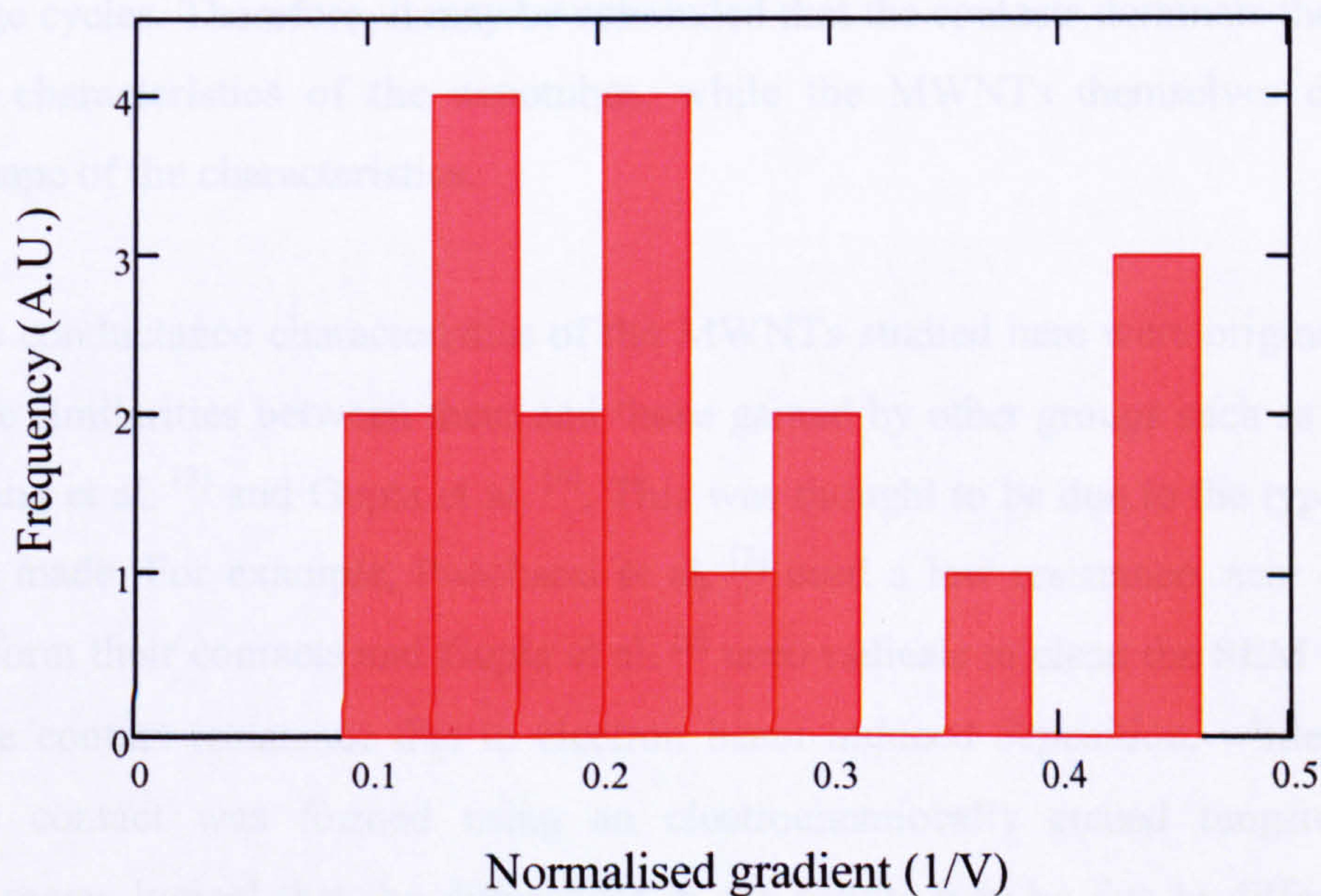


**Figure 7.22.** Graph showing the distribution of normalised gradients for all of the nanotubes tested.

Figure 7.22 shows average normalised gradient values for a number of different MWNTs that were investigated. As can be seen from this graph all of the nanotubes had values between 0.1 and 0.46 $V^{-1}$. Unlike the distributions seen for both $G_{min}$ and the gradient of the conductance, which varied over two orders of magnitude, this distribution only varied within one order of magnitude. If it is assumed that the diameters of all of the nanotubes tested were ~13 nm, then these results indicate that it is the wide range of contacts that were produced

that caused the wide variation in the observed values. It also indicates that it is appropriate to use the density of states of metallic CNTs to understand and explain the conductance because if it were not suitable, then the normalised gradient distribution for all of the MWNTs studied would be expected to still vary by two orders of magnitude.

This conclusion may be reinforced by calculating the transmission coefficients of both the contacts and the semiconducting sub-bands. $T_s$ was first calculated for the 10 μm long multi-walled carbon nanotube investigated in Figures 7.17, 7.18 and 7.21 using equation (7.6) and assuming a nanotube diameter of 13 nm. For all of the voltage cycles investigated, $T_s$ was found to have values between 0.017 and 0.036. To calculate $T_c$ these values were then substituted into equation (7.4) and the values of $T_c$ were found to be between $2 \times 10^{-3}$ and $8 \times 10^{-3}$. The smaller values of $T_c$ indicate that there is a larger amount of scattering at the contacts than in the semiconducting sub-bands of the nanotubes, while the large range of values of $T_c$ indicates that there is a large variation in the scattering at the contacts over all of the voltage cycles. Therefore, it may be concluded that the contacts dominate the scale of the electrical characteristics of the nanotubes, while the MWNTs themselves dominate the overall shape of the characteristics.

When the conductance characteristics of the MWNTs studied here were originally analysed there were similarities between them and those gained by other groups such as Poncharal et al. [2], Liang et al. [3] and Gupta et al. [6]. This was thought to be due to the type of contacts that were made. For example, Poncharal et al. [2] used a low resistance, near ohmic liquid metal to form their contacts and Gupta et al. [6] used radicals to clean the SEM chamber and reduce the contact resistance due to electron beam induced deposition, while here a high resistance contact was formed using an electrochemiocally etched tungsten probe. It therefore seems logical that the differences in the results may be due to differences in the experimental set-up and that the same normalisation procedure applied to the results of other groups should result in similar normalised gradients to those calculated here.

Indeed, calculation of normalised gradient values for the nanotubes studied by Poncharal et al. (Fig. 5 in ref. [2]), Liang et al. (Fig. 2 in ref. [3]) and Tsutsui et al. (Fig. 2 in ref. [4]) produces values of 0.25, 0.43 and 0.24 $V^{-1}$ respectively. These values are in excellent agreement with our values given the probable variation in disorder, length and diameter. Furthermore, Poncharal et al. [2] found a range of semiconducting sub-band transmission coefficients of between 0.02 and 0.03. These results are remarkably similar to those achieved

here and indicate that the MWNTs used here have comparable electronic properties to those used studied by Poncharal et al. [2], Liang et al. [3] and Tsutsui et al. [4] even though the transparencies of the contacts formed by each of the groups are obviously very different. These results also support the use of one-dimensional dependant conductivity to analyse the I-V measurements, where the transport may be either ballistic or quasi ballistic.

This work may be further extended and tested by considering the conductance characteristics of another nanotube in which a three-terminal arrangement was used as shown in Figure 7.23. The results of this investigation are shown in Figure 7.24. Initially, one probe was brought into contact with a 15.7 μm long, polymer coated MWNT as described earlier and a number of voltage cycles were run to produce characteristics similar to the set labelled sweep 1. A second probe was then brought into contact with the MWNT a distance of 3.1 μm from the first probe as is also shown in Figure 7.23 and a number of voltage cycles were run between this probe and the polymer composite to give the data set labelled sweep 2. Finally, the nanotube was broken just below the second contact and a third set of voltage cycles was run between the two probes to give the final set of data, labelled sweep 3.

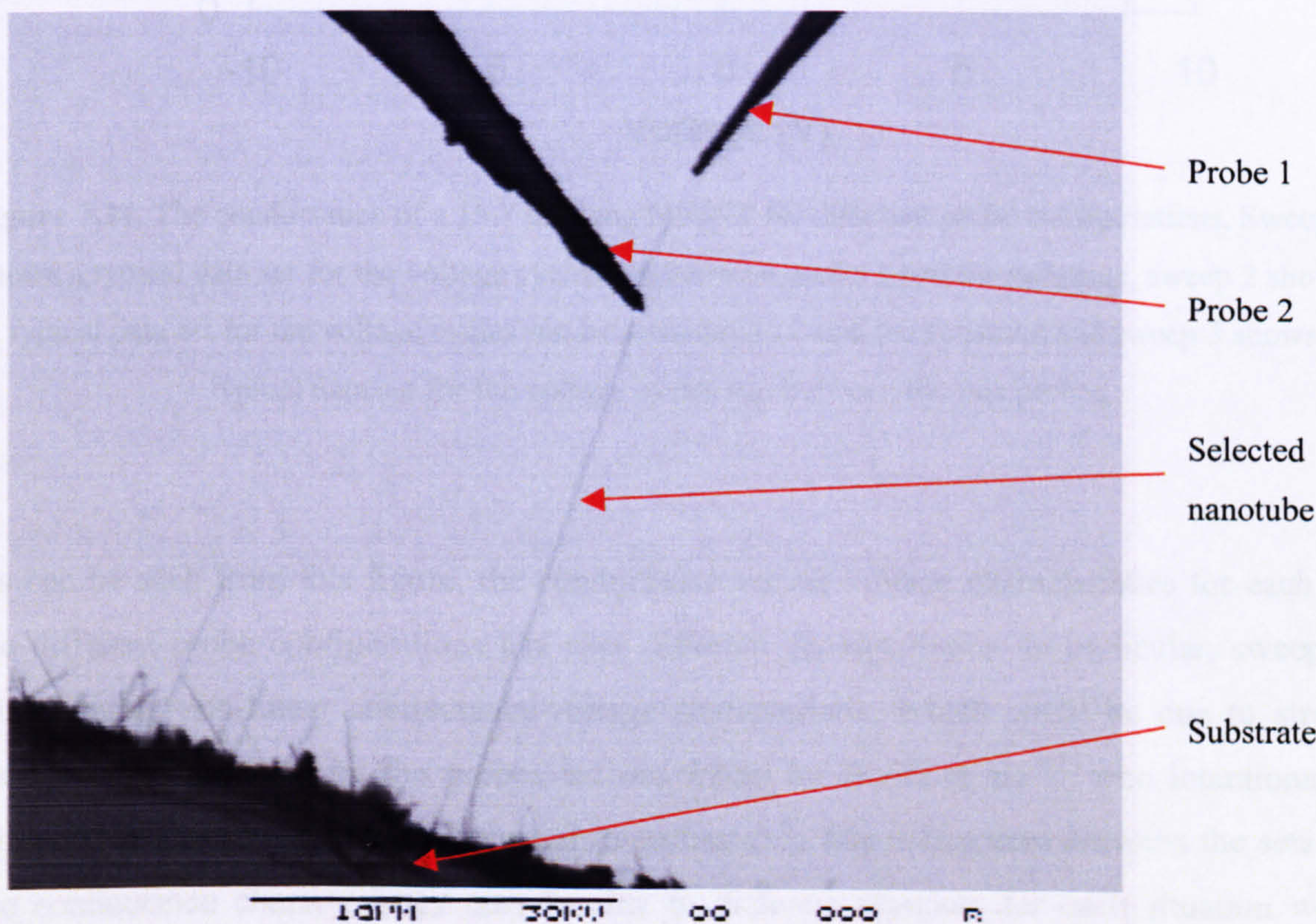


**Figure 7.23.** SEM image of a MWNT, which is attached to two sharpened metal tungsten probes. The nanotube has been enhanced in this image for clarity.

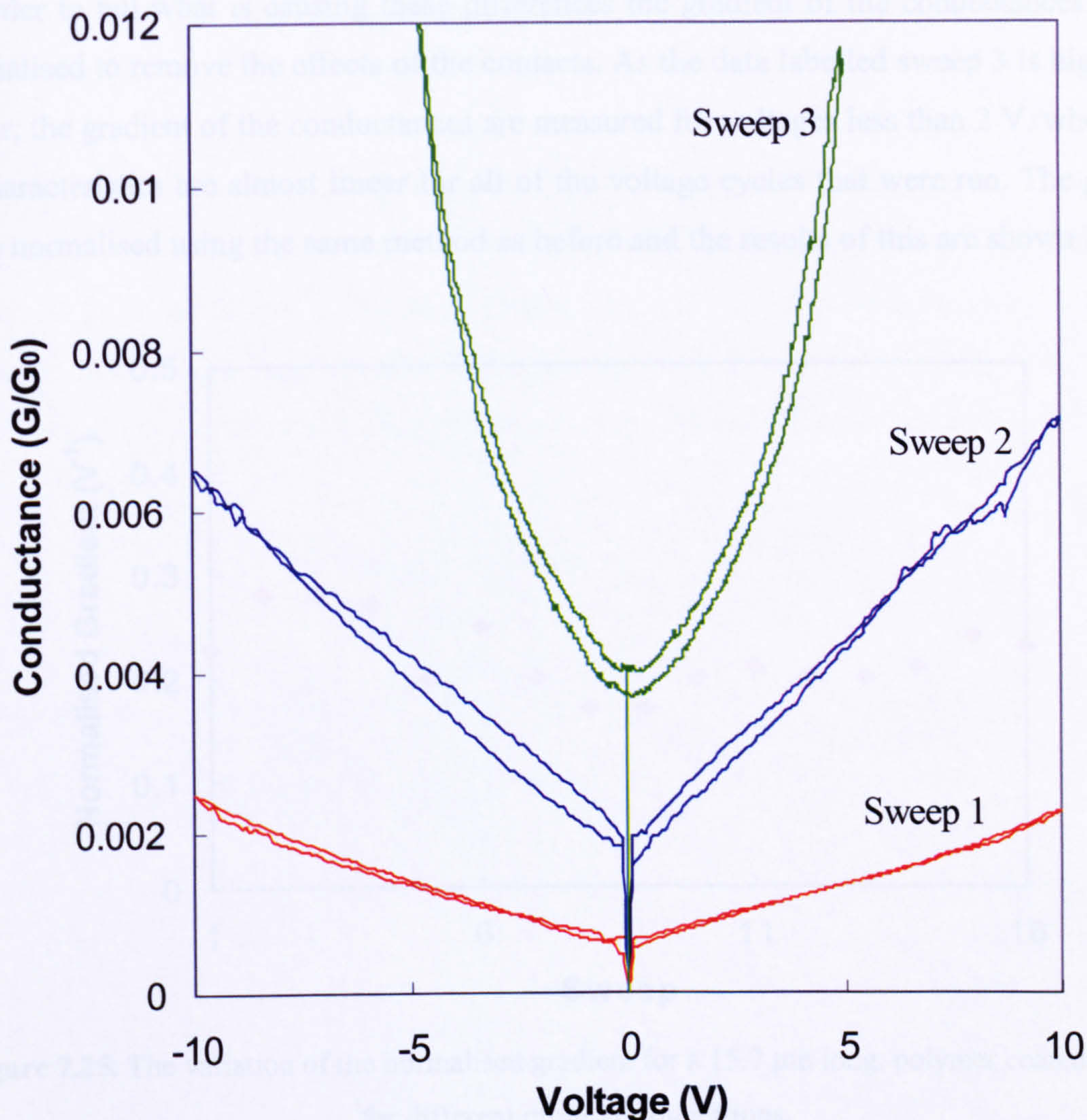


**Figure 7.24.** The conductance of a 15.7 μm long MWNT for different probe configurations. Sweep 1 shows a typical data set for the voltage cycles run between probe 1 and the substrate, sweep 2 shows a typical data set for the voltage cycles run between probe 2 and the substrate and sweep 3 shows a typical data set for the voltage cycles run between the two probes.

As can be seen from this figure, the conductance versus voltage characteristics for each of the different probe configurations has very different characteristics. In particular, sweep 3 has a highly non-linear conductance-voltage characteristic, which could be due to strain induced effects caused by the probes, as was found by Gupta et al. [6], who intentionally strained their MWNTs as was discussed in section 2.3. The differences between the sets of the conductance characteristics may be due to different contacts for each situation with different contact resistances or to varying amounts of scattering within the contacts. It may also be due to different amounts of scattering within the semiconducting sub-bands in each of the sections of the nanotube being investigated.

In order to tell what is causing these differences the gradient of the conductances must be normalised to remove the effects of the contacts. As the data labelled sweep 3 is highly non-linear, the gradient of the conductances are measured for voltages less than 2 V, where the I-V characteristics are almost linear for all of the voltage cycles that were run. The gradients were normalised using the same method as before and the results of this are shown in Figure 7.25.

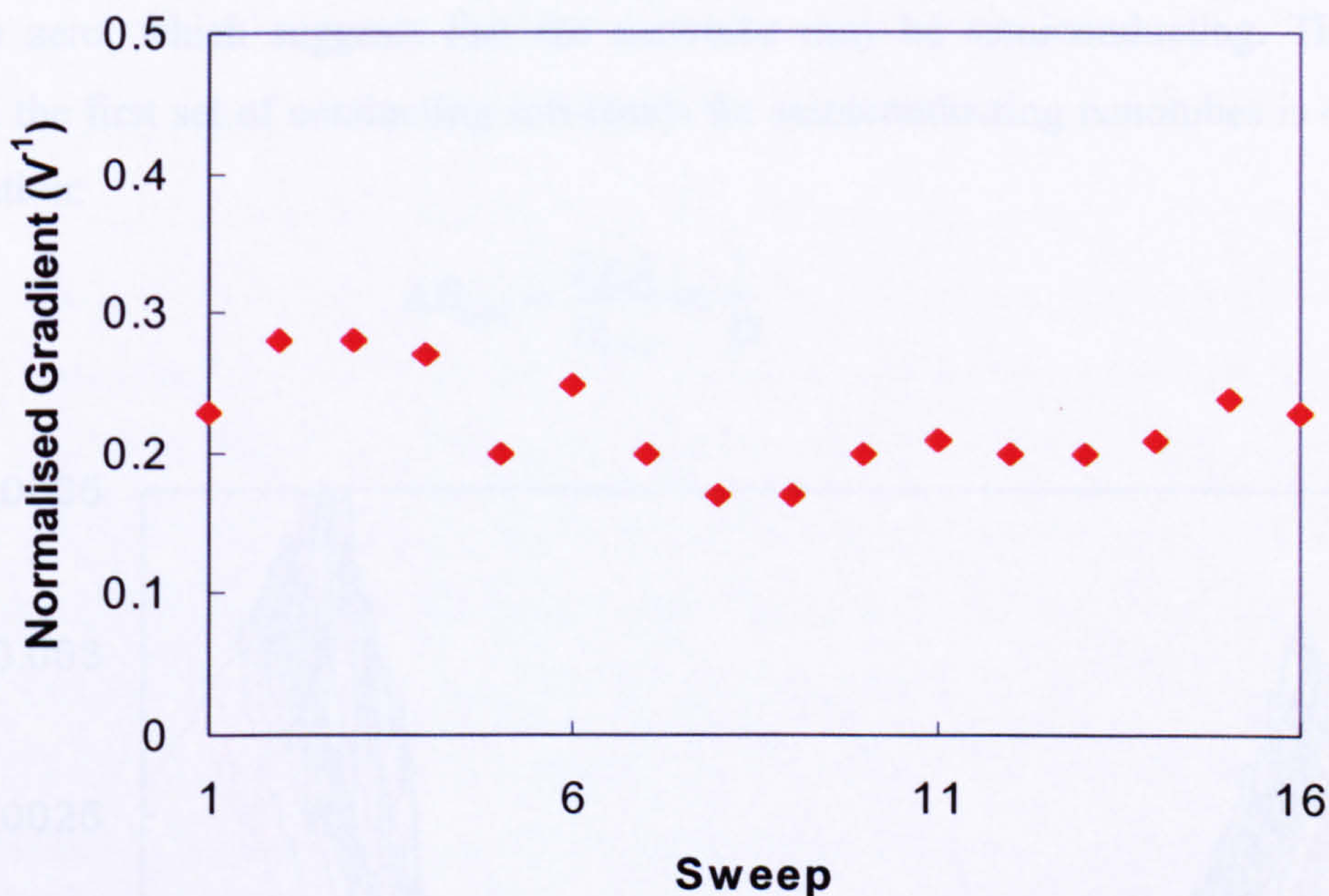


**Figure 7.25.** The variation of the normalised gradient for a 15.7 μm long, polymer coated MWNT for different probe configurations.

The data in Figure 7.25 clearly demonstrates that the normalised conductance is consistent for all voltage cycles regardless of the different probe configurations used. As explained earlier, the normalised conductance has had the contributions of the contacts removed and so the resulting data is only that of the conduction within the nanotube and has an average value of 0.24 ± 0.06 V$^{-1}$. Therefore, the differences in the un-normalised conductance measurements must be due to the differences in contact resistance.

$T_c$ and $T_s$ were also calculated for this nanotube and $T_s$ was found to have values between 0.016 and 0.028, while $T_c$ had values between 0.0003 and 0.002. Both the normalized gradient values and the calculated values of $T_c$ and $T_s$ indicate that whatever section of the nanotube is used, its conduction properties are similar and that the differences in the size of

the non-normalized measurements must be due to differences in the contacts, while their differences in the linearity may be due to strain induced effects.

Whilst this model fits the data for the majority of the carbon nanotubes analysed here, there were a number of nanotubes, which could not be investigated using this method. An example of one of these nanotubes is shown in Figure 7.26. As can be seen from this graph, $G_{min}$ is equal to zero, which suggests that the nanotube may be semiconducting. The band gap between the first set of conducting sub-bands for semiconducting nanotubes is described by the equation:

$$\Delta E_{semi} = \frac{2\gamma_0 a}{D_{CNT}} \propto \frac{1}{D} \qquad (7.7)$$

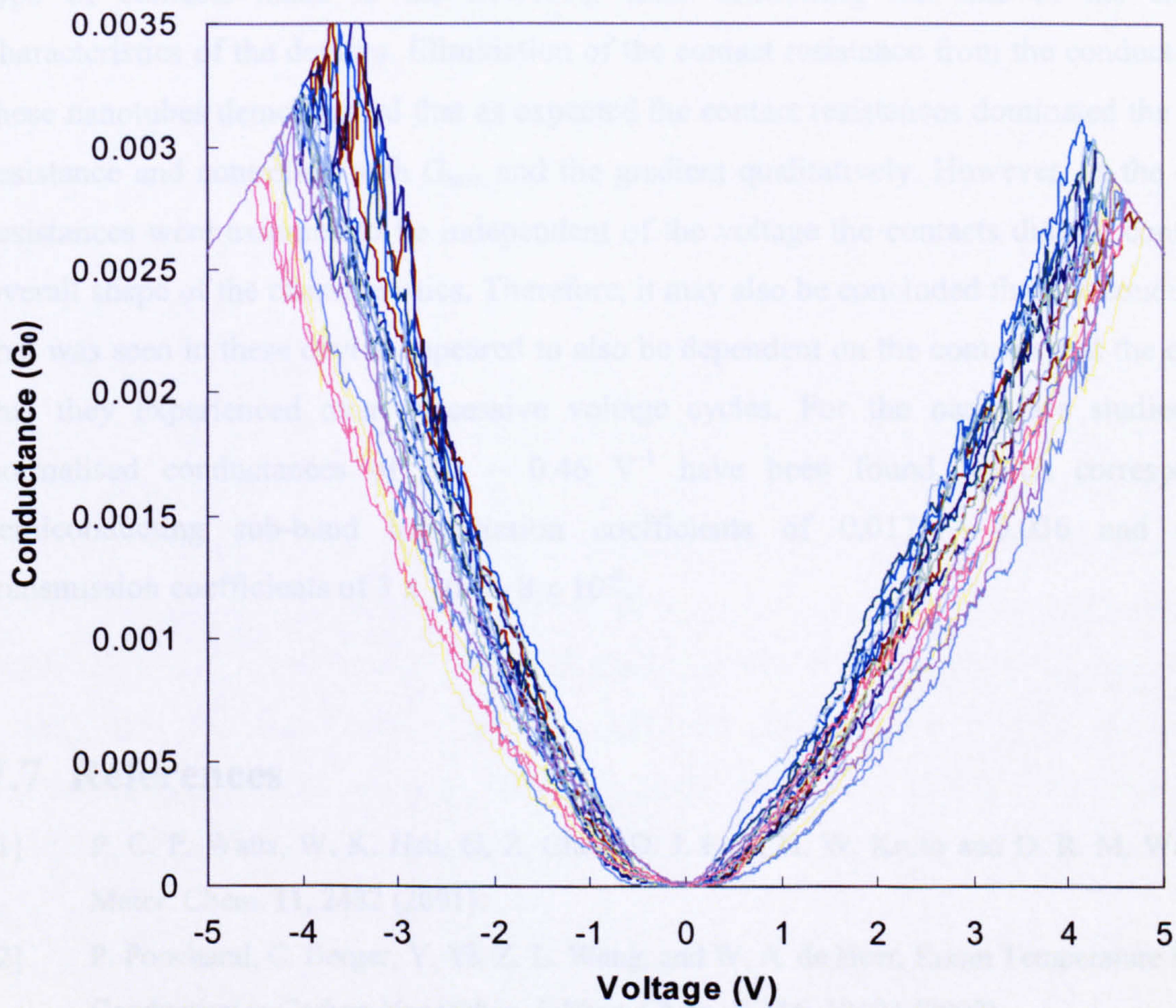


**Figure 7.26.** The conductance versus voltage characteristics of a highly resistive MWNT.

This means that for the nanotube examined in Figure 7.26, where the onset of conduction occurs at ±2 V and $\Delta E_{semi}$ = 4 V, the diameter must be 0.21 nm. This value is unphysical and

suggests that this is not a correct explanation for the conduction of this nanotube. Further examination of the conductance characteristics in Figure 7.26 also shows that the measured conductances are very low, and this along with the low value of $G_{min}$ and the high value of the onset of conduction suggests that extremely high contact resistances dominate the electrical characteristics of this nanotube.

## 7.6 Conclusions

In summary, the polymer coated multi-walled carbon nanotubes examined in this investigation showed a wide range of characteristics and varying amounts of conditioning. It was also confirmed that the large contact resistances of the devices, which were due to the type of contacts made to the MWNTs, were controlling the size of the electrical characteristics of the devices. Elimination of the contact resistance from the conductance of these nanotubes demonstrated that as expected the contact resistances dominated the overall resistance and controlled both $G_{min}$ and the gradient qualitatively. However, as the contact resistances were assumed to be independent of the voltage the contacts did not control the overall shape of the characteristics. Therefore, it may also be concluded that the conditioning that was seen in these device appeared to also be dependent on the contacts and the changes that they experienced over successive voltage cycles. For the nanotubes studied here, normalised conductances of 0.1 – 0.46 $V^{-1}$ have been found, which correspond to semiconducting sub-band transmission coefficients of 0.017 – 0.036 and contact transmission coefficients of $3 \times 10^{-4} - 8 \times 10^{-4}$.

## 7.7 References

[1] P. C. P. Watts, W. K. Hsu, G. Z. Chen, D. J. Fray, H. W. Kroto and D. R. M. Walton, J. Mater. Chem. **11**, 2482 (2001).

[2] P. Poncharal, C. Berger, Y. Yi, Z. L. Wang, and W. A. de Heer, Room Temperature Ballistic Conduction in Carbon Nanotubes, J. Phys. Chem. B **106**, 12104 (2002).

[3] Y. X. Liang, Q. H. Li and T. H. Wang, Appl. Phys. Lett. **84**, 3379 (2004).

[4] M. Tsutui, S. Mitsuya, S. Kurokawa and A. Sakai, Nanotechnol. **16**, 1863 (2005).

[5] L. C. Venema, J. W. Janssen, M. R. Buitelaar, J. W. G. Wildöer, S. G. Lemay, L. P. Kouwenhoven and C. Dekker, Phys. Rev. B **62**, 5238 (2000).

[6] R. Gupta, R. E. Stallcup II and M. in het Panhuis, Nanotechnol. **16**, 1707 (2005).

# CHAPTER EIGHT

## 8 Conclusions

Within this thesis, the use of electron beam deposited tungsten wires and multi-walled carbon nanotubes as interconnects in mictroelectronic circuits have been investigated. It has been found that EBID nanowires have the advantage over CNTs in that they can be fabricated at specific locations with nanometer accuracy whereas at present CNTs are typically dispersed using a liquid medium, which means that their location cannot be guaranteed to be 100% accurate. However, if CNTs can be grown at low temperatures, repeatedly and reliably this issue will be overcome. EBID wires also have a number of disadvantages in comparison to CNTs, which include very high resistivities and high leakage between closely spaced wires, which is undesirable in many electronic applications. As such the use of post deposition annealing and carrying out the depositions on heated substrates has been investigated in an attempt to reduce the resistivity of the deposits. It has also been found that even though these processes do improve the resistivity of the nanowires, their resistivity is still several orders of magnitude higher than it is for bulk metals. Meanwhile, CNTs have the disadvantage that although they can carry very high currents and electromigration is not an issue, their electrical characteristics are dominated by the properties of their contacts and better methods of producing ohmic contacts need to be made.

### 8.1 Electron Beam Deposition of Tungsten Interconnects

The study of the EBID of tungsten interconnects included investigating the effects of different electron beam currents, electron sources, and precursor lifetimes on the geometrical, structural and electrical properties of the deposits. From these investigations it was found that the deposition rate and the resistivity of the deposits increased with

increasing beam current and was attributed to the increasing number of electrons that were available to be involved in the deposition process. However, as the electron beam current was increased it was also found that the resolution of the process decreased. Therefore, when selecting the deposition parameters to be used in electronic applications, it is necessary to make a trade off between resistivity and resolution.

When the effects of changing the electron source were investigated, it was found that the use of brighter sources resulted in deposits with a lower resistivity and a higher growth rate. This result suggests that the choice of the most optimum source can be of benefit to EBID. This result also highlights one of the main issues with EBID, which is that depositions produced in different systems or in the same system at different times can have quite different characteristics. This means that in order for EBID to be accepted as a mainstream fabrication technique either better control of the electron sources within the deposition systems or the production of sources with more uniform properties needs to be gained. Both of these solutions are difficult to achieve.

During this thesis the effects of the precursor lifetime on the properties of the deposits was also investigated and it was found that as the precursor aged, the growth rate of the deposits decreased. However, for deposits produced using both a precursor with less than twenty hours of use and with more than 120 hours of use, the resistivity of a given height deposit was found to be constant. This result suggests that while the gas flux may vary with time, the deposited material for a given set of beam conditions does not. Therefore, in order to be able to fabricate reproducible deposits, when describing the conditions used for the depositions it is necessary to also factor in some measure of either the precursor age or the gas flux.

As all of the deposits that were produced in this thesis had high resistivities, the effects of post deposition annealing and the use of heated substrates during the deposition process were investigated to determine whether they could produce deposits with lower resistivities. For deposition at substrate temperatures between 25°C and 75°C, it was found that the deposition rate decreased with increasing temperature, while the resistivity increased. However, for a given height deposit the resistivity was actually found to be an order of magnitude better than for deposits produced at room temperature. AES was used to show that this behaviour was due to a significant decrease in the amount of carbon that was incorporated into the deposits. This result suggests that while using heated substrates can

help to improve the resistivity of the deposited material, much longer deposition times are required in order to produce reasonable height deposits. This process also has the disadvantages in that it requires a very much more complex and expensive set-up and that sample drift as the substrate is heated can be an issue with producing well defined deposits.

The use of post deposition annealing at temperatures up to 367°C was also investigated and it was found that it could improve the resistivity of the deposits by two orders of magnitude. This process does not affect the deposition process or resolution and has the advantage that by using higher annealing temperatures a more significant improvement in the resistivity of the deposits can be gained than when using heated substrates for the deposition process. However this process also has the disadvantage that in certain applications, such as when contacting to nanostructures (i.e. carbon nanotubes or nanowires), the annealing process can cause degradation or alter the properties of the nanostructures, which is undesirable when attempting to characterise the properties of these structures.

In order to determine the current carrying capability of these deposits, the deposits were also exposed to currents up to 1 mA and it was found that as the current passes through the wires was increased, the resistivity of the deposits decreased. At higher currents, in excess of 1 mA, it was found that the resistivity of the deposits continued to decrease, while their structure transformed from being completely amorphous to consisting of tungsten clusters embedded in a graphitised carbon matrix. These changes were attributed to the high resistance of the deposits causing significant ohmic heating within the deposited material at temperatures in excess of 1000°C to occur. This caused the microstructure of the deposits to change through current induced self-heating or annealing and an improvement in the resistivity of the nanowires of two orders of magnitude was achieved. The results of this work suggest that this method may be suitable for use in improving the resistivity of the deposited material for interconnect applications without the need for furnace annealing, which may cause damage to other structures on the substrate. Furthermore, the breakdown properties of these nanowires and in several cases the substrate in the area surrounding the deposit implied that significant ohmic heating was again occurring.

Throughout this experimental work every effort was made to ensure that the results were as accurate as possible as well as being reproducible. As such before carrying out any of the depositions, the same optimisation procedure was always carried out. However, even after

carrying out this procedure it was found that there was still variation in the final structures, which were attributed to both user error and variations in the system. These results suggest that further work needs to be undertaken to improve the control of the system variables such that more reproducible deposits can be fabricated across a range of similar systems.

In conclusion, these results have shown that the EBID process has a number of distinct advantages, which include the ability to produce nanometer sized interconnects at specific locations, the ability to vary the deposition parameters to achieve deposits that are suitable for individual applications and the ability to create specific three-dimensional objects at the nanometer scale. Meanwhile, the high resistivity of these deposits, the long deposition times in comparison to other similar interconnect fabrication processes such as UV lithography, the variation in interconnects produced in different systems but with the same parameters and the instability in the structural and electrical properties of the deposits suggests that further work needs to be carried out before EBID can be used as a mainstream nanofabrication technique. However, EBID is already capable of being used in a number of industrial applications where bespoke metal wiring on the micron scale is required. One of the most relevant is the use of EBID in a FIB type system for the repair and debugging of microelectronic circuits. In this application the ion beam is used to remove the incorrect or damaged tracks and then new tracks are deposited using EBID.

## 8.2 Suspended Multi-Walled Carbon Nanotubes

Another method of being able to create nanometer sized electrical connections to nanostructures that has been studied within this thesis is the use of MWNTs. These nanowires have the distinct advantage over EBID nanowires in that they are able to carry much higher current densities without degrading, and, that the leakage between closely spaced MWNTs is negligible. However, they have the disadvantage that they cannot currently be produced at specific locations, with specific dimensions. Furthermore, the research into the properties of these nanotubes to date has shown that their electrical characteristics are highly dependent on their contact geometry and the methods that are used to produce them. As such, within this thesis an alternative contact methodology was used to directly connect to arc discharge, suspended multi-walled carbon nanotubes using a two probe manipulation system installed within a SEM. This method has the unique advantage

that it can also be used to connect to and manipulate the nanotubes into the required location on a substrate. It also has the advantage that it allows for the electrical properties of the nanotubes themselves to be studied without the inclusion of any substrate-nanotube interactions.

The results of this study show that the contacts that were made to the nanotubes played a very important role and dominated the electrical characteristics. In particular, it was found that for each nanotubes studied, when multiple voltage cycles were run the resistance of the structures changed. In an attempt to understand what caused these changes the conductance mechanisms of the nanotubes was analysed and the role of the contacts factored out. The results of this analysis showed that once the contributions of the contacts had been factored out, the conductance of the nanotubes remained approximately constant over all of the voltage cycles and had normalised conductance values of 0.1-0.46 $V^{-1}$. Further analysis of the electrical characteristics of these nanotubes was also carried out and it was found that these normalised conductances corresponded to semiconducting sub-band transmission coefficients of 0.017 – 0.036 and contact transmission coefficients of $3 \times 10^{-4} - 8 \times 10^{-4}$. These values have been compared to the experimental results of others who investigated the properties of suspended MWNTs using alternative contact methodologies that were found to be similar.

## 8.3 Future Work

This section shall examine a number of different ways in which the work that has been undertaken within this thesis may be extended. Initially, it will look at how the characterisation of EBID nanowires can be extended to give a greater understanding of the effects of the different deposition parameters on the deposited structure and electrical properties of the material. It will then discuss some ways in which this work can be built upon by using the experimental results gained in this study to produce deposits suitable for several different applications. Finally, it will consider some further work that may be carried out to improve our understanding of the electrical properties of multi-walled carbon nanotubes and suggest some methods through which further nanotube investigations may be carried out.

Within this thesis, the characterisation of EBID tungsten wires only examined a number of the system variables. Therefore, it is possible that the resistivity, growth rate and structure of the deposits may be enhanced further by also analysing the effects of varying some of the other deposition variables through the use of AES, TEM, AFM and electrical measurements. These variables include the use of a greater range of electron beam currents, as well as investigating the effects of different electron beam voltages, pitches, dwell times and scanning conditions. As part of this thesis it was also shown that changing the electron source had an effect on the growth rate and resistivity of the deposits. To understand the effects of the electron sources on the results more fully, it may be of use to carry out further examination of the electron sources and their energy and compare the results of these investigations along with the resulting deposits with those of other electron sources in order to be able to factor in the differences in the electron sources to the deposition rate. Within this work it was also found that the gas flux of the precursor varies throughout its lifetime. In order to factor this variation in further measurements of the degradation in the growth rate could be made and factored to estimate the deposit heights. Alternatively, some method of measuring the gas flux through the capillary tube could also be developed and may be used to gain a greater control of the gas flux throughout the precursor lifetime.

The resistivity of the EBID tungsten interconnects fabricated using standard conditions had high resistivities. To improve the resistivity, both post deposition annealing and the use of heated substrates was investigated. To extend these investigations, annealing at yet higher temperatures could be examined to determine whether a greater improvement could be achieved. This work could also be extended by carrying out TEM and AES of these deposits to correlate the changes in the resistivity with structural and compositional changes. Meanwhile, the deposition on heated substrate work could be extended by carrying out a more detailed study into the properties of deposits produced at a greater range of temperatures. TEM may also be carried out to determine whether the changes in the resistivity are due to structural changes as well as compositional changes and should lead to an optimal temperature being determined.

When carrying out the investigations into the current carrying abilities of the nanowires at high current biases, it was found that for currents in excess of 1 mA the structure of the deposits had transformed permanently. During these investigations, the effects of the resistance changes at lower currents on the structure and composition of the deposits was not

investigated. Therefore, it may be of use to also carry out further investigations into the microstructure and composition of the deposits for a greater range of current exposures in order to build up a more detailed picture of the changes that are occurring and the reasons for this. During this work it was also found that in a number of cases the substrate in the area surrounding the deposits was damaged. This may be attributed to the substrate acting as a heat sink for the nanowires. To investigate this behaviour more fully and to gain a greater understanding of the current carrying capability of the nanowires it may also be desirable to produce free-standing or suspended nanowires, which allow for just the properties of the wires to be investigated.

Within the experimental work carried out in this thesis, the conduction mechanisms of these wires was not investigated. It may be appropriate to carry out a detailed study into the conduction of these nanowires in order to gain a greater understanding of the properties and the suitability of these wires for use in electronic applications. Furthermore, this work has only investigated the use of one precursor. EBID has been shown to also be able to be carried out for other materials, some of which may have more suitable properties for use in interconnect applications. One precursor that is similar and also holds great promise is $WF_6$. This precursor is particularly attractive because it does not contain any carbon and so should allow for deposits with a higher metallic content to be fabricated.

To date, there has also been much controversy into the contributions of the different types of electrons to the deposition process of EBID structures. It may therefore be applicable to carry out simulations and experimental work in order to build up a more complete picture of the deposition process. One possible experimental method that may be suitable is the use of different substrate materials to analyse the contributions of different BSEs to the deposition process and the use of a biased grid held just above the substrate surface that can be used to depress and enhance the contributions of the SEs to analyse the SE contributions to the deposition process.

Throughout this thesis EBID tungsten nanowires were electrically characterised in an attempt to gain a greater understanding about the factors that influence their resistivity and to determine the most suitable parameters for use when fabricating tungsten interconnects to nanostructures such as carbon nanotubes. This work may therefore be extended by selecting the most suitable deposition parameters for use in various electronic applications. One

possible application is borne out by the high bias electrical characterisation investigation. Within this section it was shown that when EBID tungsten nanowires are exposed to currents approaching 1 mA, they become hot and may even reach temperatures of 1000°C. This property may be of use for heater applications, when it is not suitable to use conventional resistive heaters. One example of this is to image the phase transformations of thin film metals as they are steadily heated on an electron transparent membrane using STEM. Another example includes the use of this material to contact to carbon nanotubes, which will be discussed in more detail later.

The work into the use of MWNTs as an interconnect material highlighted how important it is to use a suitable contact methodology so that the electrical properties of the nanotubes are not dominated by the contacts. Therefore, this work may be extended by creating multiple contacts at various points along the length of the nanotubes using the same methodology, such that the effects of the contacts and conduction mechanisms of the nanotubes themselves can be characterised more fully. Investigating the use of alternative contact geometries, which do not dominate the electrical characteristics of the nanotubes, can also extend this work. This may include the use of different contact materials, which create ohmic contacts and investigating the properties of the nanotubes while both on and off the substrate.

Finally, both sections of this thesis could be interlinked by investigating the use of EBID to produce more suitable contacts to the nanotubes. This may include dispersing MWNTs over prefabricated gold contacts and carrying out some electrical characterisation before using EBID to create a better contact between the nanotubes and the gold contact pads and carrying out further electrical characterisation. Another method which may also allow for the contacts to the nanotubes to be characterised further is to disperse the MWNTs onto a SiN membrane and then contacting them using EBID tungsten nanowires and a two probe manipulation system. This set-up would allow for the nanotubes to be both electrically characterised using the same methodology before being structurally characterised using TEM. Both of these experiments could then be extended further by carrying out post deposition annealing of the structures.